

ADA032881

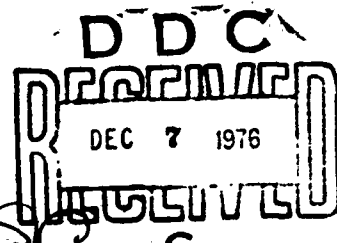
AFAPL-TR-76-65  
VOLUME II

12/8

**THE GENERATION AND RADIATION OF SUPERSONIC JET  
NOISE  
VOLUME II STUDIES OF JET NOISE, TURBULENCE  
STRUCTURE AND LASER VELOCIMETRY**

**LOCKHEED-GEORGIA COMPANY  
MARIETTA, GEORGIA 30063**

**SEPTEMBER 1976**



**TECHNICAL REPORT AFAPL-TR-76-65  
FINAL REPORT FOR PERIOD 6 NOVEMBER 1972 - 6 NOVEMBER 1975**

Approved for public release; distribution unlimited

**DEPARTMENT OF TRANSPORTATION  
OFFICE OF NOISE ABATEMENT  
WASHINGTON, D.C.**

**AIR FORCE AERO-PROPULSION LABORATORY  
AIR FORCE WRIGHT AERONAUTICAL LABORATORIES  
AIR FORCE SYSTEMS COMMAND  
WRIGHT-PATTERSON AIR FORCE BASE, OHIO 45433**

NOTICE

When Government drawings, specifications, or other data are used for any purpose other than in connection with a definitely related Government procurement operation, the United States Government thereby incurs no responsibility nor any obligation whatsoever; and the fact that the Government may have formulated, furnished, or in any way supplied the said drawings, specifications, or other data, is not to be regarded by implication or otherwise as in any manner licensing the holder or any other person or corporation, or conveying any rights or permission to manufacture, use, or sell any patented invention that may in any way be related thereto.

This final report was prepared by the Lockheed-Georgia Company, Marietta, Georgia, under Contract F33615-73-C-2032. The effort was sponsored by the Air Force Aero-Propulsion Laboratory, Air Force Systems Command, Wright-Patterson AFB, Ohio and the Department of Transportation under Project 3066, Task 14, and Work Unit 08 with Mr. Paul A. Shahady (AFAPL/TBC) as Project Engineer. Dr. Gordon Banerian was the Project Manager for the Department of Transportation. Dr. Harry E. Plumblee of Lockheed-Georgia was technically responsible for the work.

This report has been reviewed by the Information Office, ASD/OIP, and is releasable to the National Technical Information Service (NTIS). At NTIS, it will be available to the general public, including foreign nations.

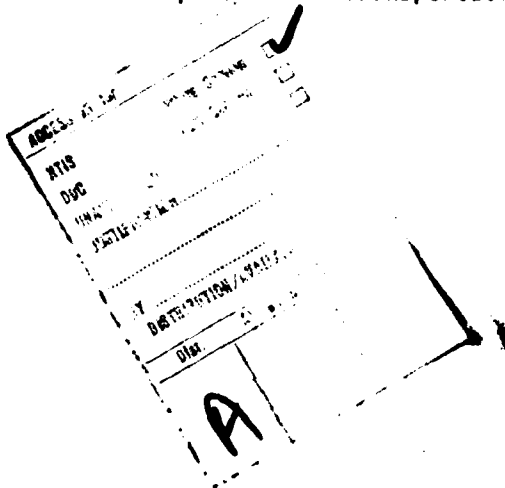
This technical report has been reviewed and is approved for publication.

*Paul A. Shahady*  
PAUL A. SHAHADY  
Project Engineer  
USAF

FOR THE COMMANDER

*Robert E. Henderson*  
ROBERT E. HENDERSON  
Manager, Combustion Technical Area

*G. Banerian*  
DR. GORDON BANERIAN  
Project Manager  
Department of Transportation



Copies of this report should not be returned unless return is required by security considerations, contractual obligations, or notice on a specific document.

## UNCLASSIFIED

SECURITY CLASSIFICATION OF THIS PAGE (When Data Entered)

REPORT DOCUMENTATION PAGE		READ INSTRUCTIONS BEFORE COMPLETING FORM
1. REPORT NUMBER AFAPL TR-76-65-Vol 2	2. GOVT ACCESSION NO.	3. RECIPIENT'S CATALOG NUMBER
4. TITLE (and Subtitle) THE GENERATION AND RADIATION OF SUPERSONIC JET NOISE. Volume II Studies of Jet Noise, Turbulence Structure and Laser Velocimetry.		5. TYPE OF REPORT & PERIOD COVERED FINAL TECHNICAL REPORT 6 NOV 72 - 6 NOV 75
6. AUTHOR(S) Harry E. Plumlee, Jr., Robert H. Burrin, Jack C. Lau, Christopher L. Morfey, Philip J. Morris, David M. Smith, H.K. "Bob" Tanna, Brian J. Tester, M. Clay Whiffen		7. REPORTING ORGANIZATION NAME & ADDRESS Lockheed-Georgia Company Marietta, Georgia 30063
8. PERFORMING ORGANIZATION NAME AND ADDRESS Air Force Aero Propulsion Laboratory/TBC Wright-Patterson AFB, Ohio 45433		9. PROGRAM ELEMENT, PROJECT, TASK AREA & WORK UNIT NUMBERS PE 62203F, Project 3866, Task 14 Work Unit 08
10. CONTROLLING OFFICE NAME AND ADDRESS		11. REPORT DATE 11 23 June 76
12. MONITORING AGENCY NAME & ADDRESS (if different from Controlling Office)		13. NUMBER OF PAGES 463 (12) 472 pa
14. DISTRIBUTION STATEMENT (of this Report)  Approved for Public Release; Distribution Unlimited.		15. SECURITY CLASSIFICATION (of this report) Unclassified
16. DISTRIBUTION STATEMENT (of the abstract entered in Block 20, if different from Report)		17. DECLASSIFICATION/DOWNGRADING SCHEDULE
18. SUPPLEMENTARY NOTES		
19. KEY WORDS (Continue on reverse side if necessary and identify by block number) Acoustics, Turbulence, Jet Noise, Laser Velocimetry, Supersonic Jets, Shock Noise.		
20. ABSTRACT (Continue on reverse side if necessary and identify by block number)  This report is published in four volumes. Volume I summarizes the work accomplished. Volume II (this volume) contains a detailed discussion of work accomplished since the publication of the interim report, and all of the major conclusions reached during the program. Volume III is a data report which presents a detailed compilation of the turbulent mixing noise 1/3-octave spectra. Volume IV, another data report, contains the narrow-band spectra for broadband shock-associated noise. (Continued)		

210 065  
bpg

*This volume discusses*

**UNCLASSIFIED**

SECURITY CLASSIFICATION OF THIS PAGE(When Data Entered)

Six topics are comprehensively presented in this volume:

- (1) Turbulent mixing noise tests and observations relative to effects of temperature and Mach number on intensity, directivity, and spectra;
- (2) Numerical solutions of the Lilley theory for sound radiated from point sources simulating small-scale turbulence noise sources, and comparisons of these solutions with experimental data relating to temperature and velocity effects on directivity and spectra;
- (3) The theory describing the development of the large-scale coherent motion of the jet structure and the far-field noise radiated from this turbulence;
- (4) The improvements made to the LV system since the interim reporting period, and an analysis of those improvements which lead to unique system characteristics.
- (5) A detailed discussion and interpretation of the jet turbulence and mean velocity data,
- (6) A comprehensive description of the shock-associated noise tests, a preliminary description of the broadband shock-associated noise model, and a discussion of shock-associated noise in the overall jet noise picture.

**UNCLASSIFIED**

SECURITY CLASSIFICATION OF THIS PAGE(When Data Entered)

## PREFACE

This report was prepared by the Lockheed-Georgia Company, Marietta, Georgia, for the Air Force Aero Propulsion Laboratory, Wright-Patterson Air Force Base under Contract F33615-73-C-2032. The report covers work done in the period 6 November 1972 through 6 November 1975. The work described herein is part of the Air Force Aero Propulsion Laboratory's joint program with the Department of Transportation to define and control the noise emission of aircraft propulsion systems.

Mr. Paul Shahady was the Air Force Aero Propulsion Laboratory's Project Engineer. The program is being conducted under Project 3066, Task 14. Dr. Gordon Banerian was the Project Manager for the Department of Transportation. Lockheed's Program Manager was Harry E. Plumlee, Jr.

Major contributors to the work performed under this contract and presented in this report are: Robert H. Burrin, Peter D. Dean, Philip E. Doak, Michael J. Fisher, Sham S. Kapur, Jark C. Lau, Geoffrey M. Lilley, William T. Mayo, Donald M. Meadows, Christopher L. Morfey, Philip J. Morris, David M. Smith, H. K. "Bob" Tanna, Brian J. Tester, and M. Clay Whiffen.

The assistance of the following individuals is gratefully acknowledged: C. Benton Reid, who operated the test facilities and data acquisition systems; Edward C. Mills, who did the electronic design for the laser velocimeter circuitry discussed in this report; J. P. McKenna, who kept up with the budget and other administrative details; and last, but certainly not least, most gracious appreciation is extended to Barbara C. Reagan for her superb typing of all the manuscripts.

Gratitude is expressed to the University of Southampton for permitting Professor Philip E. Doak, Professor Geoffrey M. Lilley, Dr. Michael J. Fisher, and Dr. Christopher L. Morfey, to participate in the performance of the research reported herein.

This report was submitted on 6 December 1975.

Publication of this report does not constitute Air Force approval of the report's findings or conclusions. It is published only for the exchange and stimulation of ideas.

## TABLE OF CONTENTS

	<u>Page</u>
<b>1. INTRODUCTION</b>	1
1.1 The National Interest in Aircraft Noise Reduction	1
1.2 Lockheed's Contract Efforts	1
1.3 Outline of This Report	2
1.4 A Special Acknowledgement	3
<b>2. TURBULENT MIXING NOISE EXPERIMENTS</b>	5
2.1 Introduction	10
2.2 Experimental Program	11
2.3 Results from Freely-Convection Quadrupole Theory	13
2.4 Velocity Dependence of Overall Intensity	15
2.4.1 Isothermal ( $T_j/T_o = 1$ ) Jet	15
2.4.2 Effect of Jet Temperature $T_j/T_o$	15
2.5 Directivity of Overall Intensity	18
2.5.1 Isothermal ( $T_j/T_o = 1$ ) Jet	18
2.5.2 Effect of Jet Temperature $T_j/T_o$	18
2.6 1/3-Octave Spectra	23
2.6.1 Isothermal ( $T_j/T_o = 1$ ) Jet	23
2.6.2 Effect of Jet Temperature $T_j/T_o$	26
2.6.3 Peak Frequency	26
2.7 Velocity Dependence of 1/3-Octave Intensity at Constant Source Strouhal Numbers	32
2.7.1 Isothermal ( $T_j/T_o = 1$ ) Jet	32
2.7.2 Effect of Jet Temperature $T_j/T_o$	36
2.8 Directivity of 1/3-Octave Intensity at Constant Source Strouhal Numbers	36
2.8.1 Isothermal ( $T_j/T_o = 1$ ) Jet	36
2.8.2 Effect of Jet Temperature $T_j/T_o$	45
2.8.2.1 Low frequency	45
2.8.2.2 High frequency	49
2.9 Concluding Remarks	49
<b>3. JET NOISE THEORY AND COMPARISON WITH EXPERIMENT</b>	55
3.1 Introduction	55
3.1.1 Density Ratio Effects on Jet Noise	62
3.1.2 Finite Mach Number Effects	65
3.2 The Jet Noise Model	65
3.2.1 Acoustic Analogy for Turbulent Shear Flows	65
3.2.2 Method of Solution	68
3.2.3 Source Model	74
3.2.4 Numerical Results	77
3.2.5 Asymptotic Solutions	77
3.2.5.1 High-frequency results (GA)	80
3.2.5.2 Low-frequency results (LF)	83

## TABLE OF CONTENTS (Cont'd)

	<u>Page</u>
3.3 Interpretation of Jet Noise Measurements	86
3.3.1 Amplification of Quadrupole Radiation by Hot Jet Flow	86
3.3.2 Amplification by Mean Shear in Isothermal Jets	92
3.3.3 Refraction, Source Convection and Noncompactness Effects	93
3.4 Conclusions	100
 4. THE FLOW AND ACOUSTIC CHARACTERISTICS OF LARGE-SCALE WAVE-LIKE STRUCTURE OF AN AXISYMMETRIC JET	101
4.1 Introduction	106
4.2 Mathematical Derivatives	109
4.2.1 The Integral Equations	109
4.2.2 Shape Assumptions for the Mean Flow and Wave-Like Fluctuations	111
4.2.2.1 The annular mixing region	111
4.2.2.2 The developed jet Region (downstream of potential core)	117
4.2.3 The Normal Velocity on a Cylindrical Control Surface	120
4.2.3.1 The annular mixing region	121
4.2.3.2 The developed jet region (downstream of potential core)	125
4.2.4 Calculation of the Far-Field Noise	127
4.3 Numerical Calculations	129
4.3.1 The Local Inviscid Stability Characteristics	129
4.3.2 The Axial Wave Development	140
4.3.3 The Normal Velocity on a Cylindrical Contour Surface	155
4.3.4 The Far-Field Noise	159
4.4 Discussion and Directions of Further Work	173
 5. LASER VELOCIMETER	177
5.1 Introduction	182
5.2 LV System Description	184
5.3 Velocity Offset	184
5.3.1 Polar Response of an LV Measurement Volume	188
5.3.2 Velocity Offset Optics	194
5.3.3 Extended Range Capability	199
5.4 Data Validation Circuitry	199
5.5 Summary	202
 6. MEASUREMENTS OF TURBULENT JET STRUCTURE	205
6.1 Introduction	210
6.1.1 Historical Development	210
6.1.2 Application of Hot-Wire Anemometer	210
6.1.3 The Laser Velocimeter	212

**TABLE OF CONTENTS (Cont'd)**

	<u>Page</u>
<b>6.2 Experimental Shop Set-up</b>	213
6.2.1 Air Supply	213
6.2.2 Hot-Wire Anemometry and Ancillary Equipment	215
6.2.3 Laser Velocimetry and Ancillary Equipment	215
<b>6.3 Comparison Between the LV and the Hot-Wire Anemometer</b>	217
6.3.1 Mean Velocity	217
6.3.2 Fluctuating Velocities	220
6.3.3 Probability Distributions of the Axial Velocity Fluctuations	225
6.3.4 Autocorrelations and Spectra	225
6.3.5 Summary	229
<b>6.4 Measurements of the Jet Flow Characteristics</b>	233
6.4.1 Radial Distributions	233
6.4.1.1 Mean velocities	233
6.4.1.2 Fluctuating Velocities	239
6.4.2 Normalized Radial Distributions	248
6.4.2.1 Mean velocities	248
6.4.2.2 Fluctuating velocities	263
6.4.3 Survey of the Flow Characteristics Along the Jet Centerline	263
6.4.4 Mach Number Effects	270
2.4.4.1 $x_c/D$ versus $M_j$	270
2.4.4.2 Spreading rate $\delta_n$ versus $M_j$	275
2.4.4.3 Relative changes in spreading on the two sides of the shear layer	277
2.4.4.4 Movement of the turbulence intensity peaks	277
2.4.4.5 Equation for the centerline velocity distribution	280
2.4.4.6 Normalization of the radial distribution	280
6.5 Conclusions	284
6.5.1 The LV as an Instrument	284
6.5.2 The Jet Flow Field	288
<b>7. SHOCK-ASSOCIATED NOISE</b>	291
7.1 Introduction	296
7.2 Experimental Program	299
7.2.1 Experimental Program Chart	299
7.2.2 Screech Suppression	302
7.3 Overall SPL Results	303
7.4 Peak Frequency and Implications	311
7.4.1 Theoretical Model for Shock-Associated Noise	311
7.4.2 Inferences from Measured Peak Frequencies	317
7.5 Comparison of Measured and Predicted Spectra	321
7.6 Conclusions and Future Work	325

TABLE OF CONTENTS (Cont'd)

	<u>Page</u>
<b>APPENDICES</b>	
3A Lilley Equation Developments	331
3B Transfer of the Quadrupole Operator from the Source Function to the Green Function [Derivation of Equation (3-17)]	347
3C Numerical Results Outside the Cone of Silence	349
3D Numerical Results Inside the Cone of Silence ("Effective Depth" Investigation)	363
3E The Influence of Temperature on Jet Noise at 90° to the Jet Axis: A Comparison Between Measured Data and a Model Based on the Unsteady Density Scattering, Dipole Source	371
3F Isothermal Jet Noise Directivity: Detailed Comparisons with Theory	381
3G Hot-Jet Noise Directivity: Detailed Comparison with Theory	407
4A The Nonlinear Integral Equations for a Compressible Axisymmetric Jet	415
4B Tensor Notation and Physical Notation	423
4C Linearized Equations of Motion for a Compressible, Viscous, Heat-Conducting Fluid in Cylindrical Coordinates and Inviscid Stability Equations	427
4D Analytical and Numerical Representation of the Mean Flow Shape Functions	433
4E Eigenfunction Distributions at $b = 2$	439
6A The Effect of Velocity Measurement Inaccuracy on the Measured Flow Statistics	453
REFERENCES	457

## 1. INTRODUCTION

### 1.1 THE NATIONAL INTEREST IN AIRCRAFT NOISE REDUCTION

The challenges faced by the aerospace industry have historically presented a web of fundamentally conflicting problems. During the late 1960's and the early 1970's, environmental problems received priority attention, particularly with respect to the noise pollution caused by military aircraft. Although the more immediately pressing problems of energy conservation have shifted some of the emphasis away from environmental effects, aircraft noise remains a severe problem that must be solved. In fact, the new concern for energy conservation makes it even more important to understand in detail how noise from aircraft engines is produced, so that designs can be created to give the required noise reduction with only minimum energy penalties.

It has been recognized that the jet exhaust comprises the major noise source for most military aircraft systems, and under proposed FAA regulations jet noise will also be a predominant source for most civil aircraft. It was thus quite logical that the U. S. Air Force and the U. S. Department of Transportation should cooperate in dealing comprehensively with their mutual noise problems. In 1971 they awarded three competitive, one-year, jet noise contracts to separate companies, including Lockheed, to conduct program-definition studies for future comprehensive research investigations. These basic studies were followed by two contracts, one awarded to Lockheed, for in-depth investigation of noise-generating mechanisms. All of these contracts were managed by the Air Force Aero Propulsion Laboratory, and in addition to a large noise-suppression contract later awarded by the Department of Transportation, have served as effective means of disseminating information throughout the aircraft industry. The attention given to the contractor reports and the semi-annual public reviews of all the studies are good indicators of the widespread government and corporate interest in aircraft noise reduction.

### 1.2 LOCKHEED'S CONTRACT EFFORTS

Lockheed's contractual role in this work has comprised a very fundamental study aimed at theoretically defining the basic jet-noise generation mechanisms and the acoustic interactions with the mean flow as the sound propagates from the sources to the receiver. Experiments have been conducted to confirm the theory and to provide data for theoretical studies. In several instances it was necessary to develop highly specialized instrumentation.

The six-volume report<sup>1-6</sup> issued at the conclusion of the Lockheed program-definition contract showed that:

- (1) Noise originating from a jet exhaust could be classified as turbulent mixing noise, shock-associated noise, and internal or upstream noise.
- (2) Turbulent mixing noise could be further identified as to type: that originating from the large-scale, coherent eddy structure; and that from the small-scale disorganized turbulence.

- (3) Shock-associated noise contains discrete frequency (screech) components and a broadband random component.
- (4) The three types of noise or noise sources could be considered separately.

These conclusions and other results of the first study also clearly indicated a work plan for the present contract program. Among the most significant features, the follow-on study would accord primary importance to turbulent-mixing noise, which is usually dominant in all realistic operating conditions. Because of the relatively meager knowledge of shock-associated noise, detailed investigations would be conducted to determine the characteristics and relative importance of the broadband shock-associated noise. Thus, the present study had the following principal objectives, all of which were satisfactorily accomplished.

- (1) Mathematically model the large-scale coherent structure of a turbulent supersonic jet, and calculate the associated sound pressure.
- (2) Interpret Lilley's acoustic/mean flow interaction theory as applied to jet noise from small-scale turbulence, and to determine the form of and numerically solve the theory for the point source functions representing the small-scale turbulence.
- (3) Develop new or modified instruments and facilities, including a laser velocimeter, for necessary measurement of appropriate turbulence and acoustic quantities.
- (4) Characterize the effects of temperature and exhaust velocity on far-field jet noise, and isolate broadband, shock-associated noise and determine how it is affected by Mach number and temperature.
- (5) Determine the mean and turbulence velocity characteristics in heated subsonic and supersonic jets.
- (6) Evaluate calculated noise results with experimentally observed results, and determine the validity of theoretical assumptions and solutions.
- (7) Construct a model and/or extend existing models for shock-associated noise prediction.

An interim report<sup>7</sup>, issued at approximately the contract mid-point, discussed preliminary numerical solutions of the Lilley theory, indicated progress in the critique and study of various models related to jet noise, and presented descriptions of the Lockheed-Georgia anechoic facility for jet noise research and of the Lockheed two-channel laser velocimeter system.

### 1.3 OUTLINE OF THIS REPORT

The present report, which completes the description of the work conducted under the current program, is published in four volumes. Volume I summarizes

the work accomplished. Volume II (this volume) contains a detailed discussion of work accomplished since the publication of the interim report, and all of the major conclusions reached during the program. Volume III is a data report which presents a detailed compilation of the turbulent mixing noise 1/3-octave spectra. Volume IV, another data report, contains the narrow-band spectra for broadband shock-associated noise.

Six topics are comprehensively presented in this volume:

- (1) Turbulent mixing noise tests and observations relative to effects of temperature and Mach number on intensity, directivity, and spectra.
- (2) Numerical solutions of the Lilley theory for sound radiated from point sources simulating small-scale turbulence noise sources, and comparisons of these solutions with experimental data relating to temperature and velocity effects on directivity and spectra.
- (3) The theory describing the development of the large-scale coherent motion of the jet structure and the far-field noise radiated from this turbulence.
- (4) The improvements made to the LV system since the interim reporting period, and an analysis of those improvements which lead to unique system characteristics.
- (5) A detailed discussion and interpretation of the jet turbulence and mean velocity data.
- (6) A comprehensive description of the shock-associated noise tests, a preliminary description of the broadband shock-associated noise model, and a discussion of shock-associated noise in the overall jet noise picture.

#### 1.4 A SPECIAL ACKNOWLEDGEMENT

The authors hope that this work will have lasting usefulness on the problem of understanding and reduction of noise from jet flows. They also wish to restate their appreciation and gratitude to the U. S. Air Force and the U. S. Department of Transportation and their respective technical managers, Mr. Paul A. Shahady and Dr. Gordon Banerian, for their support and continuous open examination of this work. It is felt that the frequent reviews by university, industry, and government experts and interested observers have not only cleared the air concerning the goals and direction of the program, but have significantly added to the overall usefulness of the final results by constructive criticism and a continual infusion of new ideas.

2. TURBULENT MIXING NOISE EXPERIMENTS

## SUMMARY

---

The characteristics, both spectral and directivity, of turbulent mixing noise in the far field from subsonic and fully-expanded supersonic jet flows are studied experimentally over an extensive envelope of jet operating conditions (jet exit velocity and temperature). The changes in detailed jet noise features with varying velocity and exhaust temperature are assessed independently.

---

The basic philosophy used in the jet noise experimental program was that each noise source should be examined independently as far as possible. Only then is it possible to study the trends and dependencies of each noise source accurately. The turbulent mixing noise tests and the shock-associated noise tests, although planned to be mutually compatible, were therefore conducted separately. During each of the two test series, the contribution from the other noise source was either eliminated completely or was kept to a minimum. The results from the turbulent mixing noise experiments are described in the present section, and the corresponding shock-associated noise results from under-expanded jets are presented in Section 7 of this Volume.

The experiments were conducted in the anechoic facility which provides a free-field environment. Four two-inch diameter nozzles were used, namely a convergent nozzle for pressure ratios up to critical, and three convergent-divergent nozzles having nominal design Mach numbers of 1.4, 1.7, and 2.0, respectively. The jet operating conditions for the entire test program are shown in Figure 2S.1. The most important features of the experimental program are as follows:

(1) The experimental program is more comprehensive than any previously reported experiments of this kind. It covers the entire envelope of jet operating conditions of practical interest.

(2) The results at super-critical pressure ratios are obtained by operating the three con-div nozzles at their design pressure ratios only. Hence, the results are not contaminated to any significant extent by shock-associated noise.

(3) The test points are carefully selected to yield results (i) at constant jet efflux temperature with varying jet velocity, and conversely, (ii) at constant jet velocity with varying jet exhaust temperature. In this manner, the effects of velocity and temperature on jet noise are assessed independently.

(4) Special care has been taken to provide results at nominally isothermal jet exit conditions. Hence, the variation of jet noise with jet efflux velocity can be examined accurately, and the results also form a base line for investigating the effects of jet heating on the radiated sound field.

(5) Since the sound field can be expected to scale on the jet static temperature rather than on the stagnation temperature (a constant stagnation temperature would yield decreasing static temperature as the pressure ratio is increased), the present experiments were conducted at constant values of jet static temperature ratio.

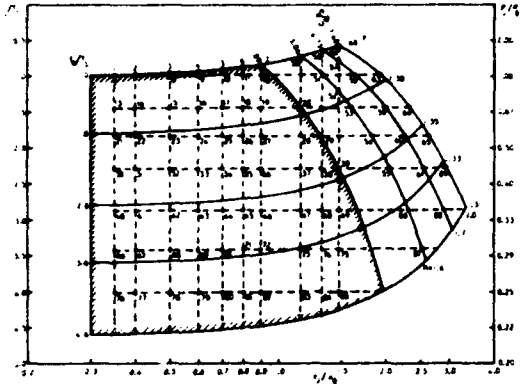


Figure 2S.1 Experimental Program Chart

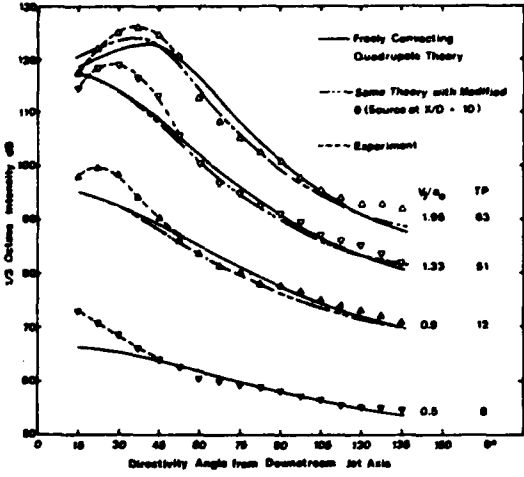


Figure 2S.2 Directivity of 1/3-Octave Intensity at  $f_s D / V_j = 0.1$ :  
 $T_j / T_0 \approx 1$

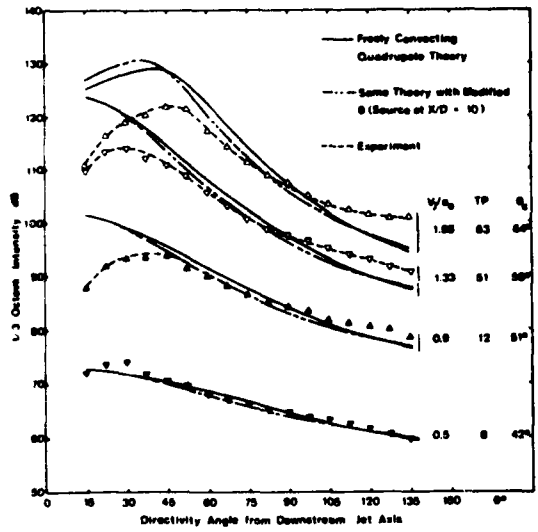


Figure 2S.3 Directivity of 1/3-Octave Intensity at  $f_s D / V_j = 0.3$ :  
 $T_j / T_0 \approx 1$

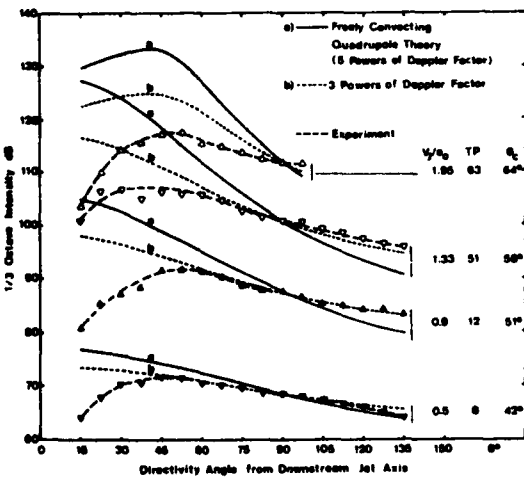


Figure 2S.4 Directivity of 1/3-Octave Intensity at  $f_s D / V_j = 1.0$ :  
 $T_j / T_0 \approx 1$

---

The results are presented in a systematic manner, and the observed trends and dependencies are discussed in detail. The isothermal jet noise results are compared with the freely-convection quadrupole theories. The discrepancies between this model and the measurements, many of which are recently shown to occur due to the presence of mean velocity and temperature gradients surrounding the sources, are obtained accurately over all jet operating conditions of interest.

---

The results at  $90^\circ$  to the jet axis were presented in Appendix III of the Interim Report, where a semi-empirical scaling law model for the prediction of noise at  $90^\circ$  was developed. The corresponding results from 75 jet exit conditions (i.e. combinations of  $T_J/T_0$  and  $V_J/a_0$ ) at all angles to the downstream jet axis ( $15^\circ \leq \theta \leq 135^\circ$ ) are presented here. For future reference, the data from the complete test program are tabulated in Volume III of this report.

The data are analyzed and presented in a suitable form so that detailed comparisons with the on-going theoretical efforts can be carried out at appropriate stages. The velocity dependence and the directivity, both for overall results and 1/3-octave band results at fixed values of source Strouhal number, are displayed in a systematic manner. (Some typical results are shown in Figures 2S.2 through 2S.8). The characteristics of turbulent mixing noise from fully-expanded jet flows, as one proceeds from the low subsonic jet velocities to high supersonic velocities, are established in detail, and the changes in jet noise features with varying velocity and exhaust temperature are assessed independently.

The basic aim of this section is to present and describe the major experimentally observed features of jet noise. Comparisons with recent theoretical work on this program are included in Section 3 of this Volume. However, the results for isothermal jet operating conditions ( $T_J/T_0 = 1$ ) are compared with the Lighthill/Ffowcs Williams/Ribner<sup>9,10,11</sup> theory of quadrupoles convected in free space (i.e. a model in which the presence of mean velocity and temperature fields surrounding the sources is neglected) in order to (i) obtain as much insight as possible using this simpler model, (ii) highlight the inadequacies of this model quantitatively, and (iii) define the regimes over which the discrepancies occur (see Figures 2S.2, 2S.3, and 2S.4).

In Section 3, it will be seen that many of the observed deviations between experiment and the basic freely convecting quadrupole model are a consequence of the shrouding of the sound sources in the jet flow by mean velocity and temperature gradients.

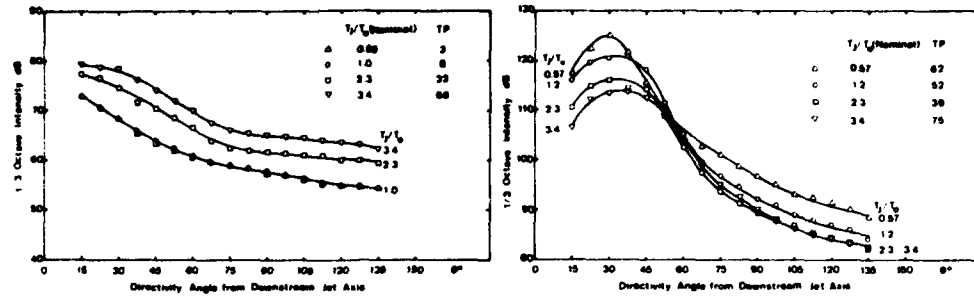


Figure 2S.5 Effect of  $T_j/T_0$  on Directivity of 1/3-Octave Intensity at  $V_j/a_0 = 0.5$ :  $f_{sD}/V_j = 0.1$

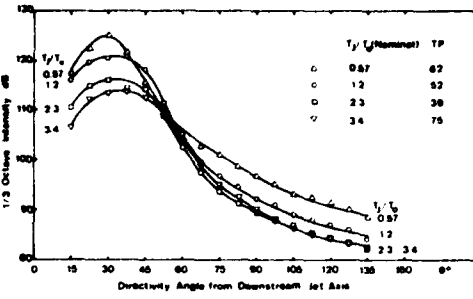


Figure 2S.6 Effect of  $T_j/T_0$  on Directivity of 1/3-Octave Intensity at  $V_j/a_0 = 1.47$ :  $f_{sD}/V_j = 0.1$

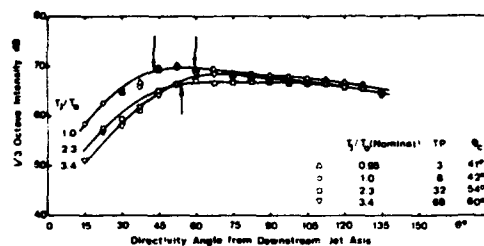


Figure 2S.7 Effect of  $T_j/T_0$  on Directivity of 1/3-Octave Intensity at  $V_j/a_0 = 0.5$ :  $f_{sD}/V_j = 3.0$

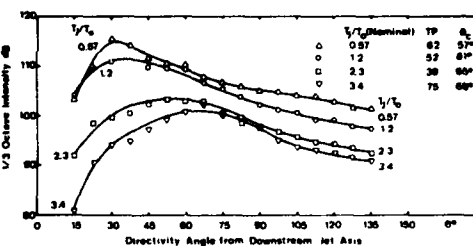


Figure 2S.8 Effect of  $T_j/T_0$  on Directivity of 1/3-Octave Intensity at  $V_j/a_0 = 1.47$ :  $f_{sD}/V_j = 1.0$

## 2.1 INTRODUCTION

The characteristics of turbulent mixing noise from unheated jets operated at subsonic exhaust velocities were examined experimentally in great detail by Lush<sup>8</sup>. The inadequacies of the freely-convection quadrupole theories<sup>9,10,11</sup>, which do not account for the changes in radiation efficiency due to the shrouding of the sound sources in a jet flow by the mean flow environment, were highlighted over this restricted regime of jet operating conditions. During the last three years, various investigations, a few of which are experimental but most are theoretical, have shown that many of the observed deviations from this theoretical model can be explained, at least qualitatively, by immersing the sound sources in a realistic mean velocity environment that is always present in a jet exhaust.

In order to study these acoustic/mean-flow interaction effects quantitatively at all jet operating conditions of interest, it is vital to obtain turbulent mixing noise data of high accuracy over extensive ranges of jet velocity and exhaust temperature. As part of the fundamental research program on the generation and radiation of supersonic hot jet noise, these results are now available, and they are presented in this section.

In the present experimental program, the characteristics, both spectral and directivity, of the sound field of supersonic shock-free jets are studied by measuring the turbulent mixing noise in the far field from four two-inch diameter nozzles, namely a convergent nozzle for pressure ratios up to critical and three convergent-divergent nozzles having nominal design Mach numbers of 1.4, 1.7, and 2.0, respectively. In order to avoid the contamination of data by shock-associated noise, these latter were operated only at their design pressure ratios (up to 7.4). The measurements were conducted in the carefully designed large anechoic room which provides a free-field environment. The facility, test procedure and the calibration tests conducted prior to the experimental program are described in detail in references 12, 13, and 14.

The ranges of various parameters defining the jet operating conditions are as follows:

Pressure Ratio,  $P_R/P_0 = 1$  to 7.4  
Stagnation or Total Temperature Ratio,  
 $T_R/T_0 = 1$  to 4.5  
Jet Exit Velocity Ratio,  $V_J/a_0 = 0.3$  to 3.0  
Static Temperature Ratio,  $T_J/T_0 = 0.5$  to 4.0  
Jet Density Ratio,  $\rho_J/\rho_0 = 0.25$  to 2.0

Results from 75 jet exit conditions ( $T_J/T_0$ ,  $V_J/a_0$ ) are presented here. The test program, described in paragraph 2.2, was carefully planned in order to obtain results (i) at constant jet efflux temperature with varying jet velocity, and conversely (ii) at constant exit velocity while varying jet efflux temperature.

The results at 90° to the jet axis were presented by Tanna *et al*<sup>13,14</sup>, where the effects of flow temperature on turbulent mixing noise "equivalent"

source strengths were identified and quantified in terms of a simple semi-empirical scaling law model to an accuracy of 1 or 2 dB. The corresponding results at all angles to the downstream jet axis ( $15^\circ \leq \theta \leq 135^\circ$ ) are presented here. The data from the entire test program are tabulated in Volume III for future reference.

The data are analyzed and presented in a suitable form so that detailed comparisons with the on-going theoretical efforts can be carried out at appropriate stages. The velocity dependence and directivity, both for overall results and 1/3-octave band results at fixed values of source Strouhal number, are displayed in a systematic manner. The characteristics of turbulent mixing noise from fully-expanded jet flows, as one proceeds from the low subsonic jet velocities to high supersonic velocities, are established in detail, and the changes in jet noise features with varying velocity and exhaust temperature are assessed independently.

Every effort is made to keep the majority of the figures self-explanatory, and the corresponding descriptions therefore are kept to a minimum. It is also pointed out that no attempt is made to formulate a general empirical prediction method from these results at this stage, although it is felt that this can be achieved very successfully by spending the required effort for it.

The basic aim of this section is to present and describe the major experimentally observed features of jet noise. Comparisons with recent theoretical work on this program are included in Section 3 of this Volume. However, the results for *isothermal* jet operating conditions ( $T_j/T_o = 1$ ) are compared with the Lighthill/Ffowcs Williams/Ribner<sup>9,10,11</sup> theory of quadrupoles convected in free space in order to (i) obtain as much insight as possible using this simpler model, (ii) highlight the inadequacies of this model quantitatively, and (iii) define the regimes over which the discrepancies occur. In addition, these comparisons provide a convenient method of data presentation.

For each aspect under examination (e.g., velocity dependence, directivity, etc.), the data are essentially presented in two parts. The first part describes the variation with jet exit velocity ratio,  $V_j/a_0$ , and hence deals with the results for which  $T_j/T_o$  is unity, whereas the second part considers the variation with jet efflux temperature ratio,  $T_j/T_o$ , at fixed jet velocities.

## 2.2 EXPERIMENTAL PROGRAM

The experimental program, summarized earlier, is now described in detail with the help of the experimental program chart shown in Figure 2.1. The chart essentially shows the envelope of jet static temperature ratio  $T_j/T_o$  (and hence also jet density ratio,  $\rho_j/\rho_o$ ), and jet exit velocity ratio  $V_j/a_0$ , as a function of stagnation temperature ratio  $T_R/T_o$ , and pressure ratio  $P_R/P_o$ . The lower limit of  $V_j/a_0$  is set by the measuring instrumentation noise, as described by Tanaka et al<sup>13,14</sup>. The four nozzles employed are the convergent nozzle and the M=1.4, 1.7 and 2.0 convergent-divergent nozzles. In this study of turbulent mixing noise, the nozzles must be operated at on-design pressure ratios so that the data will not be contaminated by contribution from shock-associated noise. The convergent nozzle therefore can be operated at any pressure ratio up to 1.89, and the corresponding ranges of  $T_j/T_o$  and  $V_j/a_0$  are

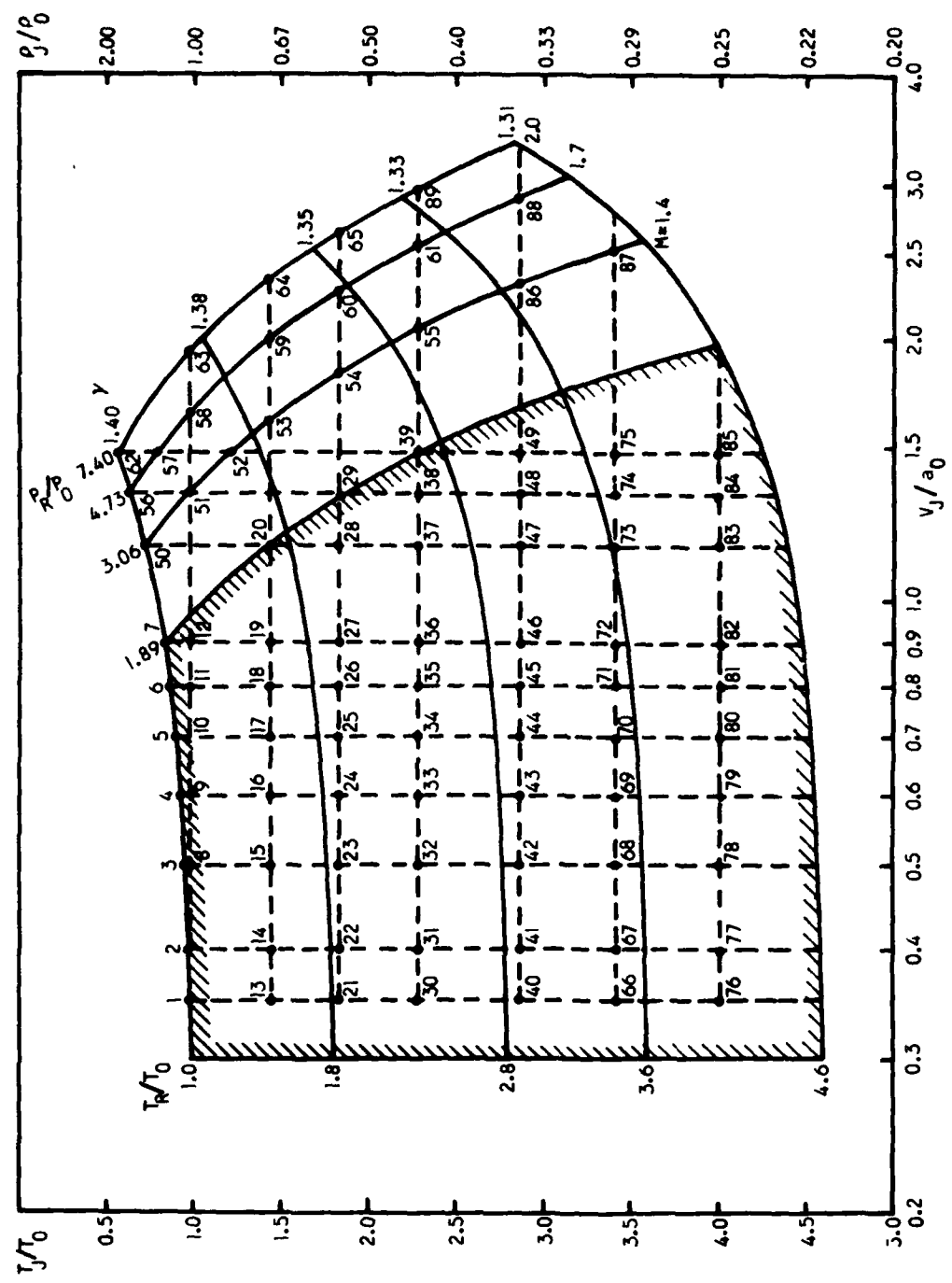


Figure 2.1 Experimental Program Chart

shown by the shaded area of the chart. In other words, the convergent nozzle can be used to obtain jet exit conditions ( $T_j/T_0$ ,  $V_j/a_0$ ) at any point within this shaded area. In contrast, the three con-div nozzles can be operated at fixed pressure ratios only, and hence the jet exit conditions available with these nozzles are represented by the three curves on the right of the shaded area. The variation of the specific heat ratio,  $\gamma$ , with temperature was incorporated in the preparation of this chart<sup>13,14</sup>.

The jet operating conditions (combinations of  $T_j/T_0$  and  $V_j/a_0$ ) originally selected for the experimental program are identified by test point numbers (TP) in Figure 2.1. Throughout this section, data will be identified in terms of these test point numbers, an approach which it is hoped will assist the reader's interpretation. It can be seen that by considering test points on each horizontal line, it is possible to keep the jet efflux temperature constant while varying the efflux velocity. Conversely, on each vertical line, constant efflux velocity is maintained while jet exit temperature is varied.

It should be noted that all data given here are obtained from 2-inch diameter nozzles with the measurement points at 72 diameters. The normal scaling laws must therefore be applied for application to other measurement configurations.

### 2.3 RESULTS FROM FREELY-CONVECTING QUADRUPOLE THEORY

In view of the comments made in paragraph 2.1, the results from the freely-convection quadrupole theories which will be used in the data presentation are quoted in this paragraph.

The far-field acoustic intensity,  $I$ , is given by the Lighthill/Ffowcs Williams/Ribner theory of quadrupoles convected in the absence of any mean velocity or temperature gradients in dimensional form as

$$I \sim \rho_m \left( \frac{\rho_m}{\rho_0} \right)^2 \frac{V_j^{8D^2}}{a_0^5 R^2} \times \frac{D(\theta)}{[(1-M_c \cos \theta)^2 + \alpha^2 M_c^2 (\cos^2 \theta + e^2 \sin^2 \theta)]^{5/2}}, \quad (2-1)$$

where

$\rho_m$  = density in the mixing region,

$\rho_0$  = density of the external fluid,

$a_0$  = ambient speed of sound,

$V_j$  = jet exit velocity,

$D$  = nozzle diameter,

$R$  = distance from the jet to the observer,

$\theta$  = angle between the direction of emission of sound and the downstream jet axis,

$D(\theta)$  = directivity of the unconvected quadrupole distribution in the jet,

$M_c$  = eddy convection Mach number (i.e., quadrupole convection speed divided by the ambient speed of sound,  $V_c/a_0$ ),

$\alpha$  = turbulence parameter expressing the rate of decay of the turbulent eddies, given by  $\omega l_1/V_c$ , where  $\omega$  is the typical frequency of turbulence observed in a reference frame moving at the eddy convection speed and  $l_1$  is the longitudinal length scale of turbulence, and

$e$  = ratio of lateral to longitudinal scales of turbulence  $l_2/l_1$ .

In Equation (2-1) the amplification due to source convection at high velocities is given by the factor

$$[(1-M_c \cos\theta)^2 + \alpha^2 M_c^2 (\cos^2\theta + e^2 \sin^2\theta)]^{-5/2}, \quad (2-2)$$

which is commonly referred to as the "convective amplification" factor.

Since the data collapse at  $90^\circ$  to the jet axis for isothermal jets reported previously was better when based on  $V_J^{-7.5}$  dependence rather than the normally accepted velocity index of 8 [see Tanna et al<sup>13,14</sup>], all comparisons presented here will be based on  $V_J^{-7.5}$  dependence. For isothermal jet operating conditions (i.e.  $\rho_m/\rho_o = 1$ ), assuming the basic unconvected quadrupole distribution in the jet to be statistically isotropic (i.e., spherical directivity,  $D(\theta) = 1$ ), and putting  $e = 1$  for convenience, Equation (2-1) for the overall intensity therefore gives

Velocity Dependence at angle  $\theta$  as

$$\left(\frac{V_J}{a_0}\right)^{7.5} [(1-M_c \cos\theta)^2 + \alpha^2 M_c^2]^{-5/2} \quad (2-3)$$

and Directivity at fixed  $V_J/a_0$  as

$$[(1-M_c \cos\theta)^2 + \alpha^2 M_c^2]^{-5/2}. \quad (2-4)$$

For the analysis of the results in 1/3-octave bands, the same Equations (2-3) and (2-4) above can be used for the velocity dependence and the directivity, except that, in this case, since the sources are being convected at eddy convection Mach number,  $M_c$ , the observed frequency  $f$  and the source frequency  $f_s$  will be related by the Doppler Factor  $F$  as

$$f_s = fF = f[(1-M_c \cos\theta)^2 + \alpha^2 M_c^2]^{1/2}. \quad (2-5)$$

Thus, if the 1/3-octave results are analyzed at constant source Strouhal number,

$$\frac{f_s D}{V_J} = \frac{f D}{V_J} [(1-M_c \cos\theta)^2 + \alpha^2 M_c^2]^{1/2} = \text{constant}, \quad (2-6)$$

then the 1/3-octave intensities will be independent of frequency, as explained in detail by Lush<sup>8</sup>. In the analysis of the results at constant source Strouhal number, the observed frequency  $f$  corresponding to the fixed source frequency  $f_s$  is first determined from Equation (2-5), and the Strouhal number correction ensures that the intensity is measured at the same point on the spectrum relative to the peak. In this manner, the source in a geometrically similar position in the jet is observed, irrespective of the emission angle, jet diameter and jet velocity.

In the following paragraphs, the velocity dependence and the directivity of both the overall intensity and the 1/3-octave intensity are studied in the manner described briefly above. In comparing the results with the freely-convection quadrupole theory,  $M_c$  is taken to be  $0.67 V_j/a_0$  and  $\alpha = 0.3$ , as measured for low velocity jets by Davies *et al*<sup>16</sup>.

Note: Throughout the rest of this section, the freely-convection quadrupole theory will be referred to as "theory" for simplicity. It should not be confused with any recent theoretical efforts at either Lockheed-Georgia or any other source.

## 2.4 VELOCITY DEPENDENCE OF OVERALL INTENSITY

### 2.4.1 Isothermal ( $T_j/T_o = 1$ ) Jet

The measured overall intensity as a function of  $V_j/a_0$  at four angles to the jet axis, namely  $135^\circ$ ,  $90^\circ$ ,  $45^\circ$  and  $22.5^\circ$ , is shown in Figure 2.2, together with the theoretical predictions for velocity dependence given by Equation (2-3). The theoretical curves at  $\theta = 135^\circ$ ,  $45^\circ$  and  $22.5^\circ$  are plotted relative to the theoretical curve at  $90^\circ$  and therefore show the correct amount of convective amplification. At  $\theta = 90^\circ$ , the theoretical velocity scaling follows the measured velocity dependence very accurately over the entire subsonic and supersonic velocity range considered here. However, in the forward arc ( $\theta > 90^\circ$ ), the theory underestimates the measurements, and at  $\theta = 45^\circ$  and  $22.5^\circ$ , the theory grossly overestimates the measured velocity dependence. The amount of overestimation in the rear arc ( $\theta < 90^\circ$ ) increases as  $\theta$  decreases or as  $V_j/a_0$  increases.

It should be noted that although the theoretical curves in Figure 2.2 can be shifted much closer to the measurements by choosing appropriate values of  $M_c$  and  $\alpha$  (e.g.  $M_c = 0.5 V_j/a_0$  and  $\alpha = 0.55$  as suggested by Ribner), there is no experimental evidence to justify this at the present time.

### 2.4.2 Effect of Jet Temperature $T_j/T_o$

The most general effect of heating can be observed by examining the velocity dependence of overall intensity at  $\theta = 90^\circ$  for various values of  $T_j/T_o$ . This is presented in Figure 2.3. As it is commonly accepted now, the effect of heating is to produce an increase in noise at low jet velocities, whereas at high jet velocities the overall level decreases with heating. The velocity exponent decreases with heating, and from the figure it appears that the value of  $V_j/a_0$ , at which the effect of heating (relative to  $T_j/T_o = 1$ ) reverses, increases as  $T_j/T_o$  increases.

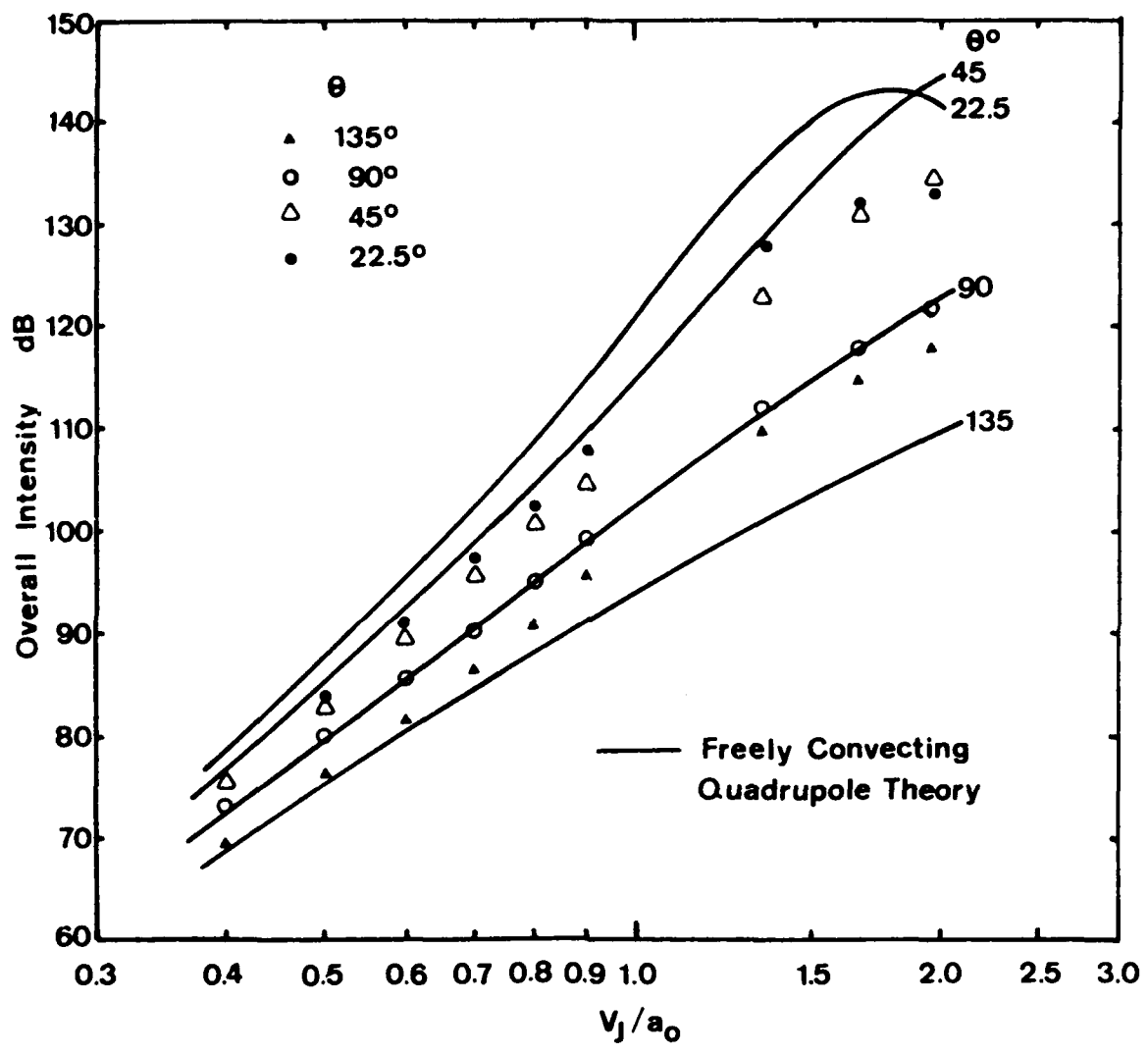


Figure 2.2 Velocity Dependence of Overall Intensity:  $T_J/T_O \doteq 1$

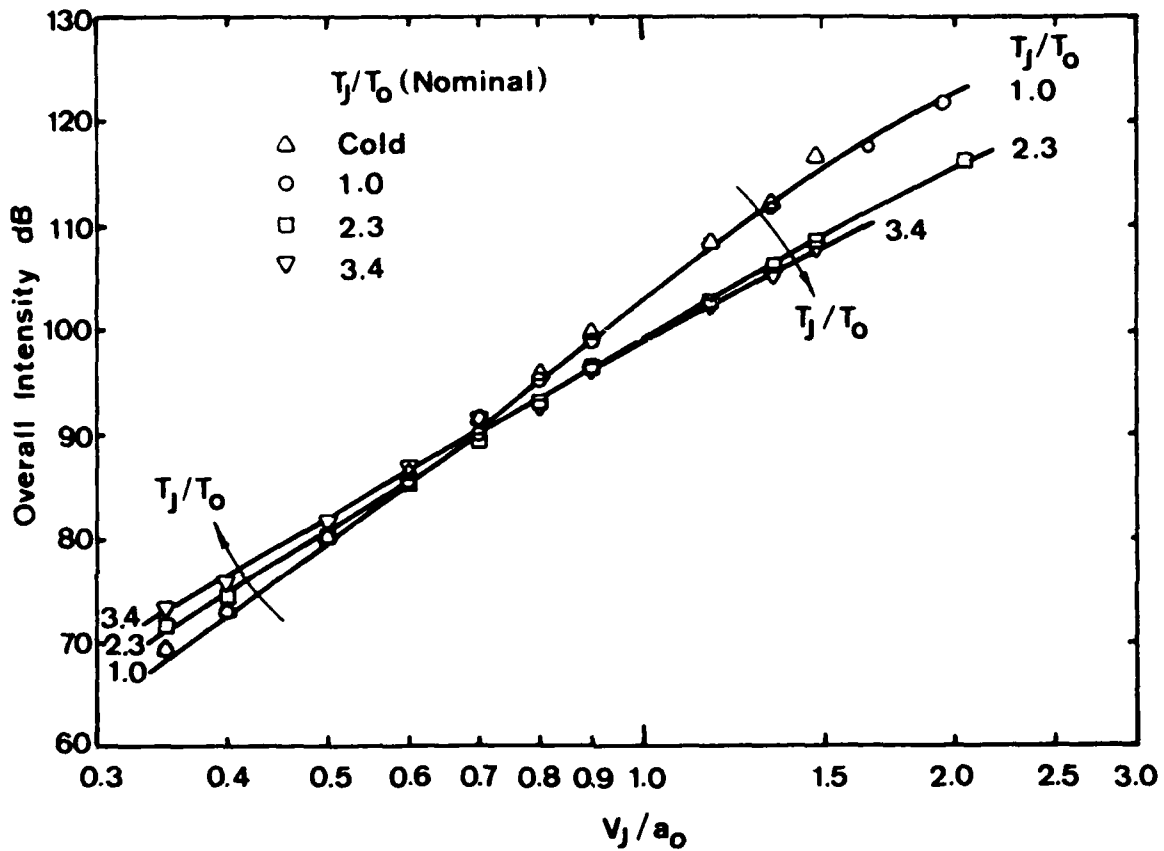


Figure 2.3 Effect of  $T_J/T_O$  on Velocity Dependence of Overall Intensity:  
 $\theta = 90^\circ$

It should be noted that no theoretical velocity dependence is implied in this figure. The full lines shown are simply lines joining experimental points. This comment in fact applies to all subsequent figures where the variation with  $T_J/T_0$  is presented.

## 2.5 DIRECTIVITY OF OVERALL INTENSITY

### 2.5.1 Isothermal ( $T_J/T_0 = 1$ ) Jet

The directivities of measured overall intensity at several values of  $V_J/a_0$  from 0.5 to 1.95 are shown in Figure 2.4. At subsonic velocities, the intensity is directional with a peak quite close ( $20^\circ - 25^\circ$ ) to the jet axis, and the effect of refraction is to produce a slight dip at angles less than approximately  $20^\circ - 25^\circ$ . At supersonic velocities, the overall intensity is highly directional; the peak angle and the dip at angles smaller than the peak angle increase progressively as the jet velocity increases. It should be noted, however, that at these high velocities, these dips at small angles to the jet axis do not arise purely due to refraction, but are a result of the combination of refraction and Mach wave radiation<sup>10</sup> that occurs when the eddy convection Mach number in the direction of the observer approaches unity (i.e.  $M_c \cos\theta \approx 1$ ). Further work is required to establish which of these two phenomena is dominant in this velocity regime.

The measured directivities are now compared with the theoretical directivities given by Equation (2-4), with  $M_c = 0.67 V_J/a_0$  and  $\alpha = 0.3$ . It should be noted that all theoretical directivities are plotted relative to the experimental value at  $\theta = 90^\circ$ , and not adjusted vertically for best fit; thus they represent true comparisons between theory and experiment. The theoretical convective amplification in the rear arc and convective "attenuation" in the forward arc are clearly too large. The deviation increases progressively as  $V_J/a_0$  increases and also as  $\theta$  increases or decreases from  $90^\circ$ . Even at the lowest jet velocity considered ( $V_J/a_0 = 0.5$ ), the agreement between theory and experiment is poor.

It is reminded that as in the case of velocity dependence (paragraph 2.4.1), the theoretical convective amplification can be reduced significantly by selecting appropriate value of  $M_c$  and  $\alpha$ , but this cannot be justified until measurements of  $M_c$  and  $\alpha$  over the entire velocity range become available.

### 2.5.2 Effect of Jet Temperature $T_J/T_0$

The influence of jet exit temperature on the directivity of overall intensity at three values of  $V_J/a_0$  is illustrated in Figures 2.5, 2.6, and 2.7. At low velocity ( $V_J/a_0 = 0.5$ ), it can be seen that the effect of heating observed previously at  $\theta = 90^\circ$  holds at all angles. That is, the noise increases with heating. The directivities for  $T_J/T_0 = 1$  and 3.4 are virtually parallel. On the other hand, at the medium jet velocity ratio of 0.9, the effect of heating is to produce a decrease in noise level. It is interesting to note that in Figure 2.6, over the range of  $T_J/T_0$  considered here, there is no effect in the vicinity of  $\theta = 40^\circ$ , and as  $\theta$  increases or decreases

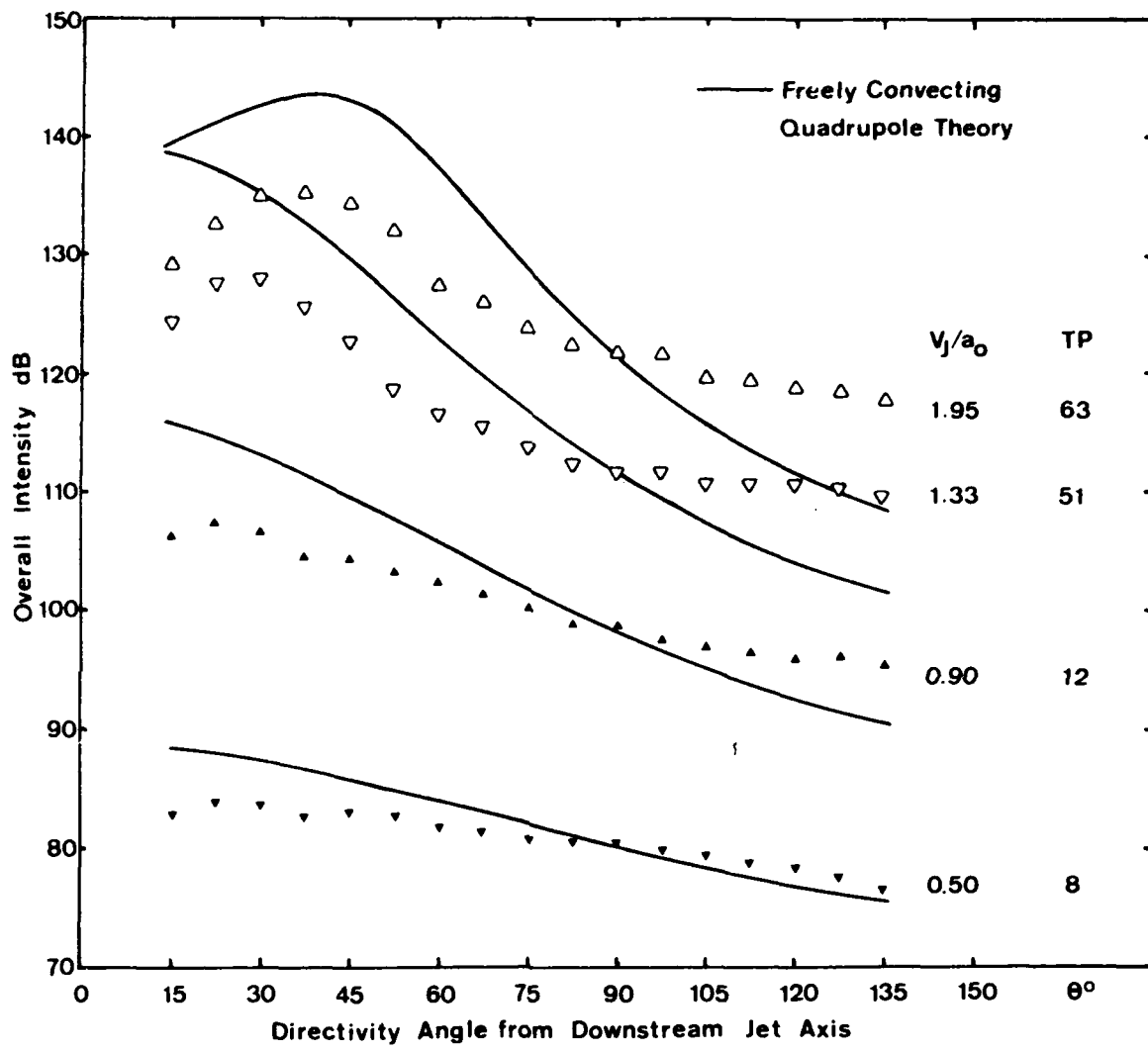


Figure 2.4 Directivity of Overall Intensity:  $T_j/T_o \doteq 1$

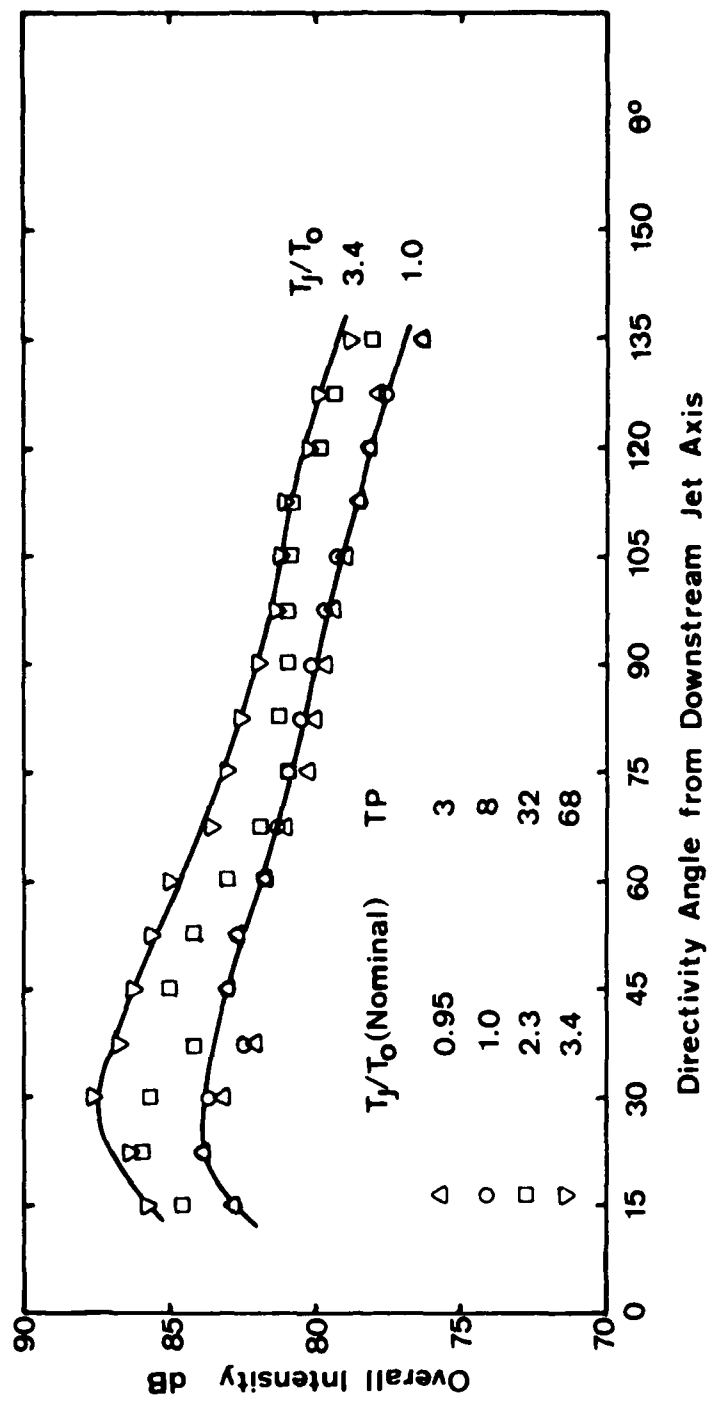


Figure 2.5 Effect of  $T_J/T_0$  on Directivity of Overall Intensity:  $v_J/a_o = 0.5$

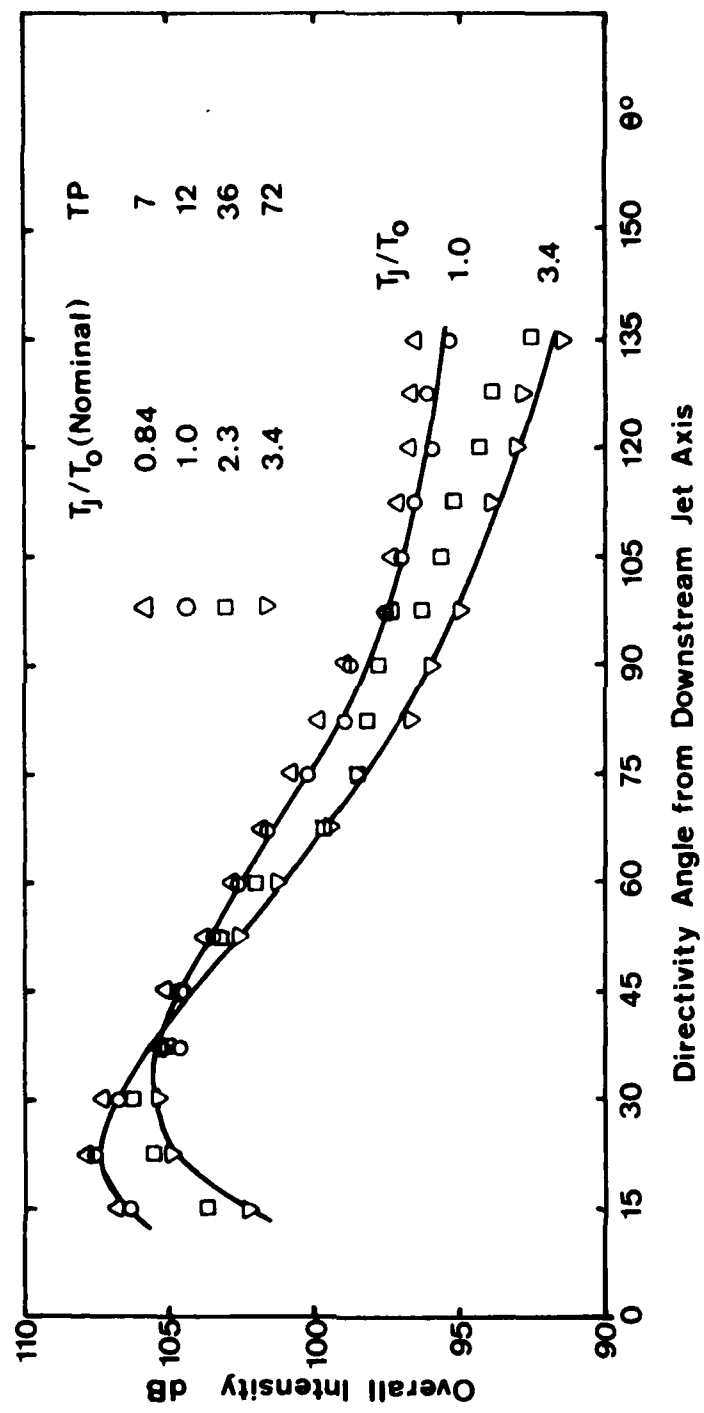


Figure 2.6 Effect of  $T_j/T_0$  on Directivity of Overall Intensity:  $V_j/a_o = 0.9$

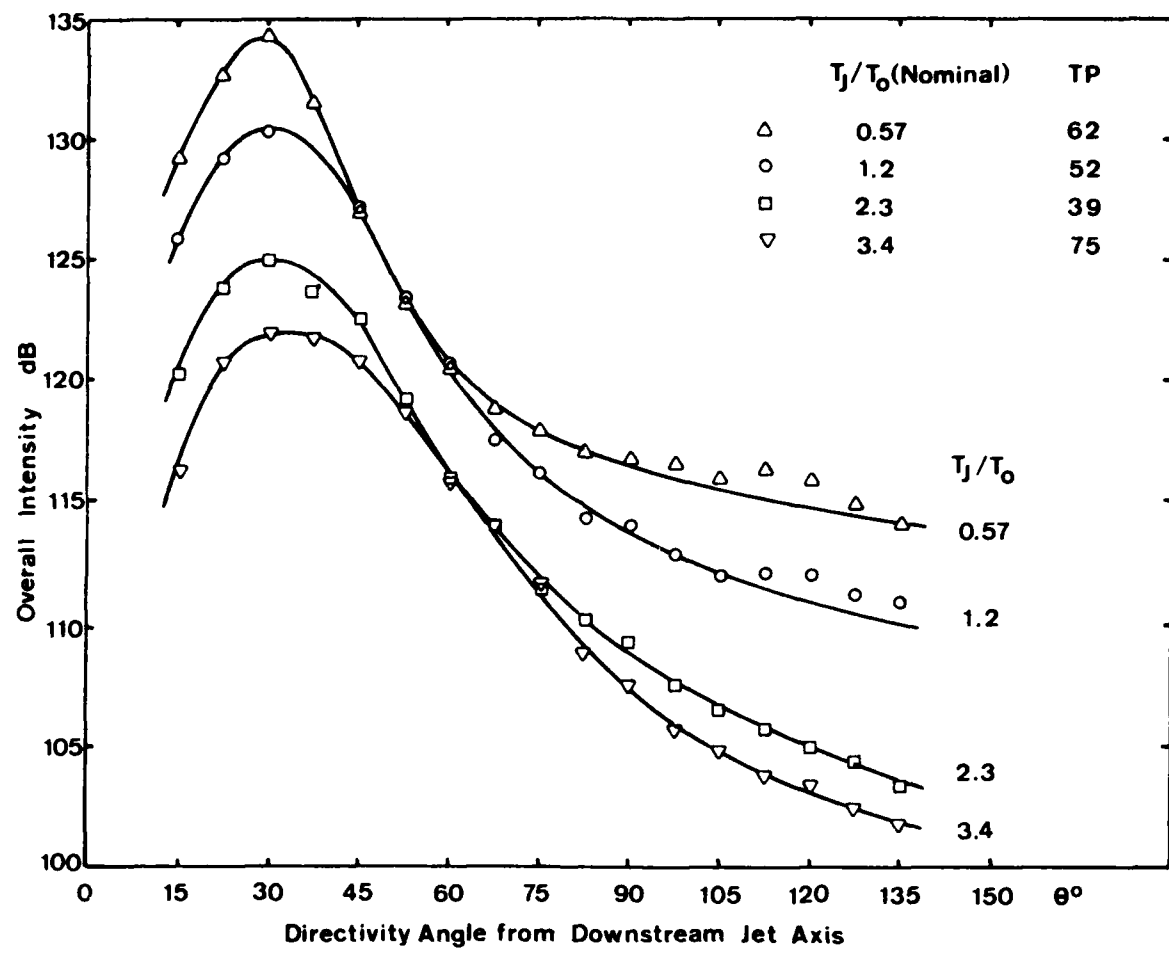


Figure 2.7 Effect of  $T_J/T_0$  on Directivity of Overall Intensity:  $V_J/a_0 = 1.47$

from 40°, there is a progressive reduction in overall intensity with heating. Finally, at  $V_J/a_0 = 1.47$  (Figure 2.7), the reductions become very large indeed, especially near the jet axis.

Comparison of peak radiation angles in Figures 2.5, 2.6, and 2.7 is most revealing. At the low and high velocities considered, the peak angle remains nearly constant ( $\theta_p \approx 30^\circ$ ). Furthermore, this peak angle does not vary significantly with jet temperature. In contrast, the peak angle for  $V_J/a_0 = 0.9$  increases convincingly with  $T_J/T_0$ .

## 2.6 1/3-OCTAVE SPECTRA

Having examined the overall characteristics of jet noise as a function of velocity and temperature, we can proceed to look at the spectral results. The purpose of this paragraph is to display, in a preliminary manner, the changes in spectral shapes where  $V_J/a_0$  and  $T_J/T_0$  are varied independently as before.

### 2.6.1 Isothermal ( $T_J/T_0 = 1$ ) Jet

The 1/3-octave spectra at various jet exit velocities in the range from  $V_J/a_0 = 0.5$  to 1.95 are shown at  $\theta = 90^\circ$  and  $30^\circ$  in Figures 2.8 and 2.9, respectively. At  $\theta = 90^\circ$ , the spectra are broad and smooth with peak frequencies scaling on the Strouhal number basis. However, at  $30^\circ$  to the jet axis, the spectrum shape changes and the peak becomes more marked and shifts to a lower frequency. Furthermore, the peak frequency does not scale as a Strouhal number and remains essentially constant at about 1400 Hz over the subsonic velocity range.

In examining the corresponding results at all angles to the jet axis (not shown here) between  $90^\circ$  and  $15^\circ$ , it was observed that the variation in spectral shapes at the supersonic velocities as one proceeds from  $90^\circ$  to  $15^\circ$  was rather interesting. At  $\theta = 90^\circ$ , the spectra throughout the velocity range are parallel in nature. This parallel "stacking" is retained as the observer angle  $\theta$  reduces to approximately  $45^\circ$ . It suggests that for  $\theta > 45^\circ$ , the eddy convection Mach number in the direction of the observer,  $M_c \cos \theta$ , is less than unity at all values of  $V_J/a_0$  up to 2.0, and therefore the convective amplification increases steadily as  $\theta$  reduces from  $90^\circ$  to  $45^\circ$ . At smaller ( $\theta < 45^\circ$ ) angles, however, it was observed that while the spectra at all subsonic velocities and the highest supersonic velocity considered ( $V_J/a_0 = 1.95$ ) essentially exhibit the parallel stacking pattern, the spectra for  $V_J/a_0 = 1.33$  and 1.65 do not conform to this pattern. At these two velocities, the spectrum levels are higher, especially at the higher frequencies, and the spectra therefore peak at frequencies which are higher than the peak frequencies for the spectra at all other velocities considered. The magnitudes of these observed effects increase as the observer moves further towards the jet axis, and at  $\theta = 30^\circ$  (Figure 2.9), the spectrum for  $V_J/a_0 = 1.65$  is in fact identical in level to the spectrum for  $V_J/a_0 = 1.95$  for frequencies above 3000 Hz. These observations suggest that at  $V_J/a_0 = 1.33$  and 1.65, the factor  $M_c \cos \theta$  in the convective amplification approaches unity at small angles to the jet axis, thus giving rise to high convective amplification. This feature of supersonic jet noise giving rise to high efficiency of convective amplification in the region of the Mach angle ( $M_c \cos \theta_m = 1$ ) has been described theoretically by

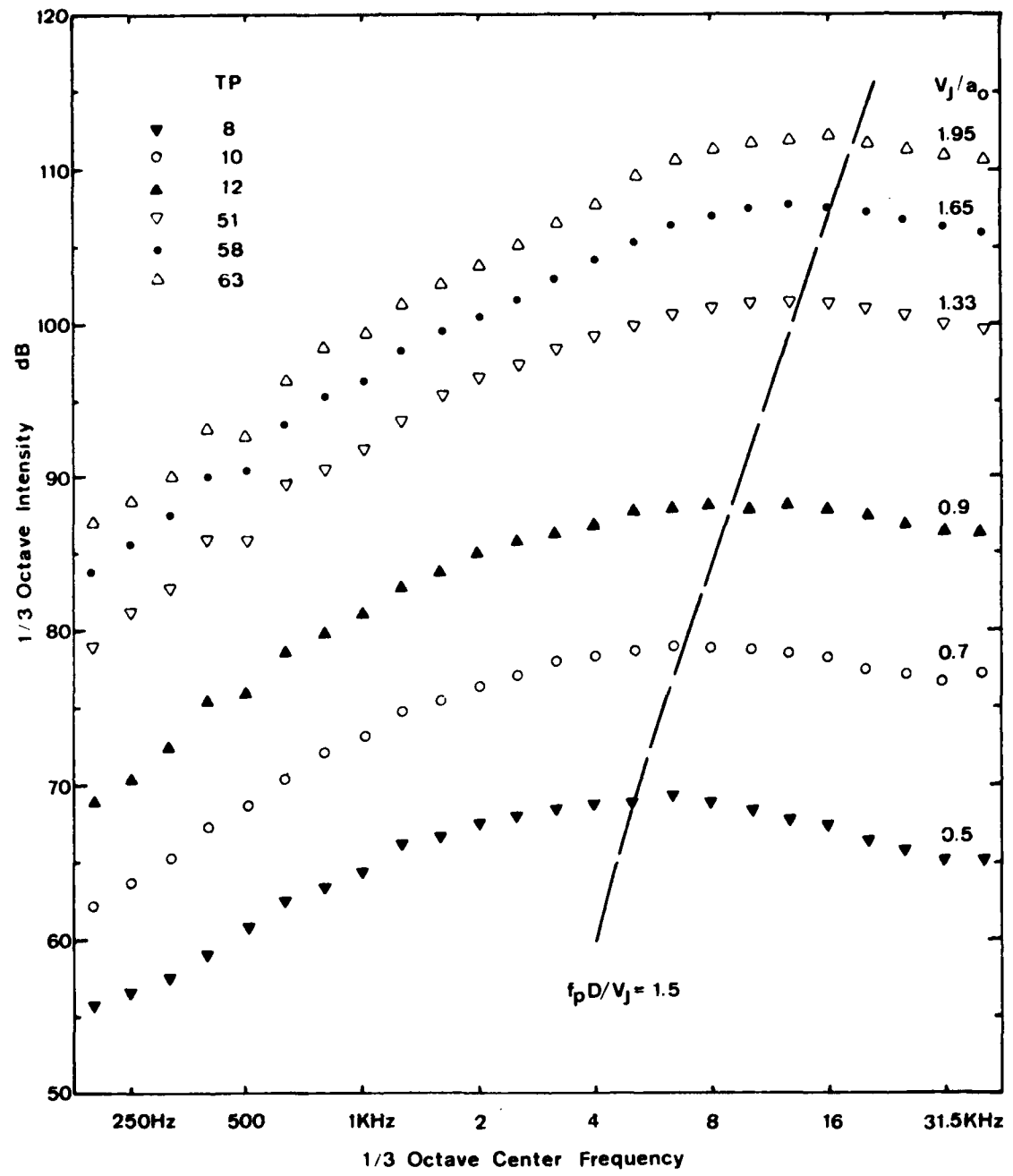


Figure 2.8 Variation of 1/3-Octave Spectra at  $\theta = 90^\circ$  with Jet Velocity:  
 $T_J/T_\infty \approx 1$

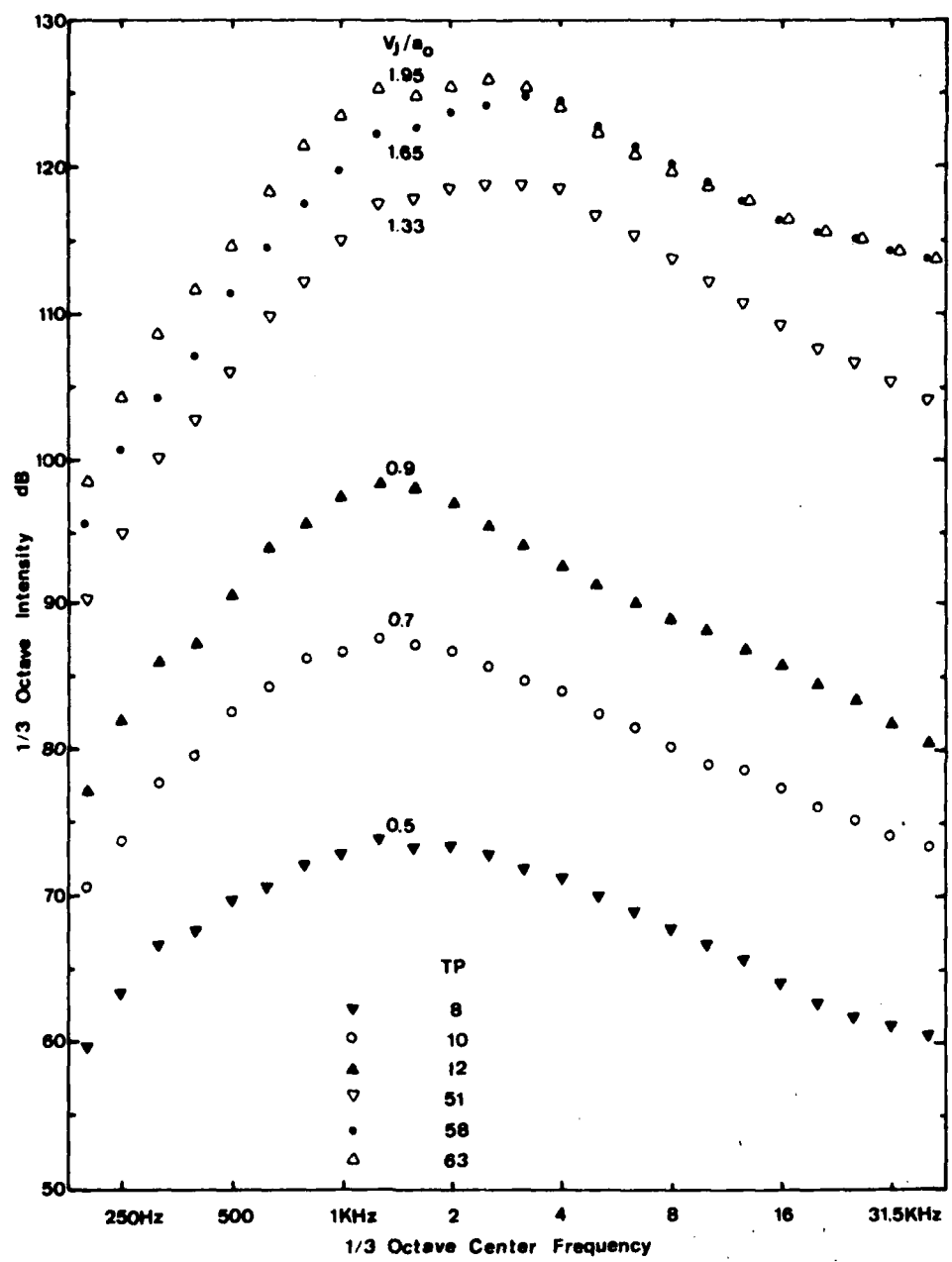


Figure 2.9 Variation of 1/3-Octave Spectra at  $\theta = 30^\circ$  with Jet Velocity:  
 $T_j/T_o \doteq 1$

Ffowcs Williams<sup>10</sup>, and the present measurements, carefully conducted to ensure the highly desirable shock-free conditions, appear to confirm the theoretical trends in a qualitative manner. Other possible explanations for these observations, for example, the refractive effects, cannot be discussed in any detail until such effects are examined and quantified at supersonic velocities. The theoretical efforts in this area are described in Section 3 of this report.

### 2.6.2 Effect of Jet Temperature $T_j/T_0$

The major effects of temperature on the noise spectrum and the variation of these effects throughout the speed range are illustrated at  $\theta = 45^\circ$  in Figures 2.10, 2.11, and 2.12. This angle is chosen for two reasons. First, the spectra at  $\theta = 90^\circ$  were presented and discussed previously by Tanna *et al*<sup>14</sup>. Second, this angle is in the vicinity of the peak radiation angle, and therefore warrants close examination.

At low jet velocity ( $V_j/a_0 = 0.5$ , Figure 2.11), the effect of elevated temperature is to provide a significant noise increase at the lower frequencies, and a significant noise reduction at the higher frequencies. As the jet velocity increases, the noise increase at lower frequencies becomes less dramatic, and at high velocities ( $V_j/a_0 = 1.47$ , Figure 2.12), the noise levels at these frequencies in fact decrease with jet heating. In contrast, the effect at higher frequencies does not reverse as one proceeds from low to high  $V_j/a_0$ ; the reductions in spectrum levels at these higher frequencies increase in magnitude as  $V_j/a_0$  increases throughout the speed range.

At all velocities considered, the effects of jet heating described above alter the peak frequencies in a consistent manner; the peak frequency decreases as the jet exit temperature ratio increases from unity. This suggests that it may be possible to scale the peak frequencies as a function of temperature, and this is discussed in the following subsection.

### 2.6.3 Peak Frequency

For *isothermal* jet operating conditions, the variation of measured peak frequency,  $f_p$ , with jet velocity at  $90^\circ$  and  $22.5^\circ$  to the jet axis is shown in Figure 2.13. At  $\theta = 90^\circ$ , the peak frequencies throughout the velocity range scale on the Strouhal number basis in the region of  $f_p D/V_j = 1.5$ , compared to the Strouhal number of 0.8 obtained by Lush<sup>8</sup> for data from an unheated jet over the subsonic velocity range. In contrast, at  $\theta = 22.5^\circ$ , the peak frequency does not scale on the Strouhal number basis. For  $V_j/a_0 < 1$ , the peak frequencies remain constant at approximately 1100 Hz, which corresponds to the Helmholtz number of  $f_p D/a_0 = 0.16$  and therefore agrees with  $f_p D/a_0 = 0.15$  obtained by Lush. As the jet velocity increases above  $V_j/a_0 = 1$ , the peak frequency at  $\theta = 22.5^\circ$  first increases, as noted previously, and then decreases as the velocity is increased beyond  $V_j/a_0 \approx 1.5$ . For  $V_j/a_0 > 2$ , the peak frequencies would presumably again scale on  $f_p D/a_0 \approx 0.16$ .

The variation of peak frequency with jet temperature was examined in detail at  $\theta = 90^\circ$ , and the results are presented in Figure 2.14. This figure represents the peak frequencies obtained from 1/3-octave spectra for

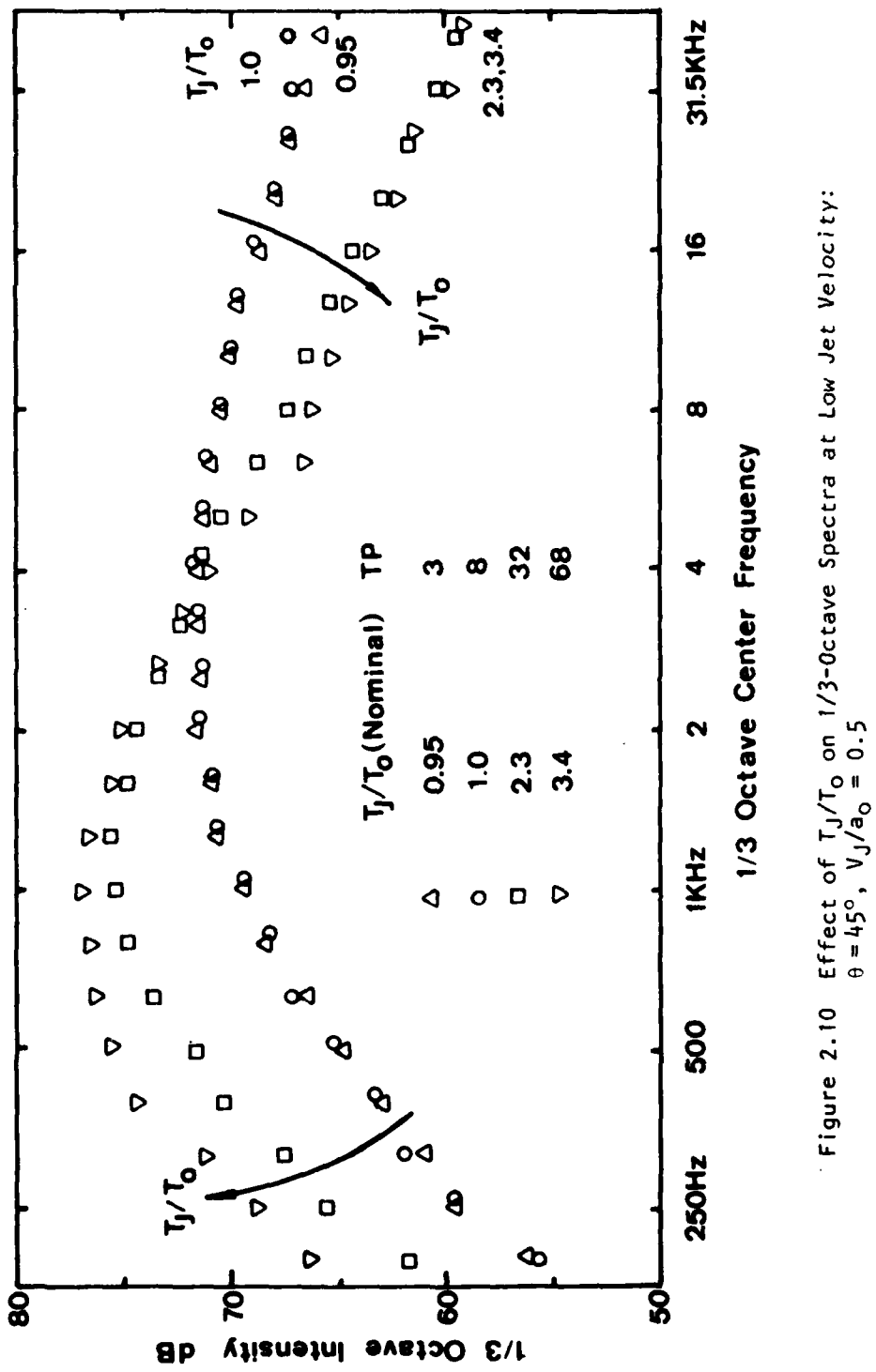


Figure 2.10 Effect of  $T_J/T_0$  on 1/3-octave Spectra at Low Jet Velocity:  
 $\theta = 45^\circ$ ,  $V_J/a_0 = 0.5$

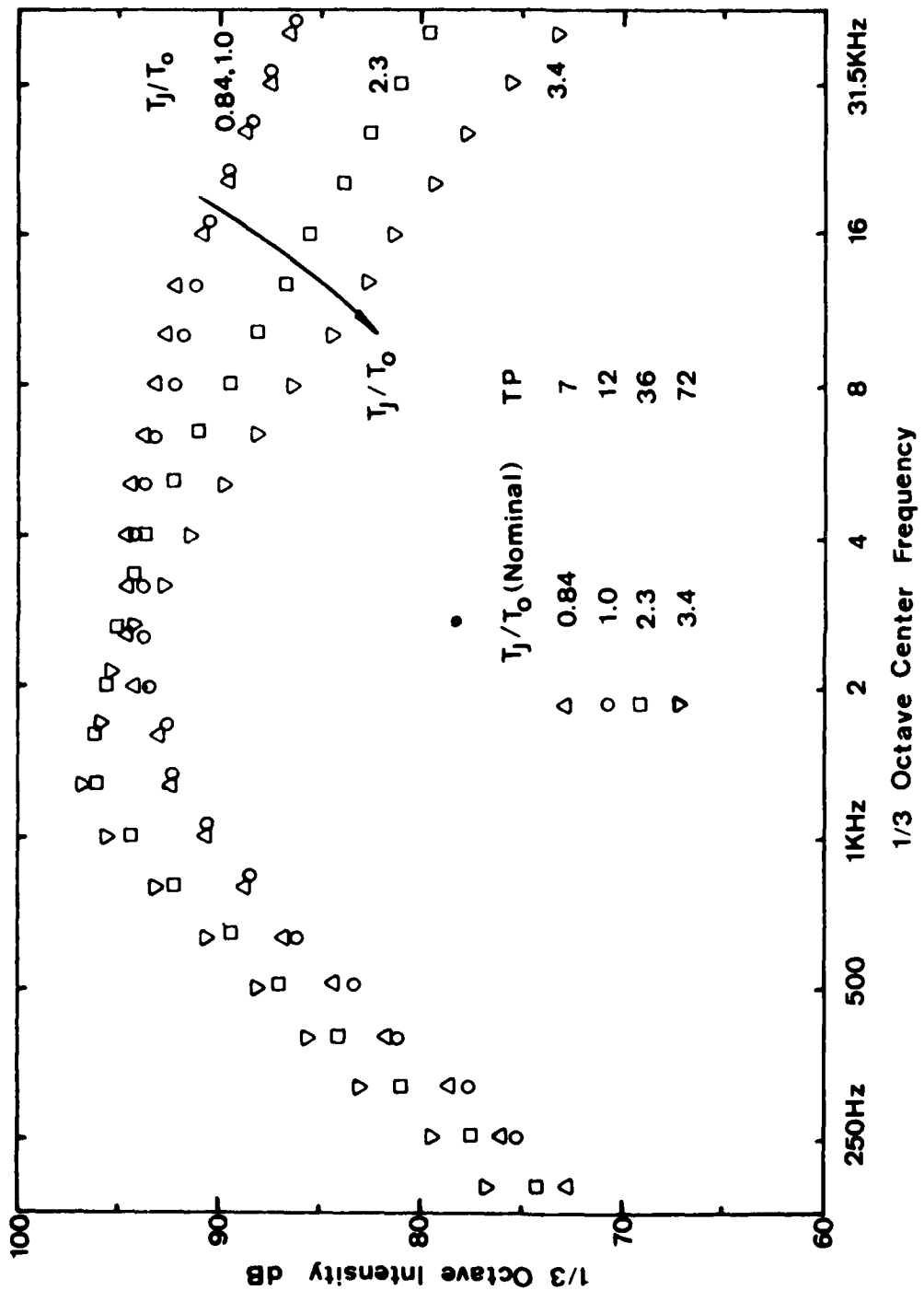


Figure 2.11 Effect of  $T_J/T_o$  on 1/3-Octave Spectra at Medium Jet Velocity:  
 $\theta = 45^\circ$ ,  $V_J/a_0 = 0.9$

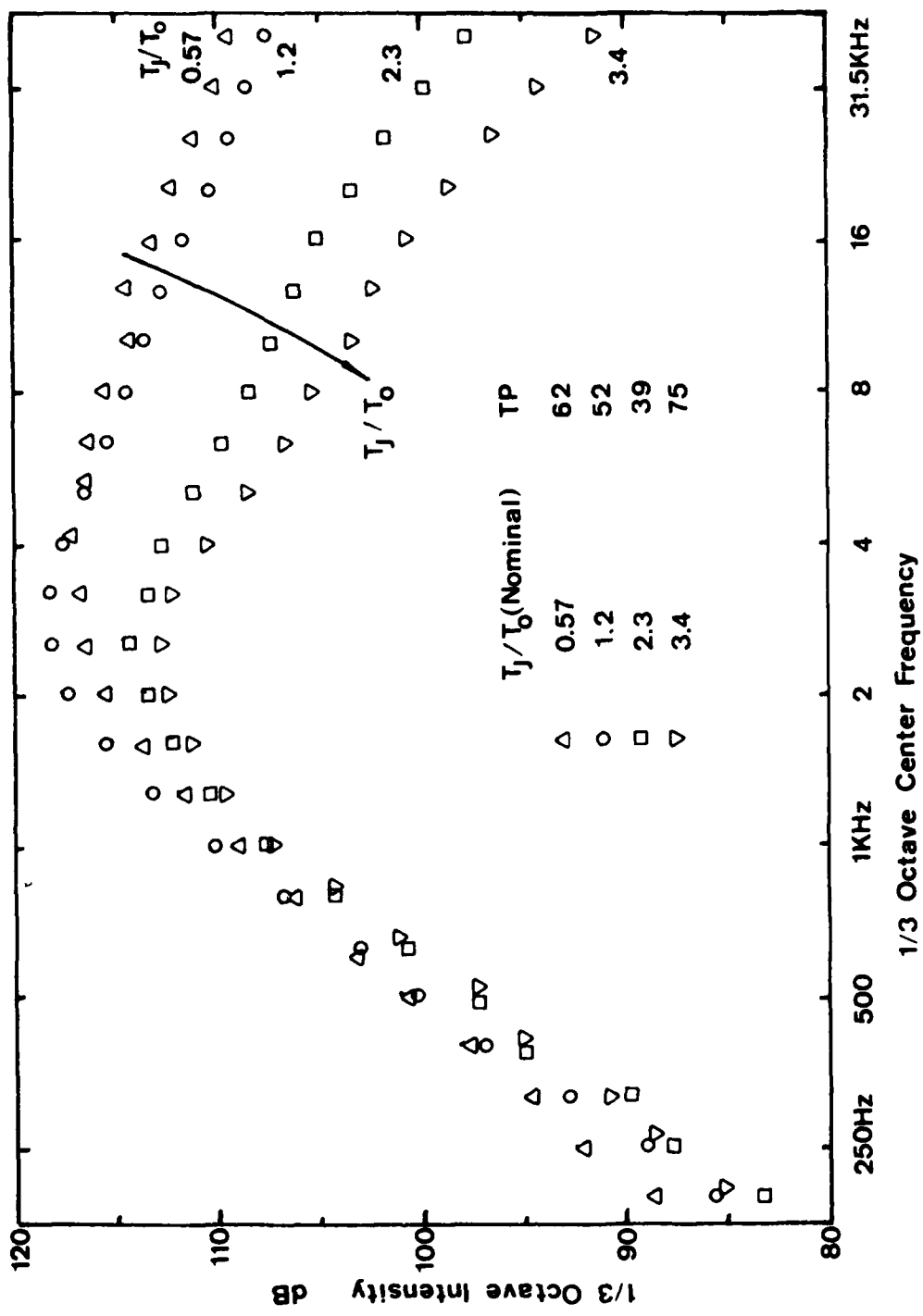


Figure 2.12 Effect of  $T_J/T_0$  on 1/3-Octave Spectra at High Jet Velocity:  
 $\theta = 45^\circ$ ,  $V_J/a_0 = 1.47$

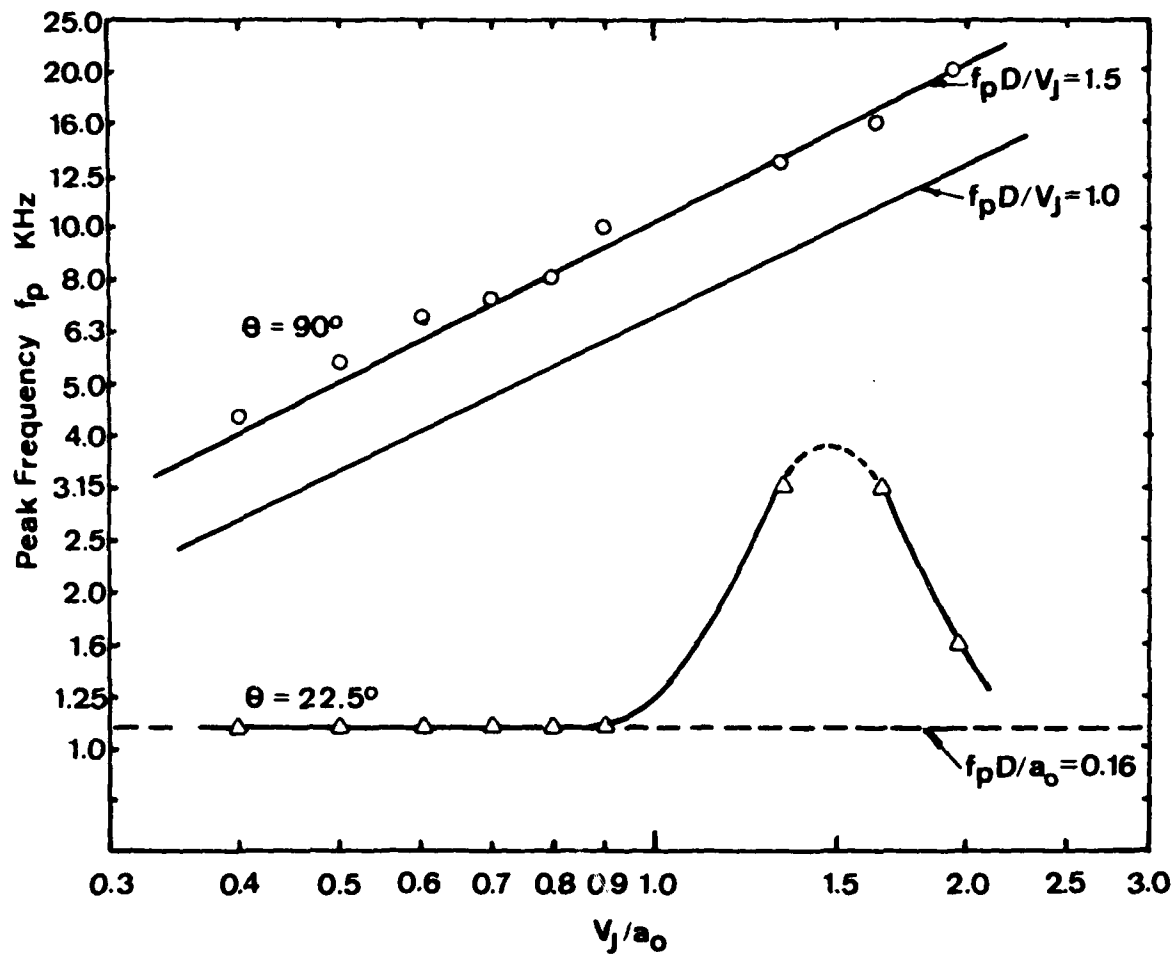


Figure 2.13 Variation of Peak Frequency with Jet Velocity:  $T_j/T_0 \approx 1$

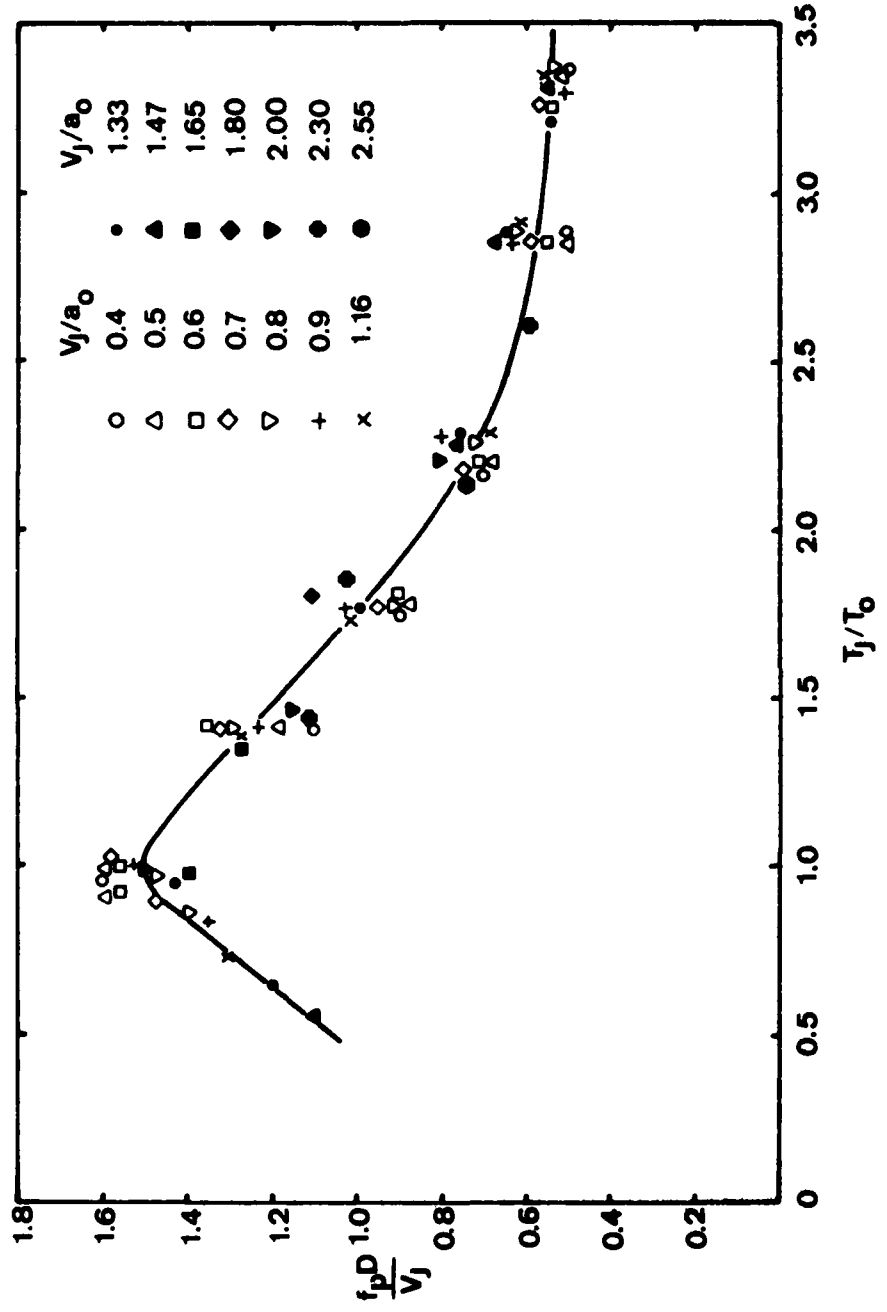


Figure 2.14 Variation of Peak Frequency with Jet Velocity and Temperature:  $\theta = 90^\circ$

approximately 70 jet operating conditions, covering the range of  $V_J/a_0$  from 0.4 to 2.55 and the range of  $T_J/T_0$  from 0.57 to 3.4. At each nominal value of  $T_J/T_0$  considered, the peak frequencies scale on the Strouhal number basis, as shown by the clusters of experimental points in Figure 2.14. The variation of the peak Strouhal number with temperature is shown by drawing a smooth curve through the points and the result is rather interesting. It shows that the peak Strouhal number is maximum when the jet exit temperature is close to the ambient temperature, and it decreases progressively as  $T_J/T_0$  either increases or decreases from unity.

## 2.7 VELOCITY DEPENDENCE OF 1/3-OCTAVE INTENSITY AT CONSTANT SOURCE STROUHAL NUMBERS

### 2.7.1 Isothermal ( $T_J/T_0 = 1$ ) Jet

The turbulent mixing noise data for isothermal jet operating conditions over the range of  $V_J/a_0$  from 0.5 to 1.95 have been analyzed in 1/3-octave bands at particular values of the source Strouhal number  $f_s D/V_J$  [Equation (2-6)], in accordance with the technique adopted by Lush and which was described briefly in paragraph 2.3. It is reminded that in all analyses presented in this section,  $M_c$  is taken to be equal to 0.67  $V_J/a_0$  and  $\alpha = 0.3$ , as suggested by jet flow measurements at low velocities<sup>16</sup>.

The dependencies of 1/3-octave intensities on jet velocity at three angles to the jet axis, namely 90°, 45° and 22.5°, are shown in Figures 2.15, 2.16, and 2.17, respectively. The five values of source Strouhal number considered are

$$\frac{f_s D}{V_J} = 0.03, 0.1, 0.3, 1.0, \text{ and } 3.0.$$

The predictions from the freely-convection quadrupole theory, Equation (2-3), are also shown on these figures.

At 90° to the jet axis (Figure 2.15), the results follow the theoretical prediction,  $I \sim (V_J/a_0)^{7.5} \times [1 + \alpha^2 M_c^2]^{-5/2}$ , at all frequencies with very high accuracy, the majority of the points being within 1 dB. We may also note in passing that an eighth power of jet velocity with a larger value of  $\alpha$  will also result into an equally good correlation between theory and experiment.

The velocity dependence at 45° (Figure 2.16) shows that the theory (solid line) fits the results well at the two lowest frequencies, i.e.,  $f_s D/V_J = 0.03$  and 0.1. At the next value of the frequency parameter, 0.3, the theory is in agreement at subsonic velocities, but overestimates the intensity as the jet velocity increases in the supersonic regime. At the two highest frequencies, i.e.,  $f_s D/V_J = 1.0$  and 3.0, the measurements (broken line) fall well below the expected variation, the magnitude of the overestimation increasing progressively with increasing frequency.

The velocity dependence at  $\theta = 22.5^\circ$  (Figure 2.17) shows similar features, except that the measurements begin to fall below the theoretical velocity

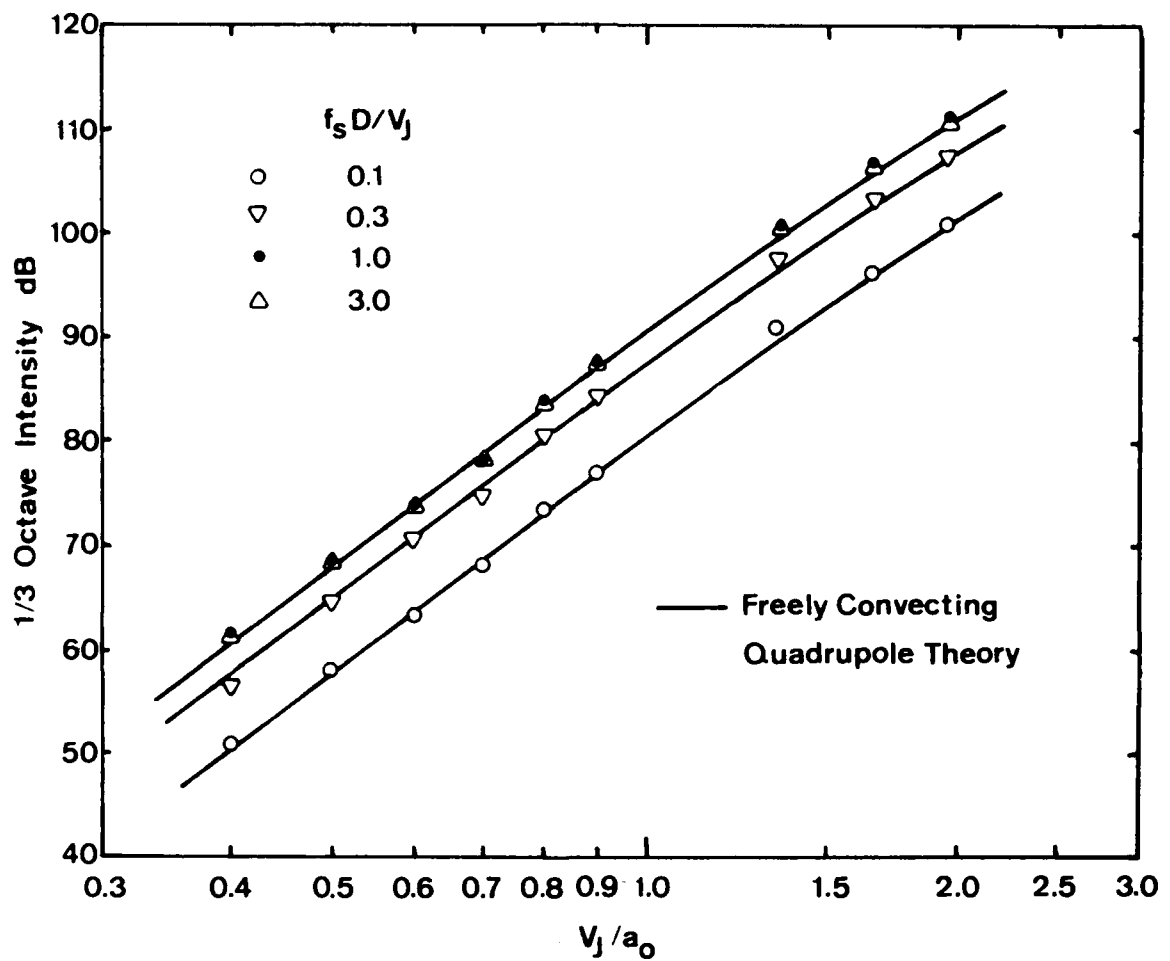


Figure 2.15 Velocity Dependence of  $1/3$ -Octave Intensity at  $\theta = 90^\circ$ :  $T_J/T_O \doteq 1$

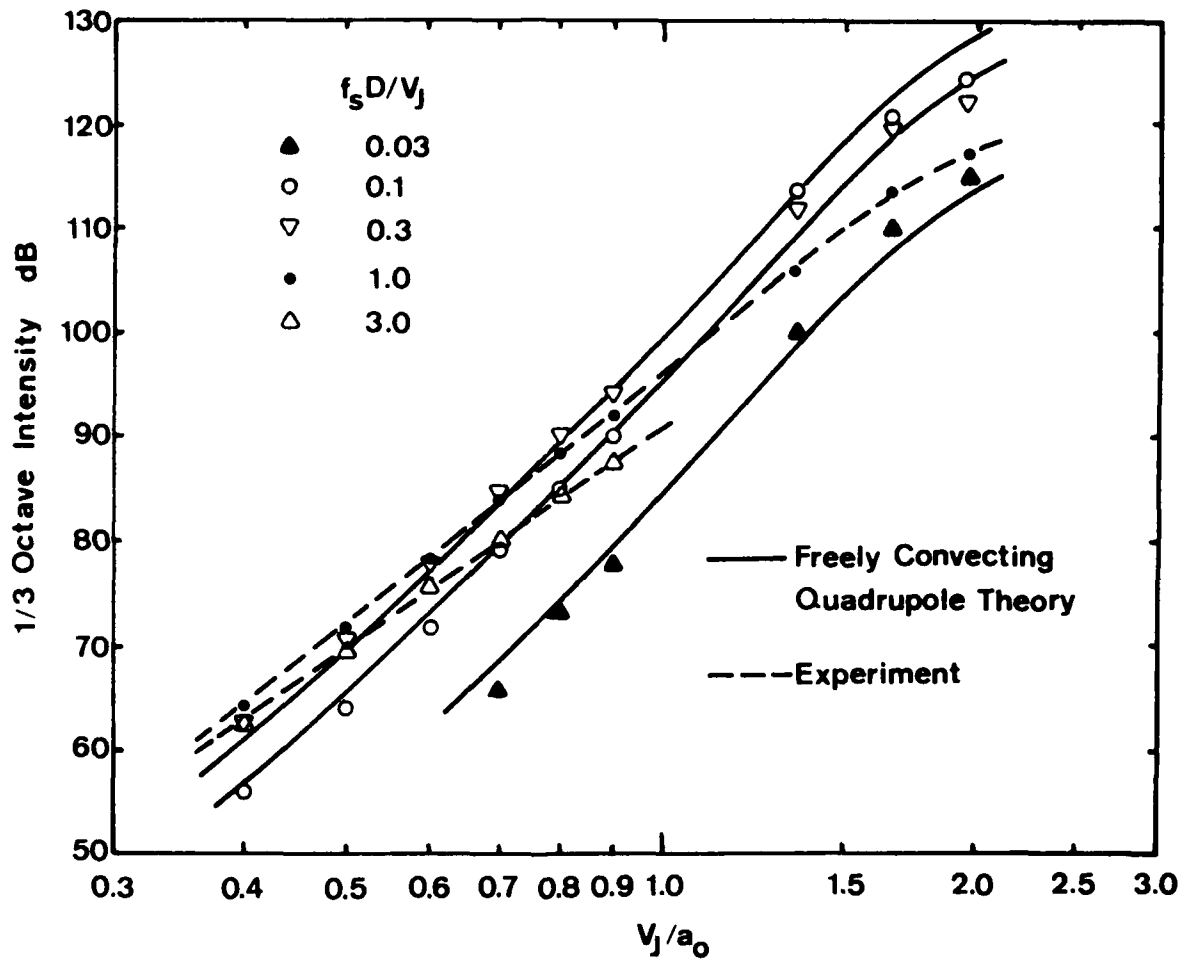


Figure 2.16 Velocity Dependence of 1/3-Octave Intensity at  $\theta = 45^\circ$ :  $T_J/T_O \approx 1$

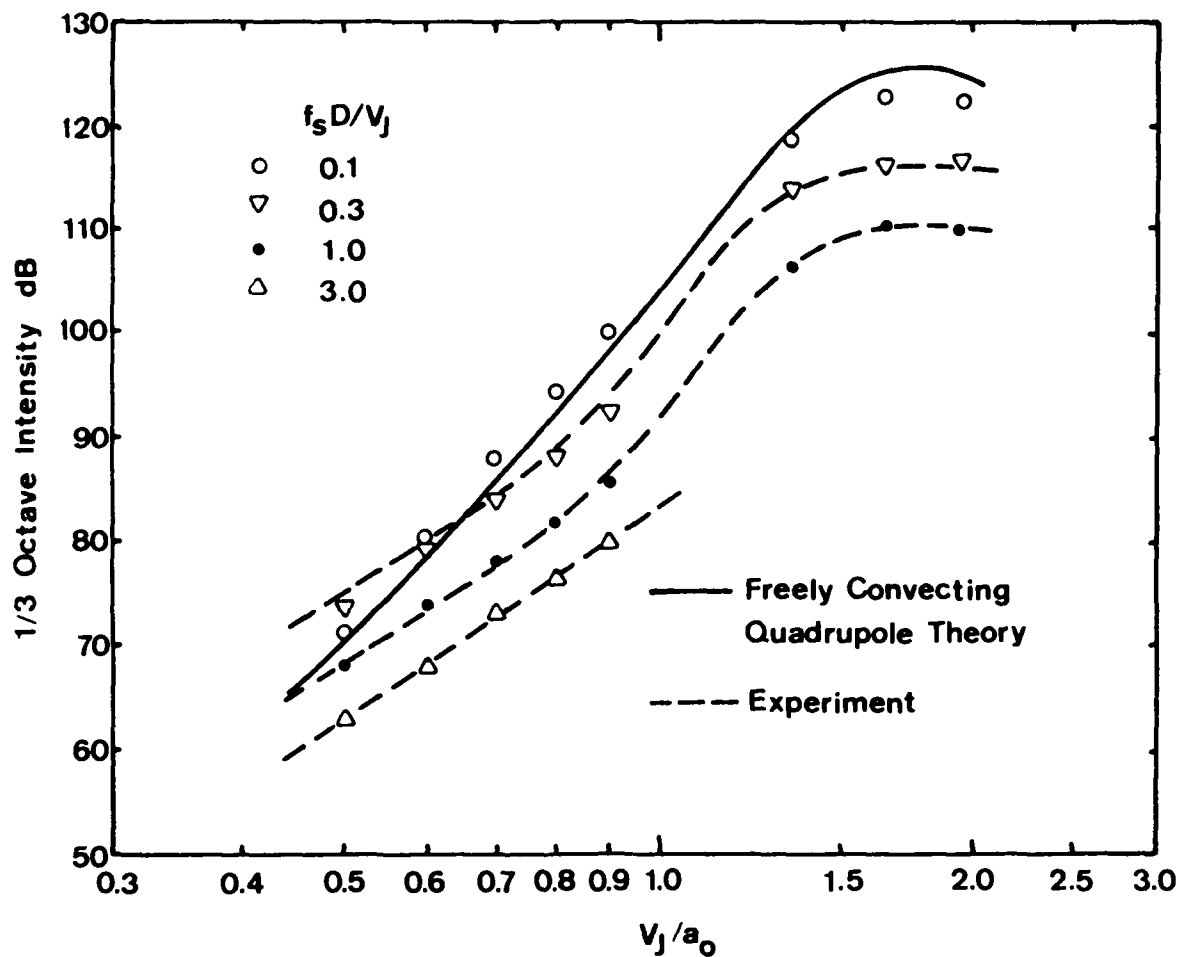


Figure 2.17 Velocity Dependence of 1/3-Octave Intensity at  $\theta = 22.5^\circ$ :  
 $T_J/T_O \approx 1$

dependence at a lower value of the frequency parameter, i.e.,  $f_s D/V_J = 0.1$ . At frequencies below this value, the predicted variation of intensity with jet velocity (solid line) is approximately in agreement with measurements, whereas at frequencies above  $f_s D/V_J = 0.1$ , the measurements (broken line) tend to fall well below the expected variation.

### 2.7.2 Effect of Jet Temperature $T_J/T_0$

The influence of temperature on the velocity dependence of 1/3-octave intensity is illustrated at  $90^\circ$  to the jet axis. The two extremes of the frequency parameter, namely  $f_s D/V_J = 0.1$  and 3.0, are considered in Figures 2.18 and 2.19, respectively. As in paragraph 2.4.2, no theoretical velocity scaling is implied in these figures. The curves through the experimental points are shown merely to illustrate the measured trends.

At low source Strouhal number ( $f_s D/V_J = 0.1$ , Figure 2.18), the effects of jet heating are qualitatively similar to the effects observed for the velocity dependence of overall intensity, described in paragraph 2.4.2. That is, the noise increases at low velocities, and the noise decreases at high velocities. The velocity exponent decreases at elevated temperatures. It also appears that the breakpoint (value of  $V_J/a_0$  at which the effect of heating relative to  $T_J/T_0 = 1$  reverses) increases as  $T_J/T_0$  increases.

At high source Strouhal number ( $f_s D/V_J = 3.0$ , Figure 2.19), this breakpoint is shifted to a much lower value of  $V_J/a_0$ . Reductions in noise levels are now measured almost throughout the velocity range considered, and the magnitudes of these reductions with heating increase significantly as  $V_J/a_0$  increases.

## 2.8 DIRECTIVITY OF 1/3-OCTAVE INTENSITY AT CONSTANT SOURCE STROUHAL NUMBERS

The directivities of turbulent mixing noise at constant source Strouhal numbers are presented first for the isothermal jet operating conditions, and later, the effects of jet efflux temperature are established at the two extremes of the frequency parameter. Although the presentation of data in this form requires a large effort, the final plots are most suitable for comparison with theoretical investigations. Using these plots, it is not only possible to quantify the discrepancies between measurements and the freely-convection quadrupole theory and define the regimes over which they exist, but they are also very convenient in testing the validity of any other theoretical model which accounts for the acoustic/mean-flow interaction phenomena throughout the frequency range.

### 2.8.1 Isothermal ( $T_J/T_0 = 1$ ) Jet

The directivities at various jet exit velocities for the same five values of  $f_s D/V_J$  considered previously are shown systematically in Figures 2.20 through 2.24. The directivities due to quadrupole convection in free space [Equation (2-4)] are also shown as solid lines, and it should be noted that since they are plotted relative to the experimental values at  $\theta = 90^\circ$  and not

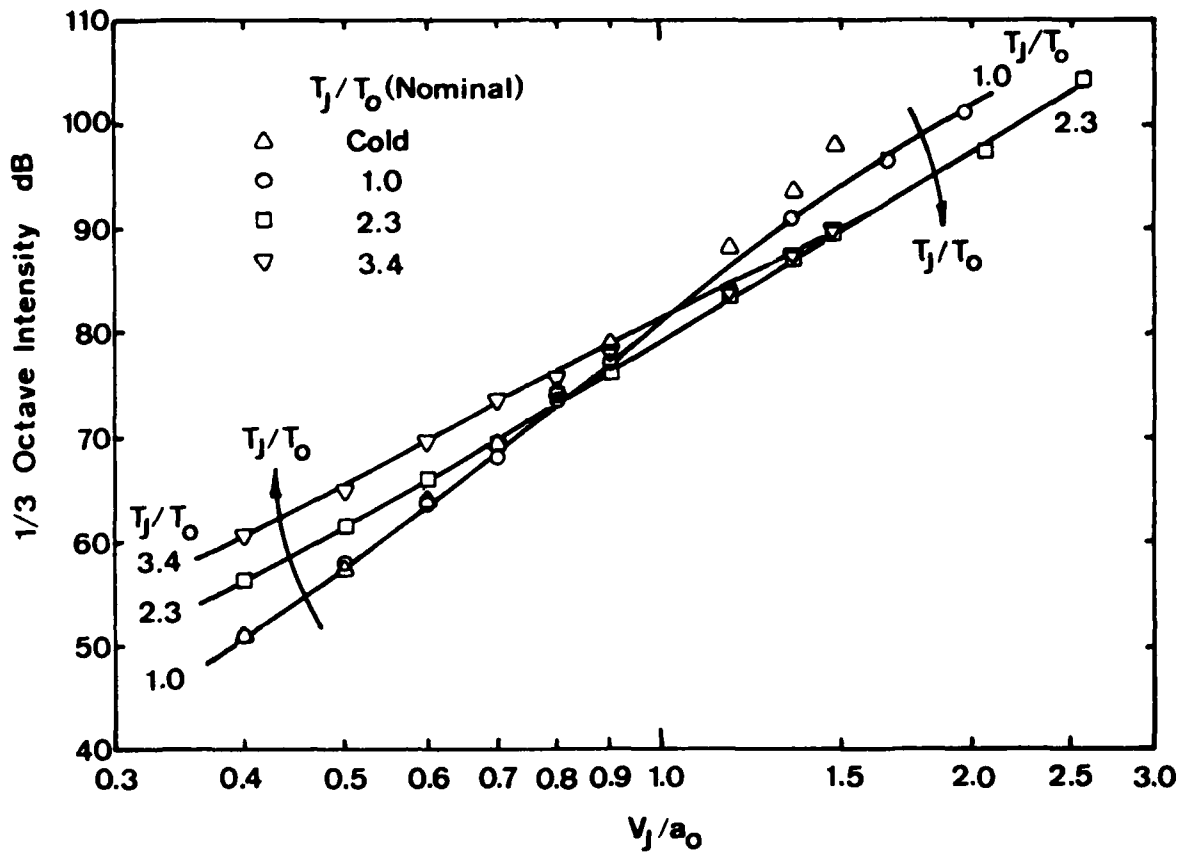


Figure 2.18 Effect of  $T_J/T_o$  on Velocity Dependence of 1/3-Octave Intensity:  
 $\theta = 90^\circ$ ,  $f_S D/V_J = 0.1$

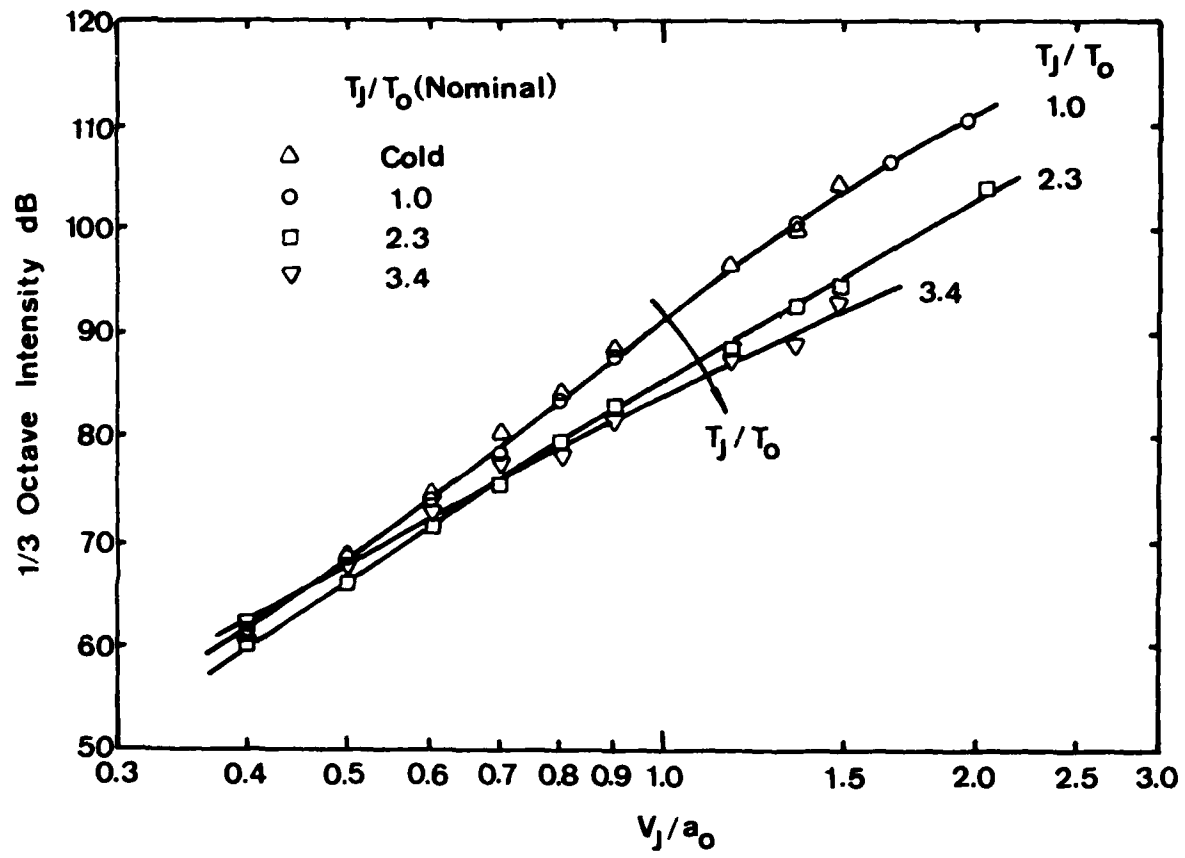


Figure 2.19 Effect of  $T_J/T_0$  on Velocity Dependence of  $1/3$ -Octave Intensity:  
 $\theta = 90^\circ$ ,  $f_s D/V_J = 3.0$

adjusted vertically to give the best fit, they represent the correct amount of convective amplification (or convective "attenuation" as the case may be) relative to the level at 90°.

At the two lowest values of the non-dimensional frequency parameter, namely  $f_s D/V_J = 0.03$  and 0.1 (Figures 2.20 and 2.21), the theoretical directivities are in fairly good agreement with measurements, except at small and large angles to the jet axis, where the measured levels are consistently higher. The amount of this underestimation at low frequencies tends to increase as the jet velocity increases. At angles between approximately 45° and 90°, the agreement between theory and experiment can be improved significantly by using the following argument. At these lower frequencies, recent source location studies indicate that the sources in the jet flow are located at some distance downstream of the nozzle exit plane. The center of the observer arc should therefore be taken in the region where the sources exist, rather than at the nozzle exit plane. In the present comparison, if the sources at these lower frequencies are assumed to be located at approximately 10 nozzle diameters downstream, which appears to be reasonable from available evidence, then the observer angles are modified and the corresponding modified theoretical directivities are also shown in Figures 2.20 and 2.21. It can be seen that while this procedure makes little difference at the extremes of observer angle (except at the highest velocity, when  $M_c \cos\theta$  becomes greater than unity at small angles), the agreement between theory and experiment at  $\theta$  between 45° and 90° is considerably improved at all jet velocities.

It is admitted that the above procedure does introduce a slight deterioration in the correlation at some angles in the forward arc, but in general, a careful examination reveals that the amount of benefit gained with this procedure outweighs the slight damage. Besides, it is physically correct to use this procedure at the lower frequencies.

At the next value of source Strouhal number,  $f_s D/V_J = 0.3$  (Figure 2.22), the agreement between theory and experiment is again reasonable between  $\theta = 45^\circ$  and 90°, and this can be improved significantly using the above argument of choosing the correct source location. At smaller angles to the jet axis, however, the theory now overestimates the 1/3-octave intensity, showing that refractive effects are beginning to emerge at this frequency. The overestimation in fact becomes worse as the jet velocity increases. Furthermore, in Figure 2.22, it is interesting to note the observation, made previously for the directivity of overall intensity, that while the directivities for  $V_J/a_0 = 0.5, 0.9$  and 1.95 are parallel in nature, the directivity for  $V_J/a_0 = 1.33$  does not fall into this pattern. The levels at smaller angles are higher for  $V_J/a_0 = 1.33$ . Whether this is due to  $M_c \cos\theta$  approaching unity or the consequence of the refractive phenomena needs to be ascertained.

At the next higher frequency given by  $f_s D/V_J = 1.0$ , Figure 2.23 shows that the effects of refraction are present even at larger angles to the jet axis. The freely-convection quadrupole theory (directivity denoted by (a) in Figure 2.23) now overestimates in the rear arc ( $\theta < 90^\circ$ ) and underestimates in the forward arc ( $\theta > 90^\circ$ ) by large amounts at this frequency. The magnitude of the discrepancy in general increases as the jet velocity increases or as the observer moves away from the 90° pivot. Also shown in Figure 2.23 are theoretical directivities based on three powers of Doppler factor [denoted by (b)], i.e.,

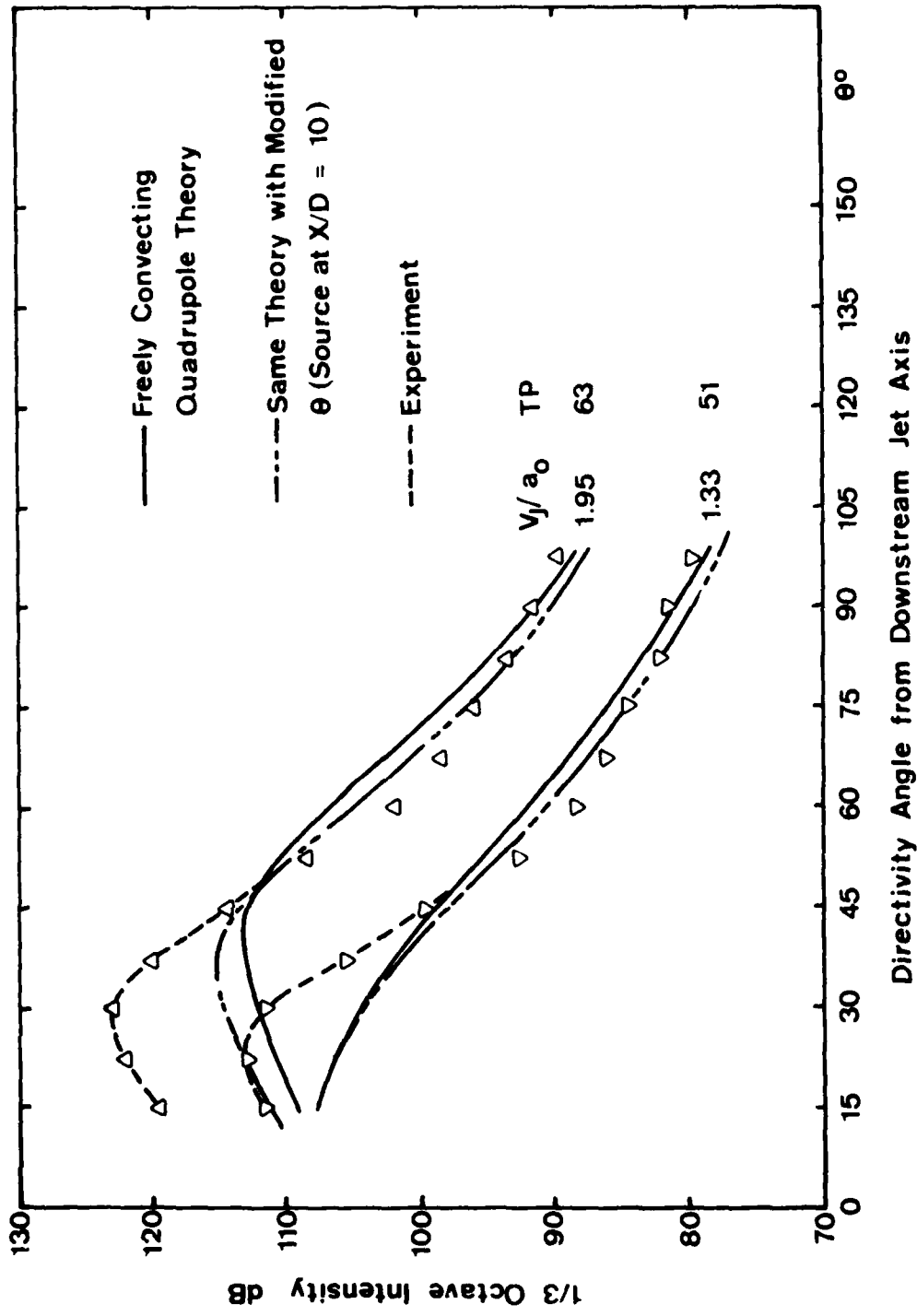


Figure 2.20 Directivity of 1/3-Octave Intensity at  $f_s D/V_J = 0.03$ :  $T_J/T_0 \approx 1$

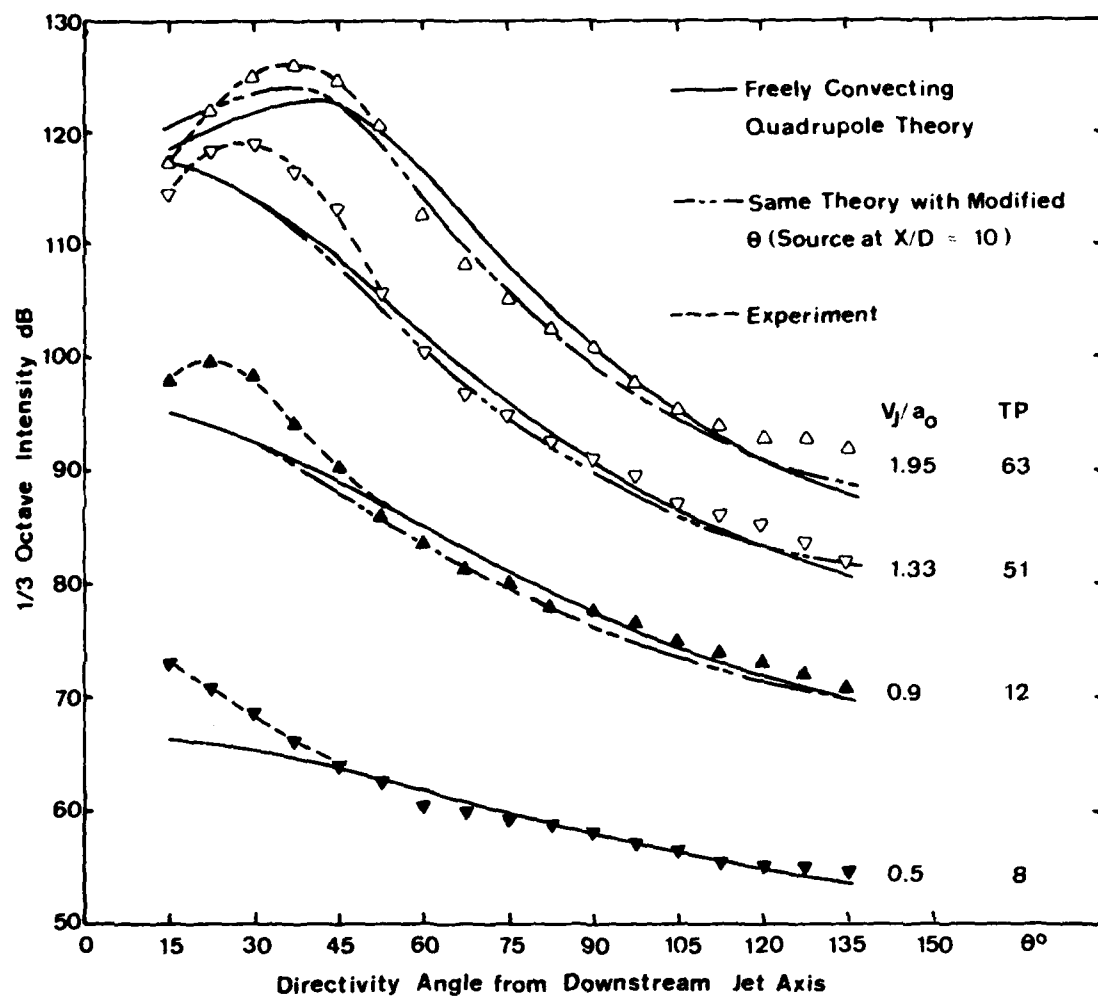


Figure 2.21 Directivity of 1/3-Octave Intensity at  $f_s D/V_J = 0.1$ :  $T_J/T_O \approx 1$

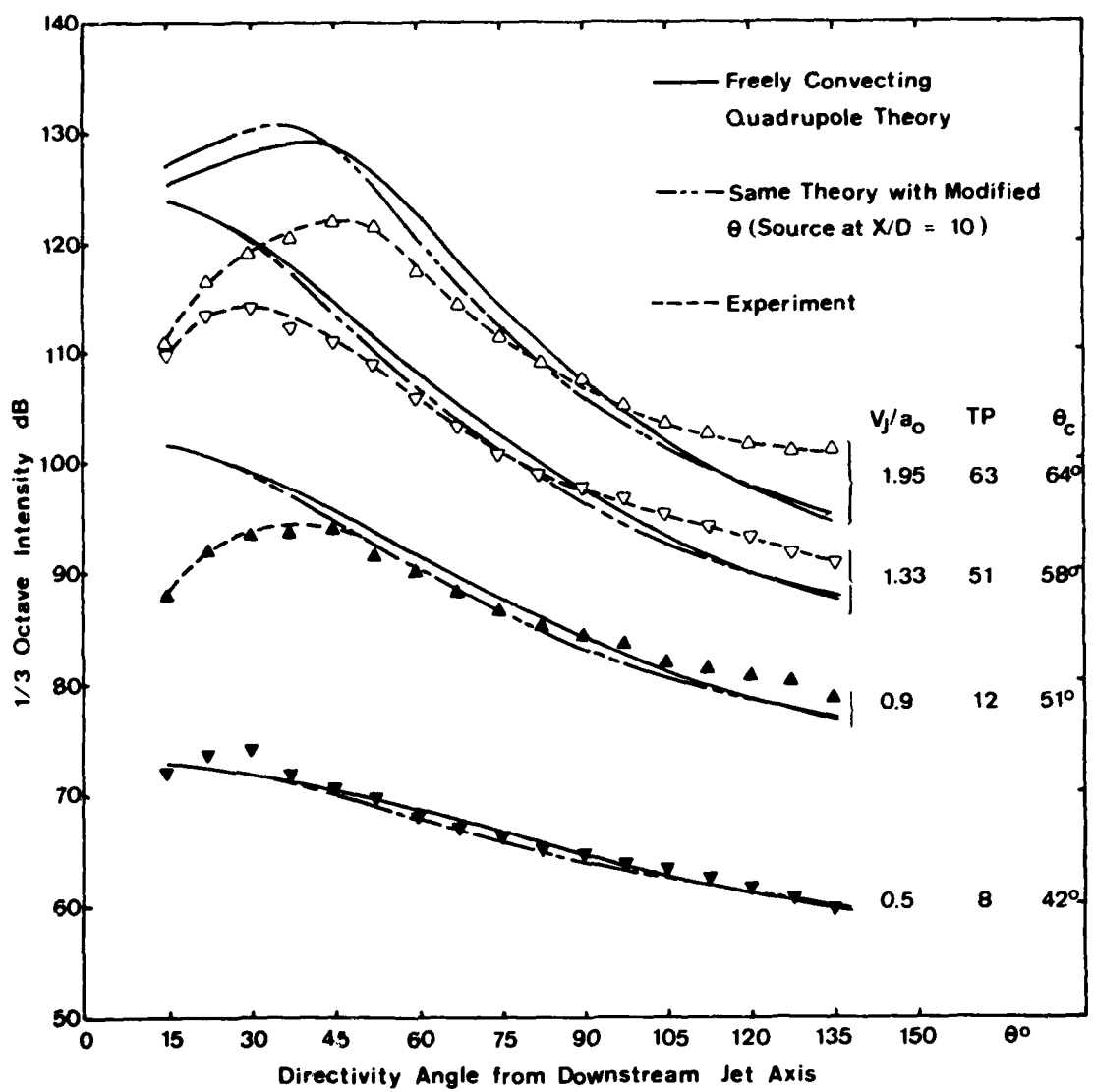


Figure 2.22 Directivity of 1/3-Octave Intensity at  $f_s D/V_J = 0.3$ :  $T_J/T_0 \approx 1$

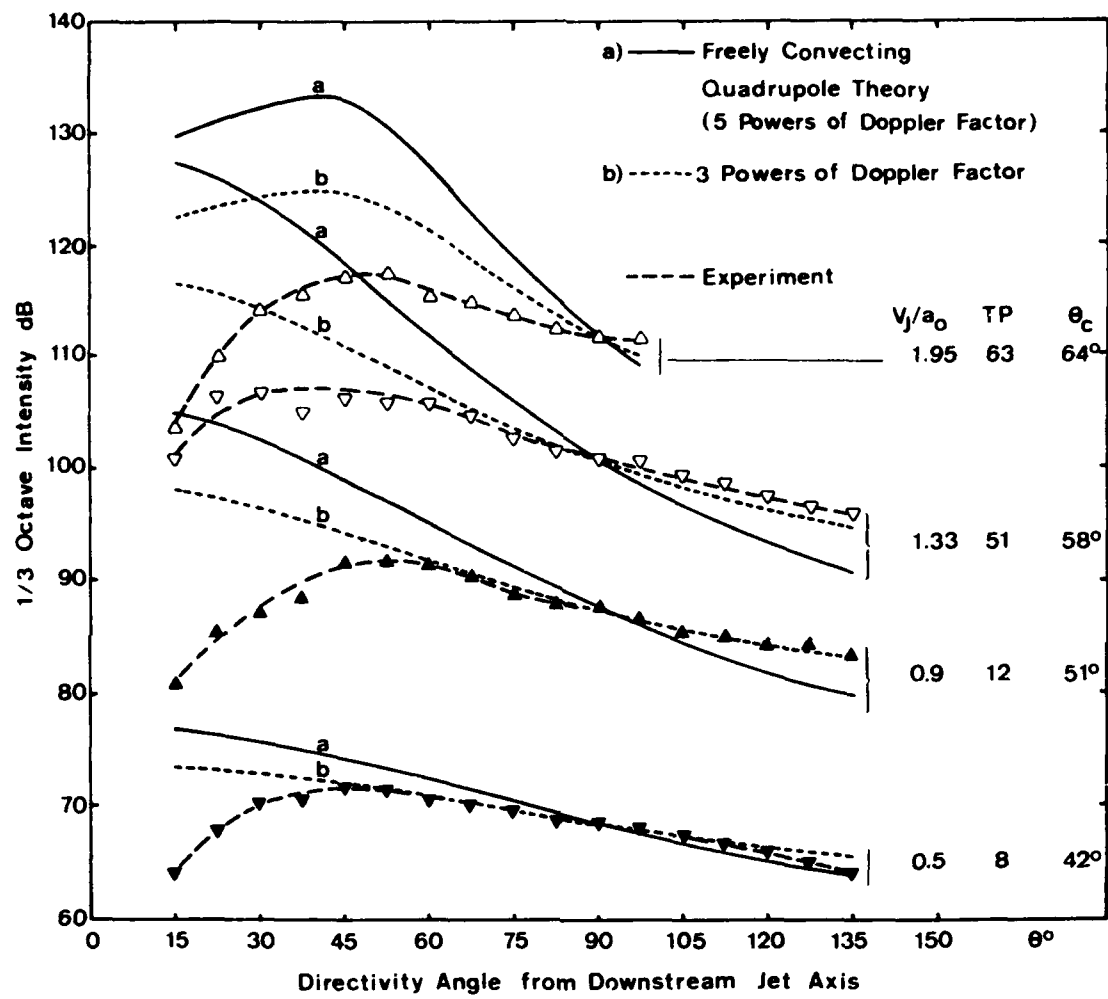


Figure 2.23 Directivity of 1/3-Octave Intensity at  $f_s D/V_J = 1.0$ :  $T_J/T_O \doteq 1$

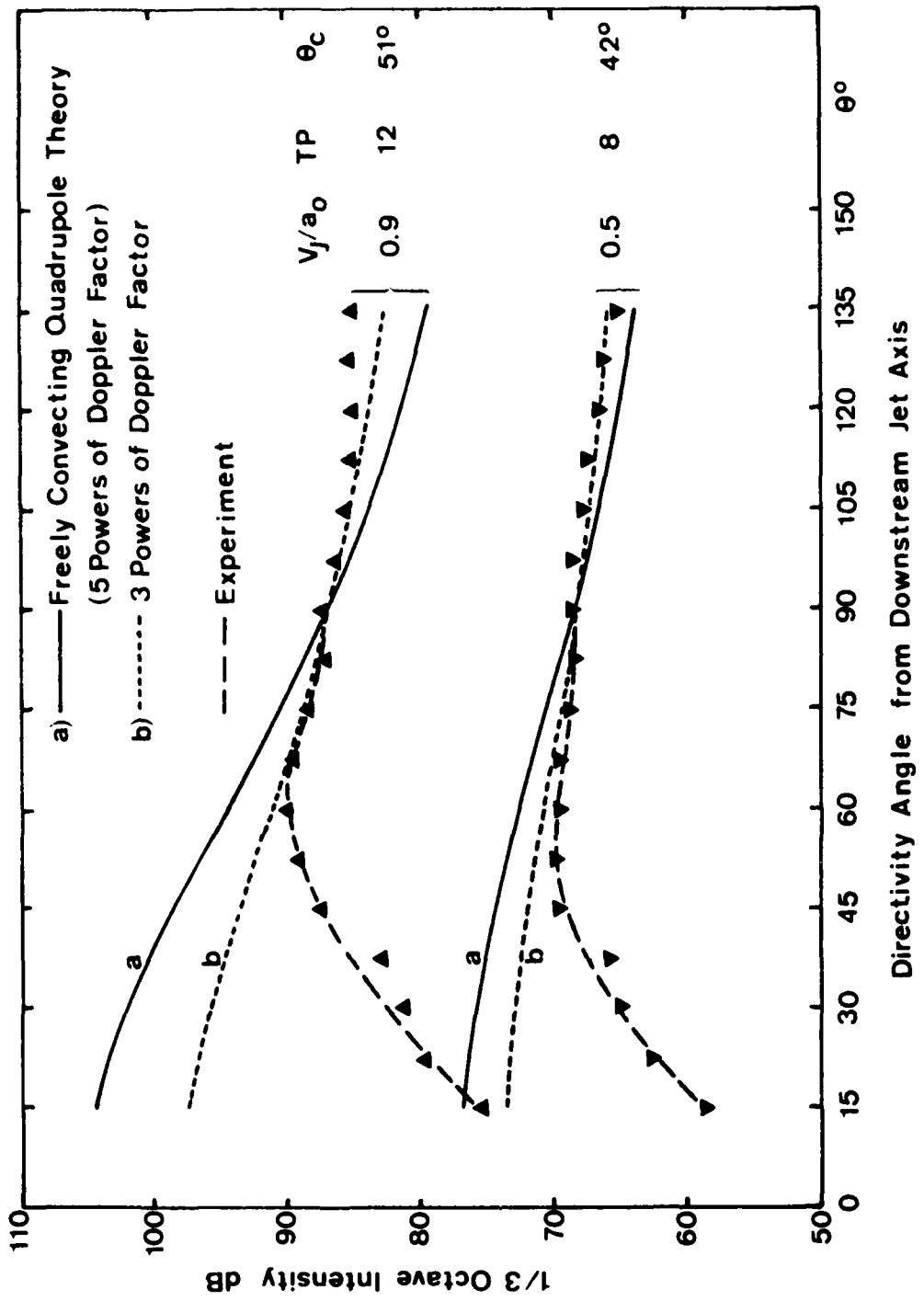


Figure 2.24 Directivity of 1/3-octave Intensity at  $f_S D/V_J = 3.0$ :  $\tau_J/\tau_o \doteq 1$

$$I = [(1 - M_c \cos \theta)^2 + \alpha^2 M_c^2]^{-3/2} \text{ with}$$

$$M_c = 0.67 V_j/a_0 \text{ and } \alpha = 0.3, \quad (2-7)$$

as opposed to the normally accepted five powers for freely convected quadrupoles. It can be seen that at angles greater than the "cone of silence" angle, given by  $\theta_c = \sec^{-1}(1 + M_c)$  from ray acoustics, the directivities predicted by three powers of Doppler factor are in very good agreement with the measurements, except at the highest velocity,  $V_j/a_0 = 1.95$ , where some overestimation still occurs. This observed angular dependence of intensity at high frequencies and at angles outside the zone of silence is in agreement with the results of the ongoing theoretical work, which is described in Section 3 of this Volume.

Finally, for the comparisons at the highest frequency given by  $f_s D/V_j = 3.0$  and shown in Figure 2.24, the above comments for Figure 2.23 apply here as well. In addition, it can be seen that since the frequency is higher in this case, the effects of refraction are even greater than those observed in Figure 2.23. The theoretical directivity given by Equation (2-4) does not resemble the measured directivity shapes at all. In contrast, the angular dependence given by Equation (2-7) is in very good agreement with the measurements roughly outside the zone of silence ( $\theta > \theta_c$ , see Figure 2.24).

### 2.8.2 Effect of Jet Temperature $T_j/T_0$

The influence of jet exhaust temperature on the directivity of 1/3-octave intensity was investigated in detail, and the purpose of this subsection is to present the major effects throughout the velocity range in sufficient detail. Specifically, the variation of directivity with temperature is presented at the two extremes of the source Strouhal number for three jet efflux velocities,  $V_j/a_0 = 0.5, 0.9$  and  $1.47$ . The results are shown in Figure 2.25 through 2.30. The curves through the experimental points in these figures are provided purely in order to illustrate the measured trends; they do not imply any theoretical scaling of angular dependence with temperature.

#### 2.8.2.1 Low frequency

At low source Strouhal number,  $f_s D/V_j = 0.1$ , the effect of  $T_j/T_0$  on the directivity as one proceeds from low  $V_j/a_0$  to high  $V_j/a_0$  is most revealing – see Figures 2.25, 2.26, and 2.27. At low velocity ( $V_j/a_0 = 0.5$ , Figure 2.25), the intensity at all angles increases with heating, and the magnitude of this increase is nearly independent of  $\theta$ ; the directivities at various  $T_j/T_0$  are virtually parallel. In contrast, at high velocity ( $V_j/a_0 = 1.47$ , Figure 2.27), the intensity decreases with heating. However, in this case, the magnitude of this reduction is indeed angular dependent. At medium values of jet exit velocity ( $V_j/a_0 = 0.9$ , Figure 2.26), the effect of  $T_j/T_0$  is not so dramatic, as observed previously for the overall intensity results. There is a slight increase in level at most angles, but a small reduction near the downstream jet axis.

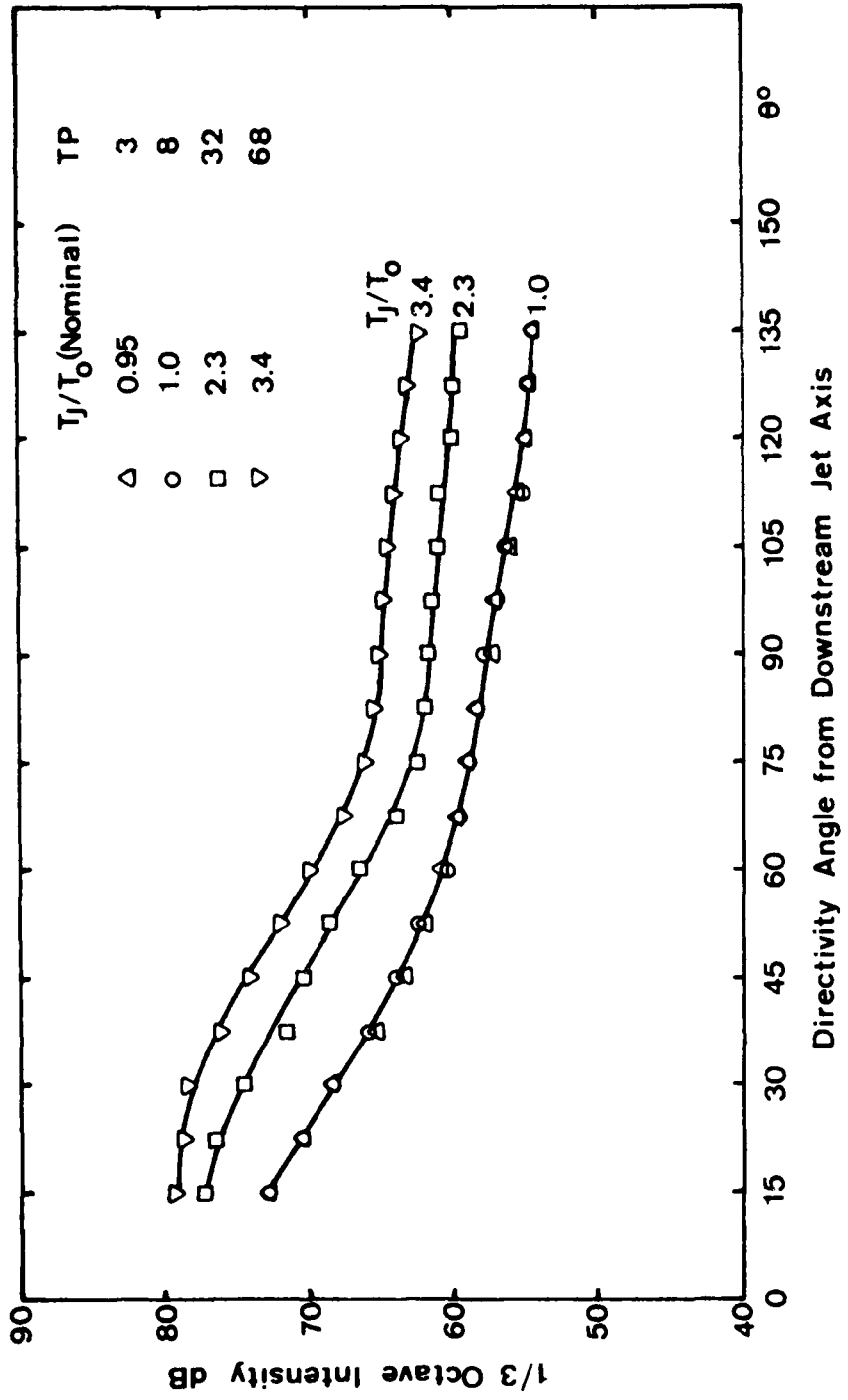


Figure 2.25 Effect of  $T_J/T_0$  on Directivity of  $1/3$ -Octave Intensity at  
 $V_J/a_0 = 0.5$ ;  $f_s D/V_J = 0.1$

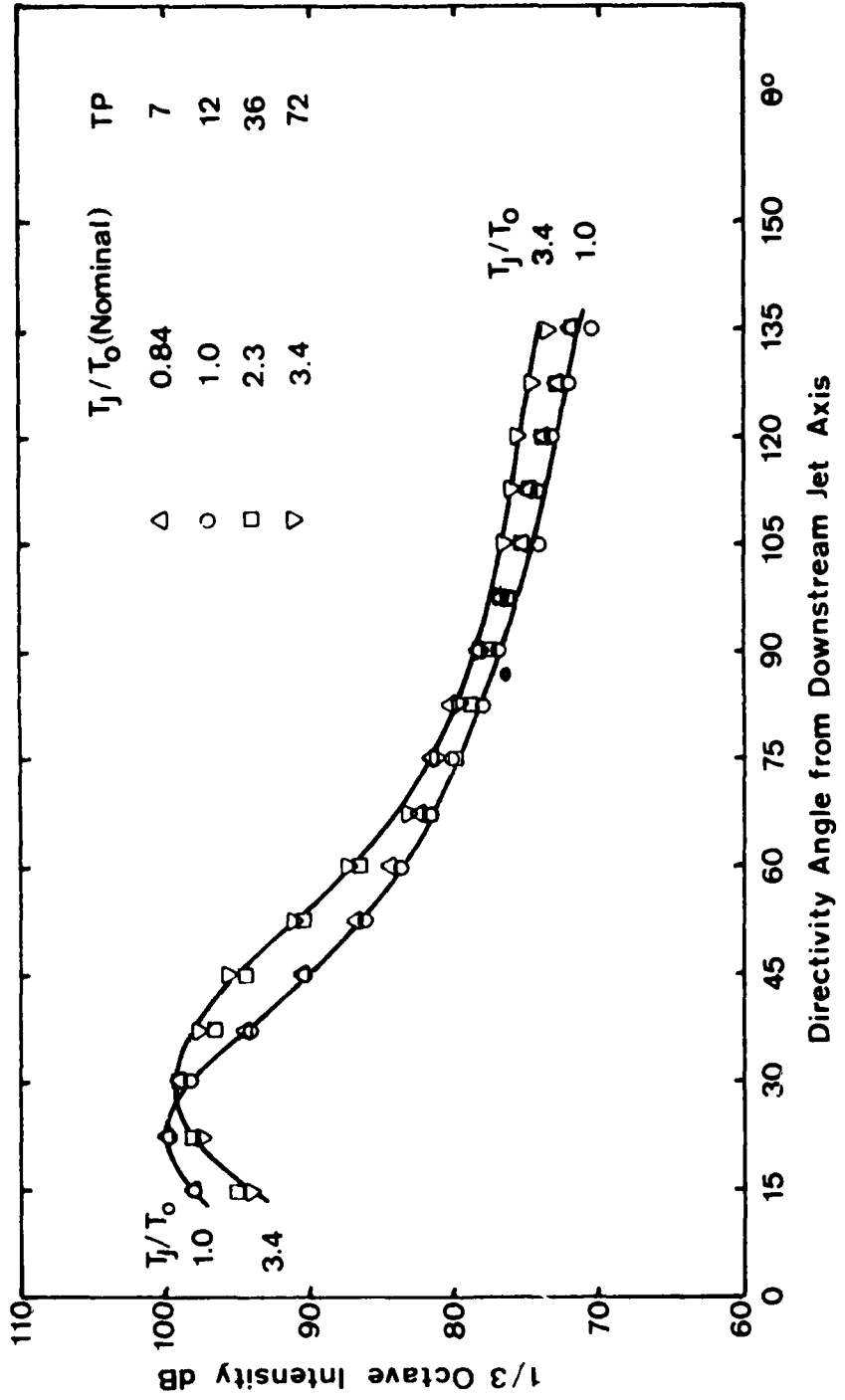


Figure 2.26 Effect of  $T_J/T_0$  on Directivity of  $1/3$ -Octave Intensity at  
 $V_J/a_0 = 0.9$ ;  $f_{SD}/V_J = 0.1$

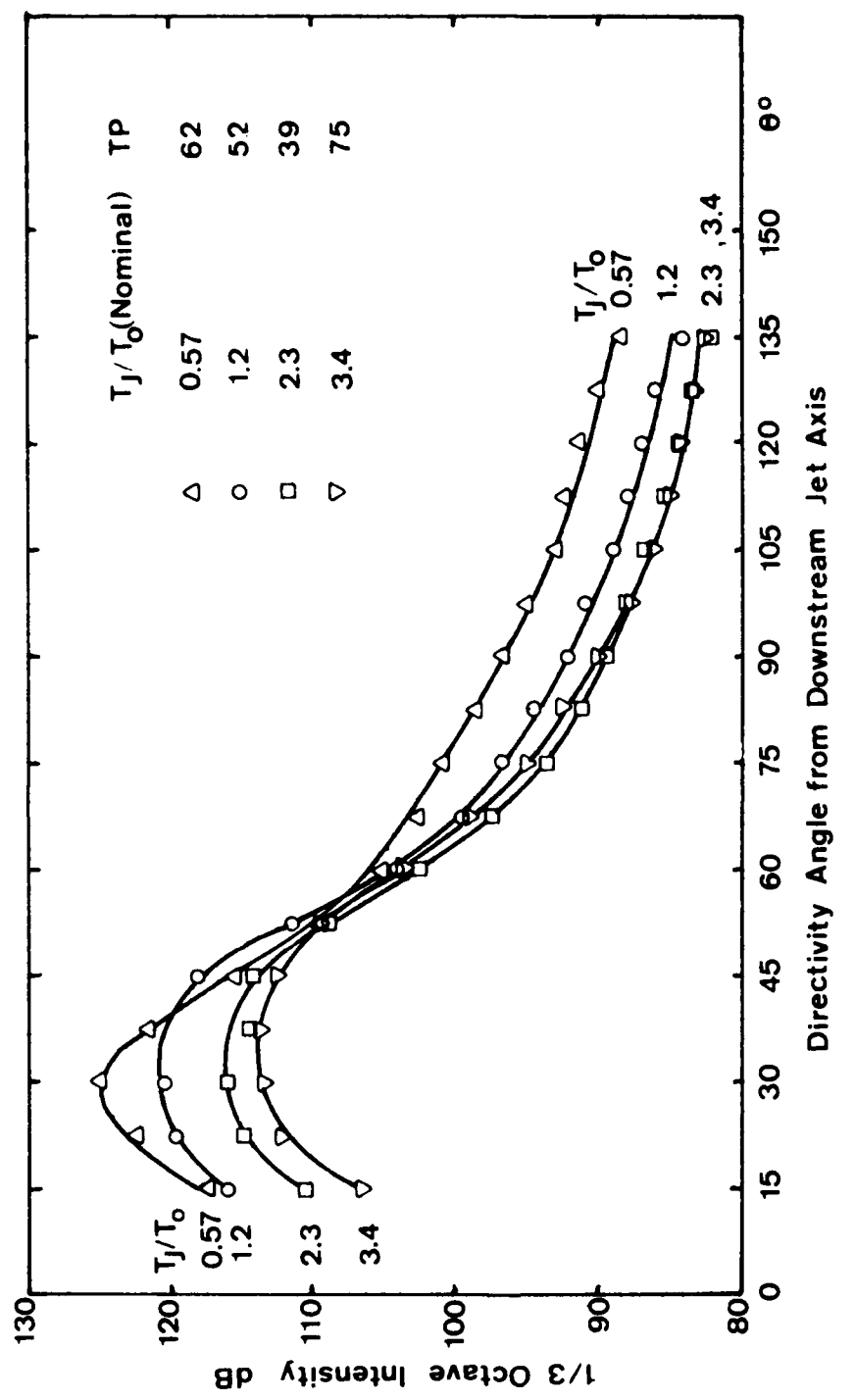


Figure 2.27 Effect of  $T_J/T_0$  on Directivity of 1/3-Octave Intensity at  $V_J/a_0 = 1.47$ :  $f_{SD}/V_J = 0.1$

### 2.8.2.2 High frequency

At high source Strouhal numbers, the effect of heating remains consistent throughout the velocity range, as can be seen in Figures 2.28, 2.29, and 2.30. That is, the noise levels decrease with increasing  $T_J/T_O$  at all velocities. In addition, these noise reductions are angular dependent at all velocities, especially at smaller angles to the jet axis. For a fixed value of  $V_J/a_0$ , the peak radiation angle,  $\theta_p$ , increases as the static temperature ratio increases. At observer angles smaller than  $\theta_p$ , the intensity falls off rapidly, and this effect is enhanced with increasing  $T_J/T_O$ .

An attempt was made to reconcile the rapid decrease in level at small angles as a function of  $T_J/T_O$  in terms of the "cone of silence angle,"  $\theta_c$ . For heated jets, this angle is given from ray acoustics as

$$\cos \theta_c = \frac{a_0}{a_s + V_c} , \quad (2-8)$$

where  $a_s$  is the speed of sound in the source region, and is related to the source temperature  $T_s$  by  $(a_s/a_0) = (T_s/T_0)^{\frac{1}{2}}$ . Using the expression for  $(T_s/T_0)$  discussed in reference 14, i.e.,

$$\frac{T_s}{T_0} = 0.7 \left\{ \frac{T_J}{T_O} - 1 \right\} + 1 , \quad (2-9)$$

and putting  $M_c = 0.67 (V_J/a_0)$ , values of  $\theta_c$  for the jet operating conditions  $(V_J/a_0, T_J/T_O)$  considered here are tabulated in Figures 2.28, 2.29, and 2.30 for the high frequency directivities. At the two subsonic velocities (Figures 2.28 and 2.29), it can be seen that for every value of  $T_J/T_O$ , the intensity increases as the observer moves from the forward arc towards the downstream jet axis, until the cone of silence angle  $\theta_c$  is reached. Beyond this, the levels fall rapidly as expected from simple physical considerations. At  $V_J/a_0 = 1.47$ , however, this concept does not appear to shed any light on the measured directivities, except at the highest temperature ratio of 3.4 - see Figure 2.30.

## 2.9 CONCLUDING REMARKS

The characteristics of turbulent mixing noise from fully-expanded, static jet exhausts have been investigated experimentally in great detail over an extensive envelope of jet operating conditions. The results, both overall and spectral, have been displayed in a systematic and comprehensive manner in the form of velocity dependence and directivity. The major features throughout the ranges of jet efflux velocity and exhaust temperature have been discussed in sufficient detail. In particular, the carefully planned experimental program has made it possible to make an independent assessment of the effects of velocity and temperature on jet noise.

The data presentation was aided by the familiar freely-convecting quadrupole model (i.e., a model in which the presence of mean velocity and

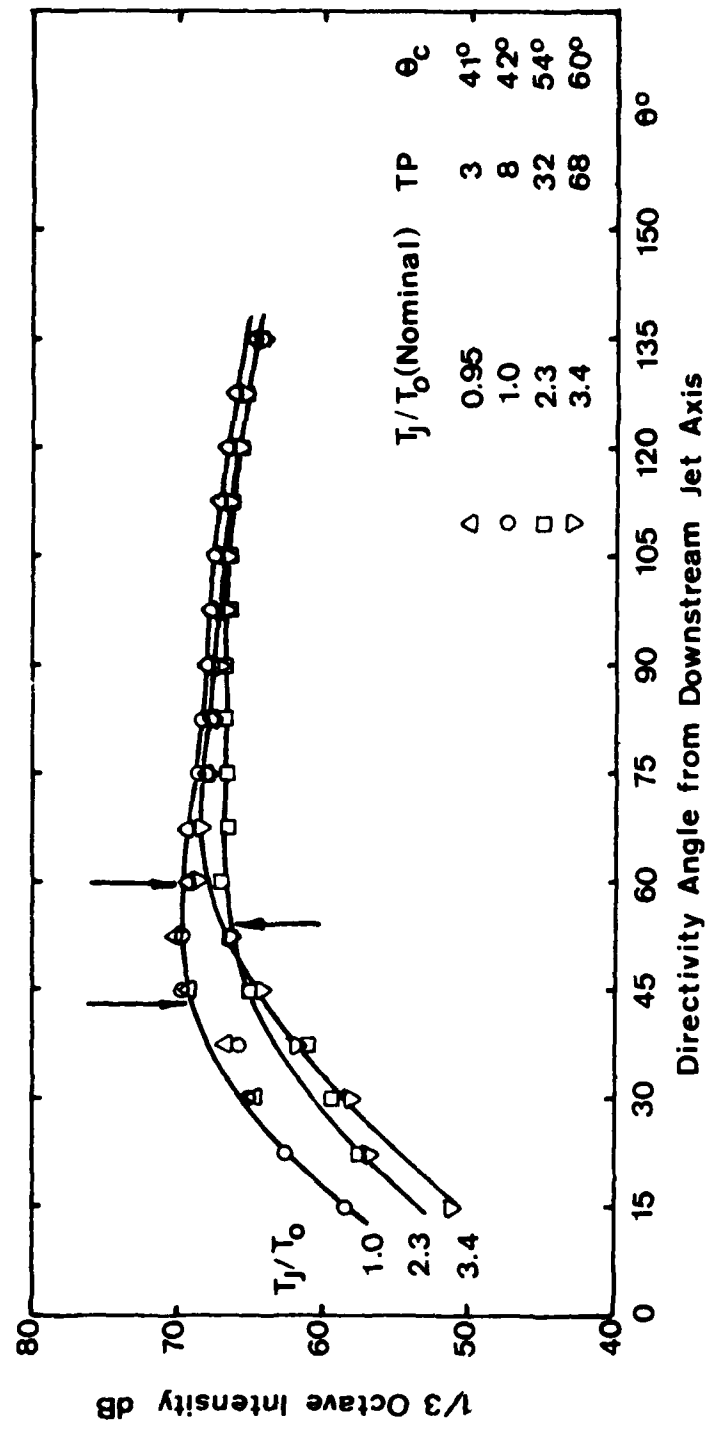


Figure 2.28 Effect of  $T_J/T_0$  on Directivity of 1/3-Octave Intensity at  
 $V_J/a_0 = 0.5$ ;  $f_{SD}/V_J = 3.0$

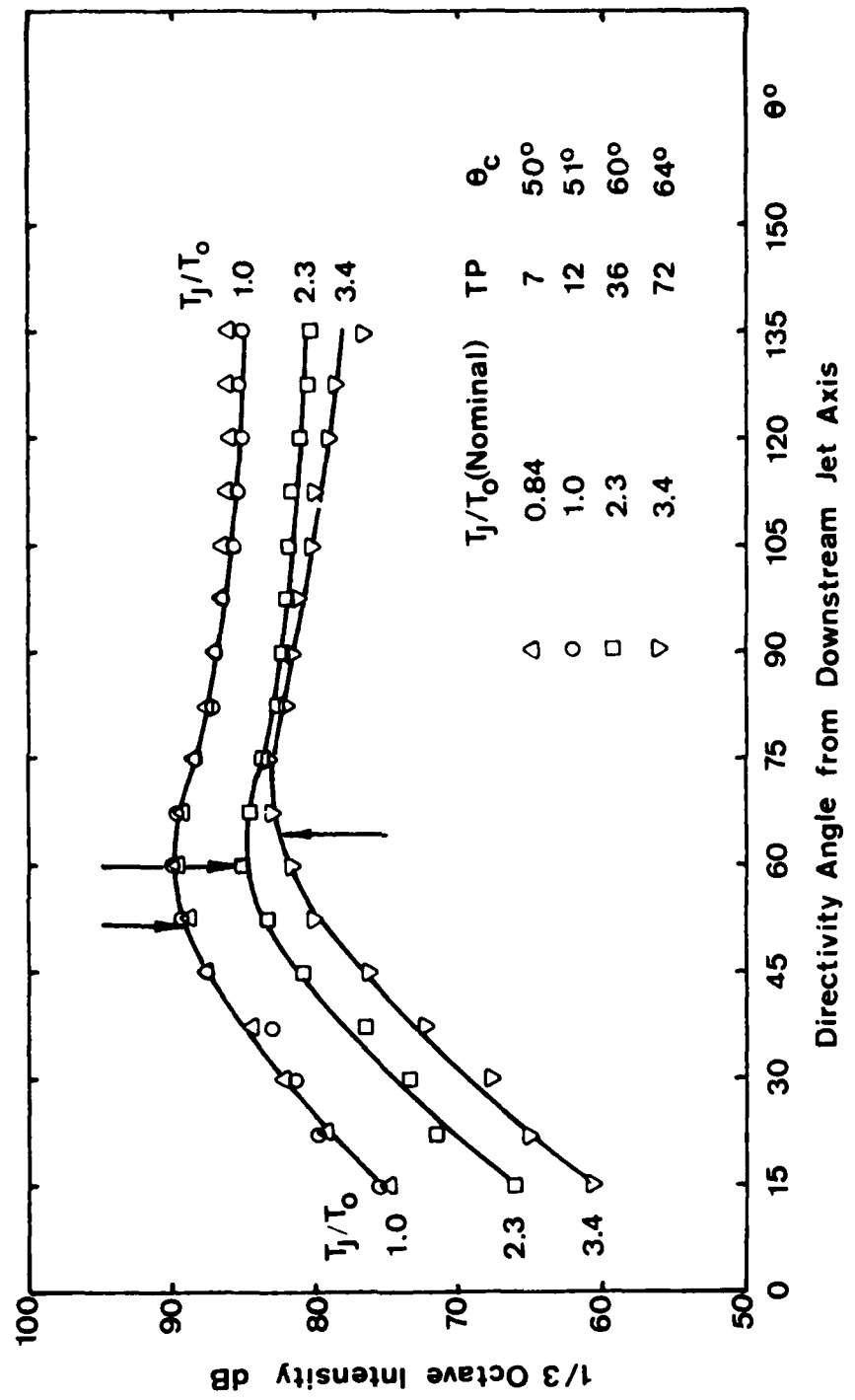


Figure 2.29 Effect of  $T_J/T_0$  on Directivity of 1/3-octave Intensity at  
 $f_s D/V_J = 3.0$ :  
 $V_J/a_0 = 0.9$ :

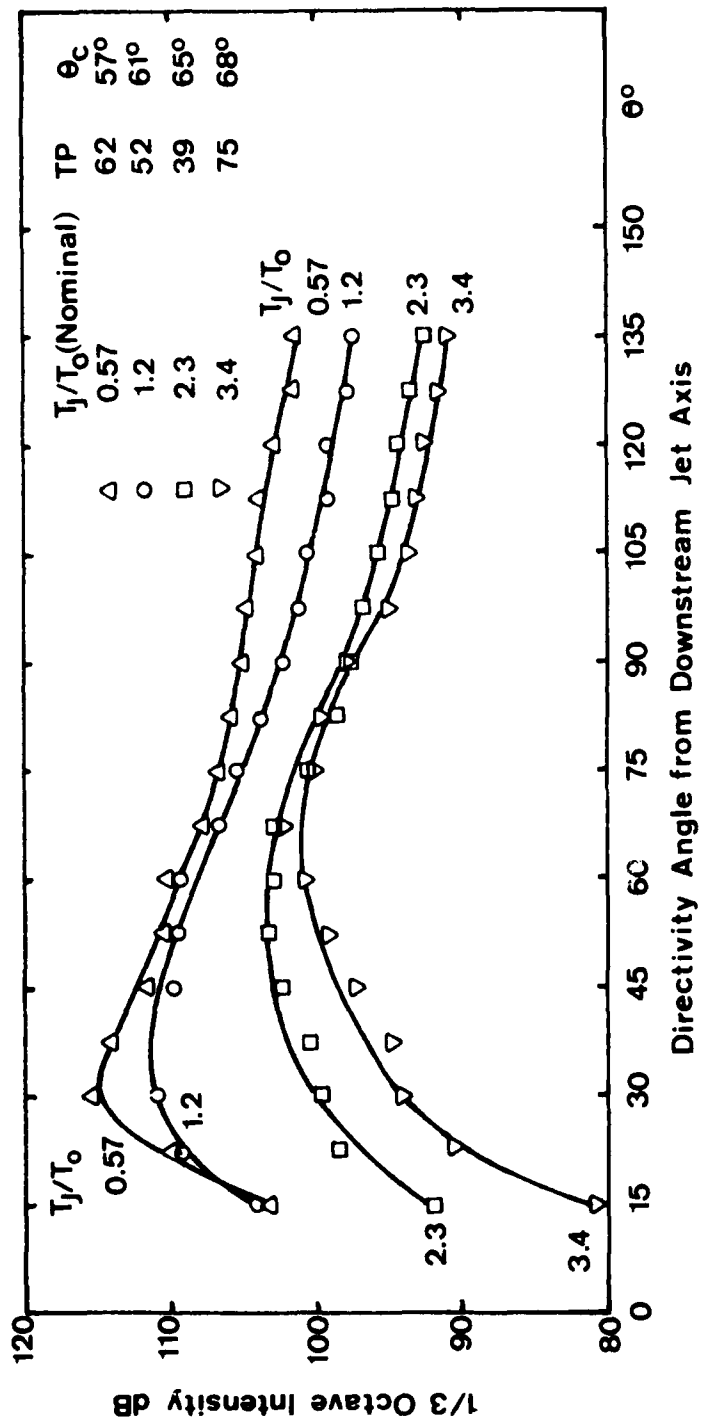


Figure 2.30 Effect of  $T_J/T_0$  on Directivity of 1/3-Octave Intensity at  
 $V_J/a_0 = 1.47$ ;  $f_{SD}/V_J = 1.0$

temperature fields surrounding the sources is neglected) for jet noise. The nature of the inadequacies of this model, the magnitudes of the discrepancies involved, and the regimes over which they exist have been studied for most aspects of data presentation.

Recent theoretical investigations rigorously indicate that many of the observed deviations between experiment and the basic freely convecting quadrupole model are a consequence of the shrouding of the sound sources in the jet flow by mean velocity and temperature gradients. (The theoretical work conducted on the current program is described in Sections 3 and 4 of this report.) In order to obtain greater physical understanding of such phenomena and to establish the effects of these acoustic/mean-flow interactions quantitatively throughout the jet operating conditions (velocity and temperature) of practical interest, the theoretical studies need to be continued. The accurate and comprehensive data obtained from the experimental program described in this section should prove most valuable in such research efforts.

Having conducted the present experimental study of turbulent mixing noise from shock-free supersonic jets, the next logical step is to examine in detail the noise characteristics of shock-containing jet flows. The measurements of shock-associated noise over a large range of supercritical pressure ratios and jet exhaust temperatures have also been conducted during the present program, and the results are discussed in Section 7 of this Volume.

3. JET NOISE THEORY AND COMPARISON WITH THEORY

## SUMMARY

---

The effect of temperature on the jet mixing noise intensity radiated normal to the axis can be predicted by the Lilley equation when a new dipole source, which represents a scattering mechanism, is added to the quadrupole source junction.

---

Measured data on hot jets at low Mach numbers ( $U_j/c_0 = 0.3$  to 0.6 where  $U_j$  is the jet exit velocity and  $c_0$  is the ambient sound speed) show significant increases in far-field intensity, relative to isothermal jets of the same velocity. At  $90^\circ$  to the jet axis, the measured velocity dependence is  $U_j^6$  in contrast to the  $U_j^8$  Lighthill prediction. Figure 3S.1 demonstrates this for a low Strouhal number,  $S = 0.1$ , where the increase in low velocity noise due to heating is quite pronounced ( $S = fD/U_j$  where  $f$  is the observed frequency and  $d$  is the jet diameter).

To illustrate the theoretical effects of heating on the noise radiation at  $90^\circ$  to the jet axis, some numerical quadrupole solutions to the Lilley equation for the sheared mean flow model indicated in Figure 3S.2 are shown in Figure 3S.3 in the form of a flow factor (the ratio of the far-field intensity to its value without the jet flow, the source strength being held constant). The horizontal scale is the nondimensional frequency parameter  $k_0\delta$ , i.e.  $2\pi(\delta/\lambda)$  where  $\lambda$  is the wavelength of sound outside the flow. Clearly,  $k_0\delta$  is a far more important parameter than the one based on the nozzle radius,  $k_0r_0$ ; the latter is varied over a wide range (specified in Figure 3S.3), but the resulting flow factor variation, indicated by the vertical band, is quite small.

For small values of  $k_0\delta$  these results show that the radiation from the (SIPQ) quadrupole source can be amplified when placed within a nonuniform density field. The amplification mechanism is the incomplete cancellation of the radial-radial quadrupole field in the presence of radial density gradients. Failure to cancel at low frequencies is due to the dependence on the local density of the radiation from each of the radial dipoles making up the  $rr$ -quadrupole. The basis for this explanation is the low frequency limit shown in Figure 3S.3, which is a new analytical solution to the Lilley equation and is discussed fully in Section 3.2.5. In that same discussion the high frequency or geometric acoustics limit is also derived. Clearly, these asymptotic results are useful over a wide range of  $k_0\delta$ .

Although the low frequency amplification mechanism can be related to the low Mach number condition, since  $k_0\delta \propto U_j/c_0$  at constant Strouhal number, it is argued that it cannot entirely explain the low Mach number increase in noise levels with heating observed in practice (e.g. see Figure 3S.1). The amplification mechanism, which can be referred to as one of scattering by the mean density gradient, is closely related to one of those described by Morfey<sup>19</sup> in his extension of the Lighthill analogy to include the case of flows of non-uniform density. However, that work<sup>19</sup> also uncovered an unsteady density field scattering mechanism: when the Lilley equation is modified to include this effect, an additional dipole source is introduced into the source function. That new source is found to explain temperature effects at  $90^\circ$  reasonably well (see Appendix 3E) and leads to excellent directivity predictions for hot jet mixing noise (see Appendix 3G) as illustrated in the final part of this summary.

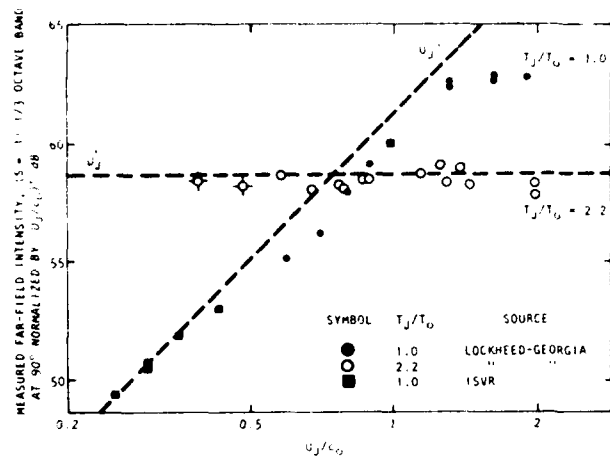


**Figure 3S.1** Effect of Heating  
On Jet Noise  
Measured at 90°:  
1/3-Octave Band  
Centered at  $S = 0.1$

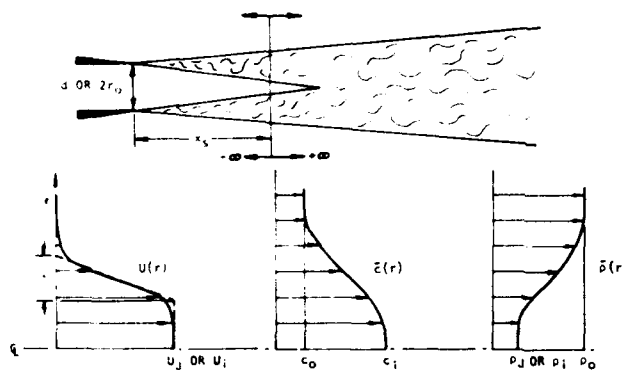


**Figure 3S.2** Typical Radial  
Profiles in Basic  
Cylindrical Flow,  
Showing Relation  
to Actual Jet Flow

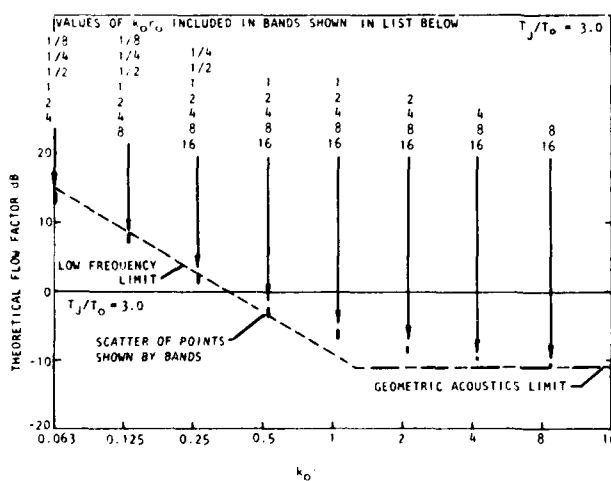


**Figure 3S.3** Lilley Equation  
Flow Factor for a  
Quadrupole Source  
in a Hot Axisym-  
metric Shear Flow  
at 90°. Radial  
Source Location  
Corresponds to  
 $\phi_s = 0.663$ . Bars  
on Graph Indicate  
 $k_0 r_0$  (or  $\delta/r_0$ )  
Dependence  
of Results

---

The directivity of isothermal supersonic jet mixing noise can be accurately predicted outside the cone of silence by the Lilley equation with the new quadrupole source model.

---

A comprehensive study of the directivity of isothermal jet mixing noise is described in Appendix 3F. The comparisons between measured data and the corresponding Lilley equation solutions cover a wide range of modified Strouhal numbers (i.e. frequencies),  $0.1 \leq S_m \leq 3.0$ ; Mach numbers,  $0.5 \leq U_j/c_0 \leq 1.95$ ; and polar angles,  $22.5^\circ \leq \theta_0 \leq 135^\circ$ . The study clearly demonstrates that outside the cone of silence the directivity shapes can be predicted from the Lilley equation solutions with considerable accuracy. This major achievement is illustrated in Figures 3S.4 and 3S.5. The improved agreement over the classical  $D_m^{-5}$  law involves only a small change at some angles, but the consistent accuracy of the new predictions and the large changes from the classical law in the forward arc demonstrate the validity of the new Lilley equation results.

In order to achieve this agreement outside the cone of silence, it has been necessary to process the measured data so that the polar origin for the directivity angle is located at the effective axial source location (as in the theoretical model) and to use an eddy convection velocity that varies with  $S_m$  in a realistic way, that is, decreasing with decreasing  $S_m$ .

Inside the cone of silence the over-prediction by the  $D_m^{-5}$  law is contrasted with an under-prediction by the Lilley equation solutions, as in Figures 3S.4 and 3S.5. The most likely reason for this large discrepancy is that the direct radiation from the large-scale turbulence structure, the subject of a parallel investigation described in the following sub-section is not included in the comparisons presented here. At the lowest Strouhal number considered,  $S_m = 0.1$ , this must be an important source of acoustic radiation inside the cone of silence. Almost of equal importance through, particularly for higher Strouhal numbers,  $S_m \geq 0.3$ , is a lack of realism in the present assumed source function model; the actual source distribution in the radial-azimuthal plane has been modeled by a ring source, that is, radially it is a point source. At angles well inside the cone of silence, the ring source of a given radius may be very effectively shielded by the flow, giving rise to low predicted levels. In reality, however, other parts of the actual source distribution nearer the outer edge of the sheared flow are less well shielded and if their contributions to the radiation levels were included, a significant increase in predicted level would result. Thus, there is an urgent need to replace the present ring source model with a radially distributed source, in order to evaluate the relative importance of the two most likely causes for the large discrepancies inside the cone of silence, the unrealistic source model and large-scale turbulent structure radiation.

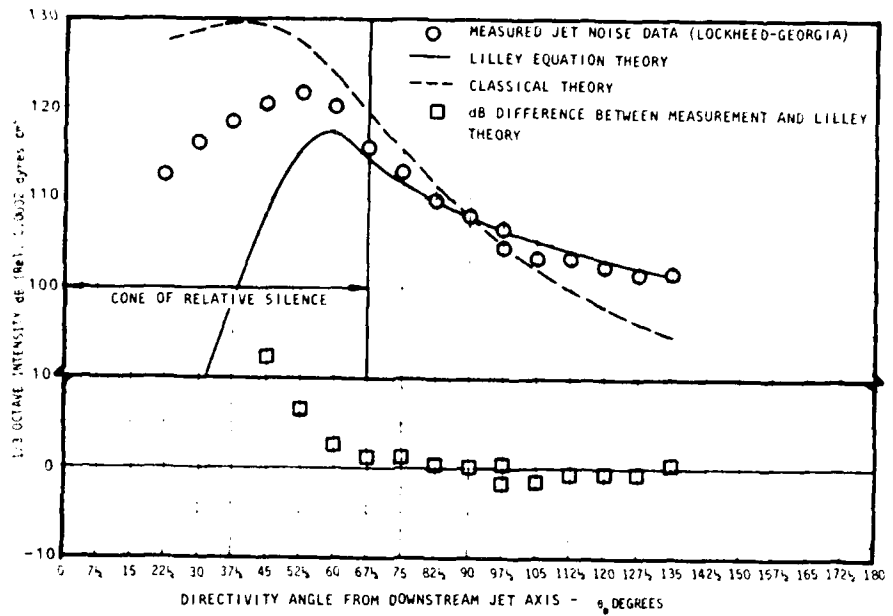


Figure 3S.4 Directivity of Supersonic Isothermal Jet Noise: Comparison of Lilley Equation and Classical Theoretical Models with Measured 1/3-Octave Data, for  $S_m = 0.3$ ,  $U_j/c_0 \approx 1.33$

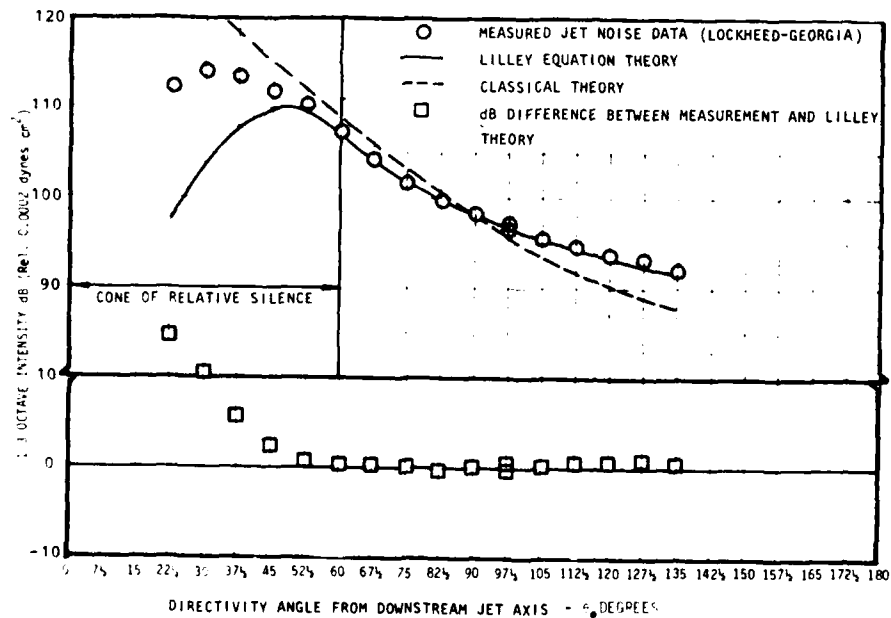


Figure 3S.5 Directivity of Supersonic Isothermal Jet Noise: Comparison of Lilley Equation and Classical Theoretical Models with Measured 1/3-Octave Data, for  $S_m = 0.3$ ,  $U_j/c_0 \approx 1.95$

The effect of temperature on the directivity of hot jet mixing noise can be accurately predicted at subsonic conditions by the modified Lilley equation.

A theoretical model for the variation of jet mixing noise with jet exit velocity and temperature at 90° to the jet axis has been evaluated and found to be in reasonable agreement with the measured data, although there are some significant deviations occurring at high velocities (see Appendix 3E). The model is based upon a source function made up of quadrupoles and dipoles, i.e. on a modified right-hand side of the Lilley equation. The dipole sources result from the scattering of turbulent pressure fluctuations by unsteady density fluctuations within non-isothermal jet flows. The relative weighting of this source combination is determined mainly from the measured isothermal and hot jet noise spectral data at 90° to the jet axis.

The Lilley equation can then be used to predict the directivity of hot or non-isothermal jet noise, given that weighted source combination. However, in the preliminary study described in Appendix 3G, an attempt has been made to separate out temperature effects from those that cause disagreement between measurement and theory at isothermal conditions, in order to test the complete theoretical model specifically with regard to temperature effects. This was accomplished by comparing calculated and measured changes with temperature in the radiation directivity. Thus, in Figure 3S.7, for example, heating the jet to an exit temperature of  $\sim 1/3$  times the ambient temperature reduces the level at 90° by  $\sim 3$  dB (relative to isothermal conditions). This determines the quadrupole/dipole relative weighting and also allows a Lilley equation directivity to be calculated for this jet temperature. The difference between it and the calculated isothermal directivity is then compared with the corresponding measured difference.

Rather than present predicted and measured differences for comparison, absolute levels are recovered by adding both to the measured isothermal levels, as in the examples of Figures 3S.6, 3S.7, and 3S.8; the Lilley equation prediction is shown as a continuous line. The agreement with the measured hot jet data is remarkably good at this jet exit condition (that is, a velocity ratio  $U_j/c_0 \approx 0.9$  and a temperature ratio  $T_j/T_0 \approx 3.3$ ). In Figures 3S.6 through 3S.8 the frequency parameter  $S_m$  takes the values 0.3, 1.0, and 3.0. At  $S_m = 0.3$  (Figure 3S.6), despite the negligible change in measured levels at 90°, the theory reproduces the trend of lower measured levels at small angles. At the higher frequencies, the measured changes at 90° of  $\sim 3$  dB and  $\sim 6$  dB (Figures 3S.7, 3S.8) remain about the same in the forward arc but both widen to  $\sim 15$  dB at the smallest angles; both features are accurately reproduced by the Lilley equation based on predictions.

Clearly in those examples and others included in Section 3, the modified Lilley equation model (with the new dipole sources) must contain an adequate description of all temperature dependent flow-acoustic interactions within subsonic, heated, or non-isothermal turbulent jets.

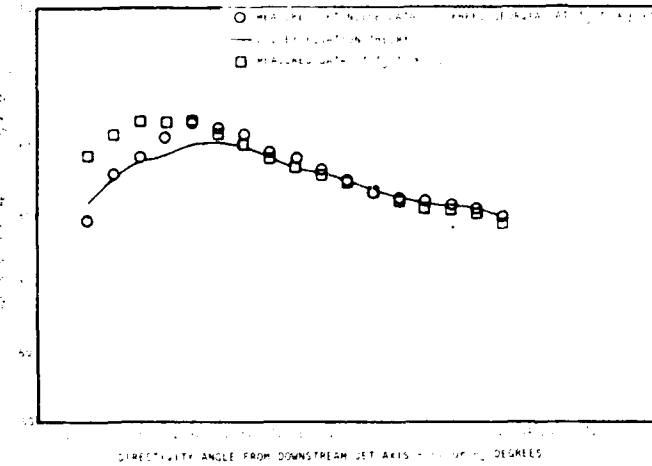


**Figure 3S.6** Directivity of Hot Jet Noise: Comparison of Lilley Equation Theoretical Model with Measured 1/3-Octave Data, for  $S = 0.3$ ,  $U_J/c_o = 0.9$ ,  $T_J/T_o = 3.37$

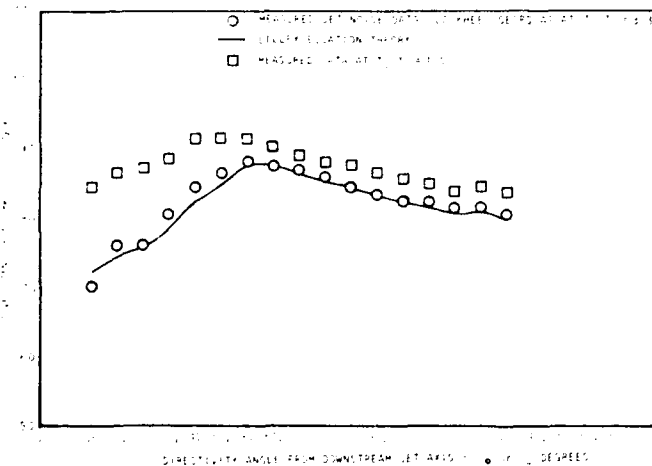


**Figure 3S.7** Directivity of Hot Jet Noise: Comparison of Lilley Equation Theoretical Model with Measured 1/3-Octave Data, for  $S = 1.0$ ,  $U_J/c_o = 0.9$ ,  $T_J/T_o = 3.37$

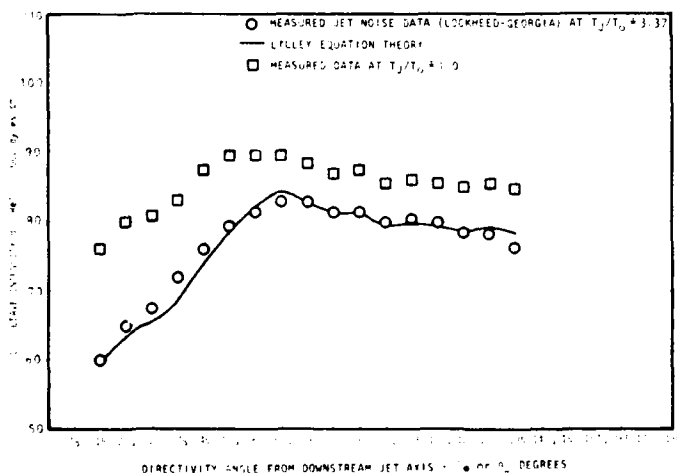


**Figure 3S.8** Directivity of Hot Jet Noise: Comparison of Lilley Equation Theoretical Model with Measured 1/3-Octave Data, for  $S = 3.0$ ,  $U_J/c_o = 0.9$ ,  $T_J/T_o = 3.37$

### 3.1 INTRODUCTION

Over the past four years, a considerable amount of accurate data has been obtained on the sound radiated from turbulent shock-free jets. Spectral information is now available over a wide range of Strouhal numbers ( $0.1 \leq S \leq 3$ , where  $S = fd/U_j$ ), for jet densities ranging from 0.3 to 2<sup>+</sup> times the ambient density and jet velocities ranging from 0.3 to 2 times the ambient sound speed. The measurements used in this paper were taken by Lockheed-Georgia<sup>13,14</sup>; ISVR, Southampton University<sup>17</sup>; and NGTE, Pyestock<sup>18</sup>.

The detailed measurements now available have revealed features of jet mixing noise not explained by earlier models and have led to further advances in aerodynamic noise theory. These include the recognition of an additional source term in the Lighthill analogy<sup>19</sup>, and the development of a shear flow analogy capable of accounting for flow effects on sound radiation from turbulence<sup>20,21,22</sup>.

The jet noise model presented in this section is a further development of the shear flow analogy mentioned above, aimed specifically at describing the sound generated by turbulent mixing in round jets. The governing equation is Lilley's equation, for which numerical solutions have been calculated for sources of quadrupole order. The numerical solutions are compared in Section 3.2 with analytical solutions for the limiting cases of low and high frequencies.

Finally, in Section 3.3 comparisons are made between theoretical predictions and measured data. Two aspects considered in detail are (1) the effects of nonuniform density which rise with low-velocity hot jets, and (2) the radiation from "isothermal" jets (temperature ratio=1) at high velocities. The experimental evidence on these aspects of jet noise is briefly reviewed below.

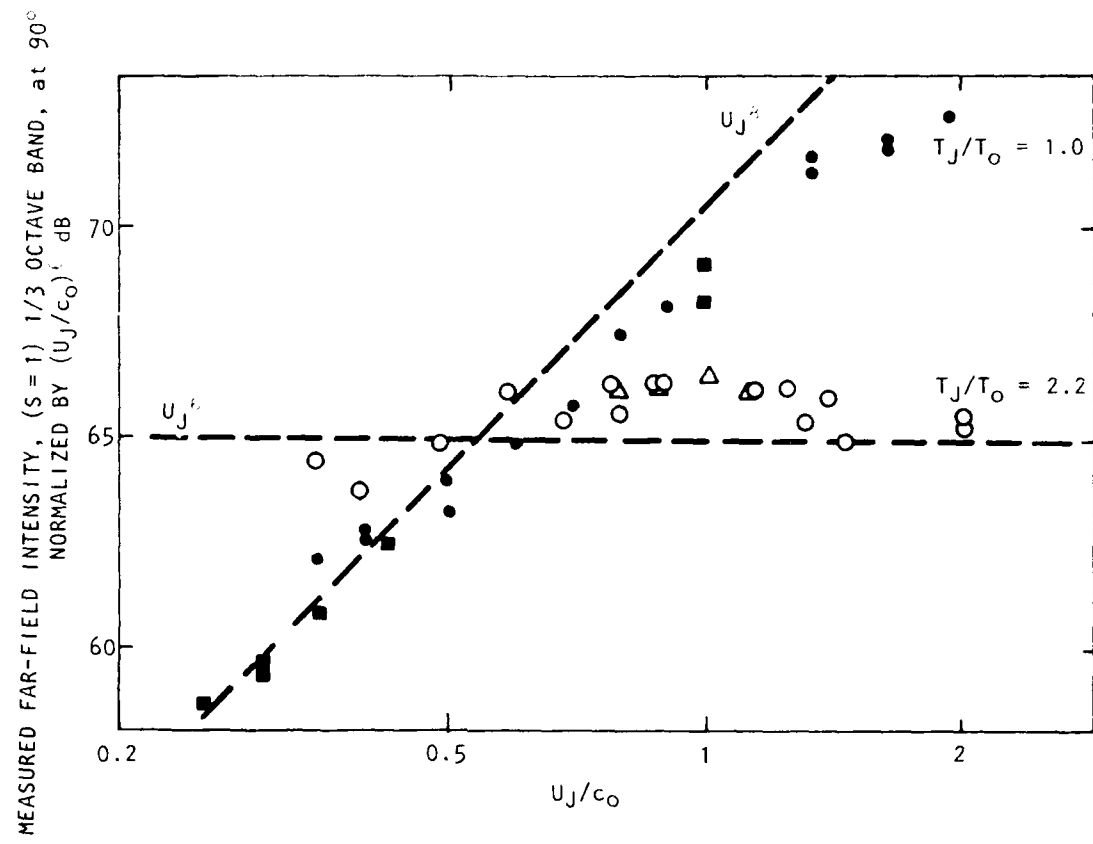
#### 3.1.1 Density Ratio Effects on Jet Noise

Data on hot jets at low Mach numbers (0.3 to 0.6) show significant increases in far-field intensity, relative to isothermal jets of the same velocity. At 90° to the jet axis, the measured velocity dependence is  $U_j^6$ , in contrast to the  $U_j^8$  Lighthill prediction. Figures 3.1 and 3.2 demonstrate this for two different parts of the spectrum ( $S=1$  and 0.1, respectively); the increase in low velocity noise due to heating is more pronounced at the lower Strouhal numbers.

The jet noise model presented in the next section provides two possible mechanisms for the increased radiation. Both mechanisms involve scattering of the local turbulent pressure field by density inhomogeneities, a process shown by Morfey<sup>19</sup> to lead to a sixth-power velocity dependence in all low Mach number flows whose density is nonuniform.

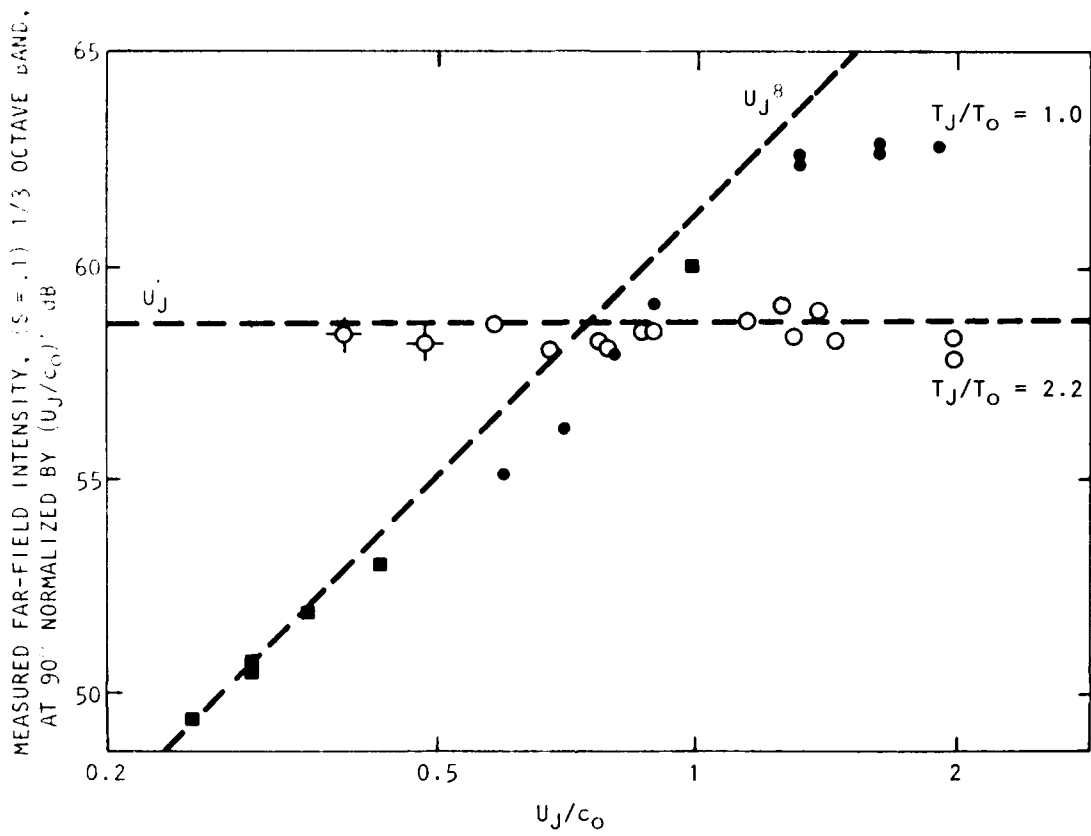
---

<sup>\*</sup>Supersonic adiabatic jet. The jet and ambient fluids are air in all cases.



SYMBOL	$T_J/T_o$	SOURCE
●	1.0	LOCKHEED-GEORGIA
○	2.2	" "
■	1.0	ISVR
△	2.2	NGTE

Figure 3.1 Effect of Heating on Jet Noise Measured at  $90^\circ$ :  $\frac{1}{3}$ -Octave Band Centered at  $S = 1.0$ . Ordinate is  $SPL(R_r) + 20 \log(R_r/10^3 d) - 20 \log(p_{\text{ambient}}/p_{\text{standard}}) - 60 \log(U_J/c_0)$ . Code: ○, Lockheed-Georgia data (13,14); ■ ISVR data (17); △ NGTE data (18). Solid symbols denote isothermal jets; open symbols denote hot jets ( $T_J/T_o = 2.2$ )



SYMBOL	$T_J/T_O$	SOURCE
●	1.0	LOCKHEED-GEORGIA
○	2.2	" "
■	1.0	ISVR

Figure 3.2 Effect of Heating on Jet Noise Measured at 90°: 1/3-Octave Band Centered at  $S = 0.1$ . Code as Fig. 3.1. Crosses Denote Low-Velocity Hot Jet Data Used to Form Figure 3.8

The first possibility, that the scattering is due to the mean density gradient, can be examined directly with the aid of the Lilleley equation and this is done in Section 3.3. The second possibility is that the scattering is predominantly from the unsteady density field; this mechanism involves additional source terms, defined in Section 3.2, which appear to be necessary to account for the observed levels.

### 3.1.2 Finite Mach Number Effects

The effects of finite Mach number — causing departures from the Lighthill  $U_j^3$  law even for isothermal jets — have long been recognized. These are refraction of the sound away from the jet axis<sup>11</sup> and turbulence noncompactness. Non-compactness and source convection effects were incorporated into Lighthill's zero-flow analogy by Ribner<sup>11</sup> and Ffowcs Williams<sup>10</sup>, but neglect of flow-acoustic interactions meant that the resulting model became increasingly inaccurate at high jet velocities — as was demonstrated by Lush<sup>8</sup> even in the subsonic velocity range.

The isothermal jet data now available, which include velocity ratios ( $U_j/c_0$ ) of 1.33, 1.65, and 1.93, offer the possibility of separating flow-acoustic interaction effects from source noncompactness and convection effects. At 90° to an isothermal jet, for example, flow-acoustic interaction may reasonably be neglected; the fact that the intensity drops below the  $U_j^3$  line at high velocities (see Figures 3.1 and 3.2) is therefore evidence of either a diminishing turbulence intensity, or turbulence noncompactness.

Figures 3.1 and 3.2 also show that at the higher jet velocities (roughly, above a jet Mach number of 0.6) the 90° levels are reduced by heating. This effect, which is more pronounced at the higher Strouhal number, is explained in Section 3.3 as due to a transition towards geometric acoustics within the jet shear layer as the ratio of the shear layer thickness to the acoustic wavelength increases.

## 3.2 THE JET NOISE MODEL

The sound field of a turbulent jet is described in terms of waves which propagate in an axisymmetric parallel shear flow. An important feature is that the source term is of second order in the turbulent velocities; all linear terms are placed on the left-hand side.

### 3.2.1 Acoustic Analogy for Turbulent Shear Flows

The unsteady pressure field of a turbulent shear layer is regarded in the present model as a set of small-amplitude waves, with real values of frequency  $\omega$  and axial wavenumber  $k_x$ , superimposed on a steady axisymmetric parallel shear flow with velocity  $[U(r), 0, 0]$ , sound speed  $c(r)$  and density  $\bar{\rho}(r)$  as sketched in Figure 3.3. The governing equation for the pressure  $p$  (relative to the uniform pressure in the assumed basic flow) is written as

$$L(p) = \bar{\rho}Q, \quad (3-1)$$

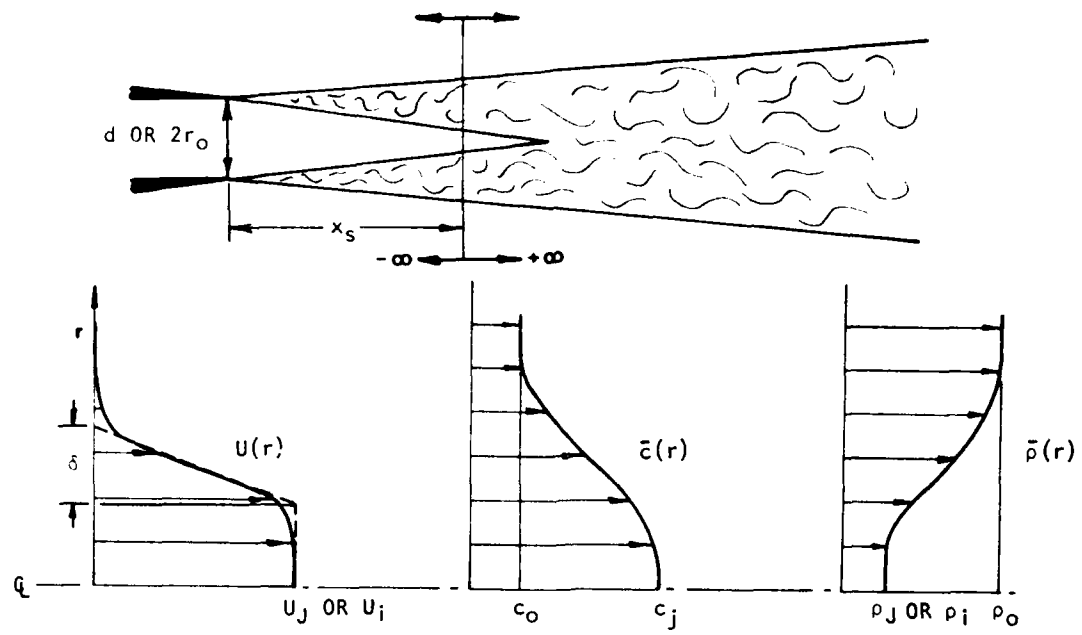


Figure 3.3 Typical Radial Profiles in Basic Cylindrical Flow, Showing Relation to Actual Jet Flow

with the linear operator  $L$  defined by

$$L = \frac{1}{c^2} \frac{\bar{D}^3}{Dt^3} - \frac{\bar{D}}{Dt} V^2 + \frac{1}{\bar{\rho}} \frac{dp}{dr} \frac{\bar{D}}{Dt} \frac{\partial}{\partial r} + 2 \frac{dU}{dr} \frac{\partial^2}{\partial x \partial r} \quad (3-1a)$$

and

$$\frac{\bar{D}}{Dt} = \frac{\partial}{\partial t} + U \frac{\partial}{\partial x}. \quad (3-1b)$$

This is a modified version of Lilley's equation<sup>20</sup>; the fluid is represented as inviscid and nonconducting, but is not limited to a perfect gas.

The source term  $Q$  is a complicated function of the pressure perturbation  $p$ , the component velocity perturbations  $v_i'$  (relative to the local basic flow  $\bar{v}_i$ ) and the specific volume perturbation  $V'$  (relative to  $\bar{V} = 1/\bar{\rho}$ ). We conjecture that the important terms in  $Q$ , for purposes of estimating far-field sound radiation from turbulent shear layers, are those of lowest order in the velocity fluctuations [see Appendix 3A for derivation of equations (3-1) through (3-5)].

The lowest-order contributions to  $Q$  are found by formally regarding the fluctuating velocity magnitude  $v'$  as a small parameter. On this basis, the leading terms in  $Q$  consist of second order velocity interactions; the local pressure fluctuation is  $O(v'^2)$ , and  $V'$  is  $O(1)$ . Explicitly,

$$Q = \frac{3}{2} \frac{\bar{D}}{Dt} \left( \frac{\partial^2 v_i' v_j'}{\partial x_i \partial x_j} \right) - \frac{\bar{D}}{Dt} \left( \frac{\partial f_j'}{\partial x_j} \right) + 2 \frac{\partial}{\partial x_i} \left( f_j' \frac{\partial \bar{v}_i}{\partial x_j} \right) + O(v'^3) \quad (3-2)$$

where  $(i, j) = 1, 2, 3$  denote Cartesian coordinate directions and the equivalent force field  $f_j'$  (per unit mass) is defined by

$$f_j' = - V' \frac{\partial p}{\partial x_j}. \quad (3-3)$$

An alternative form of  $Q$  (derived in Appendix 3A) which differs only in the  $O(v'^3)$  term is

$$Q = \frac{\bar{D}^3}{Dt^3} \left( \frac{1}{2} \frac{\partial^2 \xi_i' \xi_j'}{\partial x_i \partial x_j} - \frac{\partial \xi_i''}{\partial x_i} \right), \quad (3-4)$$

where  $\xi_i'$ ,  $\xi_i''$  are defined by

$$\frac{\bar{D} \xi_i'}{Dt} - \frac{\partial \bar{v}_i}{\partial x_k} \xi_k' = v_i', \quad \frac{\bar{D}^2 \xi_i''}{Dt^2} = f_i'. \quad (3-5)$$

The quantity  $\xi_i'$  represents, to first order in  $v'$ , the displacement of a fluid particle relative to the basic flow. Although the alternative forms (3-2) and (3-4) are equivalent second-order approximations, it will be shown below that they lead to quite different low-frequency solutions, and on this basis the

displacement form (3-4) will be adopted in Section 3.3 when jet noise model predictions are compared with measurements.

In the analysis which follows, attention is focused on the quadrupole source term above [the first term in Equation (3-4)], with the aim of showing how far this term can account for measured jet noise. The provisional conclusion is that the  $f_j$  term is negligible for isothermal jets ( $T_J = T_0$ ) at all velocities, but is probably significant for hot jets ( $T_J = 2 T_0$ ) at low velocities.

### 3.2.2 Method of Solution

The source distribution  $Q$  in Equation (3-1) is represented by

$$Q^{(v)} = \frac{\partial^v S^{(v)}}{\partial t^v} \quad (v = 1 \text{ or } 3) \quad (3-6)$$

where the auxiliary source distribution  $S^{(v)}$  of immediate interest are

$$\begin{aligned} S^{(1)} &= \frac{3}{2} M_{\alpha\beta} (v'_\alpha v'_\beta) \\ &\quad (\alpha, \beta) = (x, r, \phi) \\ S^{(3)} &= \frac{1}{2} M_{\alpha\beta} (\xi'_\alpha \xi'_\beta) \end{aligned} \quad (3-7)$$

or in general

$$S^{(v)} = M_{\alpha\beta} B_{\alpha\beta}^{(v)}$$

and the quadrupole operator  $M_{\alpha\beta}$  is given by

$$M_{\alpha\beta} = (r) \begin{bmatrix} (x) & (r) & (\phi) \\ \left[ \begin{array}{ccc} \frac{\partial}{\partial x^2} & \frac{1}{r} \frac{\partial^2 r}{\partial x \partial r} & \frac{\partial^2}{\partial x \partial \phi} \frac{1}{r} \\ \frac{1}{r} \frac{\partial^2 r}{\partial r \partial x} & \frac{1}{r} \frac{\partial^2}{\partial r^2} r & \frac{1}{r^2} \frac{\partial^2 r}{\partial r \partial \phi} \\ \frac{\partial^2}{\partial x \partial \phi} \frac{1}{r} & \frac{1}{r^2} \frac{\partial^2 r}{\partial r \partial \phi} & \frac{\partial^2}{\partial \phi^2} \frac{1}{r^2} - \frac{1}{r} \frac{\partial}{\partial r} \end{array} \right] \end{bmatrix} \quad (3-8)$$

Physically,  $S^{(1)}$  corresponds to a volume acceleration distribution and  $S^{(3)}$  to a volume displacement; both are quadrupole order, as shown by Equations (3-7) and (3-8) above.

The Fourier transform of Equation (3-1) with respect to  $x$ ,  $\phi$  and  $t$  is

$$\frac{1}{R} \frac{d}{dR} (R \frac{dp}{dR}) + \frac{1}{k_o \delta} \left( -\frac{1}{\bar{\rho}} \frac{d\bar{p}}{dx} - \frac{2}{D} \frac{dD}{dx} \right) \frac{dp}{dR} + p \left( \frac{c_o^2 D^2}{\bar{\epsilon}^2} - (k_x/k_o)^2 - \frac{n^2}{R^2} \right) = -\bar{\rho}(j\omega)^{v-1} D^{v-1} (\tilde{s}^{(v)} / k_o^2) \quad (3-9)$$

where

$$R = k_o r, k_o = \omega/c_o, D = 1 - U(x)/c_o \cdot k_x/k_o,$$

$$U = U(x)$$

$$\bar{\rho} = \bar{\rho}(x)$$

$$\bar{\epsilon} = \bar{\epsilon}(x)$$

$$x = \frac{r-r_o}{\delta} + \text{const.}$$

$\delta$  is the local shear layer thickness based on the maximum velocity gradient. The Fourier transforms, denoted by tilde, are defined by

$$\begin{aligned} \tilde{p}(k, n, \omega; R) &\equiv \tilde{p}(R) \\ &= \int_{-\infty}^{+\infty} \int_{-\pi}^{+\pi} \int_{-\infty}^{+\infty} p(x, \phi, t; R) \exp[jk_x x + jn\phi - jwt] dx d\phi dt \end{aligned} \quad (3-10)$$

and similarly for  $\tilde{s}^{(v)}$ .

Equation (3-9) has been solved numerically for the special case of a volume displacement ( $v=3$ ) radial-point source, after recasting the left-hand side in a form that removes the mean flow spatial derivatives (a computational advantage). The governing equation for this Green function,  $G^{(3)}$ , is

$$\frac{d}{dR} \left( \frac{R}{\bar{\rho} \omega^2 D^2} \frac{dG^{(3)}}{dR} \right) + \frac{RG^{(3)}}{\bar{\rho} \omega^2 D^2} \{ \kappa^2 - n^2/R^2 \} = \delta(R-R') \quad (3-11)$$

where

$$G^{(3)} \equiv G^{(3)}(k_x, n, \omega; R|R') \equiv G^{(3)}(R|R')$$

$$\kappa^2 \equiv \kappa^2(k_x/k_o, x) = [c_o^2 D^2/\bar{\epsilon}^2 - (k_x/k_o)^2]$$

The required solution to Equation (3-9) follows immediately

$$\tilde{p}(R) = \frac{1}{k_o^2} \int_0^\infty G^{(3)}(R|R') (j\omega)^{v-3} D^{v-3} (k_x/k_o, x') \tilde{s}^{(v)}(R') R' dR' \quad (3-12)$$

With the notation

$$G^{(v)}(R|R') = G^{(3)}(R|R')(j\omega)^{v-3} D^{v-3}(k_x/k_o, x') \quad (3-13)$$

and noting that

$$\tilde{s}^{(v)} = \tilde{M}_{\alpha\beta} \tilde{B}_{\alpha\beta}^{(v)} \quad (3-14)$$

where

$$\tilde{M}_{\alpha\beta} = \begin{bmatrix} -k_x^2 & -\frac{j k_x}{r} \frac{d}{dr} r & -k_x \frac{n}{r} \\ -\frac{j k_x}{r} \frac{d}{dr} r & \frac{1}{r} \frac{d^2}{dr^2} r & -jn \frac{1}{r^2} \frac{d}{dr} r \\ -k_x \frac{n}{r} & -jn \frac{1}{r^2} \frac{d}{dr} r & -\frac{n^2}{r^2} - \frac{1}{r} \frac{d}{dr} \end{bmatrix} \quad (3-15)$$

then integration by parts of the integrals

$$\tilde{p}(R) = \frac{1}{k_o^2} \int_0^\infty G^{(v)}(R|R') \tilde{M}_{\alpha\beta} \tilde{B}_{\alpha\beta}^{(v)}(R') R' dR' \quad (3-16)$$

gives

$$\tilde{p}(R) = \int_0^\infty \tilde{B}_{\alpha\beta}^{(v)}(R') N_{\alpha\beta}(R') G^{(v)}(R|R') R' dR'. \quad (3-17)$$

That is, the differential operators  $\tilde{M}_{\alpha\beta}$  are transferred from the source function to the Green function but are changed to  $N_{\alpha\beta}$  where

$$N_{\alpha\beta}(R) = \begin{bmatrix} -(k_x/k_o)^2 & j(k_x/k_o) \frac{d}{dR} & -(k_x/k_o) \frac{n}{R} \\ j(k_x/k_o) \frac{d}{dR} & \frac{d^2}{dR^2} & jn \left( \frac{1}{R} \frac{d}{dR} - \frac{1}{R^2} \right) \\ -(k_x/k_o) \frac{n}{R} & jn \left( \frac{1}{R} \frac{d}{dR} - \frac{1}{R^2} \right) & \left( \frac{1}{R} \frac{d}{dR} - \frac{n^2}{R^2} \right) \end{bmatrix} \quad (3-18)$$

(See Appendix 3B for derivation.)

The Green function  $G^{(3)}$  can be expressed in terms of two independent solutions to the homogeneous equation,  $p_o(R)$  and  $p_i(R)$ ,

$$G^{(3)}(R|R') = \frac{j\pi}{2} p_o(R) p_i(R') \left[ \frac{2\omega^2 \bar{\rho} D^2 (k_x/k_o, x') / p_o}{j\pi R' W(p_i(R'), p_o(R'))} \right]; (R \geq R') \quad (3-19)$$

where  $W(\cdot)$  is the Wronskian. The factor in the square brackets is independent of source position,  $R'$ , so that the radial derivatives in  $N_{\alpha\beta}$  operating upon  $G^{(v)}(R|R')$ , and hence  $G^{(3)}(R|R')$ , can be expressed in terms of the radial derivatives of  $p_i(R')$ . Thus, the first radial derivative is simply

$$\frac{dG^{(3)}(R|R')}{dR'} = p_i^{-1}(R') \frac{dp_i(R')}{dR'} G^{(3)}(R|R'). \quad (3-20)$$

For the second radial derivative the homogeneous wave equation is used in the form

$$\frac{d^2 p_i}{dR^2} = -\{\kappa^2 - n^2/R^2\} p_i + \frac{R}{\bar{\rho} D^2} \frac{d}{dR} \left\{ \frac{\bar{\rho} D^2}{R} \right\} \frac{dp_i}{dR} \quad (3-21)$$

to give

$$\begin{aligned} \frac{d^2 G^{(3)}(R|R')}{dR'^2} &= -\{\kappa^2 - n^2/R'^2\} G^{(3)}(R|R') \\ &+ \frac{R'}{\bar{\rho} D^2} \frac{d}{dR'} \left\{ \frac{\bar{\rho} D^2}{R'} \right\} \frac{dG^{(3)}(R|R')}{dR'}. \end{aligned} \quad (3-22)$$

Thus, both the first and second radial derivatives of  $G^{(3)}$  can be expressed directly in terms of  $G^{(3)}$  and multiplicative factors: numerical differentiation is not necessary. The factors only require numerical solution information ( $p_i$ ,  $dp_i/dR'$ ) that has been generated for the calculation of  $G^{(3)}$ .

In order to satisfy (i) the radiation condition and (ii) the finiteness condition on the centerline, the independent solutions have the following initial values.

$$(i) \quad p_o = H_n^{(2)}(\kappa_o R) \quad (3-23)$$

outside the flow,  $R \geq R_\infty$ , where

$$U \rightarrow 0, \bar{\rho} \rightarrow \rho_o, \bar{c} \rightarrow c_o$$

and

$$\kappa^2 \rightarrow \kappa_o^2 = \{1 - (k_x/k_o)^2\}.$$

$$(ii) \quad p_i = J_n(\kappa_j R) \quad (3-24)$$

at or near the centerline,  $R \leq R_j$ , where

$$U \rightarrow U_J, \quad \bar{\rho} \rightarrow \rho_J, \quad \bar{c} \rightarrow c_J$$

and

$$\kappa^2 \rightarrow \kappa_J^2 = \left\{ \frac{c_o^2}{c_J^2} \left( 1 - U_J/c_o \cdot k_x/k_o \right)^2 - (k_x/k_o)^2 \right\}$$

The solution outside the flow may be rewritten, from Equations (3-19) and (3-23), as

$$G^{(3)}(R|R') = \frac{j\pi}{2} \omega^2 \rho_o c_n^{(3)}(R') H_n^{(2)}(\kappa_o R) \quad (3-25)$$

where

$$c_n^{(3)}(R) = \rho_i(R) \left[ \frac{2\bar{\rho}(x) D^2(k_x/k_o, x)/\rho_o}{j\pi R W\{\rho_i(R), \rho_o(R)\}} \right] \quad (3-26)$$

then Equation (3-17) becomes (for  $R \geq R_\infty$ )

$$\frac{\bar{\rho}(R)}{\rho_o c_o} = (j\omega)^{v-3} \frac{j\pi}{2} k_o^2 H_n^{(2)}(\kappa_o R) \int_0^\infty \tilde{B}_{\alpha\beta}^{(v)}(R') N_{\alpha\beta}(R') c_n^{(v)}(R') R' dR' \quad (3-27)$$

where

$$c_n^{(v)}(R) = D^{v-3}(k_x/k_o, x) c_n^{(3)}(R) \quad (3-28)$$

After Fourier inversion with respect to  $k_x$  and  $n$ , the far-field ( $\kappa_o R_r \rightarrow \infty$ ) acoustic pressure is

$$\frac{\rho(R_r, \phi, \omega)}{\rho_o c_o} = - (j\omega)^{v-3} k_o^2 \frac{\exp[-jk_o R_r]}{4\pi R_r} \sum_{n=-\infty}^{\infty} A_n^{(v)} \exp[-jn\phi] \quad (3-29)$$

where

$$A_n^{(v)} = \exp[jn\pi/2] \left[ \int_0^\infty \tilde{B}_{\alpha\beta}^{(v)}(R') C_{n\alpha\beta}^{(v)}(R') R' dR' \right] \quad k_x = k_o \cos\theta_o$$

and

$$C_{n\alpha\beta}^{(v)} = N_{\alpha\beta} C_n^{(v)}.$$

$R_r$  is the distance along a line joining the far-field observer and the axial center of the source region and  $\theta_o$  is the angle between the line and the

(downstream) jet axis. In what follows, all quantities, e.g.  $N_{\alpha\beta}$ ,  $C_n^{(\nu)}$ , are evaluated with the particular value of the axial wavenumber,  $k_x/k_o = \cos\theta_o$ .

The quantities  $C_{n\alpha\beta}^{(\nu)}$ , written out explicitly, are

$$C_{nx\bar{x}}^{(\nu)} = -\cos^2\theta_o C_n^{(\nu)} \quad (3-31)$$

$$C_{nxr}^{(\nu)} = j \cos\theta_o \frac{dC_n^{(\nu)}}{dR} \quad (3-32)$$

$$C_{nrr}^{(\nu)} = \frac{d^2C_n^{(\nu)}}{dR^2} \quad (3-33)$$

$$C_{nx\phi}^{(\nu)} = -\cos\theta_o \frac{n}{R} C_n^{(\nu)} \quad (3-34)$$

$$C_{nr\phi}^{(\nu)} = j n \left\{ \frac{1}{R} \frac{dC_n^{(\nu)}}{dR} - \frac{C_n^{(\nu)}}{R^2} \right\} \quad (3-35)$$

$$C_{n\phi\phi}^{(\nu)} = \left\{ \frac{1}{R} \frac{dC_n^{(\nu)}}{dR} - \frac{n^2}{R^2} C_n^{(\nu)} \right\}. \quad (3-36)$$

Since the factor multiplying  $p_i$  in the expression for  $C_n^{(3)}$  [Equation (3-26)] is independent of  $R$ , the first and second radial derivatives in the above expressions can be evaluated with Equation (3-28) and the equations [that follow directly from (3-20) and (3-22)].

$$\frac{dC_n^{(3)}}{dR} = \frac{1}{p_i} \frac{dp_i}{dR} C_n^{(3)} \quad (3-37)$$

$$\frac{d^2C_n^{(3)}}{dR^2} = -\{\kappa^2 - n^2/R^2\} C_n^{(3)} + \frac{R}{\bar{\rho}D^2} \frac{d}{dR} \left\{ \frac{\bar{\rho}D^2}{R} \right\} \frac{dC_n^{(3)}}{dR} \quad (3-38)$$

The first radial derivative in Equation (3-38) can of course be removed with aid of Equation (3-37). In its present form Equation (3-38) shows that the radiation from a radial-radial volume displacement quadrupole of unit strength in a non-uniform flow contains a component that is identical to the radiation from a volume displacement point radial dipole at the same location, but with a source strength amplitude given by

$$\frac{R^4}{\bar{\rho}D^2} \frac{d}{dR^4} \left\{ \frac{\bar{\rho}D^2}{R^4} \right\} \quad (3-39)$$

This component is dominant at the low frequency limit analyzed in Section 3.2.5.2 [whereas the other component, the first term in Equation (3-38) takes over at the high frequency or geometric acoustics limit discussed in Section 3.2.5.1].

However unless the radial dipole radiation solution,  $dC_n^{(3)}/dR$ , is known it is not possible to infer from (3-38) any direct connection between mean flow gradients and the dipole component of the far-field radiation, for the radial dipole solution itself may depend on those gradients. The objective must be to obtain analytic or numerical solutions for  $C_n^{(3)}$  and  $dC_n^{(3)}/dR$ , or  $p_i^{-1} dp_i/dR$ , before specific conclusions can be drawn regarding the radiation dependence on flow properties at the source position.

### 3.2.3 Source Model

For purposes of investigating flow effects (including non-uniform density and sound speed) on sound radiation from jets, a simplified model is introduced to simulate the jet turbulence. For modeling acoustically compact eddies, a point quadrupole source is used which is isotropic in a statistical sense; thus, its radiated intensity in the absence of flow would be omnidirectional. Details of the source model are as follows:

(a) Initially, the source distribution is concentrated at a point, or

$$\begin{aligned} B_{\alpha\beta}^{(v)}(k_x, n, \omega; r) &\rightarrow B_{\alpha\beta}^{(v)}(k_x, n, \omega) \delta(r - r_s)/r \\ &= k_o^2 \tilde{B}_{\alpha\beta}^{(v)} \frac{\delta(R - R_s)}{R} \end{aligned} \quad (3-40)$$

so that  $A_n^{(v)}$  reduces to

$$A_n^{(v)} = k_o^2 \exp[jn\pi/2] \left[ \tilde{B}_{\alpha\beta}^{(v)} C_{n\alpha\beta}^{(v)} \right]_{R = R_s}. \quad (3-41)$$

(In what follows, subscript 's' denotes evaluation at  $R = R_s$  or  $x = x_s$ .) The term point quadrupole refers to the radial dependence of the source distribution in this model. In addition, it is recognized that the features (b) and (d) below are equivalent to taking the azimuthal average of the mean square radiated pressure due to a source distribution that is concentrated at a fixed azimuthal point.

(b) The ring source is assumed, like the jet turbulence<sup>23</sup>, to have a strength whose mean square value is independent of azimuthal position. The resulting expression for the power spectral density of the radiated pressure,  $P(R_f, \theta, \omega)$ , is therefore the sum of the spectral densities of the pressures radiated in each azimuthal mode:

$$\frac{16\pi^2 R_r^2}{k_o^8 \omega^{2\nu-6} \rho_o^2 c_o^4} \frac{P(R_r, \theta_o, \omega)}{=}$$

$$\sum_{n=-\infty}^{+\infty} \text{Limit}_{T \rightarrow \infty} \left\{ \frac{\bar{B}_{\alpha\beta}^{(\nu)} \bar{B}_{\delta\gamma}^{(\nu)*}}{2T} \right\} C_{n\alpha\beta}^{(\nu)}(R_s) C_{n\delta\gamma}^{(\nu)*}(R_s) \quad (3-42)$$

where  $T$  is an appropriate averaging time.

(c) The source excitation is statistically isotropic, or

$$\text{Limit}_{T \rightarrow \infty} \left\{ \frac{\bar{B}_{\alpha\beta}^{(\nu)} \bar{B}_{\delta\gamma}^{(\nu)*}}{2T} \right\} = \delta^{(\nu)}(k_x, n, \omega) (\delta_{\alpha\delta} \delta_{\beta\gamma} + \delta_{\alpha\gamma} \delta_{\beta\delta}) \quad (3-43)$$

where  $\delta_{ij}$  is the Kronecker delta.

(d) The azimuthal source coherence is negligible, or

$$\delta^{(\nu)}(k_x, n, \omega) \rightarrow \phi^{(\nu)}(k_x, \omega) \quad (3-44)$$

so that the azimuthal mode excitation is uniform.  $\phi^{(\nu)}(k_x, \omega)$  is a cross-power spectral density of each and every quadrupole source strength integrated over the source "volume." Here the cross-power spectral density is the two-dimensional Fourier transform of the cross-correlation function of the source strength,  $B_{\alpha\beta}^{(\nu)}$ , with respect to temporal and axial separations; radial and azimuthal coherence effects are not included in the present model.

Equation (3-42) then reduces to its final form for the stationary Statistically-Isotropic Point Quadrupole (SIPQ) model

$$\frac{16\pi^2 R_r^2 P(R_r, \theta_o, \omega)}{k_o^8 \omega^{2\nu-6} \rho_o^2 c_o^4 \phi^{(\nu)}(k_o \cos \theta_o, \omega)}$$

$$= \sum_{n=-\infty}^{\infty} C_{n\alpha\beta}^{(\nu)}(R_s) C_{n\alpha\beta}^{(\nu)*}(R_s) \quad (3-45)$$

$$= F^{(\nu)}(\omega).$$

The right-hand side of Equation (3-45) is unity in the absence of flow and hence is referred to as the Flow Factor,  $F^{(\nu)}(\omega)$ .

(e) Source convection and non-compactness effects are included by assuming that<sup>24</sup>

$$\phi^{(\nu)}(k_x, \omega) = \phi^{(\nu)}(0, \omega') \quad (3-46)$$

where

$$\omega'' = \{(\omega')^2 + (k_x U_{e1})^2\}^{1/2}$$

and

$$\omega' = \omega - k_x U_c . \quad (3-47)$$

Here  $U_c$  is the axial eddy convection velocity,  $\omega'$  is the frequency in a frame of reference moving at that velocity and  $U_{e1}$  is a wavenumber scaling velocity representing axial coherence effects in the moving frame. The modified moving-frame frequency  $\omega''$ , evaluated at the acoustic wavenumber  $k_x = k_0 \cos \theta_0$  is

$$\begin{aligned} \omega_m &= \omega f (1 - U_c \cos \theta_0 / c_0)^2 + (U_{e1} \cos \theta_0 / c_0)^2 \}^{1/2} \\ &= \omega D_m, \end{aligned} \quad (3-48)$$

where  $D_m$  is a modified Doppler factor.

Equation (3-45), rewritten in terms of  $\omega_m$ ,  $D_m$  and the modified Strouhal number  $S_m$ , where

$$2\pi S_m = (\omega_m d / U_J) , \quad (3-49)$$

is

$$\begin{aligned} 16\pi^2 \left( \frac{R_r}{d} \right)^2 \frac{\omega P(R_r, \theta_0, \omega)}{\rho_0^2 c_0^4} &= (2\pi)^{2\nu+2} \left\{ \frac{F^{(\nu)}(\omega_m / D_m)}{D_m^{2\nu+3}} \right\} S_m^{2\nu+2} \\ &\times \left\{ \frac{\omega_m \Phi^{(\nu)}(0, \omega_m) U_J^{2\nu+2}}{d^{2\nu+4} c_0^8} \right\}. \end{aligned} \quad (3-50)$$

If  $S_m$  is held constant the predicted jet noise directivity is given by the Flow Factor,  $F^{(\nu)}$ , divided by  $D_m^{2\nu+3}$ .

Jet noise measurements are commonly analyzed using a Doppler factor of the form

$$D_m = \{(1 - U_c \cos \theta_0 / c_0)^2 + (\alpha U_c / c_0)^2\}^{1/2}, \quad (3-51)$$

which differs from (3-48) in that the second term contains no  $\cos^2 \theta_0$  factor. The definition (3-51) follows in the Lighthill analogy<sup>9</sup> from assuming that the source spatial coherence is isotropic in the moving frame, rather than limited to the axial direction as in (3-48). Extension of the present shear-flow model to include radial and azimuthal coherence effects is more complicated, and will not be attempted here; for purposes of comparison with data in section 3.3 of this paper, Equation (3-51) has been used as a preliminary approximation, with  $\alpha$  taken as 0.3.

### 3.2.4 Numerical Results

Numerical solutions for the far-field radiation in any direction have been generated, for a wide range of flow parameters and source types (including the statistically-isotropic point quadrupole - SIPQ - mentioned above).

Some numerical results are presented in Figures 3.4 and 3.5 for the flow factor, defined as the ratio of the far-field intensity to its value without the jet flow, the source strength being held constant. The horizontal scale is the nondimensional frequency  $k_0 \delta$ , where  $k_0 = 2\pi f/c_0$  and  $\delta$  is the shear layer thickness based on the maximum velocity gradient.

In all the numerical calculations, the fluid is assumed to be a perfect gas with constant specific-heat ratio  $\gamma$ , and error function profiles of velocity and temperature have been used, in the form

$$\phi = \frac{U}{U_J} = \frac{1}{2} \{1 - \operatorname{erf}(\sqrt{\pi} x)\}, \quad (3-52)$$

$$\frac{T}{T_\infty} = 1 + \phi \left( \frac{T_J}{T_\infty} - 1 \right), \quad (3-53)$$

The radial similarity coordinate  $x$  is defined by

$$x = \frac{r - r_0}{\delta} + \text{const.}, \quad (3-54)$$

where the value of the constant determines the value of  $\phi$  at  $r = r_0$ . In order that  $r = r_0$  may be identified with the lip line in the jet mixing region (i.e.  $r_0$  = nozzle radius  $d/2$ ), we choose  $\phi(r = r_0)$  as 0.663 and the constant is accordingly taken as -.168. The resulting profiles contain  $\delta/r_0$  as a shape parameter; to relate  $\delta/r_0$  to axial position in the initial mixing region, the approximate relation  $x/d \approx 3.5 \delta/r_0$  may be used (corresponding to a spreading parameter  $c = 7\pi^{1/2} \approx 12.4$ ).

Both Figures 3.4 and 3.5 refer to the SIPQ source, and it is remarkable how little the results depend on the frequency parameter  $k_0 r_0$  based on nozzle radius at least outside the cone of silence. The low frequency and high frequency asymptotes shown in Figures 3.4 and 3.5 are described in the following section. It should be noted that there is no influence of the mean flow velocity on radiation at  $90^\circ$ ; that is, any flow factor at  $90^\circ$  is independent of the shear layer velocity profiles at this angle, and hence the results in Figure 3.4 are valid for both the volume acceleration and volume displacement SIPQ Flow Factors,  $F^{(1)}$  and  $F^{(3)}$ .

Other numerical results are discussed in Section 3.3 and Appendices 3C and 3D.

### 3.2.5 Asymptotic Solutions

Analytical solutions to the Lille equation have been derived, which are asymptotically valid in the low and high frequency limits ( $k_0 \delta \rightarrow 0$  and  $k_0 \delta \rightarrow \infty$ ).

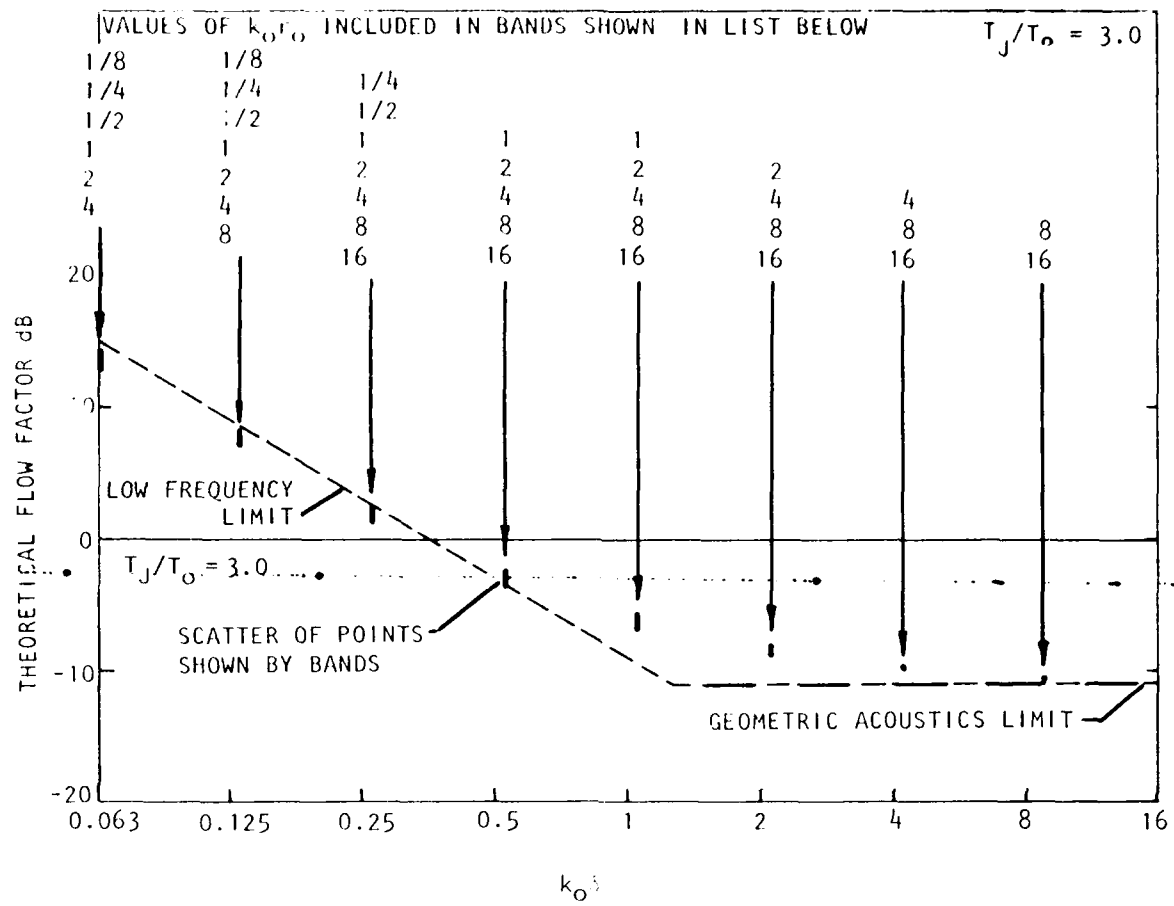


Figure 3.4 Calculated Flow Factor for a Stationary Point Displacement Quadrupole (SIPQ Source) in an Axisymmetric Shear Flow. Hot Case,  $T_J/T_o = 3.0$ ; Radiation Angle  $90^\circ$ ; Radial Source Location Corresponds to  $\phi_s = .663$ . Bars on Graph Indicate  $k_o r_o$  (or  $r/r_o$ ) dependence of results.

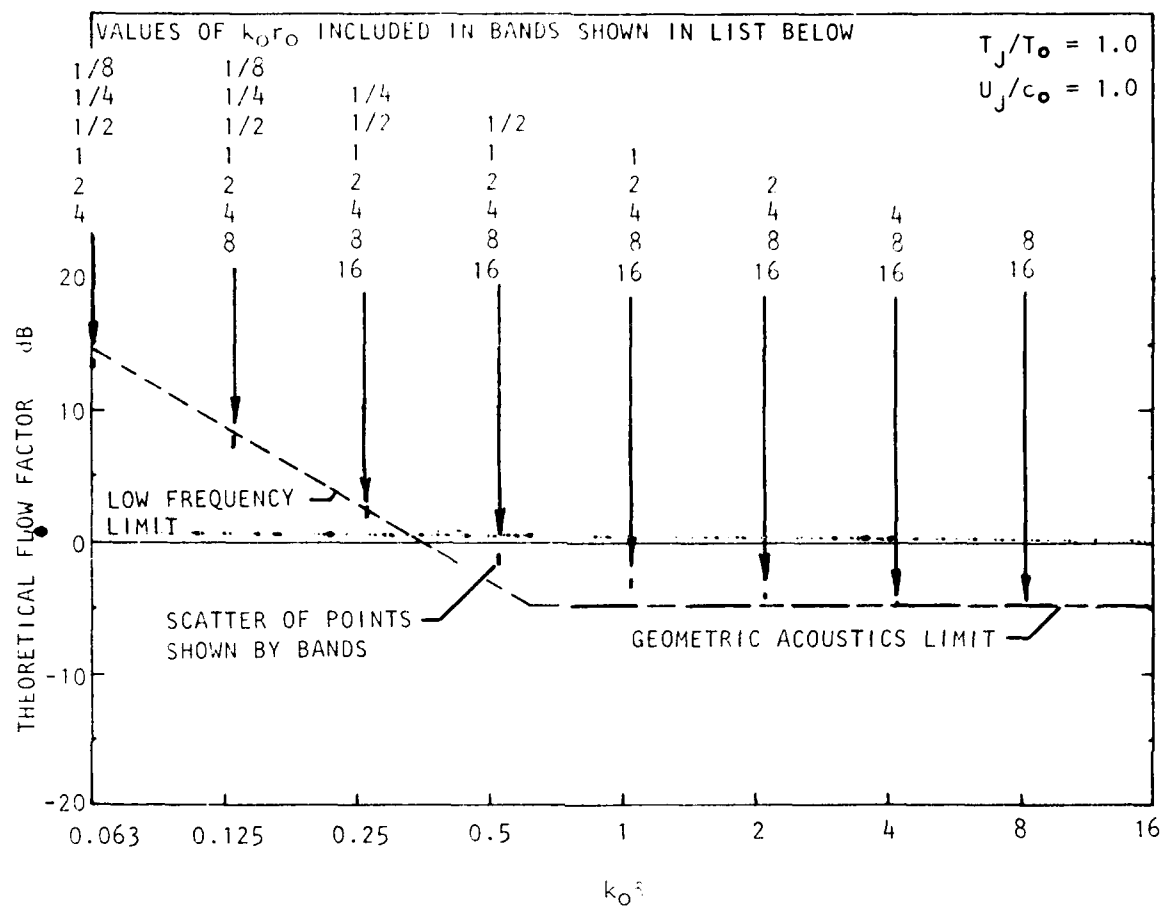


Figure 3.5 Calculated Flow Factor for a Stationary Point Displacement Quadrupole (SIPQ Source) in an Axisymmetric Shear Flow. Isothermal Case; Case,  $U_J/c_0 = 1.0$ ; Radiation Angle  $75^\circ$ ;  $i_s = .663$

The corresponding predictions for the SIPQ flow factor are shown in Figures 3.4 and 3.5, for comparison with the numerical solutions; it is clear that the asymptotic results are useful over a wide range of  $k_0$ .

The *high-frequency* asymptote is based on geometric acoustics (GA); it is a generalization to cylindrical geometry of earlier work by Csanady<sup>25</sup>, Krishnappa<sup>26</sup> and Pao<sup>27</sup>. The *low frequency* (LF) asymptote is based on a plug flow representation of the mean jet profile (i.e.  $\delta/r_0 \rightarrow 0$ ), but differs from earlier plug-flow calculations<sup>28,29</sup> in allowing the source to be placed anywhere within the shear layer. This feature is important since the LF solution thus obtained shows large increases in radiation when the SIPQ source is placed within the shear layer, rather than in the uniform jet flow region.

### 3.2.5.1 High-frequency results (GA)

In the high-frequency or geometric acoustics (GA) limit, where the acoustic wavelength is small compared with the shear layer thickness, an asymptotic result for the flow factor for any type of source can be derived outside the cone of silence using an energy conservation law, as outlined below.

- The cone of relative silence is defined for this purpose to include all angles  $\theta_0$  for which the dimensionless quantity

$$\kappa^2(\theta_0, x) = \frac{c_0^2}{\bar{c}^2(x)} D^2(\theta_0, x) - \cos^2 \theta_0 \quad (3-55)$$

remains positive for all dimensionless radii  $R \geq R_s$ , i.e. from the source radius outwards.

The derivation begins from the zero-flow result relating the power spectrum  $P(\omega)$  of the far-field pressure to the source power spectrum  $\Phi(v)(k, \omega)$ , where  $v=1$  refers to a volume-acceleration distribution and  $v=3$  to a volume-displacement distribution as before. At distance  $R_r$  from the source region, in a stationary uniform fluid of density  $\bar{\rho}_s$  and sound speed  $\bar{c}_s$ ,

$$R_r^2 P(\omega) \ll [\bar{\rho}_s^2 \Phi(v)(k, \omega)]_{k=\omega \alpha_s / \bar{c}_s} \quad (3-56)$$

Here  $\hat{g}$  is a unit vector in the wavenormal direction, and the subscript s denotes source-region properties (to be distinguished later from the ambient region, subscript o).

Equation (3-56) may be generalized to cover radiation into a *uniform flow*, parallel to the x axis of velocity  $U_s$ , by means of a Doppler transformation<sup>30</sup>. The Doppler factor  $D_s$ , relating frequencies relative to the flow frequencies in a stationary frame, is given by

$$D_s = (1 + U_s \cos \theta_s / \bar{c}_s)^{-1} \quad (3-57)$$

where  $\cos \theta_s$  is the component of  $\alpha_s$  in the axial direction. Thus, Equation (3-56) becomes, with flow included,

$$R'_r P(\omega) = \left[ \bar{\rho}_s D_s^{2\nu} \Phi^{(\nu)}(k, \omega) \right] k = \omega D_s \alpha_s / \bar{c}_s ; \quad (3-58)$$

the radiation distance  $R_r'$  is now interpreted as the distance travelled by the wavefronts through the fluid in the *downstream* direction, and so does not contain the effect of convection by the flow. Note that (3-58) depends, through  $\nu$ , on the number of  $\partial/\partial t$  derivatives in the fixed-frame source description, but does not depend explicitly on the multipole order or number of spatial derivatives.

The effect of source multipole order  $\mu$  enters through the wavenumber dependence of  $\Phi^{(\nu)}(k, \omega)$ . Thus, for a *compact* isotropic multipole source of order  $\mu$  (e.g. a point multipole),

$$\Phi^{(\nu)}(k, \omega) \propto |k|^{2\mu} ; \quad (3-59)$$

combining (3-58) and (3-59) gives the compact-source result

$$R_r'^2 P(\omega) \propto \bar{\rho}_s^2 \bar{c}_s^{-2\mu} D_s^{2\nu+2\mu} . \quad (3-60)$$

To apply this result to radiation from a point source in a cylindrical shear layer of arbitrary profile, we note that in the GA limit Equation (3-60) may be applied within the locally uniform flow surrounding the source region. The quantity  $R_r' P(\omega)$  in the source-region flow is then related, by Blokhintsev's energy conservation law<sup>31</sup>, to the corresponding quantity in the ambient fluid at rest. More precisely, it is the azimuthal averages of these quantities which are related, since the power radiated into the conical sector  $(\theta_s, \theta_s+d\theta_s)$  in the region surrounding the source must all emerge in the conical sector  $(\theta_0, \theta_0+d\theta_0)$  far from the cylindrical flow, where

$$\frac{\cos\theta_0}{c_0} = \frac{\cos\theta_s}{\bar{c}_s} D_s . \quad (3-61)$$

The relationship which follows from equating the sound power within and outside the flow is

$$\langle R_r'^2 P(\omega) \rangle_o \frac{1}{\rho_0 c_0} d(\cos\theta_0) = \langle R_r'^2 P(\omega) \rangle_s \frac{1}{\bar{\rho}_s \bar{c}_s} D_s^2 d(\cos\theta_s) . \quad (3-62)$$

where the angle brackets denote an average with respect to the azimuthal angle  $\phi$ . It follows from (3-61) and (3-62) that

$$\frac{\langle R_r'^2 P(\omega) \rangle_o}{\langle R_r'^2 P(\omega) \rangle_s} = \frac{\rho_0}{\bar{\rho}_s D_s^4} \quad (3-63)$$

Finally, a value for the flow factor  $F$  (as defined in Section 3.2.4) may be deduced from (3-60) and (3-63). The simplest case is that of a source

whose zero-flow radiation is statistically isotropic; the flow factor for radiation at polar angle  $\theta_0$  outside the flow is given by

$$F(v) = \frac{\bar{\rho}_S}{\rho_0} \left( \frac{\bar{c}_S}{c_0} \right)^{-2\mu} D_S^{2v+2\mu-4}, \quad (3-64)$$

for compact isotropic source distributions of any type ( $v$ ) or multipole order ( $\mu$ ), radiating at high frequencies to angles outside the cone of silence.

A special case of particular interest is the SIPQ displacement source ( $v=3$ ), radiating into a perfect gas of constant specific-heat ratio. Then Equation (3-64) gives

$$F^{(3)} = D_S^6 (T_S/T_0)^{-3} \quad (3-65)$$

as the flow factor in the GA limit. The asymptotes shown in Figures 3.4 and 3.5 (for high  $k_0 R$ ) are based on Equation (3-65) and show good agreement with the high-frequency numerical results.

The above results are limited to radiation outside the cone of silence, that is to angles  $\theta_0$  outside the flow such that

$$\frac{-c_0}{\bar{c}_S - U_S} < \cos\theta_0 < \frac{c_0}{\bar{c}_S + U_S} \quad (U_S/\bar{c}_S < 1) \quad (3-66)$$

On the other hand if (3-66) is not satisfied, an alternative approach to the high-frequency limit becomes necessary. It is convenient to define a modified radial wavenumber  $q$  by writing

$$q^2 = \kappa^2 - (n^2 - \frac{1}{4})/R^2; \quad (3-67)$$

radiation into the cone of silence corresponds, at high frequencies, to having the source located in a region where  $q$  is imaginary. When this is the case, approximate high-frequency solutions to the homogeneous form of (3-11) yield — for each azimuthal mode —

$$\left[ c_n^{(v)} \quad c_n^{(v)*} \right]_S = \frac{\bar{\rho}_S}{\rho_0} D_S^{2v-4} \frac{1}{2\pi R_S |q_S|} \exp \left( -2 \int_{R_S}^{R_T} |q| dR \right); \quad (3-68)$$

here  $R_T$  denotes the (single) value of  $R$  at which  $q$  changes sign, on moving radially outwards from the source.

Summation of Equation (3-68) over  $n$  gives the monopole flow factor, in the high-frequency limit, for radiation into the cone of silence. The radiation suffers an exponential decay as it propagates from the source position  $R_S$  to the transition point  $R_T$ ; Equation (3-67) shows that the decay rate increases with increasing  $n$ , so that radiation within the cone of relative silence is dominated by low-order azimuthal modes. This is in contrast to the

radiation outside the cone of silence, where the relative contribution tends to peak at mode orders  $n \sim k_s R_s$  for omnidirectional sources.

### 3.2.5.2 Low-frequency results (LF)

The LF analytic solutions for  $C_{nab}^{(v)}$  and  $F^{(v)}$  have been derived by making two approximations, which are exact in the low-frequency limit  $k_o\delta \rightarrow 0$ . First, the pressure at any position within the shear layer is equated with its corresponding initial or edge value. At the inner and outer edges of the shear layer,  $R = R_J$ ,  $R_\infty$ , the independent solutions to the homogeneous form of Equation (3-11),  $p_i$ ,  $p_o$ , take the initial values given by Equations (3-23) and (3-24). Thus, the first approximation gives

$$p_i(R) = p_i(R_J) = J_n(k_J R_J), \quad (3-69)$$

$$p_o(R) = p_o(R_\infty) = H_n^{(2)}(k_o R_\infty). \quad (3-70)$$

Second, the radial derivative of the pressure at any position within the shear layer is determined by equating the transverse particle displacement with its corresponding initial or edge value, that is (omitting the  $1/\omega^2$  factor),

$$\frac{1}{\rho D^2} \frac{dp_i(R)}{dR} = \frac{1}{\rho_J D_J^2} \frac{dp_i(R_J)}{dR} = \frac{k_J}{\rho_J D_J^2} J_n'(k_J R_J), \quad (3-71)$$

$$\frac{1}{\rho D^2} \frac{dp_o(R)}{dR} = \frac{1}{\rho_o} \frac{dp_o(R_\infty)}{dR} = \frac{k_o}{\rho_o} H_n^{(2)'}(k_o R_\infty). \quad (3-72)$$

When Equations (3-69) through (3-72) are substituted into Equation (3-26) and  $R$ ,  $R_J$  and  $R_\infty$  are replaced by  $R_o$  [the errors being  $O(k_o\delta)$ ] that equation reduces to

$$\left[ C_n^{(3)} \right]_s = \frac{\rho_J}{\rho_o} D_J^2 \frac{J_n(k_J R_o)}{E_n} \quad (3-73)$$

where

$$E_n = \frac{j\pi}{2} \left\{ \frac{\rho_J}{\rho_o} D_J^2 k_o R_o H_n^{(2)'}(k_o R_o) J_n(k_J R_o) - k_J R_o J_n'(k_J R_o) H_n^{(2)}(k_o R_o) \right\} \quad (3-74)$$

Similarly Equations (3-37), (3-69), (3-71), and (3-73) combine to give

$$\left[ \frac{dc_n^{(3)}}{dR} \right]_s = \frac{\bar{\rho}_s}{\rho_o} D_s^2 \frac{k_J J_n'(k_J R_o)}{E_n}. \quad (3-75)$$

Among the six quadrupole components making up the volume displacement flow factor [see Equations (3-31) through (3-36)], the radial-radial quadrupole is dominant in the LF limit ( $k_o \delta \rightarrow 0$ ) since it alone contains a term that is inversely proportional to ( $k_o \delta$ ). That term appears when the approximations to  $C_n^{(3)}$  and  $dC_n^{(3)}/dR$ , given by Equations (3-73) and (3-75), are substituted into Equation (3-38), after making use of the Bessel equation the resulting expression is

$$\left[ \frac{d^2 C_n^{(3)}}{dR^2} \right]_S : C_{nrr}^{(3)} = E_n^{-1} \left[ \frac{\bar{\rho}_s}{\rho_o} D_s^2 \kappa_J^2 J_n''(k_J R_o) + J_n'(k_J R_o) \left\{ \frac{\bar{\rho}_s}{\rho_o} D_s^2 \kappa_J^2 - \frac{\rho_J}{\rho_o} D_J^2 \kappa_s^2 + \frac{n^2}{R_o^2} \left( \frac{\rho_J}{\rho_o} D_J^2 - \frac{\bar{\rho}_s}{\rho_o} D_s^2 \right) \right\} + \left\{ \frac{1}{(k_o \delta)} \left[ \frac{d}{dx} \left( \frac{\bar{\rho}}{\rho_o} D^2 \right) \right]_S \kappa_J J_n'(k_J R_o) \right\} \right], \quad (|R - R_o| \leq k_o \delta) \quad (3-76)$$

The second and third terms in this expression vanish when the radial source position is at the inner edge of the shear layer ( $\bar{\rho}_s, D_s, \kappa_s \rightarrow \rho_J, D_J, \kappa_J$ ); the term that remains, the first one containing the second derivative of  $J_n$ , is identical to the standard, plug flow model result with the source placed inside the plug flow but adjacent to the vortex sheet. When the radial source position is at the outer edge of the shear layer ( $\bar{\rho}_s, D_s, \kappa_s \rightarrow \rho_o, 1, \sin \theta_o$ ) only the third term vanishes and again the remaining terms are identical to the standard plug flow result with the source placed outside the plug flow but adjacent to the vortex sheet. Otherwise, Equation (3-76) is a new result that (a) describes a smooth transition between those standard results by allowing for an arbitrary radial source position within the shear layer and (b) reveals the existence of a new sound generation mechanism. That mechanism is described by the third term in the expression for  $C_{nrr}^{(3)}$  and will be referred to as low-frequency scattering by the mean velocity and mean density gradient. Scattering of a different kind is represented by the second term: the mismatch of the mean flow velocity and mean density at the source position with that of the inner uniform flow, or jet column, causes radiation that can be described in the standard plug flow model only when the source is entirely outside the shear layer. The relevance of the new mechanism to jet noise is discussed in Section 3.3.

When  $R_o \ll 1$  ( $R_o = k_o r_o$ ) the usual Bessel function approximations can be used to further simplify the expression for  $C_{nrr}^{(3)}$  and then only the  $n = -1, +1$  azimuthal modes need be considered, that is, the flow factor can be approximated by

$$F^{(3)} = 2 |C_{1rr}^{(3)}|^2 = \frac{2 \sin^2 \theta_o}{(1 + \rho_J D_J^2 / \rho_o)^2} \left\{ \frac{1}{(k_o \delta)} \times \left[ \frac{d}{dx} \left( \frac{\bar{\rho}}{\rho_o} D^2 \right) \right]_S + \frac{1}{(k_o r_o)} \left( \frac{\rho_J}{\rho_o} D_J^2 - \frac{\bar{\rho}_s}{\rho_o} D_s^2 \right) \right\}^2 \quad (3-77)$$

At  $90^\circ$  and neglecting the jet column scattering term, this reduces to

$$F^{(1)} = F^{(3)} = 2 \left\{ \frac{1}{(\rho_0 + \rho_J)} \frac{1}{k_0 \delta} \left[ \frac{d\bar{\rho}}{dx} \right]_S \right\}^2 = \frac{2}{k_0^2} \left\{ \frac{1}{(\rho_0 + \rho_J)} \left( \frac{d\bar{\rho}}{dr} \right)_S \right\}^2 \quad (3-78)$$

Equation (3-78) defines the low-frequency asymptote shown in Figure 3-4. Similarly for an isothermal shear layer it reduces to

$$F^{(3)} = 2 \left\{ \frac{\sin 2\theta_0 (1 - U_s \cos \theta_0 / c_0)}{1 + (1 - U_J \cos \theta_0 / c_0)^2} \frac{1}{k_0 \delta} \cdot \left[ \frac{dU/c_0}{dx} \right]_S \right\}^2 \quad (3-79)$$

Equation (3-79) defines the low-frequency asymptote shown in Figure 3.5. Note that the factor  $[d(U/c_0)/dx]_S/k_0 \delta = [dU/dr]_S/\omega$  may be expressed in non-dimensional terms using the Strouhal number  $S$ , as  $(\pi S)^{-1} [d(U/U_J)/d(r/r_0)]_S$ ; this suggests an alternative view of (3-79) as being a low Strouhal number asymptotic result, for a given value of  $U_J/c_0$ .

Corresponding LF solutions for a volume acceleration quadrupole source distribution ( $v=1$ ) follow directly from Equation (3-28) and its first and second radial derivatives:

$$\left[ \frac{dC_n^{(v)}}{dR} \right]_S = D_S^{v-3} \left[ \frac{dC_n^{(3)}}{dR} \right]_S + (v-3) \frac{D_S^{v-4}}{(k_0 \delta)} \left[ \frac{dD}{dx} \right]_S \left[ C_n^{(3)} \right]_S \quad (3-80)$$

$$\begin{aligned} \left[ \frac{d^2C_n^{(v)}}{dR^2} \right]_S &= D_S^{v-3} \left[ \frac{d^2C_n^{(3)}}{dR^2} \right]_S + 2(v-3) \frac{D_S^{v-4}}{(k_0 \delta)} \left[ \frac{dD}{dx} \right]_S \left[ \frac{dC_n^{(3)}}{dR} \right]_S \\ &\quad + (v-3) D_S^{v-4} \left\{ (v-4) D_S^{-1} \left[ \frac{dD}{dx} \right]_S^2 \right. \\ &\quad \left. + \left[ \frac{d^2D}{dx^2} \right]_S \right\} \frac{\left[ C_n^{(3)} \right]_S}{(k_0 \delta)^2} \quad (3-81) \end{aligned}$$

These derivatives can be evaluated with LF expressions for  $C_n^{(3)}$  and its first and second radial derivatives, given by Equation (3-73), (3-75), and (3-76). Equations (3-80) and (3-81) with Equations (3-31) and (3-36) indicate that the mean velocity gradient scattering term appears in all the LF quadrupole results,  $C_{nab}^{(v)}, v \neq 3$ , with the exception of  $C_{nxx}^{(v)}$  (axial-axial) and  $C_{nxz}^{(v)}$  (axial-azimuthal) while the LF volume acceleration radial-radial quadrupole radiation amplitude [Equation (3-81)] also contains a component that is proportional to square of the mean shear and its radial derivative, and hence to  $(k_0 \delta)^{-2}$ .

### 3.3 INTERPRETATION OF JET NOISE MEASUREMENTS

Two principal effects of flow-acoustic interaction have been identified in the preceding section: (1) low-frequency scattering by the mean velocity and density field; (2) high-frequency refraction and the emergence of a cone of relative silence as the geometric acoustics limit is approached. The significance of these effects in jet noise is examined below in the light of the measurements available.

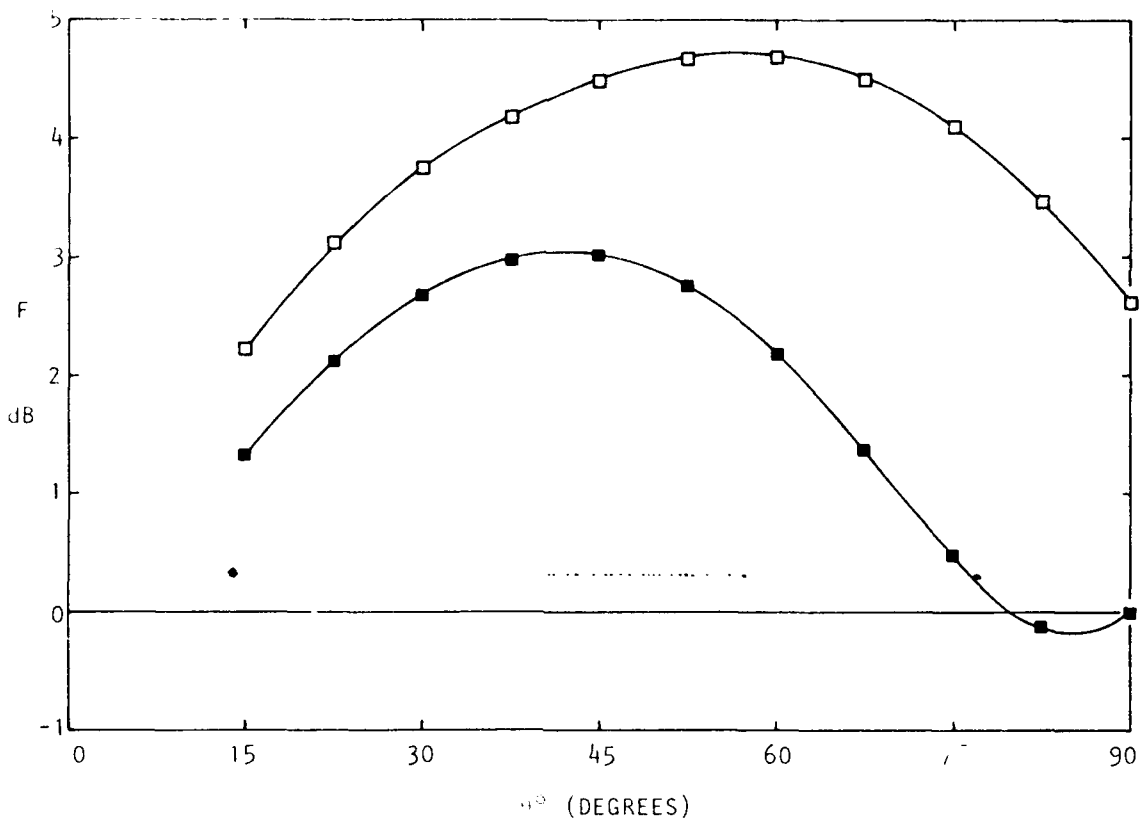
#### 3.3.1 Amplification of Quadrupole Radiation by Hot Jet Flow

The numerical results of Figure 3.4 and the analytical results of Section 3.2.5.2, have shown that the radiation from a quadrupole source can be amplified at low frequencies by placing the source in a nonuniform density field. Assuming the density field to be axisymmetric, the principal amplification mechanism is the incomplete cancellation of the radial-radial quadrupole field in the presence of radial density gradients. Failure to cancel at low frequencies is due to the dependence on local density of the radiation from each of the radial dipoles making up the rr-quadrupole.

In the present section we investigate the possibility that the same amplification mechanism is responsible for the increases in low velocity jet noise on heating which have been noted earlier (Figures 3.1 and 3.2). To begin with, we note from Figure 3.4 that, at least for density profiles typical of hot jets and for radial source locations representative of turbulent mixing noise, any low-frequency amplification at  $90^\circ$  is determined by  $k_0\delta$  and in fact closely follows the  $(k_0\delta)^{-2}$  dependence given by the asymptotic theory. Since the frequency parameter  $k_0\delta$  may be expressed as  $2\pi(f\delta/U_j)(U_j/c_0)$ , and  $f\delta/U_j$  is a jet similarity parameter, amplification of jet noise by the mean density field is expected to become apparent at low  $U_j/c_0$  values and to yield a  $(U_j/c_0)^{-2}$  factor on intensity in the low-velocity limit.

This prediction is consistent with the  $90^\circ$  data shown in Figures 3.1 and 3.2, but there are two points which require further discussion: (a) whether the predicted increase in radiated intensity has the observed directional dependence; (b) whether the source locations implied by the observed increases in intensity at various Strouhal numbers are physically realistic.

The directional dependence of the predicted low-frequency is illustrated in Figure 3.6, which compares the flow factors calculated for an SIPQ displacement source in two flow fields of the same velocity profile ( $U_j/c_0 = 0.5$ ;  $\delta/r_0 = 1.05$ , i.e. about  $3\frac{1}{2}$  to 4 diameters downstream) but different temperature profiles (isothermal and  $T_j/T_0 = 2$ ). The source frequency corresponds to a Strouhal number of 0.16, and has been chosen so that the increase in intensity at  $90^\circ$  is of the same order as observed experimentally. However, the angular trend is for the predicted increase to become smaller as the jet axis is approached, falling to around half the  $90^\circ$  value at angles of  $45^\circ$  and less, whereas experimentally the  $90^\circ$  increase is more than maintained throughout the rear arc down to  $15^\circ$  (see Figure 25 of Tanna and Dean<sup>32</sup>) This discrepancy, although only of order 3 dB, is too large to be explained by errors in the measured data.



$U_J/c_O$	$k_{O\infty}$	$\psi_c$	$T_J/T_O$
.5	.25	50°	2.0
.5	.25	40°	1.0

Figure 3.6 Comparison of Hot and Isothermal Flow Factors, Showing Increase of Displacement Quadrupole Radiation Due to Heating at Low Frequency ( $k_O^{-1} = .26$ ). Source: SIPQ at  $\psi_s = .600$ . Profile parameter  $\delta/r_O = 1.05$ ; Center Velocity Ratio  $U_J/c_O = 0.5$ ; Strouhal Number  $S = 0.16$ .

The second point, concerning the source locations implied by the observed increases in jet noise intensity, will be examined using  $90^\circ$  data at four different Strouhal numbers (0.1, 0.316, 1.0, 3.16). The sensitivity of the predicted SIPQ flow factor to source location, in a hot jet flow at low frequencies, is due mainly to the dependence of the mean density gradient on position within the jet. If the radial source location is assumed to correspond to the maximum intensity of turbulence across the shear layer, an effective axial location in the jet can be deduced at any given frequency from the measured increase in  $90^\circ$  intensity on heating.

Figure 3.7 shows in detail how the  $90^\circ$  SIPQ amplification is determined by the temperature ratio  $T_J/T_O$  and the frequency parameter  $k_O\delta$ , for a range of temperature profile shapes. The computed flow factor shows a strong dependence on  $k_O\delta$  in the amplification region, with a relatively insignificant dependence on the profile shape parameter  $\delta/r_O$ . Also shown in Figure 3.7 are the curves obtained by adding the low and high frequency flow factor asymptotes for each case; the agreement is close enough to justify using the asymptote approximation to interpret the measurements.

Based on these theoretical results, the axial source location required to account for the  $90^\circ$  hot jet measurements is obtained as follows. Let  $I$  denote the far-field intensity at a given  $U_J/c_O$  value for the hot jet, normalized as in Figure 3.1 and 3.2, and  $I_O$  the corresponding normalized intensity at the same  $U_J/c_O$  for an isothermal jet. An SIPQ source is assumed to represent the jet turbulence; moreover, any source alteration with jet temperature is neglected.\* Then,  $I/I_O$  is to be interpreted as the  $90^\circ$  SIPQ flow factor, which according to Figure 3.7 may be approximated by summing the GA and LF asymptotes to give

$$F^{(+)}) = (T_S/T_O)^{-3} + 2(K/k_O)^2 \quad (3-82)$$

where

$$K = \frac{1}{r_J + r_O} \left( \frac{d\bar{\rho}}{dr} \right)_S \quad (3-83)$$

Note that  $K$  is a function only of  $T_J/T_O$ , for the family of profiles represented by Equations (3-52) and (3-53), once the radial source location is specified in terms of  $\delta_S$ .

It follows from (3-82) that

$$(k_O\delta)^2 = \frac{2 I_O (k\delta)^2}{1 - I_O (T_S/T_O)^{-3}} .$$

---

\*This is in line with the high-velocity data of Figures 3.1 and 3.2, where the reduction in intensity with increasing jet temperature can be accounted for by the air flow factor  $(T_S/T_O)^{-3}$  — see Equation (3-75).

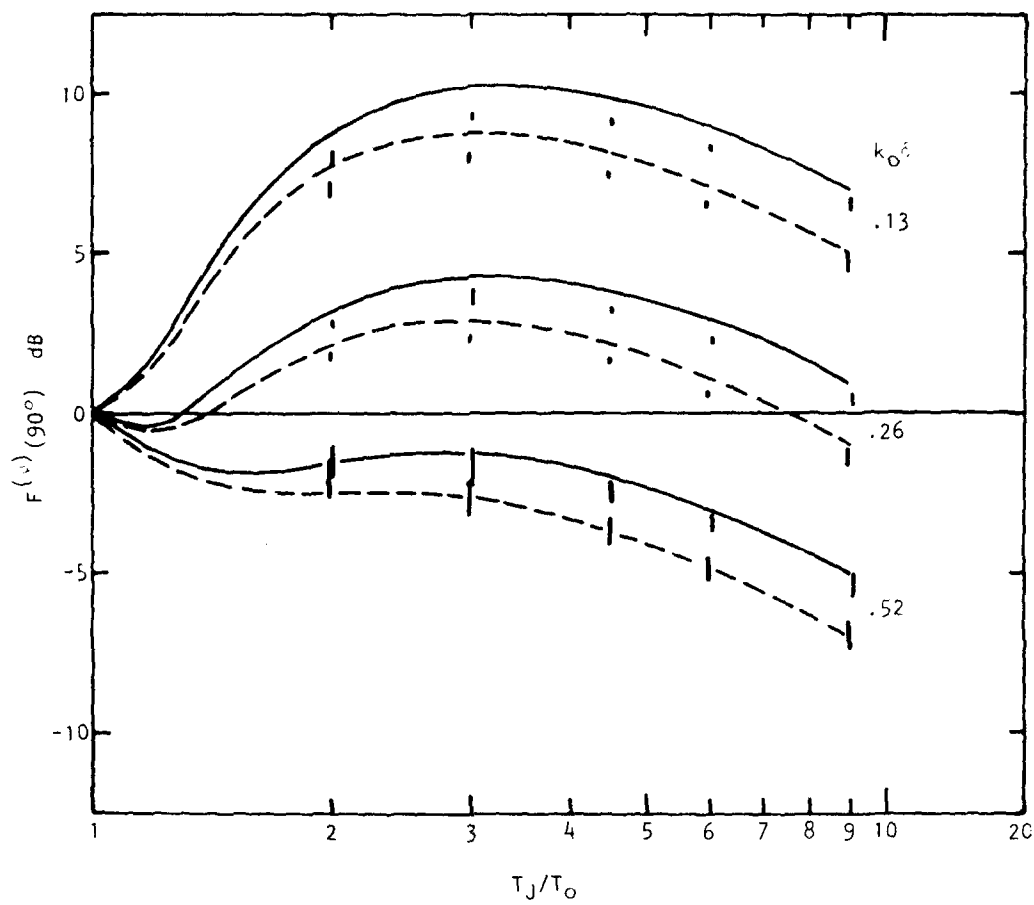


**Figure 3.7** Temperature and Frequency Dependence of  $90^\circ$  Flow Factor, for SIPQ Source in an Axisymmetric Shear Flow. Range of Numerical Results is Indicated by Bars (Based on  $\delta/r_0 = .26, .52, 1.05$ ); Upper And Lower Values are for  $\phi_s = .600$  and  $\phi_s = .663$ , respectively. Corresponding Lines Represent Addition of Low- and High-Frequency Asymptotes.

But  $k_0\delta$  may be written as  $\pi S(\delta/r_0)(U_j/c_0)$ ; thus

$$\left(\frac{\delta}{r_0}\right)^2 = \frac{2}{\pi^2 S^2} I_0(U_j/c_0)^{-2} G^{-1}, \quad (3-84)$$

where

$$G = \{1 - I_0(T_s/T_0)^{-3}\}/(K\delta)^2 \quad (3-85)$$

is obtained experimentally from a plot of normalized intensity versus  $(K\delta)^2$  as shown in Figure 3.8. Ideally, the data used to form this type of plot would be at such a low jet velocity that subtraction of the  $I_0(T_s/T_0)^{-3}$  term from  $I$  would make no significant difference; but in practice, although only the low end of the test velocity range was used, the correction was not negligible. The box heights in Figure 3.8 are therefore drawn to include both uncorrected and corrected data points, thus indicating the limits within which the asymptotic low-velocity data should lie.

For each of the four Strouhal numbers mentioned above, a value of  $G$  was obtained by plotting hot jet normalized intensities as in Figure 3.8. Also, a value of  $I_0(U_j/c_0)^{-2}$  was found from the low-velocity asymptote to the iso-thermal data, as defined for example in Figures 3.1 and 3.2. The resulting  $\delta/r_0$  values, converted to  $x_s/d$  values by multiplying by 3.5, are listed in Table 3-1 below.<sup>†</sup>

$S$	0.1	0.32	1	3.2
$x_s/d$	$4 - 5^{\ddagger}$	$1 - 1\frac{1}{2}$	$\sim \frac{1}{2}$	$\sim 1/5$

Table 3-1. Source locations required to account for hot jet noise by mean gradient scattering.

Thus, the entire jet radiation at  $S = .32$ , for example would have to be scattered at a density profile typical of  $1 - 1\frac{1}{2}$  diameters downstream, in order to account for the measured  $90^\circ$  levels of hot jet noise. This appears improbable in view of the source location evidence mentioned below. We conclude that there is a strong density scattering effect in hot jets at low velocities, but that it is mainly associated with the *unsteady* density field.

(See Appendix 3E for comparisons between measured data and a model based on scattering by the unsteady density field.)

<sup>†</sup>These  $x_s/d$  values would be increased by about 15 per cent if  $\phi_g$  were taken as .600, rather than .663.

<sup>‡</sup>Assuming the centerline temperature does not deviate significantly from  $T_j$ ; for lower Strouhal numbers, this assumption would evidently break down.

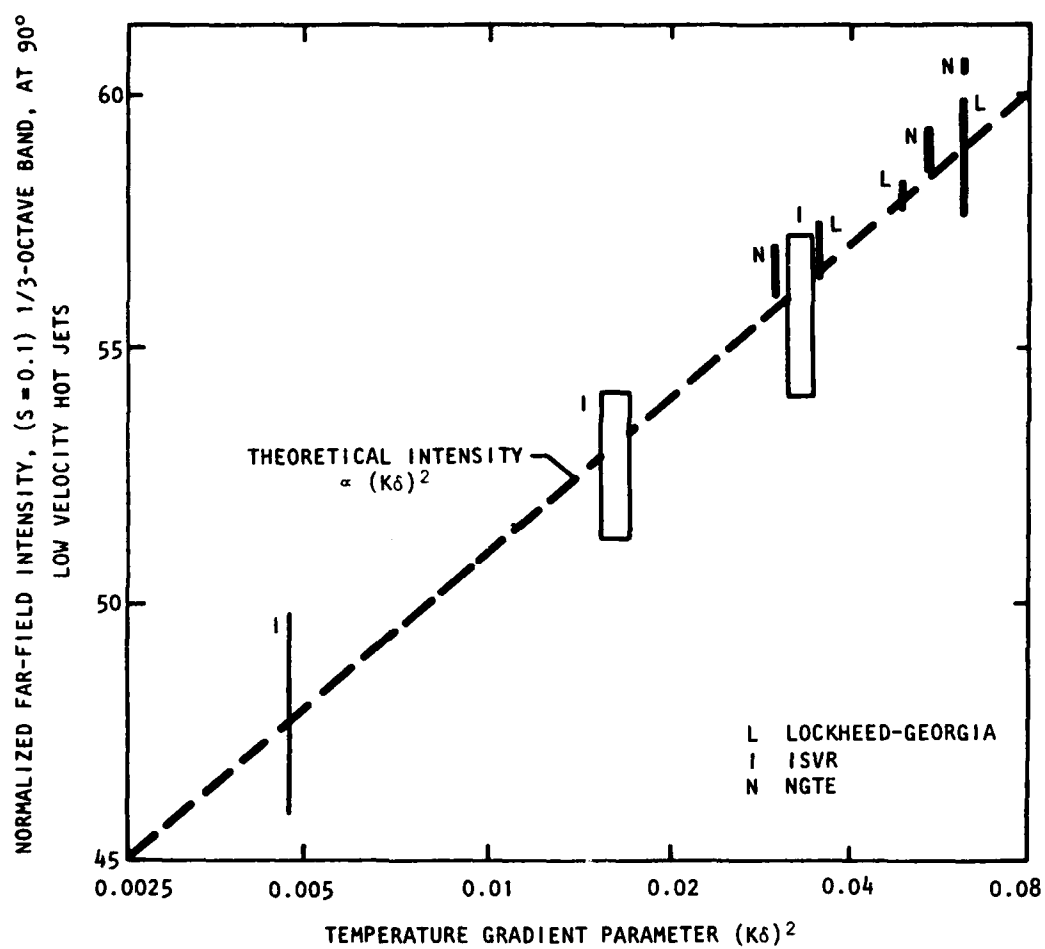


**Figure 3.8** Temperature Dependence of Low Velocity Jet Noise; for  $S = 0.1$  (based on measurements as in Fig. 3.2). Ordinate is Normalized Intensity as in Figs. 3.1 and 3.2. Code: L, Lockheed-Georgia Data (Nominal  $T_J/T_0$  Values 1.7, 2.2, 2.85); I, ISVR data (1.2, 1.4, 1.7); N, NGTE data (1.7, 2.3, 3.0).  $(K\delta)^2$  Values Based on  $\phi_s = .663$  (Experimental Range Indicated by Box Width).

### 3.3.2 Amplification by Mean Shear in Isothermal Jets

The possibility that jet noise is amplified by mean velocity gradients – particularly in the region of intense shear near the nozzle exit – was first put forward by Lighthill<sup>9</sup> over twenty years ago, but has not yet been satisfactorily resolved. In the framework of the present shear flow analogy, mean shear amplification can be studied as a flow-acoustic interaction effect, rather than as a contribution to the source term as in the zero-flow analogy, and is correspondingly easier to assess.

The mean shear effect is most easily studied at low jet Mach numbers, where the low-frequency asymptotic results of Section 3.2.5.2 apply. The same  $rr$ -quadrupole scattering term responsible for the hot-flow amplification at  $90^\circ$  (see Figures 3.4 and 3.7) gives rise to a mean-shear amplification in the low frequency limit  $k_o\delta \rightarrow 0$  (Figure 3.5), when the source is a radial-radial displacement quadrupole.

The implications for jet noise of this low frequency scattering mechanism are most clearly seen by rewriting the analytical approximations for the isothermal flow factor  $F^{(3)}$ , Equation (3-79), in terms of the Strouhal number  $S$  and the profile parameter  $\delta/r_o$ . This gives

$$F^{(3)} \sim \left(\frac{\delta}{r_o}\right)^{-2} S^{-2}, \quad (\delta/r_o, U_j/c_o, S \rightarrow 0) \quad (3-86)$$

for LF scattering of SIPQ radiation in a shear flow with no density gradients. The amplification due to mean shear is evidently independent of  $U_j/c_o$  at low Mach numbers, in contrast to the density-gradient effect discussed in the previous section.

It is at this point that the need to use a *displacement* quadrupole source, rather than an *acceleration* quadrupole source, in the shear flow analogy becomes apparent. For the choice of  $v=1$  – corresponding to an acceleration source – in place of  $v=3$  leads, via Equations (3-28) and (3-81) to the asymptotic LF result

$$\begin{aligned} F^{(1)} &= (k_o\delta)^{-4} \left\{ (D^{-2})_S^{\prime\prime} \right\}^2, \quad (\delta/r_o \rightarrow 0, k_o r_o \rightarrow 0) \\ &= (k_o\delta)^{-4} \frac{4}{D_S^6} \left\{ \left[ \frac{d^2 D}{dx^2} \right]_S - \frac{3}{D_S} \left[ \left( \frac{dD}{dx} \right)^2 \right]_S \right\}^2. \end{aligned} \quad (3-87)$$

Expressing  $F^{(1)}$  in terms of  $S$  then gives, corresponding to (3-86) above,

$$F^{(1)} \sim \left(\frac{\delta}{r_o}\right)^{-4} \left(\frac{U_j}{c_o}\right)^{-2} S^{-4}; \quad (\delta/r_o, U_j/c_o, \delta \rightarrow 0) \quad (3-88)$$

In other words a *volume-acceleration* distribution of *rr-quadrupole* type<sup>†</sup> would give rise to a  $U_j^6$  velocity dependence for turbulent jet noise at low Mach numbers, in direct contradiction to both observation and the established Lighthill theory for jets of uniform density. For this reason, the numerical results and comparisons with jet noise data presented in this paper are limited to the displacement source model ( $\nu = 3$ ). Detailed numerical results given in Appendix 3C support the trends indicated by the approximate analytic results given above.

Returning to Equation (3-86), the low-frequency theory shows that mean shear amplification increases, for a given velocity profile shape, as  $S$  decreases. This is demonstrated in Figure 3.9 for two different Strouhal numbers, 0.32 and 0.16. Suppression of the mean shear scattering term reduces the SIPQ flow factor  $F^{(3)}$  by at most  $1\frac{1}{2}$  dB at  $S = 0.32$ , whereas at half the Strouhal number the flow factor is reduced by up to 3 dB. The inference from Figure 3.9 is that for the profile with  $\delta/r_0 = 1.05$ , typical of a subsonic isothermal jet at  $3\frac{1}{2}$  to 4 diameters downstream of the nozzle, the mean shear amplification mechanism ceases to have a significant effect at Strouhal numbers of around 0.32 and above.

The question which remains is whether jet noise at Strouhal numbers of order 0.16 to 0.32 originates from a region of the jet around 4 diameters or less from the nozzle, or from further downstream where the mean shear is too small to cause significant amplification. A partial answer is provided by the acoustic source location measurements of Grosche<sup>33</sup> and Laufer, Kaplan and Chu<sup>34</sup>; the relevant curve from Grosche's results is reproduced in Figure 3.10, which indicates that most of the radiation in the Strouhal number range mentioned originates between 5 and 10 diameters downstream of the nozzle.

The provisional conclusion, then, is that the mean-shear amplification mechanism appears not to make an important contribution to isothermal jet noise at Strouhal numbers of around 0.3. The same conclusion may be extended by similarity arguments to the whole Strouhal number range, since according to Equation (3-79) the ratio of shear-scattered direct radiation is proportional to  $(dU/dr)_s/w$ , and this quantity is expected to remain roughly constant with axial position in both the initial mixing region and the fully developed jet.

### 3.3.3 Refraction, Source Convection and Non-Compactness Effects

At high frequencies, where the sound wavelength is comparable with or less than the shear layer thickness, the theoretical calculations of Section 3.2 indicate an approach to geometric acoustics. The value of  $k_0\delta$ , for radiation from a turbulent jet at a given Strouhal number, scales as  $U_j/c_0$ ; so a transition from low-frequency to high frequency behavior is expected with increasing velocity ratio, if  $S$  is held constant.

Such a transition has been observed by Lush<sup>8</sup> at  $S \sim .3$  and 1; it becomes apparent at any given angle in the rear arc as the cone of silence moves out

---

<sup>†</sup>The same applies to a  $\phi\phi$ -quadrupole if higher-order  $\delta/r_0$  terms are retained.

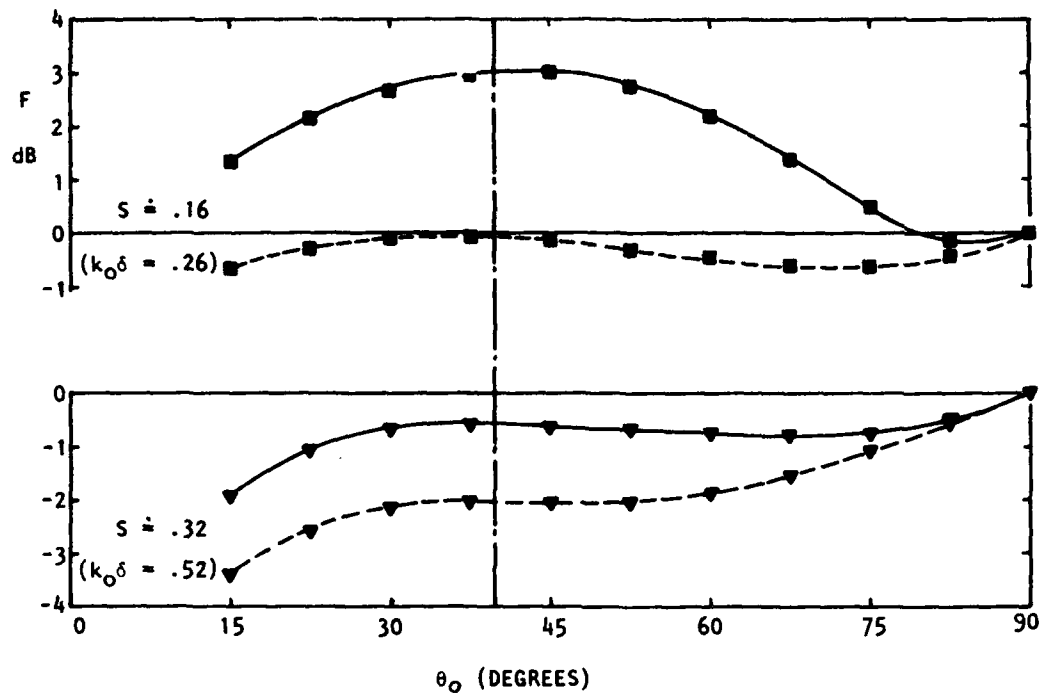


Figure 3.9 Contribution of Mean Shear Scattering to Radiation from Displacement Quadrupole Source, at Two Different Frequencies in an Isothermal Shear Flow. Code: — Flow Factor with Scattering Included; --- Flow Factor with Mean Velocity Gradient Term Suppressed. Source: SIPQ at  $\phi_s = .600$ . Profile Parameter  $\delta/r_0 = 1.05$ ; Centerline Velocity Ratio  $U_j/c_o = 0.5$ .

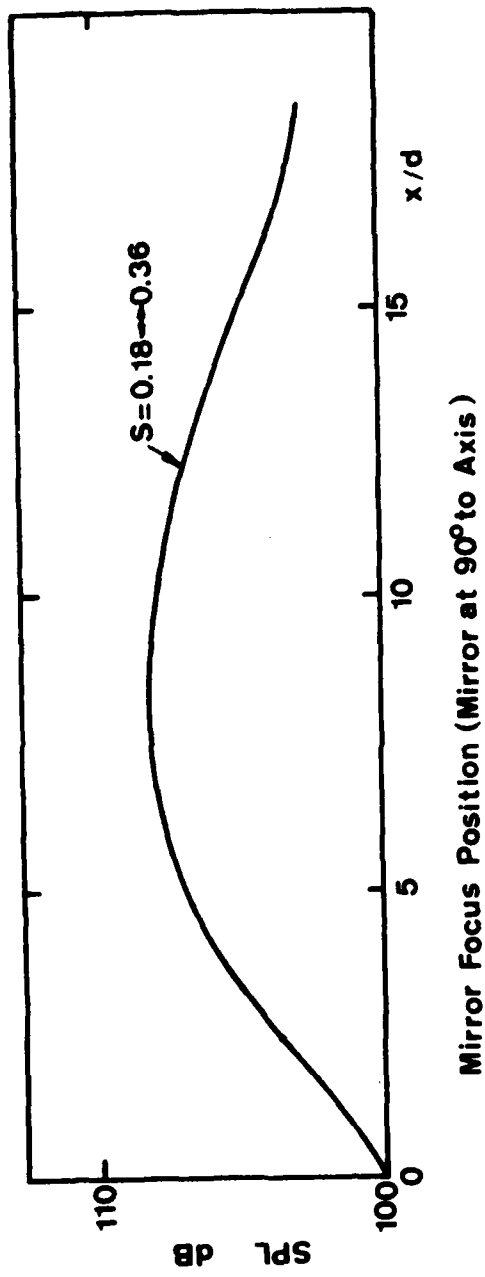


Figure 3.10 Distribution Along Jet Axis of Octave-Band Intensity as Focused by Mirror. Data from Grosche (33); Unheated Jet,  $U_j/c_0 = .91$ .

(with increasing  $U_j/c_0$ ) to enclose the observation point. The cone of silence or refraction valley, is the one feature of high-speed jet noise which most dramatically demonstrates the breakdown of the zero-flow acoustic analogy.

At the same time, the scattering effect of the nonuniform velocity field will tend to persist into the high- $k_0\delta$  region as  $U_j/c_0$  is increased with  $S$  held constant; the mean shear amplification, for example, was shown in the previous section to be independent of  $U_j/c_0$  in the limits  $U_j/c_0 \rightarrow 0$ ,  $S \rightarrow 0$ . The transition from small to large  $k_0\delta$  does not, therefore, necessarily imply that jet noise can be described by geometric acoustics at high values of  $U_j/c_0$  — whether or not this is so depends on the axial distribution of source strength as a function of Strouhal number, since this determines the extent of mean shear amplification.

In Figures 3.11 and 3.12, measurements of isothermal jet noise directivity at modified Strouhal numbers  $S_m = 1, 3$  are compared with predictions based on numerical solution of the Lilleby equation. For this purpose a displacement source model has been used ( $\nu = 3$ ) so that the predicted directivity is proportional to  $F^{(3)} D_m^{-9}$  [from Equation (3-50)]. It is clear that the present shear-flow analogy — with a reasonable choice of velocity profile and source location — gives significantly better agreement than the  $D_m^{-5}$  directional factor of Ribner<sup>11</sup> and Ffowcs Williams<sup>10</sup>, which is based on an acceleration source model in conjunction with a zero-flow acoustic analogy. Further comparisons between jet noise directivity measurement and predictions for isothermal jets are given in Appendix 3F and for hot jets in Appendix 3G. In Appendix 3F it is concluded that at the low Strouhal numbers there is evidence of another jet noise radiation mechanism and also that a sensible choice for the eddy convection velocity is necessary in order to achieve agreement outside the cone of relative silence.

The effects of axial non-compactness and source convection have been allowed for in Figures 3.11 and 3.12 by holding the modified Doppler-shifted frequency constant as the angle is varied (see Section 3.2.3); such effects become increasingly important in jet mixing noise as  $U_j/c_0$  is increased. A further effect at high jet velocities is the static temperature variation across the shear layer which occurs even when  $T_j/T_0 = 1$ ; this has been incorporated in the predictions by assuming the stagnation temperature profile follows the velocity profile, so that  $T_{tot}$  replaces  $T$  in Equation (3-53), and assuming a constant specific-heat ratio of  $\gamma = 1.4$ .

Finally, Figure 3.13 shows a breakdown of the directivity prediction for  $S_m = 3$  and  $U_j/c_0 = 0.9$  into its component factors,  $D_m^{-9}$  and  $F^{(3)}$ . The cone of silence boundary is at approximately  $59^\circ$ , and just below this angle the flow factor curve turns sharply downward due to the exponential decay factor mentioned in Section 3.2.5.1. In the range  $60^\circ$  to  $130^\circ$ , the numerically calculated SIPQ flow factor follows fairly closely the trend of the GA prediction for angles outside the cone of silence [Equation (3-65)]; but around  $140^\circ$  a peak appears which is not accounted for by the asymptotic GA result, and is in fact associated with a single azimuthal mode ( $n = 6$ ).

Since the agreement between measured and predicted jet noise directivity is particularly good over the angle range where Equation (3-65) holds, it is of interest to note that the theoretical directivity given by the flow factor approximation (3-65) together with the convected source model of Section 3.2.3 is

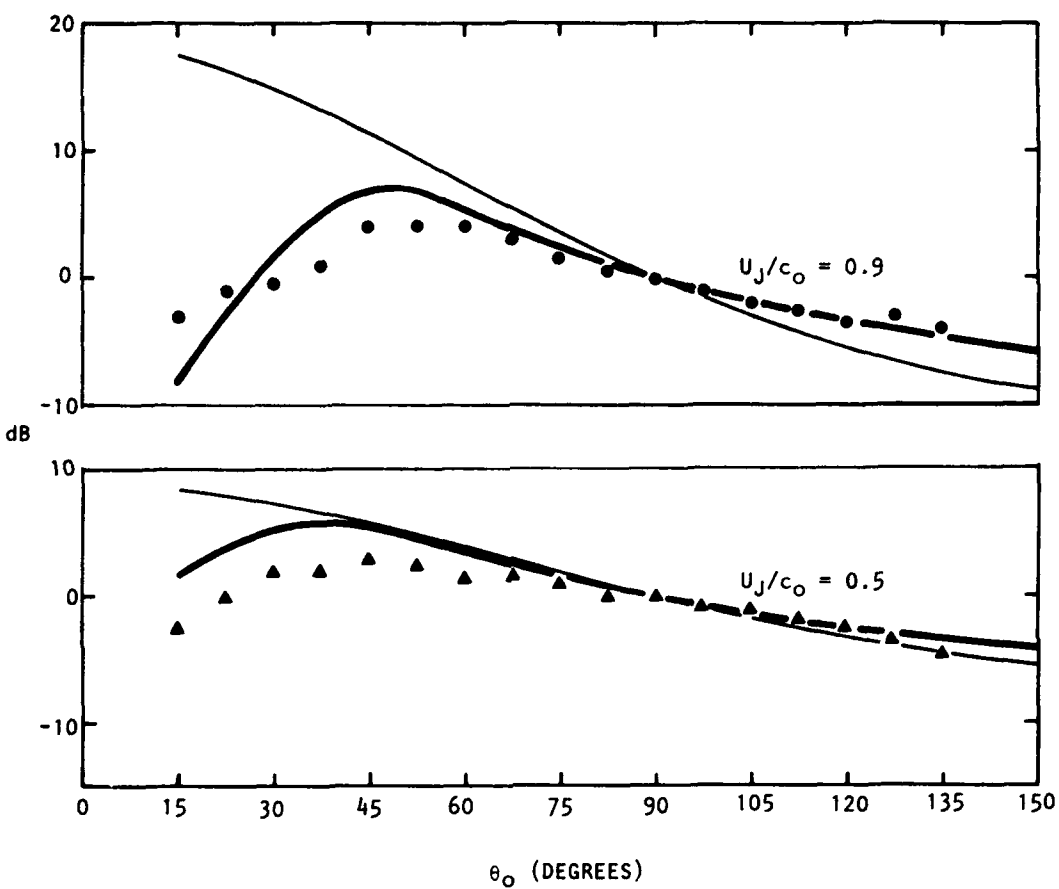


**Figure 3.11** Directivity of Isothermal Jet Noise: Comparison of Theoretical Models with 1/3-Octave Data, for  $S_m = 1.0$ . Code:  $\blacktriangle$ ,  $\bullet$  Lockheed-Georgia Measurements (32); —  $D_m^{-5}(\theta_0)/D_m^{-5}(90^\circ)$ , where  $D_m$  is the Modified Doppler Factor Defined in Equation (3-51), with  $U_c = .67 U_j$  and  $\alpha = 0.3$ ; —  $D_m^{-9}(\theta_0)F^{(3)}(\theta_0)/(D_m^{-9}(90^\circ)F^{(3)}(90^\circ))$ , where  $F^{(3)}$  is the Flow Factor Calculated by Present Theory for a Displacement Quadrupole Source at  $\phi_s = .679$ ,  $\delta/r_0 = 1.05$ .

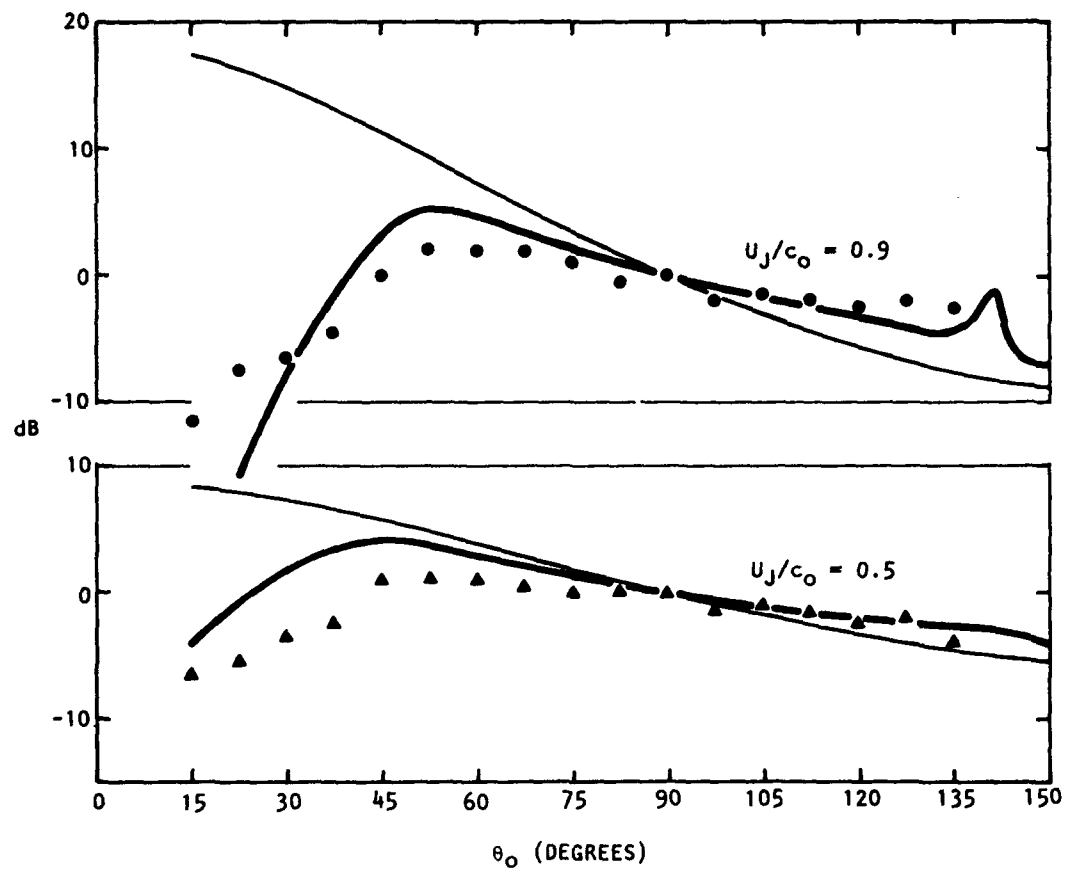


**Figure 3.12** Directivity of Isothermal Jet Noise: Comparison of Theoretical Models with 1/3-Octave Data, for  $S_m = 3.0$ . Code: as Fig. 3.11, Except that  $\delta/r_0 = .525$  for Flow Factor Calculation

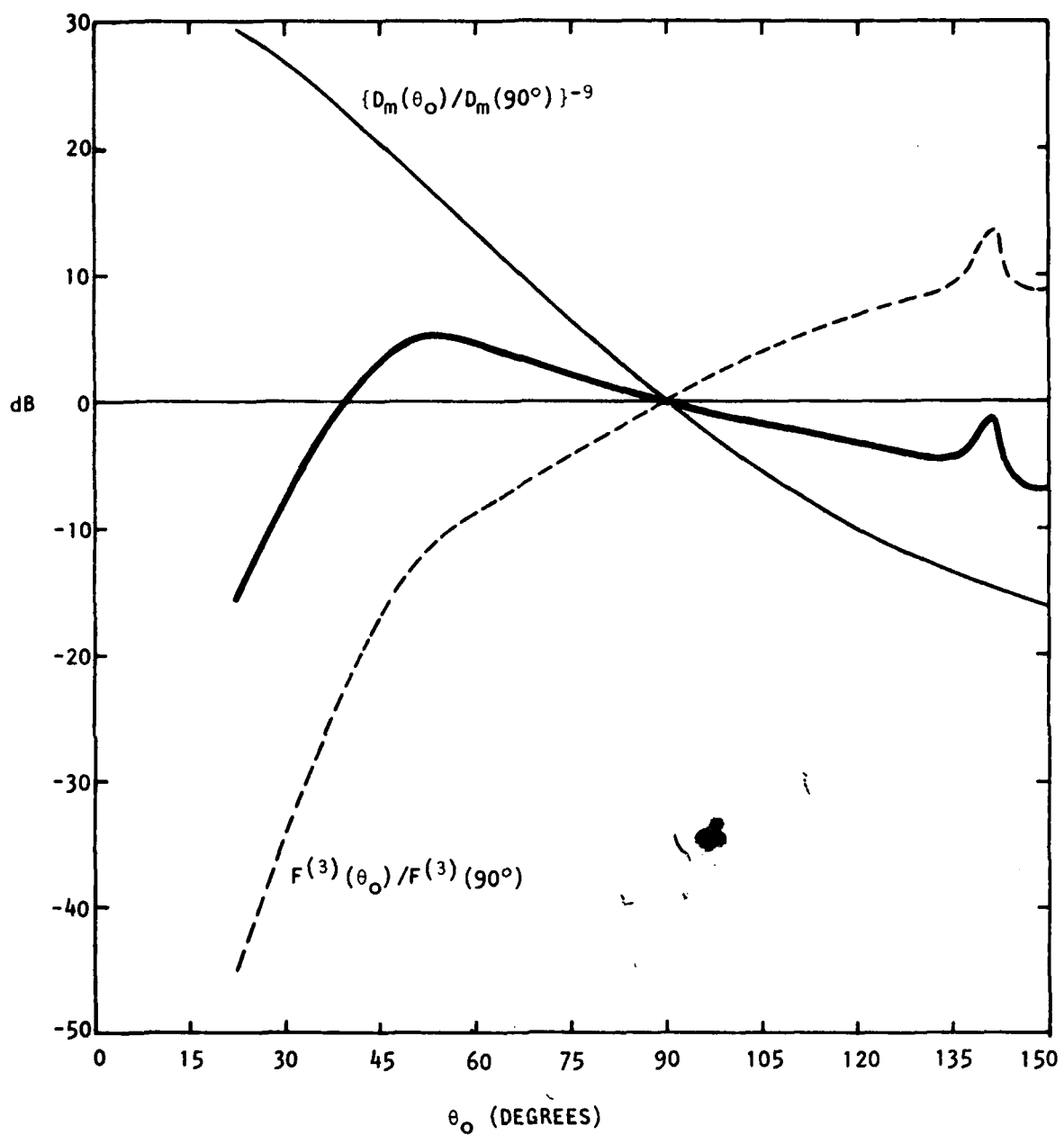


Figure 3.13 Breakdown of Directivity Prediction from Present Theory for  $S_m = 3.0$ ,  $U_j/c_0 = 0.9$ . Code: —  $\{D_m(\theta_0)/D_m(90^\circ)\}^{-9}$ ; ---  $F^{(3)}(\theta_0)/F^{(3)}(90^\circ)$ ; — Resulting Directivity Formed from Product of Two Curves.

$$\omega P(\omega) \propto D_s^6/D_m^9 \quad (\text{displacement SIPQ, } v=3) \quad (3-89)$$

or

$$\omega P(\omega) \propto D_s^2/D_m^5 \quad (\text{acceleration SIPQ, } v=1) \quad (3-90)$$

the modified Strouhal number being held constant in both cases. At moderate values of  $U_j/c_0$ , both these expressions yield a directivity similar to the  $D_m^{-3}$  factor proposed by Goldstein<sup>35</sup>, although Goldstein's result was based on a different governing equation, obtained by modifying the Lighthill analogy equation, and the similarity is therefore coincidental.

### 3.4 CONCLUSIONS

- (1) A shear-flow analogy model of jet noise has been set up based on Lilley's Equation (3-6), and leading source terms have been identified.
- (2) The governing equations can be solved numerically; solutions for multipole source distributions of any order are derived analytically from a single basic solution.
- (3) Closed-form analytical solutions are available for the limiting cases of high and low frequency.
- (4) At low frequencies, the radiation from quadrupole sources in a sheared mean flow is dominated by scattering from mean gradients.
- (5) For modeling jet mixing noise sources according to the shear-flow analogy, an acceleration quadrupole distribution is inappropriate, and a displacement quadrupole distribution must be used in order to give the correct asymptotic result at low jet velocity.
- (6) Amplification by mean shear of the radiation from radial-radial displacement quadrupoles seems to be of marginal significance for isothermal jets.
- (7) Corresponding amplification by mean density gradients may partially account for the  $U_j^6$ -dependent intensity radiated by hot low-speed jets, but a more likely explanation is scattering from the *unsteady* density field.
- (8) At high frequencies, the model predicts a rapid approach towards geometric acoustics. Combined with a simple isotropic source model, it reproduces the main features of high-speed isothermal jet radiation, including the cone of relative silence.
- (9) The simplicity of the geometric acoustics approximation, particularly outside the cone of silence, makes it attractive for detailed investigation of source convection and noncompactness effects.

4. THE FLOW AND ACOUSTIC CHARACTERISTICS OF  
THE LARGE-SCALE WAVE-LIKE STRUCTURE OF  
AN AXISYMMETRIC JET

## SUMMARY

---

A wave-model is developed for the large-scale coherent structure of subsonic and supersonic axisymmetric jets. Calculations of the associated near-field pressures are made.

---

An instantaneous fluctuation in the jet flow is regarded as being separable into three components: a time-averaged component, a periodic wave-like component, and a random small-scale component. This last component is considered to play a number of roles in the flow model. In the region of the jet exit, these fluctuations act as a driving or source mechanism for the large-scale component. Its dominant role, however, in the present model is dissipative in that the shear stresses due to the small-scale fluctuation are to be regarded as providing an enhanced viscosity. The interaction between the small-scale turbulence and the mean flow is modeled by an eddy viscosity which is a function of axial distance only. The interaction between the small-scale turbulence and the wave-like component is a very complicated process and no attempt is made to model it in this work though the effect of using a simple eddy viscosity approach is examined. An energy balance model is developed which examines the interchange of energy between the mean flow and the large-scale motion. This leads to a set of differential equations for the axial development of the wave-like component and the mean flow. The local distributions of the wave-like fluctuations are obtained from inviscid stability theory. Calculations are performed for an isothermal jet with a jet exit Mach number of 1.4. Though the axial development of the wave is described by an integral analysis, some aspects of the wave behavior can be determined from the local stability analysis. The phase velocity as a function of jet width for the helical,  $n=1$  mode is shown in Figure 4S.1. If the phase velocity predicted by linear theory is supersonic with respect to the ambient speed of sound, then a linear coupling of the propagating wave and the acoustic field occurs leading to direct far-field radiation.

The variation of the amplitude of the  $n=1$  mode, which is characterized by the relative wave kinetic energy flux, is shown in Figure 4S.2. This variation of amplitude with axial distance is found to provide a mechanism by which a wave which has a subsonic phase velocity, calculated from local linear stability theory, may radiate noise to the far field. The Strouhal number 0.3 wave is seen to reach the greatest amplitude.

Since the small-scale time-dependent component is by definition confined to the jet flow region, the fluctuations in the near field are associated with the wave-like structure. Typical contours of sound pressure level in the near field for the axisymmetric,  $n=0$ , mode and a Strouhal number of 0.3 are shown in Figure 4S.3. The higher Strouhal number modes are found to peak closer to the jet exit and the lower Strouhal number modes peak further downstream.

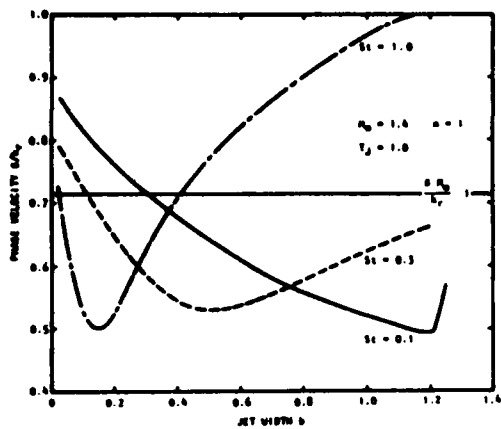


**Figure 4S.1** Variation of Phase Velocity with Jet Width:  $n = 1$

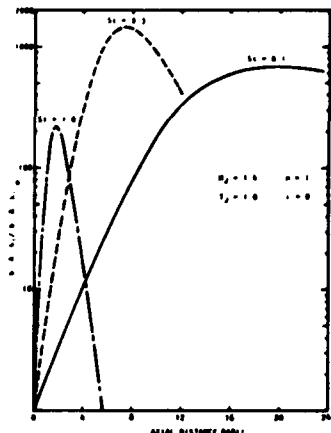


**Figure 4S.2** Axial Variation of Relative Kinetic Energy Flux Integral Amplitude:  $n = 1$

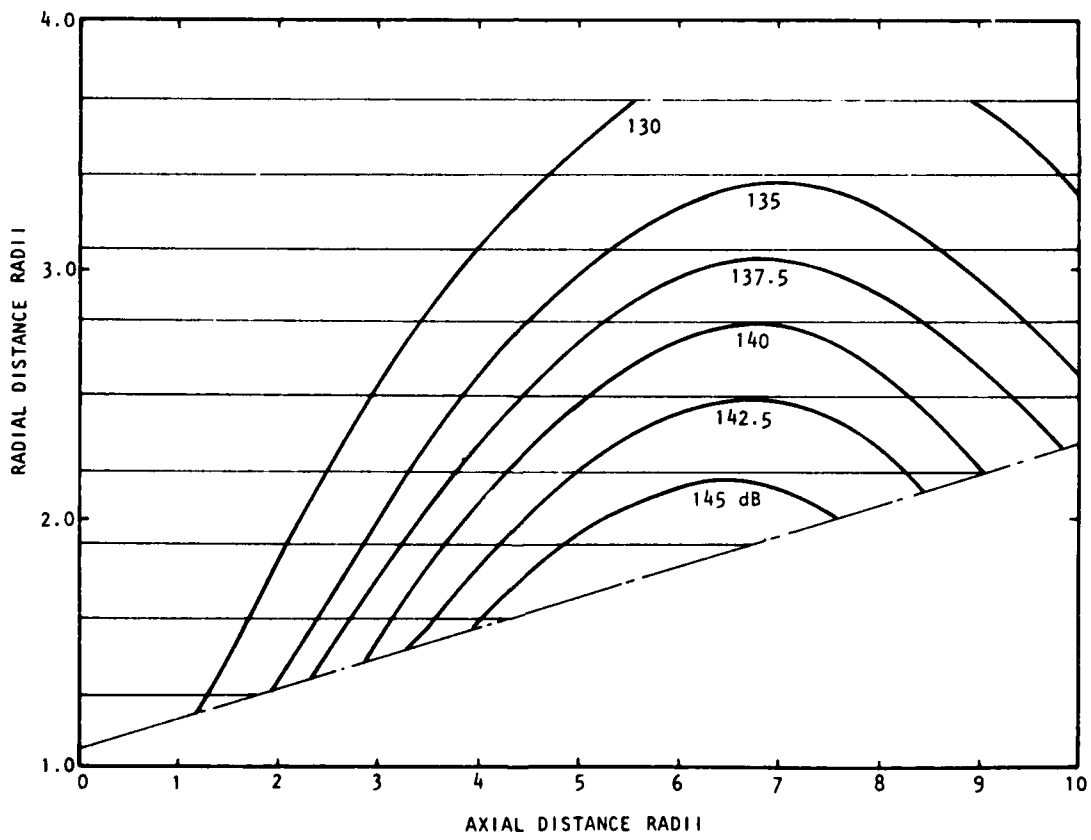


**Figure 4S.3** Contours of Sound Pressure Level in the Near Field:  $St = .3$

---

*The far-field noise radiation from the large-scale wave-like structure of an axisymmetric jet is calculated by determining the associated normal velocity on a cylindrical control surface surrounding the jet flow.*

---

A model is proposed for the mechanism by which a propagating wave-like component of the turbulence radiates noise to the far-field. As the component travels downstream, its amplitude changes as a function of axial distance. Even though the phase velocity, predicted by local inviscid stability theory is subsonic, the wave-number component spectrum, associated with the complete axial behavior of the wave, will contain wave-number components giving rise to sonic phase velocities and hence radiation to the far field.

In order to provide a boundary condition for determining the far-field radiation, a cylindrical control surface is constructed in the ambient medium surrounding the jet flow. In order to determine the wave-like radial velocity fluctuation on this surface, a correction for flow divergence effects is applied to the value predicted by local parallel-flow inviscid stability theory. The correction is based on a first-order iteration of the continuity and momentum equations. For a control surface at a large distance from the jet flow, this correction can dominate the predicted radial velocity fluctuation. This is seen in Figure 4S.1 for the  $n=1$ ,  $St=.3$  mode with a control surface radius,  $R_B$ , of  $1+\lambda/2$ , where  $\lambda$  is the acoustic wavelength.  $\hat{v}_p$  is the parallel flow radial velocity,  $\Delta\hat{v}_c$  is the correction to the radial velocity in order to satisfy continuity in the diverging flow, and  $\Delta\hat{v}_m$  is the correction to the radial velocity in order to prevent a momentum imbalance for the diverging flow.  $\hat{v}$  is the corrected radial velocity fluctuation. A typical wave number component spectrum associated with the radial velocity fluctuation is shown in Figure 4S.2 for  $n=0$  and  $St=.3$ . Far-field radiation is possible for  $-BM_0 \leq k \leq BM_0$ . The peak in the spectrum is close to this permissible range of wave numbers since the phase velocity predicted by local inviscid stability theory is close to sonic.

The predicted far-field radiation for the  $n=1$  mode and three Strouhal numbers is shown in Figure 4S.3. Though the directivity patterns peak close to the jet axis, there is still an appreciable amount of noise radiated at  $90^\circ$ . The far-field directivity patterns found by summing over  $n=0, \pm 1, \pm 2$  are shown in Figure 4S.4.

The results presented show that the mechanism proposed for radiation by wave-like structures is reasonable. However, it is argued that the method for calculating the far-field radiation is too inaccurate an approximation to provide accurate noise predictions. It is proposed to develop a deterministic source function, based on the large-scale motion, for the Lilley equation and then calculate the associated far field with retarded time effects included.

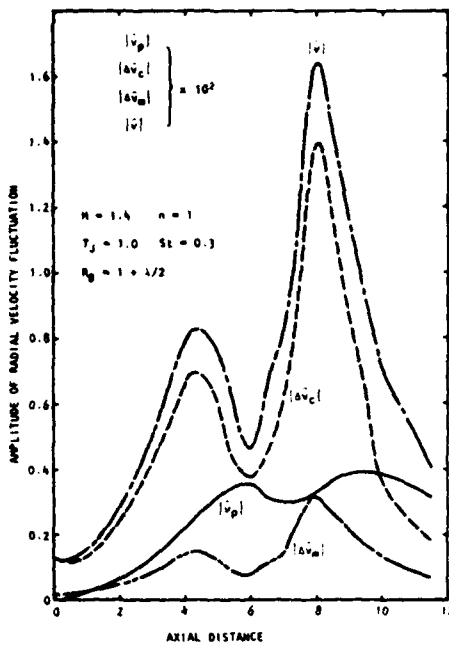


Figure 4S.4 Components of Radial Velocity Fluctuation:  
 $n = 1$

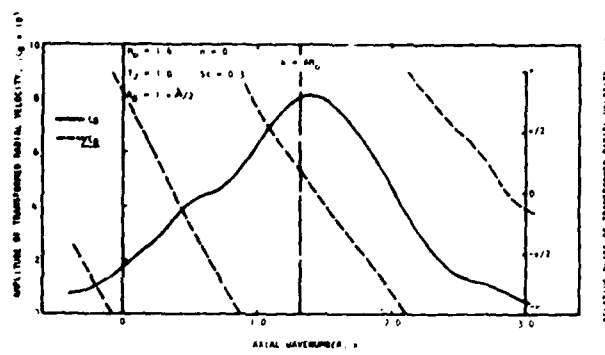


Figure 4S.5 Wavenumber Component Spectrum of Radial Velocity Fluctuation

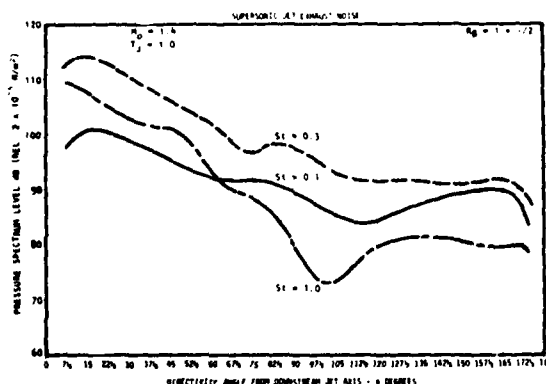


Figure 4S.6 Variation of Directivity Pattern with Strouhal Number:  $n = 1$

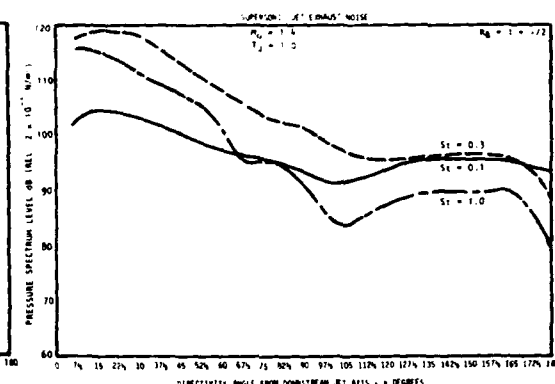


Figure 4S.7 Far-Field Directivity Patterns as a Function of Strouhal Number

#### 4.1 INTRODUCTION

The proposition that a turbulent shear flow contains or supports a large-scale coherent structure has considerable importance in the field of aero-acoustics. Speculation has occurred as to the role that such a structure would play in the noise radiated by the turbulent flow. If the turbulent motion itself contained a naturally occurring coherent structure, this component might prove a much more efficient noise emitter than the random fluctuations. It is also possible that the turbulent jet might act as an acoustic amplifier which selectively amplifies disturbances propagating from upstream of the jet exit. The model of the coherent structure of a turbulent jet to be presented here contains elements of both these concepts insofar as the radial distributions of the wave-like component are the local "natural" solutions, depending on the local conditions, whose amplitude is determined in part by the fluctuation amplitude at the jet exit.

The large-scale coherent structure of the turbulent shear flow may be assumed to have a wave-like form or may be Fourier decomposed into wave components. The development of these wave-like components, and the physical mechanisms used to maintain or drive them, will differ depending on the basic "stability" of the turbulent flow. Landahl<sup>36</sup> decomposed the turbulent fluctuations in a turbulent boundary layer into their periodic components using a Fourier transformation. The resulting equation for the fluctuations was a nonhomogeneous form of the Orr-Sommerfeld equation. The nonlinear terms on the right-hand side of this equation, which represented the fluctuating turbulent shear stresses, were regarded by Landahl as a forcing function. Thus, the small-scale turbulent fluctuations were regarded as providing a continuous input to maintain the wave-like larger scale structure. Landahl also proposed that the cross-spectral density of the pressure fluctuations would be dominated by the least-attenuated mode. Landahl's calculations of the streamwise decay of the cross-spectral density showed good agreement with the measurements, though some improvements were obtained if an eddy viscosity were used. The experiments of Reynolds and Hussain<sup>37</sup> also indicated that in a bounded turbulent shear flow wave-like disturbances behaved like local instabilities of a laminar flow. There are a number of conceptual difficulties which arise out of these simplified wave models. Firstly, it is essential that any wave-component be decaying, since there exists a continuous forcing function which would otherwise drive the component to infinite amplitude. Sharma<sup>38</sup> showed that, even for the turbulent boundary layer profile considered by Landahl there were weakly *amplifying* components. However, these growing modes would probably not present a problem physically since they would not reach an appreciable amplitude by the time that, even a very slowly diverging flow, would cause their decay. (This is also without considering the effects of flow divergence on the local growth rate.) There also exists the difficulty of local inflectional profiles in the boundary layer leading to rapid local rates of growth of the wave components. The simplicity of Landahl's model also depended on there being only a single least stable mode which dominated the cross-spectral density function.

All of the difficulties associated with a continuous forcing wave-model of the turbulent shear flow, which were of little importance in the bounded flow problems have considerable significance in the free turbulent shear flow. Consider the axisymmetric jet case. The mean flow profile, particularly close to the jet exit, is unstable to periodic disturbances. There exist many separate modes of the fluctuation all of which have similar growth rates. The experiments of Brown and Roshko<sup>39</sup> show the dominating large-scale instability motion in a free-mixing layer. Crow and Champagne<sup>40</sup> also showed how wave-like disturbances, introduced at the jet exit, propagate and amplify in the manner of waves in hydrodynamic stability theory. Thus, it can be seen that the wave-guide model of Landahl<sup>36</sup> is not appropriate in the free turbulent shear flow problem. The model that will be presented here makes use of the dual-role, driving and limiting, of the small-scale fluctuations and also takes essential account of the development of the mean flow.

Though there is substantial evidence that the local fluctuations in a turbulent shear flow may be described well in terms of local solutions of a stability-type equation, the amplitude of these fluctuations is more realistically set by the overall axial propagation of a fluctuation of a given frequency through the jet flow. If the local growth rate of a particular frequency component were large enough, its amplitude would more likely be governed by a local amplitude self-limitation criterion. But this is certainly not the case in an axisymmetric jet, which is a comparatively stable free shear flow, particularly at high Mach numbers. In fact far downstream of the jet exit, all azimuthal mode number and frequency components are decaying, unlike the free-mixing layer or two-dimensional jet. The greatest amplitude will be achieved by those modes and frequencies which are stimulated close to the jet exit. Thus, in the present model the wave-like structure of the flow is made up of components of all azimuthal mode numbers and frequencies which are generated at the jet exit plane and propagate through the pre-existing turbulent mean flow.

The instantaneous fluctuation in the flow is regarded as having three separately identifiable components. The first is the time-averaged or mean flow component. The second is the periodic, wave-like, large-scale component. The third is the random, small-scale turbulent component. This last component plays a number of different roles in the present model. For the case of a jet which has no external stimulus, to phase-lock the wave-like structure, the small-scale fluctuations, in the region of the jet exit, act as the initial driving mechanism. In this way the small-scale turbulence acts in the manner proposed by Landahl, that of a forcing function. However, the dominant role of the small-scale turbulence in the present model is dissipative. Liepmann<sup>41</sup> proposed that a flow containing a small-scale turbulent motion would be regarded as a "turbular" fluid. In such a fluid the shear stresses could be regarded as an apparent viscosity due to the small-scale motion. Liepmann<sup>41</sup> also indicated that the turbular fluid would most likely be non-Newtonian. However, momentum and heat transfer of a turbulent free shear flow can be described well using the enhanced viscous and heat-conducting properties of a turbular fluid. It should be recalled that both Landahl<sup>36</sup> and Reynolds and Hussain<sup>37</sup> obtained good agreement with measurements using an enhanced viscosity. The small-scale turbulence is thus seen to control the development of the mean flow acting as an eddy viscosity and is also likely to dissipate the large-scale wave-like structure. The interaction between the large-scale motion and the small-scale turbulence is an extremely complicated process. The

experiments of Crow and Champagne<sup>40</sup> indicated that though the small-scale motion may dissipate the periodic structure, the large-scale motions appeared to extract or concentrate the broadband energy of the fine-scale turbulence around the frequencies of the excited large-scale motion. No attempt, in the present work, has been made to model this complicated process.

With the functions and properties of the various components of the instantaneous motion defined, the development of the large-scale wave-like structure can be examined. Ko, Kubota and Lees<sup>42</sup> showed how an energy integral approach could be used to describe the development of finite amplitude instabilities in an incompressible wake flow. This work which contained many results similar to those of Stuart<sup>43</sup>, has been subsequently extended by Liu and Lees<sup>44</sup>, Liu<sup>45</sup>, Morris<sup>46</sup>, Chan<sup>47</sup>, Liu<sup>48</sup>, Morris<sup>49</sup>, and Merkine and Liu<sup>50</sup>. The technique shows how an interchange of energy takes place between the mean flow and the wave-like component which leads to initial growth and eventual decay of the wave. This energy transfer mechanism provides the physical reason why waves of a particular frequency do not grow infinitely. Two factors control the amplitude of the fluctuation. As the component propagates downstream the local energy exchange process alters until the dissipative action of the small-scale turbulence and a return of energy from the wave to the mean flow leads to a decay of the wave amplitude. If the amplitude of the wave is sufficiently large, it can influence the development of the mean flow directly causing more rapid onset of decay. A simplified version of Ko, Kubota and Lees'<sup>42</sup> and Stuart's<sup>43</sup> analysis shows that there is an absolute limit to the wave amplitude. For the case of an axisymmetric jet, this latter effect of amplitude self-limitation is of little importance unless the jet is strongly excited.

The growth and eventual decay of the wave-like component which has been physically explained by the energy exchange mechanism is of considerable importance from the point of view of noise generation. Since there appears such a close relationship between the unstable spatially growing waves of stability theory and the observations of wave-like structure in a jet, it is tempting to examine the noise radiated by such a growing wave. Tam<sup>51</sup> examined the directional acoustic radiation generated by such a shear layer instability. The results showed that two types of solution existed. Close to the downstream jet axis there was a spatially growing periodic solution and at larger angles to the jet axis the wave decayed exponentially. Tam noted that the exponentially growing solution was only meaningful close to the nozzle exit before the amplitude became sufficiently large. It is possible to obtain the noise radiated, at all angles, to the far-field by truncating the linear, exponentially growing solution at some downstream location. However, this renders the problem completely arbitrary. The energy exchange approach which is used in the present work provides a physically realistic mechanism for the decay of the wave-like solutions and thus any noise generated by the wave-like structure as a consequence of its axial development is not arbitrary.

The model of the flow field used in the present work has been previously used to describe the near field of the flow (Liu<sup>48</sup>, Merkine and Liu<sup>50</sup>). The only attempt to calculate the noise radiation associated with the wave-like structure is that by Tam<sup>52</sup>. However, the model used by Tam is somewhat singular in its interpretation of the noise generation mechanism. The total energy of the wave components of the flow was taken as being confined at one

single frequency. This frequency was set by an interaction between the unstable solution and the weak cellular structure of the nearly ideally expanded jet. Any broadening of the radiated noise spectrum was associated with turbulence scattering and the random time of occurrence of the propagating waves. Clearly, the mechanism is confined to supersonic flows and the spectral broadening is unlikely to account for the observed broad spectrum. In the present model the same noise generation mechanism exists at supersonic and subsonic jet exit velocities. Noise can be radiated by propagating disturbances with locally subsonic phase velocities. There is no shock-selection mechanism to extract a particular frequency and all frequency components may radiate noise to a lesser or greater extent. There is some evidence of the existence of the noise radiation mechanism proposed by Tam in the experiments by McLaughlin *et al*<sup>53</sup> though it is not clear whether the phenomenon may be more realistically thought of as a shock-noise component.

In the subsequent sections of this report the governing equations for the development of a large-scale wave-like fluctuation will be derived. The near-field pressure fluctuations will be presented for a number of Strouhal number components. It will be shown how the radial velocity fluctuation on a cylindrical control surface surrounding the flow can be calculated including corrections for the divergence of the mean flow. The noise radiated by the large-scale wave-like components will then be computed based on a matching of the wavenumber component spectrum of the radial velocity fluctuation with the far-field acoustic solution. Finally, the direction that further work will take will be discussed.

## 4.2 MATHEMATICAL DERIVATIVES

### 4.2.1 The Integral Equations

The nonlinear integral equations for a compressible axisymmetric jet are derived in Appendix 4A. It will be seen in the present computations that the magnitude of periodic fluctuations is very small and the integral form of the momentum equations then relates the local momentum flux of the mean flow to its value at the jet exit. To this end the covariance of the density and axial velocity fluctuation is neglected so that the integral equations of Appendix 4A may be reduced to

$$\int_0^{\infty} [\bar{\rho} \bar{u}^2] r^* dr^* = \left[ \int_0^{\infty} \bar{\rho} \bar{u}^2 r^* dr^* \right]_{z^*=0} \quad (4-1)$$

$$\frac{d}{dz^*} \int_0^{\infty} \bar{\rho} \frac{\bar{u}^3}{2} r^* dr^* = \int_0^{\infty} \bar{\rho} \bar{u} \bar{v} \frac{\partial \bar{u}}{\partial r} r^* dr^* - \int_0^{\infty} \bar{\rho} \left( \frac{\partial \bar{u}}{\partial r} \right)^2 r^* dr^*, \quad (4-2)$$

and

$$\frac{d}{dz^*} \int_0^\infty \frac{1}{2} \bar{\rho}^* \bar{u}^* (\bar{u}^{*2} + \bar{v}^{*2} + \bar{w}^{*2}) r^* dr^* = - \int_0^\infty \left[ \bar{v}^* \frac{\partial \bar{p}^*}{\partial r^*} + \frac{\bar{w}^*}{r^*} \frac{\partial \bar{p}^*}{\partial \phi} + \bar{u}^* \frac{\partial \bar{p}^*}{\partial z^*} \right] r^* dr^*$$

$$- \int_0^\infty \bar{\rho}^* \bar{u}^* \bar{v}^* \frac{\partial \bar{u}^*}{\partial r^*} r^* dr^* - \int_0^\infty \phi^* r^* dr^*, \quad (4-3)$$

where the dissipation term  $\phi^*$  is defined in Appendix 4A. Only the largest wave energy production term has been included in Equation (4-2) and asterisks denote dimensional quantities.

Equations (4-1) through (4-3) may be nondimensionalized with respect to the jet radius, jet exit velocity, ambient pressure, density, and viscosity, giving

$$\int_0^\infty \bar{\rho} \bar{u}^2 r dr = \frac{1}{2 T_J} \quad (4-4)$$

$$\frac{d}{dz} \int_0^\infty \bar{\rho} \bar{u}^3 r dr = 2 \int_0^\infty \bar{\rho} \bar{u} \bar{v} \frac{\partial \bar{u}}{\partial r} r dr - \frac{2}{R_J} \int_0^\infty \bar{\rho} \bar{\epsilon} \left( \frac{\partial \bar{u}}{\partial r} \right)^2 r dr \quad (4-5)$$

and

$$\frac{d}{dz} \int_0^\infty \bar{\rho} \bar{u} (\bar{u}^2 + \bar{v}^2 + \bar{w}^2) r dr = - \frac{2}{\gamma M_0^2} \int_0^\infty \left[ \bar{v} \frac{\partial \bar{p}}{\partial r} + \frac{\bar{w}}{r} \frac{\partial \bar{p}}{\partial \phi} + \bar{u} \frac{\partial \bar{p}}{\partial z} \right] r dr$$

$$- 2 \int_0^\infty \bar{\rho} \bar{u} \bar{v} \frac{\partial \bar{u}}{\partial r} r dr - \frac{2}{R_J} \int_0^\infty \phi r dr \quad (4-6)$$

where

$$M_0 = \frac{\bar{u}_J^*}{\bar{a}_0^*}, \quad R_J = \frac{\bar{\rho}_0^* \bar{u}_J^* r_J^*}{\bar{\mu}_0^*},$$

the flow properties are assumed to be constant across the jet exit, and the subscripts J and o refer to jet exit and ambient conditions, respectively.

Equations (4-4), (4-5), and (4-6) provide the basis of the present calculations. Being of integral form, the detailed radial distributions of the mean and fluctuating components of the flow do not directly affect the interaction between the mean flow and the wave-like fluctuation. In the next

sections the mean flow will be described by a number of shape functions which will define the local mean flow distributions in terms of a local coordinate system. The flow in the annular mixing region of the jet is discussed first.

#### 4.2.2 Shape Assumptions for the Mean Flow and Wave-like Fluctuations

##### 4.2.2.1 The annular mixing region

In order to appropriately define a local coordinate system which characterizes the radial mean flow distribution in terms of a shape function, it is convenient to divide the jet into two regions: the annular mixing region and the flow downstream of the end of the potential core which will be called the developed jet flow. This latter nomenclature does not imply the existence of any strict conditions of self-preservation or even similarity but is used for convenience. It will be seen that downstream of the potential core a transition region exists where an axially varying shape function is used.

The local coordinate system used in the annular mixing region of the jet is shown in Figure 4.1a. The local mean velocity profile in this region can be defined as

$$\left. \begin{array}{ll} \bar{u} = 1 & r \leq h \\ \bar{u} = U(\eta) & r > h \end{array} \right\} \quad (4-7)$$

where                     $\eta = (r - h)/b,$

$h$  is the potential core radius and  $b$  is the half-velocity thickness of the mixing region (Appendix 4D). Thus, the radial distance to the half-velocity point is given by  $(h+b)$ . The choice of mean velocity shape function is discussed in some detail in Appendix 4D. In the present calculations the shape function takes the form,

$$U(\eta) = .5 [1 - \operatorname{erf} \{1.8984 (\eta - 1)\}]. \quad (4-8)$$

This shape function corresponds to that given by Townsend<sup>54</sup> transformed into the present coordinate system. The shape function  $U(\eta)$  is shown in Figure 4.2.

The density is related to the velocity using a Crocco relationship , such that

$$\tilde{\rho} = \{1 + (T_J - 1) \bar{u} + \frac{(\gamma-1)}{2} M_0^2 \bar{u}(1-\bar{u})\}^{-1}. \quad (4-9)$$

Substituting Equations (4-7) and (4-9) into Equations (4-4) through (4-6) leads to

$$(h^2 - 1) + 2hb T_J \beta_1 + 2b^2 T_J \beta_2 = 0, \quad (4-10)$$

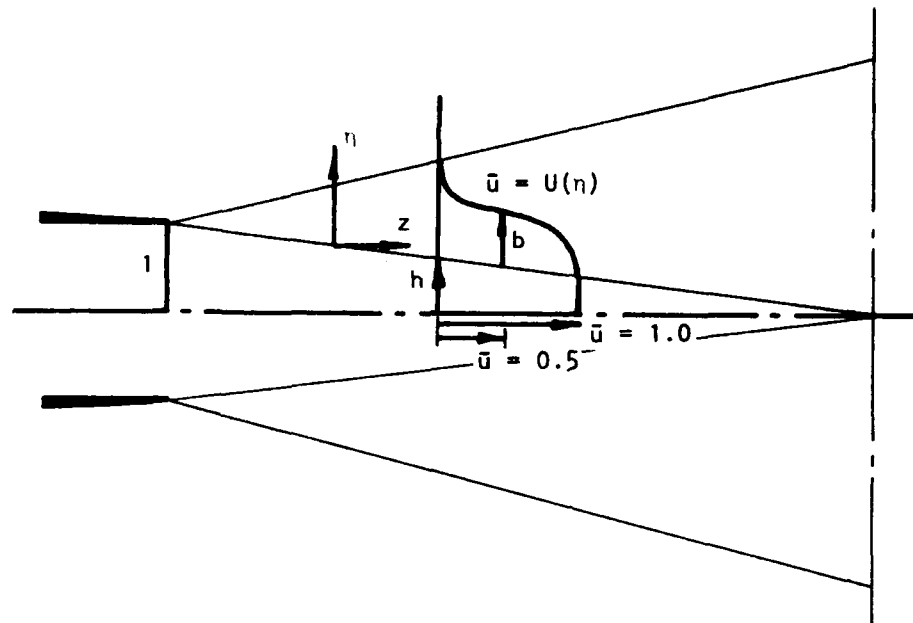


Figure 4.1 (a) Coordinate System in Annular Mixing Region

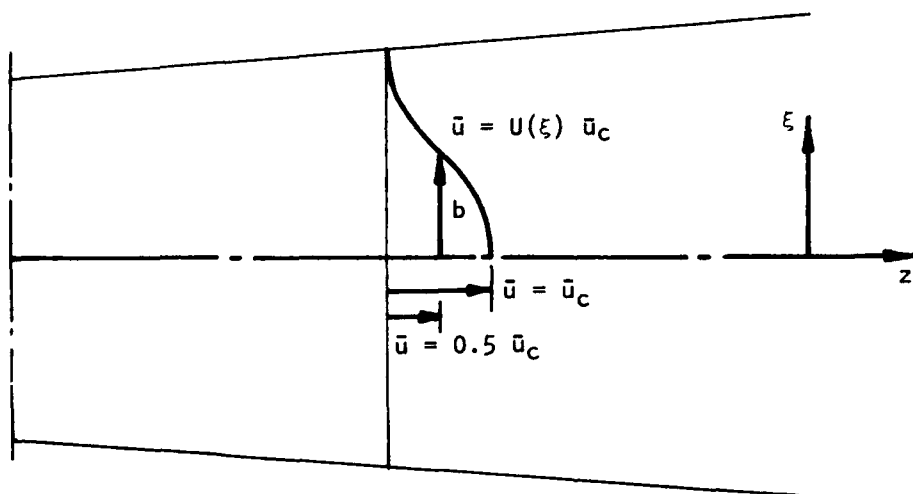


Figure 4.1(b) Coordinate System in Developed Jet Region

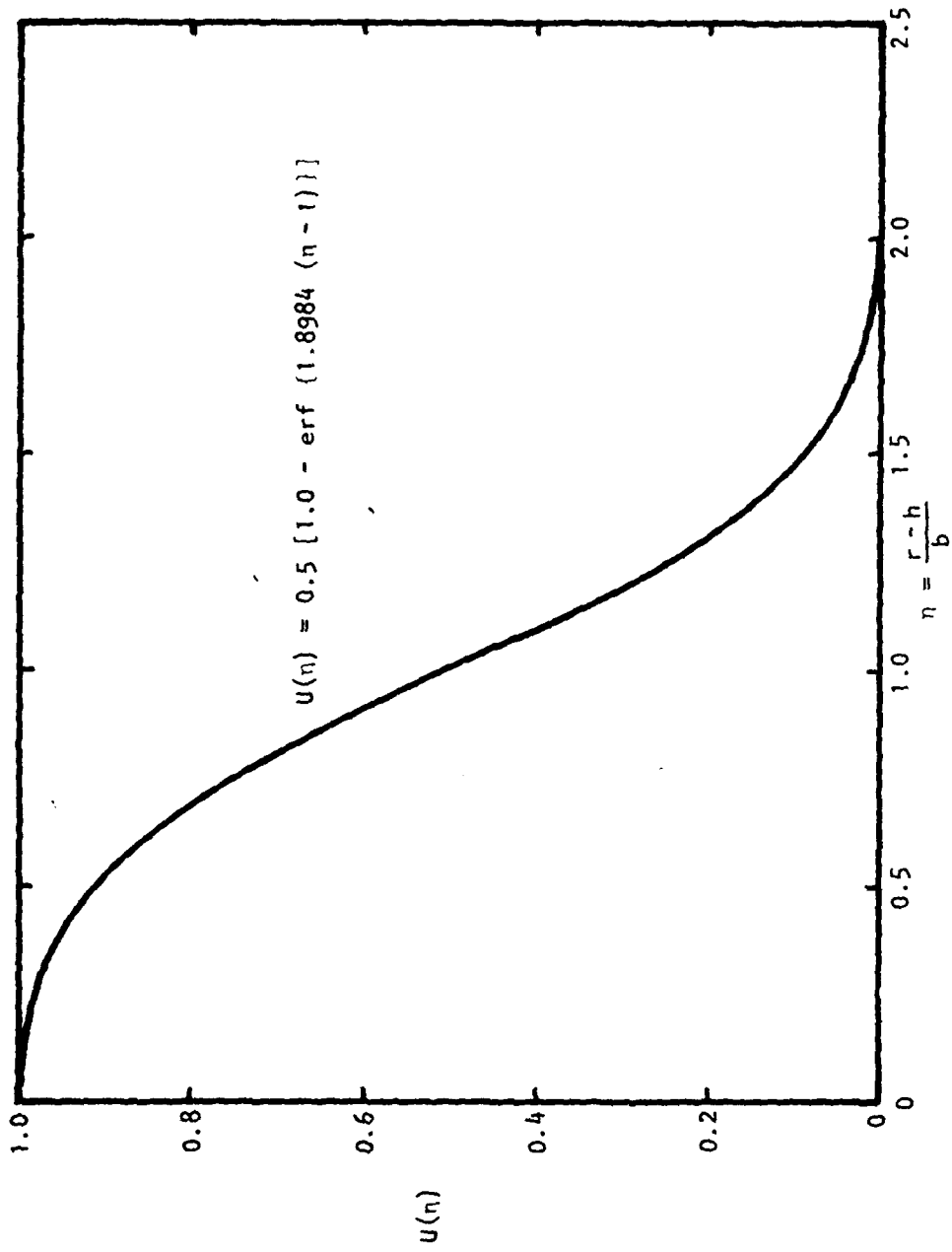


Figure 4.2 Mean Velocity Shape Function in Annular Mixing Region

$$\frac{d}{dz} \left( \frac{h^2}{2T_J} + hb\beta_3 + b^2\beta_4 \right) = 2bI_4 - \frac{2\bar{\epsilon}}{R_J} \left( \frac{h}{b} \beta_5 + \beta_6 \right), \quad (4-11)$$

and

$$\frac{d}{dz} \{b^2 I_1\} = - \frac{2b}{\gamma M_0^2} I_2 - 2bI_4 - \frac{2\bar{\epsilon} I_5}{R_J}, \quad (4-12)$$

where

$$\beta_1 = \int_0^\infty \bar{\rho} U^2 d\eta; \quad \beta_2 = \int_0^\infty \bar{\rho} U^2 \eta d\eta;$$

$$\beta_3 = \int_0^\infty \bar{\rho} U^3 d\eta; \quad \beta_4 = \int_0^\infty \bar{\rho} U^3 \eta d\eta;$$

$$\beta_5 = \int_0^\infty \bar{\rho} \left( \frac{dU}{d\eta} \right)^2 d\eta; \quad \beta_6 = \int_0^\infty \bar{\rho} \left( \frac{dU}{d\eta} \right)^2 \eta d\eta;$$

$$I_1 = \int_0^\infty \bar{\rho} U (\tilde{u}^2 + \tilde{v}^2 + \tilde{w}^2) \xi d\xi;$$

$$I_2 = \int_0^\infty \left[ \overline{\tilde{v} \frac{\partial \tilde{p}}{\partial \xi}} + \overline{\tilde{w} \frac{\partial \tilde{p}}{\partial \phi}} + \overline{\tilde{u} \frac{\partial \tilde{p}}{\partial \psi}} \right] \zeta d\zeta$$

$$I_4 = \int_0^\infty \bar{\rho} \overline{\tilde{u} \tilde{v}} \frac{dU}{d\xi} \xi d\xi;$$

$$I_5 = \int_0^\infty \bar{\rho} \left[ 2 \left[ \overline{\left( \frac{\partial \tilde{v}}{\partial \xi} \right)^2} + \frac{1}{\xi^2} \left( \frac{\partial \tilde{w}}{\partial \phi} + \tilde{v} \right)^2 + \overline{\left( \frac{\partial \tilde{u}}{\partial \psi} \right)^2} \right] - \frac{2}{3} \left| \frac{\partial \tilde{v}}{\partial \xi} + \frac{1}{\xi} \left( \frac{\partial \tilde{w}}{\partial \phi} + \tilde{v} \right) + \frac{\partial \tilde{u}}{\partial \psi} \right|^2 \right. \\ \left. + \left| \frac{1}{\xi} \frac{\partial \tilde{u}}{\partial \phi} + \frac{\partial \tilde{w}}{\partial \psi} \right|^2 + \left| \frac{\partial \tilde{u}}{\partial \xi} + \frac{\partial \tilde{v}}{\partial \psi} \right|^2 + \left| \frac{1}{\xi} \frac{\partial \tilde{v}}{\partial \phi} - \frac{\tilde{w}}{\xi} + \frac{\partial \tilde{w}}{\partial \xi} \right|^2 \right] \xi d\xi,$$

$$\psi = z/b, \quad \text{and} \quad \xi = r/b.$$

The local wave-like fluctuation is assumed to take the form,

$$\begin{aligned} \bar{u}(\xi, \phi, \psi, t') \\ \bar{v}(\xi, \phi, \psi, t') \\ w(\xi, \phi, \psi, t') \\ -\frac{p}{\gamma M_0}(\xi, \phi, \psi, t') \end{aligned} = \text{Re.} \left\{ A(\psi) \begin{bmatrix} \bar{u}(\xi; \psi) \\ \bar{v}(\xi; \psi) \\ \bar{w}(\xi; \psi) \\ \hat{p}(\xi; \psi) \end{bmatrix} e^{i(n\phi - \omega t')} \right\} \quad (4-13)$$

where  $t' = t/b$  the local time, and  $\omega$  is the local frequency

The local axial derivatives of the fluctuations are written in terms of the local wavenumber such that,

$$\frac{1}{A(\psi)} \frac{dA(\psi)}{d\psi} = i\alpha. \quad (4-14)$$

The radial distributions of the wave-like fluctuations are obtained from local linear inviscid stability theory. This does not permit the explicit influence of the small-scale turbulence, acting as an eddy-viscosity, to be included. However, the inviscid solution does permit a proper matching to take place across the turbulent/nonturbulent interface, Reynolds 55, and the integral approach used to describe the development of large-scale wave-like motion does eliminate the need for a detailed radial description. (This will be seen to be an over-simplification which can lead to over-estimation of the local dissipating effect of the small-scale turbulence on the wave.)

The equation describing the local pressure distribution is derived in Appendix 4C and may be written,

$$\frac{d^2 \hat{p}}{d\xi^2} + \left\{ \frac{1}{r} - \frac{1}{\bar{\rho}} \frac{d\bar{\rho}}{d\xi} - \frac{2\alpha}{(\alpha U - \omega)} \frac{dU}{d\xi} \right\} \frac{d\hat{p}}{d\xi} - \left\{ \lambda^2 + \left( \frac{n}{\xi} \right)^2 \right\} \hat{p} = 0, \quad (4-15)$$

where

$$\lambda^2 = \alpha^2 - (\alpha U - \omega)^2 M_0^2 \bar{\rho}. \quad (4-15a)$$

Using these wave-like forms for the periodic fluctuations equations (4-11) and (4-12) become,

$$\frac{d}{dz} \left\{ \frac{h^2}{2T_J} + hb\beta_3 + b^2\beta_4 \right\} = 2b|A|^2 k_4 - \frac{2}{R_T} \{ h\beta_5 + b\beta_6 \}, \quad (4-16)$$

and

$$\frac{d}{dz} \{ b^2 |A|^2 k_1 \} = -2b|A|^2 \left\{ k_2 + k_4 + \frac{k_5}{R_T} \right\}, \quad (4-17)$$

where

$$k_1 = \frac{1}{2} \int_0^\infty \bar{\rho} U (|\hat{u}|^2 + |\hat{v}|^2 + |\hat{w}|^2) \xi d\xi, \quad (4-18)$$

$$k_2 = \frac{1}{2} \int_0^\infty \text{Re.} \left\{ \hat{v}^* \frac{d\hat{p}}{d\xi} + \hat{w}^* \frac{i\eta p}{\xi} + \hat{u}^* i\alpha \hat{p} \right\} \xi d\xi, \quad (4-19)$$

$$k_4 = \frac{1}{2} \int_0^\infty \text{Re.} \left\{ \hat{u}^* \hat{v} \right\} \bar{\rho} \frac{dU}{d\xi} \xi d\xi, \quad (4-20)$$

$$\begin{aligned} k_5 = \frac{1}{2} \int_0^\infty \bar{\rho} & \left[ 2 \left\{ \left| \frac{d\hat{v}}{d\xi} \right|^2 + \left| \frac{i\eta \hat{w}}{\xi} + \hat{v} \right|^2 + \left| i\alpha \hat{u} \right|^2 \right\} - \frac{2}{3} \left\{ \left| \frac{d\hat{v}}{d\xi} + \frac{i\eta \hat{w}}{\xi} + v + i\alpha \hat{u} \right|^2 \right\} \right. \\ & \left. + \left| \frac{i\eta \hat{u}}{\xi} + i\alpha \hat{w} \right|^2 + \left| \frac{d\hat{u}}{d\xi} + i\alpha \hat{v} \right|^2 + \left| \frac{i\eta \hat{v}}{\xi} - \frac{\hat{w}}{\xi} + \frac{d\hat{w}}{d\xi} \right|^2 \right] \xi d\xi, \end{aligned} \quad (4-21)$$

where a star denotes the complex conjugate and

$$\bar{R}_T = \bar{u}_J^* b^*/\bar{\varepsilon}^* \quad \text{and} \quad \tilde{R}_T = \tilde{u}_J^* b^*/\bar{\varepsilon}^*. \quad (4-21a)$$

The eigenfunctions are normalized so that  $|A|^2$  is the kinetic energy of the wave per unit b, so that,

$$|A|^2 = \frac{1}{2} \int_0^\infty \bar{\rho} (\bar{u}^2 + \bar{v}^2 + \bar{w}^2) \xi d\xi, \quad \text{or} \quad (4-22a)$$

$$\frac{1}{4} \int_0^\infty \bar{\rho} (|\hat{u}|^2 + |\hat{v}|^2 + |\hat{w}|^2) \xi d\xi = 1. \quad (4-22b)$$

Equation (4-17) can be integrated directly to give,

$$\frac{b^2 |A|^2 k_1}{(b^2 |A|^2 k_1)_0} = \exp \left[ -2 \int_0^z \left\{ \frac{k_2 + k_4 + k_5 / \bar{R}_T}{bk_1} \right\} dz \right]. \quad (4-23)$$

It can be shown that,

$$(k_2 + k_4)/k_1 = \alpha_{ij}, \quad (4-24)$$

where  $\omega_{ij}$  is the imaginary part of the wavenumber calculated from local inviscid stability theory. So that Equation (4-23) may be written,

$$\frac{b^2 |A|^2 k_1}{(b^2 |A|^2 k_1)_0} = \exp \left[ -2 \int_0^z \frac{\omega_{ij}}{b} dz \right] \cdot v_c(z). \quad (4-25)$$

$v_c(z)$  is a dissipative correction to be kinetic energy flux which accounts for the interaction between the small-scale turbulence, acting as an eddy viscosity, and the wave-like structure.

Making use of Equation (4-10) the potential core radius can be written in terms of the jet width as,

$$h = b\beta_1 T_J + \{b^2 T_J (\beta_1^2 T_J - 2\beta_2) + 1\}^{\frac{1}{2}}, \quad (4-26)$$

so that the local mean flow and hence fluctuation distributions may be expressed solely as a function of  $b$ . Equation (4-16) may be written as a first order differential equation for  $b$  as,

$$f(h, b, T_J) \frac{db}{dz} = 2b|A|^2 k_4 - \frac{2}{\bar{R}_T} \{h\beta_5 + b\beta_6\}, \quad (4-27)$$

where

$$f(h, b, T_J) = \left\{ \frac{h^2 (\beta_3 - \beta_1) + 2hb (\beta_4 - \beta_2) + 2b^2 T_J (\beta_1 \beta_4 - \beta_2 \beta_3)}{(h + b\beta_1 T_J)} \right\} \quad (4-27a)$$

The development of the mean flow and the growth and decay of the wave-like fluctuations in the annular mixing region of the jet can thus be obtained by simultaneous solution of Equations (4-26), (4-27), and (4-17).

In the next section the corresponding set of equations for the developed jet are derived.

#### 4.2.2.2 The developed jet region (downstream of potential core)

The local coordinate system used downstream of the end of the potential core is shown in Figure 4.1b. The local mean velocity profile in this region can be defined as,

$$\bar{u} = \bar{u}_c U(\xi), \quad (4-28)$$

where  $\bar{u}_c$  is the jet centerline velocity. A detailed definition of the mean flow shape function in this region is given in Appendix 4D. The shape function does vary with jet width, most rapidly close to the end of the potential core in the transition region. These shape functions are obtained by a finite difference solution of the time-averaged boundary layer equations using a two-equation model of the turbulence described by Launder *et al* 56.

The mean flow shape functions for several values of jet half width  $b$  are shown in Figure 4.3. Making use of Equation (4-9), the density may be written as a function of  $\xi$  as

$$\bar{\rho}(\xi) = \{1 + (T_J - 1) \bar{u}_c + \frac{(\gamma-1)}{2} M_0^2 \bar{u}_c U(1 - \bar{u}_c)\}^{-1} \quad (4-29)$$

Substituting Equations (4-28) and (4-29) into Equations (4-4), (4-5), and (4-6) leads to

$$b^2 \bar{u}_c^2 = 1/2 T_J \gamma_2, \quad (4-30)$$

$$\frac{d}{dz} (b^2 \bar{u}_c^3 \gamma_4) = 2b \bar{u}_c^3 I_4 - 2 \frac{\bar{u}_c^2 \tilde{\epsilon}}{R_J} \gamma_6, \quad (4-31)$$

and

$$\frac{d}{dz} (b^2 \bar{u}_c^3 I_1) = -2 \bar{u}_c b I_2 - 2 \bar{u}_c^3 b I_4 - \frac{\bar{u}_c^2}{R_J} \tilde{\epsilon} I_5, \quad (4-32)$$

where

$$\begin{aligned} \gamma_2 &= \int_0^\infty \bar{\rho} U^2 \xi d\xi; & \gamma_4 &= \int_0^\infty \bar{\rho} U^3 \xi d\xi; \\ \gamma_6 &= \int_0^\infty \bar{\rho} \left( \frac{dU}{d\xi} \right)^2 \xi d\xi. \end{aligned}$$

The local fluctuations take the form,

$$\begin{aligned} \hat{u}(\xi, \phi, \psi, t') \\ \hat{v}(\xi, \phi, \psi, t') \\ \hat{w}(\xi, \phi, \psi, t') \\ \frac{P}{M_0^2} (\xi, \phi, \psi, t') \end{aligned} = \text{Re.} \left\{ A(\psi) \begin{bmatrix} \bar{u}_c \hat{u}(\xi; \psi) \\ \bar{u}_c \hat{v}(\xi; \psi) \\ \bar{u}_c \hat{w}(\xi; \psi) \\ \bar{u}_c^2 \hat{p}(\xi; \psi) \end{bmatrix} e^{i(n\phi - \omega t')} \right\}$$

and the local axial derivatives are given by Equation (4-14).

Equations (4-31) and (4-32) can then be written,

$$\frac{d}{dz} \{b^2 \bar{u}_c^3 \gamma_4\} = 2b^2 \bar{u}_c^3 \gamma_4 \left\{ \frac{|A|^2 k_4}{b \gamma_4} - \frac{1}{b R_c} \frac{\gamma_6}{\gamma_4} \right\} \quad (4-34)$$

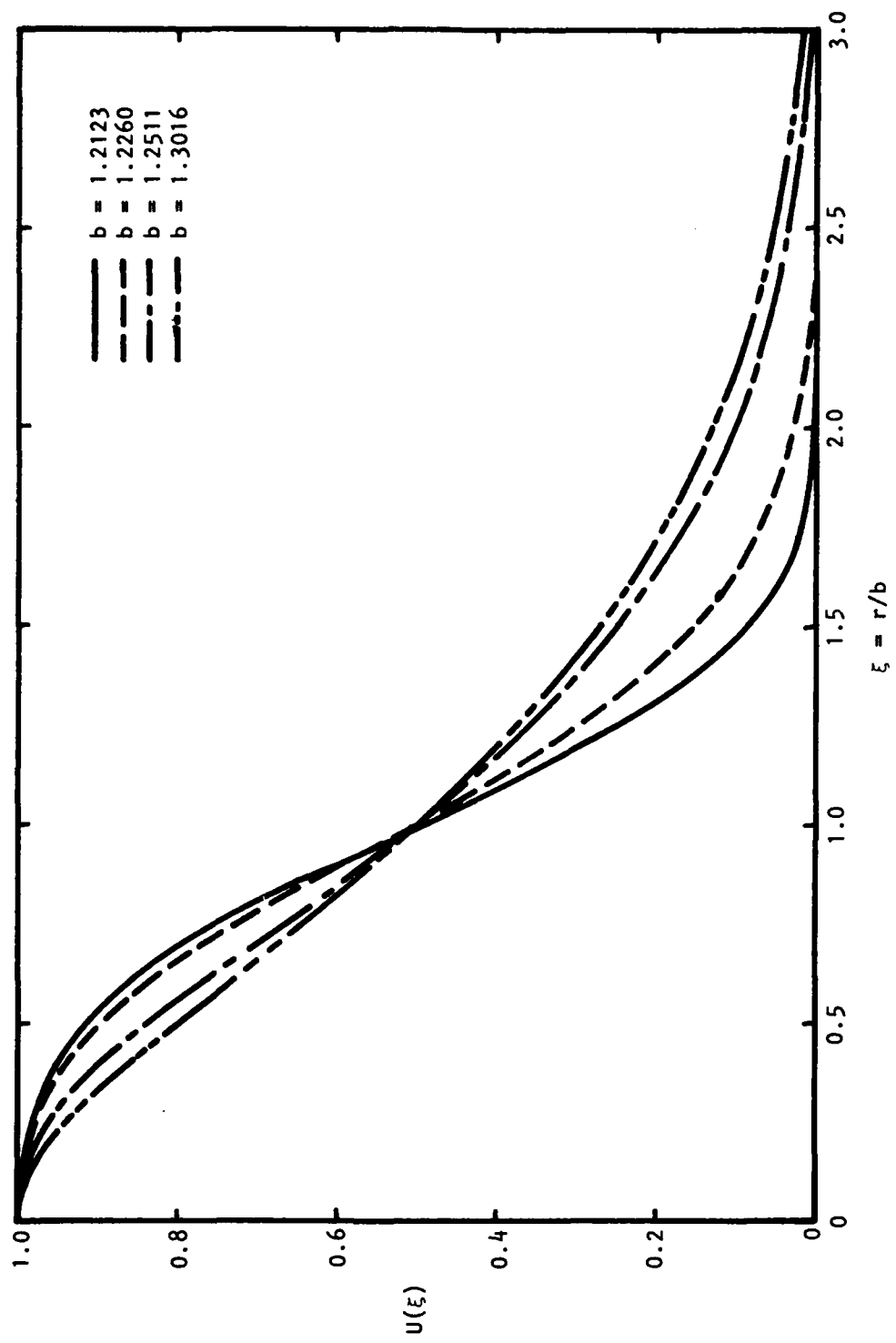


Figure 4.3 Mean Velocity Shape Functions in Developed Jet Region

and

$$\frac{d}{dz} \{ b^2 \bar{u}_c^3 |A|^2 k_1 \} = - 2|A|^2 b \bar{u}_c^3 \{ k_2 + k_4 + k_5/\tilde{R}_c \} \quad (4-35)$$

where

$$\bar{R}_c = \frac{\bar{u}_c^* b^*}{\bar{\epsilon}^*} \quad \text{and} \quad \tilde{R}_c = \frac{\bar{u}_c^* b^*}{\bar{\epsilon}^*} \quad (4-36)$$

Equations (4-34) and (4-35) may be integrated directly and on using Equations (4-30) it follows that,

$$\frac{\bar{u}_c \gamma_4}{\gamma_2} = \left\{ \frac{\bar{u}_c \gamma_4}{\gamma_2} \right\}_{z_c} \exp \left\{ 2 \int_{z_c}^z \left[ \frac{|A|^2 k_4}{b \gamma_4} - \frac{1}{b \tilde{R}_c} \frac{\gamma_6}{\gamma_4} \right] dz \right\}, \quad (4-37)$$

and

$$b^2 \bar{u}_c^3 |A|^2 k_1 = \left\{ b^2 \bar{u}_c^3 |A|^2 k_1 \right\}_{z_c} \exp \left\{ -2 \int_{z_c}^z \frac{\alpha_{ij}}{b} dz \right\} \cdot v_c(z) \quad (4-38)$$

where  $\alpha_{ij}$  is the local inviscid growth rate given by Equation (4-24) and  $v_c(z)$  is the viscous correction to the wave kinetic energy flux given by,

$$v_c(z) = \exp \left\{ -2 \int_{z_c}^z \frac{k_5}{k_1 b \tilde{R}_c} dz \right\} \quad (4-39)$$

$z_c$  is the axial location of the end of the potential core which is the value of  $z$  at which the width is given by

$$b^2 = 1/2T_j \gamma_2. \quad (4-40)$$

The simultaneous solution of Equations (4-30), (4-34), and (4-35) gives the axial development of the mean flow and the growth and decay of the fluctuation amplitude in the developed region of the jet.

#### 4.2.3 The Normal Velocity on a Cylindrical Control Surface

In the preceding sections the amplitude of a wave-like disturbance propagating in an axisymmetric jet flow was derived. This analysis provides the following information:

- (i) the development of mean flow:  $b(z)$ ,  $h(z)$ ,  $\bar{u}_c(z)$ ,
- (ii) the local eigenvalues based on parallel flow theory:  $\alpha(z)$ ,
- (iii) the amplitude of the wave-like fluctuation:  $A(z)$ , and
- (iv) the local radial distributions of the fluctuation:  $\hat{u}(r)$ ,  $\hat{v}(r)$ ,  $\hat{w}(r)$ ,  $\hat{p}(r)$ , etc.

Since these local radial distributions of the fluctuations have been obtained assuming locally parallel flow, it is necessary to correct these values to account locally for the effects of flow divergence. The radial velocity and pressure fluctuations on some boundary surrounding the flow region control the radiated noise. The continuity equation and radial and azimuthal momentum equations will be used to derive these flow divergence corrections and the corrected radial velocity fluctuation on a cylindrical control surface surrounding the flow will be derived. As in the previous sections, the jet flow is divided into two regions; the annular mixing region and the developed jet region. These two will be treated separately.

#### 4.2.3.1 The annular mixing region

The nondimensional form of the continuity equation for the wave-like fluctuation may be written,

$$\frac{\partial \tilde{p}}{\partial t} + \frac{1}{r} \frac{\partial}{\partial r} [\tilde{\rho} \tilde{v} + \tilde{\rho} \tilde{v}] r + \frac{1}{r} \frac{\partial \tilde{\rho} \tilde{w}}{\partial \phi} + \frac{\partial}{\partial z} (\tilde{\rho} \tilde{u} + \tilde{\rho} \tilde{u}) = 0. \quad (4-41)$$

The eigenfunctions based on parallel flow, denoted by the subscript p, satisfy the relationship,

$$\frac{\partial \tilde{p}_p}{\partial t} + \frac{1}{r} \frac{\partial}{\partial r} [\tilde{\rho} \tilde{v}_p] r + \tilde{\rho} \left\{ \frac{1}{r} \frac{\partial \tilde{w}_p}{\partial \phi} + \frac{\partial \tilde{u}_p}{\partial z} \right\} + \tilde{u} \frac{\partial \tilde{p}_p}{\partial z} = 0. \quad (4-42)$$

The difference between the radial velocity fluctuation satisfying Equation (4-41) and that satisfying the parallel flow equations is denoted by  $\Delta \tilde{v}_c$ . Then,  $\Delta \tilde{v}_c$  satisfies the equation

$$\frac{1}{r} \frac{\partial}{\partial r} [\tilde{\rho} \Delta \tilde{v}_c + \tilde{\rho}_p \tilde{v}] r + \tilde{u}_p \frac{\partial \tilde{p}}{\partial z} + \tilde{\rho}_p \frac{\partial \tilde{u}}{\partial z} = 0. \quad (4-43)$$

Equation (4-43) may be integrated from the jet axis to a control boundary at  $r = R_B$ , giving,

$$[\tilde{\rho} \Delta \tilde{v}_c + \tilde{\rho}_p \tilde{v}]_B R_B = - \int_0^{R_B} \left\{ \tilde{u}_p \frac{\partial \tilde{p}}{\partial z} + \tilde{\rho}_p \frac{\partial \tilde{u}}{\partial z} \right\} r dr, \quad (4-44)$$

where the subscript B denotes the value at  $r = R_B$ , the control boundary.

Assuming  $\Delta \tilde{v}_c$  takes the same periodic form as the parallel flow solutions, viz,

$$\Delta \tilde{v}_c (r, \phi, z, t) = \text{Re} \left\{ A(z) e^{i(k_r z + n_\phi - \beta t)} \Delta \hat{v}_c(r) \right\}, \quad (4-45)$$

then

$$\Delta \hat{v}_c = -\frac{\hat{\rho}_{PB}}{\bar{\rho}_B} \bar{v}_B - \frac{1}{\bar{\rho}_B R_B} \frac{d}{dz} \left\{ b^2 \int_0^{\xi_B} (\bar{\rho} \hat{u}_p + \hat{\rho} \bar{u}_p) \xi d\xi \right\}, \quad (4-46)$$

where  $\xi_B = R_B/b$  and  $\bar{u}$  and  $\bar{\rho}$  are defined in Equations (4-7) and (4-9).

The radial mean velocity at  $r=R_B$  can be obtained by integrating the time-averaged continuity equation such that,

$$\bar{v}_B = \frac{1}{\bar{\rho}_B R_B} \int_0^{R_B} \frac{\partial \bar{\rho} \bar{u}}{\partial z} r dr \quad (4-47)$$

Making use of the mean velocity shape function, Equation (4-47) may be written

$$\bar{v}_B = \frac{1}{\bar{\rho}_B R_B} \frac{d}{dz} \left\{ \frac{h^2}{2T_J} + hb\beta_{10} + b^2\beta_{11} \right\}, \quad (4-48)$$

where

$$\beta_{10} = \int_0^{\eta_B} \bar{\rho} U d\eta \quad \text{and} \quad \beta_{11} = \int_0^{\eta_B} \bar{\rho} U \eta d\eta, \quad (4-49)$$

and  $\eta_B = (R_B - h)/b$ .

The relationship between  $h$  and  $b$  given in Equation (4-10) may be used to simplify Equation (4-48), giving,

$$\bar{v}_B = -\frac{g(h, b, T_J)}{\bar{\rho}_B R_B} \frac{db}{dz}, \quad (4-50)$$

where

$$g(h, b, T_J) = \frac{\{h^2(\beta_{10} - \beta_1) + 2hb(\beta_{11} - \beta_2) + 2b^2T_J(\beta_1\beta_{11} - \beta_2\beta_{10})\}}{\{h + bT_J\beta_1\}} \quad (4-51)$$

Letting  $k_{11}$  be given by

$$k_{11} = \int_0^{\xi_B} (\bar{\rho} \hat{u}_p + \hat{\rho} \bar{u}_p) \xi d\xi, \quad (4-52)$$

$\Delta\tilde{v}_c$  may be written in the form,

$$\Delta\tilde{v}_c(r, \phi, z, t) =$$

$$\text{Re.} \left\{ \frac{A(z)e^{i(k_r z + n\phi - \beta t)}}{\bar{\rho}_B R_B} \cdot \left[ \frac{\bar{\rho}_B}{\bar{\rho}_B} g(h, b, T_J) \frac{db}{dz} - \frac{d}{dz} (b^2 k_{11}) \right] \right\} \quad (4-53)$$

In order to calculate momentum imbalance caused by assuming locally parallel flow the radial and azimuthal momentum equations are used. These equations, including terms of order unity in the boundary layer approximations, may be written,

$$\bar{\rho} \frac{\partial \tilde{v}}{\partial t} + \frac{1}{r} \frac{\partial}{\partial r} (2\bar{\rho}\tilde{v}\tilde{v}r) + \frac{\bar{\rho}\tilde{v}}{r} \frac{\partial w}{\partial \phi} + \frac{\partial}{\partial z} (\bar{\rho}\tilde{u}\tilde{v}) = - \frac{\partial \tilde{p}}{\partial r} + \begin{cases} \text{viscous} \\ \text{terms} \end{cases}, \quad (4-54)$$

and

$$\bar{\rho} \frac{\partial \tilde{w}}{\partial t} + \frac{1}{r} \frac{\partial}{\partial r} (\bar{\rho}\tilde{v}\tilde{w}r) + \frac{\bar{\rho}\tilde{v}\tilde{w}}{r} + \frac{\partial}{\partial z} (\bar{\rho}\tilde{u}\tilde{w}) = - \frac{1}{r} \frac{\partial \tilde{p}}{\partial \phi} + \begin{cases} \text{viscous} \\ \text{terms} \end{cases} \quad (4-55)$$

It will be assumed that the inviscid eigenfunctions satisfy closely the viscous parallel flow momentum equations. The difference between the pressure fluctuation satisfying Equations (4-54) and (4-55) and that satisfying the parallel flow equations is denoted by  $\Delta\tilde{p}$ .  $\Delta\tilde{p}$  takes the form,

$$\Delta\tilde{p}(r, \phi, z, t) = \text{Re.} \left\{ A(z) \Delta\tilde{p}(r) e^{i(k_r z + n\phi - \beta t)} \right\}, \quad (4-56)$$

and satisfies the equations,

$$- \frac{\partial \Delta\tilde{p}}{\partial r} = \frac{1}{r} \frac{\partial}{\partial r} (2\bar{\rho}\tilde{v}\tilde{v}_p r) + \tilde{v}_p \frac{\partial \tilde{p}\tilde{u}}{\partial z} + \frac{\bar{\rho}\tilde{v}}{r} \frac{\partial \tilde{w}_p}{\partial \phi}, \quad (4-57)$$

and

$$- \frac{1}{r} \frac{\partial \Delta\tilde{p}}{\partial \phi} = \frac{1}{r} \frac{\partial}{\partial r} (\bar{\rho}\tilde{v}\tilde{w}_p r) + \tilde{w}_p \frac{\partial \tilde{p}\tilde{u}}{\partial z} + \frac{\bar{\rho}\tilde{v}}{r} \tilde{w}_p. \quad (4-58)$$

Following the general method suggested by the work of Tam<sup>52</sup>, new coordinates are introduced, given by

$$x = r\cos\phi \quad \text{and} \quad y = r\sin\phi, \quad (4-59)$$

so that Equations (4-57) and (4-58) become,

$$\begin{aligned}
-\frac{\partial \tilde{\Delta p}}{\partial x} = & \frac{1}{r} \frac{\partial}{\partial r} (2\bar{\rho} \bar{v} \bar{v}_p \cos\phi - \bar{\rho} \bar{v} \bar{w}_p \sin\phi) r + \frac{\partial \bar{u}}{\partial z} (\bar{v}_p \cos\phi - \bar{w}_p \sin\phi) \\
& + \frac{\bar{\rho} \bar{v}}{r} \frac{\partial \bar{w}_p}{\partial \phi} \cos\phi - \frac{\bar{\rho} \bar{v}}{r} \bar{w}_p \sin\phi,
\end{aligned} \tag{4-60}$$

and

$$\begin{aligned}
-\frac{\partial \tilde{\Delta p}}{\partial y} = & \frac{1}{r} \frac{\partial}{\partial r} (2\bar{\rho} \bar{v} \bar{v}_p \sin\phi + \bar{\rho} \bar{v} \bar{w}_p \cos\phi) r + \frac{\partial \bar{u}}{\partial z} (\bar{v}_p \sin\phi + \bar{w}_p \cos\phi) \\
& + \frac{\bar{\rho} \bar{v}}{r} \frac{\partial \bar{w}_p}{\partial \phi} \sin\phi + \frac{\bar{\rho} \bar{v}}{r} \bar{w}_p \cos\phi.
\end{aligned} \tag{4-61}$$

The fluctuating forces acting in the vertical and transverse planes per unit length of the jet corresponding to the fluctuating pressure  $\tilde{\Delta p}$  are given by

$$\tilde{F}_y = - \int_{-x}^x \tilde{\Delta p} dx, \tag{4-62}$$

and

$$\tilde{F}_x = - \int_{-y}^y \tilde{\Delta p} dy. \tag{4-63}$$

From the form of fluctuations and Equations (4-60) and (4-61), it can be seen that the fluctuating forces are only non-zero for  $n=1$ , and are given by,

$$\begin{aligned}
\tilde{F}_x = \text{Re.} \left\{ \left[ \pi \frac{d}{dz} \left( \int_0^{R_B} \bar{\rho} \bar{u} (\hat{v}_p - i \hat{w}_p) r dr \right) + \pi \bar{\rho}_B \bar{v}_B R_B (2 \hat{v}_p - i \hat{w}_p)_B \right] \right. \\
\left. \cdot A(z) e^{i(k_r z - \beta t)} \right\}, \tag{4-64}
\end{aligned}$$

and

$$\begin{aligned}
\tilde{F}_y = \text{Re.} \left\{ \left[ \pi \frac{d}{dz} \left( \int_0^{R_B} \bar{\rho} \bar{u} (i \hat{v}_p + \hat{w}_p) r dr \right) + \pi \bar{\rho}_B \bar{v}_B R_B (2i \hat{v}_p + \hat{w}_p)_B \right] \right. \\
\left. \cdot A(z) e^{i(k_r z - \beta t)} \right\}. \tag{4-65}
\end{aligned}$$

The fluctuating forces per unit jet length may be associated with rate of change of fluctuating velocities in their respective directions, such that,

$$\tilde{F}_y = -\bar{\rho}_B R_B^2 \pi \frac{\partial \tilde{v}_y}{\partial t} \quad \text{and} \quad \tilde{F}_x = -\bar{\rho}_B R_B^2 \pi \frac{\partial \tilde{v}_x}{\partial t}, \quad (4-66)$$

where  $v_y$  and  $v_x$  are the associated fluctuating velocities in the  $y$  and  $x$  directions, respectively. The radial component of these velocity fluctuations, denoted by  $\Delta \tilde{v}_m$  is given by,

$$\Delta \tilde{v}_m = \cos\phi \tilde{v}_y + \sin\phi \tilde{v}_x,$$

so that

$$\Delta \tilde{v}_m = \text{Re.} \left\{ \frac{1}{\beta \bar{\rho}_B R_B^2} \left[ \frac{d}{dz} \left( \int_0^{R_B} \bar{\rho} \bar{u} (\hat{v}_p - i\hat{w}_p) r dr + \bar{\rho}_B \bar{v}_B R_B (2\hat{v}_p - i\hat{w}_p)_B \right) \cdot A(z) e^{i(k_r z - \beta t)} \right] \right\}. \quad (4-67)$$

Letting

$$k_{12} = \int_0^{\xi_B} \bar{\rho} \bar{u} (\hat{v}_p - i\hat{w}_p) \xi d\xi$$

and noting that the Strouhal number  $St = 2f^* r_j^* / \bar{u}_j^*$  is given by  $St = \beta/\pi$ , the normal velocity correction  $\Delta \tilde{v}_m$  is then given by,

$$\Delta \tilde{v}_m = \text{Re.} \left\{ \frac{1}{\pi St \bar{\rho}_B R_B^2} \left[ \frac{d}{dz} (b^2 k_{12}) - (2\hat{v}_p - i\hat{w}_p)_B g(h, b, T_J) \frac{db}{dz} \right] \cdot A(z) e^{i(k_r z - \beta t)} \right\} \quad (4-68)$$

Thus, the radial velocity fluctuation on a cylindrical control surface surrounding the flow region is given by,

$$\tilde{v}_B = \tilde{v}_{p_B} + \Delta \tilde{v}_c + \Delta \tilde{v}_m. \quad (4-69)$$

In the next section the corresponding analysis for the flow downstream of the potential core will be examined.

#### 4.2.3.2 The developed jet region (downstream of potential core)

The continuity equation nondimensionalized with respect to the ambient density, the jet radius and the jet centerline velocity may be written,

$$\frac{\partial \tilde{p}}{\partial t} + \frac{1}{r} \frac{\partial}{\partial r} [\tilde{p}\tilde{v} + \tilde{\rho}\tilde{v}]r + \frac{1}{r} \frac{\partial \tilde{p}\tilde{w}}{\partial \phi} + \frac{1}{\bar{u}_c} \frac{\partial}{\partial z} [(\tilde{\rho}\tilde{u} + \tilde{\rho}\tilde{u})\bar{u}_c] = 0, \quad (4-70)$$

where  $\bar{u}_c(z)$  is the jet centerline velocity.

The eigenfunctions given by locally parallel flow, denoted by the subscript p, satisfy the parallel mean flow continuity equation (4-46), so the difference between the radial velocity satisfying Equation (4-70) and that satisfying the parallel flow equation, denoted by  $\Delta\tilde{v}_c$  is given by

$$\frac{1}{r} \frac{\partial}{\partial r} [(\tilde{\rho}\Delta\tilde{v}_c + \tilde{\rho}_p \tilde{v})r + \frac{\tilde{u}_p}{\bar{u}_c} \frac{\partial \tilde{\rho}\bar{u}_c}{\partial z} + \frac{\tilde{\rho}_p}{\bar{u}_c} \frac{\partial \bar{u}\bar{u}_c}{\partial z}] = 0. \quad (4-71)$$

Integration radially to a boundary at  $r=R_B$  then gives,

$$\bar{u}_c \Delta\tilde{v}_c = - \bar{u}_c \frac{\tilde{v}_B \hat{\rho}_p B}{\bar{\rho}_B} - \frac{1}{\bar{\rho}_B R_B} \frac{d}{dz} \{b^2 \bar{u}_c k_{15}\}, \quad (4-72)$$

where

$$k_{15} = \int_0^{\xi_B} (\tilde{\rho} \hat{u}_p + U \hat{\rho}_p) \xi d\xi, \quad (4-73)$$

where  $U(\xi)$  is defined in Equation (4-28).

The time averaged continuity equation may be integrated from  $r=0$  to  $r=R_B$  giving,

$$\bar{\rho}_B R_B \tilde{v}_B \bar{u}_c = - \frac{d}{dz} \{b^2 \bar{u}_c \gamma_{11}\}, \quad (4-74)$$

where

$$\gamma_{11} = \int_0^{\xi_B} \bar{\rho} U \xi d\xi. \quad (4-75)$$

The normal velocity correction  $\Delta\tilde{v}_c$  is assumed to take the same periodic form as the parallel flow solution which gives,

$$\bar{u}_c \Delta\tilde{v}_c = \text{Re} \cdot \left\{ \frac{A(z)}{\bar{\rho}_B R_B} e^{i(k_r z + n\phi - \beta t)} \left[ \frac{\hat{\rho}_p B}{\bar{\rho}_B} \frac{d}{dz} \{b^2 \bar{u}_c \gamma_{11}\} - \frac{d}{dz} \{b^2 \bar{u}_c k_{15}\} \right] \right\}. \quad (4-76)$$

The derivation of the radial velocity correction which leads to satisfaction of the radial and azimuthal momentum equations in the developed jet flow follows, in an analogous manner, the analysis for the annular mixing region; Equations (4-54) through (4-67). This leads to

$$\Delta \tilde{v}_m = Re \left\{ \frac{1}{\beta R_B^2 \bar{\rho}_B} \left[ \frac{1}{\bar{u}_c^2} \frac{d}{dz} \left( \int_0^{R_B} \bar{\rho} \bar{u} \bar{u}_c^2 (\hat{v}_p - i\hat{w}_p) r dr \right) + \bar{\rho}_B \bar{v}_B R_B (2\hat{v}_p - i\hat{w}_p)_B \right] \cdot A(z) e^{i(k_r z - \beta t)} \right\}. \quad (4-77)$$

Letting

$$k_{17} = \int_0^{\xi_B} \bar{\rho} U (\hat{v}_p - i\hat{w}_p) \xi d\xi$$

and noting that the Strouhal number is given by  $St = \bar{u}_c^\beta / \pi$ , then Equation (4-74) can be used to obtain,

$$\bar{u}_c \Delta \tilde{v}_m = Re \cdot \left\{ \frac{1}{St \pi \bar{\rho}_B R_B^2} \left[ \frac{d}{dz} \{ b^2 \bar{u}_c^2 k_{17} \} - \bar{u}_c (2\hat{v}_p - i\hat{w}_p)_B \frac{d}{dz} \{ b^2 \bar{u}_c \gamma_{11} \} \right] \cdot A(z) e^{i(k_r z - \beta t)} \right\}. \quad (4-78)$$

Then the radial velocity fluctuation on a cylindrical control surface surrounding the flow region, normalized with respect to the jet exit velocity, is given by,

$$\Delta \tilde{v}_B = \Delta \tilde{v}^*/\bar{u}_j^* = \bar{u}_c (\tilde{v}_{p_B} + \Delta \tilde{v}_c + \Delta \tilde{v}_m). \quad (4-79)$$

The corrected radial velocity fluctuation given by Equations (4-69) and (4-79) can be used to calculate the noise radiated by the wave-like fluctuations in the jet. This analysis is considered in the next section.

#### 4.2.4 Calculation of the Far-Field Noise

The fluctuating pressure in the ambient medium around the jet satisfies the equation

$$\bar{a}_o^{*2} \nabla^2 \tilde{p}^* - \frac{\partial^2}{\partial t^{*2}} \tilde{p}^* = 0. \quad (4-80)$$

Equation (4-80) may be nondimensionalized with respect to the ambient density, the jet exit velocity and the jet radius. Assuming a periodic form for the pressure fluctuation,

$$\tilde{p}(r, \phi, z, t) = \text{Re.} \left\{ x(r, z) e^{i(n\phi - \beta t)} \right\}, \quad (4-81)$$

Equation (4-80) may be written,

$$\bar{a}_o^2 \left\{ \frac{\partial^2 x}{\partial r^2} + \frac{1}{r} \frac{\partial x}{\partial r} + \frac{\partial^2 x}{\partial z^2} - \frac{n^2 x}{r^2} \right\} + \beta^2 x = 0. \quad (4-82)$$

The Fourier transform of  $x$  with respect to  $z$  is defined by

$$\pi(r, k) = \frac{1}{2\pi} \int_0^\infty x(r, z) e^{-ikz} dz, \quad (4-83)$$

The transformed form of Equation (4-82) may be solved for  $\pi(r, k)$ , giving

$$\pi(r, k) = B \cdot H_n^{(1)} \left[ \left\{ \frac{\beta^2}{\bar{a}_o^2} - k^2 \right\}^{\frac{1}{2}} r \right]. \quad (4-84)$$

On the control surface at  $r = R_B$  the pressure fluctuation is related to the radial velocity fluctuation by,

$$\left[ \tilde{p} \frac{\partial \tilde{v}}{\partial t} = - \frac{\partial \tilde{p}}{\partial r} \right]_{r=R_B} \quad (4-85)$$

Letting

$$\tilde{v}(r, \phi, z, t) = \text{Re.} \left\{ \psi(r, z) e^{i(n\phi - \beta t)} \right\}$$

and

$$\zeta_B(R_B, k) = \frac{1}{2\pi} \int_{-\infty}^{\infty} \psi(R_B, z) e^{-ikz} dz, \quad (4-86)$$

leads to,

$$\pi(r, k) = \frac{i \tilde{\rho}_B \beta \zeta_B(R_B, k) \cdot H_n^{(1)}[\Omega r]}{\Omega H_n^{(1)}, [\Omega R_B]} \quad (4-87)$$

where

$$\Omega^2 = [\beta^2 / \bar{a}_o^2 - k^2]. \quad (4-88)$$

$$(4-88)$$

The pressure fluctuation  $\tilde{p}$  may then be obtained from the inverse Fourier transform,

$$\tilde{p}(r, z, \phi, t) = \text{Re.} \left\{ \int_{-\infty}^{\infty} \pi(r, k) e^{ikz} dk \cdot e^{i(n\phi - \beta t)} \right\} \quad (4-89)$$

In the far field,  $\Omega r \gg \infty$ , the Hankel function in equation (4-87) may be replaced by its asymptotic form,

$$H_n^{(1)}\{\Omega r\} \approx \sqrt{\frac{2}{\pi \Omega r}} \cdot \exp \left[ i \left| \Omega r - \frac{\pi}{4} - \frac{n\pi}{2} \right| \right]. \quad (4-90)$$

The integral in Equation (4-89) may then be evaluated by the method of steepest descents, Brekhovskikh<sup>57</sup>, so that the far-field pressure can be written,

$$\begin{aligned} p(R, \phi, \theta, t) = \text{Re.} & \left\{ \frac{2i\bar{\rho}_B \bar{a}_O}{R \sin \theta} \frac{\zeta_B(R_B, \beta \cos \theta / \bar{a}_O)}{H_n^{(1)} \left| \beta R_B \sin \theta / \bar{a}_O \right|} \right. \\ & \left. \cdot \exp \left[ i \left( \frac{\beta R}{\bar{a}_O} + n\phi - \beta t - \frac{\pi(n+1)}{2} \right) \right] \right\}. \end{aligned} \quad (4-91)$$

Thus, the mean square pressure may be written,

$$\overline{\tilde{p}^2} = \frac{2\bar{\rho}_B^2}{R^2 \sin^2 \theta M_O^{-2}} \left| \frac{\zeta_B(R_B, \beta M_O \cos \theta)}{H_n^{(1)} \left| (R_B \beta M_O \sin \theta) \right|} \right|^2, \quad (4-92)$$

since  $\bar{a}_O = \bar{a}_O^*/\bar{u}_J^* = M_O^{-1}$ .

In the following sections numerical solutions for the near and far-field jet structure will be described.

### 4.3 NUMERICAL CALCULATIONS

#### 4.3.1 The Local Inviscid Stability Characteristics

The analysis given in the preceding sections showed how the eigensolutions to the local inviscid stability equation described the local radial distributions of the wave-like fluctuations. In the theory of the stability of parallel flows, the sign and magnitude of the imaginary part of the eigenvalue govern the growth or decay of the fluctuation. For spatial stability analyses, the complex wavenumber is the eigenvalue. However, in the present analysis, the local radial distributions of the fluctuations, integrated across the jet, rather than the imaginary part of the wavenumber, govern the amplitude change of the wave-like fluctuations. Thus, the local growth rate is not directly used in the calculations. However, several relevant features of the wave development can be seen by examining the local inviscid stability characteristics.

The numerical calculations were performed for an ideally-expanded, isothermal (jet exit static temperature equal to ambient temperature),

axisymmetric jet exhausting into still air. The jet Mach number was 1.4. This Mach number was chosen for several reasons. The high exhaust velocity was chosen as it was felt that the noise radiated by the wave-like components of the flow would be more significant, and hence more easily recognizable, under these conditions. However, the Mach number was not significantly high that there would be any significant linear coupling between the convecting wave-like structure and the radiated noise field. This coupling, which only occurs at high supersonic velocities and is usually referred to as eddy Mach wave radiation exists as a special case of the present noise generation mechanism. Choice of a low supersonic Mach number attempted to avoid confusion between the present general formulation and eddy Mach-wave radiation. It was found, for  $n=0$  and  $St=.1$ , that the phase velocity was supersonic at the neutral point and an eddy Mach wave radiation was possible for these conditions. This test condition also corresponded to a test point in the mixing noise measurement program so that comparisons were possible.

Stability calculations were carried out numerically using an iterative integration with variable step-size on the proper contour of integration to permit the solutions to be obtained for decaying modes. Calculations were performed for the first three azimuthal modes; the axisymmetric mode,  $n=0$ ; the helical mode,  $n=1$ , and the  $n=2$  mode. Three frequencies were considered, corresponding to Strouhal numbers, based on the jet exit velocity and diameter of .1, .3 and 1. The calculated phase velocities, defined as the real frequency divided by the real part of the axial wavenumber,  $\beta/k_r$ , are shown in Figure 4.4, 4.5, and 4.6 for the  $n=0$ , 1, and 2 modes, respectively. All the modes and Strouhal numbers exhibited similar characteristics of first decreasing and then increasing phase velocity with jet width. The minimum phase velocity in all cases occurred close to the neutral local stability solution. Also shown on the figures is the sonic phase velocity line,  $\beta M_0/k_r = a_0$ . It can be seen that the minimum phase velocity in each case, which was close to the neutral point, was subsonic which eliminated the direct coupling between the linear solutions and the far-field acoustic solutions. For a particular Strouhal number the lower the azimuthal mode number the higher was the phase velocity. For the  $n=0$  mode and a Strouhal number of .1 a discontinuity occurred at  $b=1.12$ . This corresponds to a change in the least stable mode type.

The induced propagation angle of an amplifying or decaying wave is dependent on the complex phase velocity. Liu<sup>48</sup> noted that the direction of the local intensity vector in the ambient region can be defined by

$$\tan(\textcircled{H}) = \frac{\bar{p}_v}{\bar{p}_u}$$

where  $(\textcircled{H})$  is the angle from the z axis. The line perpendicular to this direction is the wave front induced by the travelling instability wave. This angle depends, by definition on the complex phase velocity,  $\beta/k$ , rather than the real phase velocity as would be appropriate for a travelling neutral disturbance. For a two-dimensional flow this direction,  $(\textcircled{H})$ , is explicitly independent of vertical position and is a function of the local wavenumber, frequency and Mach number alone. However, in the axisymmetric case, it can be shown that,

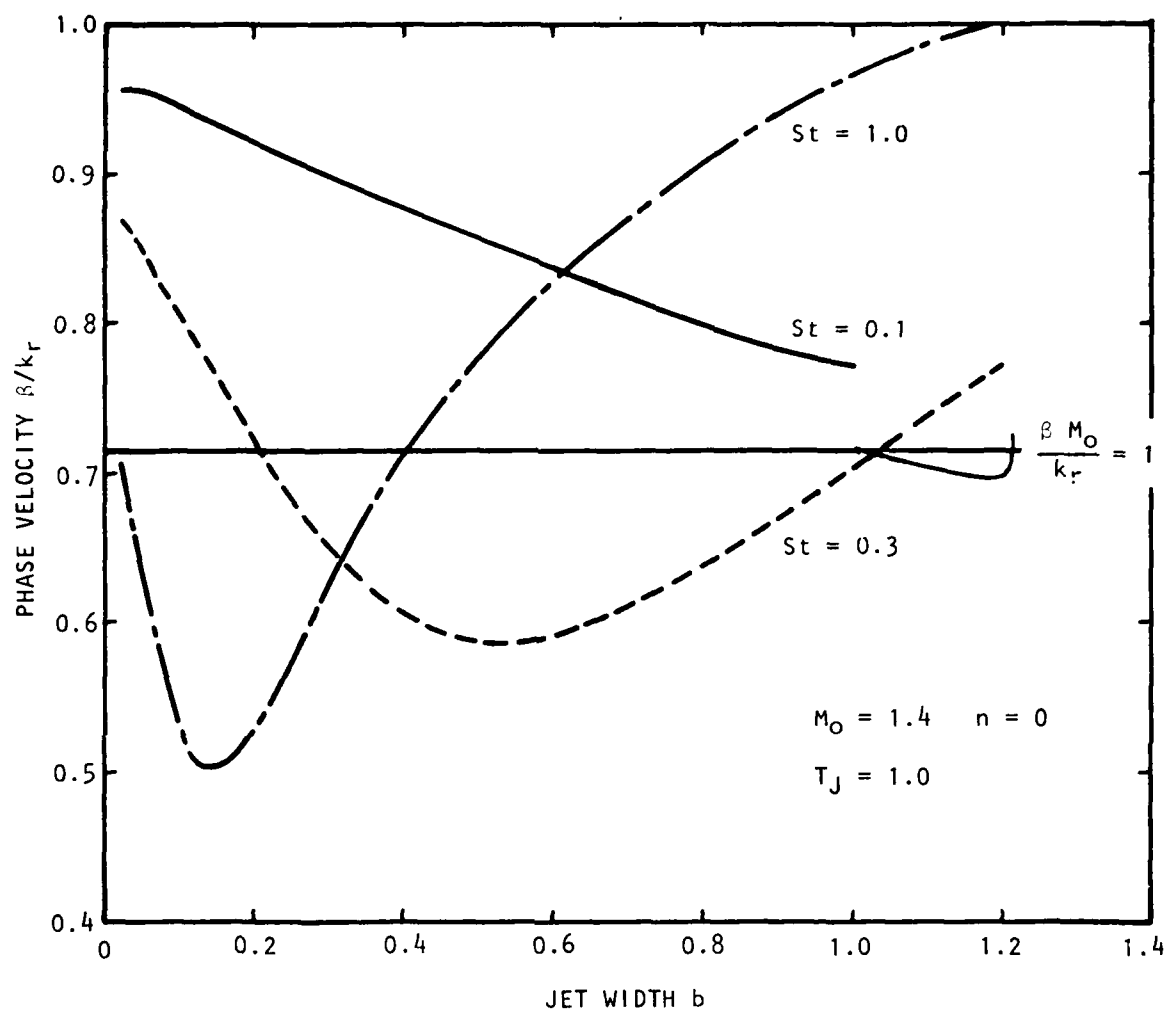


Figure 4.4 Variation of Phase Velocity with Jet Width:  $n = 0$

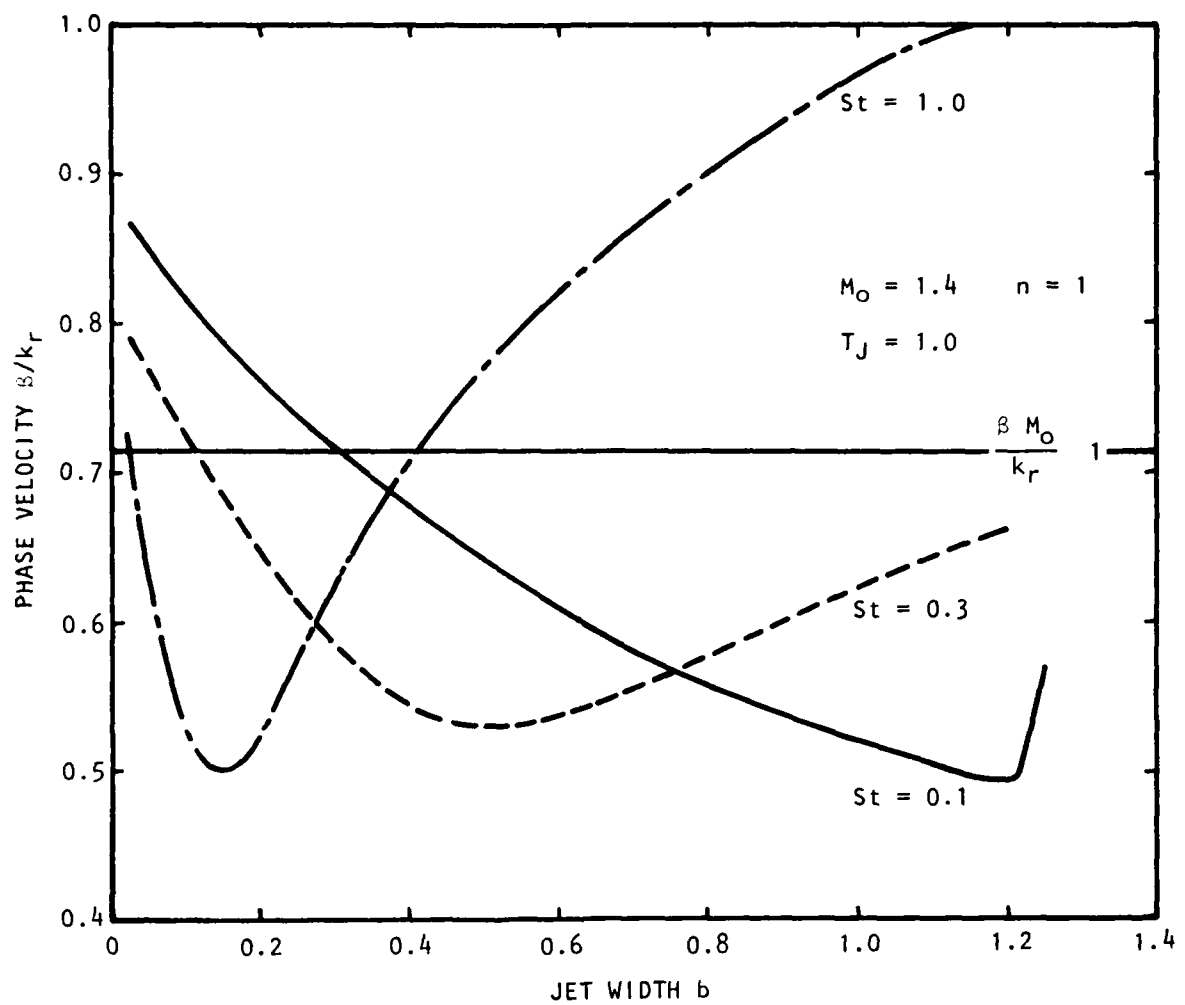


Figure 4.5 Variation of Phase Velocity with Jet Width:  $n = 1$

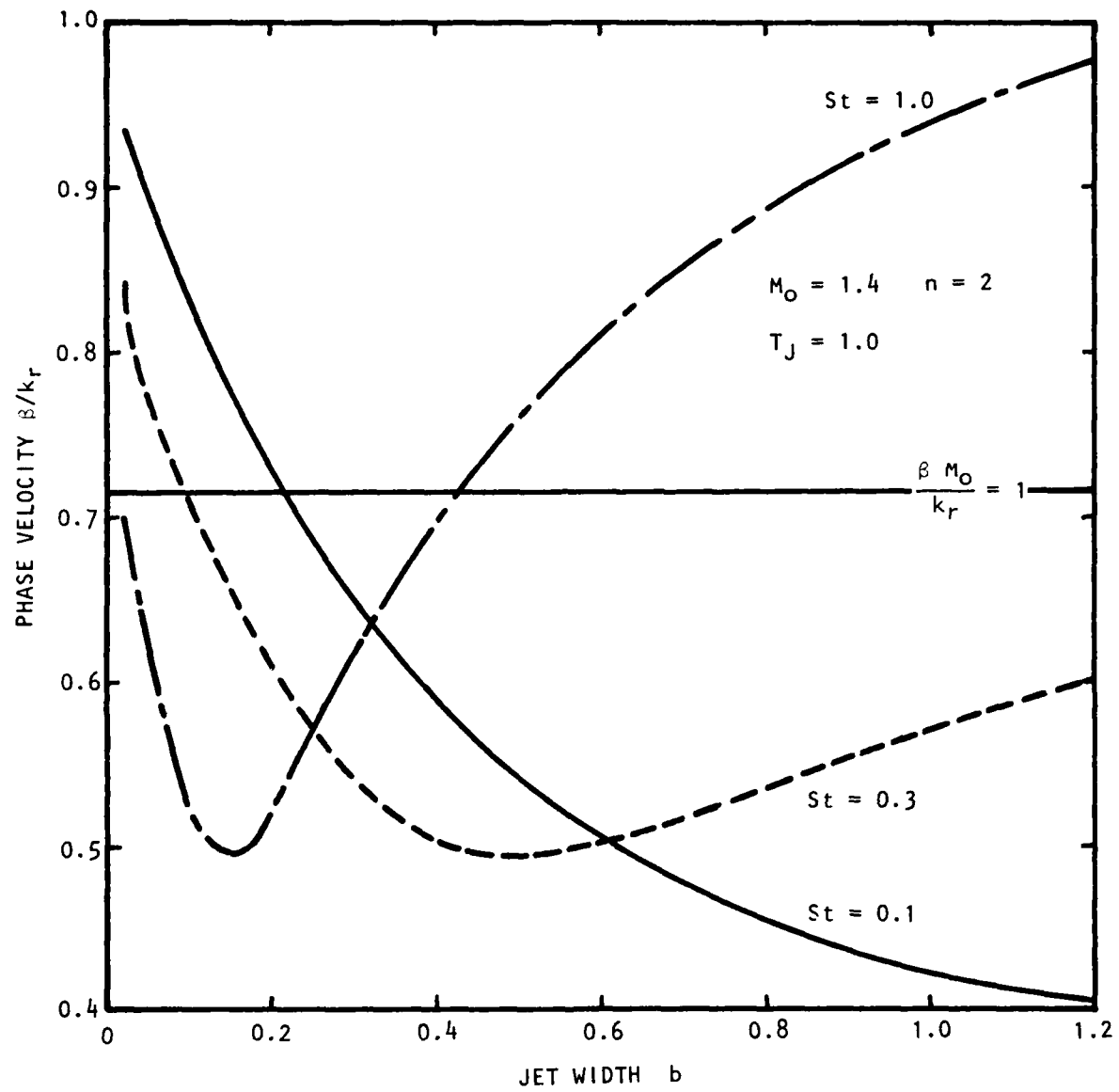


Figure 4.6 Variation of Phase Velocity with Jet Width:  $n = 2$

$$\tan \Theta = \frac{\operatorname{Re} \left[ H_n^{(1)*}(i\lambda r) H_n^{(1)}(i\lambda r) \cdot \lambda/B \right]}{|H_n^{(1)}(i\lambda r)|^2 \cdot \operatorname{Re} \{k/B\}}, \quad (4-93)$$

where  $\lambda$  is given by,

$$\lambda^2 = k^2(1 - M_0^2 c^2),$$

and

$$c = B/k. \quad (4-94)$$

Clearly the induced wave front direction is a function of radial distance. From the form of the Hankel function it can be shown that as the radial distance increases so the angle  $\Theta$  decreases, and for sufficiently large values of  $\lambda r$  the two-dimensional result is recovered,

$$\tan \Theta = \frac{1}{\sqrt{2}} \left\{ (A + (A^2 + B^2)^{\frac{1}{2}})^{\frac{1}{2}} \pm \frac{k_i}{kr} (-A + (A^2 + B^2)^{\frac{1}{2}})^{\frac{1}{2}} \right\}, \quad (4-95)$$

where

$$A = M_0^2 (c_r^2 - c_i^2) - 1$$

and

$$B = 2M_0^2 c_r c_i. \quad (4-96)$$

The choice of sign in Equation (4-95) depends on whether the wave is locally amplifying or decaying. Equation (4-95) was evaluated for  $n=0$  and  $St=.1, .3$  and  $1$  and is shown in Figure 4.7. As a wave propagates downstream so the induced propagation angle in the ambient fluid decreases till the neutral condition is reached. The induced propagation angle then increases with jet thickness as the wave decays. Since the lowest frequency mode is convecting supersonically over the range of jet widths considered, its induced propagation angle never reaches zero. If it were possible to separate out the wave fronts associated with a particular frequency component, a phase velocity could be calculated based on zero amplification where the phase velocity is given in terms of the induced propagation angle by,

$$c_{rN} = (\tan^2 \Theta + 1)^{\frac{1}{2}}/M_0. \quad (4-97)$$

Here the subscript N denotes a neutral or zero amplification assumption. The values of  $c_{rN}$  as a function of jet width were compared with the true phase velocity  $B/k_r$ . The comparison is shown in Figure 4.8. The values of  $c_{rN}$  were always higher than the true phase velocities and were always greater than or equal to the speed of sound in the ambient medium. For  $St=.1$  the two calculations yielded the same result, as they must, for a true supersonically convecting neutral disturbance. Thus, the inference of a particular phase velocity based on wave propagation angle in the near field is not possible without a detailed knowledge of the stability characteristics of the waves in the flow. In practice the induced wavefield is composed of multiple frequency components. If the most amplifying disturbance is assumed to dominate the local flow structure (Morris<sup>49</sup>), then it is possible to infer the variation of wave propagation angle with jet width or axial distance. Table I

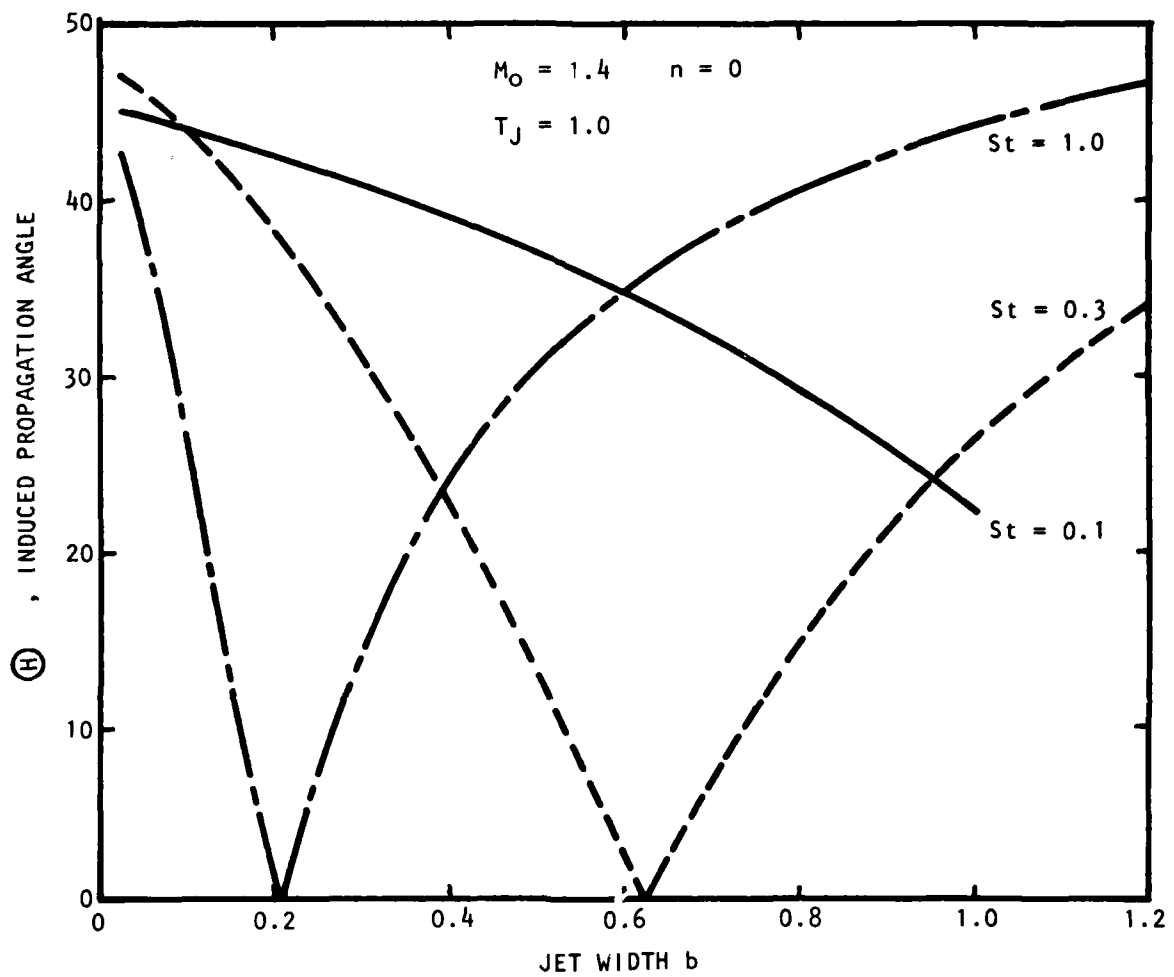


Figure 4.7 Variation of Induced Wave Propagation Angle with Jet Width

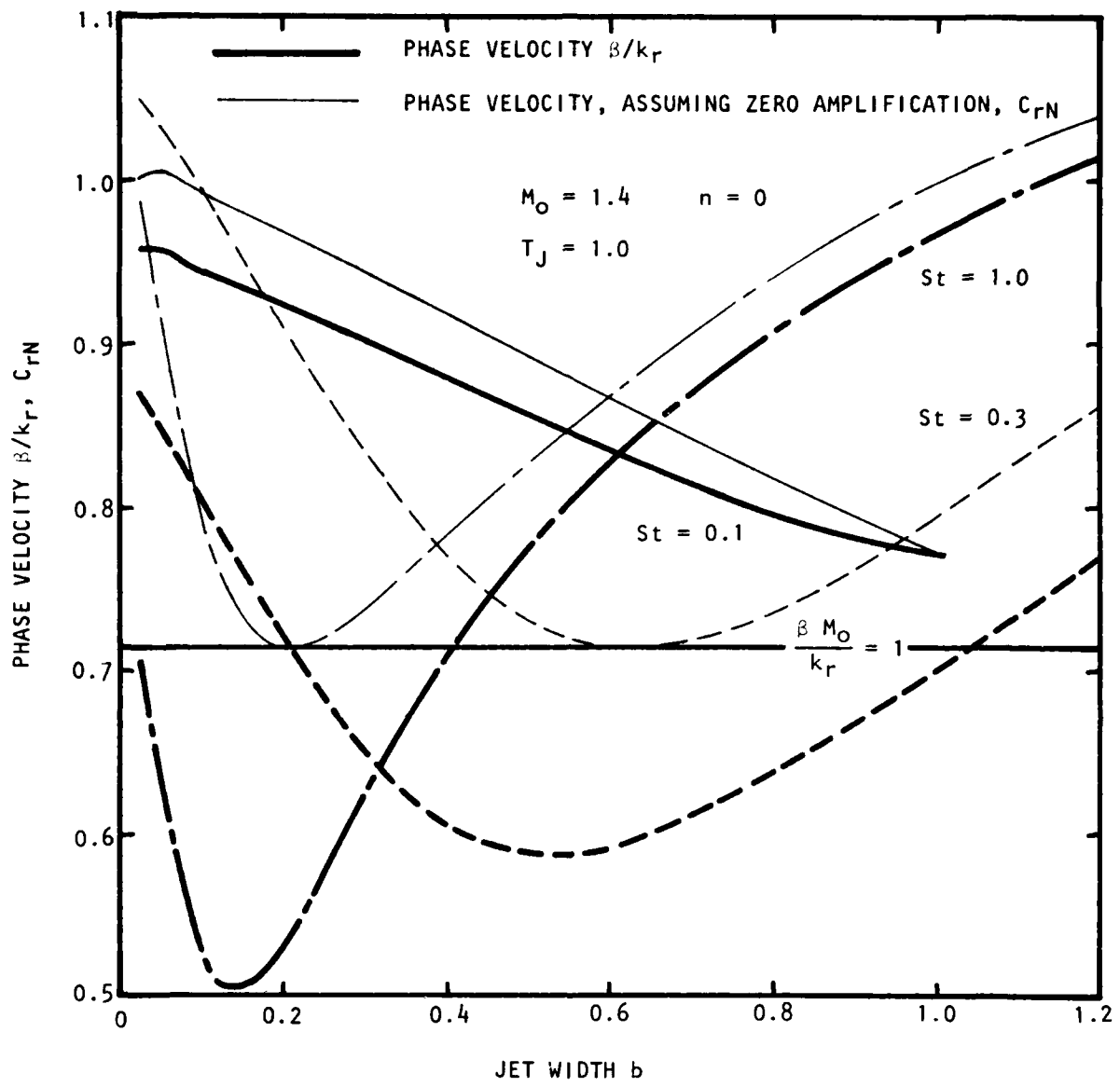


Figure 4.8 Comparison of Phase Velocity  $\beta/k_r$  and Phase Velocity Calculated from the Induced Propagation Angle Assuming Zero Amplification

shows the variation of induced propagation angle with jet width calculated in this manner. The induced angle increases with jet width, though the angular variation is small. This trend is supported by schlieren photographs (Eggers<sup>58</sup>, figure 2). Though the induced propagation angle is a function of radial position, as can be seen from Equation (4-93), the variation is very slight. The variation of angle with radial distance is given in Table II for several jet widths and  $n = 0$ ,  $St = .3$ . Thus, the wave fronts are very nearly locally parallel.

St	b max. amp.	$\Theta$
1	.1	26
.3	.3	31
.1	.6	35

Table I Variation of Induced Propagation Angle with Jet Width for Maximum Local Amplification:  $n = 0$ .

b	$\Theta$ , $r = 1.5$	$\Theta$ , $r = 2$	$\Theta$ , $r = 2.5$	$\Theta$ , $r = 3$	$\Theta$ , $r = 3.5$	$\Theta$ , EQN.95
.1	44.46	44.26	44.14	44.08	44.04	43.90
.3	--	31.21	31.11	31.06	31.02	30.89
.6	--	2.737	2.722	2.713	2.707	2.69
1.2	--	--	34.80	34.59	34.46	34.12

Table II Variation of Induced Propagation Angle with Radial Distance:  $n = 0$ ,  $St = .3$ .

In the present formulation the local growth or decay of the wave-like structure is determined from integrals of the local eigenfunctions rather than the local growth rate given by the imaginary part of the wavenumber (eigenvalue). The amplitude and phase of these eigenfunctions, which is typical of the usual distributions, determined from locally parallel stability theory, are shown in Figures 4.9(a) and 4.9(b), respectively, for  $n = 1$ ,  $St = 3$ , and  $b = .2$ . The  $\hat{u}$  eigenfunction experiences a rapid phase reversal in the outer region of the jet mixing layer whereas the phase of pressure eigenfunction remained nearly constant across the layer. The phase reversal is characteristic of the inviscid solution and is observed experimentally, Michalke<sup>59</sup>. A complete set of the eigenfunctions at  $b = .2$  for all modes and frequencies is given in Appendix 4E.

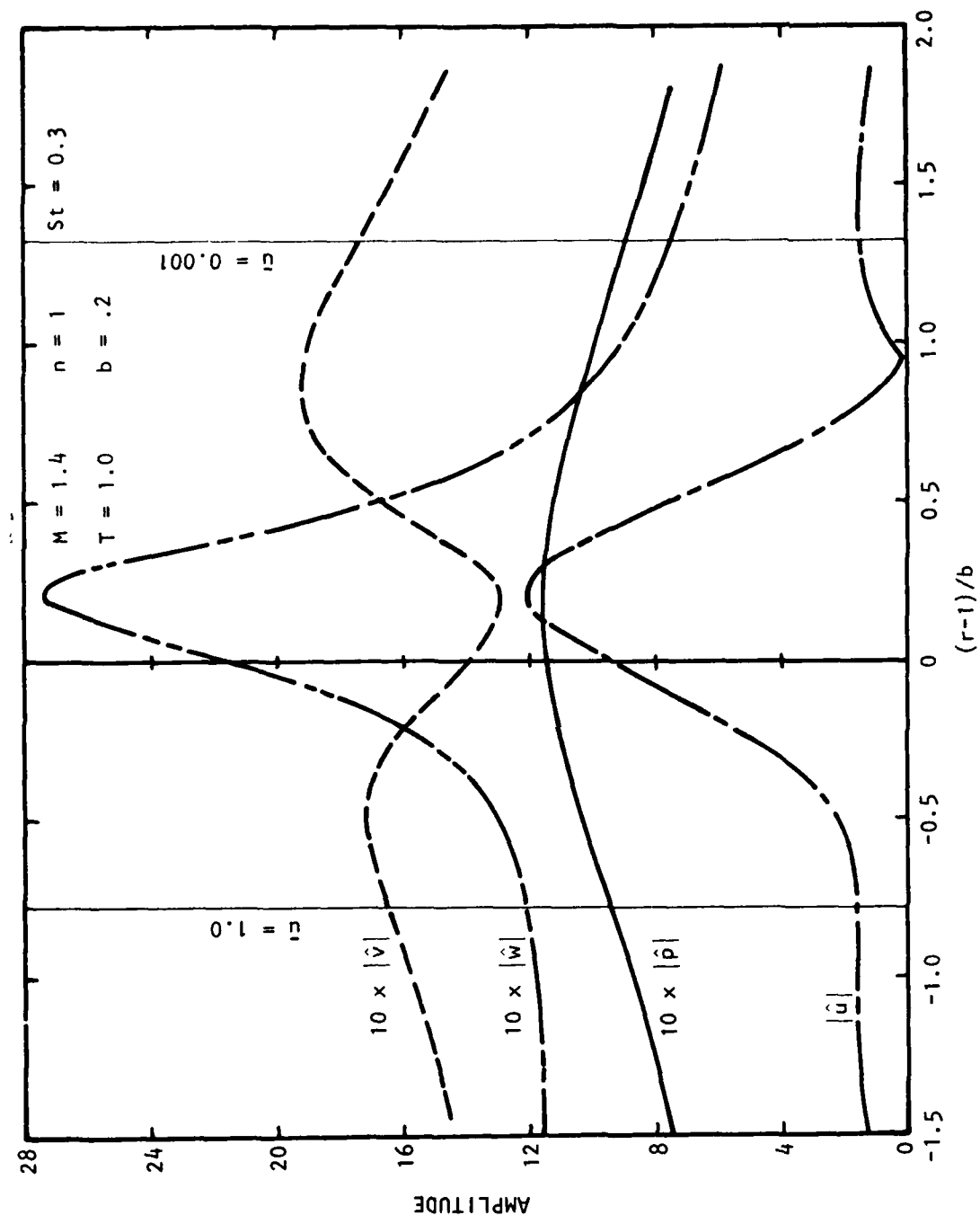


Figure 4.9(a) Radial Variation of Amplitude of Inviscid Eigenfunctions,  $b = 2$

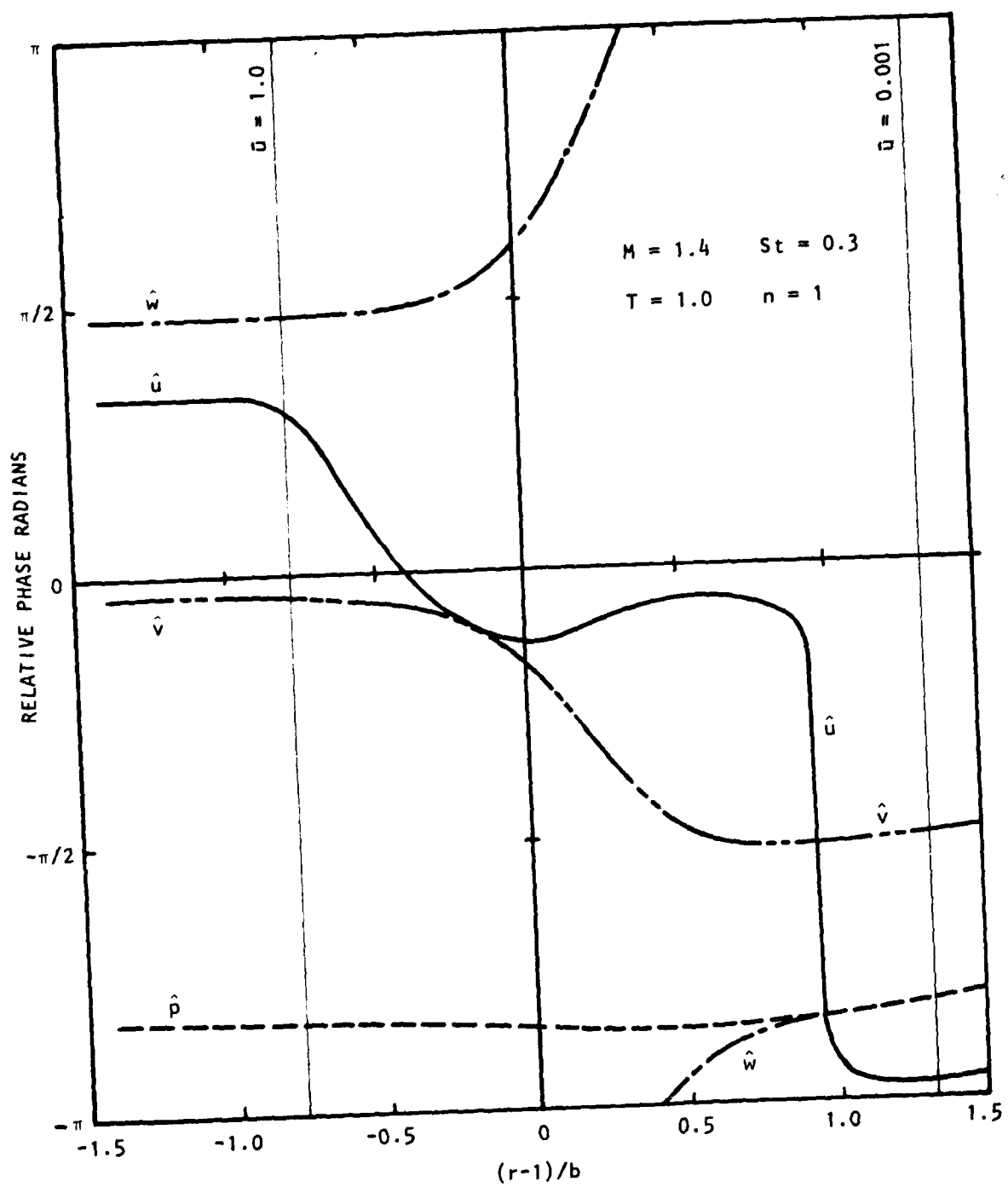


Figure 4.9(b) Radial Variation of Relative Phase of Inviscid Eigenfunctions,  $b = 2$

In Equations (4-25) and (4-38) it was shown that the amplitude of the wave kinetic energy flux could be related to the local inviscid growth rate modified by a viscous convection factor depending on the eddy viscosity relating the random shear stresses to the wave rate of strain. In the present calculations this eddy viscosity was taken as being very small so that, unless otherwise stated, the local inviscid growth rate taken from the imaginary part of the local wavenumber does represent closely the local amplitude variation. The imaginary part of the wavenumber is shown in Figures 4.10, 4.11, and 4.12 for the  $n=0$ , 1, and 2 azimuthal modes, respectively. In each case the neutral point,  $k_1 = 0$ , occurred at increasing jet thickness for decreasing Strouhal numbers. Also, the  $n=1$  mode amplified over the largest range of jet widths. Close to the jet exit the  $n=2$  mode was the most amplifying.

#### 4.3.2 The Axial Wave Development

With the local radial distributions of the mean flow and the wave-like fluctuations calculated from the local stability analysis, the axial development of the periodic structure could be obtained by simultaneous solution of equations for the jet width and wave kinetic energy flux in the annular mixing region and the jet centerline velocity and wave kinetic energy flux in the developed jet flow.

Inspection of the appropriate equations in Section 4.2.2 shows that the only as yet undefined parameters are  $\tilde{R}_T$  and  $\tilde{\epsilon}_T$ .  $\tilde{R}_T$  is a turbulent Reynolds number based on an eddy viscosity,  $\tilde{\epsilon}$ , relating the time-averaged fluctuating shear stresses to the rate of strain of the mean flow. Its numerical value will therefore be representative of the usual eddy viscosity chosen to solve the boundary layer equations.  $\tilde{R}_T$  is a turbulent Reynolds number based on an eddy viscosity,  $\tilde{\epsilon}$ , relating the time independent fluctuating shear stresses to the rate of strain of the periodic disturbances. Since the typical length scale of the wave-like structure is of the same order as the scale of the mean flow, the interaction between the random fluctuations and the mean and wave-like components of the flow will be of the same order. Liu<sup>48</sup> and Chan<sup>47</sup> assumed that  $\epsilon = \tilde{\epsilon}$  in their calculations. However, when the axial development is determined through a set of radially integrated equations and an inviscid local fluctuation shape assumption is made, as was the case in the present work as well as that of Liu and Chan, some difficulty is experienced. The magnitude of the integrated viscous dissipation term,  $I_5$ , depends not only on  $\tilde{\epsilon}$  but on the radial derivatives of the fluctuations. The inviscid eigenfunctions vary more rapidly radially than do the viscous solutions and thus the local growth rate can be greatly underestimated. The effect of the choice of  $\tilde{\epsilon}$  on the axial wave development will be examined below; however, in the present calculations  $\tilde{\epsilon}$  was set to zero. Tam<sup>52</sup> chose, for different and arguable reasons, a value of  $\tilde{\epsilon} = .1\bar{\epsilon}$ . This assumption will be shown to be little different from the present assumption of  $\tilde{\epsilon} = 0$ . The value chosen for  $\tilde{\epsilon}$  was based on the work of Peters and Phares<sup>60</sup> who used a hybrid integral turbulent kinetic energy analysis of free shear flows. These calculations showed the turbulent Reynolds number based on the local jet thickness and the jet centerline velocity was constant in the potential core region and decreased downstream of the potential core. The values used in the present calculations were

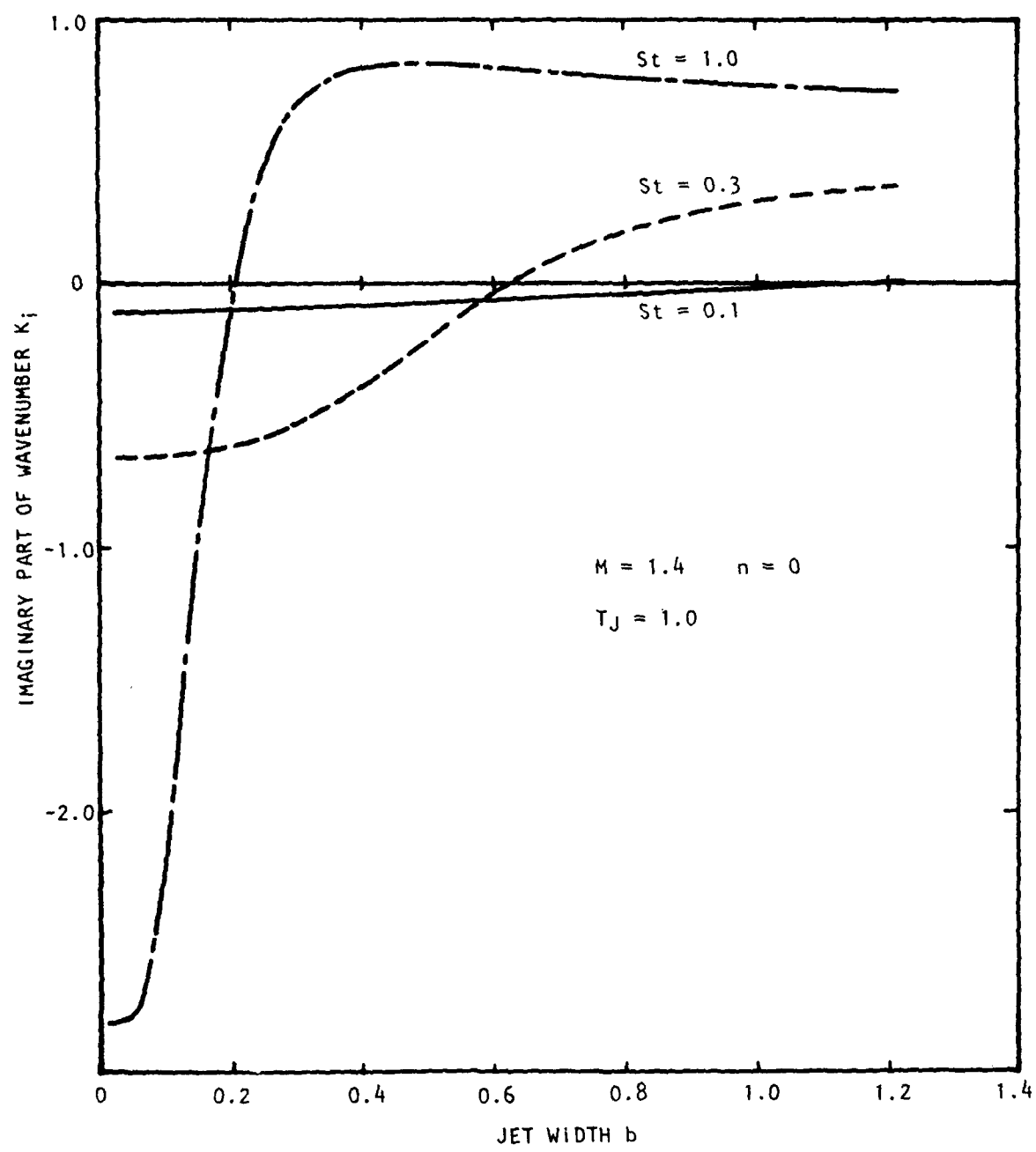


Figure 4.10 Variation of the Imaginary Part of the Wavenumber with Jet Width:  $n = 0$

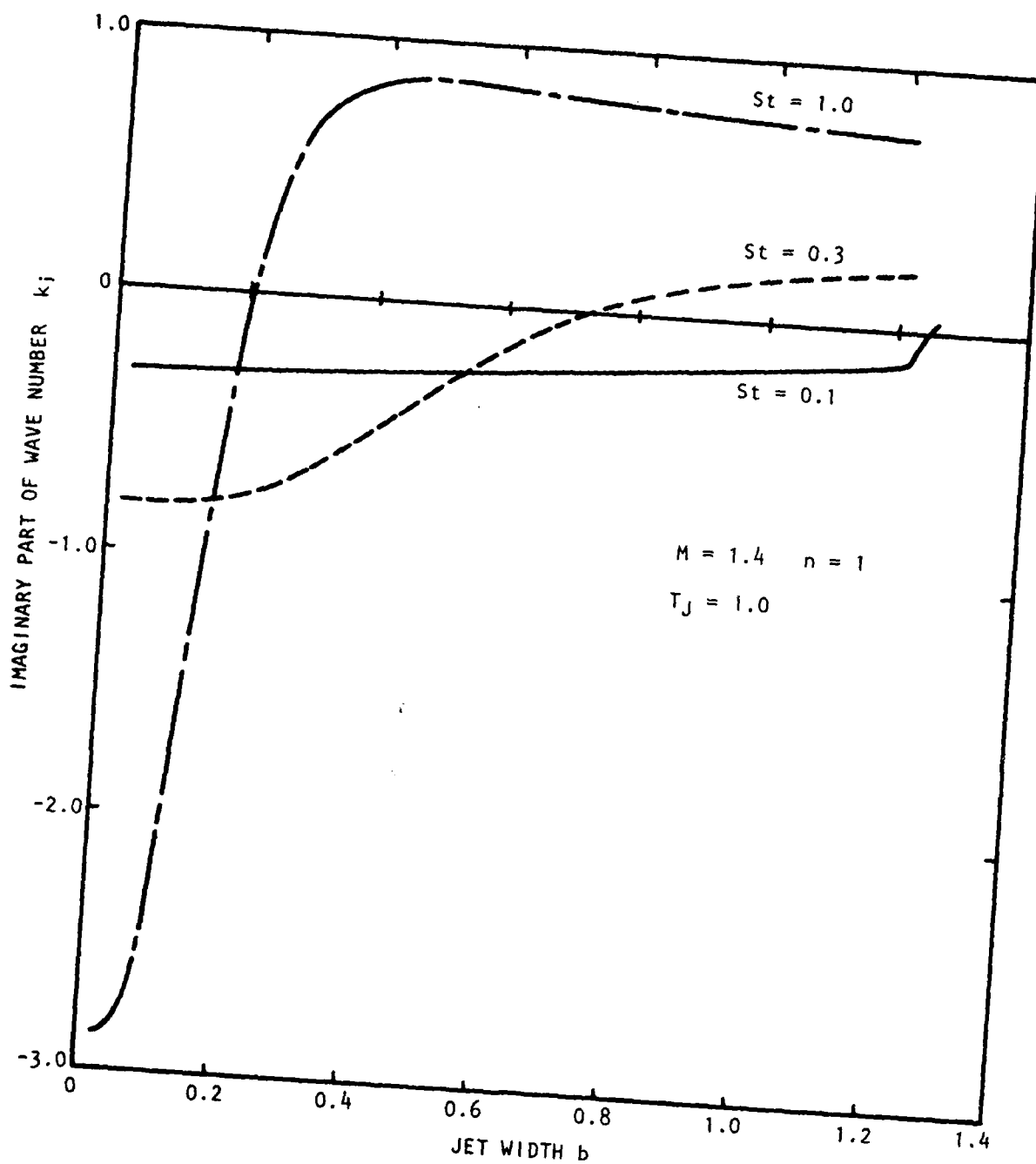


Figure 4.11 Variation of the Imaginary Part of the Wavenumber with Jet Width:  $n = 1$

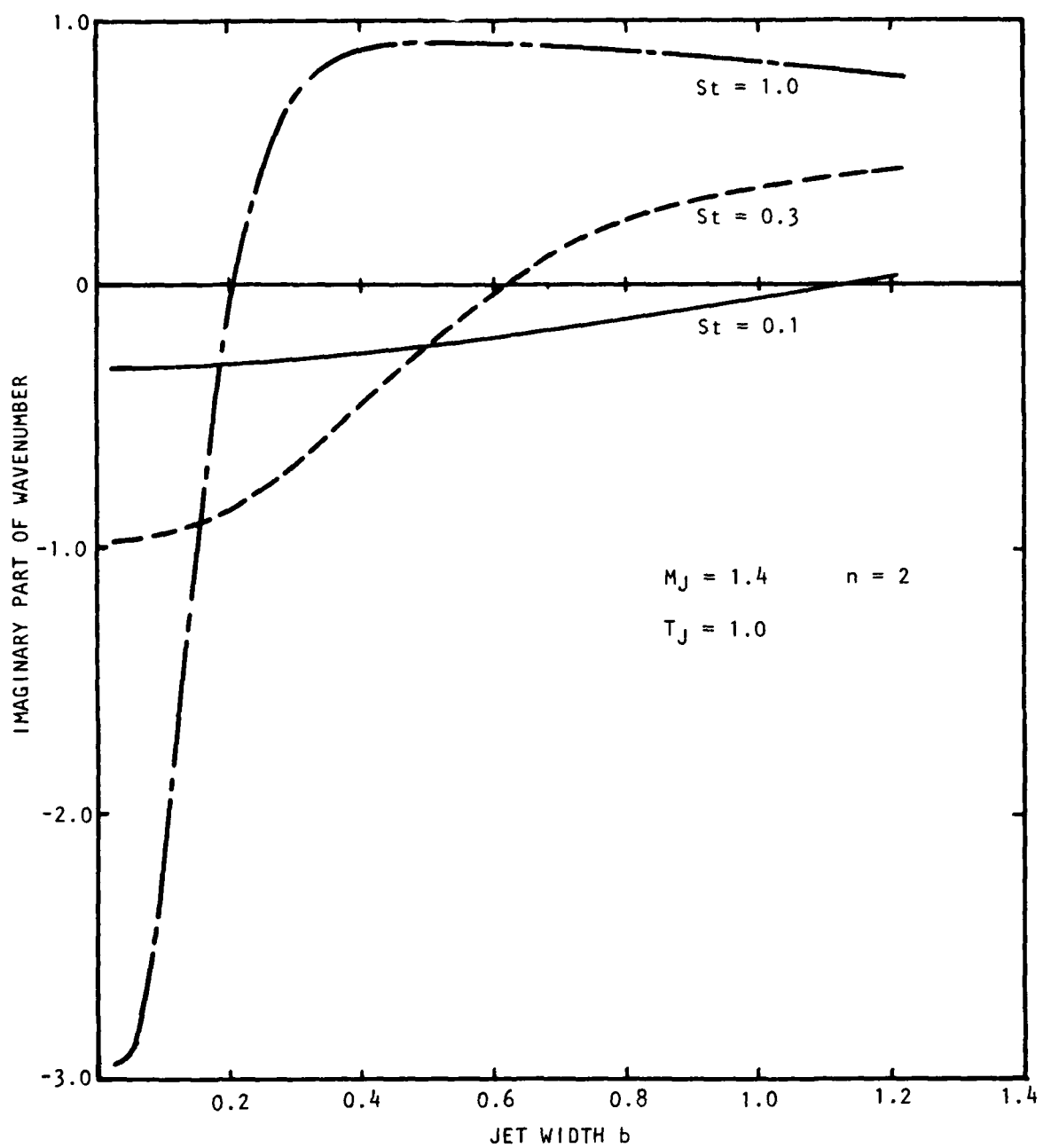


Figure 4.12 Variation of the Imaginary Part of the Wavenumber with Jet Width:  $n = 2$

$$\begin{aligned}\bar{\epsilon}^* &= .006 \ b^* \bar{u}_j^* & x \leq x_c, \\ \bar{\epsilon}^* &= .019 (1 - .82/b) b^*/\bar{u}_c^* & x > x_c,\end{aligned}\quad (4-98)$$

where  $x_c$  is the potential core length. The turbulent Reynolds numbers were thus given by

$$\begin{aligned}\bar{R}_T &= 167 & x \leq x_c \\ \bar{R}_C &= 52.63/(1 - .82/b) & x > x_c,\end{aligned}\quad (4-99)$$

where  $\bar{R}_T$  and  $\bar{R}_C$  are defined in Equations (4-21a) and (4-36), respectively.

The local radial distributions of the integrands in Equations (4-18) through (4-21) provide the radial variation of the wave energy balance. These integrands are shown in Figure 4.13 for  $n=0$ ,  $St=.3$  at  $b=.2$ . The kinetic energy flux and turbulence production peaked close to the location of the maximum mean shear. The pressure work term was positive over most of the mixing region indicating a transfer of energy from the wave into thermal energy fluctuations. The dissipation term peaked on the inner and outer edges of the mixing layer where the wave fluctuation radial derivatives were greatest.

The variation with jet width of the corresponding integrals,  $k_1$ ,  $k_2$ ,  $k_4$ , and  $k_5$  is shown in Figure 4.14 for  $n=0$ ,  $St=.3$ . For this frequency the inviscid local neutral solution occurred at  $b \approx .6$ . The turbulence production integral,  $k_4$ , changed sign at this point indicating a return of energy from the fluctuation into the mean flow. The pressure work integral,  $k_2$ , oscillated between positive and negative sign indicating an interchange of wave kinetic and thermal energy. The dissipation integral,  $k_5$ , reached a minimum value close to the inviscid neutral point. The wave kinetic energy flux integral,  $k_1$ , varied little with jet width. It should be remembered that the integrals,  $k$ , do not reflect the fluctuation amplitude but are merely relative integral terms based on the local fluctuation shape assumptions normalized using Equations (4-22a) and (4-22b).

The variation of the wave kinetic flux integral,  $b^2|A|^2k_1$ , was obtained from Equations (4-26), (4-16) and (4-17) in the annular mixing region and Equations (4-30), (4-34) and (4-35) in the developed jet flow. The relative variation in amplitude is shown in Figures 4.15, 4.16, and 4.17 for azimuthal modes,  $n=0$ , 1, and 2, respectively. The initial values used in the solution were

$$\begin{aligned}\{b^2|A|^2k_1\}_0 &= 1 \times 10^{-7} \\ b_0 &= .05 \\ z_0 &= 0\end{aligned}\quad (4-100)$$

This initial value corresponds approximately to a thirty percent total turbulence level across the initial mixing layer with constant spectrum level and a bandwidth of 10 KHz. For this initial amplitude there was negligible effect

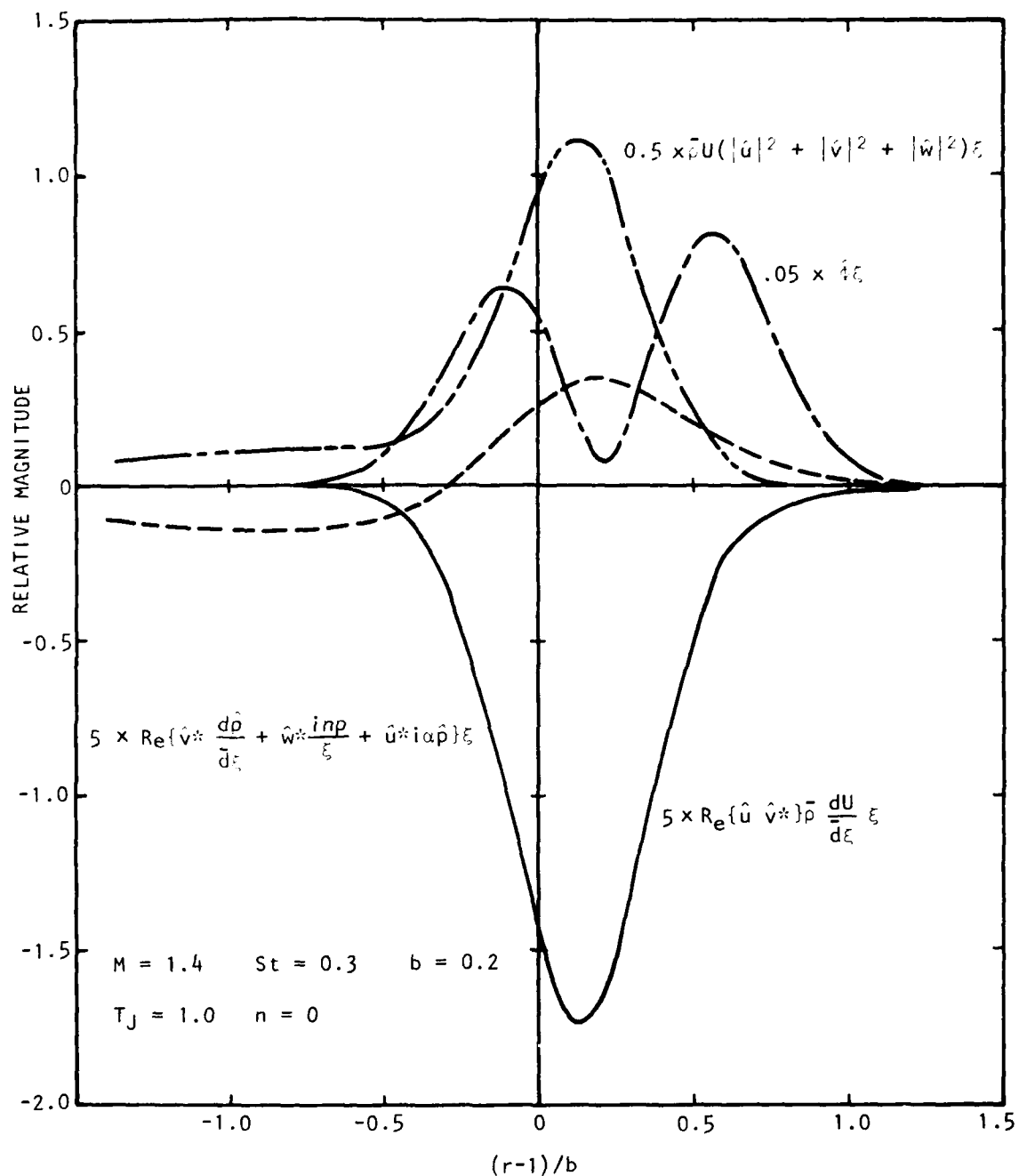


**Figure 4.13** Radial Distribution of Integrands in Wave Energy Balance,  $n = 0$

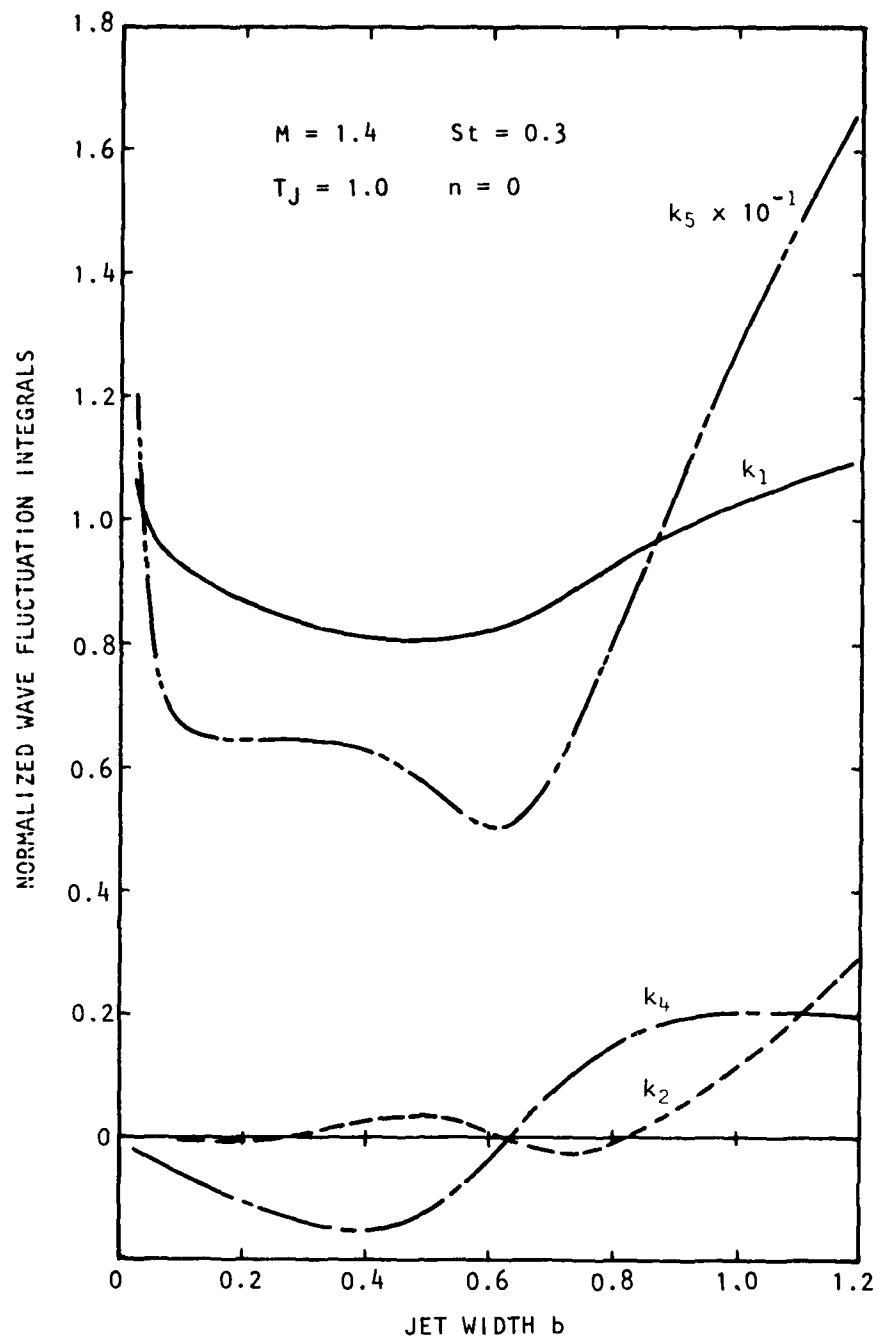


Figure 4.14 Variation of Wave Fluctuation Integrals with Jet Width:  $n = 0$

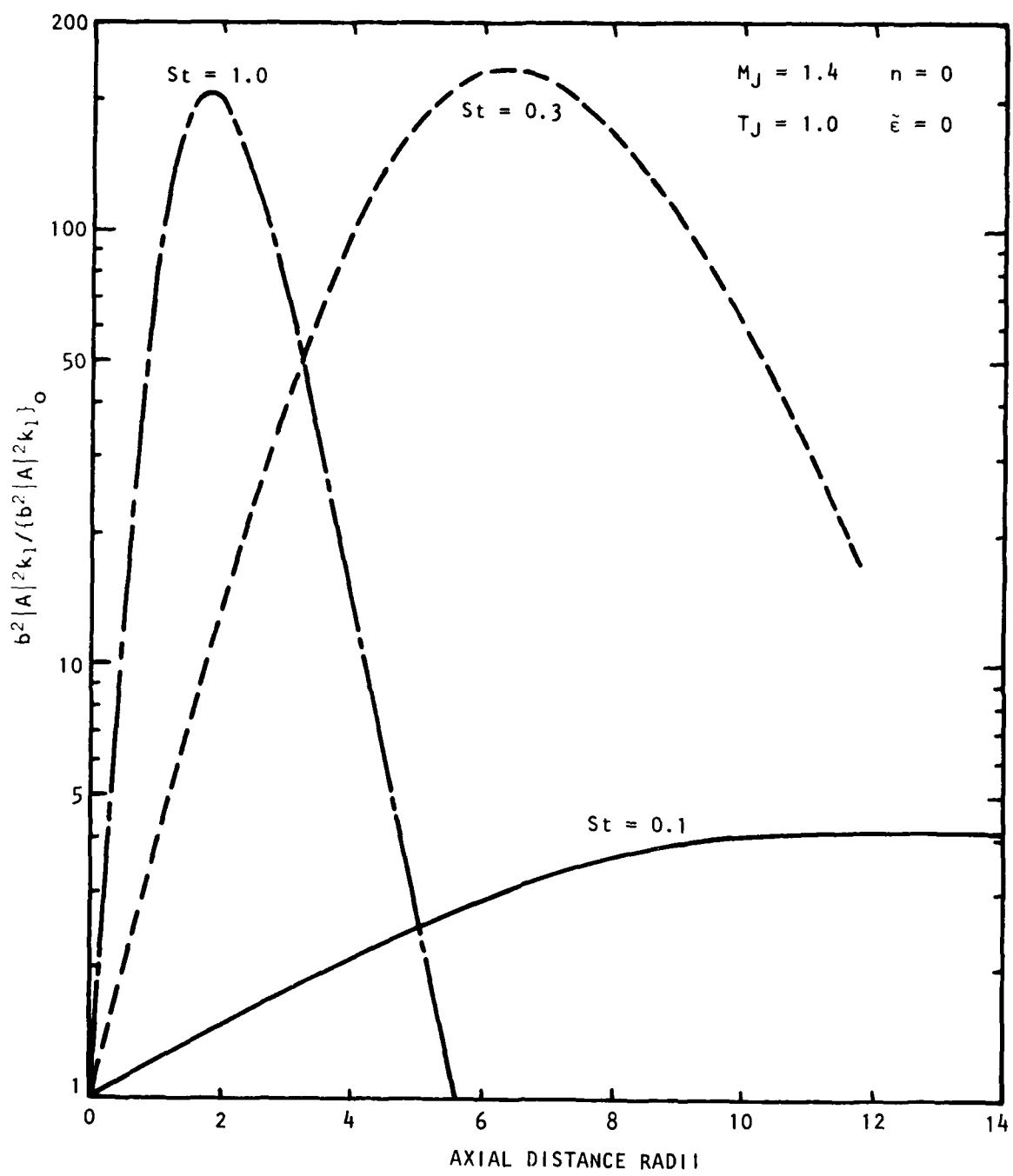


Figure 4.15 Axial Variation of Relative Kinetic Energy Flux  
Integral Amplitude:  $n = 0$

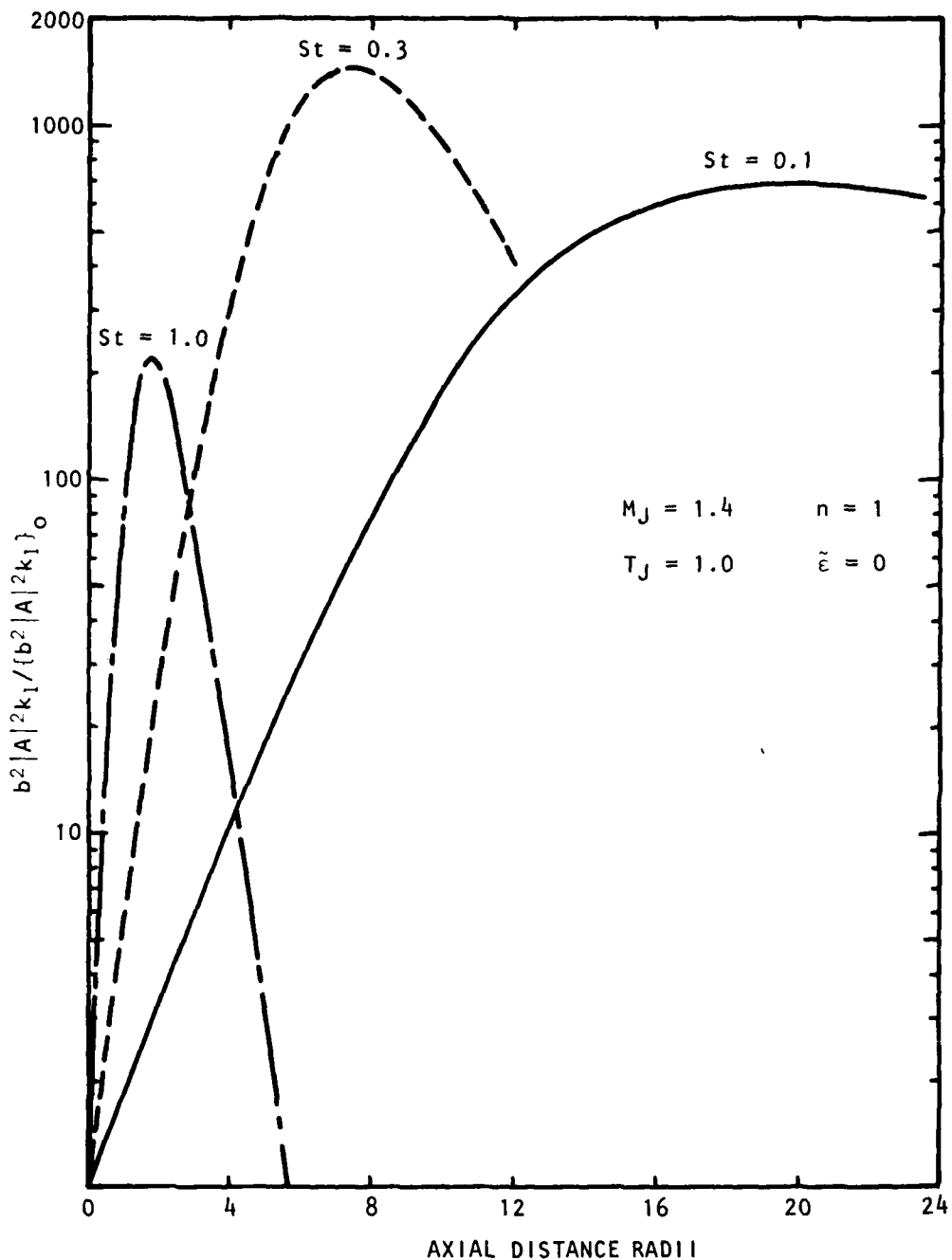


Figure 4.16 Axial Variation of Relative Kinetic Energy Flux  
Integral Amplitude:  $n = 1$

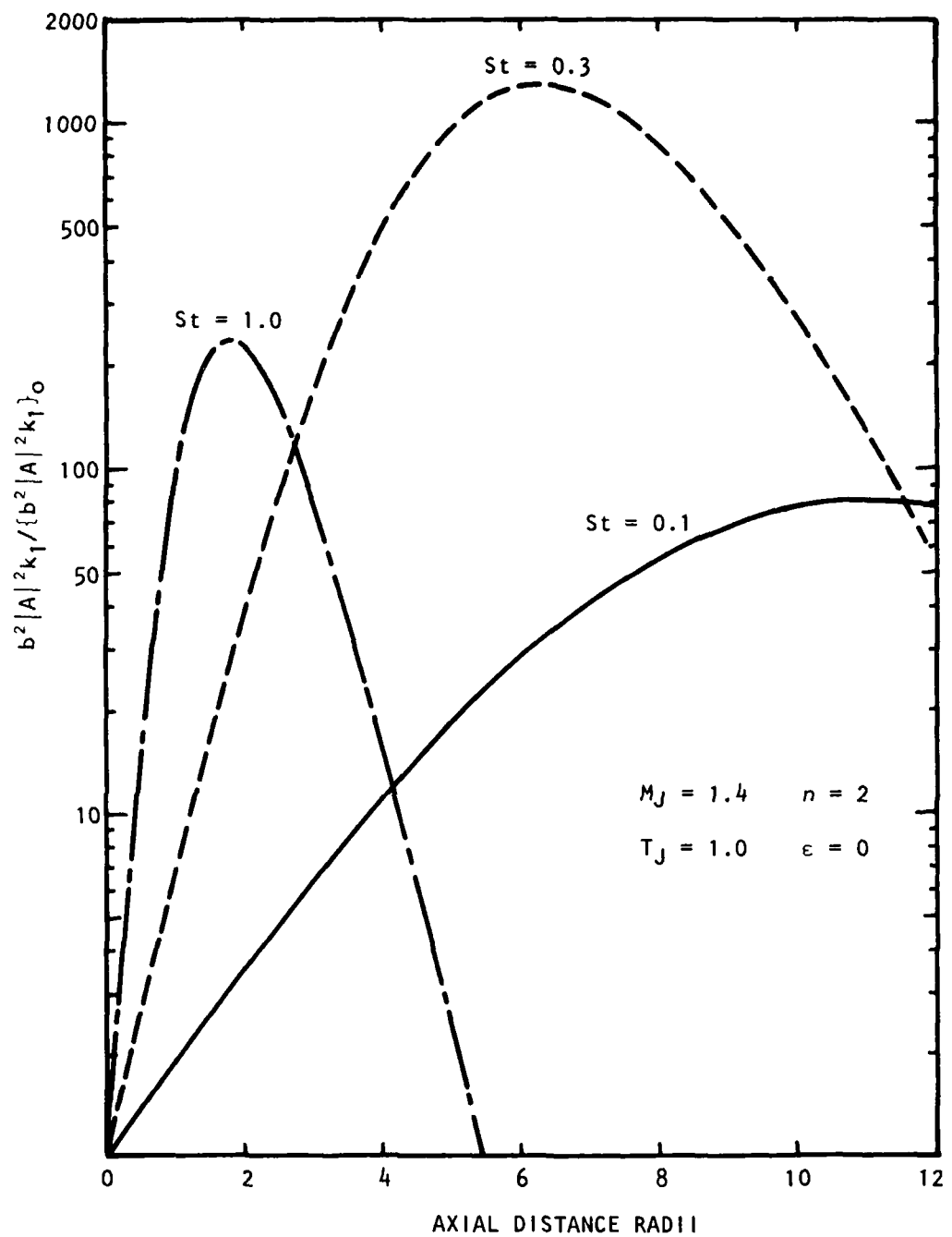


Figure 4.17 Axial Variation of Relative Kinetic Energy Flux Integral Amplitude:  $n = 2$

of the wave-development on the mean flow development. For all modes the maximum amplitude occurred progressively further downstream with decreasing Strouhal number. The  $n=1$  mode achieved the greatest relative amplitude for each Strouhal number and peaked the farthest downstream.

In the above calculations it was assumed that there was no direct interaction, represented by an eddy viscosity, between the random turbulent fluctuations and the wave-like structure, that is  $\tilde{\epsilon} = 0$ . The effect of eddy viscosity  $\tilde{\epsilon}$  on the axial development of the periodic structure is illustrated in Figure 4.18 for  $n=1$  and  $St = .1$ . For  $\tilde{\epsilon} = \bar{\epsilon}$  there was an unrealistic decay of the energy flux integral close to the jet exit and the maximum relative amplitude was 2.2 peaking at 9 radii downstream. For  $\tilde{\epsilon} = .1 \bar{\epsilon}$ , the value used by Tam<sup>52</sup>, the relative amplitude peaked at 13 radii, just downstream of the end of the potential core, with a value of 190. For  $\tilde{\epsilon} = 0$  the maximum relative amplitude was 700 occurring at about 20 radii. Without complete solution of the compressible viscous stability equations, with appropriate boundary conditions, or extensive experimental comparisons, there is no way to validate any of these assumptions. For the purpose of definition, however,  $\tilde{\epsilon}$  was taken to be zero in all the calculations. This restriction will be removed when further analysis and experimental information is available.

Though there is thus no direct interaction between the wave-like fluctuations and the random turbulent fluctuations, there does exist an important direct energy transfer from the mean flow to the wave-like structure. For any given jet thickness the energy transfer is fixed by the mean flow shape which governs the local growth or decay of the wave. However, since the amplitude of the wave-like fluctuation depends on an integral over the axial distance, rather than the jet width, as can be seen in Equation (4-23), variation of jet width with axial distance can affect the amplitude of the fluctuation. For example, consider the mean flow energy equation (4-27) in the annular mixing region.  $f(h, b, T_j)$  is always negative. So for  $k_4$  negative, which gives local wave growth, the jet width increases more rapidly. For  $k_4$  positive, which gives local wave decay, the jet width increases more slowly. The influence of this term clearly depends on the amplitude of the wave-like fluctuation. Since all frequency and modes eventually lead to a decaying or neutral condition, this energy transfer can lead to an amplitude self-limitation of the wave-like structure. This effect can be seen by altering the initial amplitudes of the wave. Figure 4.19 shows the relative amplitude of the energy flux integral for different initial amplitudes. The notation,  $E_0 = \{b^2 |A|^2 k_1\}_0$ , has been used for convenience. For small values of  $E_0$ , less than  $10^{-7}$ , there was little interaction between the wave and the mean flow and the relative amplitude reached a maximum of 234 at 6.3 radii. As the initial amplitude was increased, so the peak relative amplitude decreased and the peak occurred closer to the jet exit. For  $E_0 = 10^{-3}$ , corresponding to a strong periodic excitation at the jet exit, the peak relative amplitude was reduced to 23 occurring at 3.5 radii. This saturation process is also shown in Figure 4.20 where the maximum amplitude is shown as a function of initial amplitude. This figure is comparable to that of Crow and Champagne<sup>40</sup>, figure 10, through quantitative comparison is not possible due to the different jet flow conditions. (Increasing the Mach number stabilizes the flow.) This saturation effect is also observed in the mean flow development. The variation of jet half-velocity width with axial distance, in the annular mixing region, is shown in Figure 4.21. The jet width increased more rapidly as the initial

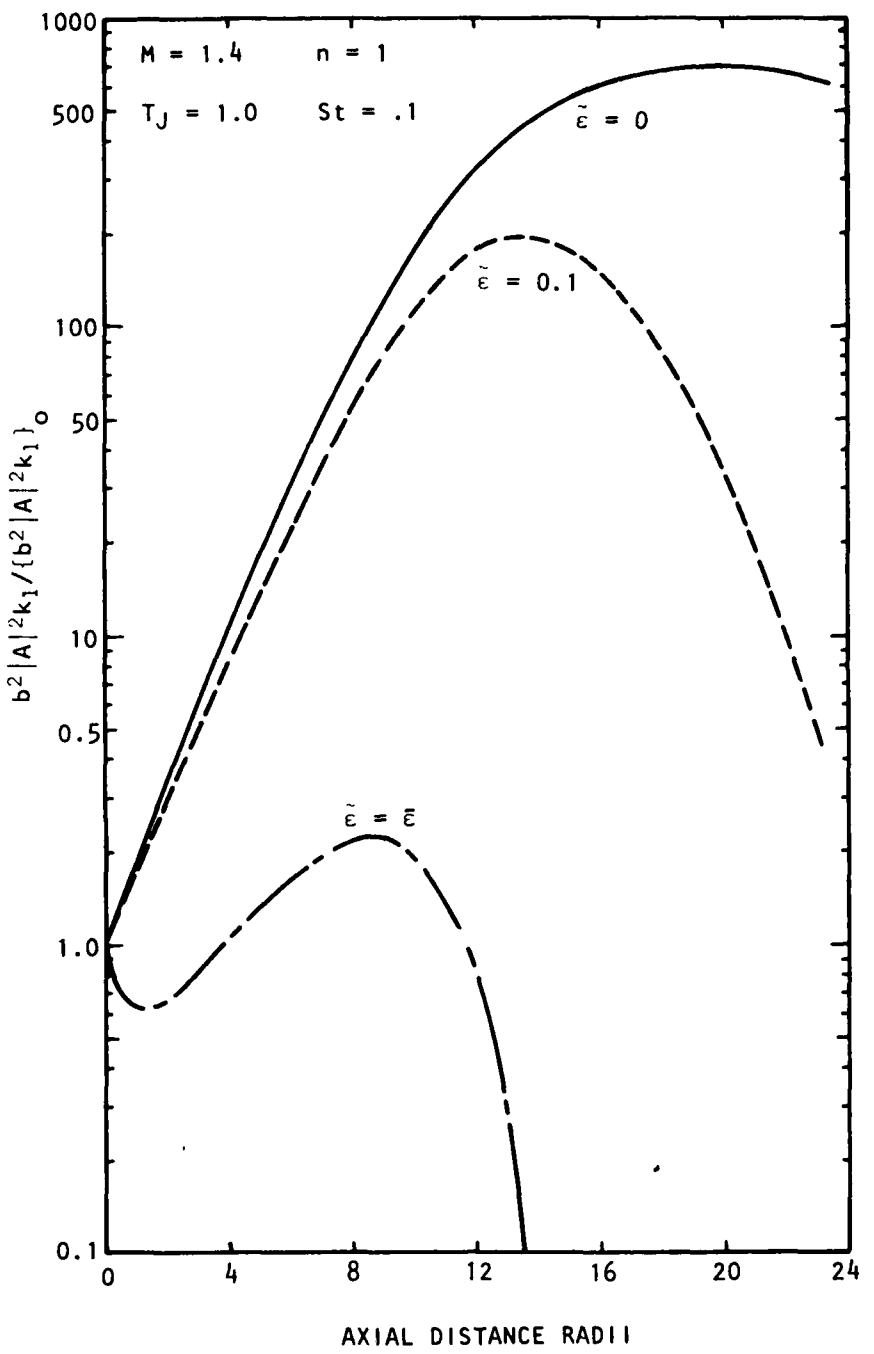


Figure 4.18 Effect of  $\epsilon$  on Growth of Wave-like Component:  $n = 1$

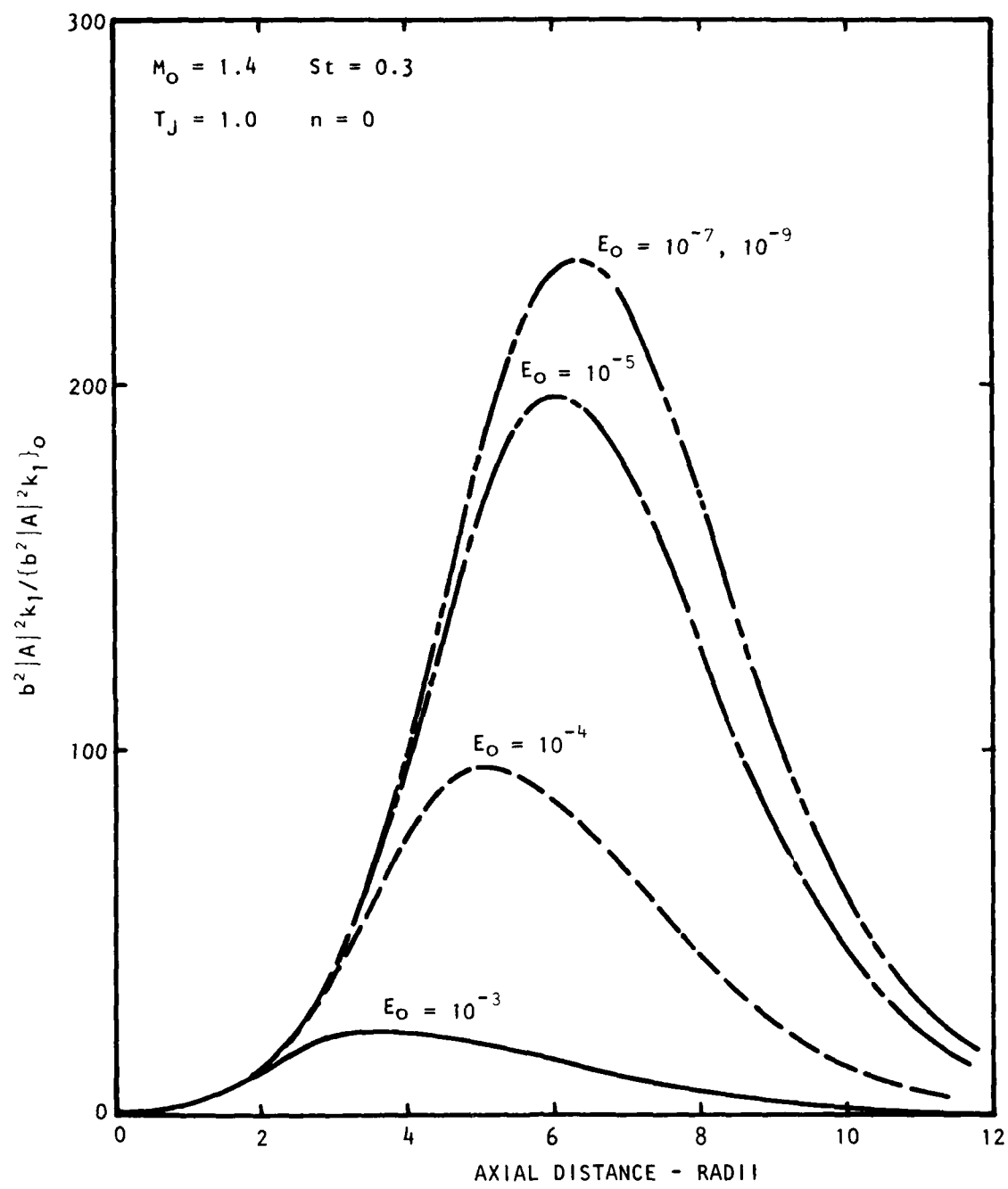


Figure 4.19 Axial Variation of Relative Wave Kinetic Energy Flux Integral Amplitude for Different Initial Amplitudes

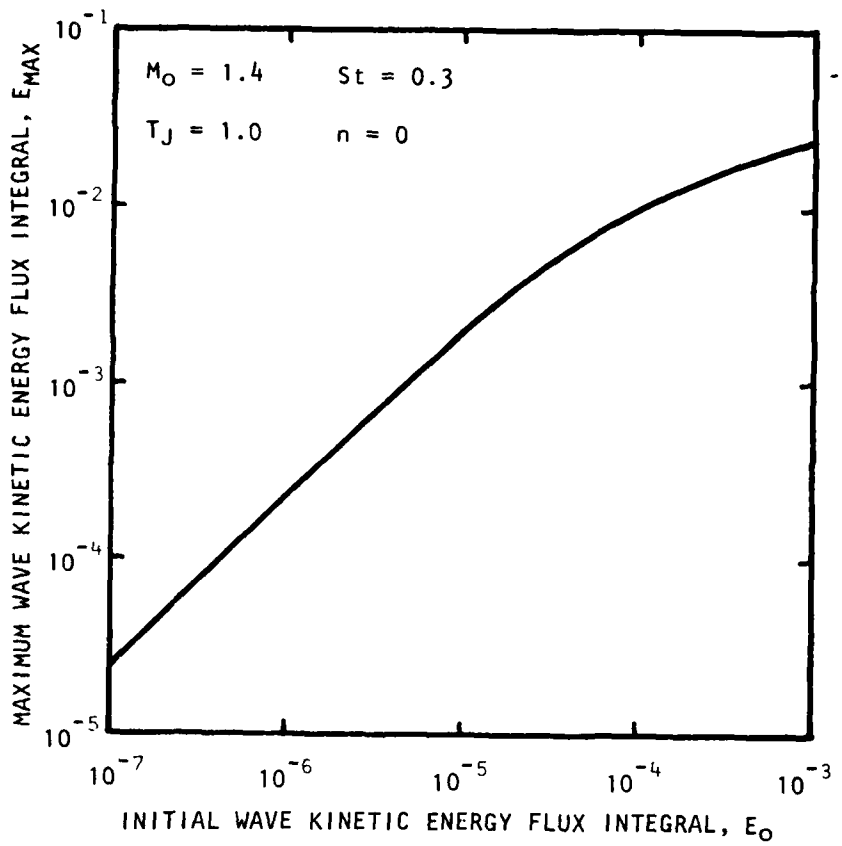


Figure 4.20 Variation of Maximum Wave Energy Integral Amplitude with Initial Amplitude

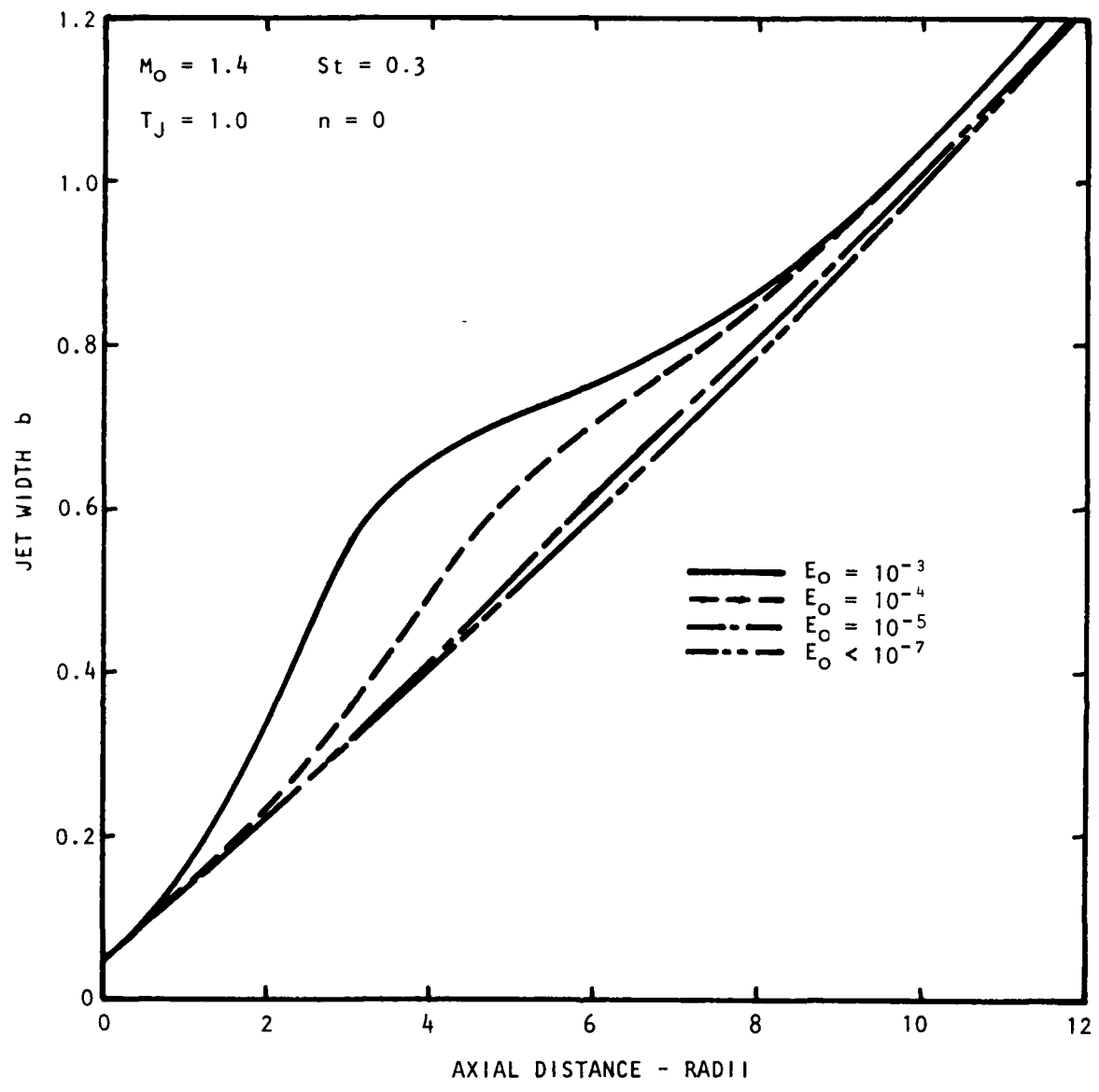


Figure 4.21 Axial Variation of Jet Width for Different Wave Kinetic Energy Flux Integral Initial Amplitudes

wave energy amplitude increased. However, the potential core length, corresponding to a value of  $b$  of about 1.2, changed very little. This was due to the reverse process of energy return from the wave to the mean flow. Although in the present calculations with  $\tilde{\epsilon} = 0$  there is a clear change in jet width variation as the wave grows and then decays, reflected in the sign change of  $k_4$ , this relation would not hold if some kinetic energy were dissipated by the action of the small-scale turbulence. Under a condition where  $\tilde{\epsilon}$  were not equal to zero, the wave could be decaying in amplitude yet still extracting energy from the mean flow, that is,  $k_4$  still negative.

The small-scale random fluctuations, which have been considered in the present analysis through an eddy viscosity hypothesis, are confined to regions of non-zero mean flow gradients. However, the wave-like components of the flow field extend beyond the edges of the jet flow decaying as Hankel functions of the first kind. Thus, the near-field pressure fluctuations of the jet may be associated with the wave-like components of the flow so long as the distance from the edge of the jet is not sufficiently large to make the local parallel flow eigensolutions invalid. The pressure spectrum level in the ambient medium may be obtained from the local eigensolutions and the axial variation of fluctuation amplitude and can be written,

$$SPL = 10 \log_{10} \left\{ \frac{|\hat{p}|^2}{2} |A|^2 \frac{\bar{\rho}_o^{*2} \bar{u}_j^{*2}}{4} \right\} + 80 \text{ dB}$$

relative to  $2 \times 10^{-5} \text{ N/m}^2$  (4-101)

where  $\bar{\rho}_o^{*2} \bar{u}_j^{*2}$  has units  $\text{N/m}^2$ : ( $1 \text{ psf} = 47.88 \text{ N/m}^2$ ). Figures 4.22, 4.23, and 4.24 show the near-field SPL contours calculated in this manner for  $n=0$ ,  $St = 1$ ;  $n=0$ ,  $St = .3$  and  $n=1$ ,  $St = .1$ , respectively. As the Strouhal number decreased so the lobe pattern moved downstream which coincides with experimentally observed near-field SPL patterns. The lower the Strouhal number, the greater was the axial extent of a particular SPL contour.

Thus, it has been shown that the near-field of the supersonic round jet may be described in terms of the large-scale wave-like components of the jet flow. The far-field radiated noise of these modes will now be examined.

#### 4.3.3 The Normal Velocity on a Cylindrical Contour Surface

In the present formulation, described in Section 4.2.3, the normal velocity is calculated on a cylindrical boundary surrounding the jet flow region. This normal velocity is different from the local parallel flow solution in that it is corrected for the effects of flow divergence. The far-field noise may then be obtained by matching the normal velocity on the cylinder with the far-field acoustic solution. Crow<sup>61</sup>, Liu<sup>48</sup>, and Crighton<sup>62</sup> have indicated that the Lighthill integral can be evaluated (without neglect of retarded time differences) in terms of the wave-like fluctuations. This eliminates the need to match on an arbitrary cylindrical boundary. The use of this technique including proper account of flow/acoustic interactions is to be examined. The results presented do not, however, attempt to define an integral noise source term within the jet flow as such, but rather define a boundary condition for acoustic propagation outside the jet flow.

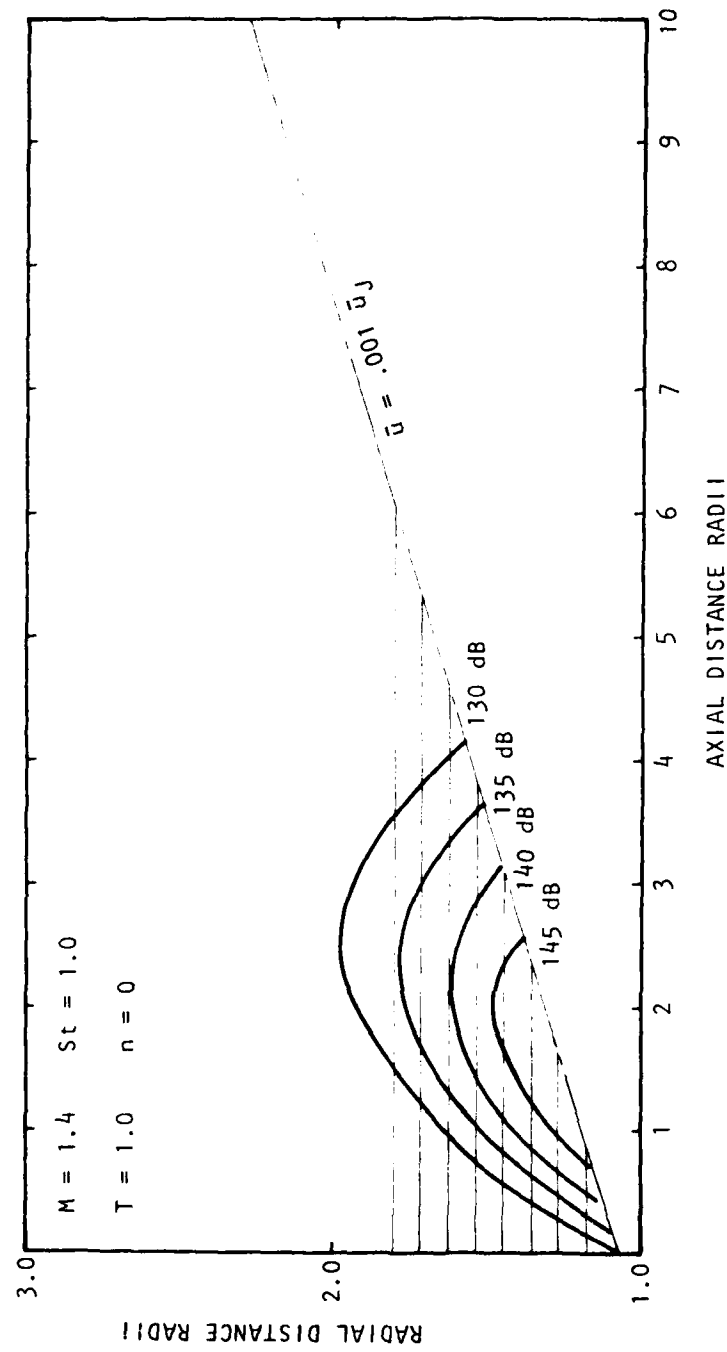


Figure 4.22 Contours of Sound Pressure Level in the Near Field:  $St = 1.0$

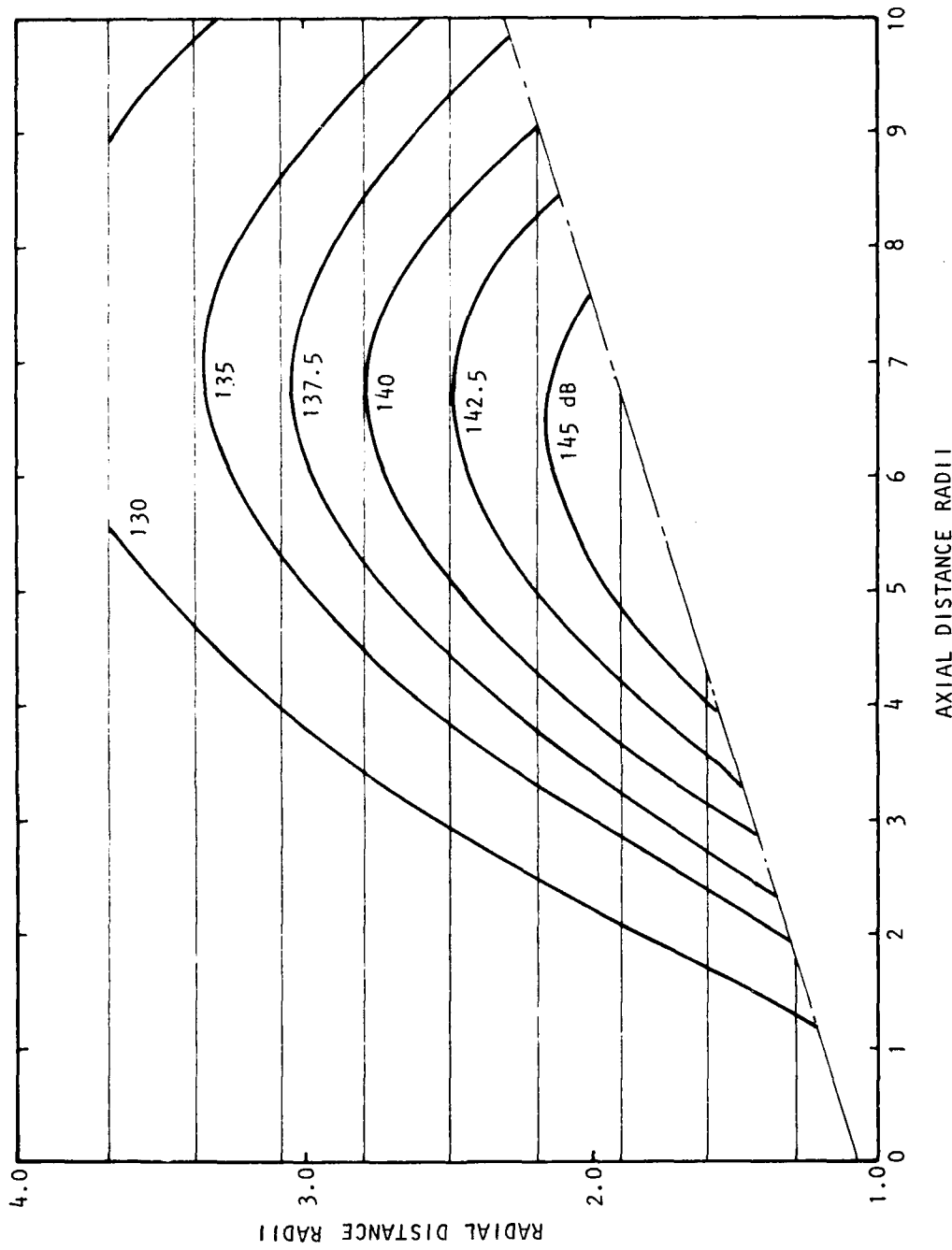


Figure 4.23 Contours of Sound Pressure Level in the Near Field:  $St = .3$

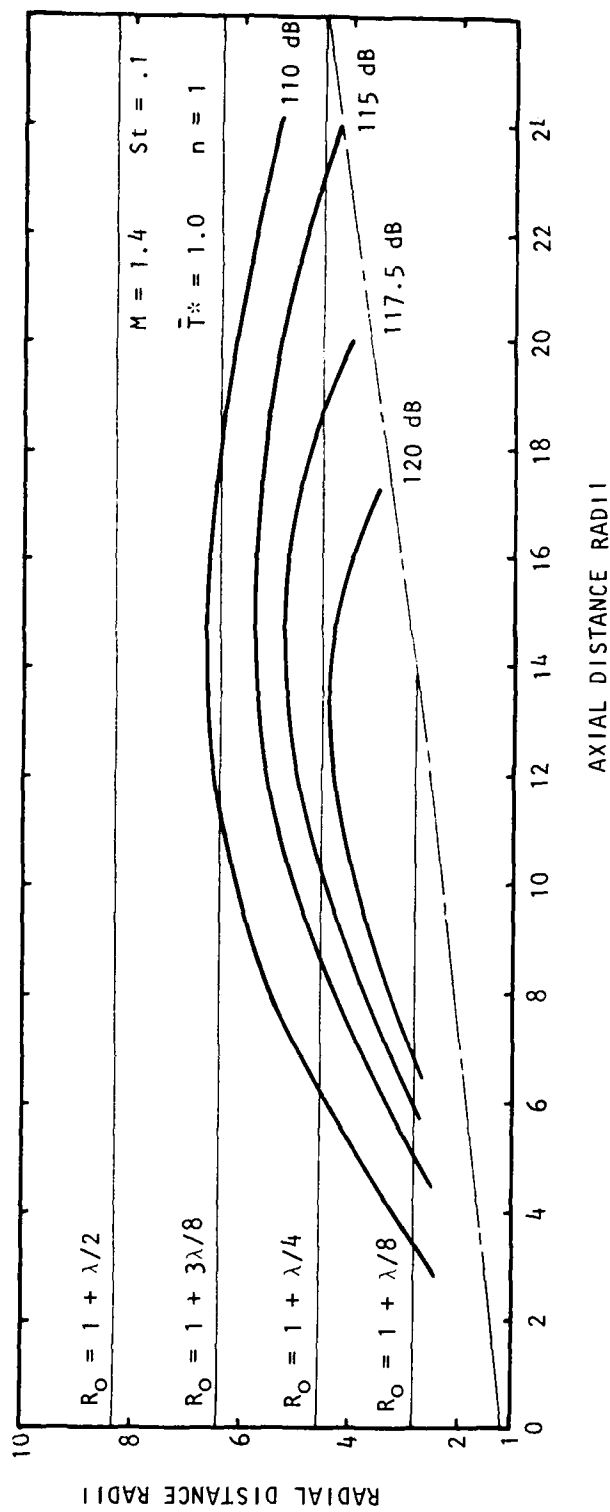


Figure 4.24 Contours of Sound Pressure Level in the Near Field:  $St = .1$

In Section 4.2.3 it was shown that an integral approach could be used to calculate the normal velocity fluctuation on a cylindrical control surface of radius  $R_B$  including corrections for the effects of flow divergence. The integral terms needed to correct for the effects of flow divergence were  $\beta_{10}$  and  $\beta_{11}$  and  $\gamma_{11}$  which were used to represent the radial mean flow velocity, and  $k_{11}$ ,  $k_{12}$ ,  $k_{15}$  and  $k_{17}$  which represented the coupling between the fluctuations and the mean axial velocity gradient. (Note that the definitions of  $k_{11}$  and  $k_{12}$  in the annular mixing region are equivalent to the definitions of  $k_{15}$  and  $k_{17}$  in the developed jet flow.) The variations of  $k_{11}$  and  $k_{12}$  with jet thickness are shown in Figure 4.25 and 4.26, respectively. The most rapid changes of  $k_{11}$  and  $k_{12}$  took place at small values of jet width.

Using these variations of  $k_{11}$  and  $k_{12}$  with jet width, it was possible to calculate the corrected normal velocity fluctuation as the sum of three terms, as given in Equations (4-69) and (4-79).  $\tilde{v}_{pB}$  was the normal velocity fluctuation based on a locally parallel flow assumption.  $\Delta\tilde{v}_c$  was the normal velocity which permitted the fluctuation continuity equation for a diverging mean flow to be satisfied.  $\Delta\tilde{v}_m$  was the normal velocity correction obtained by satisfying the radial and azimuthal momentum equations for a diverging mean flow,  $\Delta\tilde{v}_m$  was zero, except for the helical azimuthal mode,  $n=1$ . The parallel flow normal velocity and the corrections were calculated on cylindrical surfaces at cylindrical surfaces several fractions of the acoustic wavelength from the jet lip radius. This enabled the effect of the choice of control surface radius to be examined. Since the control surface radius was related to the acoustic wavelength of the wave-like fluctuation the control surfaces were further from the jet lip line for lower Strouhal number fluctuations. In this way the outer control surfaces did not cut the diverging jet flow in regions where the fluctuation amplitude was large. The five evenly spaced control surfaces between the lip line and half an acoustic wavelength are shown in Figure 4.24. It can be seen that only the surfaces at  $R_B = 1$  and  $R_B = 1 + \lambda/8$  cut the jet flow at locations where the fluctuation had a significant amplitude.

The relative contributions to the corrected normal velocity for the three azimuthal modes considered are shown in Figures 4.27, 4.28, and 4.29. It can be seen that over most of the jet flow and particularly close to the jet exit the magnitude of the normal velocity correction from the diverging flow continuity equation dominated the total normal velocity. The normal velocity correction from the diverging flow momentum equations,  $|\Delta\tilde{v}_m|$ , which is only non-zero for  $n=1$ , had a relatively small effect.

#### 4.3.4 The Far-Field Noise

With the radial velocity fluctuation calculated on the control surfaces, the wavenumber component spectrum, defined in Equation (4-26), could be calculated numerically using a fast Fourier transform routine. The wavenumber component spectrum for  $n=0$ ,  $St=.3$  on a surface at  $R_B = 1 + \lambda/2$  is shown in Figure 4.30. The wavenumber spectrum peaked at  $k = 1.38$  which was typical of the wavenumber obtained from the local stability calculations. From the equation for the far-field sound pressure, Equation (4-91), it can be seen that only wavenumber components in the range  $-\beta M_0 \leq k a_0 \leq \beta M_0$  contribute to the far-field sound. The wavenumber component at  $k = \beta M_0$  is related to the noise radiated along the downstream axis and the component at  $k = 0$  is related to the radiated noise at 90 degrees to the jet axis. As the jet Mach number increases, so the

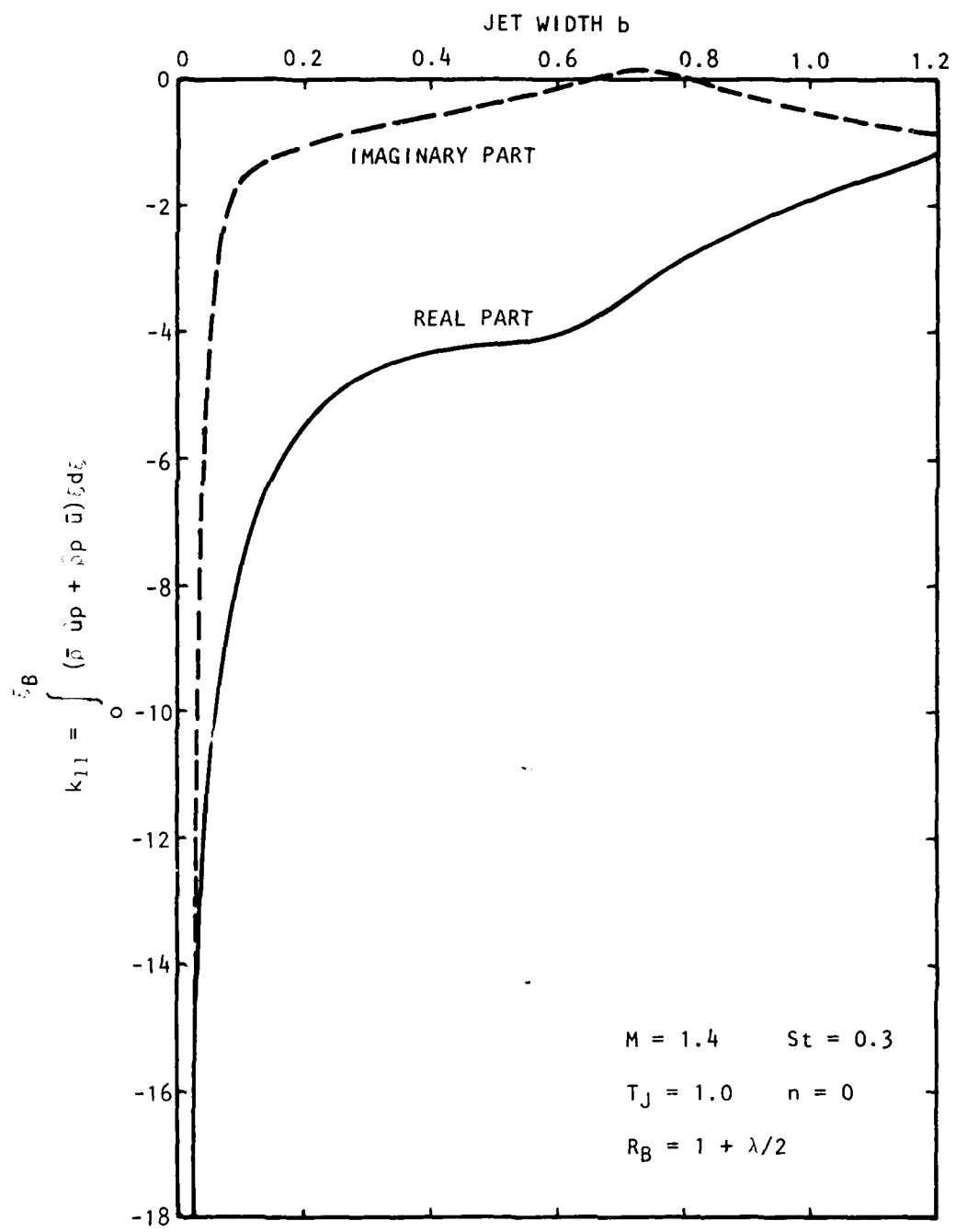


Figure 4.25 Variation of  $k_{11}$  with Jet Width

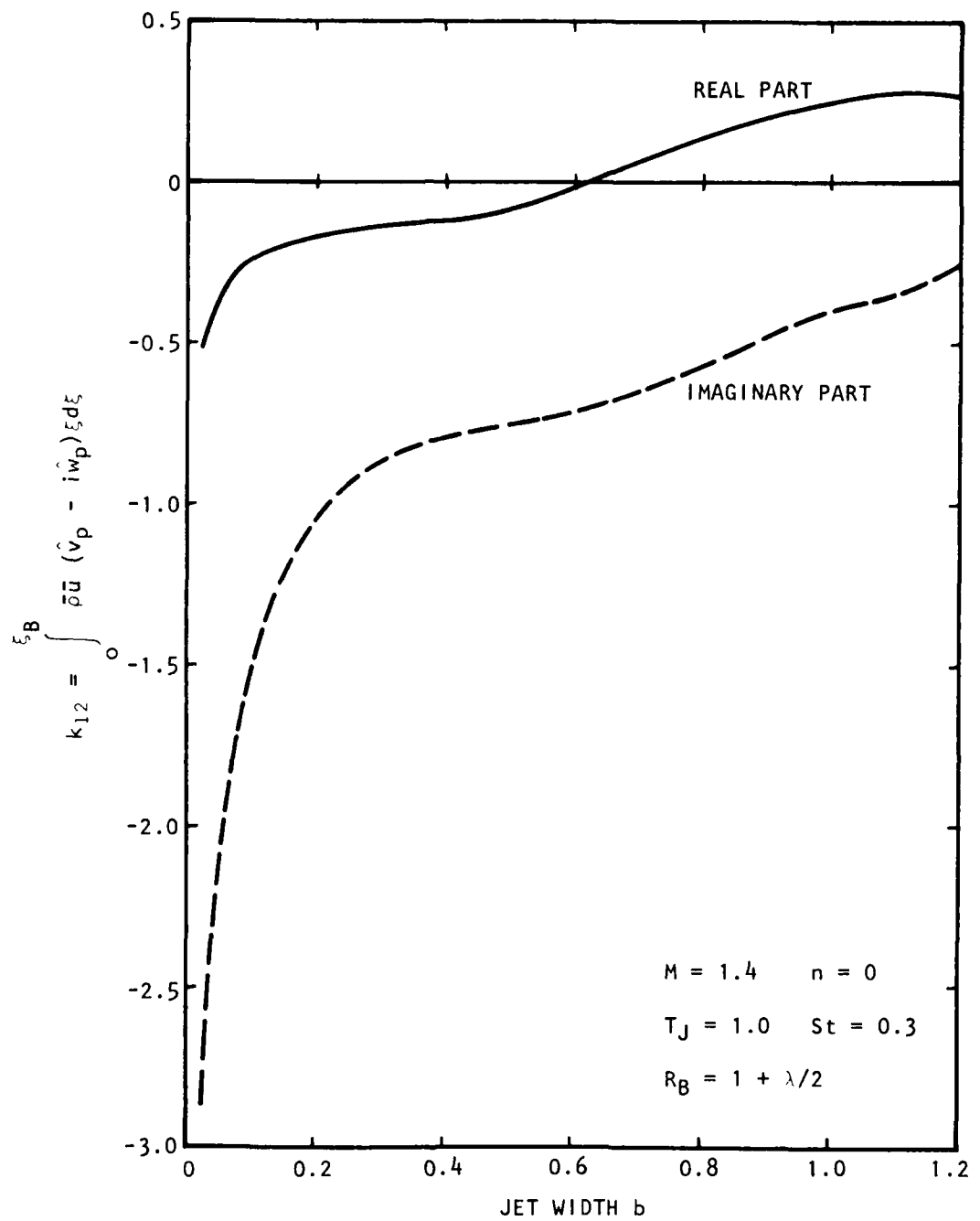


Figure 4.26 Variation of  $k_{12}$  with Jet Width

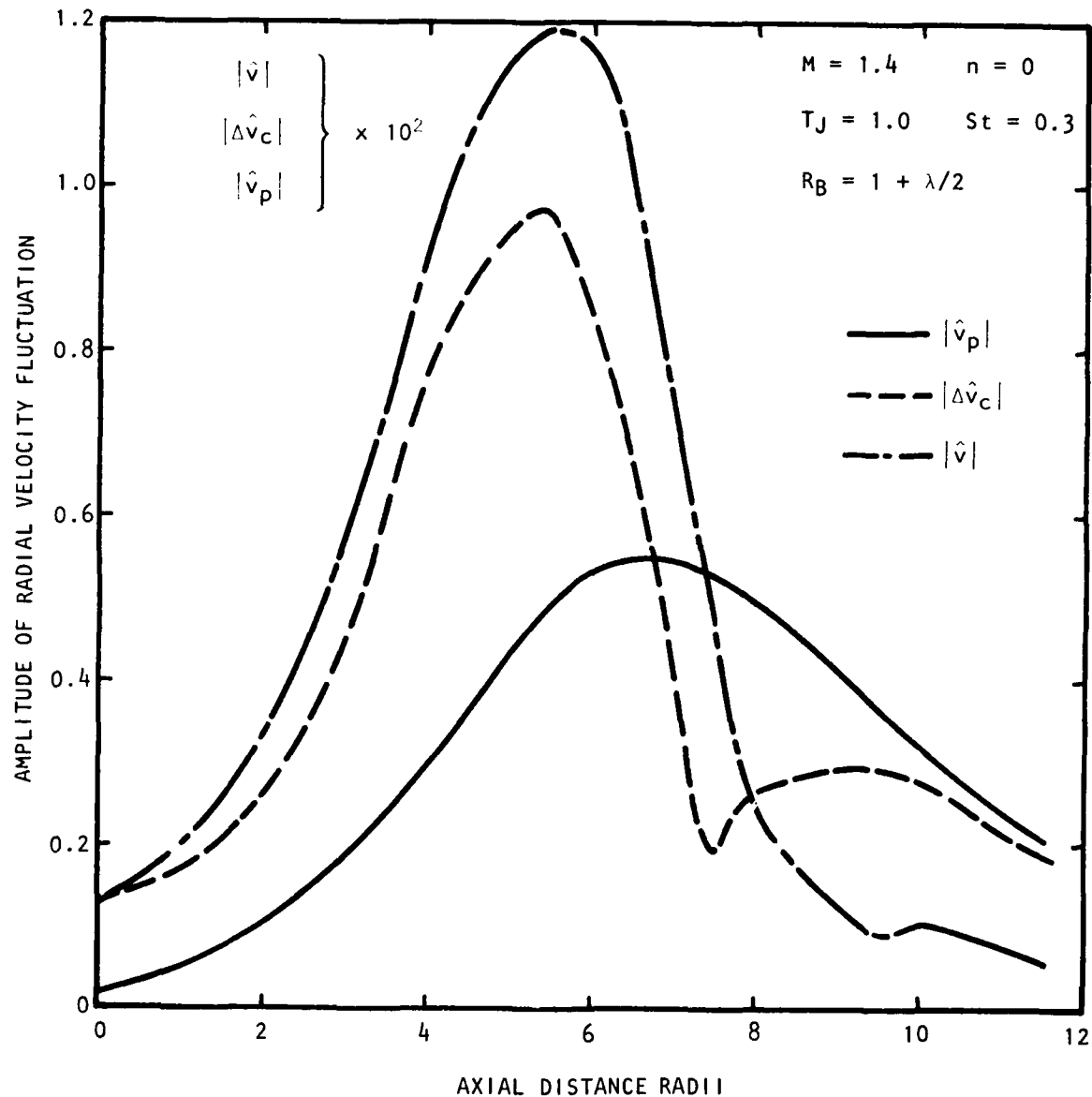


Figure 4.27 Components of Radial Velocity Fluctuation:  $n = 0$

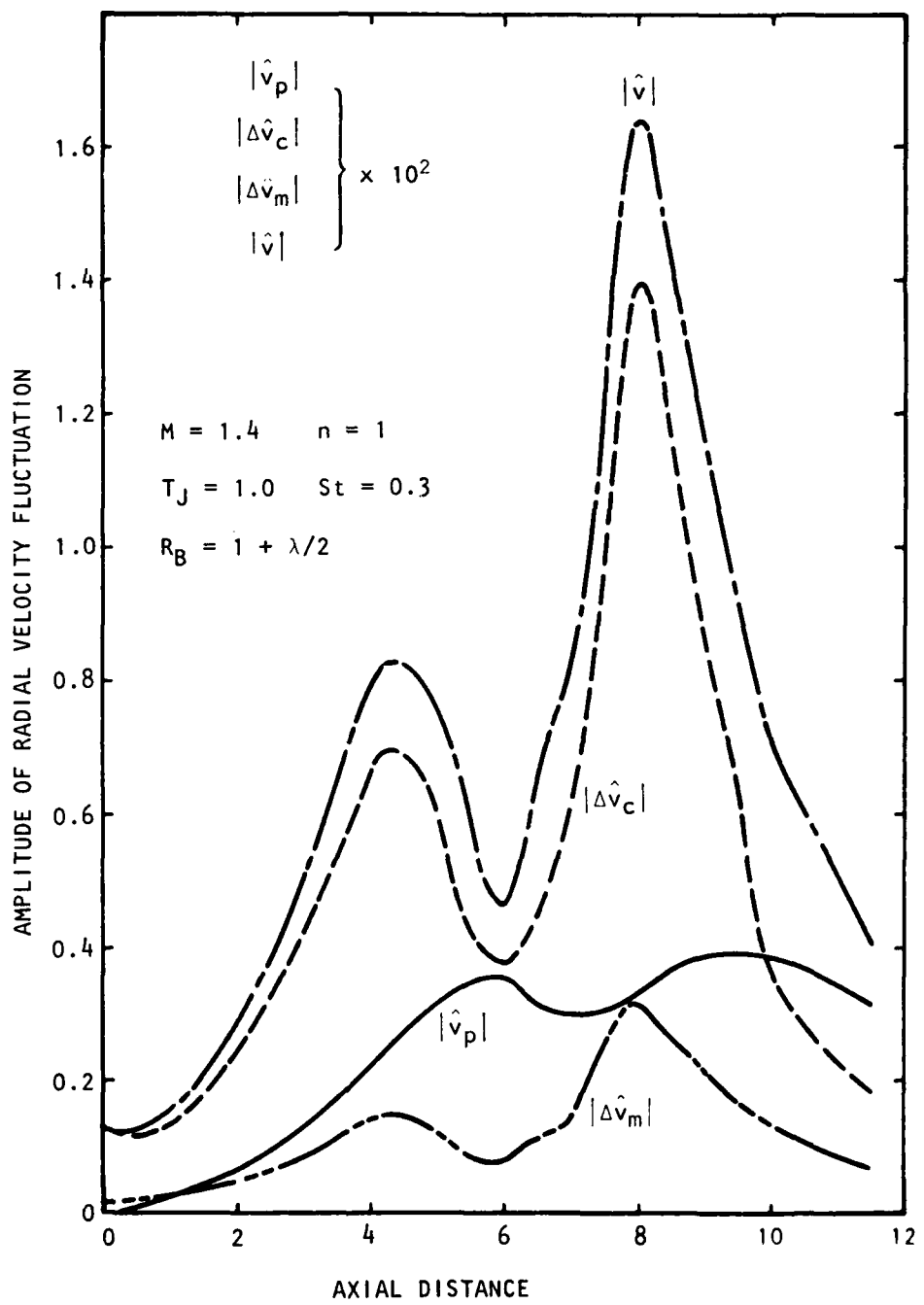


Figure 4.28 Components of Radial Velocity Fluctuation ( $n = 1$ )

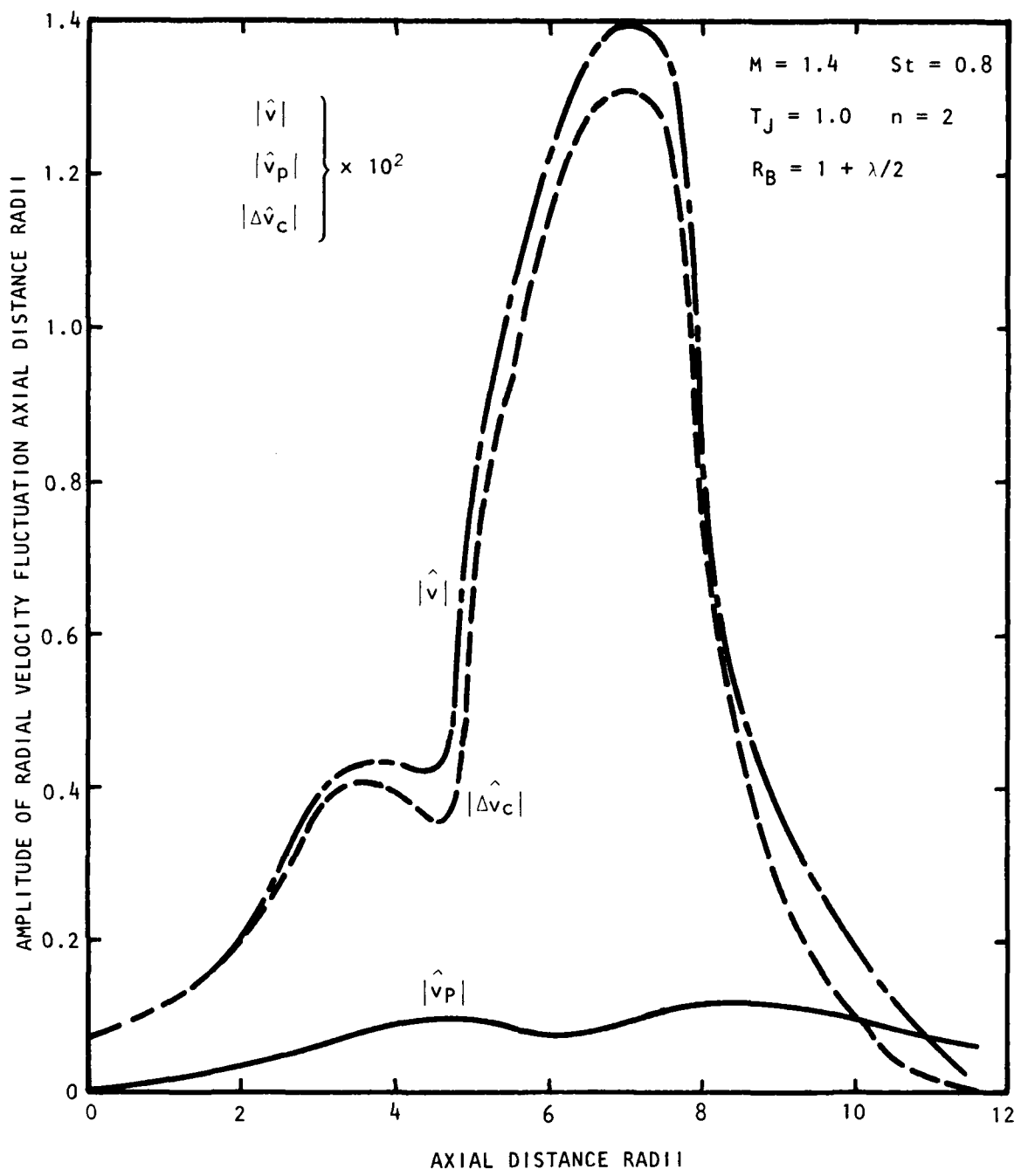


Figure 4.29 Components of Radial Velocity Fluctuation:  $n = 2$

RE, TIVE PHASE OF TRANSFORMED RADIAL VELOCITY,  $\zeta_B$

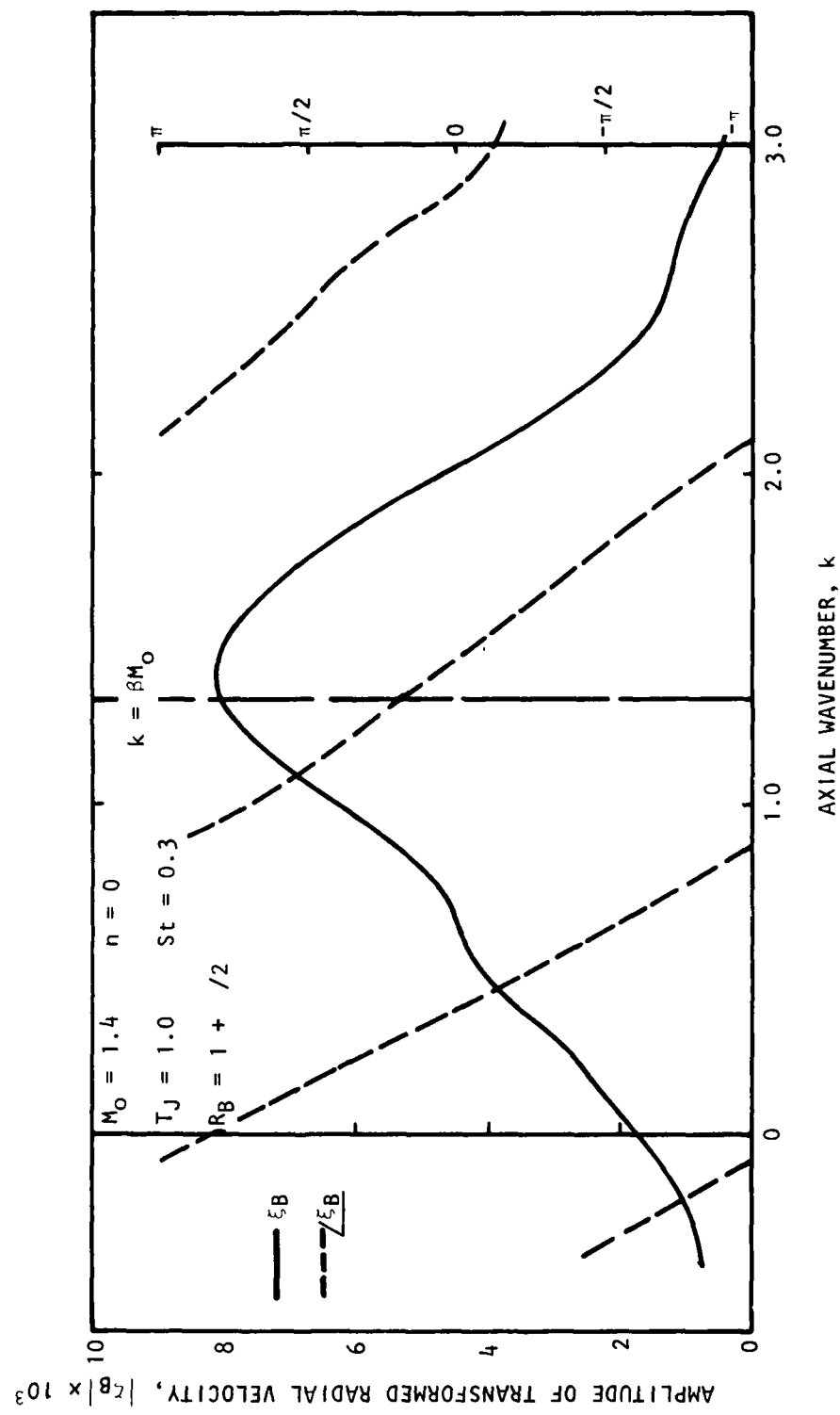


Figure 4.30 Wavenumber Component Spectrum of Radial Velocity Fluctuation

peak in the wavenumber component spectrum will move to lower wavenumbers for all the azimuthal mode numbers. The resulting highly directional noise radiation is due to the linear phase velocity coupling of the near-field fluctuations and the radiated noise giving rise to eddy Mach wave radiation.

Using Equation (4-92) the far-field sound pressure spectrum level was calculated for all the frequencies and azimuthal modes considered. Figure 4.31 shows the effect of the choice of control surface radius on the predicted far-field pressure level and directivity. It can be seen that as the control surface radius was increased so the directivity pattern tended to some limit. This indicates that the corrections for flow divergence do play an important role in the calculation of the radial velocity on the control surface and hence the far-field directivity. The importance of these flow divergence corrections could be seen again if the far-field directivity patterns were calculated using the parallel flow normal velocity,  $\tilde{v}_p$ , alone on the control surface. The resulting far-field directivity is shown in Figure 4.32. Clearly, there was no tendency of the directivity to reach a limiting value and the radius of the control surface became a non-arbitrary parameter in the solution.

The predicted far-field directivity pattern for the first three azimuthal modes and  $St = .1, .3$ , and  $1$ , are shown in Figures 4.33, 4.34, and 4.35, respectively. The initial wave kinetic energy flux integral was the same for all the frequencies. In practice the spectrum level would be expected to decrease with increasing Strouhal number. The calculated directivity patterns showed several trends. Clearly, there was a significant sound pressure level at all angles, except close to the upstream and downstream axis of the jet for the non-axisymmetric modes, for all modes and frequencies. There was no tendency at this Mach number for highly directional radiation which would be the case with eddy-Mach wave radiation at higher Mach numbers. For a fixed azimuthal mode number the peak radiation angle moved closer to the jet axis with increasing frequency. The change of noise level with radiation angle increased with increasing frequency. For a particular frequency increasing the azimuthal mode number moved the angle of peak noise radiation further from the jet axis.

The present calculations only considered the characteristics of the first three azimuthal modes. This restriction was based only on the computational time involved. However, it may be conjectured that the far-field radiation will be dominated by the lower azimuthal mode numbers particularly at low frequencies. Michalke<sup>63</sup> concluded that the most effective sound emitters and the corresponding most important turbulence components were those with  $|n| = 0, 1, 2$ . A decomposition of the near-field pressure into azimuthal components by Michalke and Fuchs<sup>64</sup> showed the dominance of these low azimuthal mode numbers. In order to calculate the total sound pressure level for a fixed Strouhal number the contributions from each of the first three azimuthal modes was added incoherently. It should be noted that the non-zero mode number contributions must be weighted by a factor of two. The directivity patterns calculated in this manner are shown in Figure 4.36 for each Strouhal number. For the Mach number considered,  $M_0 = 1.4$ , the radiated noise peaked within 15 degrees of the jet axis at all Strouhal numbers. As was evident from the behavior of individual azimuthal modes, the rate of change of sound pressure level with angle increased with frequency.

Though, as has been discussed before, no absolute comparison with measured far-field spectrum levels may be made, it is useful to compare the trends

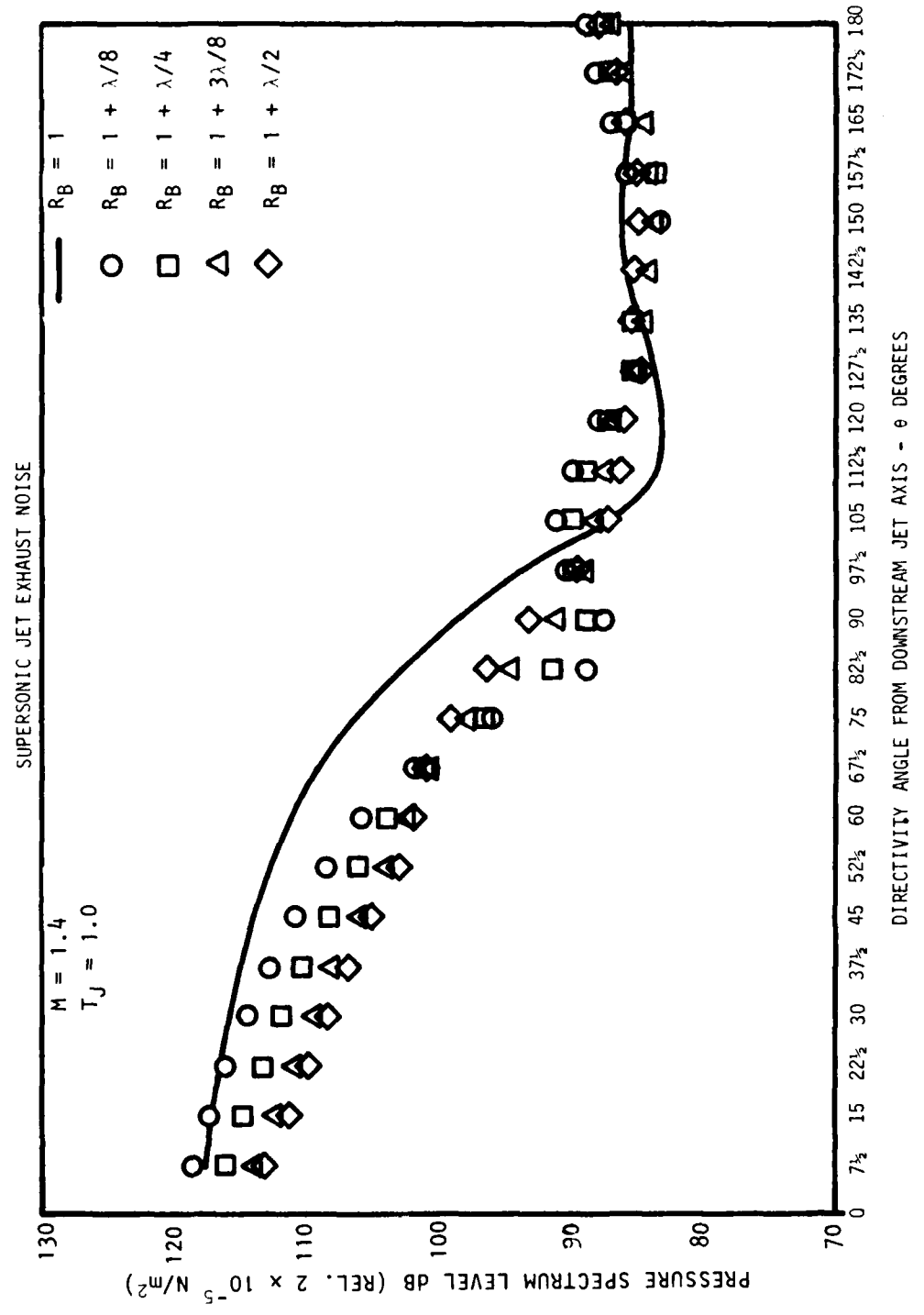


Figure 4.31 Predicted Far-Field Directivity Pattern:  $n = 0$ ,  $St = .3$

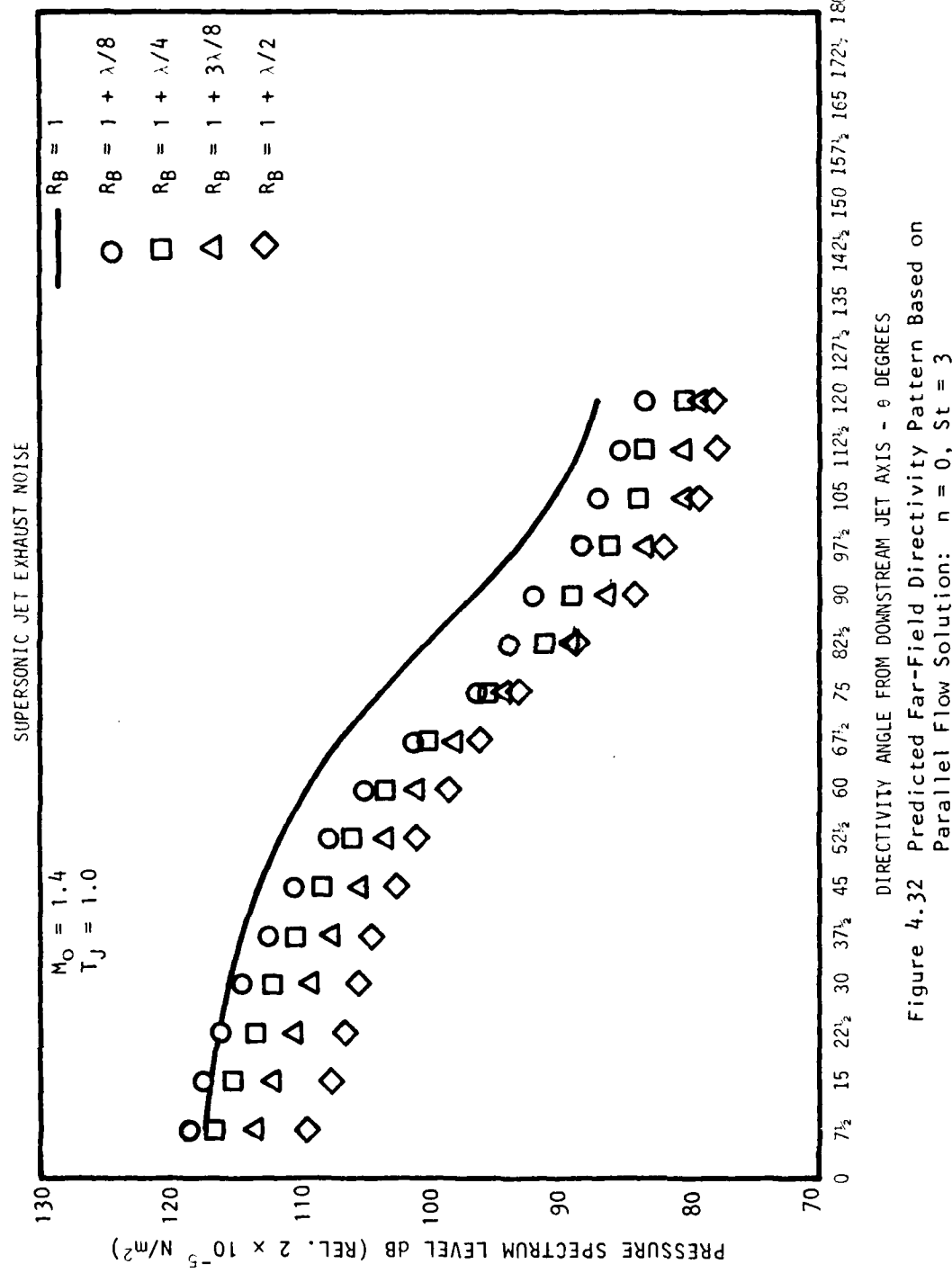


Figure 4.32 Predicted Far-Field Directivity Pattern Based on  
Parallel Flow Solution:  $n = 0$ ,  $St = 3$

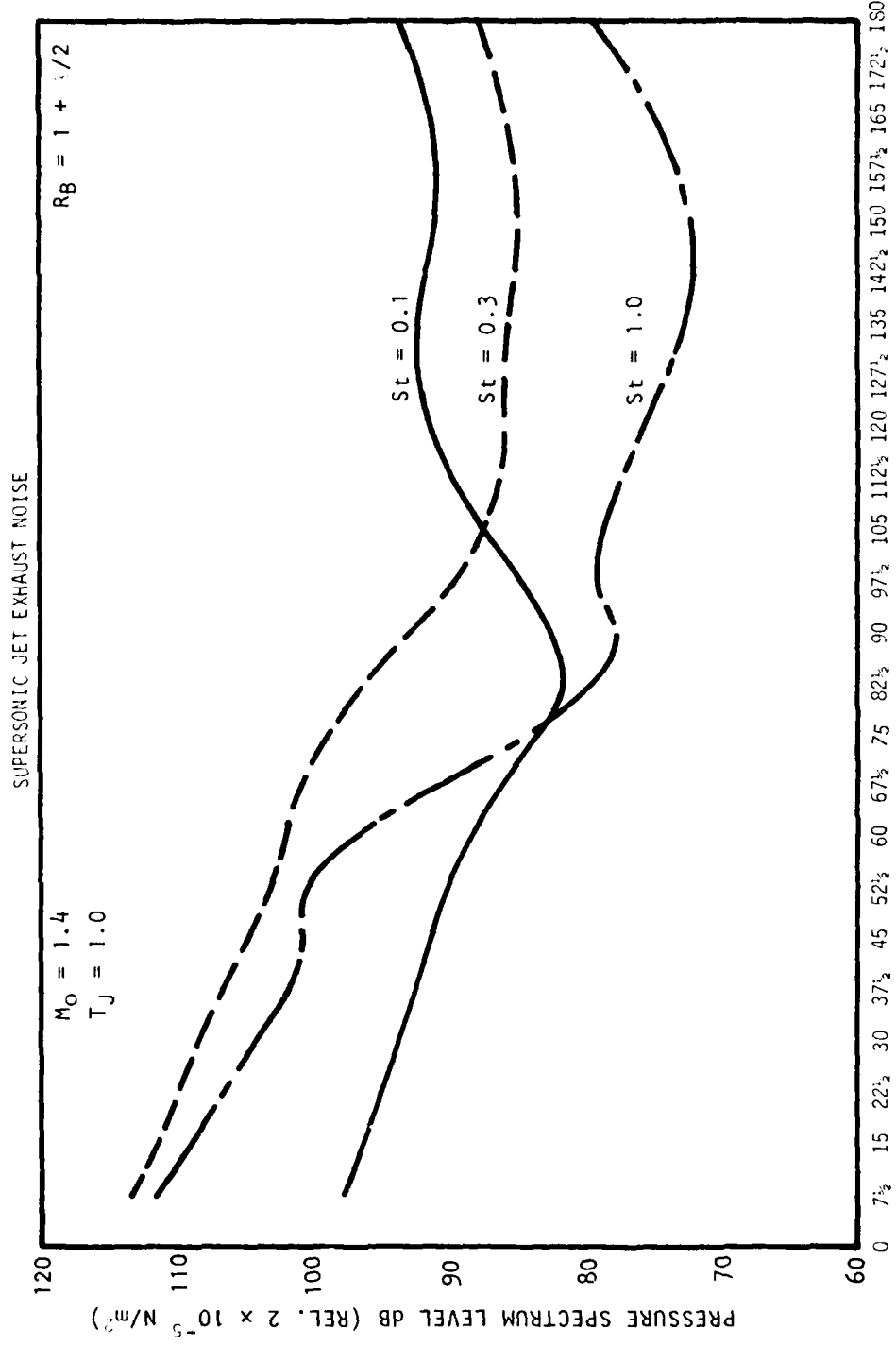


Figure 4.33 Variation of Directivity Pattern with Strouhal number:  $n = 0$

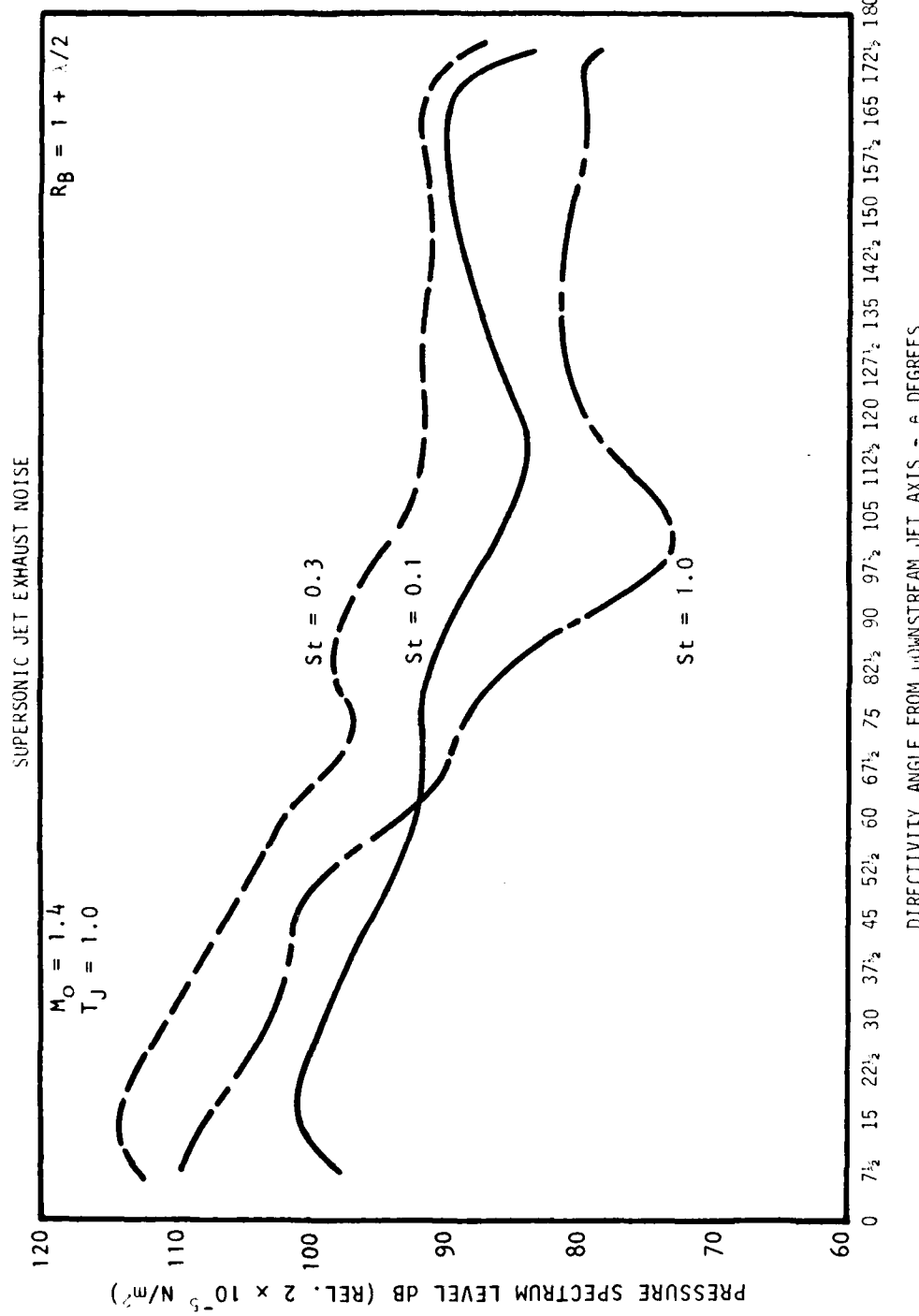


Figure 4.34 Variation of Directivity Pattern with Strouhal Number:  $n = 1$

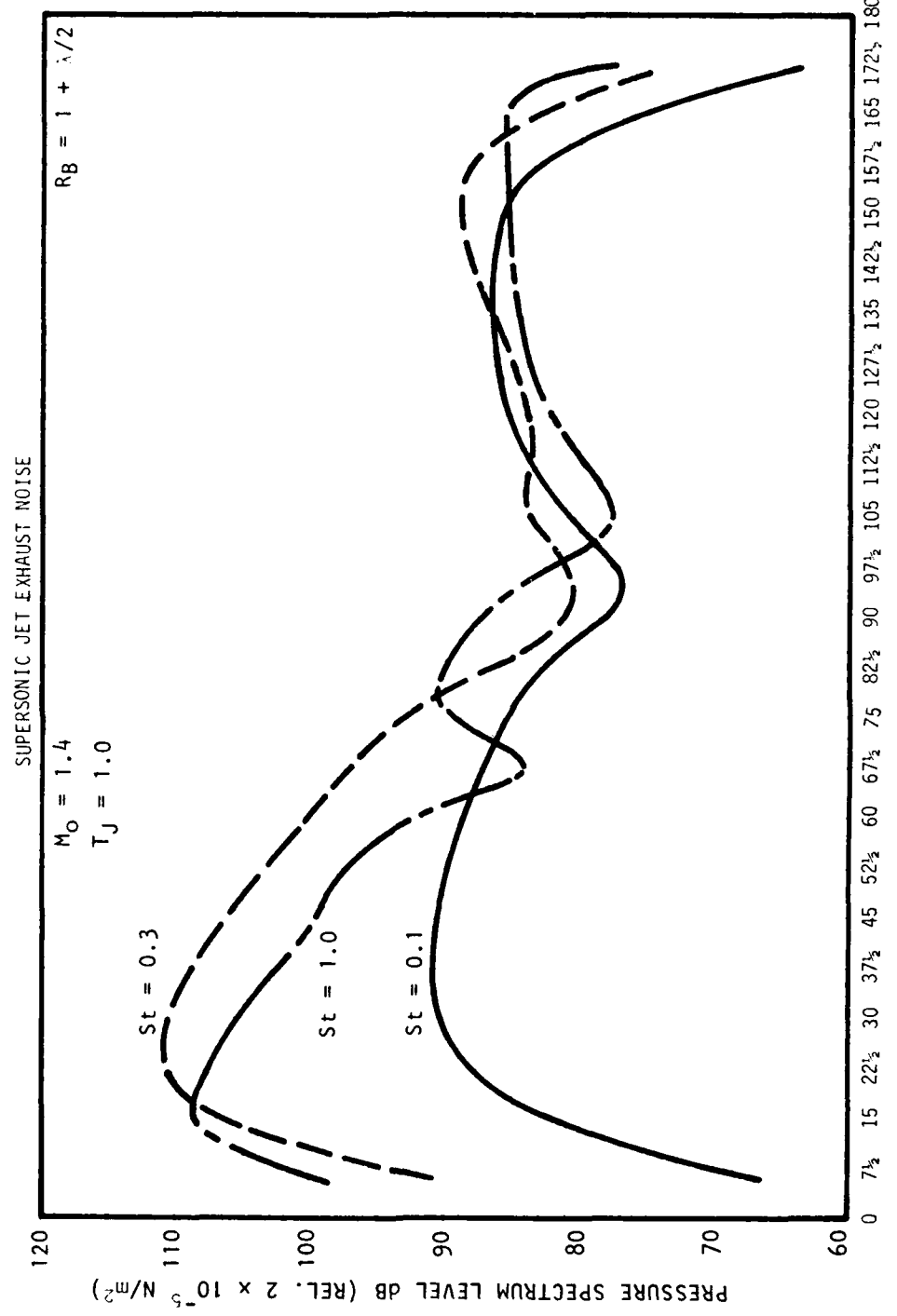


Figure 4.35 Variation of Directivity Pattern with Strouhal Number:  $n = 2$

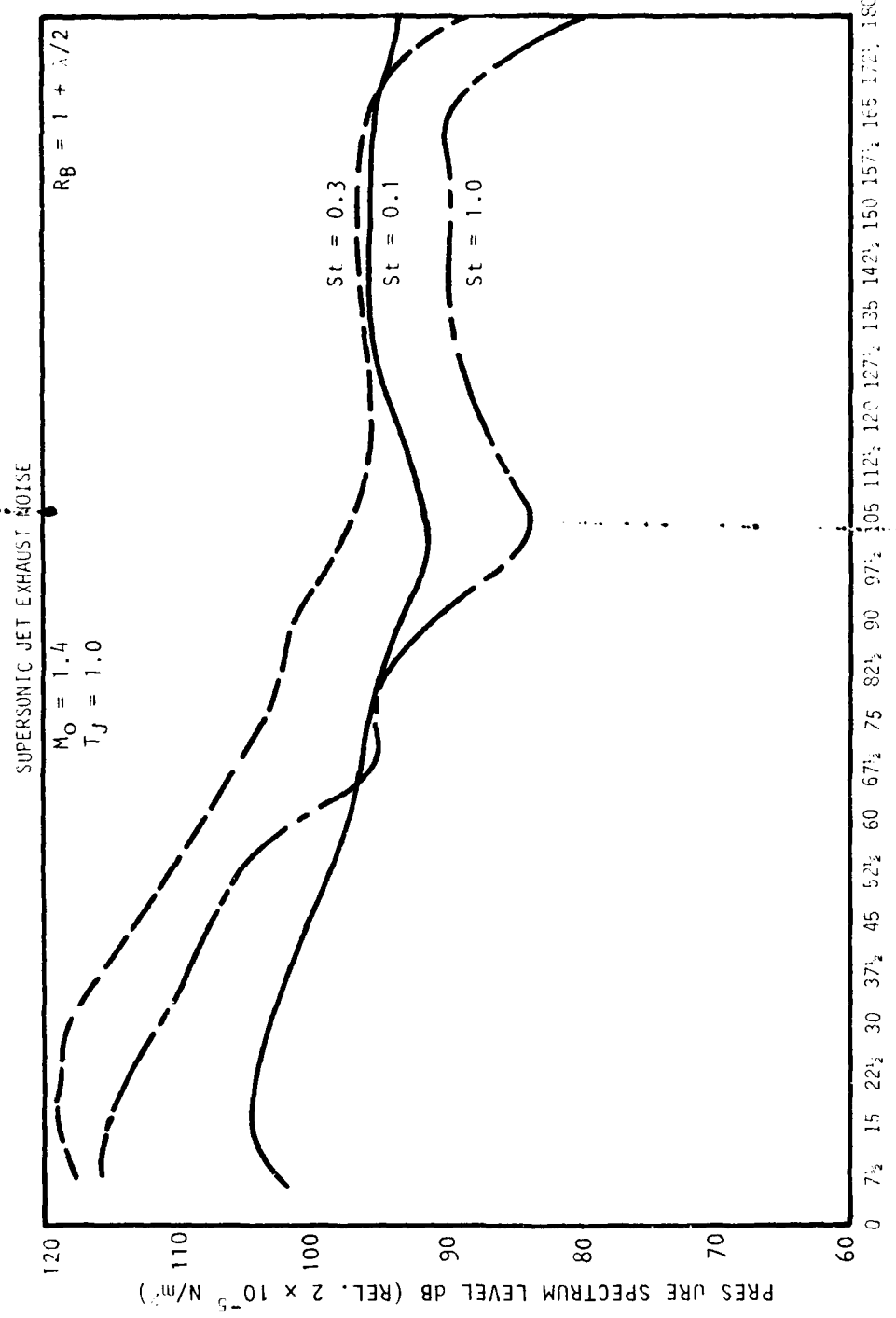


Figure 4.36 Far-Field Directivity Patterns as a Function of Strouhal Number

predicted above with the measurements. It should be emphasized that the experimentally determined directivity patterns contain contributions from all aerodynamic sound sources; both radiation associated with the small-scale turbulence as well as any contribution from the large-scale wave-like structure. The measured directivity patterns are shown in Figure 4.37. The measured third-octave data was converted to power spectrum levels. The variation of pressure level with angle decreased with increase in frequency. Although the higher Strouhal number measurements peaked closer to the jet axis which was the trend predicted by the computations, the peak occurred much further from the jet axis than predicted.

Clearly there are discrepancies between the measured trends and the predictions in the far field. These differences will be discussed in the next section and directions for continuing work will also be examined.

#### 4.4 DISCUSSION AND DIRECTIONS OF FURTHER WORK

In the preceding section it was shown how the near-field structure of the jet flow could be described in terms of large-scale wave-like fluctuations. The mechanism by which these fluctuations were able to radiate sound to the far-field was also demonstrated. However, there clearly existed significant differences between the predicted far-field pressure levels and the measured values. In this section the deficiencies and the problems of the present analytical framework are examined and the direction of further work will be discussed.

Why does the present acoustic model appear not to work? The technique requires the detailed wave number/frequency description of the wave-like structure on a cylindrical control surface surrounding the jet flow. In order for the free space wave equation to be satisfied outside this surface it must, by definition, be in the ambient medium. The distance of the surface from the edge of the jet flow can thus be large. The basic jet flow is diverging and will, at some axial location intersect the cylindrical control surface. Since wave-like components of a particular frequency have a significant amplitude over a relatively limited axial extent, this intersection of the control surface and the mean jet flow may not be important. Close to the jet exit plane, and particularly at low frequencies, the control surface is many shear thicknesses away from the edge of the jet. Under these circumstances, it is necessary to examine the local parallel flow assumptions and flow divergence corrections used in the present analysis. The corrections for flow divergence effects used in the present analysis represent approximations based on the locally parallel flow distributions. The magnitude of the correction was seen to be of the same order of, and in many cases greater than, the first parallel flow approximation, on the control surface appropriate to a given wave frequency. Thus if the far-field pressure is to be calculated using a boundary matching condition, two methods of approach are possible. If the matching control surface remains cylindrical, then the wave-like disturbances within the boundary should be calculated on the basis of a proper diverging flow solution such as that using the method of multiple scales, Bouthier<sup>65</sup>. The second improvement would be to use a control surface which more naturally reflected the diverging flow characteristics of the jet such as a conical boundary. The use of a boundary which closely follows the edge of the flow eliminates the need for retarded potential calculations.

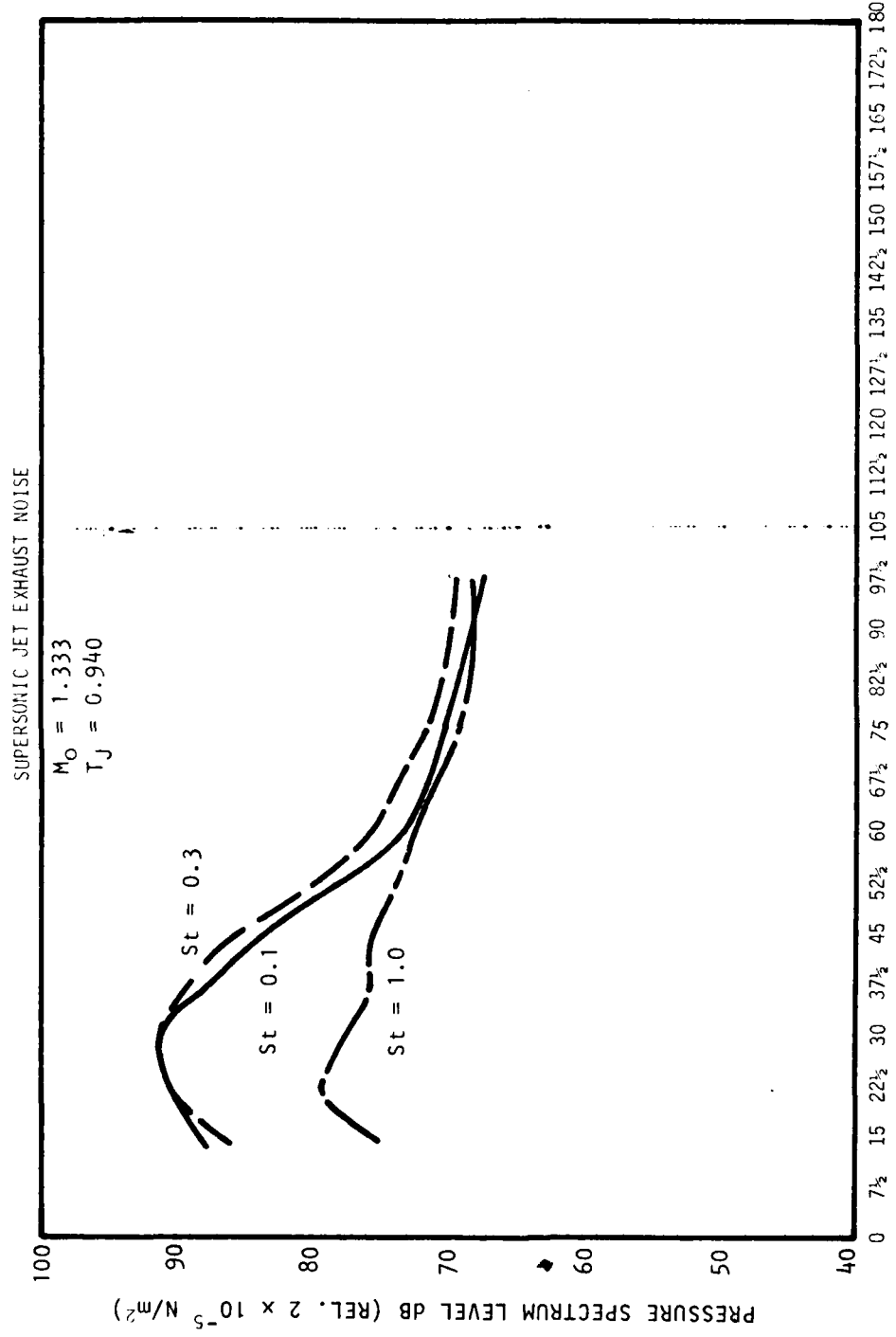


Figure 4.37 Measured Far-Field Sound Pressure Spectrum Levels

The method which will ultimately lead to the best description of the far-field noise radiation by the wave-like components of the flow is likely to be that which defines a "source function," within the framework of a convected wave equation, in terms of the wave-like components. Such a method has been proposed by Liu<sup>48</sup> and Crighton<sup>62</sup>. Crow<sup>61</sup> defined the components of the stress tensor in terms of a simple model of the wave-like structure and obtained the radiated noise by a direct evaluation of the Lighthill integral without neglect of retarded time differences. Such a direct evaluation of the noise radiation is only possible if the Lighthill equivalent source model is adopted. In order to account for the flow/acoustic interaction effects, the more complicated but more physically realistic shear flow wave equations must be used.

From the preceding analysis and discussion, it is clear that considerable further work is necessary. The most important tasks that need to be addressed are:

- (1) The determination of the interaction and energy exchange between the small-scale random turbulent fluctuations and the wave-like components.
- (2) Calculation of the effects of flow divergence on the near-field solutions using a multiple-scale analysis.
- (3) Calculation of the far-field noise radiation, defining a wave-like source term and solving a shear-flow wave equation.
- (4) Experimental evaluation of noise radiation from wave-like components of the flow using a non-acoustic jet excitation experiment.

## 5. LASER VELOCIMETER

177

PRECEDING PAGE BLANK-NOT FILMED

## SUMMARY

---

The laser velocimeter developed during this contract has been successfully qualified as an advanced instrument for simultaneously measuring two components of mean and turbulence velocity, including spectral, correlation, and histogram characteristics, in heated supersonic flows. In addition to measurements in high velocity flows the instrument has the ability to measure the quantities listed above in mixing flows where the turbulence level exceeds the local mean or in instantaneous reversed flow situations.

---

A laser velocimeter is an electro-optical device which measures localized velocities in a fluid flow field by detecting the laser light scattered by contaminant particles suspended in and moving with the fluid. Such systems are potentially capable of measuring instantaneous bi-directional velocity vectors in a turbulent flow field to velocities greater than Mach 4. The measurements do not disturb the flow field and are made in a localized region with cylindrical volume dimensions typically of 0.3 millimeters diameter and one millimeter length. As a consequence of the feature of noninterference, a wide range of flow characteristics may be investigated without distorting or destroying the characteristic under study.

The Lockheed-Georgia Company has developed an advanced laser velocimeter (Figures 5S.1 and 5S.2) which provides the unique capability of measuring two simultaneous, orthogonal flow velocity vectors at very high repetition rates. The minimum time between samples is 3 microseconds and the maximum continuous throughput rate for valid data is 18.75 kHz. The velocimeter system operates over a velocity range of -1000 to +2500 fps with an instantaneous sample accuracy of better than 1%. The ability to achieve these capabilities is based on four major system features:

- (1) a set of unique and highly efficient color separator beam splitter optics provide the basis for generating the multicolor laser beams necessary for multivector capability;
- (2) extremely high-speed processing electronics (using a 500 MHz clock rate), and error checking circuitry;
- (3) direct coupling of the LV to an on-line, high data rate mini-computer which provides unusual flexibility in data formatting and in changing or adding outputs or calculations; and
- (4) the utilization of an acousto-optic modulator in the LV optics provides a velocity shift to the instrument. The velocity shift yields polar response characteristics (Figure 5S.3) which, by proper choice of condition, are both isotropic and directionally sensitive.

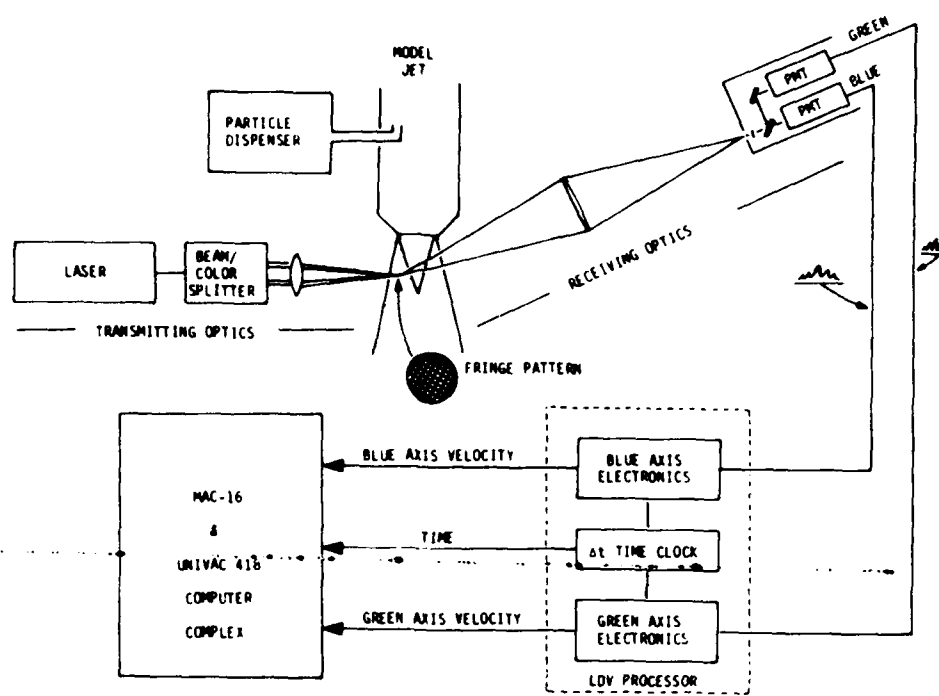


Figure 5S.1 Laser System Block Diagram



Figure 5S.2 LDV Test Configuration

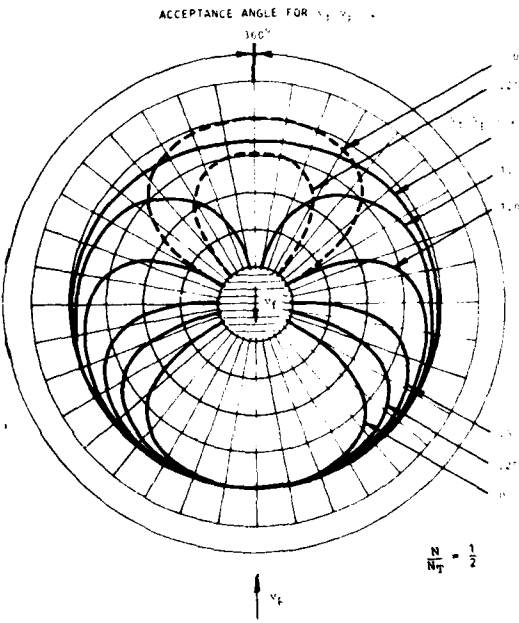


Figure 5S.3 Polar Response of Moving Fringe Pattern

*An analysis of the polar response of the LV measurement volume led to a method for making accurate measurements in highly turbulent flows. Comparisons with hot-wires in reversed flow situations show that the LV is clearly superior.*

Earlier application of the LV to measurements in highly turbulent flows was severely restricted both by instrument limitations and by a lack of knowledge about the implications of these limitations. Measurements of mean velocity made with the LV in the mixing region of a jet appeared to be significantly higher than either theory or hot-wire measurements indicated. A detailed analysis of the LV showed that its response to particles passing parallel to its measurement axis was good; but when the particle trajectory was at large angles to the measurement vector, the LV response decreased to zero at angles approaching 90°; i.e., the particle was travelling nearly parallel to the fringe planes (Figure 5S.4a). When this LV configuration was used to make axial velocity measurements in highly turbulent flows where the velocity probability distribution might even contain negative velocities (Figures 5S.4b), the LV virtually ignores most of the particles with low axial velocity components since these particles likely passed the measurement volume at large angles to the measurement vector. The LV, therefore, reported an erroneously high mean velocity as seen in Figure 5S.4b.

A similar analysis was applied to the hot-wire anemometer. Its response is essentially planar; i.e., it responds equally to all flow velocities in the plane normal to the axis of the wire. The single hot wire, therefore, does not ignore flows with high angles, as the LV does, but measures the vector velocity in the measurement plane (Figure 5S.5a), not the axial vector, as desired. Crossed hot wires can, however, make the desired vector measurement, but neither configuration can resolve flow direction. Thus assuming a velocity probability distribution as in Figure 5S.5b, the hot wire reports the negative velocities as positive, which results in an erroneously high measurement.

Lockheed's recent development of the velocity shifted LV has produced an instrument capable of essentially isotropic response along with the ability to resolve flow direction. The shift is accomplished by using an acousto-optic modulator to shift the light frequency of one of the two laser beams used to generate the fringe pattern. The fringe pattern, then, moves through the measurement volume at velocities up to 2500 fps. Therefore, particles with velocity vectors positive and negative with respect to the fringe velocity vector produce unique signal frequencies so that flow direction can be resolved. The polar response is a function of the ratio of fringe velocity,  $V_f$ , to particle velocity,  $V_p$ , as in Figure 5S.3.

A comparison of velocity probability distributions measured by the hot wire and the LV are shown in Figure 5S.6. The LV is seen to correctly measure the positive and negative portions of the distribution while the hot wire is obviously in error.

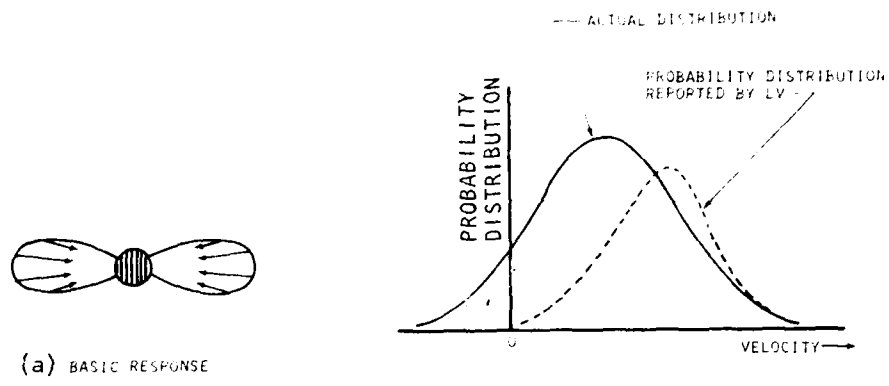


Figure 5S.4 Fixed Fringe LV Response to Reverse Flow

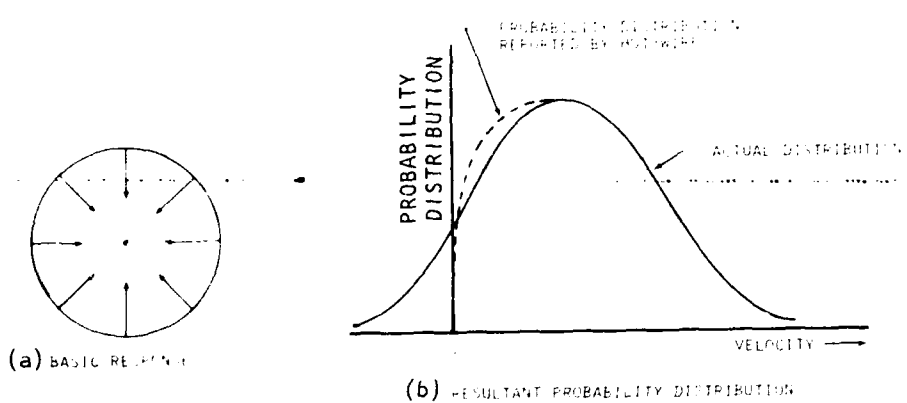


Figure 5S.5 Hot-Wire Response to Reverse Flow

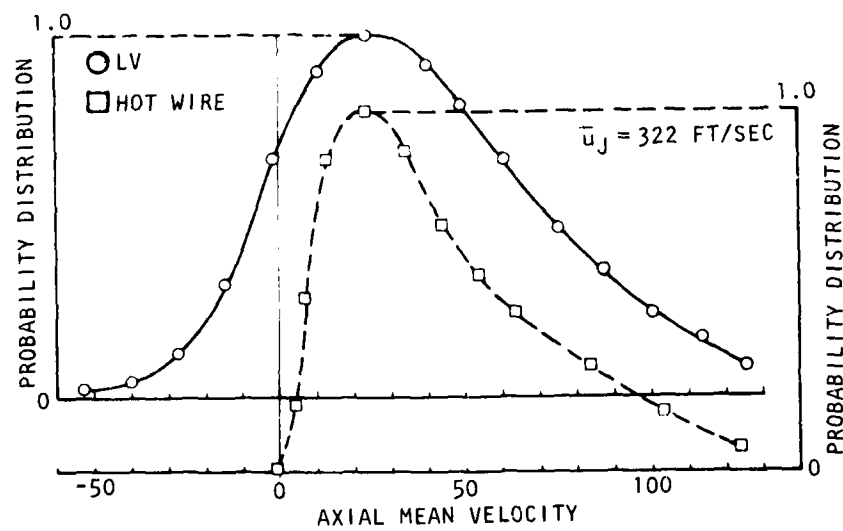


Figure 5S.6 Polar Response of Moving Fringe Pattern

## 5.1 INTRODUCTION

For a number of years conventional techniques of anemometry such as the hot-wire or pitot tube have proven highly satisfactory methods for measuring air flow at low speeds and under limited environmental conditions. However, analytical and experimental understanding of more complex aerodynamic and acoustic phenomena has improved to the stage that the limitations of these methods of measurement are now too restrictive. The limitations are basically caused by the need to insert a mechanical device in the airstream. When inserted in the airstream, the mechanical device and its supports will often not only alter the flow characteristics being measured, but will also frequently suffer mechanical damage where they are subjected to high-speed and high-temperature flows. The physical device also has the disadvantage that it provides the measurement over a relatively large region rather than at a point.

Laser anemometry seeks to resolve many of these problems by providing an instrument which will measure, by optical means, the velocity of microscopic particles introduced in the flow. The flow is therefore not disturbed except for the introduction of very small particles at low seeding density, and optical techniques can ensure that the volume in which the velocity is measured is small compared with conventional techniques.

There are a number of optical techniques for remotely detecting the velocity of particles, and these techniques are now well documented in the literature<sup>65</sup>. The technique adopted by Lockheed and described in reference 7 is based on the interference pattern of light formed in the measurement volume region by the intersection of two coherent monochromatic light beams. These intersecting beams interfere with one another producing an array of separated planes of light of which a section is shown in Figure 5.1. As a microscopic particle passes through this region, light is scattered from the particle and is detected by a photo-sensor. The sensor output signal is a burst of radio frequency energy whose frequency is proportional to the spacing of the interference pattern fringes and the vector velocity of the particle (Figure 5.2). Since the spacing of the fringes is fixed by the geometry of the optics, the particle vector velocity is readily derived from the signal frequency.

If a second set of fringes is oriented at right angles to the first, a cross-hatch pattern results as shown in Figure 5.3, and a velocity vector may then be computed which is perpendicular to the first vector. The second interference pattern may be formed using a different wavelength of light such that its signals are readily distinguishable from those of the first pattern. These different wavelengths do not necessarily require different lasers, but may be derived from a laser that operates with several color lines present simultaneously; most argon lasers, for example, provide this feature.

The Lockheed laser velocimeter system, which was used to obtain the data presented in this report, was described in detail in reference 7 with the exception of two significant changes which will be discussed herein. These changes are the addition of a velocity offset and improvements in the data validation circuits. They have resulted in an instrument which is capable of

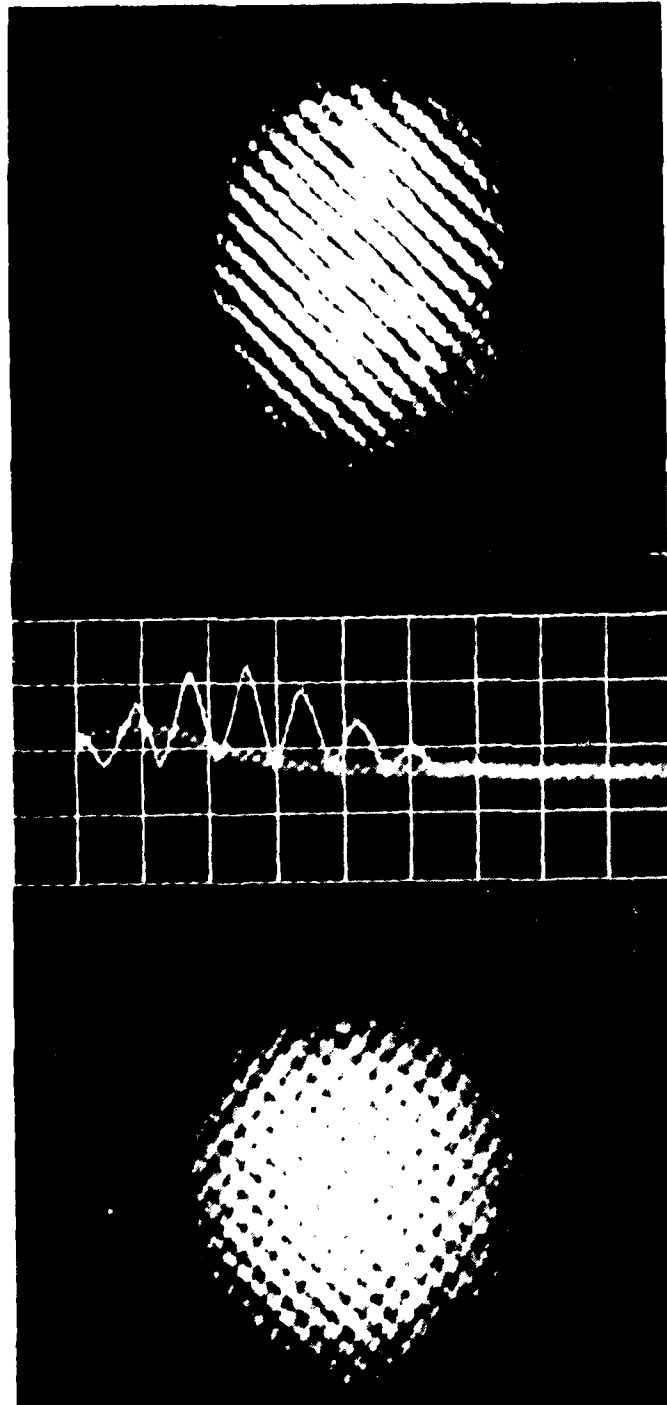


Figure 5.1  
Interference Fringe Pattern

Figure 5.2  
Detected Particle Signal

Figure 5.3  
Orthogonal Fringe Pattern

making measurements which have not been previously possible. The LV has been compared to more common instruments, e.g. pitot tube and hot wire anemometer, and has been found superior, particularly in its ability to withstand severe flow environments.

## 5.2 LV SYSTEM DESCRIPTION

The Lockheed LV is a two-vector system using color to separate the signals from each of two orthogonal fringe patterns. One pattern is generated by the green (5145Å) line from an Argon laser and the other pattern by the blue (4880Å) line. The measurement volume, which is formed by the fringe patterns, is positioned in the jet flow as shown in Figure 5.4. Figure 5.5 shows the LV optics in position around the two-inch jet. The size of this measurement volume is about 300 microns in diameter by about a millimeter long. Particles injected into the flow, both inside and outside the jet plenum, pass through the fringes scattering light at each fringe crossing. Since the physical spacing of the fringes is accurately known, the frequency of the light bursts is proportional to the velocity of the particle. Filters separate the scattered light so that each color is directed to separate photomultiplier tubes where the light bursts are converted into electrical pulses. The processor electronics convert the period of eight of these fringe pulses to digital words which, together with the time between particles, are accumulated by a mini-computer, resolved, if necessary, into the axial and radial components, and stored on both disc and tape. The mini-computer computes the mean velocity and turbulence intensity of each component and outputs these data along with a velocity histogram at a computer teletype terminal adjacent to the LV processor. A separate off-line facility stores the data on tape and disc for more complex analysis such as auto- and cross-correlation estimates and power spectral density calculations.

The processor electronics are, by necessity, quite complex, and the circuitry represents the state of the art in high-speed digital and analog techniques. The processor functional block diagram is shown in Figure 5.6. The input circuitry has a frequency range capability of 100 KHz to 100 MHz. However, because of the extended range of capability offered by recent optical improvements discussed below, the necessity for this large range has been relaxed. This has relieved a number of compromises required throughout the system to achieve the large range, and the circuitry is now optimized for the range of 4 MHz to 30 MHz. The validation circuits use analog circuitry which has been developed since the previous report 7.

## 5.3 VELOCITY OFFSET

Although the two vector LV described in Section 2 above apparently performed satisfactorily in steady flows such as the potential core of the jet, in more turbulent regions, e.g., in the jet mixing region, the LV computes a mean velocity higher than expected. In these regions the turbulence intensity, referred to the local mean, was expected to be in excess of 20%. In this previous configuration the LV system, like many other flow measuring instruments, e.g. hot-wire anemometer, could not resolve the flow direction and, as will be shown later, even ignored most of the particles with low axial velocity

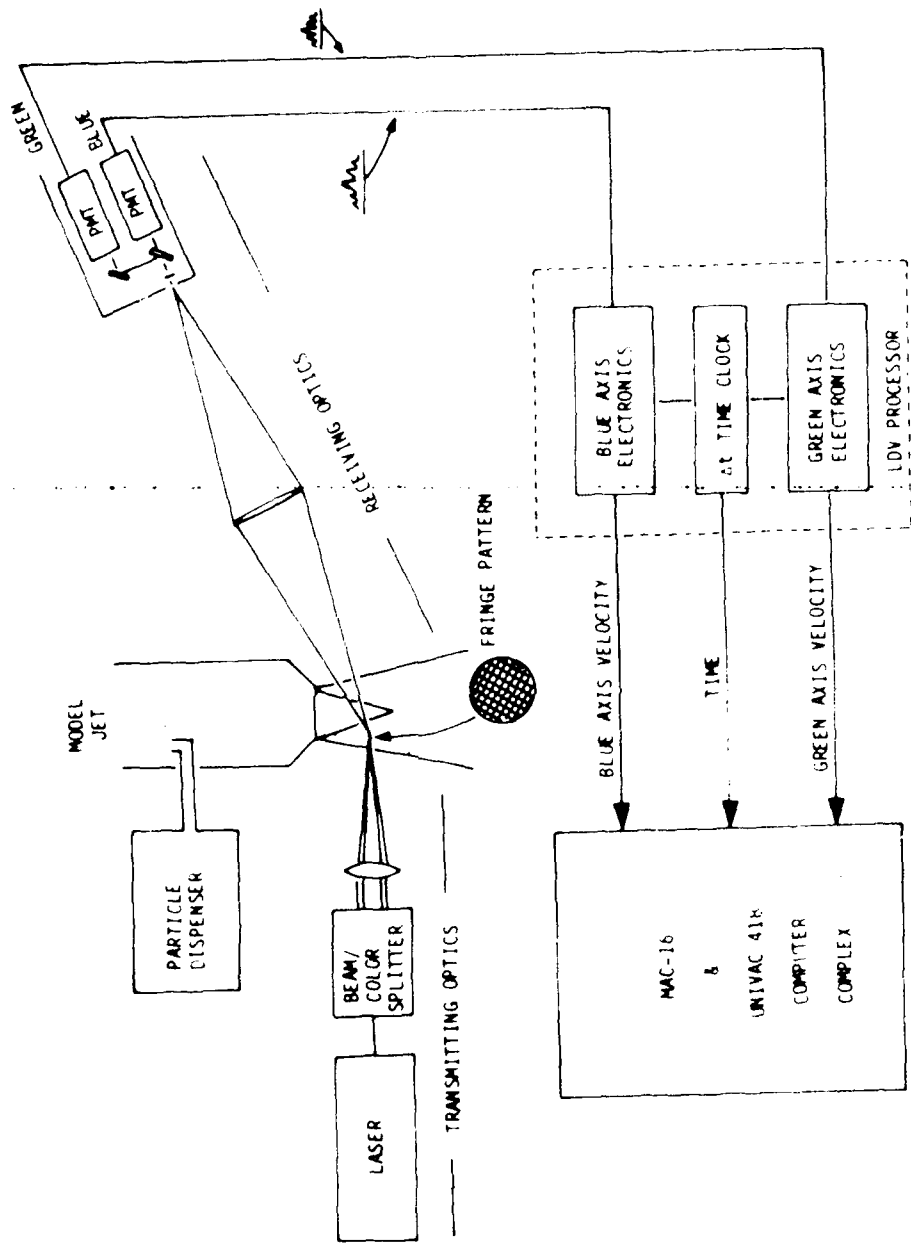


Figure 5.4 LV System Block Diagram

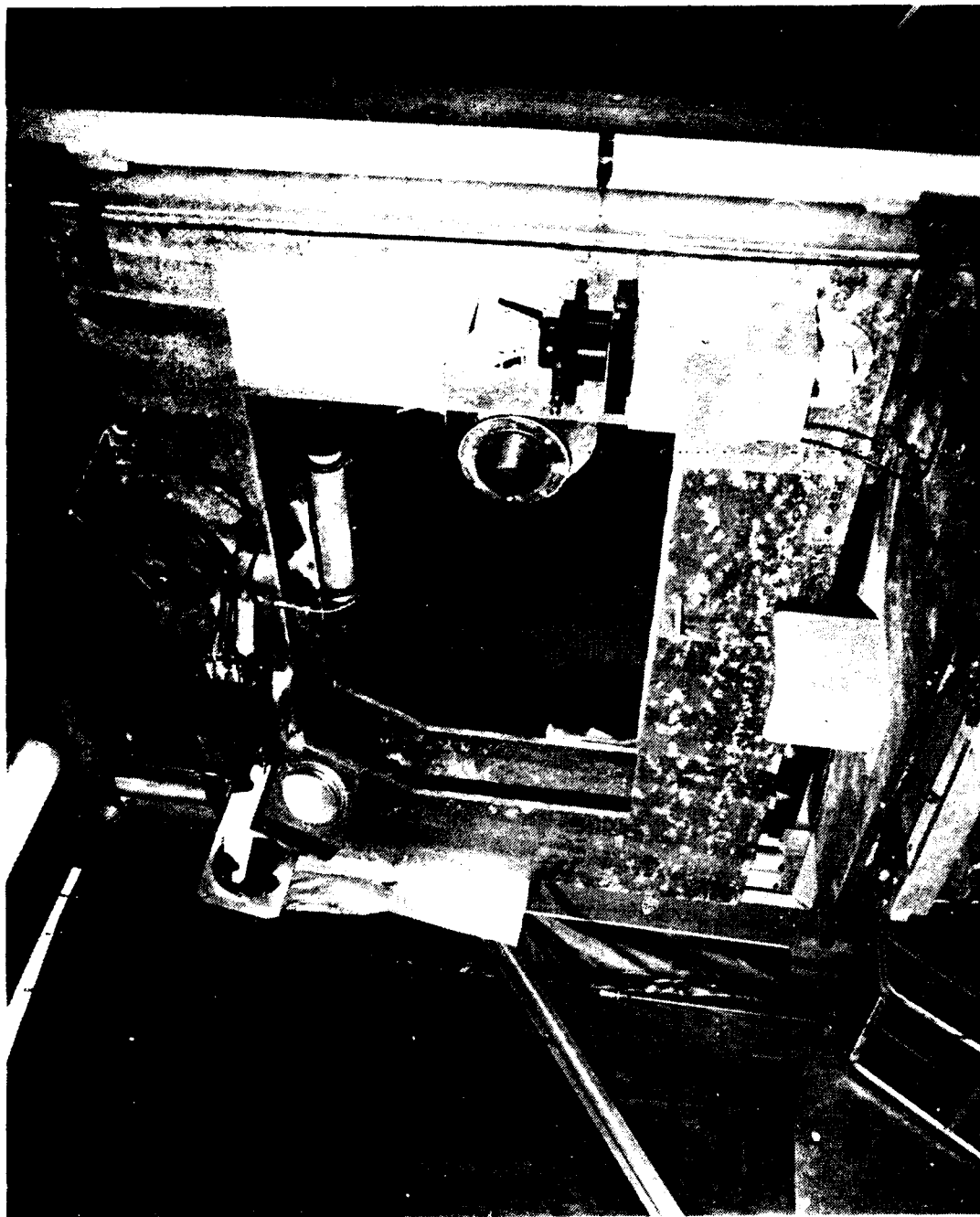


Figure 5.5 LV System Installed in Turbulence Facility

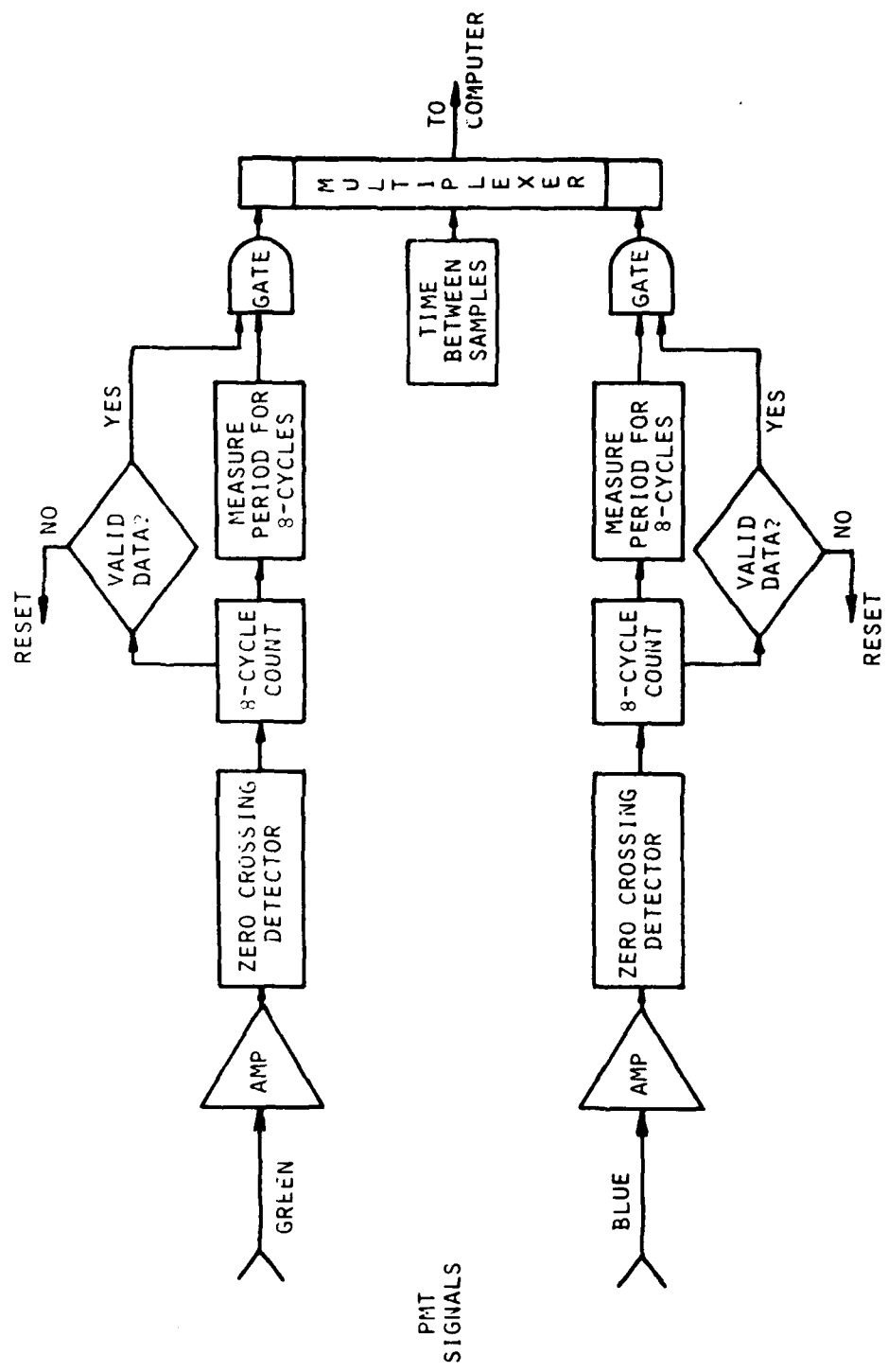


Figure 5.6 LV Processor Block Diagram

components. Consideration of the local turbulence intensity led to the conclusion that under these highly turbulent conditions one might expect a significant number of instantaneous velocity samples directed upstream. This meant that, not only the LV, but also the hot-wire anemometer, would be biased high. Further conclusions, based on the polar response calculations discussed below, indicate that the LV should be biased even higher than the hot wire and this agreed with the experimental observations. The solution to the problem was to introduce a velocity offset into the optical system. Data taken with this configuration show no evidence of bias and therefore confirm the analyses as to the sources of the bias.

### 5.3.1 Polar Response of an LV Measurement Volume

It is well known that an LV system without a velocity offset is not capable of resolving the direction of flow since the particle generates the same frequency burst regardless of the direction it passes through the measurement volume. In addition, it is also obvious that a particle whose direction is nearly parallel to a set of fringes would not cross the eight fringes necessary for a velocity measurement. In general, the probability of detection of a particle passing through a fringe pattern varies as some function, not only of the system parameters, but also of its angle of approach to the measurement volume. In an effort to describe this probability of particle detection, the polar response of a measurement volume was derived.

Assuming a homogeneous distribution of particles within the flow, we may express the probability of particle detection as a function of the effective cross-sectional area of the measurement volume as seen by the approaching particles. Only the two-dimensional case need be considered for the LV optics being used for this study, since the measurement volume is described by two cylinders intersecting at a  $30^\circ$  angle and is, therefore, essentially cylindrical throughout most of its useful volume. We consider only the particle trajectory as projected onto the circular plane normal to the LV optical axis (Figure 5.7). Since the length-to-diameter ratio of the measurement volume is three or more, the change in detection probability due to velocity components perpendicular to this plane is small compared to those due to components in the plane. A particle's probability of detection is therefore assumed to be limited entirely by its velocity component in the plane normal to the optical axis.

The effective cross-sectional area may be expressed as a function of the number of fringes required for a measurement,  $N$ ; the total number of fringes in the measurement cross section,  $N_T$ ; the spacing of the fringes,  $S$ ; and angle of incidence of the particle. Since we are interested in the probability of particle detection, all areas are normalized by the area seen by a particle travelling normal to the fringes so that the fringe spacing does not appear in the expression.

Consider a particle approaching a measurement volume from some angle,  $\alpha$ , as in Figure 5.7. The minimum distance a particle can travel through the measurement volume and cut the  $N$  fringes required for a measurement, is given by the chord  $C$ . This defines an effective measurement width,  $w$ . The relationship between the minimum fringe count and the particle angle of approach is

$$NS = C \cos \alpha .$$

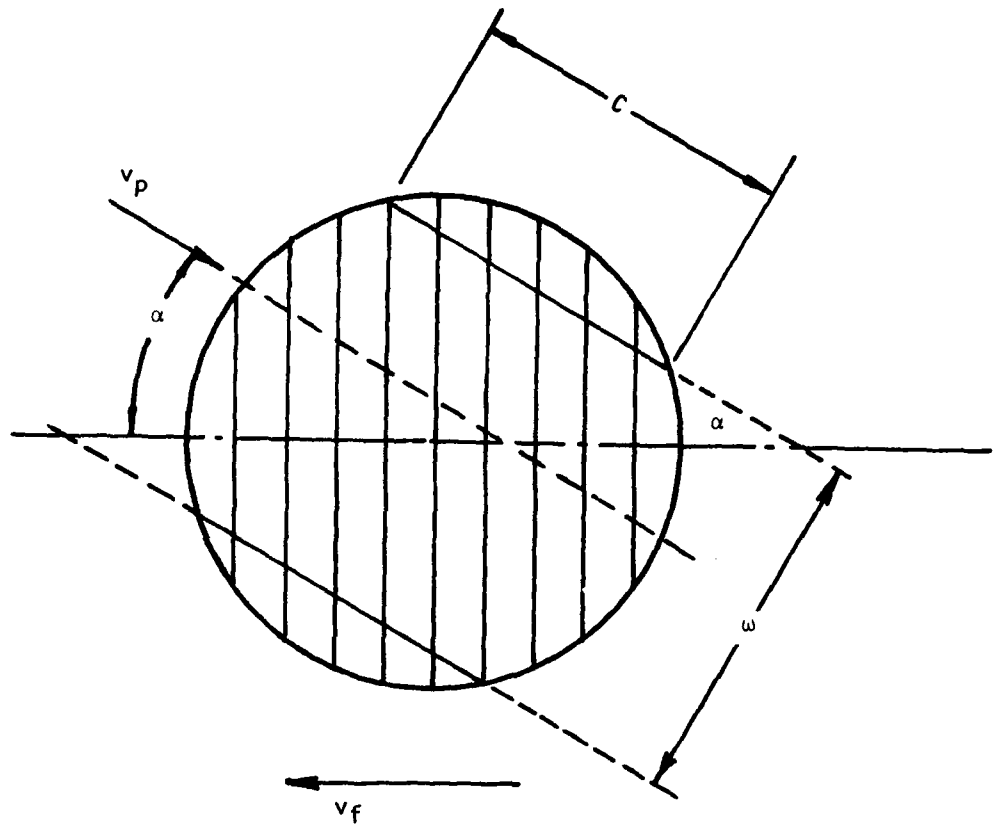


Figure 5.7 Measurement Volume Cross-Section

The diameter of the measurement volume is  $N_T S$ , so that

$$w^2 = (N_T S)^2 - C^2,$$

and thus,

$$w = N_T S \sqrt{1 - (N/N_T \cos\alpha)^2} \quad (5-1)$$

The probability of particle detection (PPD) of a single pattern,  $PPD_1$ , is then:

$$PPD_1 = \frac{w(\alpha)}{w(0)} = \sqrt{\frac{1 - (N/N_T \cos\alpha)^2}{1 - (N/N_T)^2}} \quad (5-2)$$

This analysis yields the polar response pattern shown in Figure 5.8. The ratio  $N/N_T$  is assumed to be 1/2 in the calculation since this is typical of the Lockheed system. The solid lobe represents the response of a particle incident from the nominal flow direction which is from the bottom of the figure, and the dotted lobe is the ambiguous response to a particle travelling opposite to the nominal flow. The "acceptance angle" is arbitrarily defined as that angle through which the  $PPD_1$  is 0.9 or greater. For this pattern the acceptance angle is about  $75^\circ$ . The  $PPD_1$  for a particle incident from  $90^\circ$  is zero, thus a two-vector system must have each set of fringes oriented at some angle to the nominal flow to ensure that the particles have a significant  $PPD_1$ . In the Lockheed LV configuration with fixed fringes, the two sets of fringes are orthogonal and oriented  $45^\circ$  to the nominal flow.

In order to compare theoretical flow analysis with measured flow parameters, it is necessary to describe flow turbulence in terms of its radial,  $r$ , and axial,  $x$ , components. However, since the fringe patterns are oriented at  $45^\circ$  to the  $x-r$  axes, the velocity of each individual particle must be resolved into its  $x-r$  components which requires coincident samples on each channel. To ensure that the velocity measurements being processed in each channel of the LV was derived from the same particle, it was necessary to use circuitry which accepted only those particles whose arrival times were within some coincidence window short enough to exclude the possibility of combining measurements from different particles. This coincidence requirement reduces the data rate by 80% to 90%. The PPD of the orthogonal  $45^\circ$  fringe configuration with coincidence,  $PPD_2$ , may be described as the product of the PPD for two single patterns:

$$PPD_2(\theta) = \frac{PPD_1(\theta + 45^\circ) \times PPD_1(\theta - 45^\circ)}{PPD_1(45^\circ)}$$

The resulting polar response is shown in Figure 5.9. Here the acceptance angle is reduced to only  $14^\circ$  and two more spurious lobes are generated.

When this fringe configuration is used to make measurements in turbulent flows, those particles incident on the measurement volume from angles greater than  $7^\circ$  to  $10^\circ$ , have little likelihood of being detected and are virtually ignored by the system. Since it is these particles that have low axial velocity components, the mean derived from such measurements will be severely

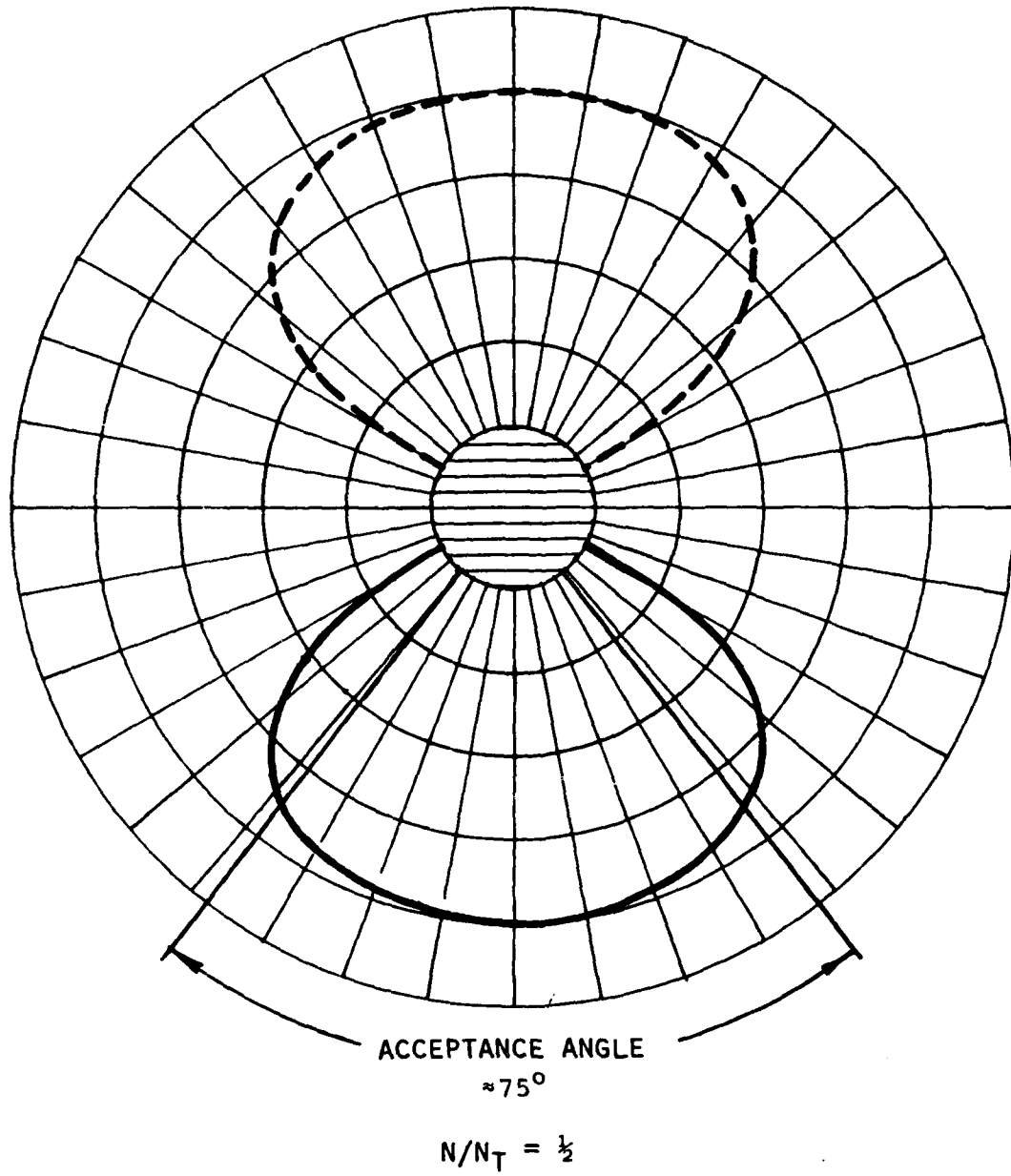
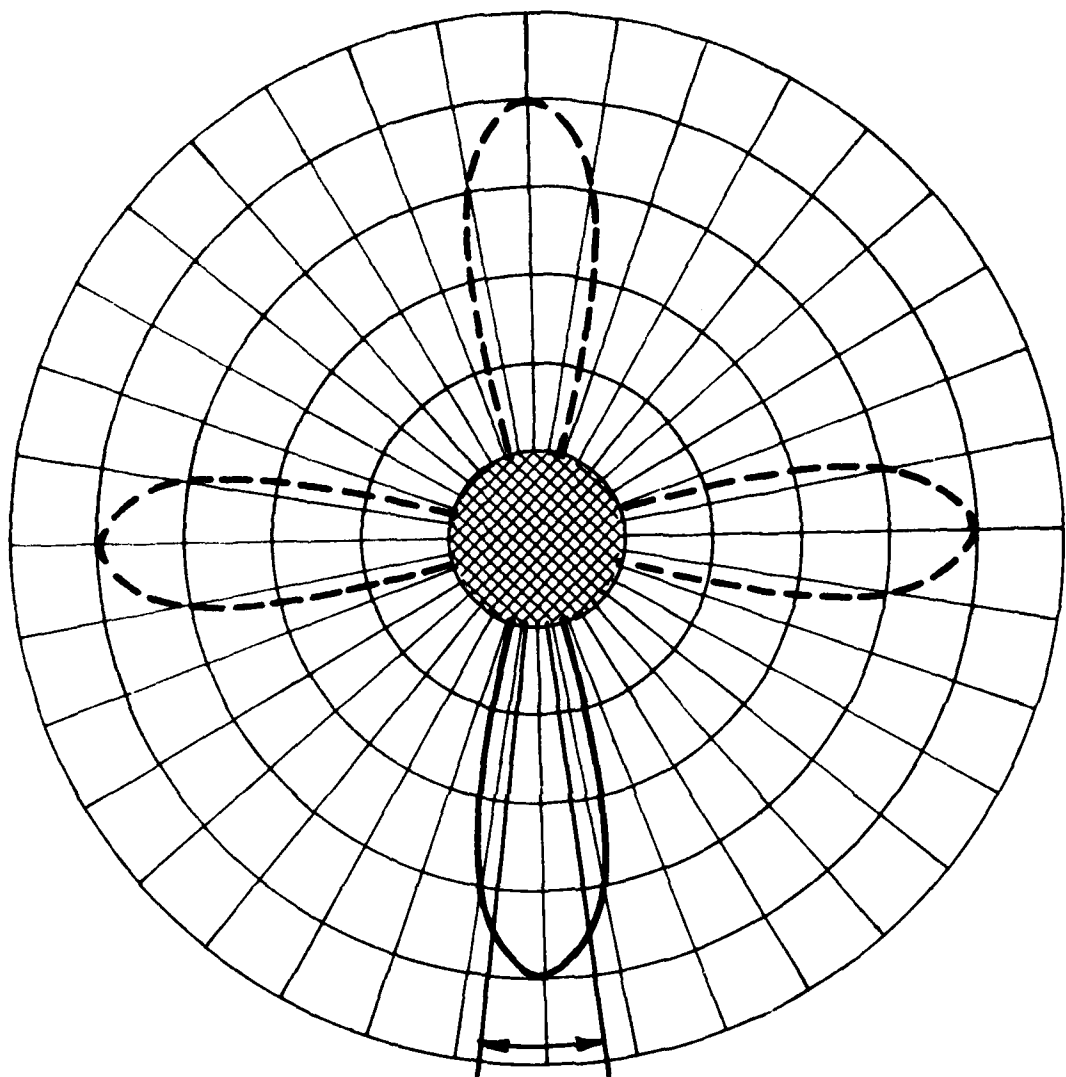


Figure 5.8 Polar Response of Fringe Pattern for Typical Total Fringe Count



ACCEPTANCE ANGLE

$\approx 14^\circ$

$N/N_T = \frac{1}{2}$



Figure 5.9 Polar Response of Two  $45^\circ$  Vector Patterns with Coincidence

biased on the high side. If the turbulence intensity is high enough, there will be a significant part of the velocity probability distribution with negative axial velocities, and here even the hot wire must be biased high also because, like the fixed fringe LV, it cannot resolve flow direction and recognizes all flow perturbations as positive velocity excursions. However, the LV, particularly the two-vector LV, is biased higher than the hot wire because, unlike the hot wire, it virtually ignores all perturbations outside of  $10^\circ$  to the nominal flow.

In order to relieve these limitations a velocity offset was added to the existing LV system. The offset is achieved by producing the same fringes and measurement volume but having the fringes move through the volume at a known and controlled velocity. A stationary particle, located in the measurement volume, will therefore produce a continuous signal proportional, in frequency, to the fringe velocity,  $V_f$ . When the particle is moving, the signal frequency is the algebraic sum of the particle velocity,  $V_p$ , and the fringe velocity,  $V_f$ . To determine  $V_p$  from the measurement, the fringe velocity, i.e. offset velocity, is subtracted from the measured velocity, which provides the capability to resolve the directional ambiguity. It is necessary to determine the new polar response and its relationship to the fringe velocity. Referring again to Figure 5.7, it is now assumed that the fringes are moving with a velocity,  $V_f$ , towards the nominal flow direction. The derivation of the PPD is carried out in terms of the residence time of a particle in the measurement volume since it is this that determines the number of fringes cut by the particle.

If, as before,  $\omega$  is assumed to be the maximum width within which the particle will cut  $N$  fringes, the minimum transit time,  $t_t$ , may be expressed:

$$t_t = \frac{\sqrt{(N_T S)^2 - \omega^2}}{V_p} \quad (5-3)$$

The relative velocity between the fringe velocity and the particle velocity normal to the fringes is  $(V_p \cos\alpha + V_f)$ , so  $N$  is given by

$$N = \frac{1}{S} (V_p \cos\alpha + V_f) \cdot t_t. \quad (5-4)$$

Combining Equations (5-3) and (5-4) and solving for  $\omega$ :

$$\omega = N_T S \sqrt{1 - \left( \frac{N/N_T}{\cos\alpha + V_f/V_p} \right)^2} \quad (5-5)$$

Normalizing the maximum  $\omega$  at  $0^\circ$ , we get  $PPD_m$  for a moving fringe system:

$$PPD_m(\theta) = \frac{\omega(\alpha)}{\omega(0^\circ)} = \sqrt{\frac{1 - \left( \frac{N/N_T}{\cos\alpha + V_f/V_p} \right)^2}{1 - \left( \frac{N/N_T}{1 + V_f/V_p} \right)^2}} \quad (5-6)$$

It is seen that  $PPD_m$  is a function of the ratio of fringe velocity to particle velocity and Figure 5.10 shows several patterns calculated for a range of  $V_f/V_p$  from 0 to 2. The previous calculation of the single fixed fringe configuration is repeated here as a special case where  $V_f/V_p = 0$ . As  $V_f/V_p$  is increased the spurious back lobes disappear and the front lobe becomes broader, until at a  $V_f/V_p = 2$ , the acceptance angle is  $360^\circ$ , i.e. the response is virtually isotropic. As long as  $V_f/V_p$  can be maintained at 2 or more, this LV system will respond properly to particles incident from any direction. It thus becomes possible to orient the two orthogonal patterns in the desired x-r axes, eliminating the coincidence requirement, which leads to a considerable improvement in data rate for the two-axis system.

### 5.3.2 Velocity Offset Optics

The velocity offset is achieved by using acousto-optic modulation to shift the light frequency of one of the two converging beams that form the measurement volume. The modulator is a Bragg cell capable of approximately 90% efficiency in the first-order deflection, which is the frequency-shifted beam. The acousto-optic modulator uses Bragg angle light diffraction by ultrasonic waves travelling in a solid glass block. Acoustic waves propagating from a piezoelectric transducer into the glass block form planar wavefronts travelling in the glass. A light beam passing through the glass at a very small, fixed angle to the acoustic wave fronts is diffracted by the phase grating formed by the acoustic waves. When the light strikes the acoustic wave fronts at the proper angle, the light is diffracted from these fronts. This is known as Bragg reflection. The Bragg angle,  $\theta$ , is defined by the equation:

$$\sin\theta = \frac{\lambda}{2n\Lambda} \quad (5-7)$$

where  $\lambda$  is the light wavelength in air,  $\Lambda$  is the acoustic wavelength and  $n$  is the index of refraction of the glass. Referring to Figure 5.11 the deflection angle formed by the undeflected and deflected beams is

$$\phi \approx \sin\phi = \frac{\lambda}{\Lambda} \quad (5-8)$$

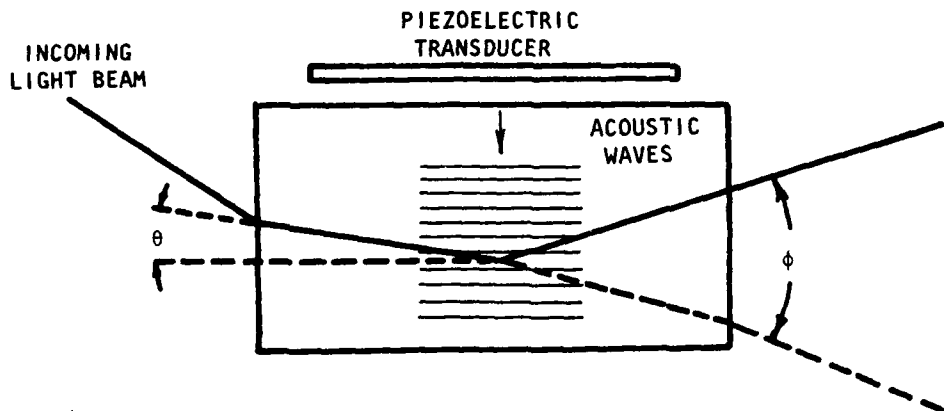


Figure 5.11 Acousto-Optic Modulator

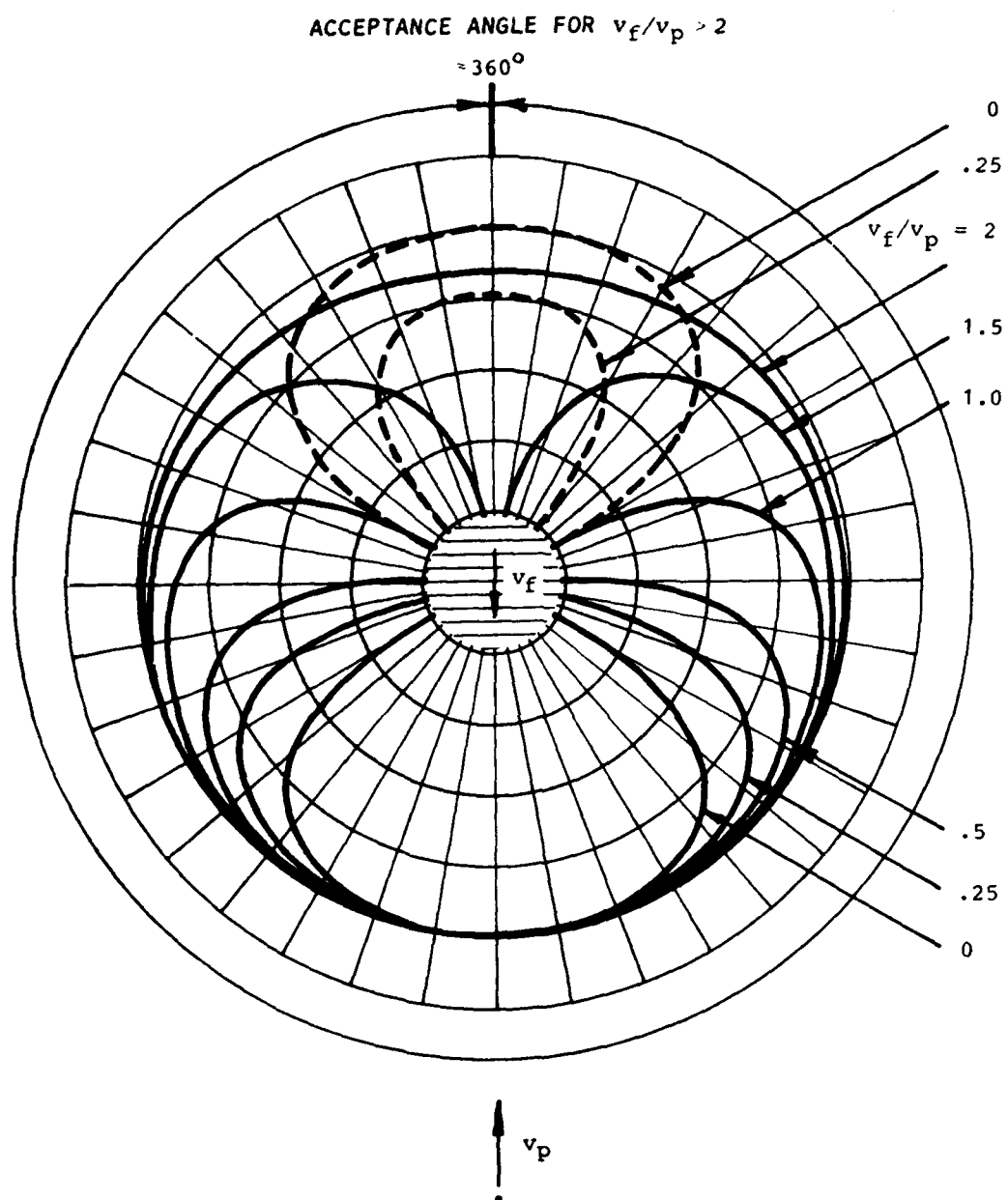


Figure 5.10 Polar Response of a Moving Fringe Pattern

Using the arrangement shown in Figure 5.12 a single acousto-optic cell shifts the frequency of both the blue and green beams. The acousto-optic cell has been used as a part of the beam splitter/color separator optics reported previously . A path length compensator was inserted in the second beam to correct for the decreased light velocity in the acousto-optic cell. The correction keeps the two path lengths within the coherence length of the laser precluding the necessity of an etalon and its inherent instabilities. It should be noted that although the Bragg angle adjustment described by Equation (4-7) should be slightly different for each different wavelength of light, in practice this difference is small and a single adjustment does not result in a significant power loss in either color. Equation (5-8) shows that the exiting beam will not only be deflected from the incoming beam but also that the deflection angle will be slightly different for each color. In order that the subsequent optics may form coincident measurement volumes and fringe patterns for both colors, this deflection must be accurately corrected for each color. This is accomplished by an achromatic prism.

The achromatic prism consists of a pair of wedge prisms fabricated from different glasses. The wedge angles are calculated to correct the deflection angle of each color beam to be parallel to its direction incident on the Bragg cell. Assuming small angles and using Snell's law of refraction, it can be seen from Figure 5.13 that,

$$\theta_G = \beta_1(n_{1G} - 1) - \beta_2(n_{2G} - 1)$$

$$\theta_B = \beta_1(n_{1B} - 1) - \beta_2(n_{2B} - 1)$$

where  $n$  is the index of refraction of the glass, the subscripts 1 and 2 refer to the respective prisms and the subscripts G and B refer to green and blue beams, respectively. This leads to the following expressions for  $\beta_1$  and  $\beta_2$ :

$$\beta_2 = \frac{\theta_B - \theta_G}{\frac{(n_{1B} - 1)}{(n_{1G} - 1)}} \quad (5-9)$$

$$\frac{(n_{2G} - 1)(n_{1B} - 1)}{(n_{1G} - 1)} - (n_{2B} - 1)$$

and

$$\beta_1 = \frac{\theta_B - \theta_G}{(n_{1B} - 1)} \quad (5-10)$$

Equations (5-9) and (5-10) were evaluated for available glass and deflection angles of interest. Since some concern was felt concerning the use of the small angle approximation, a computer program was written to obtain an exact solution. It was found that the difference was less than 1% in the calculated prism angles which is well within the adjustment tolerance.

Three degrees of freedom exist in this optics configuration which allow exact alignment of each color within the same measurement volume. Firstly, the total deflection angle,  $\phi$ , [Equation (5-8)] can be varied by changing the

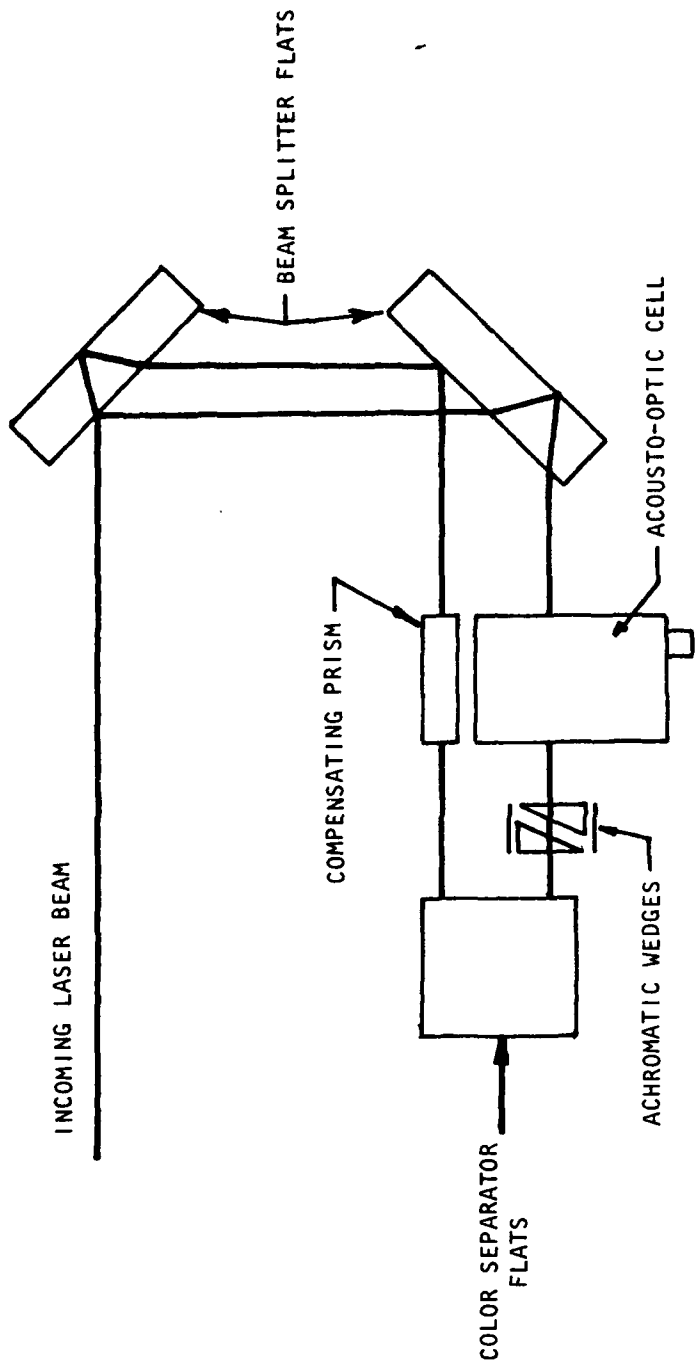


Figure 5.12 Beam Splitter/Color Separator and Acousto-optic Cell Arrangement

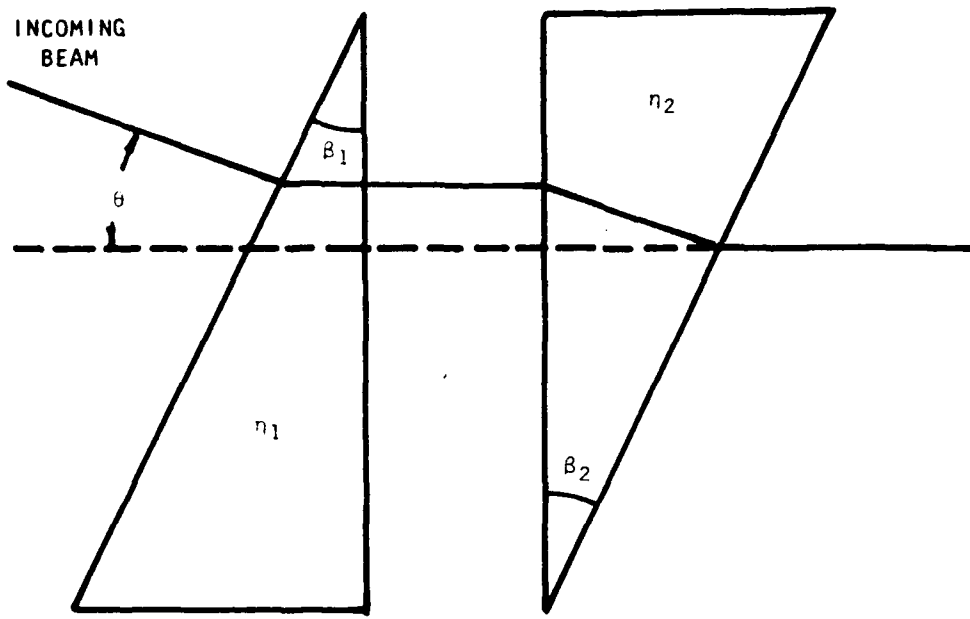


Figure 5.13 Achromatic Prisms

acousto-optic cell drive frequency. Secondly, the relationship  $\theta_G$  and  $\theta_B$  [Equations (5-9) and (5-10)] can be varied by rotating the prisms relative to one another; and last, the total angle  $\theta$  can be varied by rotating both prisms. In practice the alignment procedure involves placing a lens at the focal point (measurement volume) and adjusting the three parameters until both beams intersect at that point. This degree of adjustment was provided due to the difficulty of fabricating wedge angles with the necessary accuracy. Figure 5.14 shows the actual mounting arrangement.

### 5.3.3 Extended Range Capability

It was suggested earlier that the measurement range of the LV could be changed merely by changing the fringe velocity. However, as may be seen in Equation (5-8), a change in the fringe velocity involves a change in  $\phi$  which would result in having to change the alignment of the optics. This problem may be overcome since it is possible to heterodyne the offset frequency to any point within the processor range with a balanced mixer. The result is exactly the same as if the cell drive frequency were changed. With this capability, the resulting range of the instrument is illustrated by Figure 5.15. Here the high velocity limit is imposed by both processor upper frequency limit and the polar response necessary to accommodate the turbulence. The low velocity limit is imposed by the processor low frequency limit and the polar response,  $V_f/V_p = 2$ . The area where spurious data is possible represents the conditions under which directional ambiguity lobes appear on the PPD chart and is separated from the region of good data by a buffer zone. The measurement range of each fringe pattern may be controlled separately as shown in Figure 5.16. This allows the radial channel, for instance, to measure a range of  $\pm 500$  fps with  $360^\circ$  acceptance angle while the axial channel has a range of -250 to +1250 fps with an acceptance angle of  $120^\circ$ .

### 5.4 DATA VALIDATION CIRCUITRY

The original digital data validation circuitry has been described previously 7. That circuitry utilized a digital comparison to determine whether the period of the first four fringe crossings was the same as the period of the second four fringe crossings. In addition, a capability was added to compare the relative times for three fringes crossings and five fringe crossings. The circuits improved the ability of the system to reject data triggered by noise. However, there is still a tendency for erroneous data to be validated.

The efficiency of the validation circuits, i.e. their ability to reject erroneous data, may be described as a function of the error tolerated by the period comparisons. The window may be described by the following relationships:

$$t_4(1-\omega) < t'_4 < t_4(1+\omega) \quad \text{for the 4/4 test}$$

$$t_3(1-\omega) < t'_5 \cdot 3/5 < t_3(1+\omega) \quad \text{for the 3/5 test}$$

$$t_8(1-\omega) < t'_N \cdot 8/N < t_8(1+\omega) \quad \text{for the N/8 test}$$

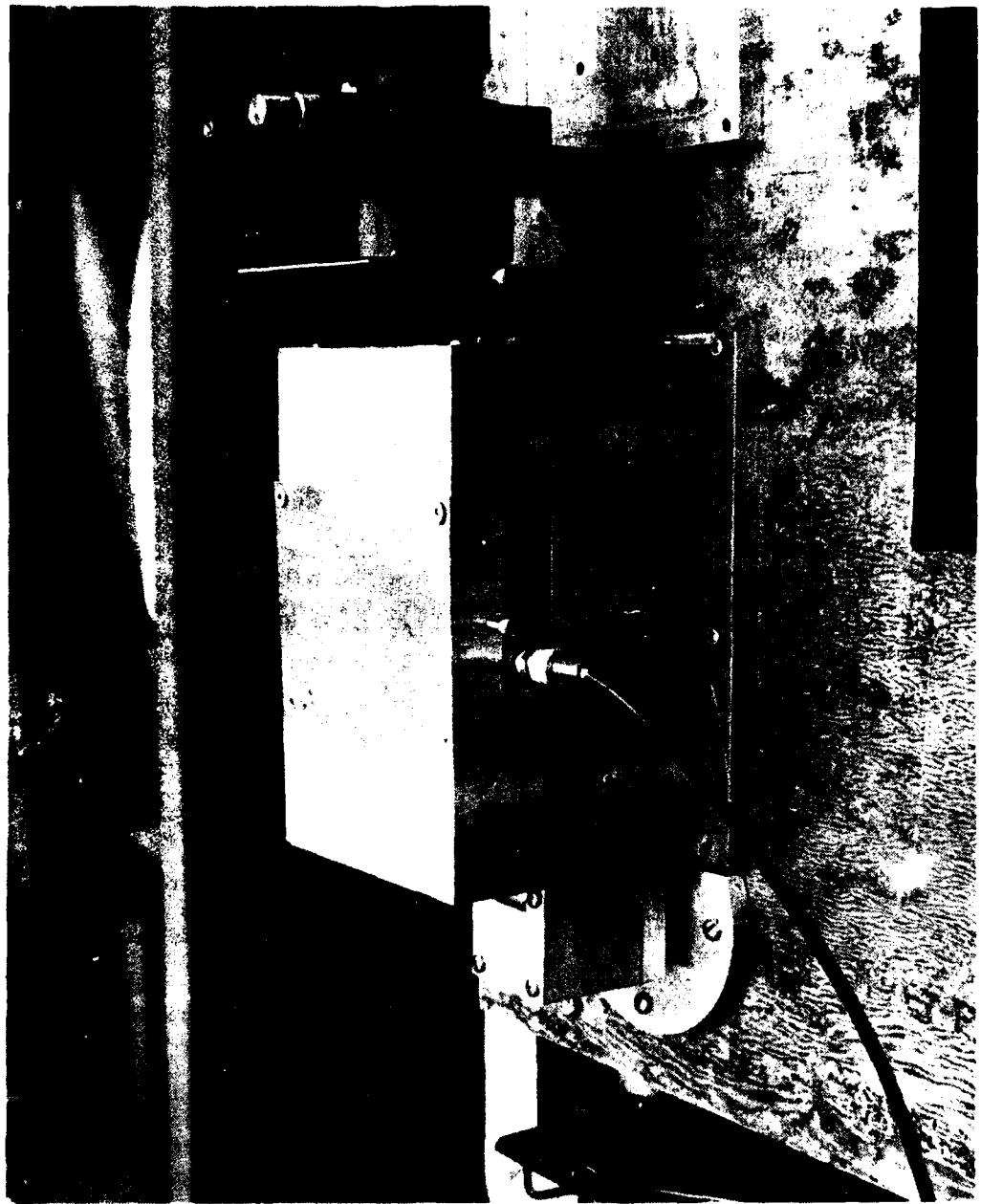
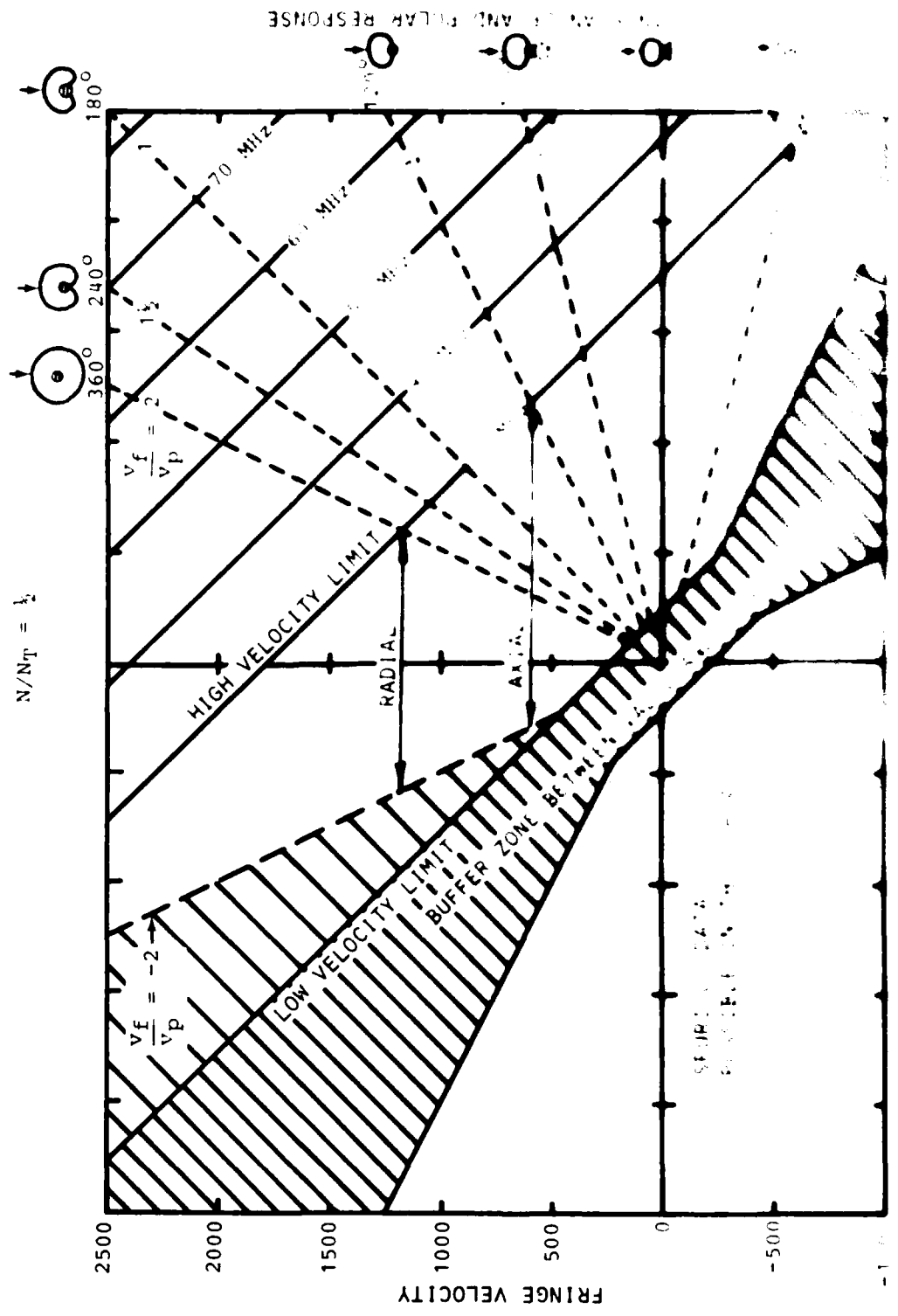


Figure 5.14 Bragg Cell



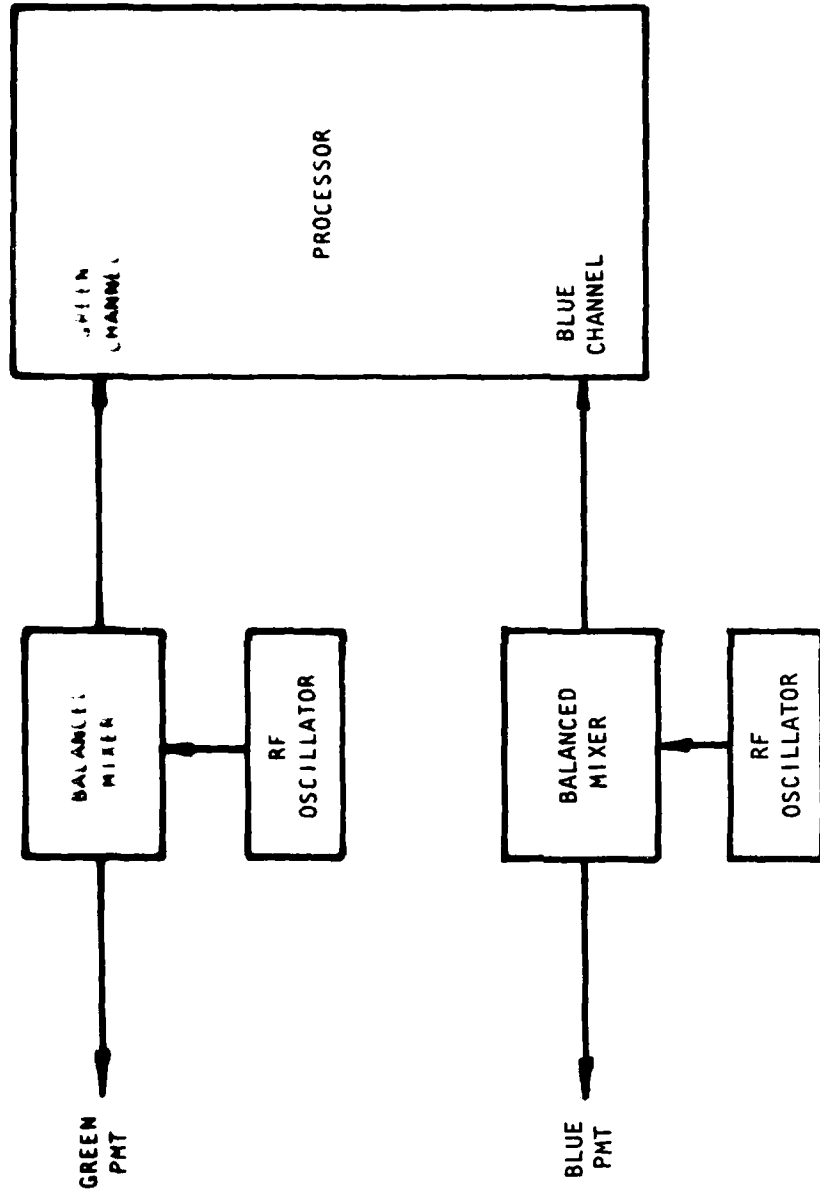


Figure 5.16 Fringe Velocity Control

where  $t_N$  is the time for  $N$  fringe crossings,  $t'_N$  is the time for a second group of  $N$  crossings taken from the same signal burst,  $N$  is any number of fringe crossings and  $w$  is the window width.

The digital comparison circuit yielded the window function plotted in Figure 5.17. While the window width of  $\pm 1\%$  to  $\pm 3\%$  is relatively small, the data reflected the discontinuities in the window function, exhibiting peaks of spurious data on the probability distributions.

An analog circuit was devised to eliminate the discontinuities and the resulting window function is shown in Figure 5.17. It may be seen that the window in this case is somewhat narrower and the continuous function yields a greatly improved validation efficiency.

### 5.5 SUMMARY

The laser velocimeter has been shown to have the potential of being the standard of comparison for future flow measuring instruments. The velocity offset capability has yielded an instrument which not only can resolve direction but has a directional response that can be made virtually isotropic. Its application has been extended to flow measurements in both supersonic and high temperature jets. It is now feasible to expand the capability of the LV to encompass a wider range of measurements aimed at defining turbulence structure and other complex flow details.

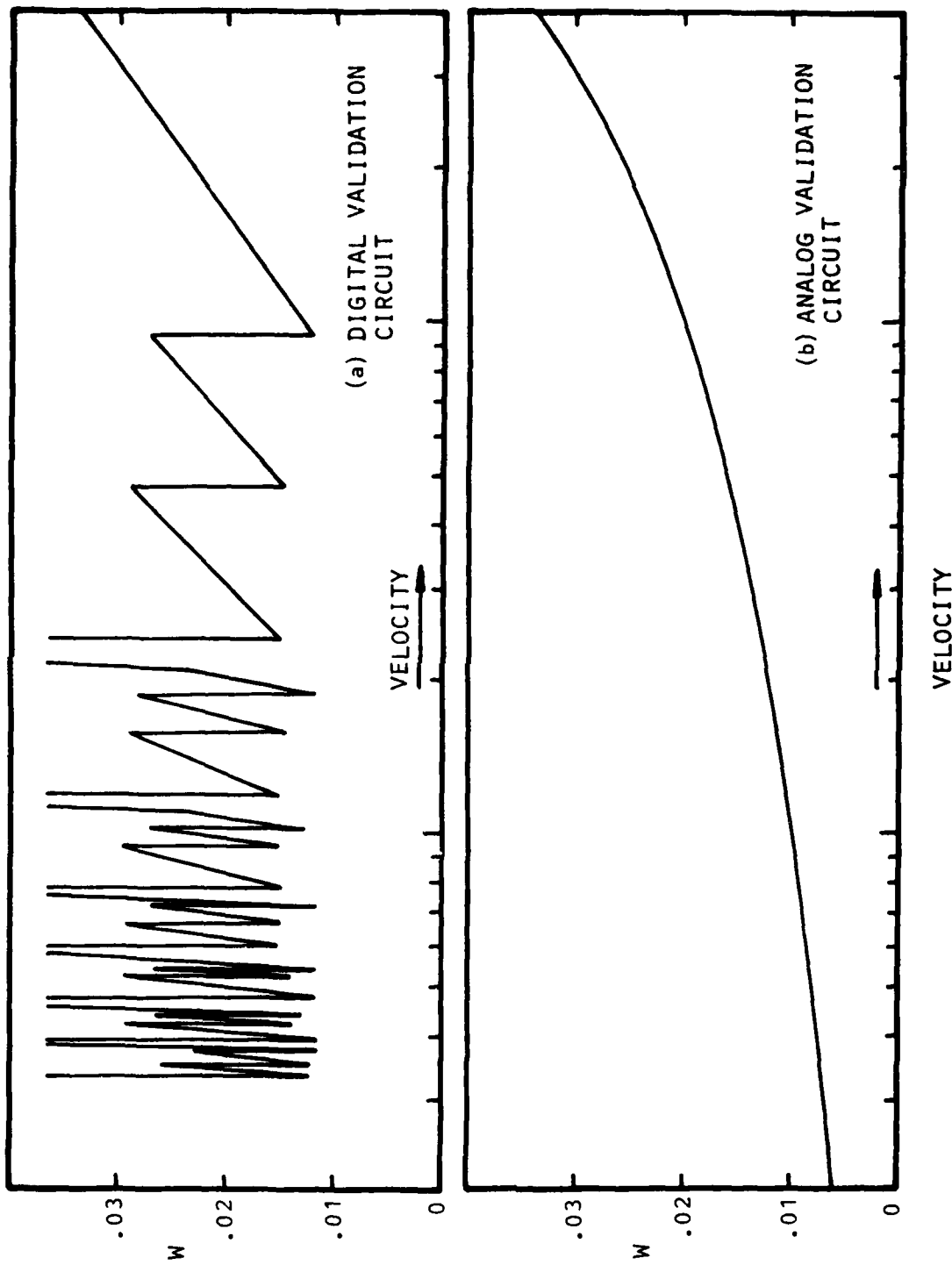


Figure 5.17 Validation Circuit Test Windows

## 6. MEASUREMENT OF TURBULENT JET STRUCTURE

## SUMMARY

To assess the capabilities of the laser velocimeter, measurements were made in a Mach 0.28 free jet using the laser velocimeter and compared with those obtained with a hot-wire anemometer. The measurements demonstrated that the laser velocimeter was a viable instrument for turbulence research. In some respects, the laser velocimeter has shown superiority over the hot-wires as an instrument for measuring velocities. One of its superior features is its capability of distinguishing between forward and reversed flow velocities. Another feature is that the velocity component in any direction may be measured with the same degree of accuracy irrespective of the direction of the mean flow. Turbulence characteristics were also obtained. These included correlograms and spectra of turbulent signals, and good agreement was achieved between laser velocimeter and hot-wire data.

The experimental study with the laser velocimeter was conducted in two phases. The first phase was aimed at trying to determine the full capabilities of the laser velocimeter system to make measurements in a turbulent flow environment. For this purpose, corresponding measurements were made in a Mach 0.28 free jet using the laser velocimeter and a hot-wire anemometer, and comparisons were then made. The measurements included the mean velocity, the turbulence intensities, probability density distributions of the fluctuating signals and the correlograms and spectra.

Figure 6S.1 shows the radial distribution of the mean axial velocity obtained with the laser velocimeter and the hot-wire. The velocity is normalized by the jet efflux velocity,  $U_j$ , and the radial distance by the nozzle radius,  $r_o$ . The agreement between the two sets of results is good. The laser velocimeter measurements of mean velocity were found to be influenced by the origin of the predominant portion of the seeds reaching the measurement volume. However, experience showed that if the jet was seeded evenly from the inside and the outside, data comparable to hot-wire data could be obtained.

Figure 6S.2 compares the probability density distributions of the velocity at the outer part of the jet using the laser velocimeter and the hot-wire anemometer. The distinct advantage of the LV over the hot-wire anemometer in being able to distinguish between forward and reversed flows is demonstrated here. It is evident from the laser velocimeter results that a high probability of negative velocities exists at this location in the jet. Yet, the hot-wire results do not show this. Instead, there is an indication that the negative values are rectified and shown as positive values.

Figure 6S.3 shows the radial distributions of the axial turbulence intensity. The laser velocimeter gives higher values than the hot-wire across the cross-section of the jet. The discrepancy persists even after allowance has been made to account for possible errors in the processing of the laser velocimeter data and in the interpretation of hot-wire data in the region of high turbulence. On the basis of some independent studies on the calibration of hot-wires for turbulence measurements, it would seem that the laser velocimeter data are probably more correct.

Figure 6S.4 shows a comparison between spectra obtained with a laser velocimeter and a hot-wire anemometer in the potential core of the jet. The two peaks of the spectra coincide and give a Strouhal number of 0.5, which agrees with results of other studies in this part of the jet. Agreement was also found between the laser velocimeter and hot-wire spectra at other locations in the jet.

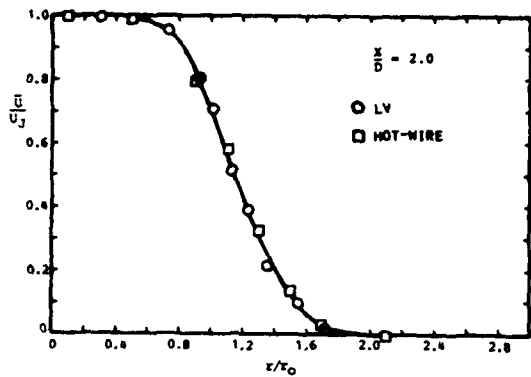


Figure 6S.1 Comparison between LV and Hot-Wire Results:  
 $\bar{U}/U_J$ , ( $M_J = 0.28$ )

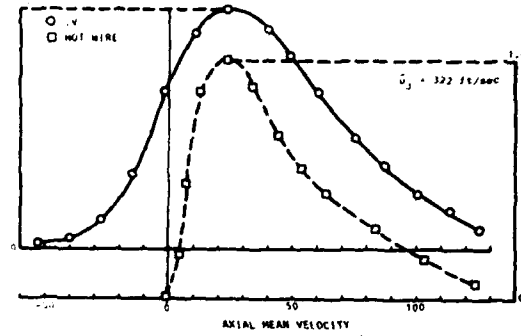


Figure 6S.2 Probability Density of Axial Velocity Fluctuations ( $X/D = 2.0$ )

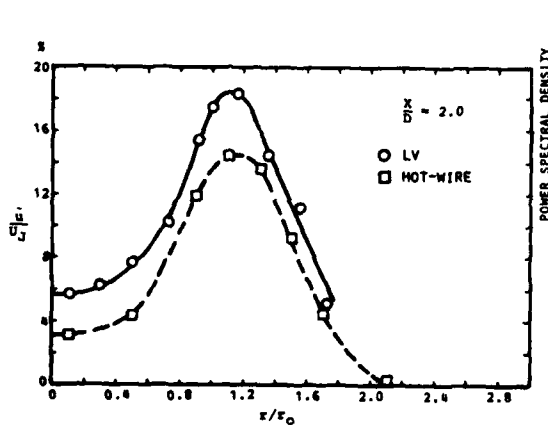


Figure 6S.3 Comparison between LV and Hot-Wire Results:  $\bar{U}/U_J$ , ( $M_J = 0.28$ )

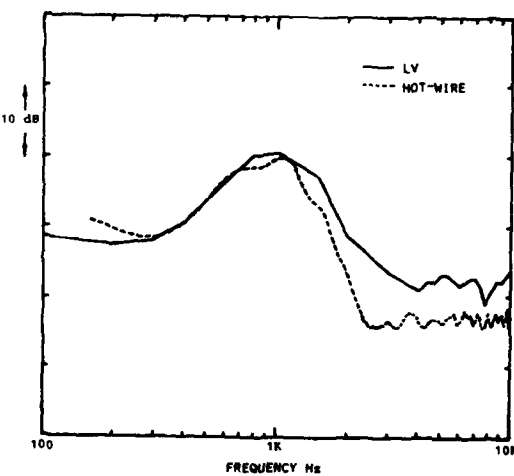


Figure 6S.4 Comparing LV and Hot-Wire Spectra ( $M_J = 0.28$ )

New insight into the jet structure at high speeds and its variation with Mach number was gained. Radial and centerline distributions of axial and radial, mean and fluctuating velocities indicated a decrease in mixing layer spreading rate ( $\delta_n$ ) with increasing Mach number and a corresponding lengthening of the potential core ( $x_0$ ), showing a jet Mach number squared variation. A collapse of radial and centerline distributions of mean velocity at varying Mach numbers was obtained. The peaks of normalized turbulence intensity decreased with increased distance downstream and Mach number. Jet heating increased the spread rate and reduced the potential core length.

The second phase of the study consisted of a detailed survey of the jet flow field under varying Mach number and temperature conditions.

Radial and centerline distributions of basic flow quantities (e.g. mean velocity and turbulence intensity) were obtained. Radial distributions of  $U/U_j$  were found to be similar for a given Mach number when based on  $\eta^*$ ,  $(r - r_{0.5})/x_0$ . The axial distance to which similarity could be achieved increased with Mach number and was approximately two potential core lengths.

Mixing layer spread rate decreased with Mach number, causing a corresponding change in the width of the radial distributions. An empirical equation was derived relating the spread rate to Mach number for isothermal conditions and is  $\delta_n = 0.165 - 0.045 M_j^2$ . Changes in radial distributions of mean velocity due to Mach number were collapsed by normalizing the radial distance by the spread rate (i.e.  $\eta^*/\delta_n$ ) as shown in Figure 6S.5.

Radial distributions of the turbulence intensities ( $\bar{u}'/U_j$  and  $\bar{v}'/U_j$ ) and the covariance  $\bar{u}'\bar{v}'/U_j^2$  did not collapse in terms of  $\eta^*$ . However, the width of the curves was consistent and at locations where similarity of the mean velocity distributions existed, the peaks of the turbulence intensity distributions tended to be oriented at  $\eta^* = 0$ . Figures 6S.6 and 6S.7 show representative radial distributions of the axial and radial turbulence intensity, respectively. A comparison of the peaks for various Mach numbers showed that the peaks at corresponding axial locations tended to fall with Mach number and axial location.

Centerline distributions of the mean velocity and the turbulence intensities moved downstream with increasing Mach number and was apparently related to the stretching of the potential core. A good collapse of the centerline distributions of mean velocity was achieved when the axial distance was normalized by the potential core length (Figure 6S.8) but that was not possible for turbulence intensity. As with the radial distributions, the peaks of the turbulence intensity distributions decreased with increasing Mach number. The relationship between the potential core length and Mach number was found to be:  $x_c/D = 4.3 + 1.1 M_j^2$ .

The heated jet was not studied in as great detail as were those at ambient temperature. However, sparse data did indicate that for a constant Mach number of 0.9, jet heating had the effect of increasing mixing layer spread rate with a corresponding reduction in potential core length. When the comparison was made with jets at the same velocity, the effect of heating was found to be more pronounced.

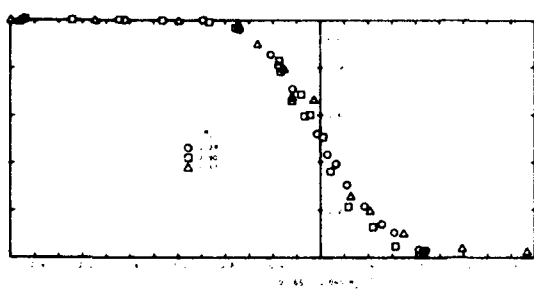


Figure 6S.5  $\bar{u}/U_J$  vs  $\eta^*$   $(0.165 - 0.045 M_J^2)^{-1}$

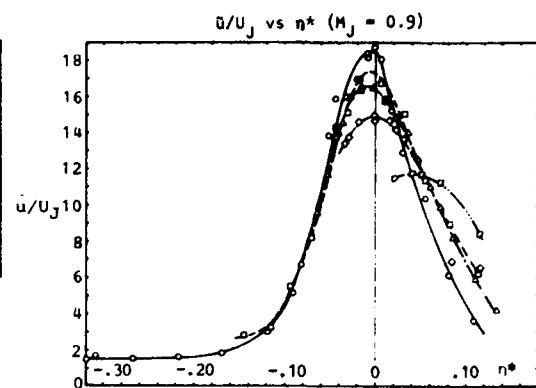


Figure 6S.6  $\bar{u}/U_J$  vs  $\eta^*$

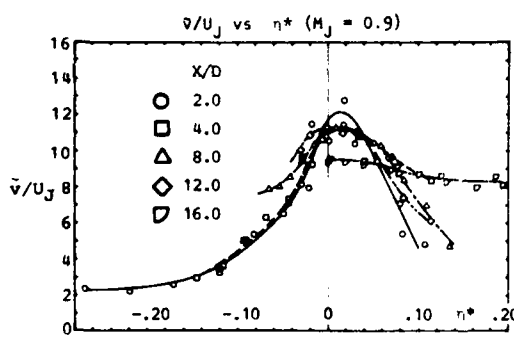


Figure 6S.7  $\bar{v}/U_J$  vs  $\eta^*$

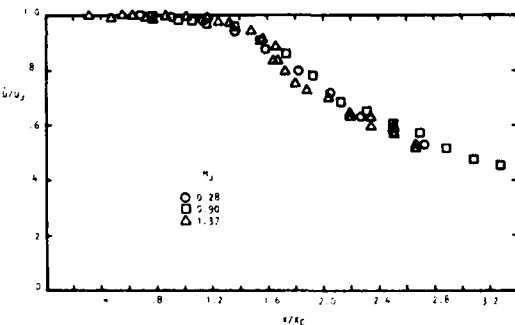


Figure 6S.8  $\bar{u}/U_J$  vs  $X/X_C$

## 6.1 INTRODUCTION

### 6.1.1 Historical Development

Scientific interest in the characteristics of round jets began long before the application of the turbojet engine for aircraft propulsion and the urgent need to reduce the attendant jet noise. Initial interest arose out of a general desire for increased understanding of the flow-separation phenomenon, particularly the mixing process in the shear layer of such flows. This knowledge was of practical importance because, in many engineering operations involving fluid flow, the problem of flow separation and its inherent effects became major factors of concern. Thus, studies in the field of jet flow were just a part of a larger study effort which included shear flows of parallel streams, wakes, and backward- and forward-facing steps.

The increasing use of jet engines for commercial aircraft in the past two decades and the corresponding search for quieter engines brought intensified urgency to the quest for a better knowledge of jet-flow characteristics. The problem centered around identifying and describing the sources of jet noise to discover generating mechanisms and methods of noise prediction, and ultimately to derive systematic and definitive design procedures for altering the structure of the sources and the mean flow environment to produce the desired noise reduction.

The change in the purpose and the direction of jet flow studies introduced a new dimension to the problem. In the past, experimental studies at low subsonic speeds were sufficient, but it now became obvious that the objectives could be achieved with practical effect only if it were possible to perform experiments at high subsonic and supersonic speeds. With the introduction of the high by-pass engine, which essentially provided a solution to the problem of jet noise at low subsonic speeds, attention was turned to the search for solutions to the high-speed cases. It was clear that new facilities and instruments had to be developed to allow measurement of the flow characteristics at these high speeds.

### 6.1.2 Application of Hot-Wire Anemometer

Traditionally, because of the broad interest in separated flow problems, the introduction of new instruments has always been followed quickly by experiments in which such flows are studied using the new instruments. In 1947, soon after the development of the constant-current, hot-wire anemometer, Liepmann and Laufer<sup>66</sup> undertook measurements of the mean and fluctuating velocities in the two-dimensional shear layer. In the same year, Corrsin<sup>67</sup>, and later, Corrsin and Uberoi<sup>68</sup>, made hot-wire measurements in the round jet. New techniques of data processing were also quickly exploited, such as the extensive use by Laurence<sup>69</sup> of the newly developed correlation and spectral analysis techniques in his careful study of the round jet. In the intervening years, the hot-wire anemometer has become a powerful instrument for research into separated flows, especially with the emergence of the constant-temperature instrument and new linearization techniques. Very useful insights into the jet structure have thus been obtained with the help of hot-wire techniques (e.g. Laurence<sup>69</sup>;

Davies, Fisher, and Barrat<sup>16</sup>; Bradshaw, Ferriss, and Johnson<sup>70</sup>; Wygnanski and Fiedler<sup>71</sup>; and Lau and Fisher<sup>72</sup>).

Although there has been widespread use of the hot-wire anemometer for measurements in various flow configurations, some of the problems associated with its use have yet to be fully resolved. In the measurement of the component of velocity which is normal to the mean flow, there is still no consensus on how the yawed or crossed hot-wire results should be interpreted. The problem lies in the fact that the directional sensitivity of the hot wire does not follow a simple relationship. Although some significant efforts have been made to resolve this question (e.g. Champagne and Sleicher<sup>73</sup>), there is no direct method available for verifying the results. Associated with this difficulty is that the hot-wire anemometer is not able to sense changes in the direction of the velocity vector in a plane normal to the wire. This causes errors in the measured results if the hot-wire is used in a region where the temporal changes in the velocity vector are significant, as in the highly turbulent region of the shear layer of a jet. Rose<sup>74</sup> and Hekestad<sup>75</sup> analyzed the problem and derived approximate corrections needed to account for this shortcoming of the hot-wire anemometer. However, the correction factors assume precise knowledge of the turbulence quantities, which are still not sufficiently defined.

Perry<sup>76</sup> recently reported some experimental results which cast doubt on the validity of directly applying static calibrations of hot-wire anemometers to dynamic measurements. His experiments indicated that, when a calibrated hot-wire was plunged into a stream of known mean flow, the instrument registered a sustained value which was about 8 percent lower than the value expected.

In spite of these difficulties encountered in various applications, the hot-wire anemometer continues to be a useful instrument for fluid-mechanics research. However, in the effort to achieve the new objectives in jet-structure research, the hot-wire anemometer has some very serious limitations. In measurements at high speed, it would be difficult to keep the hot-wire anemometer intact long enough to allow meaningful results to be obtained. Although Kolpin<sup>77</sup> was able to obtain results from a jet running at Mach 0.9, the approach of most researchers<sup>69,16,70,71</sup> has been to restrict the use of the hot-wire anemometer to regions where the Mach number is less than 0.4. Another serious limitation is that the hot-wire anemometer cannot be exposed to high temperatures, and thus a further barrier to its use in jet-structure research is imposed. Moreover, there is the question of interpretation of hot-wire data at these conditions, since the hot-wire anemometer measures mass flux instead of velocity.

A persistent question which arises when measurements are made with an instrument inserted into the flow is the extent to which the instrument affects the environment which is being measured. It appears from low-subsonic jet-structure studies that the insertion of an instrument in the "developed" regions of the flow does not alter the main structure of the jet<sup>78</sup>. However, it is to be expected that the influence of the instrument would be greater if the instrument were placed in an inherently less stable

region of the jet. This question, of course, becomes more crucial as the jet speed approaches sonic and supersonic speeds, when the instrument introduces its own shock waves into the flow field.

#### 6.1.3 The Laser Velocimeter

The physical difficulties and interpretation problems encountered in the use of the hot-wire anemometer largely prompted the development of a number of remote optical techniques for studying the various flow characteristics. Of these, the laser velocimeter (LV) has come into special prominence in the past few years. As will be evident from the measurements reported here, it is possible to obtain most of the characteristic data with the LV that are possible with the hot-wire anemometer, while avoiding the physical limitations inherent in the hot-wire technique. It should be pointed out that, with the present LV, it is necessary to introduce particles (or seeds) into the flow, and there is some question regarding the influence of these seeds on the flow. In practice, however, very small particles (0.1 to 1 micron) of a light material (e.g. Aluminum Oxide), are interspersed so that they form a part of the flow. It is presumed that this will minimize the effect, which, in the jet would probably be small<sup>6</sup>. Therefore, on balance, the LV appears to be an ideal instrument for the kind of jet research contemplated.

Laser velocimeter systems come in many forms, and Fisher, et al<sup>6</sup> provide an extensive bibliography of the work which has been carried out with various types. The report also analyzes in some detail the relative merits of the spectrum analyzer, the frequency tracker, and the burst counter systems as applied to supersonic flow studies. The laser velocimeter used in the present study is of the burst-counter type.

#### 6.1.4 Scope of This Work

The present study was conducted in two phases. In the first phase, the capability of the LV was ascertained against a background of the various kinds of measurements which have been made with the hot-wire anemometer. To accomplish this, measurements were made of:

- (a) Mean and turbulent velocities
- (b) Probability distributions of these velocities
- (c) Skewnesses and kurtoses
- (d) Autocorrelations and spectra

The results were individually compared with those obtained with a conventional hot-wire anemometer.

The second phase, directed toward the main objective of the effort, was to map out in detail the various flow characteristics of a circular jet, and to assess, through changes in the flow conditions, the various effects brought about by changes in the jet Mach number and jet temperature ratio. Due to the limited time available, a modest test program was set up, essentially comprising a study of four jet conditions:

		$T_j/T_o$	$M_j$	$V_j/a_o$
Case I	Subsonic	1.00	0.28	0.28
Case II	Subsonic	1.00	0.90	0.90
Case III	Supersonic	1.00	1.37	1.37
Case IV	Subsonic	2.32	0.90	1.37

From Cases I to III, the static jet exit temperature was kept the same as that of the ambient air, while the Mach number of the jet was progressively increased from 0.28 to 1.37. The conditions were chosen to provide insight into the effect of changes in the Mach number of isothermal jets. In Case IV, the jet was operated at a Mach number of 0.9, but it was heated so that the absolute exit velocity of the jet was the same as that of Case III (supersonic jet). The rationale was that a comparison of Cases II, III, and IV would throw light on the effects of heating and provide a determination of whether the jet structure was primarily a function of velocity or Mach number.

Case IV was not fully exploited due to a failure of the sudden expansion burner used for heating the jet. Fortunately, however, sufficient data were acquired before the failure to provide indications of heating effects on the jet structure.

## 6.2 EXPERIMENTAL SET-UP

### 6.2.1 Air Supply

Figure 6.1 shows a schematic diagram of the air system. Dry air was supplied from a plant compressor facility at 300 psi. Upstream of the jet facility, the air line divided into two branches, one going to the sudden expansion (SUE) burner, and the other leading directly to the mixing chamber, which was also connected to the outlet from the SUE burner. The desired plenum temperature was achieved by an appropriate mixture of the hot and cold air streams. The plenum was 12 inches in internal diameter and 10 feet long. No acoustic treatment was provided inside the plenum. A small-angle diffuser was used at the plenum entrance giving a smooth transition from the supply pipe to the plenum. The nozzles were attached to a converging segment of a pipe at the end of the plenum.

Two types of nozzles were used: a converging nozzle for studying Cases I, II, and IV; and a converging-diverging nozzle operating at the design condition of Mach 1.37<sup>5</sup>. The flow may thus be considered to be essentially shock-free. Both nozzles had a 2-inch exit diameter.

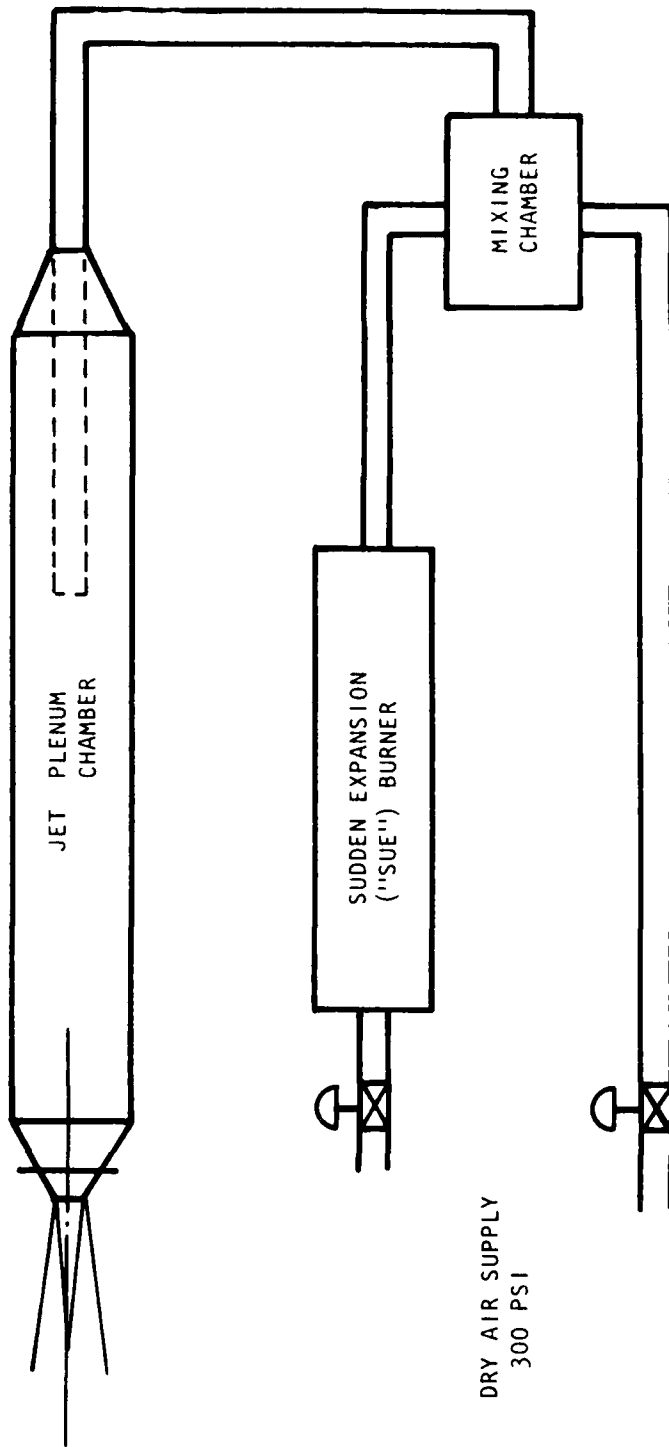


Figure 6.1 Schematic of the Air Supply System

### 6.2.2 Hot-Wire Anemometry and Ancillary Equipment

A DISA 55D01 constant-temperature, hot-wire anemometer was used in conjunction with a DISA 55D10 linearizer for obtaining the hot-wire data. The hot-wire itself was made from 5-micron tungsten wire, suitably plated at the two ends.

The DC level of the anemometer output was measured with a Hewlett-Packard Digital Voltmeter and the r.m.s. level with a B & K 2416 Electronic Voltmeter. The probability density of the hot-wire signals was obtained by feeding the anemometer signal into a Hewlett-Packard 3721A Correlator, which performed the probability density analysis. The Correlator was also used for autocorrelating the hot-wire signals, and spectral densities were obtained by coupling with a Hewlett-Packard 3720A Spectra Display.

### 6.2.3 Laser Velocimetry and Ancillary Equipment

The laser velocimeter has already been described in the previous chapter. Further details are also available in Appendix IV of Reference 7. However, to provide points of future reference, the physical components of the instrument are briefly described here.

The LV (Figure 6.2) consists essentially of an optical transmitter system which sends out two pairs of beams (one blue and one green), and an optical receiver system which is focused onto the very small region in the jet where the four beams intersect. A pair of photomultiplier tubes behind the receiving optics transform the variations in light intensity at the observation region into oscillating voltage signals. The variation of light intensity is caused by the passage of small (0.1 to 1 micron) particles through the interference fringes formed at the intersection region of the four beams.

The transmitting and receiving optical systems are mounted on a frame which is set on a lathe bed. The frame can be moved in three orthogonal directions, thus changing the position of the measurement volume. The positioning of the measurement volume is accurate to 0.03 inch.

Electrical signals from the photomultiplier tubes are fed into the electronic processor which, with the aid of an on-line MAC 16 computer, converts signal periods into a measure of the instantaneous particle velocity. With these data, the mean and standard deviation (or turbulence intensity) of the velocity at the measurement volume may be obtained.

The raw particle velocity data are stored on tape and can be further processed to provide statistical data such as skewness, kurtosis, auto-correlation, and spectrum.

Operation of the LV requires the presence of tracer particles in the flow. In the present set-up, these particles are introduced on the inside and outside of the jet. The particles for the inside enter the plenum at a point upstream of the nozzle. Seeding the outside of the jet is done through a

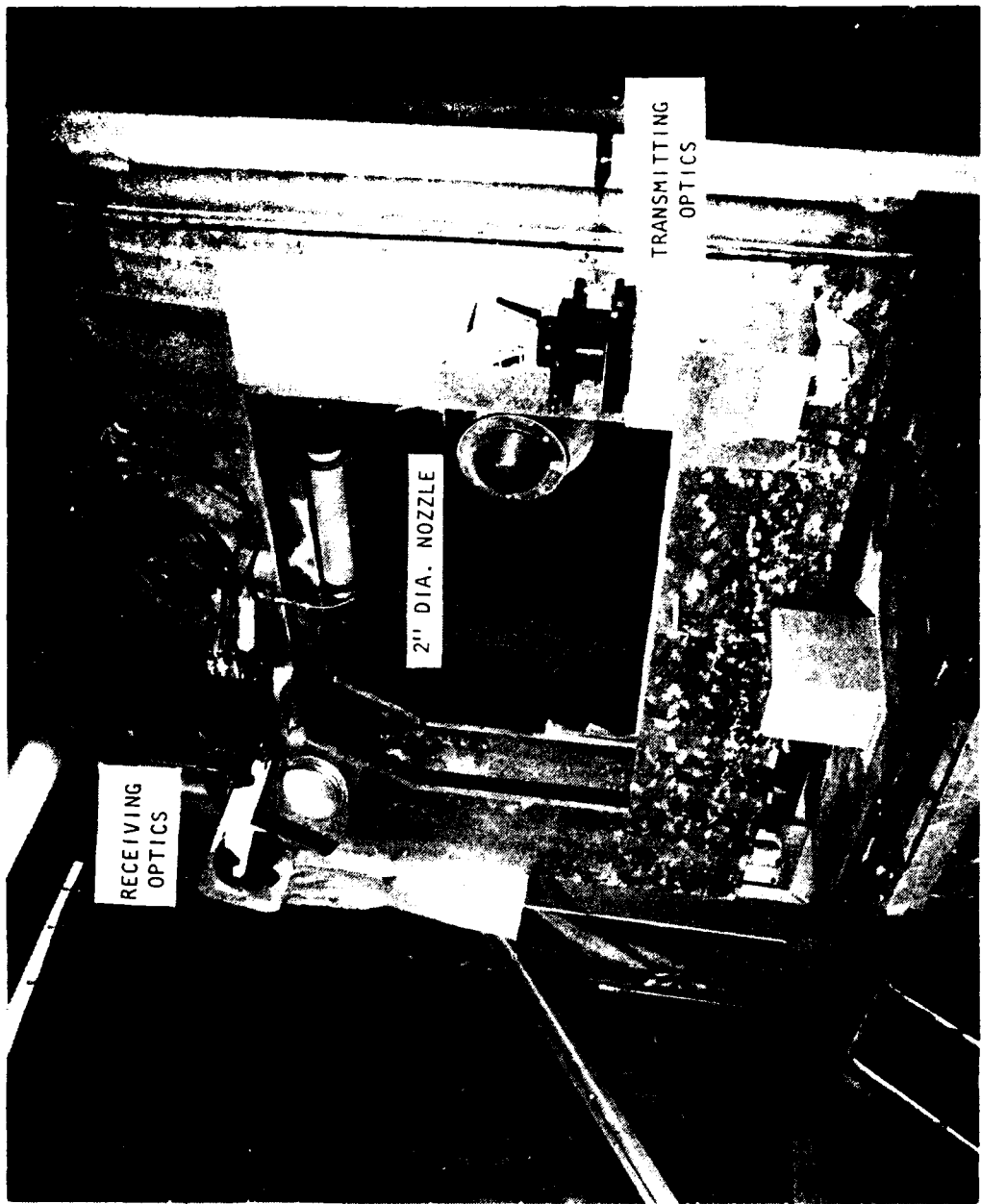


Figure 6.2 Photograph of Jet and LV Set-up

pipe placed on the supporting framework above the measurement volume. The seeds are blown slightly upstream of the measurement volume and are allowed to settle into the ambient air and subsequently mix with the jet flow.

### 6.3 COMPARISON BETWEEN THE LV AND THE HOT-WIRE ANEMOMETER

To assess the full capability of the LV as an instrument for turbulence studies, a series of comparative measurements were made with the LV and a hot-wire anemometer. On comparing the anemometer results of the many researchers working on essentially the same flow set-up, it appears that the quantities measured in different jets do not necessarily match in all details, although trends may be fully reproducible. (This is particularly true of measurements of the fluctuating velocities). For a valid comparison of LV and hot-wire anemometer data, therefore, it was decided that the two sets of measurements would have to be performed wherever possible on the same jet. In the hot-wire measurements undertaken in the present study, only the axial component of velocity was available. Therefore, in the comparison of results in which the radial component is involved, it will be necessary to use results obtained in other studies of circular jets.

#### 6.3.1 Mean Velocity

Figure 6.3 shows the radial distribution of the mean axial velocity at two axial stations in the jet obtained with the LV and with the hot-wire anemometer. The velocity in these figures is normalized by the jet efflux velocity,  $U_j$ , and the radial distance by the nozzle radius,  $r_o$ . The top figure is for  $x/D = 2$ . It is evident that there is good agreement between the two sets of results. The lower figure, for  $x/D = 4.0$ , shows generally good agreement on the inner part of the jet (i.e., for  $r/r_o < 1$ ). In the outer part, the LV data appear to give a higher value. The discrepancy may be explained by considering the constituents of the mean velocity. It may be envisaged that the mean conditions at any point in the jet constitutes an average of the effects of fluid coming to the point from both inside and outside the jet. This would especially be true in the mixing layer of the jet, where there is a constant transfer of mass from one side of the layer to the other<sup>72</sup>. Therefore for a correct assessment of the mean conditions, it would be necessary to have a representative sampling of the fluid from inside and outside the jet. If the seeding is poor from the outside, as in this case, there will be a tendency to bias the mean velocity high. By the same token, insufficient seeding from the inside would bias the readings low. This effect is perhaps brought out more clearly in Figure 6.4 which shows the centerline traverse of the mean velocity derived from the LV with seeding introduced either from the inside or the outside. Also shown is the result from a pitot tube traverse along the same centerline. (The pitot readings have been corrected for errors due to unsteady flow interactions<sup>78</sup>). Seeding from the inside alone tends to bias the results toward higher mean values, and the opposite is true of seeding the jet from the outside. The pitot readings lie between the two sets of LV readings.

It is not clear at present what constitutes a correct balance of internal and external seeding in order to obtain an unbiased measurement of

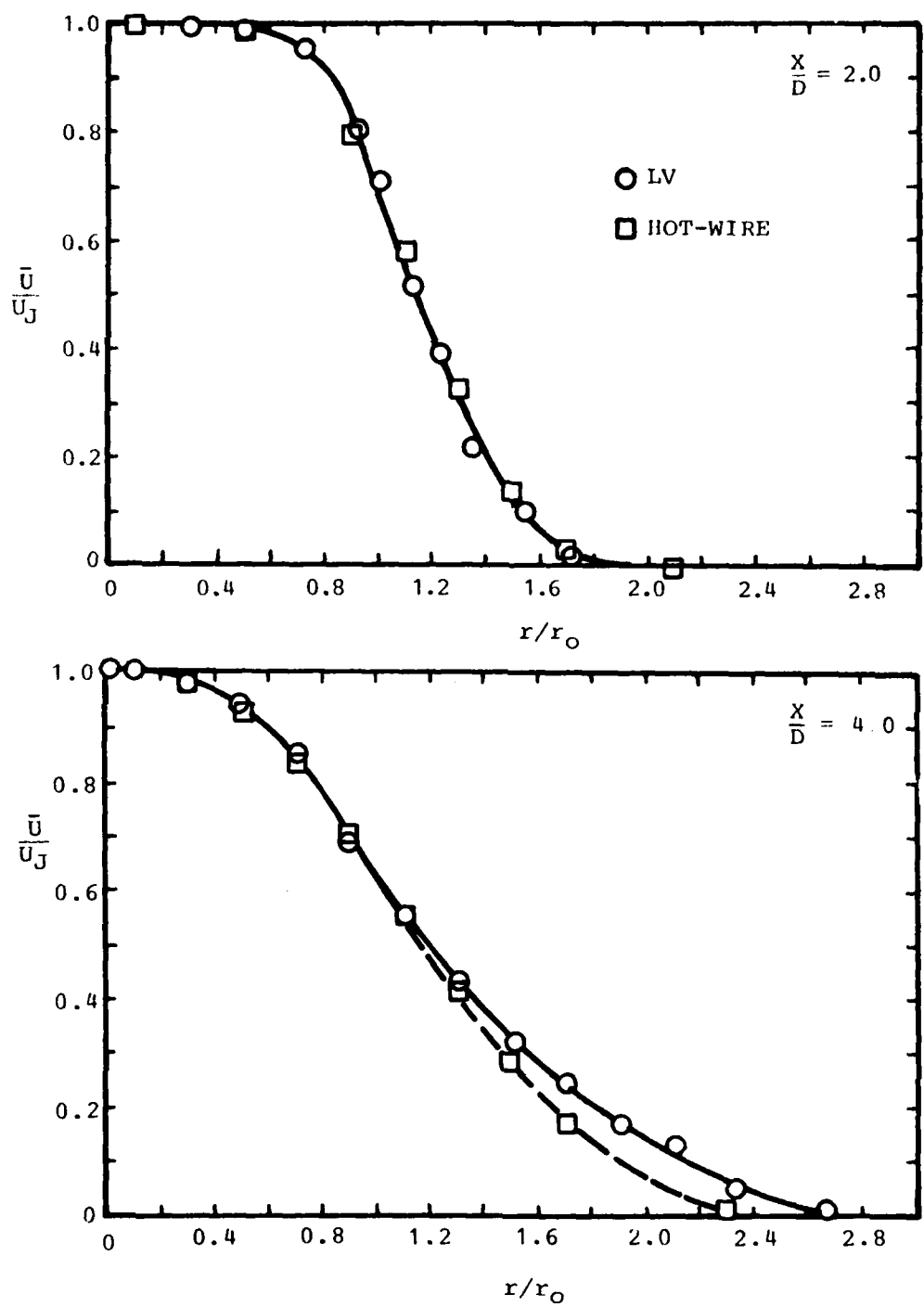


Figure 6.3 Comparison between LV and Hot-Wire Results:  $\bar{U}/U_J$ , ( $M_J = 0.28$ )

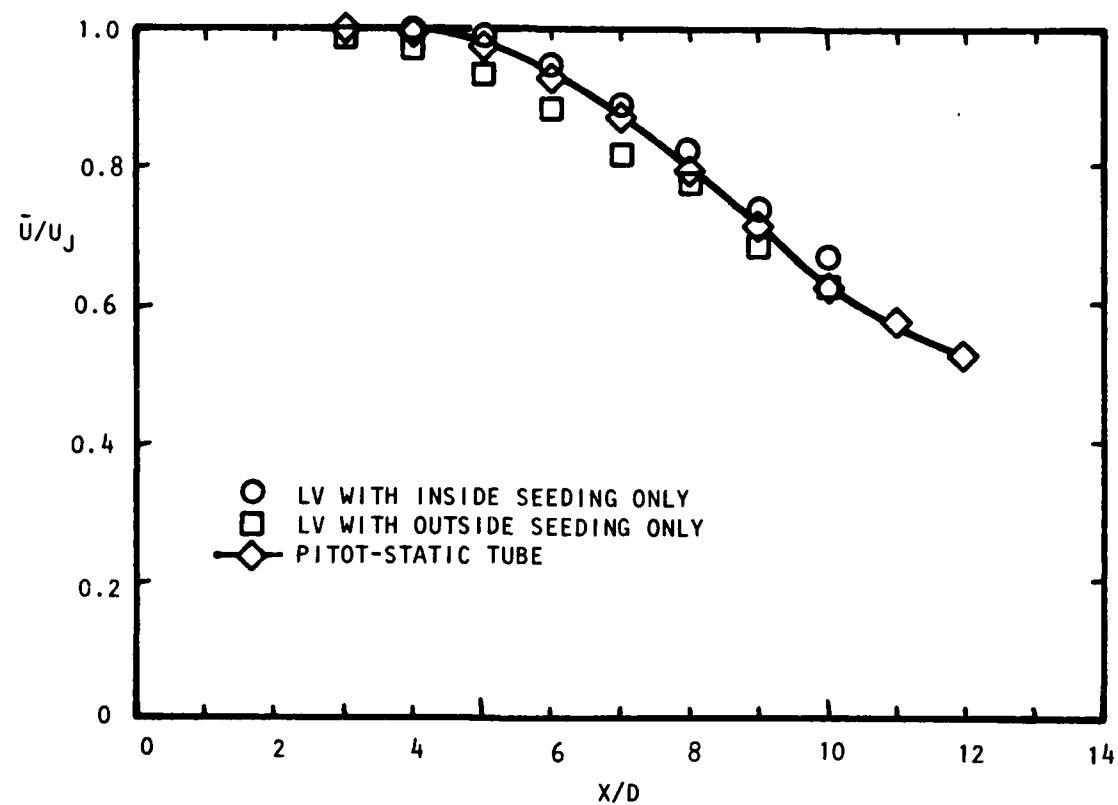


Figure 6.4  $U/U_J$  vs  $X/D$  on Centerline ( $M_J = 0.28$ )

velocity. In the present measurements care has been taken to ensure that seed is introduced internally and externally, but the measurements shown in Figure 6.3 were obtained before a reliable external seeding device was available. Studies are to be made of simple two-component flows, such as the two-dimensional shear layer, to examine more closely the seeding effect.

It should be pointed out that, while mean flow measurements were strongly influenced by whether there was sufficient seeding from inside and outside the jet, the turbulence intensity did not appear to be significantly affected.

### 6.3.2 Fluctuating Velocities

Figure 6.5 shows the radial distributions of the axial turbulence intensity at the same axial stations. The distributions of LV and hot-wire data exhibit the same trends. However, the LV results appear higher in general than those of the hot-wire. The discrepancy varies as we move radially outwards, from about 2½% on the jet centerline to about 4% on the lip line, and falls off in the outer part of the jet.

In the present study, the hot-wire data were not corrected for directional insensitivities such as those alluded to in the Introduction. Based on the correction factors which Hekestad<sup>75</sup> worked out for his own jet, it is estimated that this would raise the levels of hot-wire results by about 1½% in turbulence level in the region of the lip, the correction tapering off to zero on the jet centerline. If one were to allow for these corrections, it seems that there would be a nearly constant discrepancy between LV and hot-wire data of about 2½% in turbulence level spanning the jet from  $r/r_0 = 0$  to 1.6 at least, for the two cases considered here. (At radial positions beyond  $r/r_0 = 1.6$ , it is perhaps not valid to define the turbulence measured by a normal wire as the axial turbulence level, since the mean direction of the flow is not axial).

An analysis was made of the errors which might arise as a result of inaccuracies in the measurement of the velocity with the LV (Appendix 6A). It was ascertained that the measured standard deviation of the velocity,  $\sigma_m$ , would (in the presence of these inaccuracies) be related to the correct standard deviation,  $\sigma$ , by the formula:

$$\sigma_m^2 = \sigma^2 + \frac{a^2}{3} \quad (6-1)$$

if the probability distribution of the inaccuracy is assumed to be rectangular, extending from  $-a$  to  $+a$ .

It has been pointed out in the previous chapter that error testing circuits are incorporated in the electronic processor to validate the instantaneous particle velocities sampled by the instrument. Due to limitations of the electronic components the circuits have an inherent tolerance window, and data of velocity are accepted for analysis if they fell within the limits of the window. Moreover, in the analysis of the statistical quantities, the

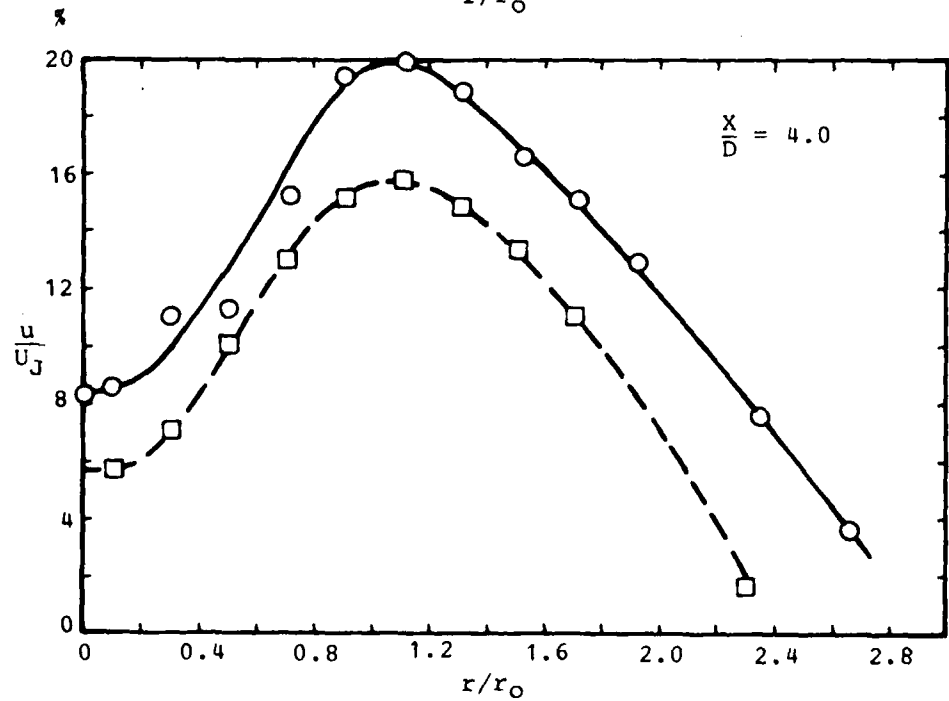
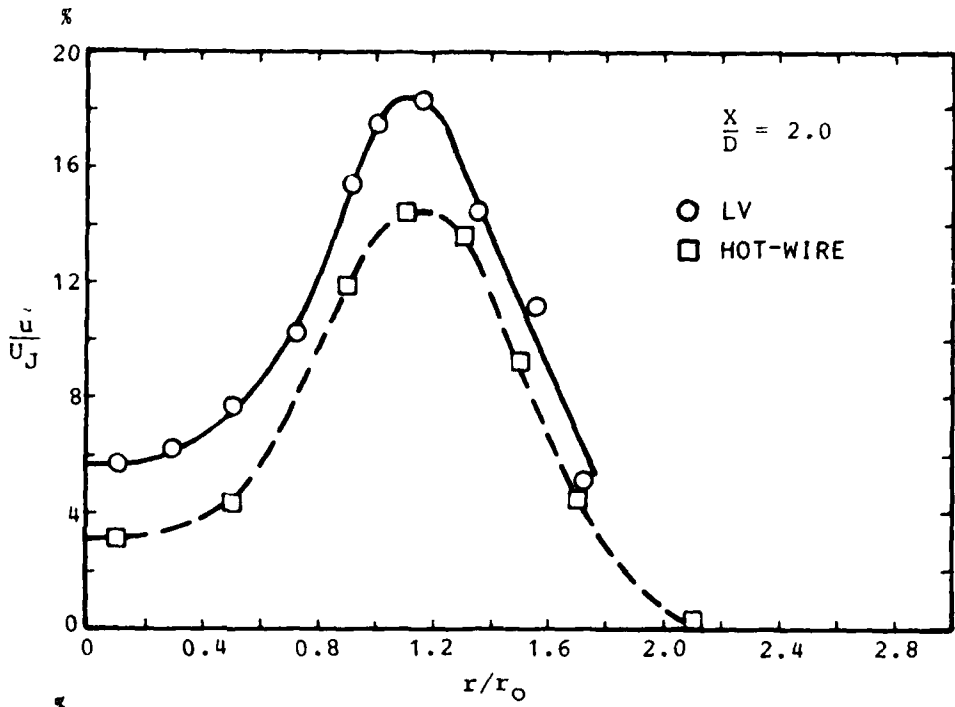


Figure 6.5 Comparison between LV and Hot-Wire Results:  $\frac{u}{u_J}$ , ( $M_J = 0.28$ )

velocities are placed in histograms which have velocity blocks of finite size. This would tend to bias turbulence readings higher also. A more detailed discussion of the processing techniques is given in Reference 80.

When these inaccuracies were evaluated, it was found that, in the worst possible case, the correction would cause an increase of the LV results by no more than 0.6% in turbulence level. Modifications are being made to the processor to further improve the system accuracy.

In the case of the hot-wire anemometer, the extent to which the phenomenon reported by Perry<sup>76</sup> would affect measured turbulence results is not yet clear, but some influence is expected. Further work is planned to assess the differences between LV and hot-wire turbulence measurements.

In the present LV set-up, the radial velocity of the jet can simultaneously be obtained with the axial velocity. Since the principle used in the LV is the same for the measurement of the two components of velocity, it is reasonable to expect that the accuracy of the LV measurements of the radial component of velocity would be the same as that in the measurements of the axial component. No attempt was made in the present program to measure the radial component of velocity with the hot-wire anemometer, partly because of time limitations. Therefore, a direct comparison between LV and hot-wire anemometer measurements of the radial component of velocity was not carried out. In view of the present uncertainties associated with the interpretation of yawed hot-wire anemometer data, a direct comparison at this stage would probably not be very fruitful. An indirect approach at comparison was thus chosen. Figure 6.6 shows comparisons of the turbulence levels of the axial and the radial velocity components obtained in the present set-up with the LV [Figure 6.6(a)], and in another 2-inch diameter jet using hot-wires<sup>81</sup> [Figures 6.6(b)]. In both sets of results, the radial components of velocity are lower than those of the axial. In particular, the peaks in the radial velocity turbulence intensity are about three-fourths as high as those of the axial velocity turbulence intensity. Thus, there appears to be a common trend in the two sets of results.

The velocity covariance  $\overline{u'v'}$ , which is related to the Reynolds stress, constitutes a very important parameter in the description of turbulence, and there is a capability in the present facility for measuring this quantity. However, as this information was not extracted until the latter part of the program, no data are available on the Reynolds stress for the lower jet speed. Figure 6.7 shows a plot of the radial distribution of  $\overline{u'v'}/U_j^2$  for a Mach number of 1.37. It shows  $\overline{u'v'}/U_j^2$  rising from about  $1 \times 10^{-3}$  near the jet centerline to about  $8 \times 10^{-3}$  at the maximum. As an order-of-magnitude comparison, the radial plot of  $\overline{u'v'}/U_j^2$  obtained by Bradshaw *et al*<sup>70</sup> at  $x/D = 3$  for a jet running at a Mach number of 0.3 is also shown. It is encouraging that the trends of the curves compare well. Work is now underway to extract this kind of data for the other flow conditions. The similarity of the two curves suggests that the qualitative behavior of the flow in the mixing layer does not differ much from a subsonic to a supersonic jet. There is more evidence of this in subsequent results.

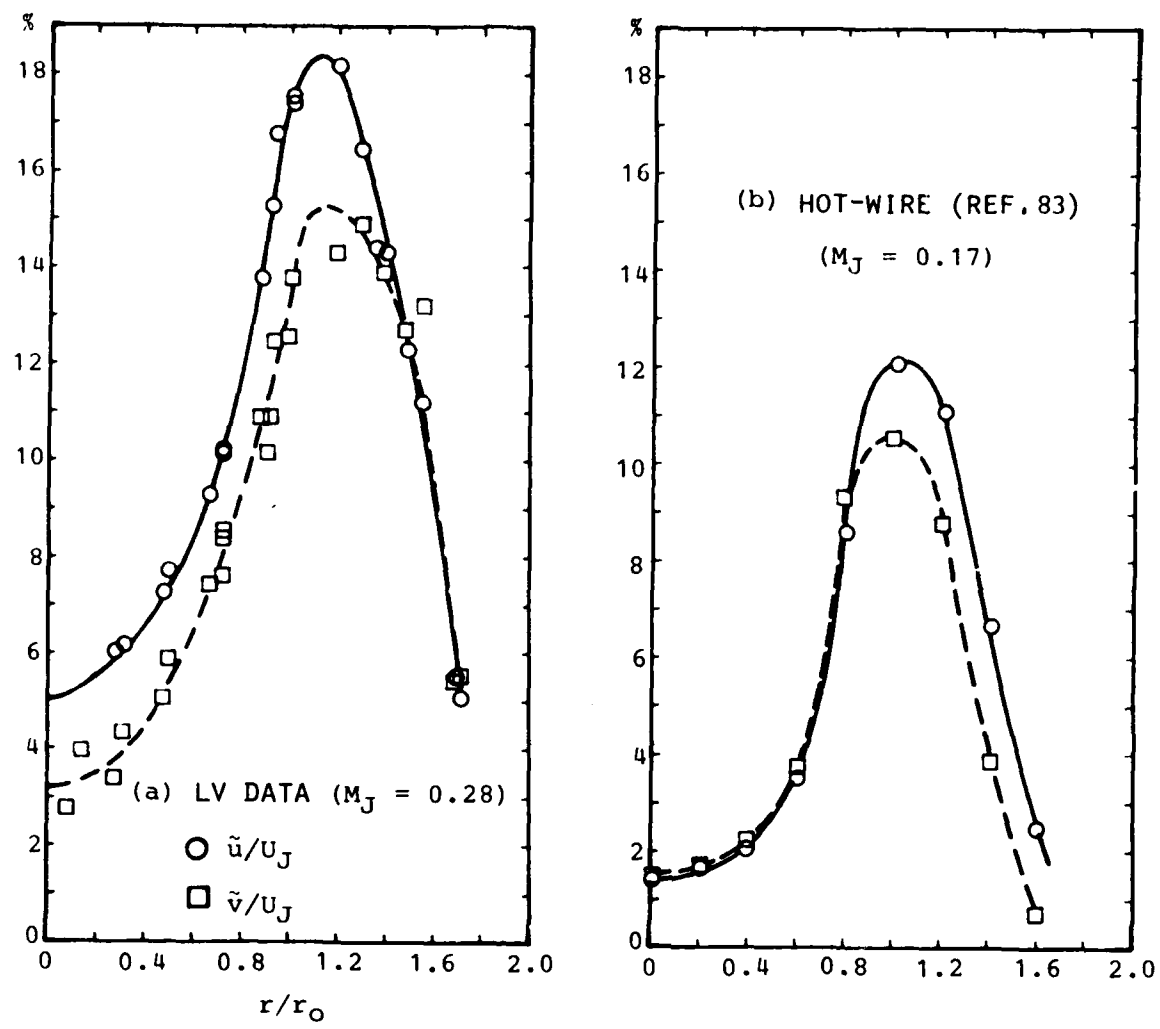


Figure 6.6 Comparing  $\tilde{u}/U_J$  and  $\tilde{v}/U_J$  Distributions (a) LV (b) Hot-Wire  
(Ref. 83),  $X/D = 2.0$

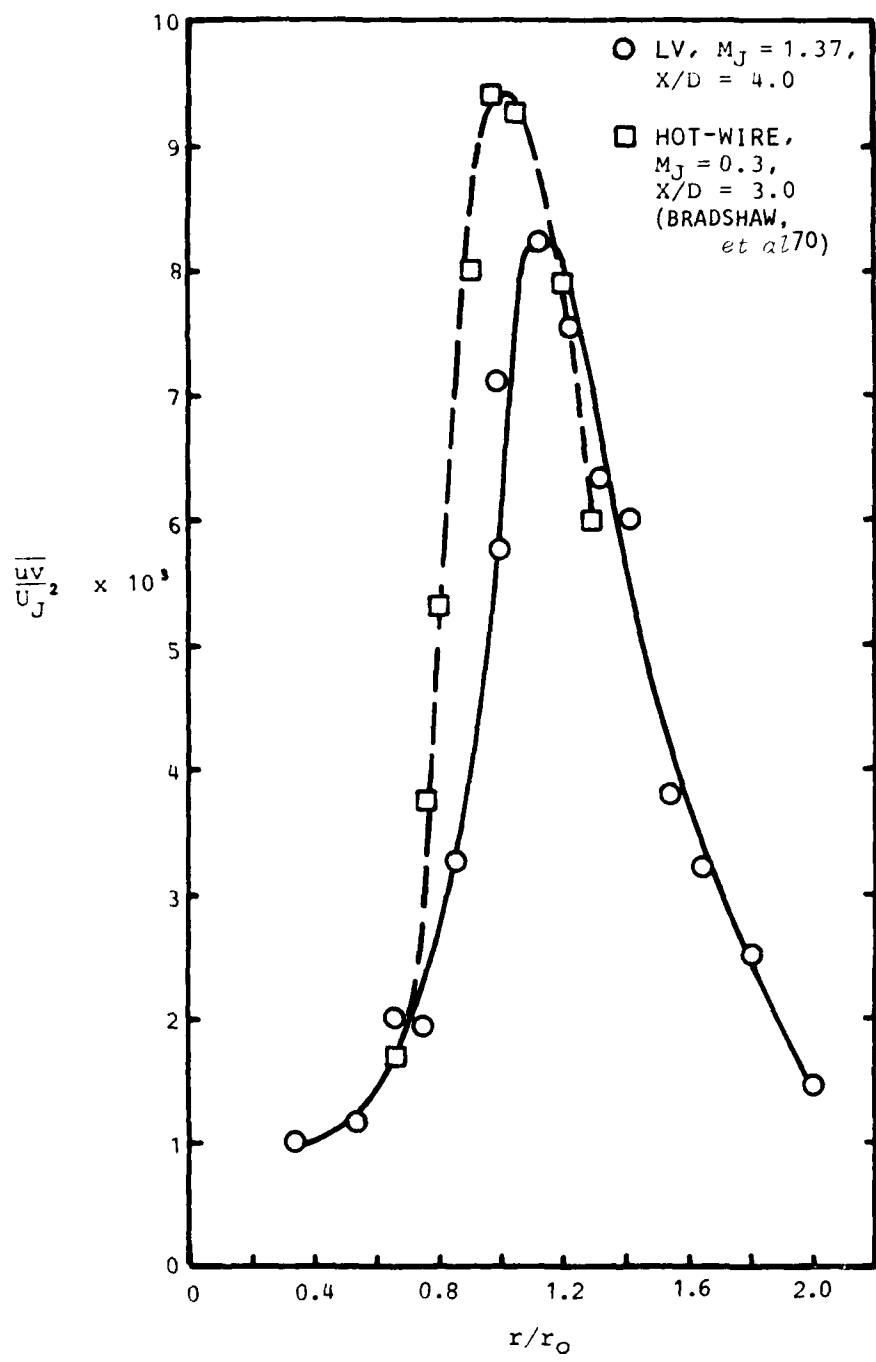


Figure 6.7  $\bar{uv}/U_J^2$  vs  $r/r_0$

### 6.3.3 Probability Distributions of the Axial Velocity Fluctuations

Figure 6.8 shows the probability distributions of the axial velocity fluctuations at a plane two diameters from the nozzle. The successive figures show the distributions at increasing radius from the centerline, and they show identical trends for LV and hot-wire data. Considering the first row of figures, the distributions begin with a nearly symmetrical form. Moving outward, the distributions assume a shape with a negative skewness. Then, further out they become symmetrical again at  $r/r_0 = 1.0$ . This behavior was reported in some detail by Fisher and Davies<sup>82</sup>. Still further outward in the jet (beginning with the first distribution on the second row), the probability distributions become positively skewed. Although the LV and hot-wire anemometer both show this tendency, careful scrutiny of the LV and hot-wire distributions at these locations show that, while the LV indicates that there are instantaneous velocities in the negative direction, the hot-wire anemometer, which is insensitive to the velocity vector direction, records these values as positive. This results in a steep rise in the probability density near zero velocity. The effect becomes worse as the proportion of negative-going velocities increases. It is evident from these LV results that there is a sizable proportion of negative velocities in the outer parts of the jet, further casting doubt on the accuracy of hot-wire anemometer data in this part of the jet.

Differences in the shapes of these probability distributions are quantified by the skewness and kurtosis, which are third and fourth moments of the distributions, suitably normalized by the standard deviation. Figure 6.9 shows the plots of the skewness and kurtosis as a function of radial position. Negative values of  $\eta^*$  essentially represent radial positions inside the nozzle lip line, and positive values of  $\eta^*$  outside the lip line. Also shown are results reported by Davies<sup>83</sup> for a 1-inch-diameter jet obtained with a hot-wire anemometer. The present results exhibit the same behavior as that indicated by the curves given by Davies. Wherever a deviation exists between the two sets of data, the LV always shows the lower magnitude. Part of the discrepancy in the outer part of the jet is brought about by the rectification of the hot-wire velocity signal. However, in view of the previous discussion on the relative accuracies of LV and hot-wire measurements of turbulence, an extensive comparison of the precise magnitudes of skewness and kurtosis obtained with the two different facilities would not be appropriate at this time. Until a better understanding of the LV as well as the hot-wire measurements is available, we will be limited to comparing only the trends of these results.

### 6.3.4 Autocorrelations and Spectra

The autocorrelation function of the axial velocity fluctuations on the axis of the jet two diameters from the nozzle is shown by the full line in Figure 6.10. The truncation of the first trough of the oscillating shape is not a real effect but results from a graph plotter limitation. Also shown are results given by Davies<sup>83</sup>, adjusted for difference in speed and diameter according to the Strouhal number criterion. Both correlation functions have a value of one at zero time delay. There is very good agreement between the two results.

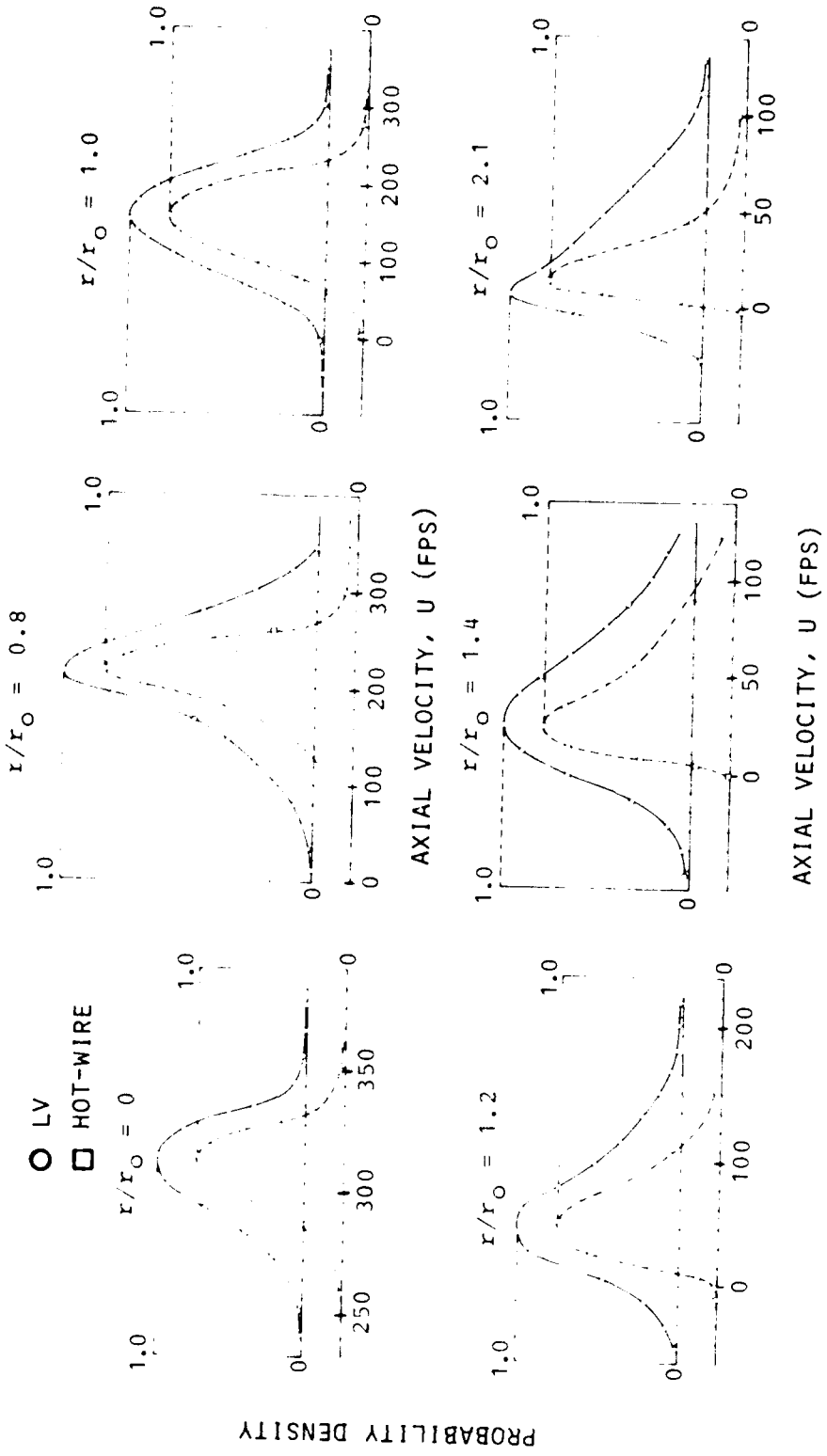


Figure 6.8 Probability Density of Axial Velocity Fluctuations ( $X/D = 2.0$ )

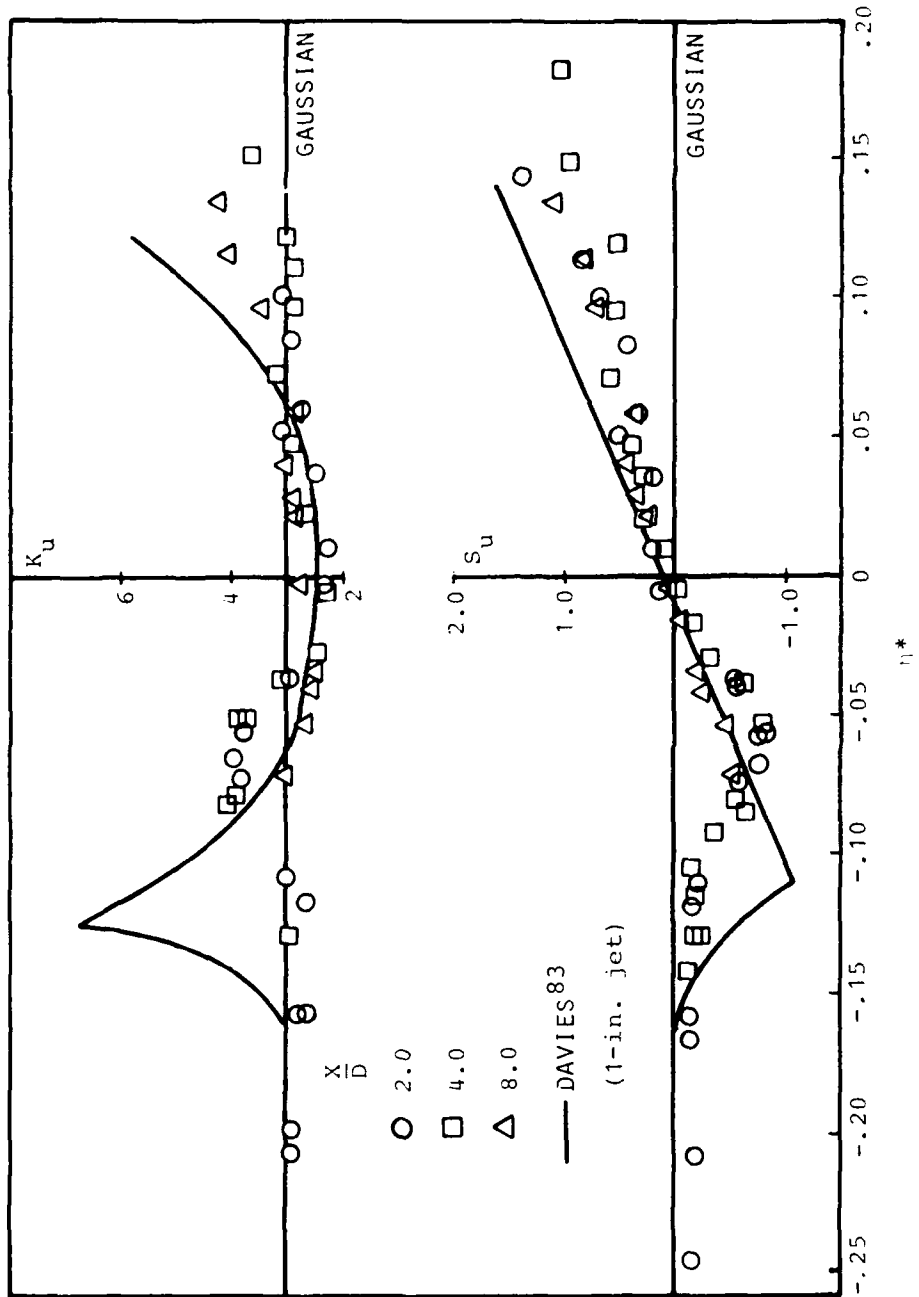


Figure 6.9 Probability Moments of Axial Velocity Fluctuations ( $M_J = 0.28$ )

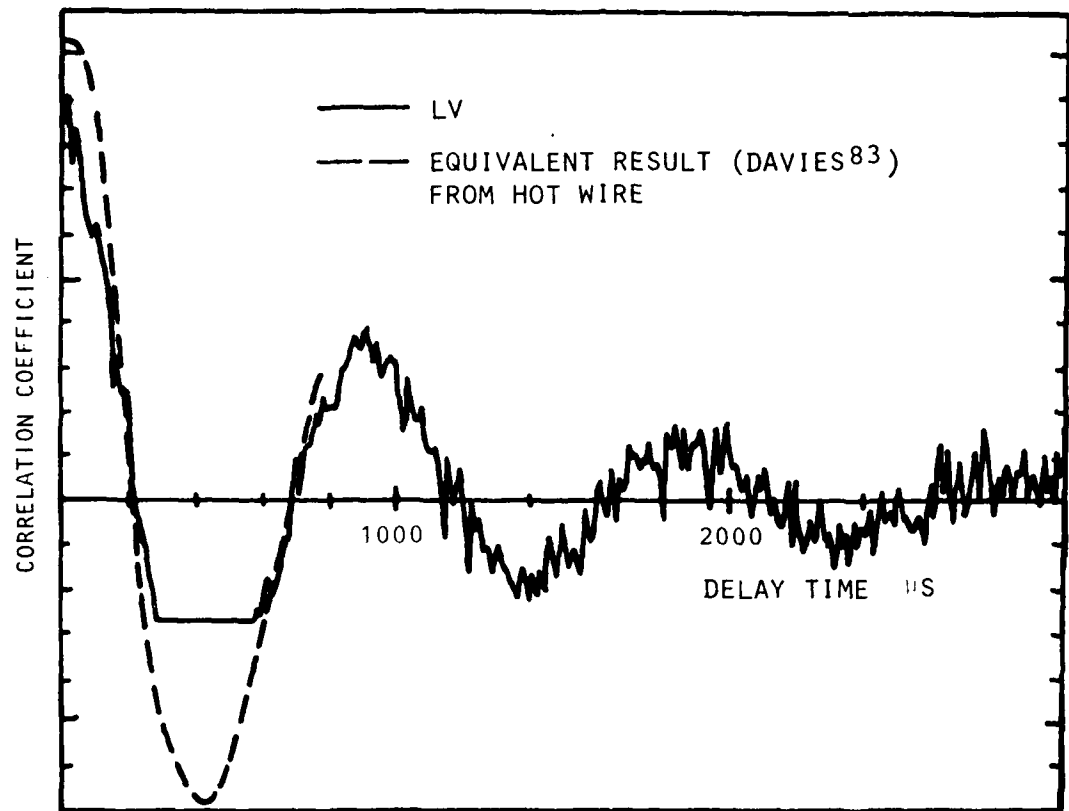


Figure 6.10 Comparison of Correlograms from LV and Hot-Wire Measurements

Figure 6.11 shows the spectrum of the axial velocity fluctuations obtained with the LV at the same point in the jet. The spectrum shows a peak at the frequency of about 1 kHz, which on normalizing with the jet efflux velocity,  $U_j$ , and the nozzle diameter,  $D$ , gives a Strouhal number ( $fD/U_j$ ) of 0.5, which is a well established number from hot-wire measurements for this part of the jet<sup>70,79,81</sup>. The equivalent hot-wire spectrum taken under the same conditions in the same jet is also shown. Very good agreement is achieved between the two spectra. The only significant difference is that LV results tend to be a little higher at the high-frequency side of the peak. This is the result of an insufficient sampling rate, a deficiency which has been rectified.

Figure 6.12(a) shows a family of curves of the spectra of axial velocity fluctuations at a number of radial positions in the jet. The results were obtained at the same axial position as for the spectrum above. As the radial position is increased, the peak in the spectrum slowly dissolves into a flat spectrum. This is reminiscent of similar displays of spectra obtained with a hot-wire anemometer. A family of hot-wire spectra, obtained under the same jet flow conditions as above, is shown for comparison in Figure 6.12(b).

It has been proposed, based on hot-wire measurements that the peak spectral frequency scales with the jet efflux velocity and the diameter of the jet. Use was made of this fact in the adjustment made earlier of the Davies' Autocorrelation curve. Figure 6.13 shows the spectra at two different speeds, and it may be seen that the spectral peak shifts to a higher frequency as the jet speed is increased. The Strouhal number in each case worked out to be 0.5, as was expected.

### 6.3.5 Summary

There is sufficient evidence that the LV is a suitable and reliable instrument for measuring the mean and fluctuating velocities in the flow field of a jet. The mean velocities can be measured accurately if care is taken to ensure a balanced supply of seeding from the inside and the outside of the jet. The turbulence intensities can also be measured, though there is a discrepancy of about 2% in the measured intensity magnitude between the LV and the hot-wire anemometer. The absolute accuracy of LV and hot-wire anemometer measurements will be assessed in future comparisons using simple flow configurations. The available evidence suggests that if discrepancies in hot-wire data are as high as recent experiments<sup>76</sup> have indicated, the uncertainty of the LV data would be substantially less than 2%. Auto-correlations and spectra are also obtainable.

Thus, all the basic characteristics of the jet structure which are now measured with a hot-wire anemometer, with the exception of conditionally sampled measurements, have been measured with the present LV system. In the work to be described in the next section, this capability was exploited and measurements were made in the jet with conditions extending into the supersonic range.

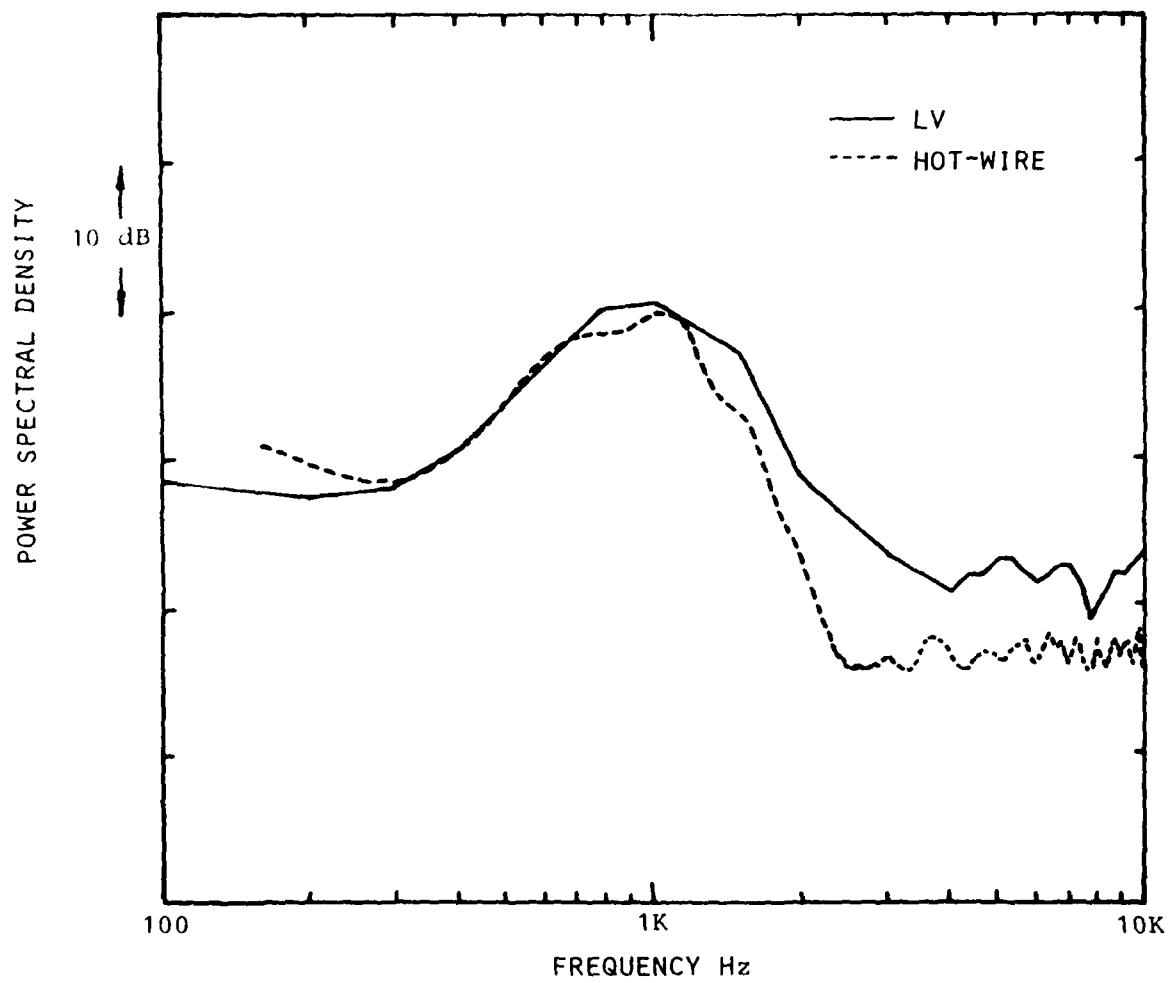


Figure 6.11 Comparing LV and Hot-Wire Spectra ( $M_J = 0.28$ )

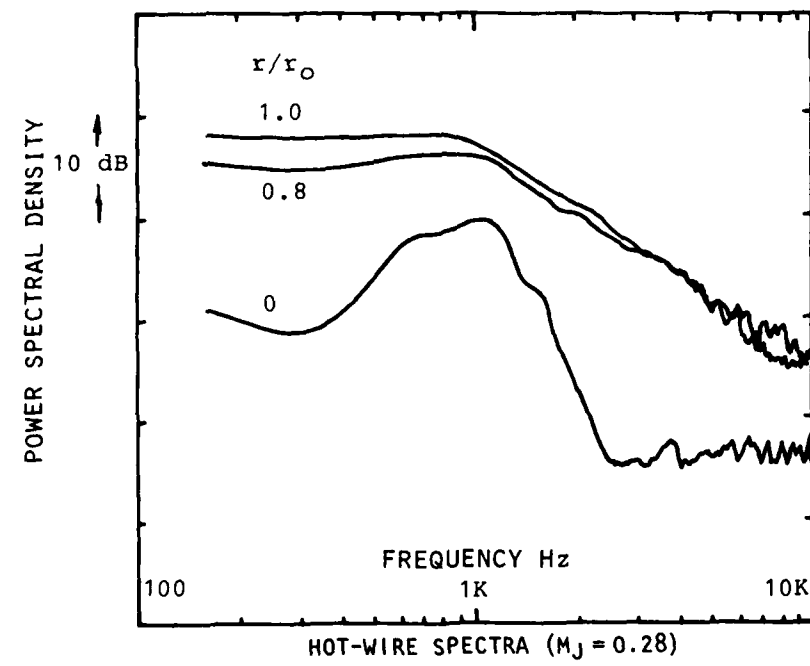
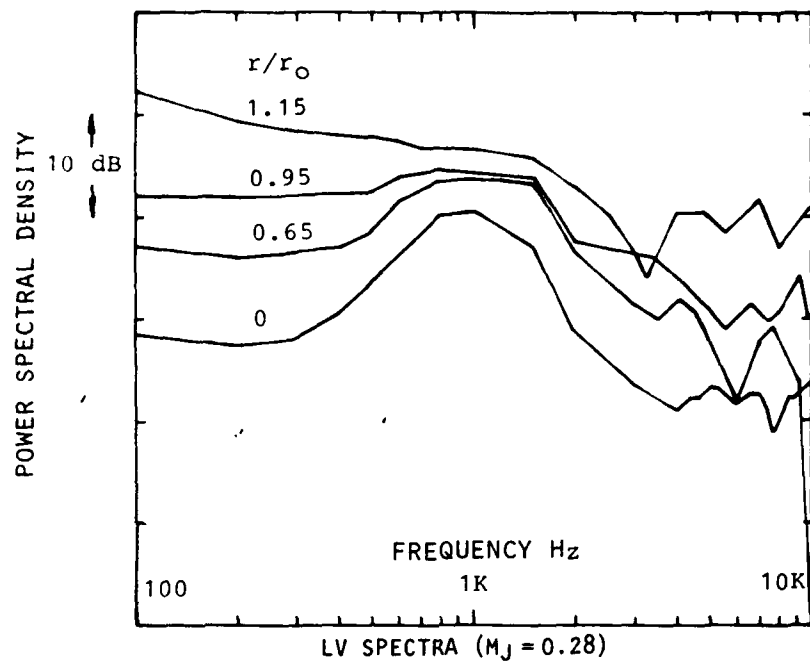


Figure 6.12 Spectra at Various Radial Positions ( $X/D = 2.0$ )

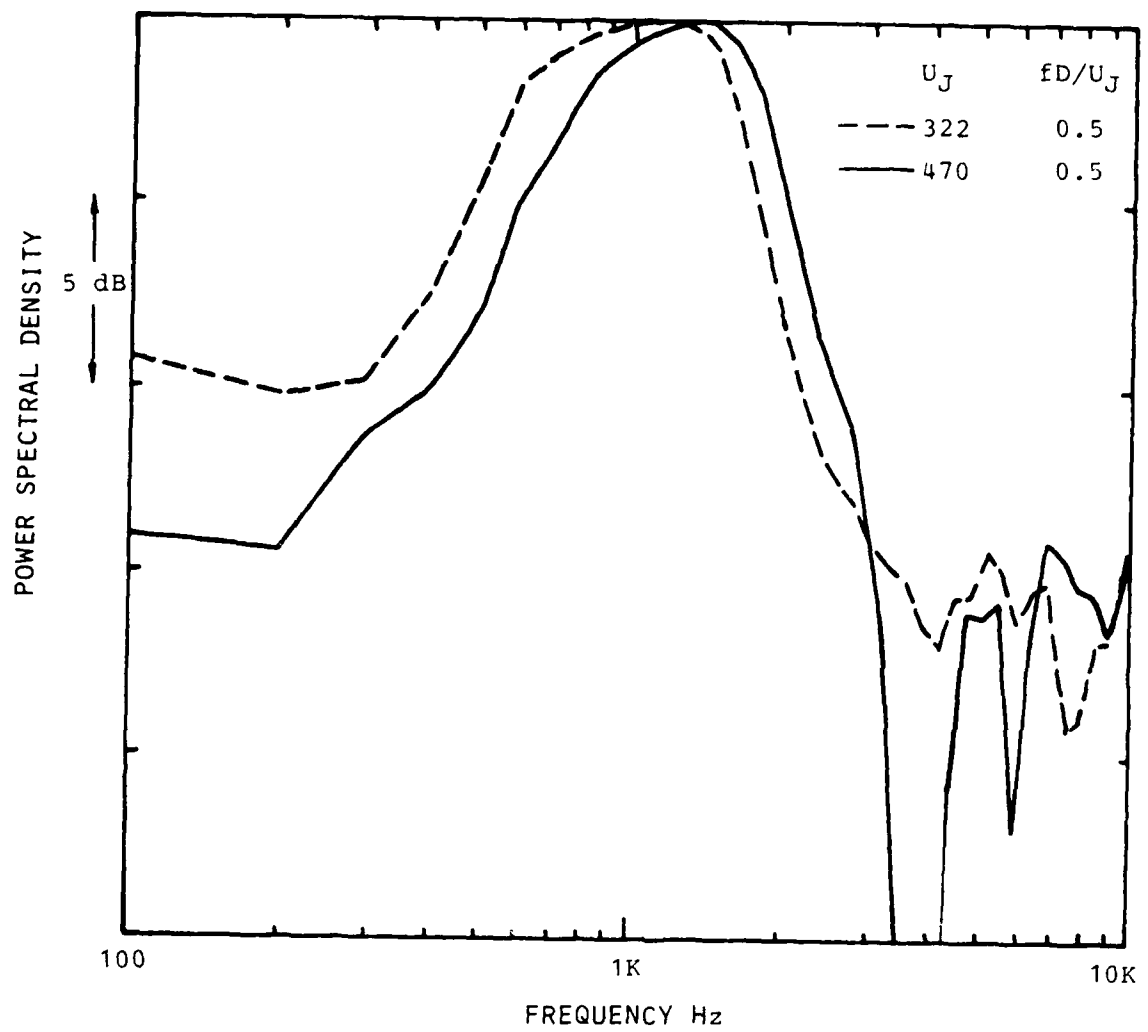


Figure 6.13 Comparing LV Spectra at Two Speeds ( $X/D = 2.0$ , Jet Centerline)

## 6.4 MEASUREMENTS OF THE JET FLOW CHARACTERISTICS

The work discussed here is an attempt to map the various relevant characteristics over the flow field of the jet. The aim is to observe how these flow characteristics vary with position in the jet, and how changes in Mach number and temperature affect the distribution of these characteristics.

Radial distributions of the flow characteristics will first be presented to illustrate in general how these quantities will change over the jet flow field. An attempt will next be made to achieve some degree of collapse of these results so that the effects of Mach number and temperature may be more clearly displayed. Results of the variation of the flow quantities on the jet centerline will next be presented, reinforcing some of the insights gained from the radial distributions. Finally, a review will be made of the conclusions regarding Mach number and temperature effects, and an attempt will be made to obtain some empirical formulation for the effect of Mach number.

### 6.4.1 Radial Distributions

#### 6.4.1.1 Mean velocities

Figure 6.14 shows the radial distribution of the mean axial velocity at a Mach number of 0.28 for three axial stations along the jet. The first two axial stations lie within the region where the potential core is known to exist, and the third station is about two core lengths downstream. The radial distributions exhibit a familiar behavior, with the distributions spreading radially with downstream distance and the centerline velocity falling after the potential core is passed.

Similar trends may be observed in Figures 6.15, 6.16, and 6.17 which respectively represent the results obtained with isothermal jets at Mach numbers of 0.9 and 1.37, and the heated jet at a Mach number of 0.9. A careful study of each of these figures shows that the effect of the increasing spread of the distribution with downstream distance results in a lowering of the velocities on the inner side of the jet, and a lifting of the velocities on the outer side.

For comparison, the LV results presented by Knott and Mossey<sup>84</sup> of the General Electric Company are plotted in Figure 6.18. Their LV works on basically the same principle as that used here, using the burst-counter approach. The results, obtained at a Mach number of 0.5, show a tendency for decreasing velocities on the inside of the jet as the axial distance is increased, but the expected velocity increase in the outer region of the jet is less well defined. It is suspected that this lack of definition on the outer side may be associated with some problem in their method of seeding the jet.

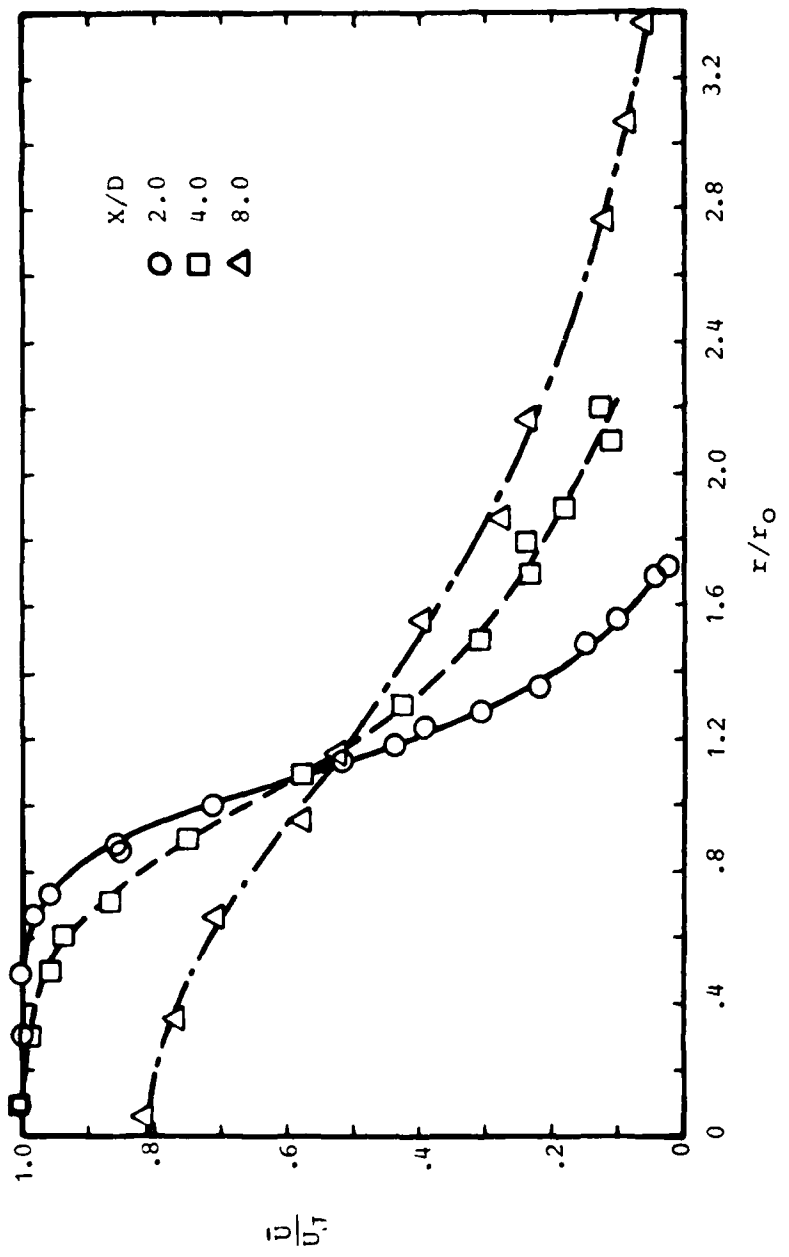


Figure 6.14  $\bar{U}/U_J$  vs  $r/r_o$  ( $M_J = 0.28$ )

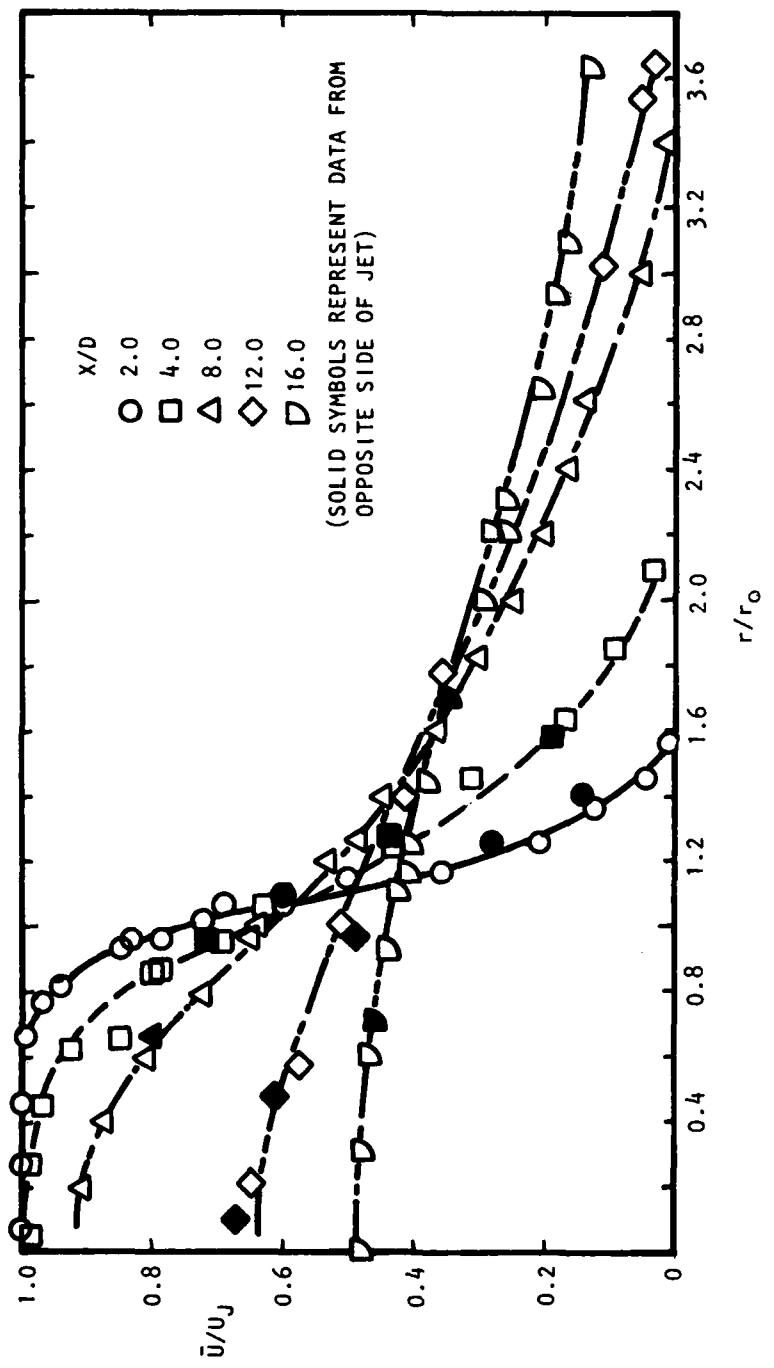


Figure 6.15  $\bar{U}/U_J$  vs  $r/r_0$  ( $M_J = 0.9$ )

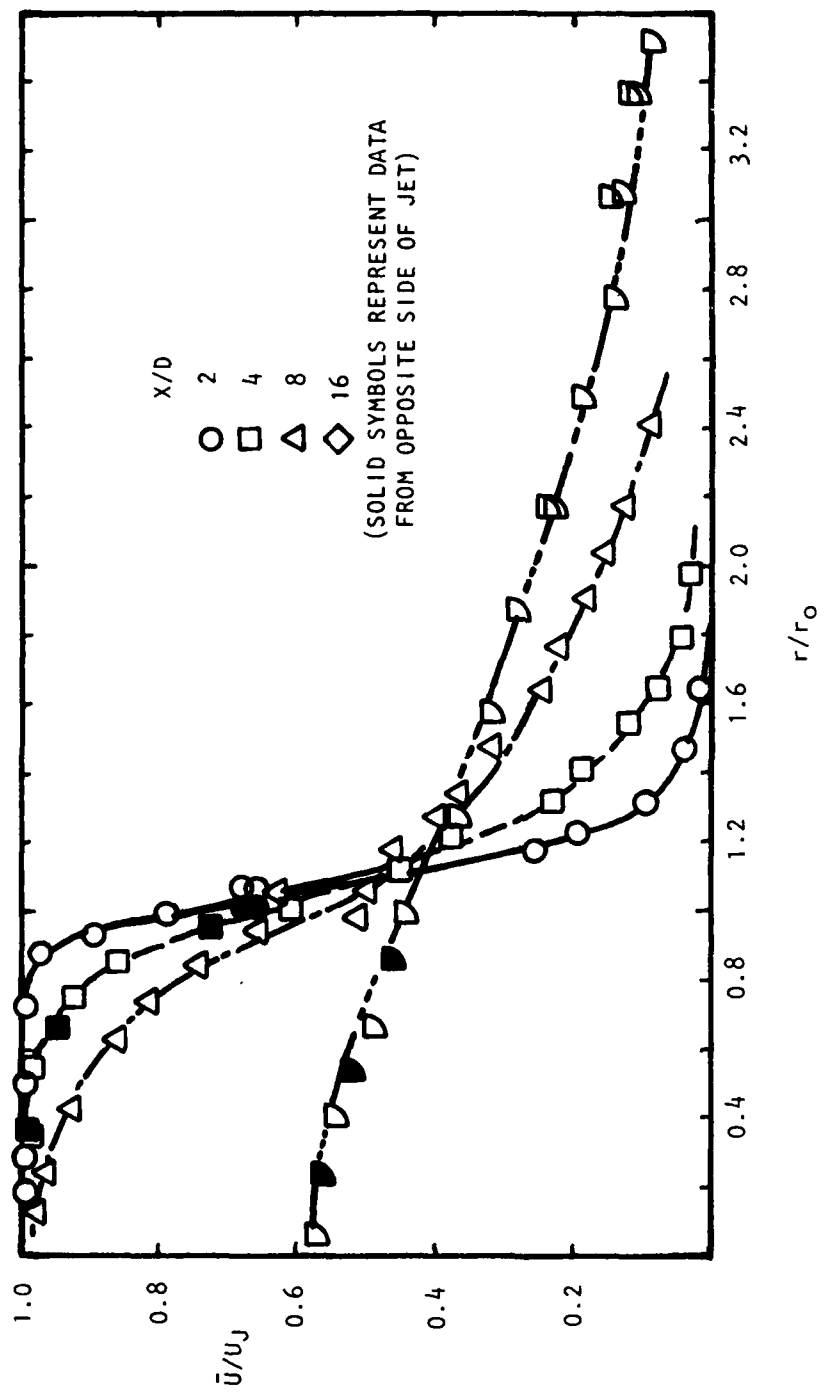


Figure 6.16  $\bar{U}/U_J$  vs  $r/r_0$  ( $M_J = 1.37$ )

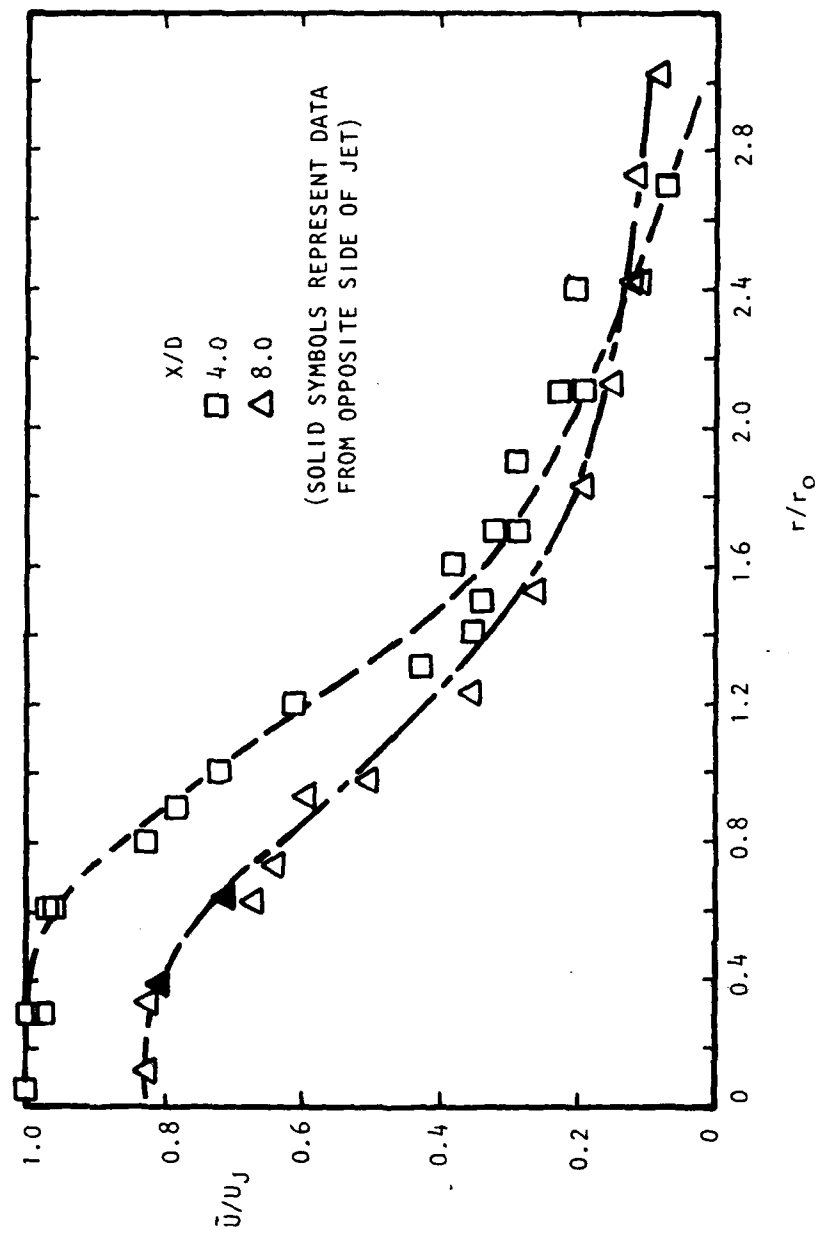


Figure 6.17  $\bar{U}/U_J$  vs  $r/r_0$  ( $M_J = 0.9$ , HEATED)

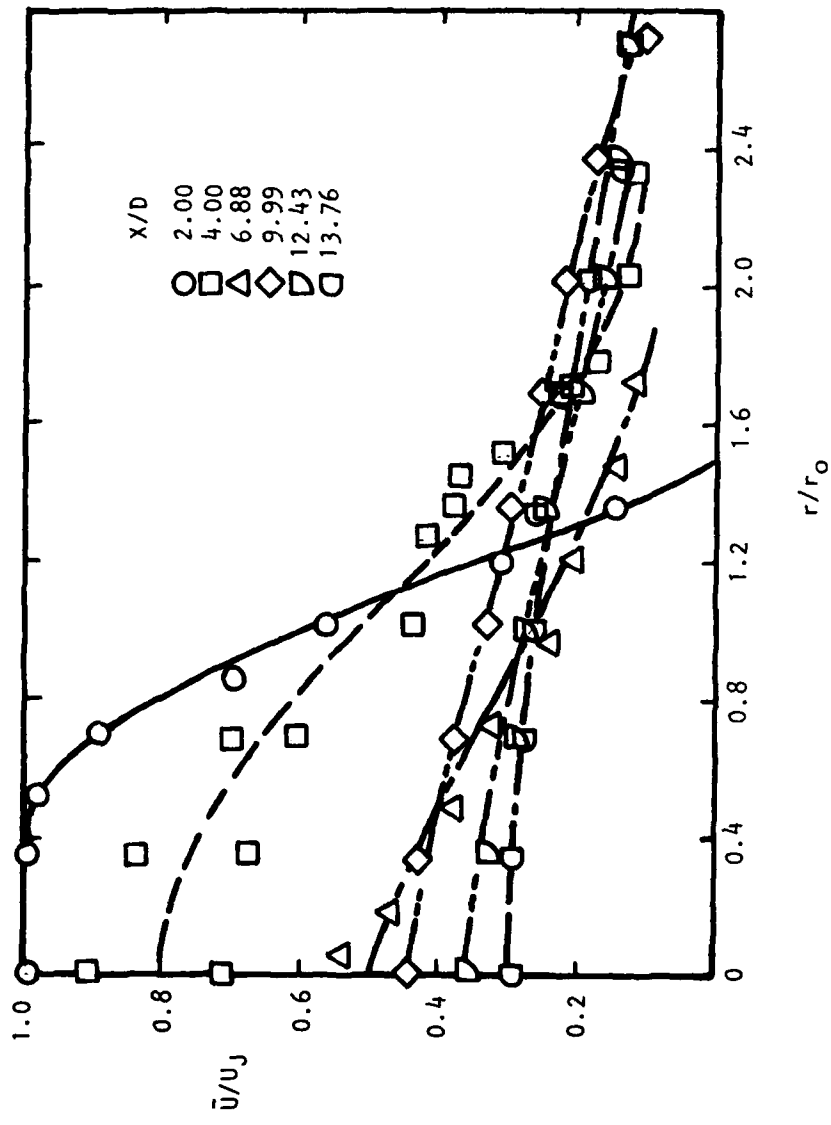


Figure 6.18  $\bar{U}/U_J$  vs  $r/r_O$  (G.E. Data<sup>84</sup>,  $M_J = 0.5$  Cold)

Figures 6.19 and 6.20 show the radial distributions of the mean radial velocity at different axial positions for jet Mach numbers of 0.28 and 0.9, respectively. For axial stations close to the nozzle, the mean radial velocity is zero in the potential core, and rises to a peak just outside of the lip line. The positive sign indicates a mean outflow of fluid from the potential core into the mixing region. The mean radial velocity then falls, and there are indications that it would fall to negative values in the outer region of the jet. In harmony with the concept of a spreading mixing layer in the jet, the distributions increase in radial extent with axial distance, and the peaks move gradually outward. The point where the change in sign takes place also appears to move outward. The magnitudes of the peaks fall with axial distance. Similar distributions may be found in the work by Sami et al 85. Given the results of the mean axial velocity and the requirement of continuity, the above results are as might be expected. However, no computations were carried out to relate the mean axial velocity to the radial velocity through the use of the continuity equation.

Figure 6.21 shows the radial distributions of mean radial velocity at an axial station  $x/D = 4.0$  for different Mach numbers. The outstanding feature is that, although the distributions were obtained at the same axial station, the distributions have quite different widths. A potential core is clearly seen to exist in the results for Mach numbers of 0.9 and 1.37. As will be shown later, the shear-layer thickness at any given axial station decreases with increasing Mach number, and this must be reflected as an increase in the potential core length.

#### 6.4.1.2 Fluctuating velocities

Figure 6.22 shows the radial distribution of the axial turbulence intensity at a Mach number of 0.28 for three axial stations. The value of the turbulence intensity on the axis rises with distance downstream, and the radial extent of the distributions increases with axial position in a way similar to that observed for the mean velocity. These qualities are also present in Figures 6.23 to 6.25, which give the results of measurements made on the isothermal jets at Mach numbers of 0.9 and 1.37 and on the heated jet at a Mach number of 0.9.

In considering the peaks of the curves in more detail, two features emerge. First, it appears that there is a general indication that the magnitude of the peaks on the curves falls as we move downstream, especially as the potential core is passed. Second, there is a suggestion that the peaks would move inward towards the jet centerline with increase in axial distance. It is interesting to note that, in the results of the mean axial velocity distribution, if the locus is traced out of the points where the mean velocity is one-half of the jet efflux velocity, this will show a curve which moves towards the jet centerline also. This is illustrated in Figure 6.26, which shows plots of the loci of the peak turbulence intensity and the half-velocity points. This phenomenon is a characteristic which will be discussed in a coming publication.

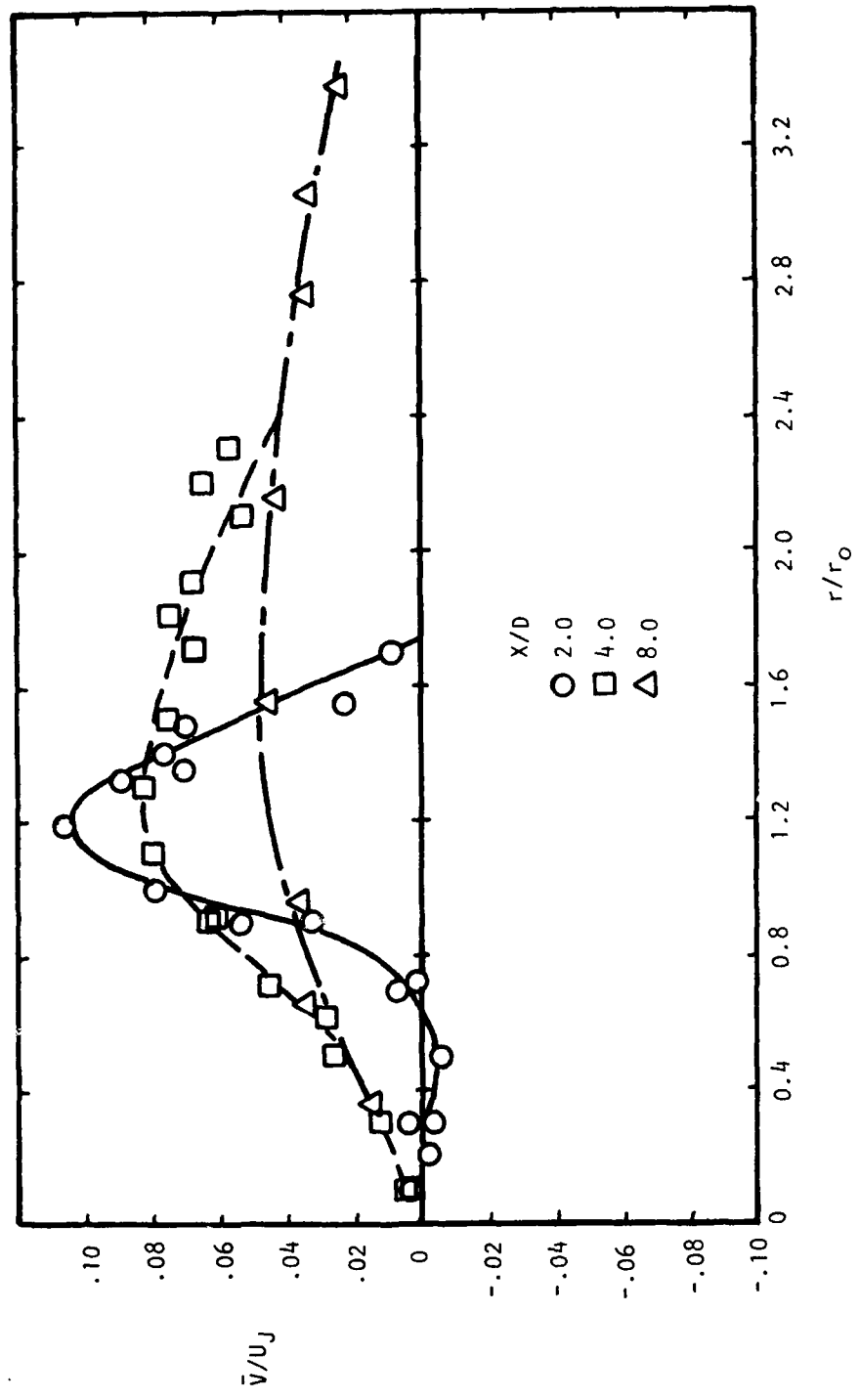


Figure 6.19  $\bar{V}/U_J$  vs  $r/r_O$  ( $M_J = 0.28$ )

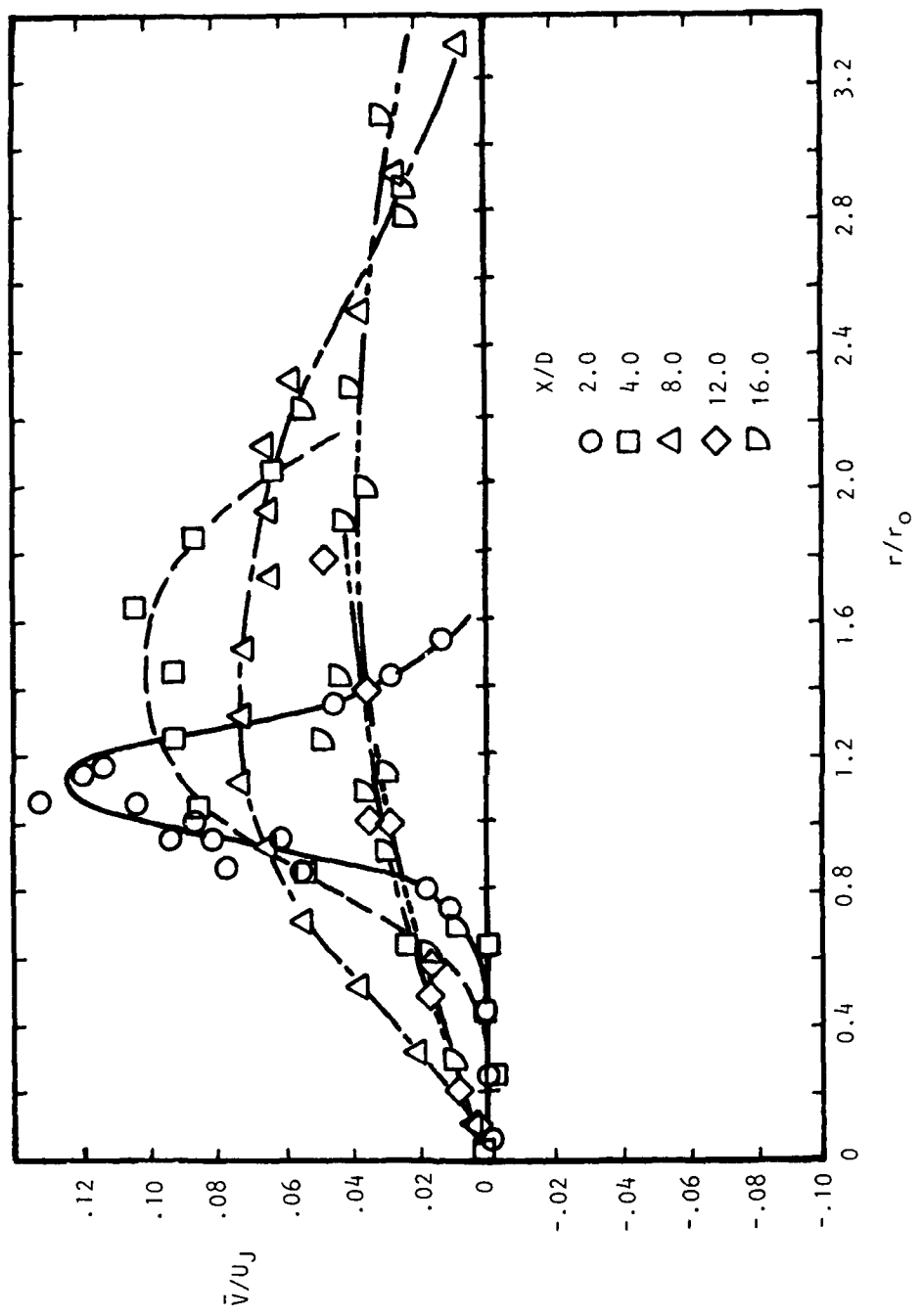


Figure 6.20  $\bar{V}/U_J$  vs  $r/r_O$  ( $M_J = 0.9$ )

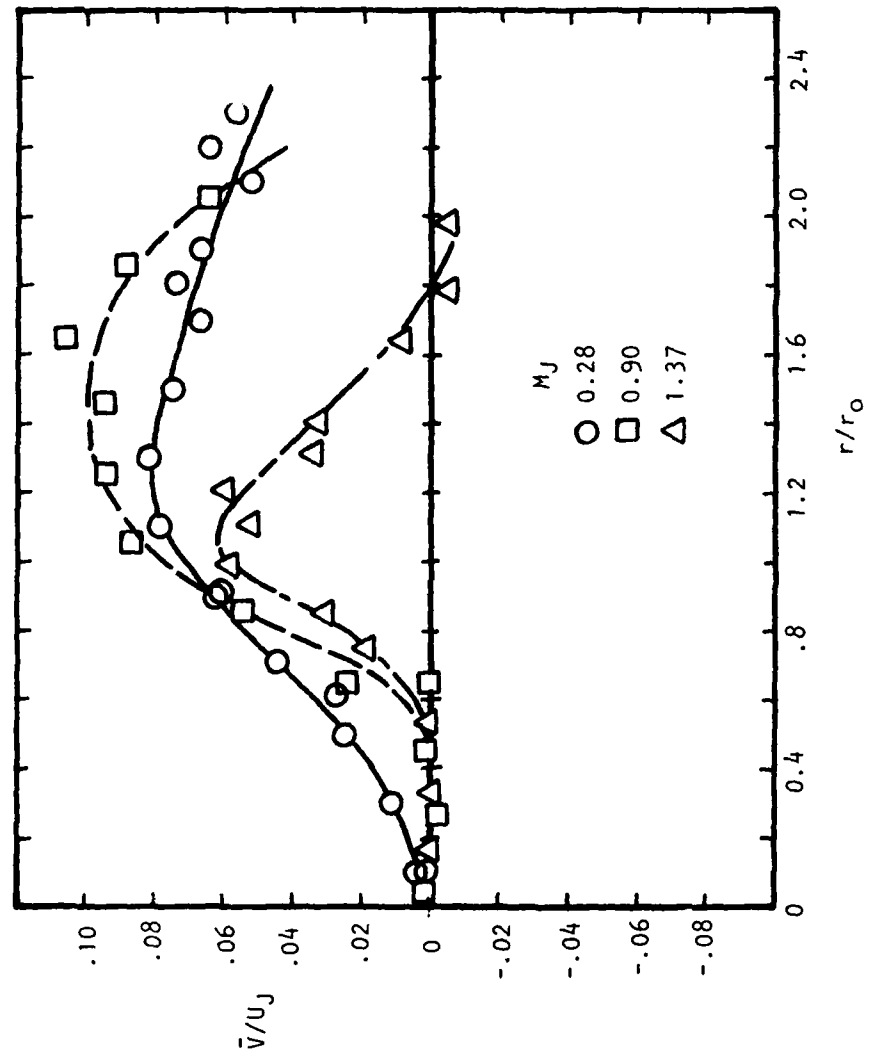


Figure 6.21  $\bar{v}/U_J$  vs  $r/r_O$  ( $x/D = 4, 0$ )

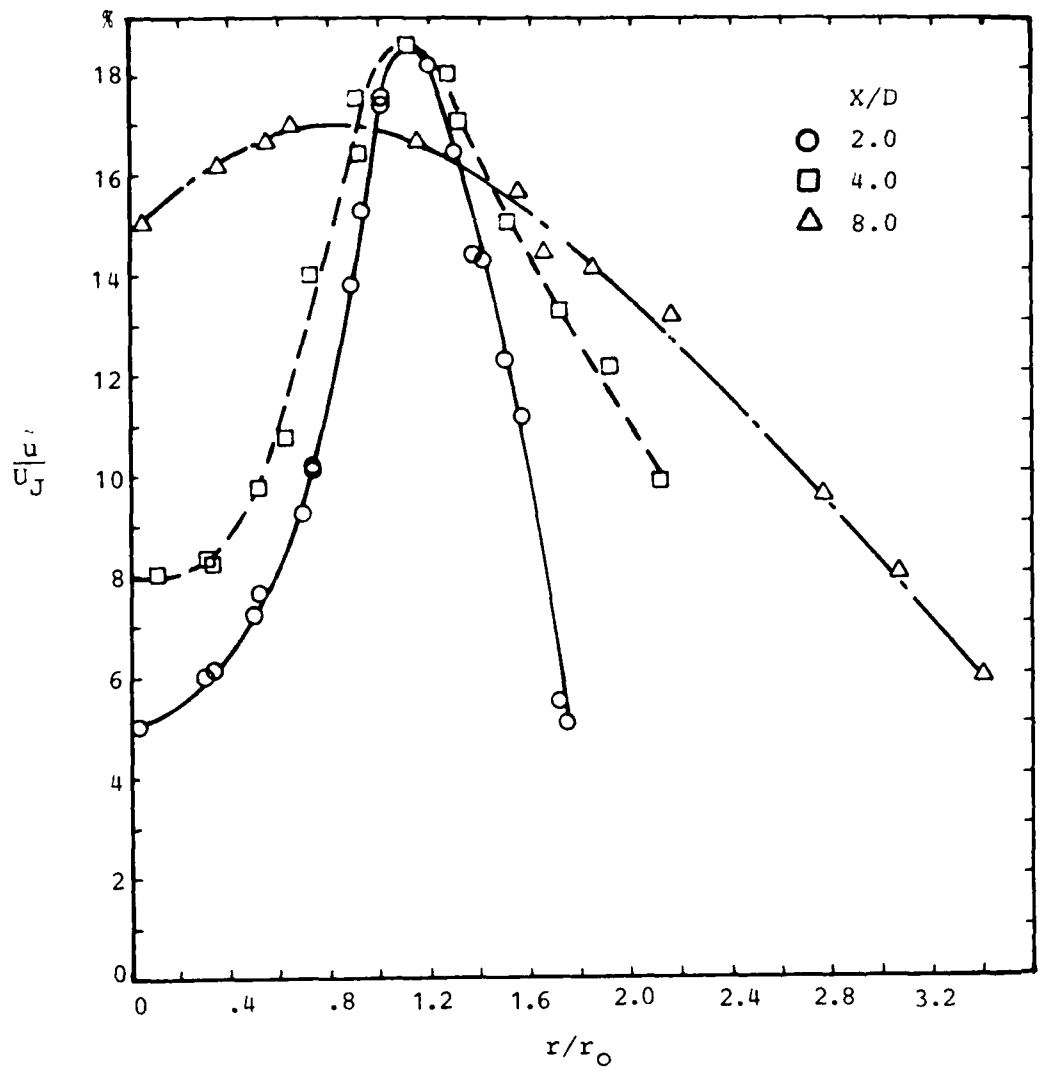


Figure 6.22  $\tilde{u}/U_J$  vs  $r/r_o$  ( $M_J = 0.28$ )

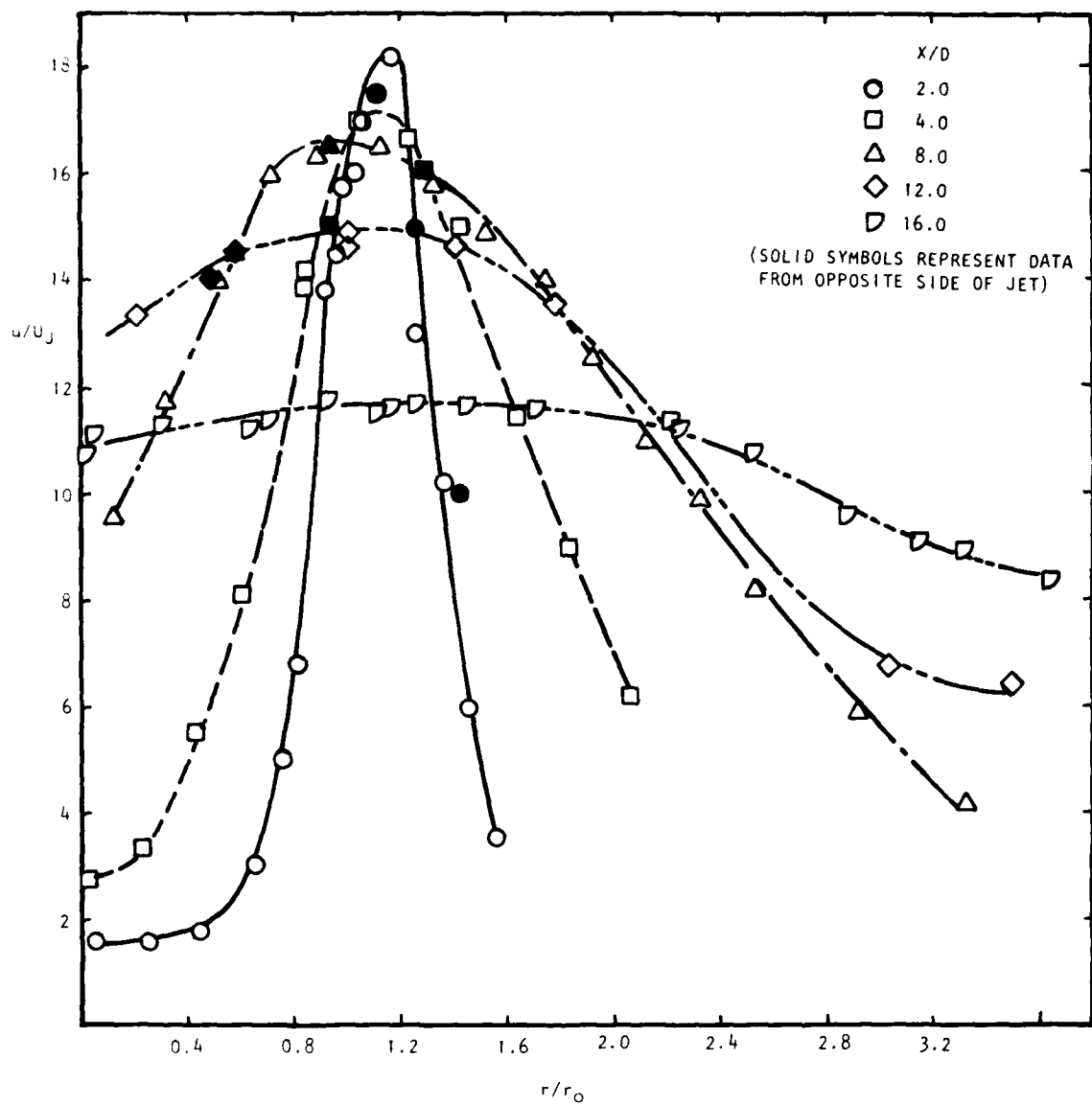


Figure 6.23  $\tilde{u}/U_J$  vs  $r/r_0$  ( $M_J = 0.9$ )

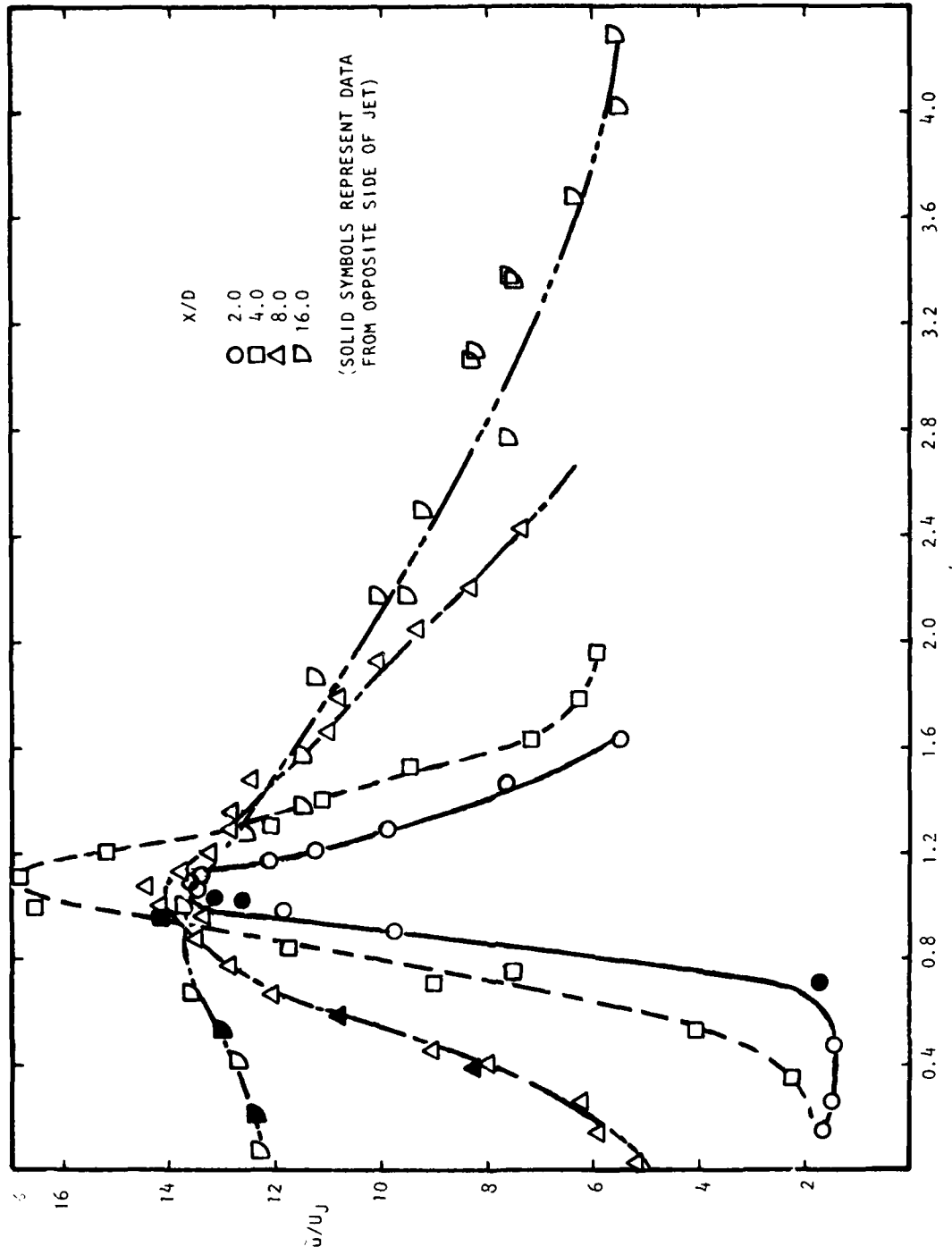


Figure 6.24  $\bar{u}/U_J$  vs  $r/r_0$  ( $M_J = 1.37$ )

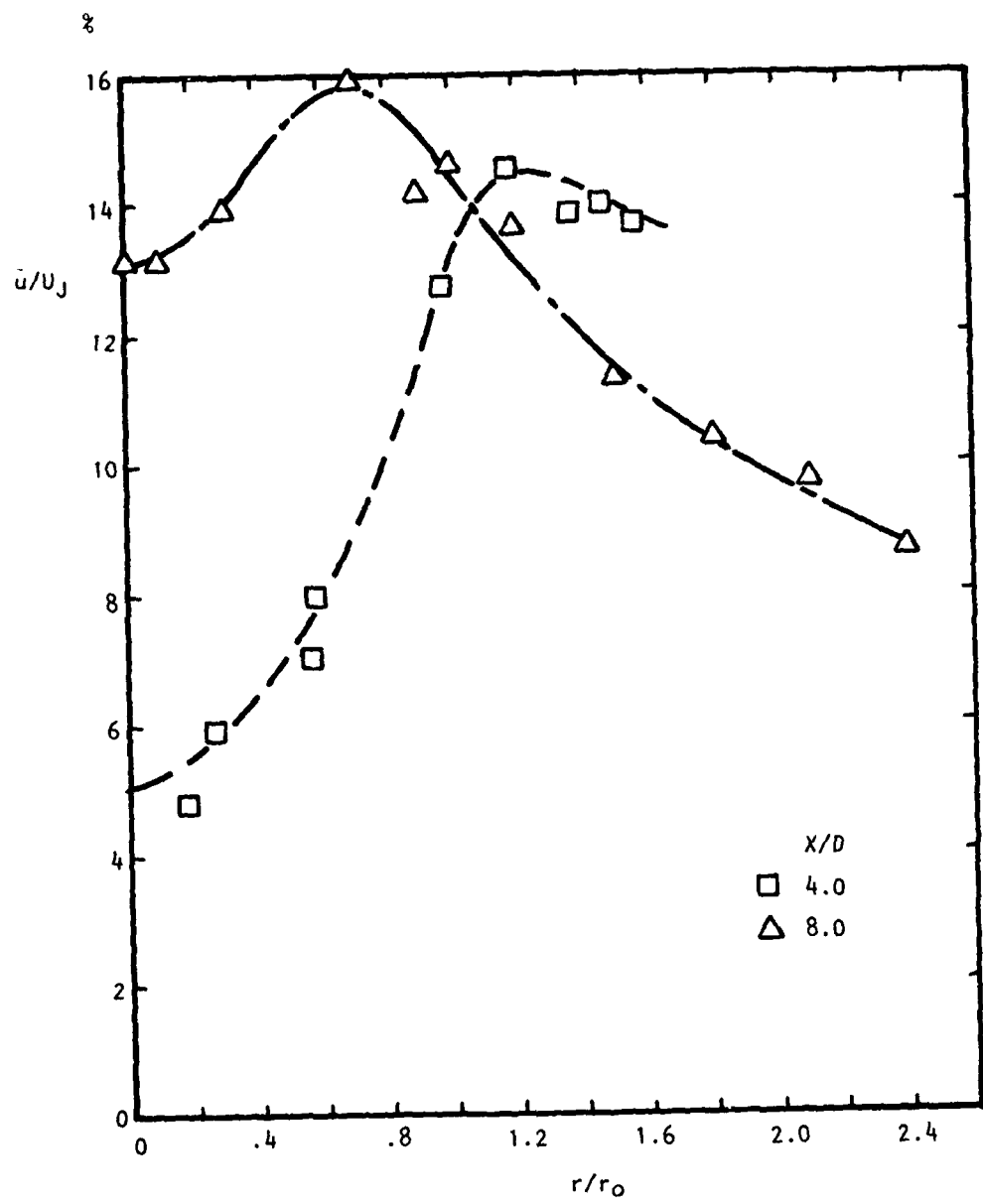


Figure 6.25  $\bar{u}/U_J$  vs  $r/r_0$  ( $M_J = 0.9$ , HEATED)

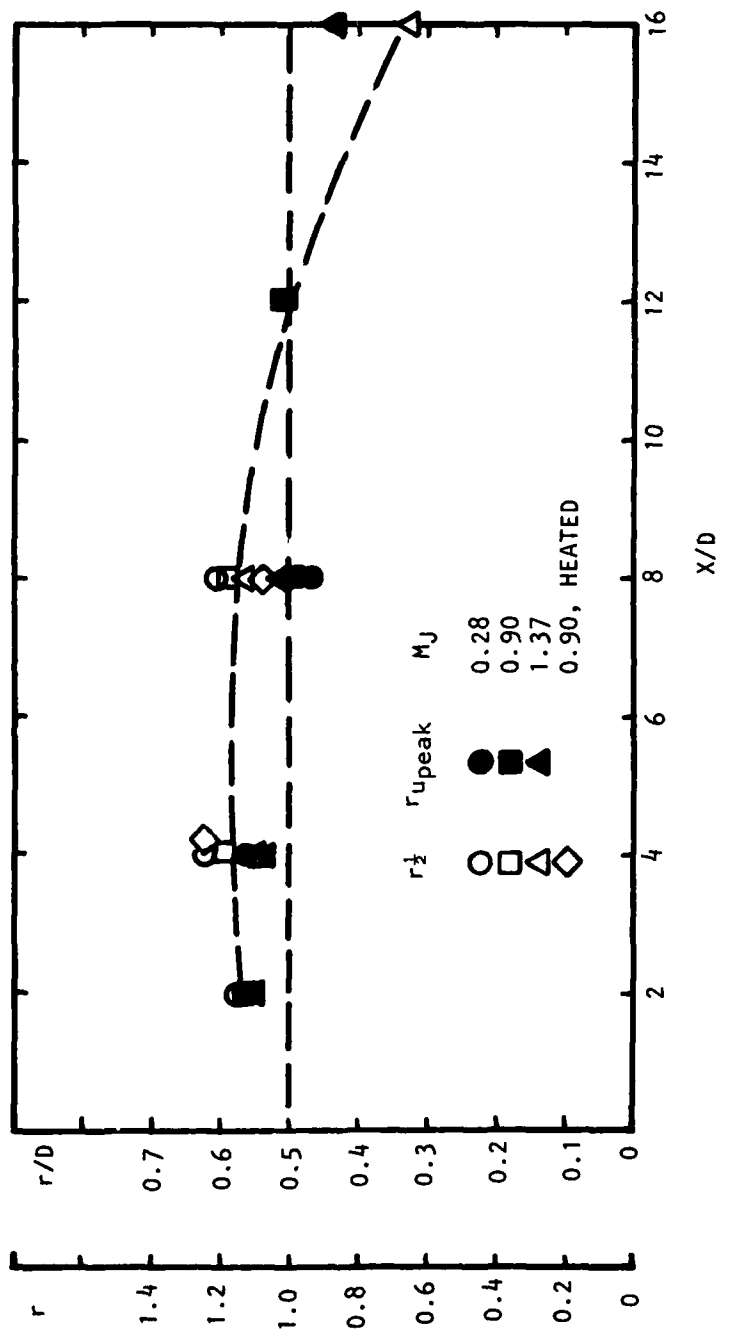


Figure 6.26 Loci of  $(\bar{u}/U_J)_{\text{peak}}$  and  $(\bar{u}/U_J = 1/2)$

The radial distributions of the axial turbulence intensity obtained by Knott and Mossey<sup>84</sup> are shown in Figure 6.27. The curves were plotted from the available data in their report. It was not possible with the limited available data to make meaningful comparisons.

Figures 6.28 to 6.31 show radial distributions of the radial velocity turbulence intensity for different axial positions at the four Mach numbers and temperature conditions studied. The trends which were brought out in the above discussion of the axial velocity turbulence seem to be repeated here. Basically, for a fixed Mach number and temperature, the level of turbulence on the jet centerline increases with distance downstream. The radial extent of the distributions also increases downstream. The magnitude of the peaks tends to move toward the jet axis with increasing downstream position.

The peaks of the radial velocity fluctuations do not reach the magnitudes found in the axial velocity fluctuations. In general, the radial velocity fluctuations are 25% to 30% lower than their corresponding counterparts in the axial velocity fluctuation. Sami et al<sup>85</sup> and Bradshaw et al<sup>70</sup>, both working on round jets with hot-wire anemometers, provided respective figures of 50% and 10% for this difference, and as pointed out in subsection 6.3.2 there are other hot-wire results which suggest that this difference might be about 25%.

The large variation in the hot-wire results is due primarily to differences in interpretation of yawed and crossed wire data, and underscores the need for a more definitive method of measuring velocities normal to the mean flow. The LV, within the limitations discussed above, would appear to fulfill this need.

#### 6.4.2 Normalized Radial Distributions

##### 6.4.2.1 Mean velocities

To isolate the changes in the velocity distribution with Mach number from those associated with differences in position, it would be advantageous to be able to collapse the curves of velocity distribution at the various axial positions into one single curve. Since experience has shown that there is similarity in the mean velocity distributions, such an agglomeration of curves is possible.

Figure 6.32 shows one commonly used method of achieving this goal. In this case, the radial position is normalized to give  $n$ , which is defined by  $n = \frac{r - r_0}{x}$  where  $r_0$  is the nozzle radius. The various curves at the three axial stations do tend to converge. Figure 6.33 shows another approach, and the collapse of the curves is much better. In this case, the radial position is expressed in terms of  $n^* = \frac{r - r_1}{x}$ , where  $r_1$  is the position at which the mean velocity is half of the jet velocity. Also shown are the results of a mean-fit curve computed by Hallen<sup>86</sup> from data taken from nine studies of two-dimensional shear layers. Görtler's<sup>87</sup> well-known analytical results for a

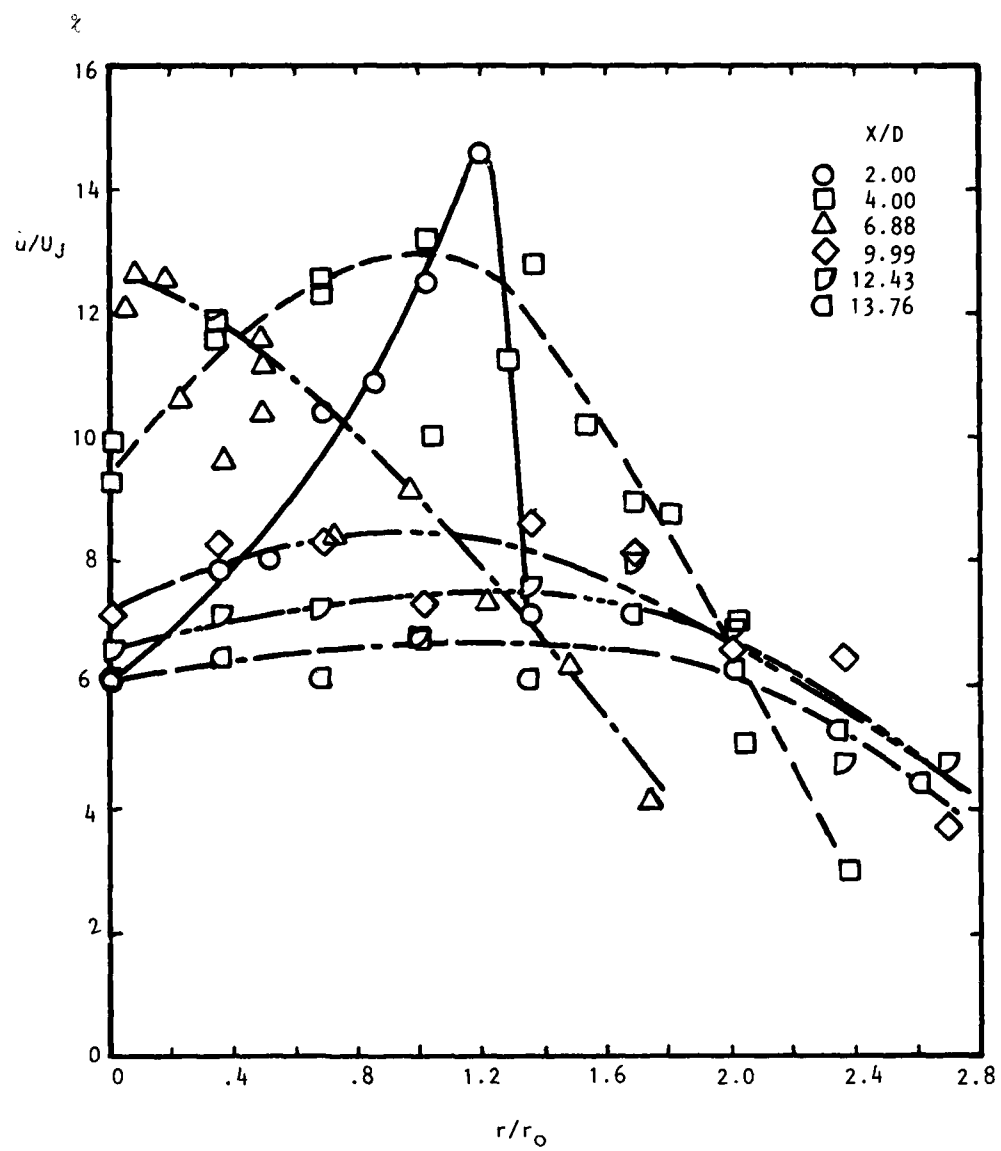


Figure 6.27  $\dot{u}/U_J$  vs  $r/r_o$  (G.E. Data<sup>84</sup>)

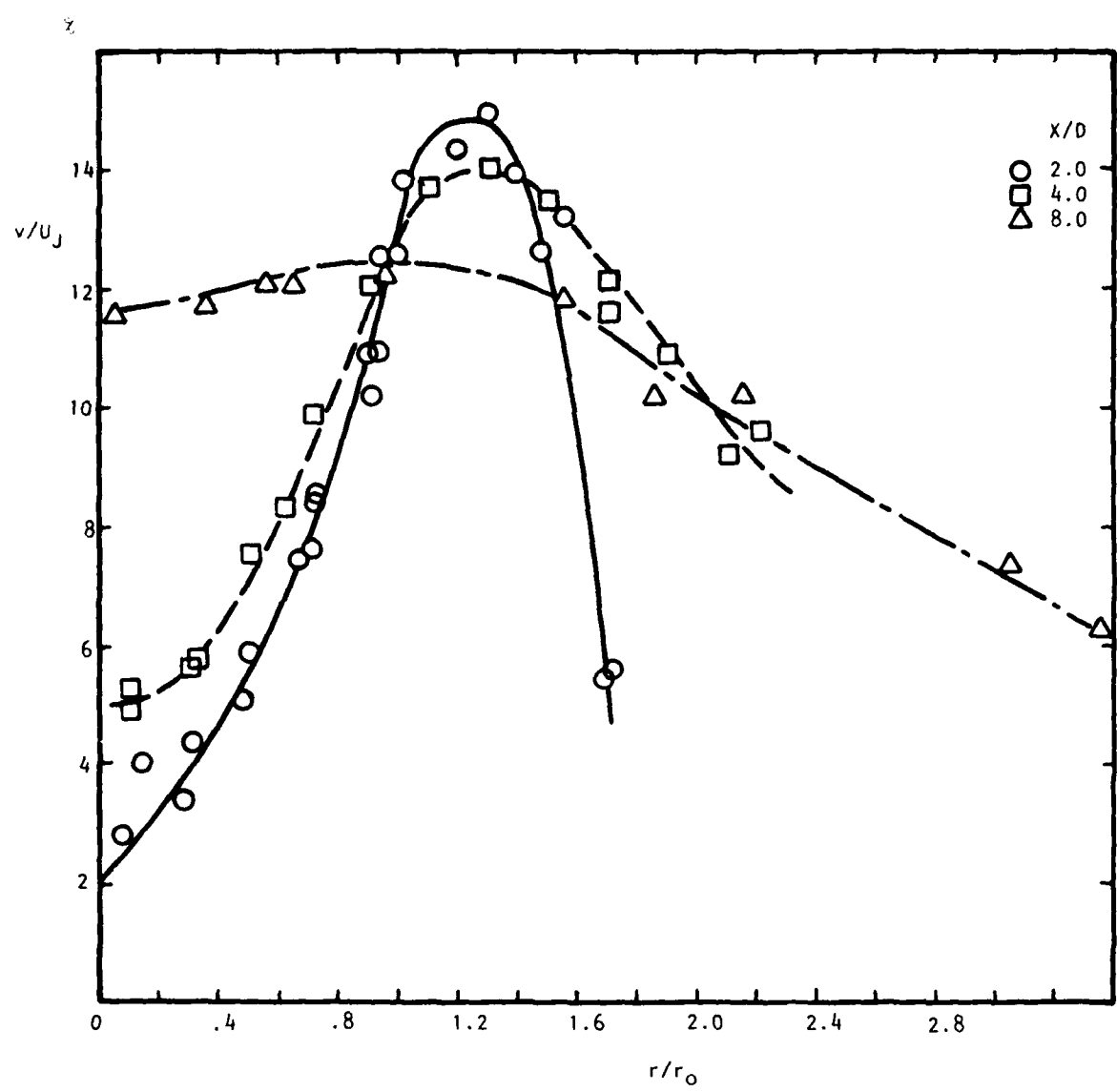


Figure 6.28  $u/U_J$  vs  $r/r_0$  ( $M_J = 0.28$ )

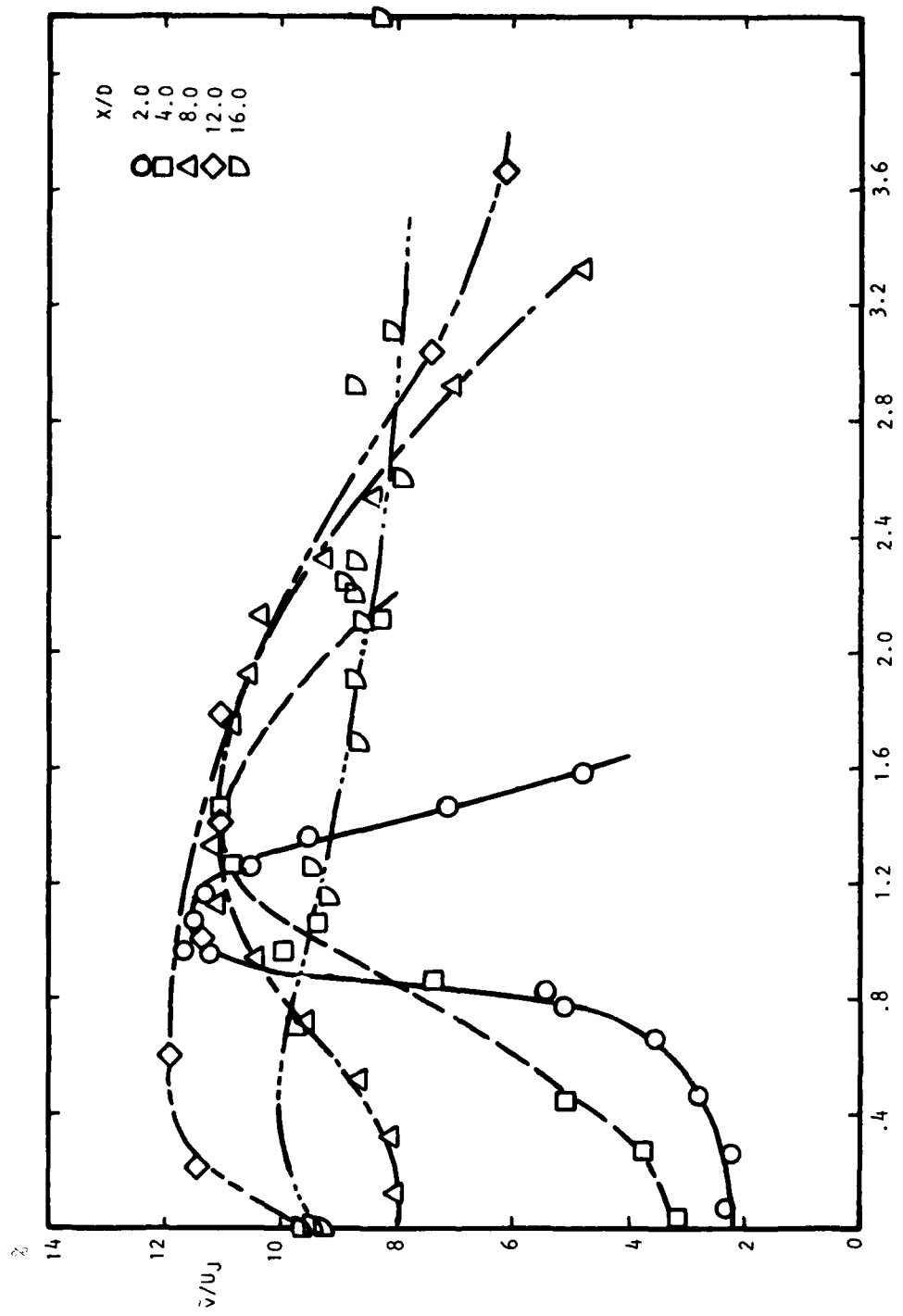


Figure 6.29  $v/v_J$  vs  $r/r_0$  ( $M_J = 0.9$ )

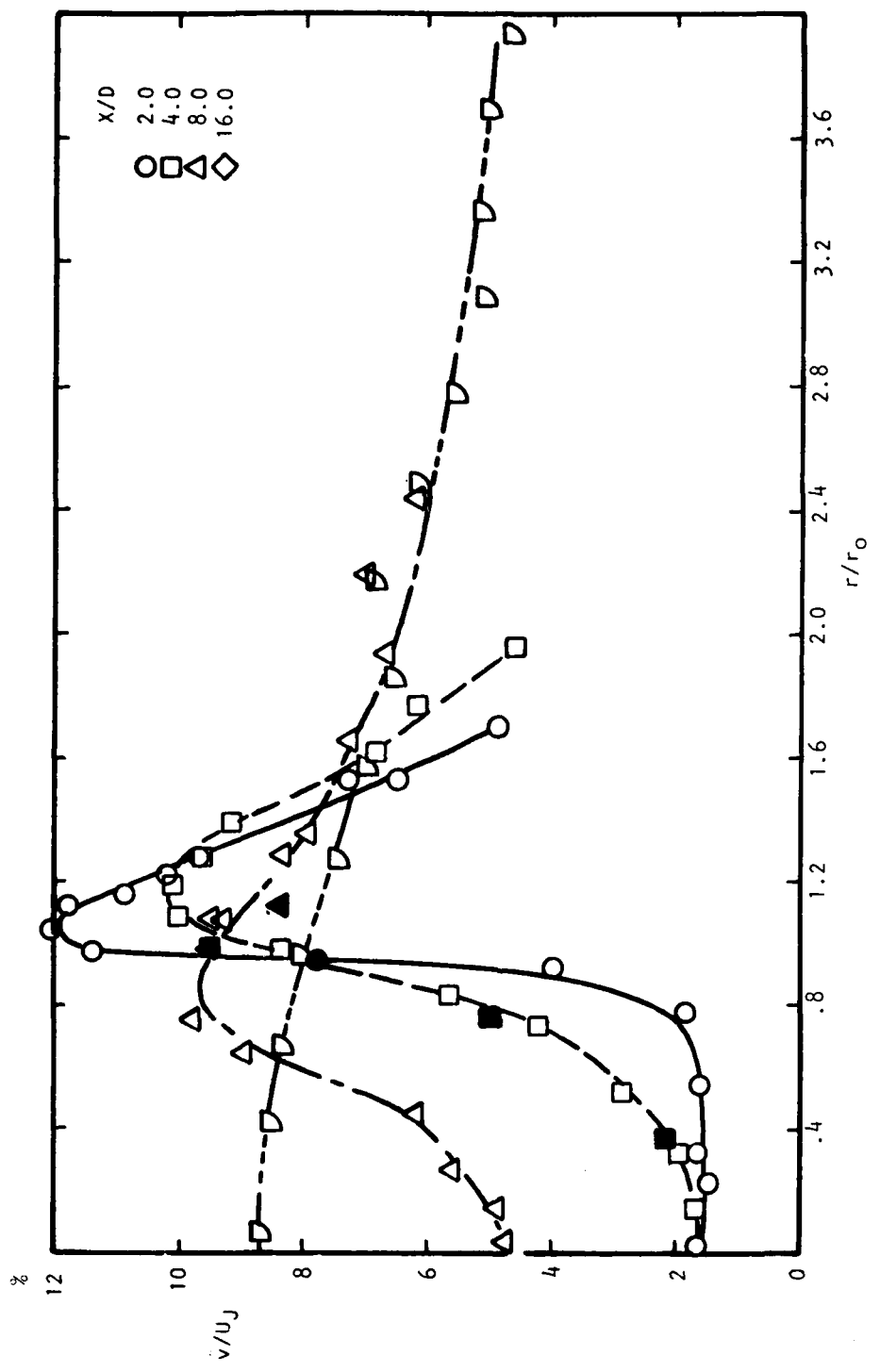


Figure 6.30  $\tilde{v}/v_{UJ}$  vs  $r/r_0$  ( $M_J = 1.37$ )

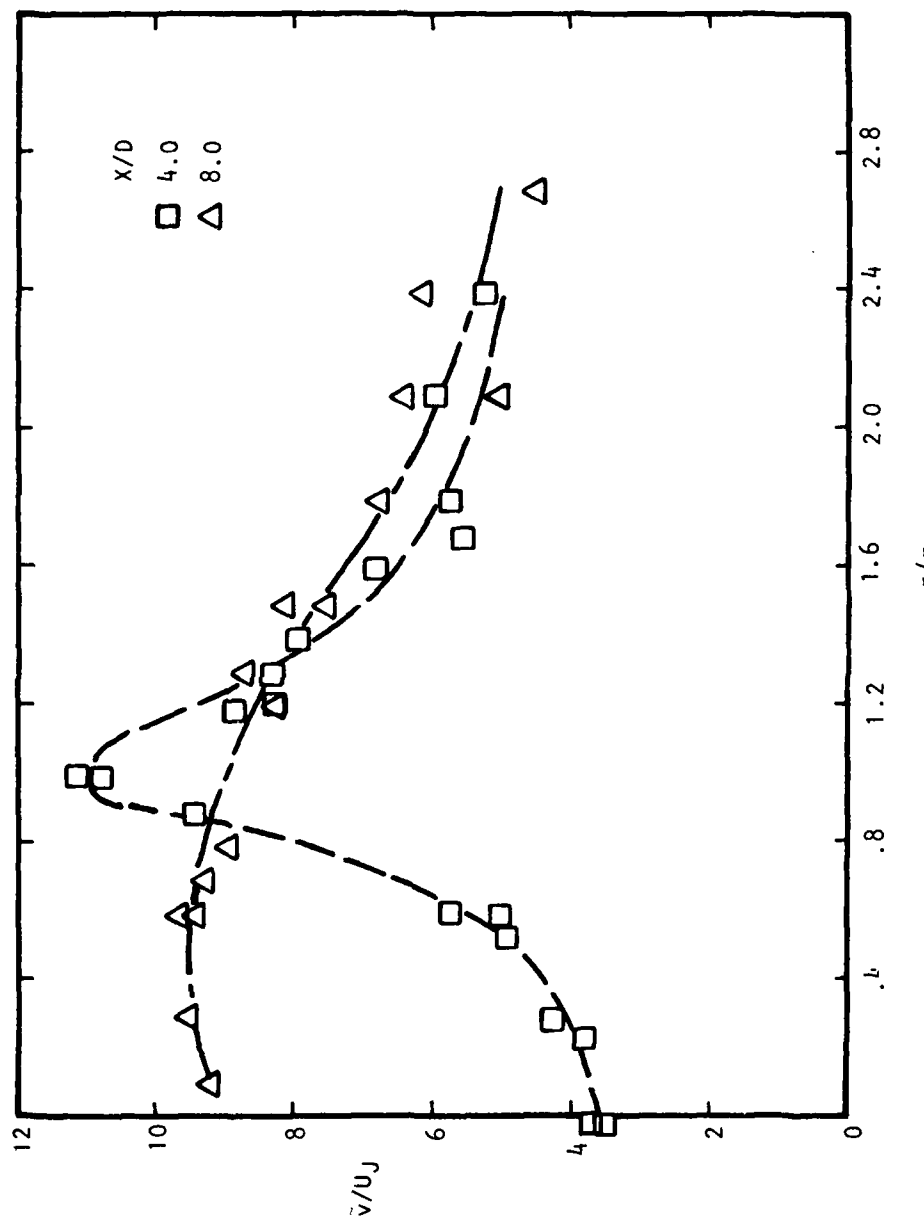


Figure 6.31  $\bar{v}/U_J$  vs  $r/r_0$  ( $M_J = 0.9$ , HEATED)

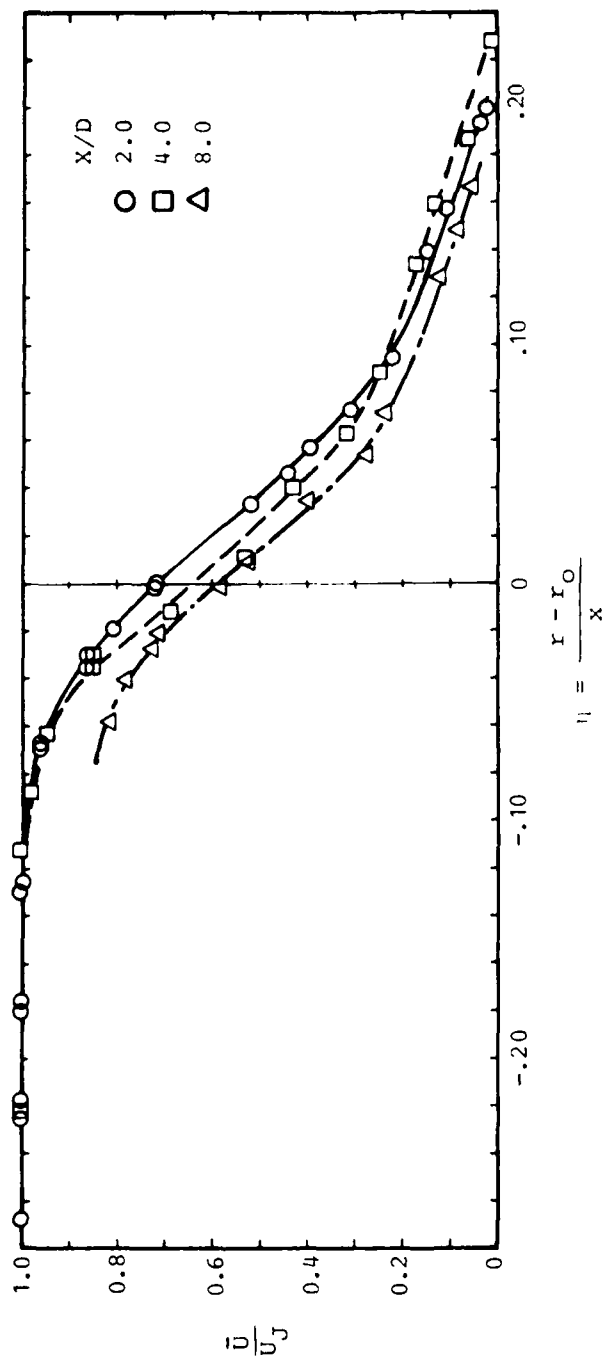


Figure 6.32  $\bar{U}/U_J$  vs  $\eta$  ( $M_J = 0.28$ )

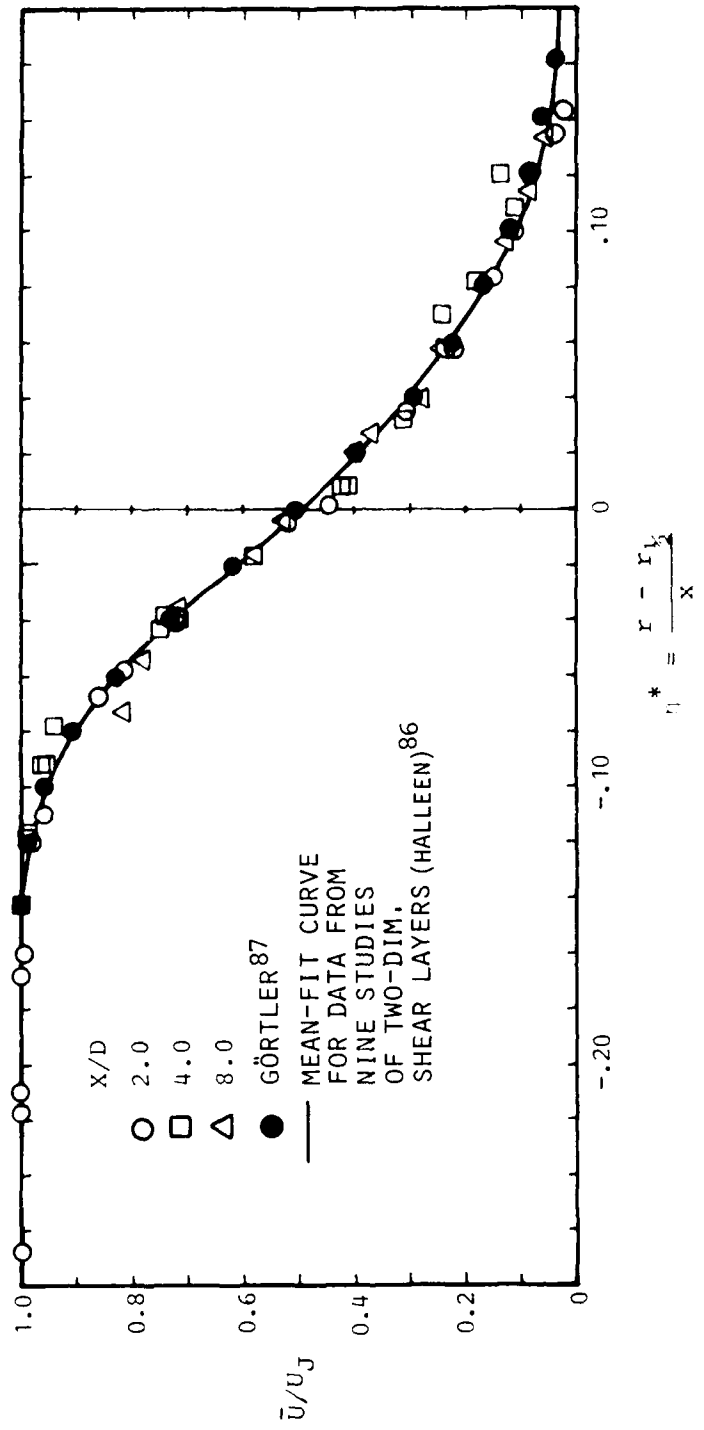


Figure 6.33  $\bar{U}/U_J$  vs  $r^*$  ( $M_J = 0.28$ )

two-dimensional shear layer are also shown. Such a collapse was also achieved previously by Lau<sup>81</sup> in measurements on another 2-inch circular jet using hot-wire anemometers. The ability to bring results as far downstream as eight diameters from the nozzle into a collapse with two-dimensional shear layer data is perhaps intuitively unreconcilable, especially when it is considered that the potential core ends at round  $4\frac{1}{2}$  diameters. However, the use of  $\eta^*$  seems to allow this reduction of the many curves into one. As such, it will be adopted as the method for presenting subsequent data.

Figure 6.34 shows the radial distribution of the mean axial velocity for a Mach number of 0.9 plotted in terms of  $\eta^*$ . The results extend over larger axial distances downstream than for the previous case. In general, there is good collapse of the data on the inner part of the jet (i.e.,  $\eta^*$  negative), but significant deviations appear in the outer part, from around  $\eta^* = 0.05$ . Closer scrutiny reveals, however, that the very large deviations are found only in the results at  $x/D = 16$ . Thus, if the data for  $x = 16$  are excluded, there would appear to be a collapse of the data, and a faired curve may then be drawn through the points. Kolpin's experiments<sup>77</sup> with a cold jet produced a similar distribution (his results are shown by the solid symbol).

Figure 6.35 shows the radial distribution at  $M_j = 1.37$ . Good collapse of the data is achieved even for  $x/D = 16$ . It would seem that the similarity of the mean velocity curves is preserved for a longer distance as the Mach number is increased. In subsection 6.4.1.1 it was noted that the potential core increases in length with increasing Mach number. On this basis, it would appear that the distance, to which similarity may still be found in the mean velocity distribution, is related to the potential core length. An estimate based on present results would place this distance at between two and two and one-half times the length of the potential core. This characteristic will be discussed in more detail later when Mach number effects are specifically considered. As before, a faired curve is drawn through the results.

Figure 6.36 gives the results of the radial distribution of the heated jet at  $M_j = 0.9$ . Unfortunately, a failure in the burner during the experiments prevented as extensive a study at this condition as was possible at the other conditions. However, the data for the two axial stations lie on one curve and a faired curve is drawn through the results.

The four faired curves passing through the experimental data are taken from Figures 6.33 to 6.36 and plotted in a composite graph in Figure 6.37. The radial extent of the curves expressed in  $\eta^*$ , which is an expression of the relative spreading rate of the shear layer, shows a systematic variation with Mach number. The shear layer for  $M_j = 0.28$  extends from  $\eta^* = -0.14$  to around 0.18 (taking  $U/U_j = 0.05$  as the lower cut-off point). For  $M_j = 1.37$  the shear layer extends from  $\eta^* = -.08$  to 0.12.

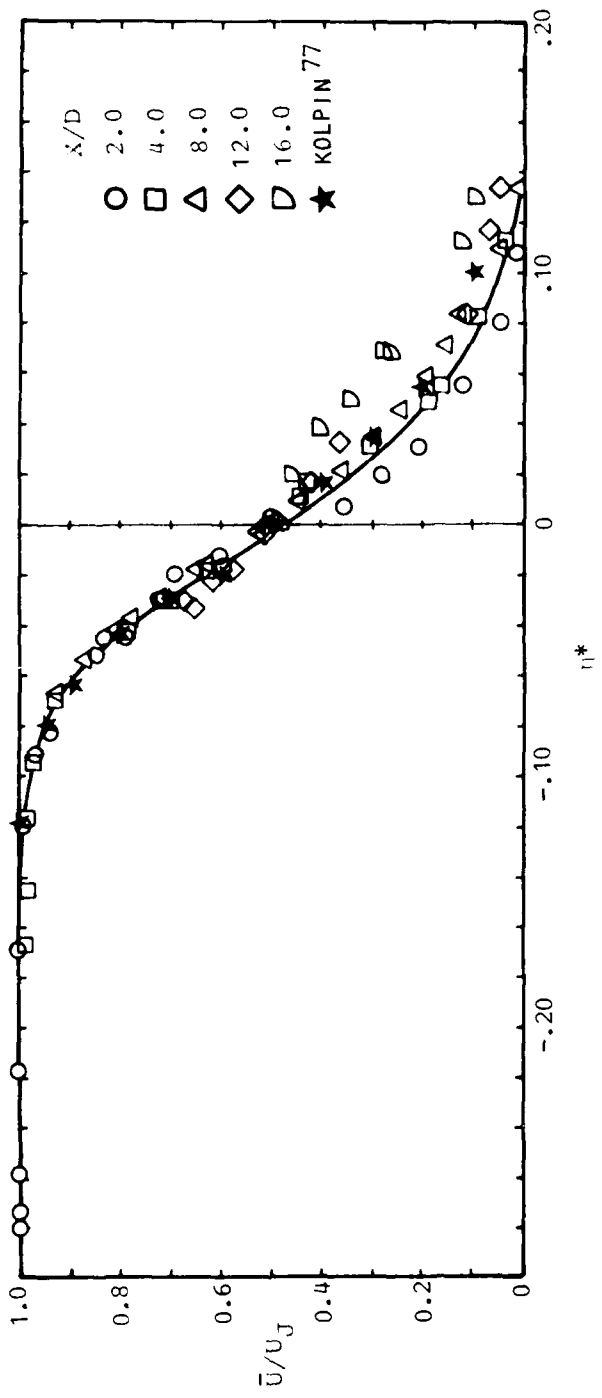


Figure 6.34  $\bar{U}/U_J$  vs  $r_1^*$  ( $M_J = 0.9$ )

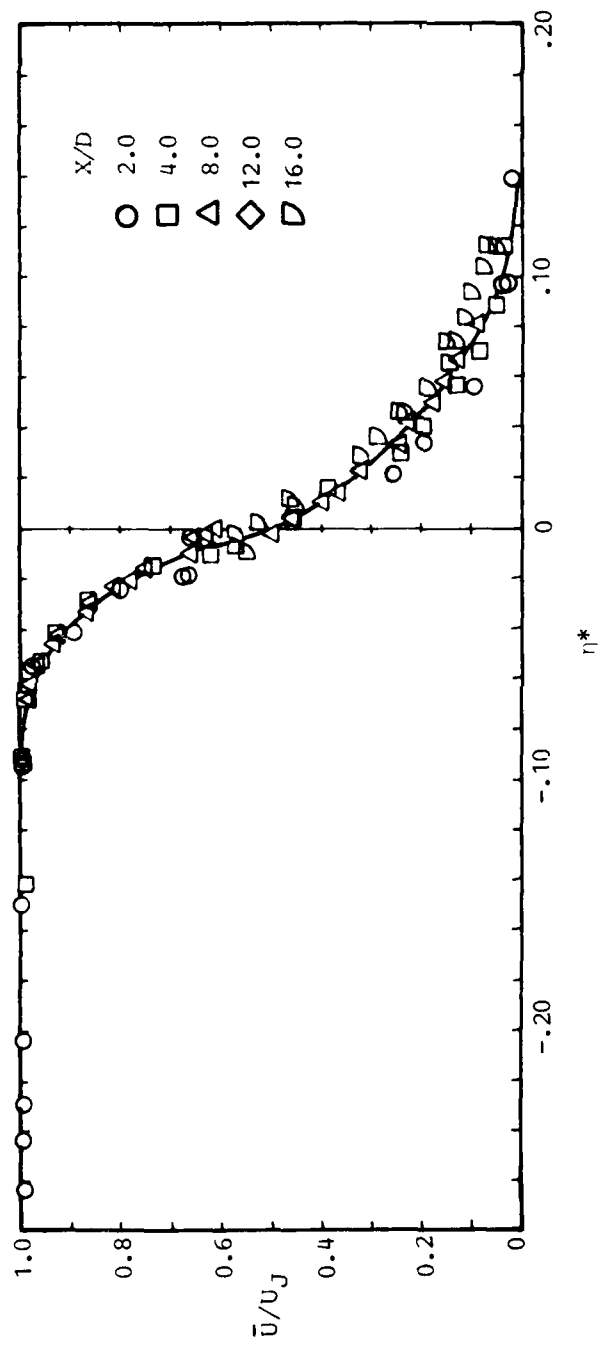


Figure 6.35  $\bar{U}/U_J$  vs  $\eta^*$  ( $M_J = 1.37$ )

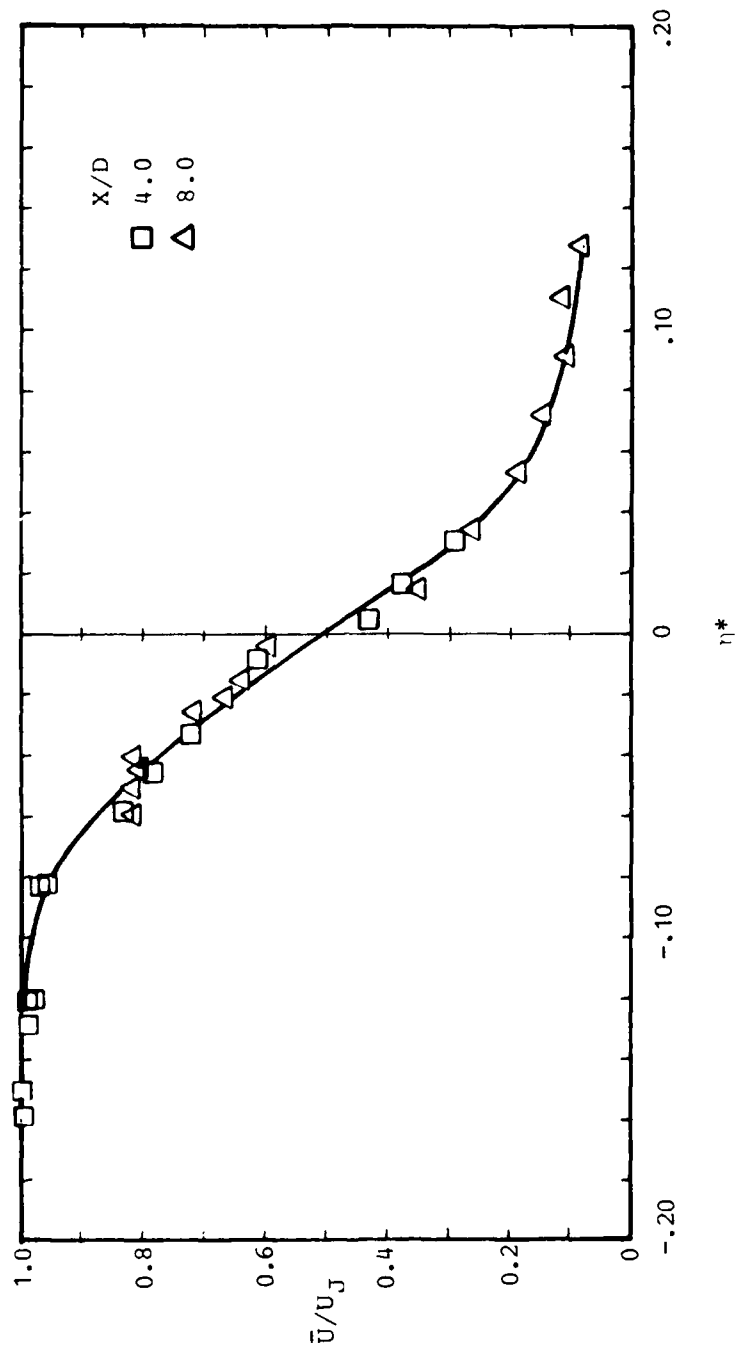


Figure 6.36  $\bar{U}/U_J$  vs  $\eta^*$  ( $M_J = 0.9$ , HEATED)

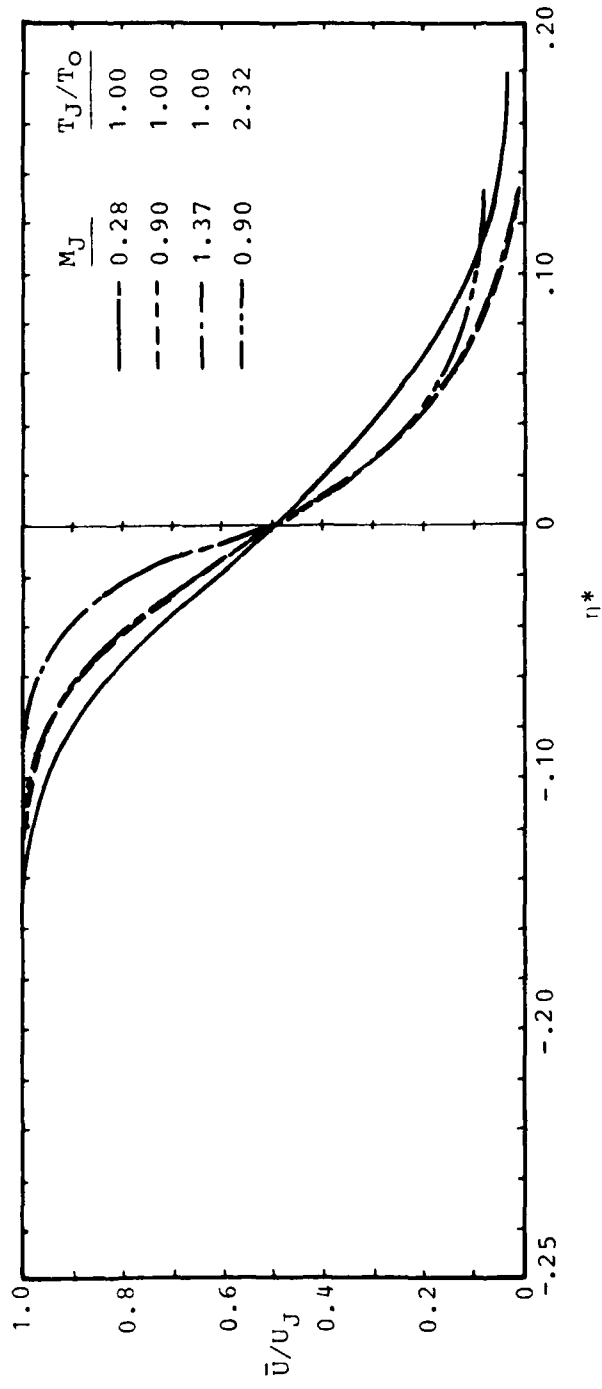


Figure 6.37 Variation of the Mean Velocity Distribution with  
Mach Number and Temperature Ratio

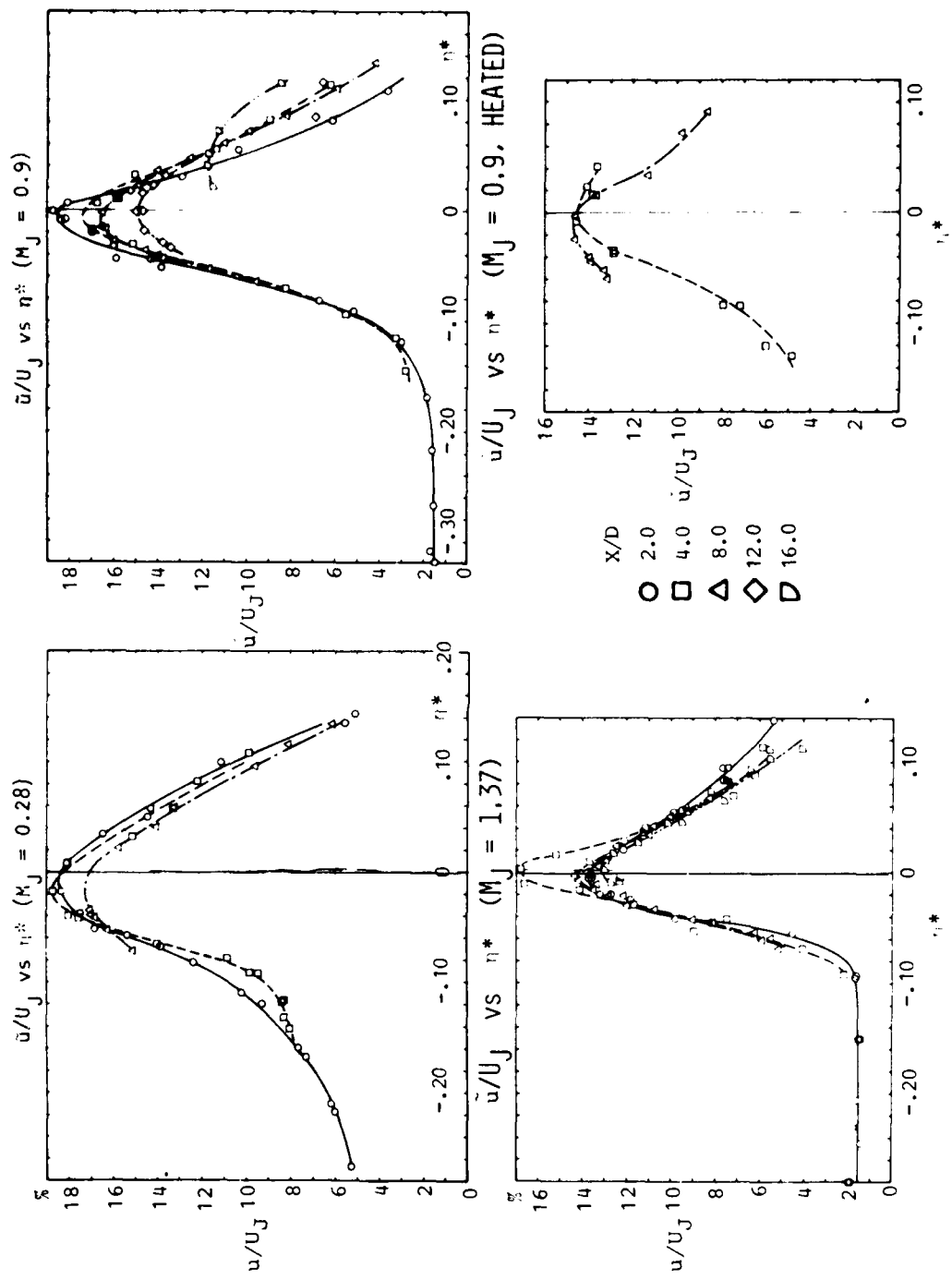


Figure 6.38  $\tilde{u}/U_J$  vs  $\eta^*$

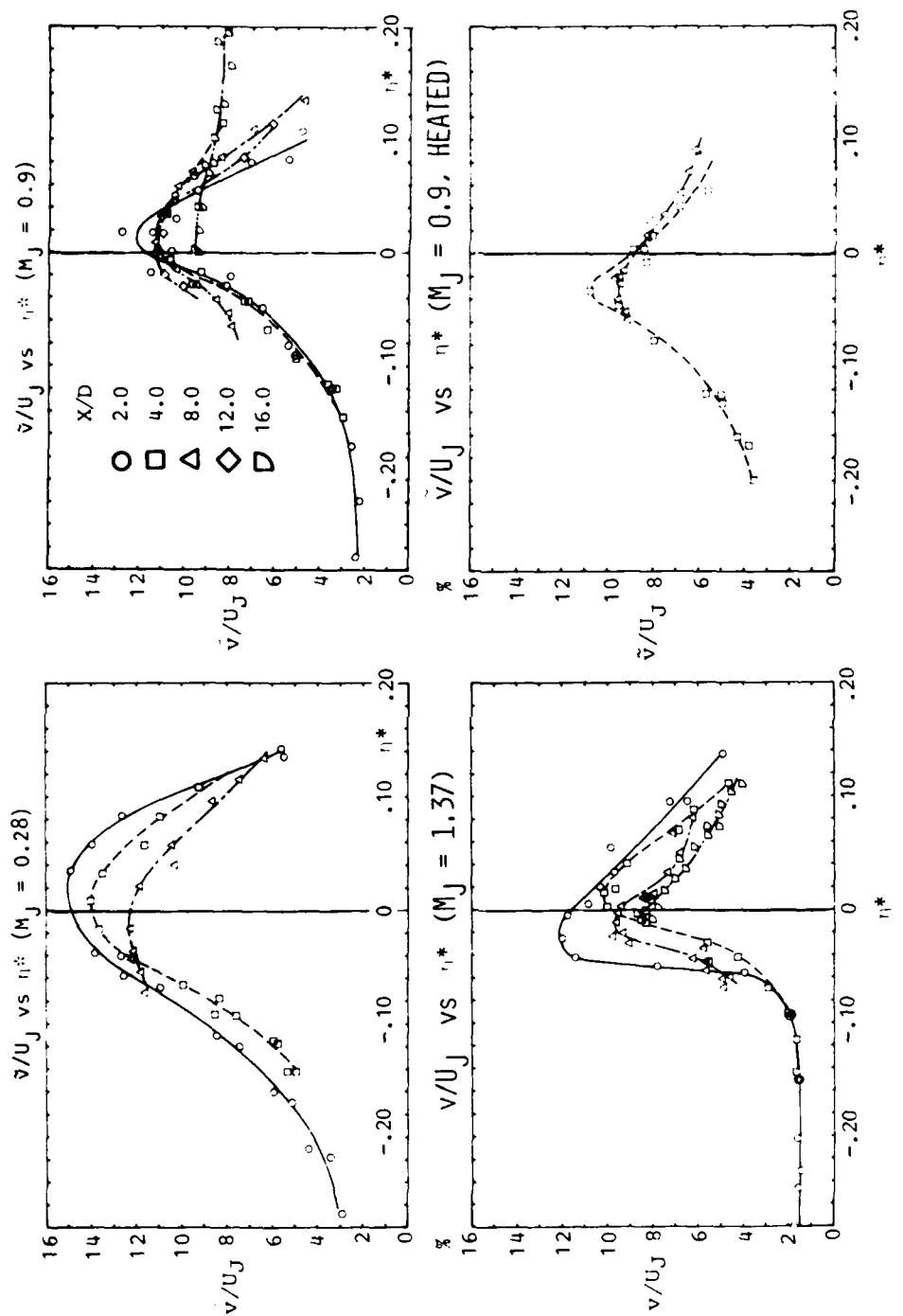


Figure 6.39  $\tilde{v}/U_J$  vs  $v_t/U_J$  vs  $\eta^*$

Between the two extreme cases are those for  $M_J = 0.9$  (isothermal and heated). The curve for the heated jet seems to follow that for the isothermal jet in the inner region, but deviates from it in the outer region. It would thus seem that the effect of heating is to broaden the shear layer by increasing the spreading rate. Additional data presented in the next section reinforces this observation.

It should be noted that the efflux velocity of the heated jet at  $M_J = 0.9$  is the same as that for the isothermal supersonic case ( $M_J = 1.37$ ). It may be recalled that the spreading rate of the shear layer in the latter case was actually smaller than for the Mach 0.9 isothermal case. The changes in the spreading rate of the shear layer are therefore not identifiable with a change in jet efflux velocity alone. It would probably be more appropriate to consider the shear-layer spreading rate as a function of Mach number and temperature.

The present data are not sufficient to allow any formulation for describing the effect of temperature changes but work will be continued in this direction. However, the effects due to Mach number change are better defined, and an effort is made in subsection 6.4.4 to make some projections of Mach number effects.

#### 6.4.2.2 Fluctuating velocities

Figure 6.38 shows the radial distributions of the axial turbulence intensity with the radial position expressed in terms of  $\eta^*$ . The velocity is, as in previous plots, normalized by  $U_J$ . As they are plotted, the curves tend to orientate themselves in such a way that their peaks lie close to the position of  $\eta^* = 0$ . The only result which does not exhibit this quality is at the position of  $\frac{x}{D} = 16$  for a Mach number of 0.9. It may be recalled that there was also a breakdown in the similarity of the results of the mean velocity at this point. The changing spread of the shear layer of the jet with increasing Mach number is shown in this sequence of graphs. No systematic, consistent trend can be detected in the value of the peaks in the turbulence intensity, but the maximum turbulence intensity largely tends to fall with increasing axial distance from the nozzle and as the Mach number of the jet is increased.

Figure 6.39 shows the radial distribution of the radial turbulence intensity. The results show practically the same trends as for the axial turbulence intensity.

#### 6.4.3 Survey of the Flow Characteristics Along the Jet Centerline

Figure 6.40 shows the axial distribution of the mean velocity on the jet axis for different Mach numbers. Examining first the three isothermal jet results, there is a consistent trend in which the curves move downstream as the Mach number is increased. This shift in the curves agrees with the earlier suggestion that the potential core of the jet would increase in length as the Mach number is increased.

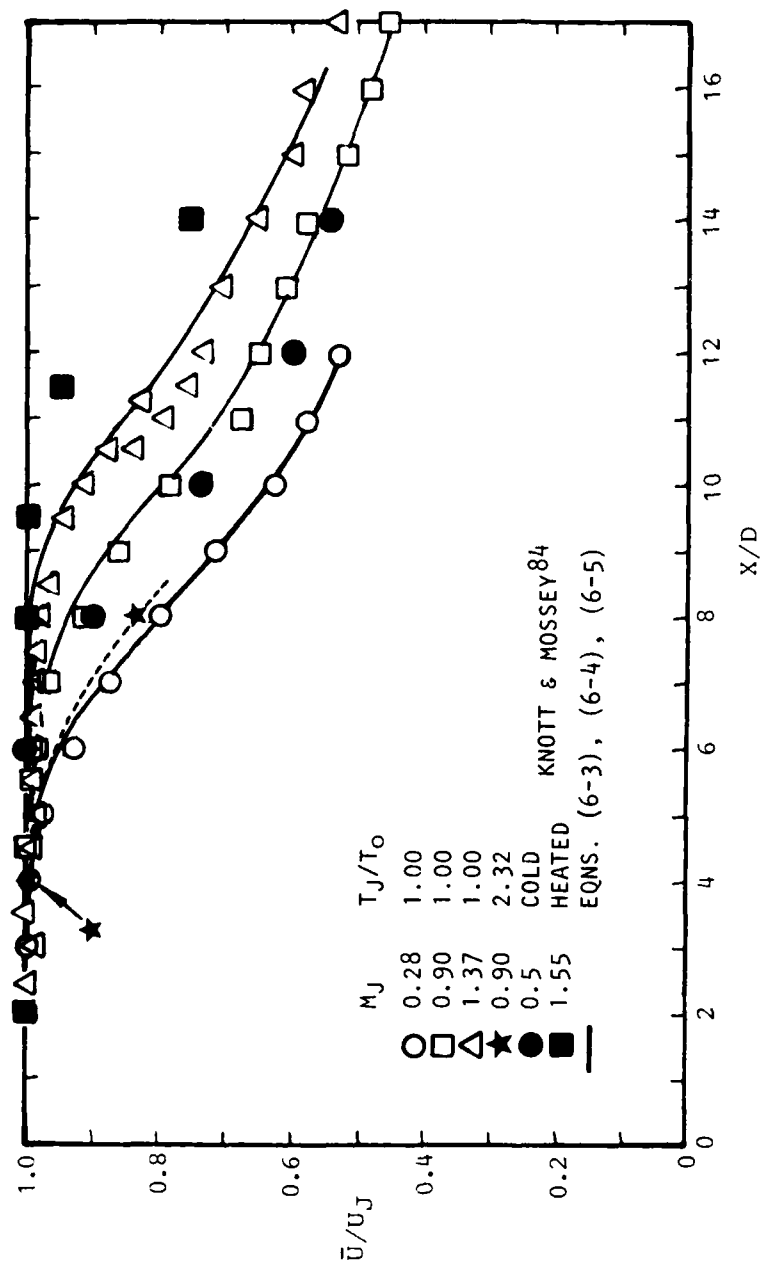


Figure 6.40 Axial Distribution of  $\bar{U}/U_J$  (JET CENTERLINE)

Earlier observations about the effect of heating also appear to be borne out here. The results for the heated jet lie upstream of those for the isothermal jet at the same Mach number of 0.9. This confirms the earlier statement that the potential core shortens with heating for a fixed jet efflux velocity or jet Mach number.

The results of Knott and Mossey<sup>84</sup> are also shown. They generally appear to fit into the pattern which is suggested in the present set of results. For instance, their results for a cold jet at  $M_J = 0.5$  lie between the curves for the isothermal jets of  $M_J = 0.28$  and  $M_J = 0.9$ , and tend to be biased closer to the curve for  $M_J = 0.9$  rather than that for  $M_J = 0.28$ . Such a tendency would be consistent with what has just been said about the effects of jet heating. Presumably, cooling the jet would have the kind of opposite effect seen here. Their results for the heated jet at  $M_J = 1.55$  lie downstream of all the results presented so far, which is not altogether unreasonable. However, on the basis of the foregoing remarks, these results should lie upstream of those for an equivalent isothermal jet running at the same Mach number. This question will be examined more fully in Section 6.4.4, within a closer study of Mach number effects, when extrapolations of the present results will be made to cover other Mach number cases.

The distribution of the mean velocity on the jet centerline was analyzed by Witze<sup>88</sup>, who proposed that the distribution would be of the form:

$$\frac{U}{U_J} = 1 - \exp \left\{ -\frac{1}{2\xi} \right\} \quad (6-2)$$

where, for an isothermal jet,  $\xi = a \left( \frac{x}{D} - \frac{x_c}{D} \right)$ . The constants "a" and " $x_c$ " are determined from experimental results by plotting  $\xi$ , which is defined by  $\{-2 \ln (1-U/U_J)\}^{-1}$ , against  $x/D$ . The slope of the straight line would give the value of "a", and the abscissa intercept would give  $x_c/D$ . Figure 6.41 shows such plots of  $\xi$  against  $x/D$  for the three isothermal jets studied. In each case, the data for the downstream portion tend to fall on a straight line. However, close to the tail of the potential core, the data points deviate from the straight line. The straight lines have different slopes, depending on the Mach number, and the abscissa intercepts are different. From an analysis of these straight lines, the values of "a" and " $x_c$ " may be determined, to give the following equations for the centerline distribution of the mean velocity:

$$\frac{U}{U_J} = 1 - \exp \left( 5.75 \frac{D}{4.4D-x} \right) \quad \text{for } M_J = 0.28 \quad (6-3)$$

$$\frac{U}{U_J} = 1 - \exp \left( 7.18 \frac{D}{5.2D-x} \right) \quad \text{for } M_J = 0.9 \quad (6-4)$$

$$\frac{U}{U_J} = 1 - \exp \left( 8.47 \frac{D}{6.4D-x} \right) \quad \text{for } M_J = 1.37 \quad (6-5)$$

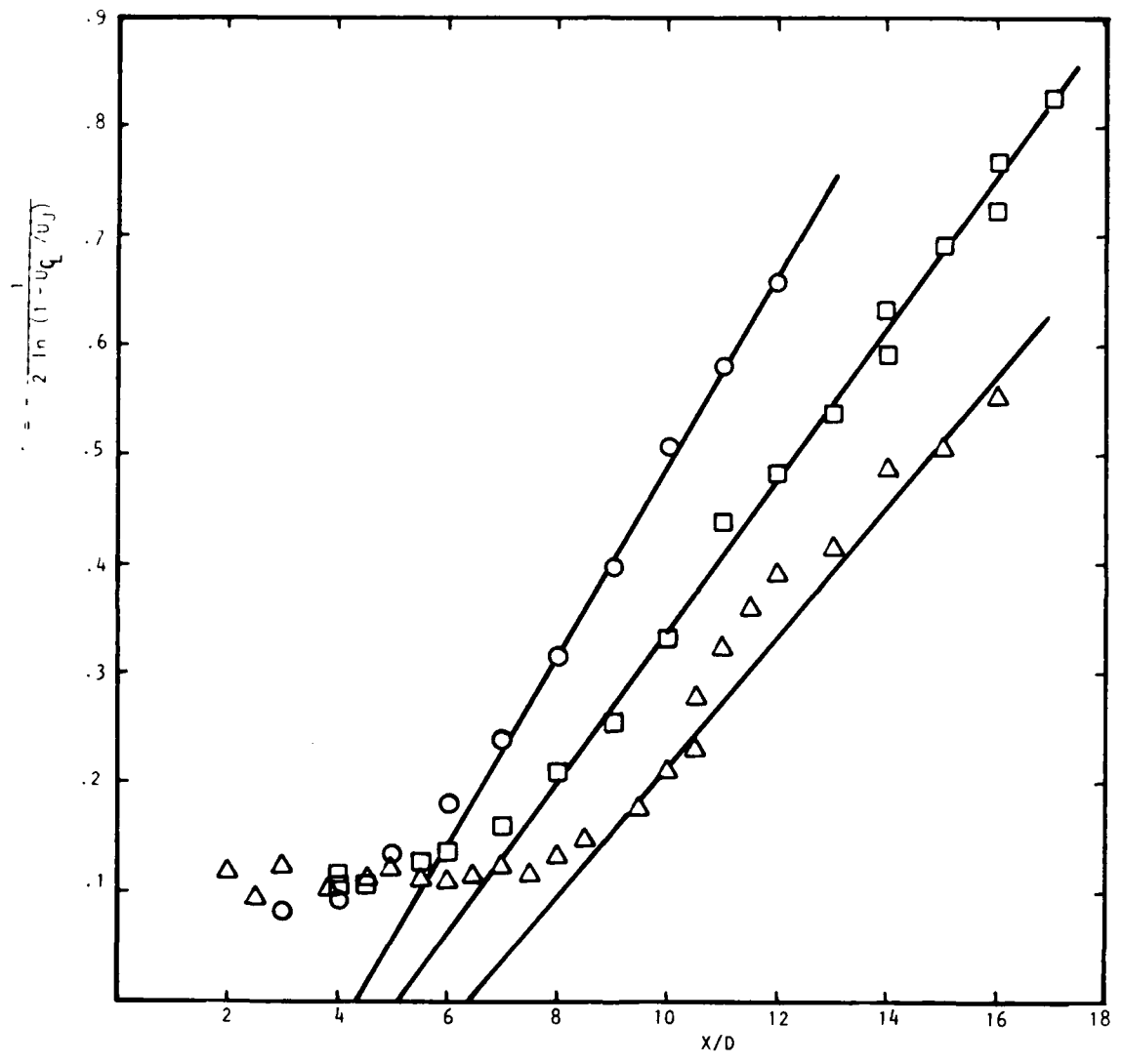


Figure 6.41 Plot of  $\xi$  vs  $X/D$

It was found by Kleinstein (please see Witze<sup>88</sup>) that the product  $2ax_c/D$  has a universal value of 0.70. The values obtained in the present study were 0.76, 0.72 and 0.76 for Mach numbers of 0.28, 0.9 and 1.37, respectively, which would tend to agree with the concept of a universal value although the value of the product may not agree with Kleinstein.

It should be noted that Witze's formula provides a definitive method for finding the end of the potential core. From the abscissa intercepts of the straight lines in Figure 6.41, the lengths of the potential core,  $x_c$ , were determined and found to be 4.4, 5.2, and 6.4 diameters for Mach numbers of 0.28, 0.9, and 1.37, respectively. Curves for these equations were plotted in Figure 6.40; the curves follow their respective data points in the downstream part of the jet as expected, but near the tails of the potential core, the data and the curves deviate.

Figure 6.42 shows the variation of the axial turbulence intensity on the jet centerline for the various jet flow conditions tested. The turbulence intensity rises with axial distance and reaches a peak value downstream of the potential core, before finally falling off. The decrease in turbulence level downstream of the peak is much more gradual than the rapid increase upstream of the peak.

The curves tend to move bodily downstream as the Mach number is increased, in keeping with the trend observed in the axial mean velocity distributions. The position of the peaks in these curves appear to bear some relationship with the length of the potential core, and the discussion in a later section will establish this relationship.

As in the radial distributions, the peak value of turbulence intensity appears to fall with increasing Mach number.

The results of Knott and Mossey are also shown in Figure 6.42. The magnitudes of their turbulence levels are in general lower than those of the present study, which is not inconsistent since their data have also tended to show a lower value in the radial distributions. However, the curves generally follow the trends which the present results have indicated. In particular, the peak for the Mach 0.5 cold jet falls between those for the Mach 0.28 and 0.9 cases of the present study. The results for the heated jet tested in this study are also shown; as expected, they lie between the results of the isothermal jets at Mach 0.28 and 0.9.

Figure 6.43 shows the axial distributions of the radial turbulence intensity on the jet centerline for different Mach numbers. As in the axial turbulence intensity, the levels rise with axial distance, reaching a peak at some point downstream of the potential core, and falling gradually further downstream. The positioning of the curves for the various Mach number configurations of jet is similar to the earlier description of the axial turbulence intensity distributions. The peaks of the curves lie close to the positions where the peaks of the axial turbulence intensity distributions may be found.

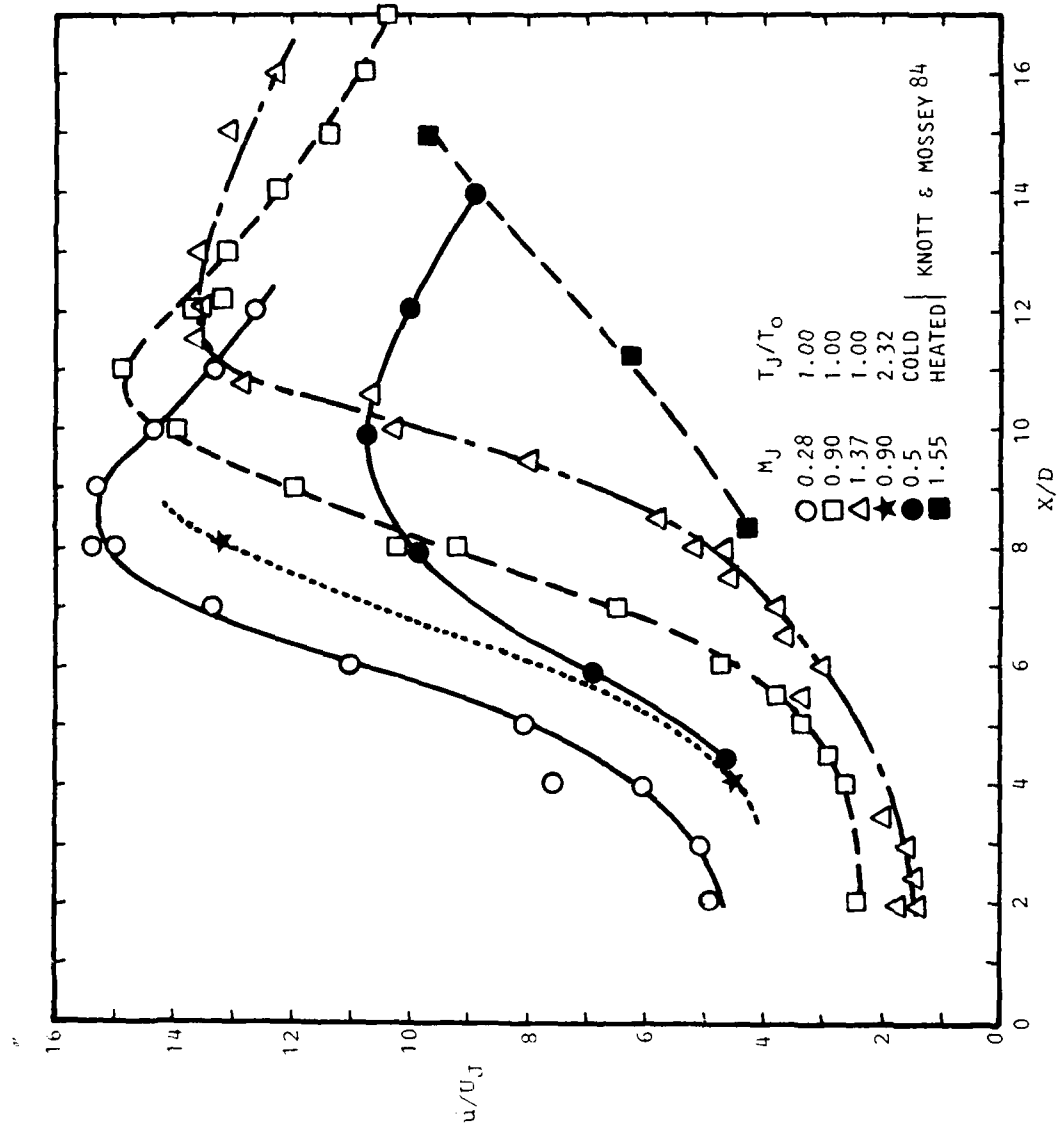


Figure 6.42 Axial Distribution of  $u/U_J$  (Jet Centerline)

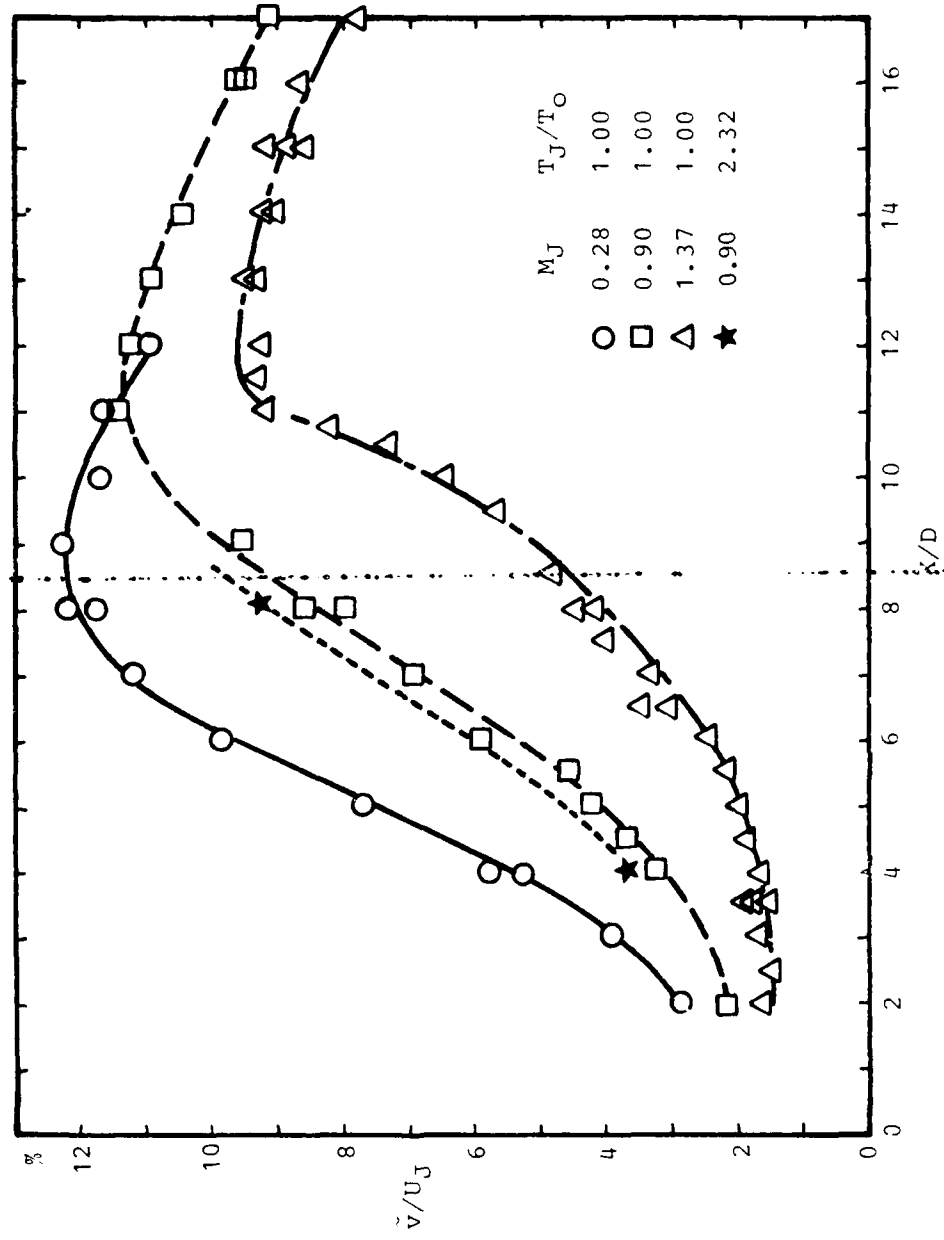


Figure 6.43 Axial Distribution of  $\bar{v}/U_j$  (Jet Centerline)

The apparent relationship between the shapes of the axial distributions and the points where the potential core ends suggests that there might be some means of normalization of the axial position involving the potential core length,  $x_c$ , which would allow a collapse of the respective curves. As an initial attempt, the axial position,  $x$ , is normalized by dividing it by  $x_c$ . Figures 6.44 to 6.46 represent the results of such an effort.

Figures 6.44 shows the variation of the mean axial velocity and a good collapse of data is achieved for the three Mach numbers. The distribution of the axial turbulence intensity is shown in Figure 6.45. The normalization of the axial position with potential core length appears to be satisfactory and the peaks lie close to each other, at about  $x/x_c = 2.0$ . The results however do not collapse and would suggest that the turbulence intensity needs to be normalized differently, to take count of Mach number effects. The same observations may be made of the distributions of the radial turbulence intensity shown in Figure 6.46. Specifically the peaks are located at about  $x/x_c = 2.0$ , and the results generally suggest that  $x_c$  is a good parameter with which to normalize the axial distance.

#### 6.4.4 Mach Number Effects

In the previous discussions of the radial and axial distributions of the mean velocity and the turbulence intensities, reference was made to some of the more noticeable effects of Mach number changes. For instance, it was pointed out that the spreading rate of the turbulent shear layer decreased when the Mach number was increased, and in turn that this caused a lengthening of the potential core. It was also brought out that, although no systematic change could be observed, the general trend was for the maximum axial and radial turbulence intensity in the radial or the axial distribution to fall with increasing Mach number.

An attempt is made in this section to quantify some of these observable effects, and possibly to build up with the available data, a set of formulae which may be used to extrapolate the results to other Mach numbers.

##### 6.4.4.1 $x_c/D$ versus $M_j$

The variation of the potential core length,  $x_c$ , with Mach number,  $M_j$ , is shown in Figure 6.47. It is seen that the potential core length increases monotonically with Mach number across the range from subsonic to supersonic. The change should be continuous and preliminary results of the present study have generally supported that view. The experimental results from eight studies of heated and unheated subsonic round jets and five studies of unheated supersonic jets compiled by Witze<sup>88</sup> are shown by the solid line and they pass through the present results for isothermal jets.

Witze<sup>88</sup> used the experimental results of these thirteen studies of heated and unheated jets and derived an empirical formula for the variation of the potential core length with Mach number. Provision is made in the formula for density differences between the jet and the ambient medium. The formula has a different form in locally subsonic and supersonic flow regions. The

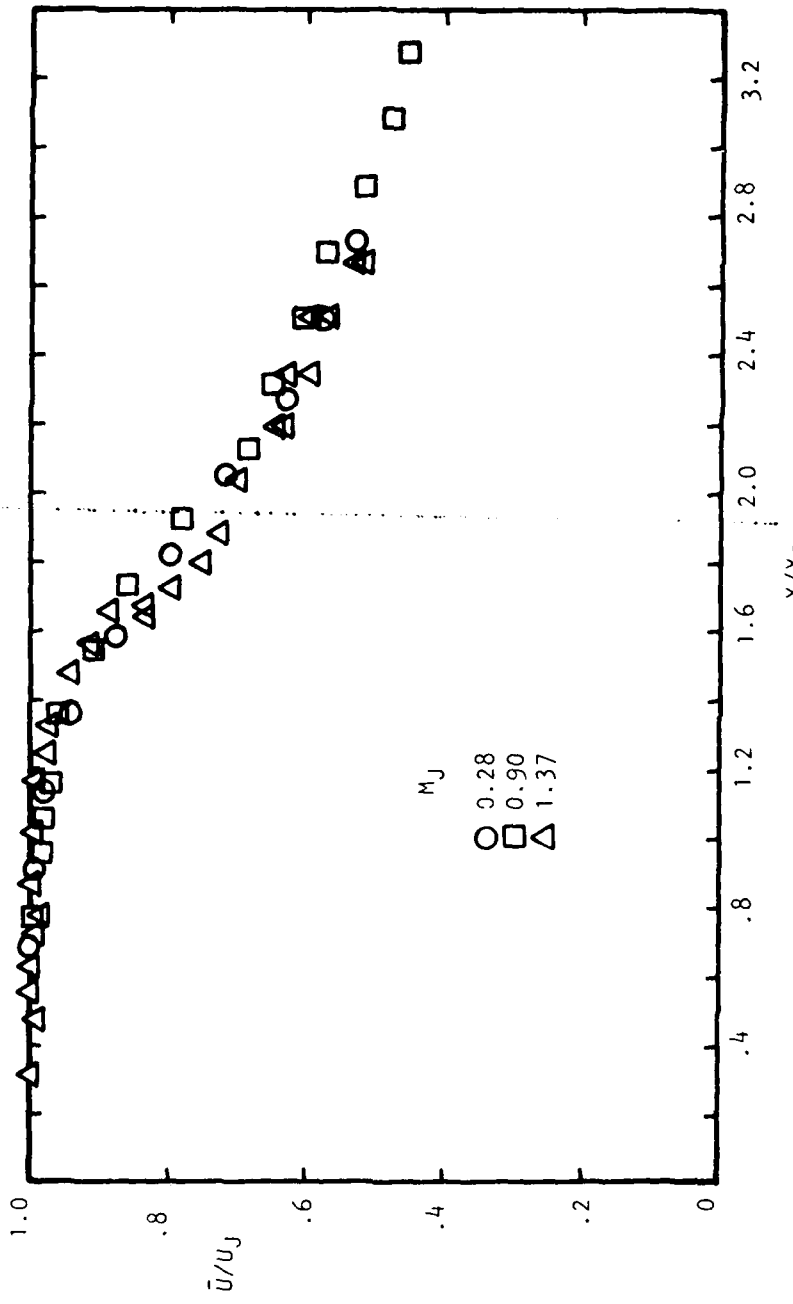


Figure 6.44  $\bar{U}/U_J$  vs.  $X/X_C$

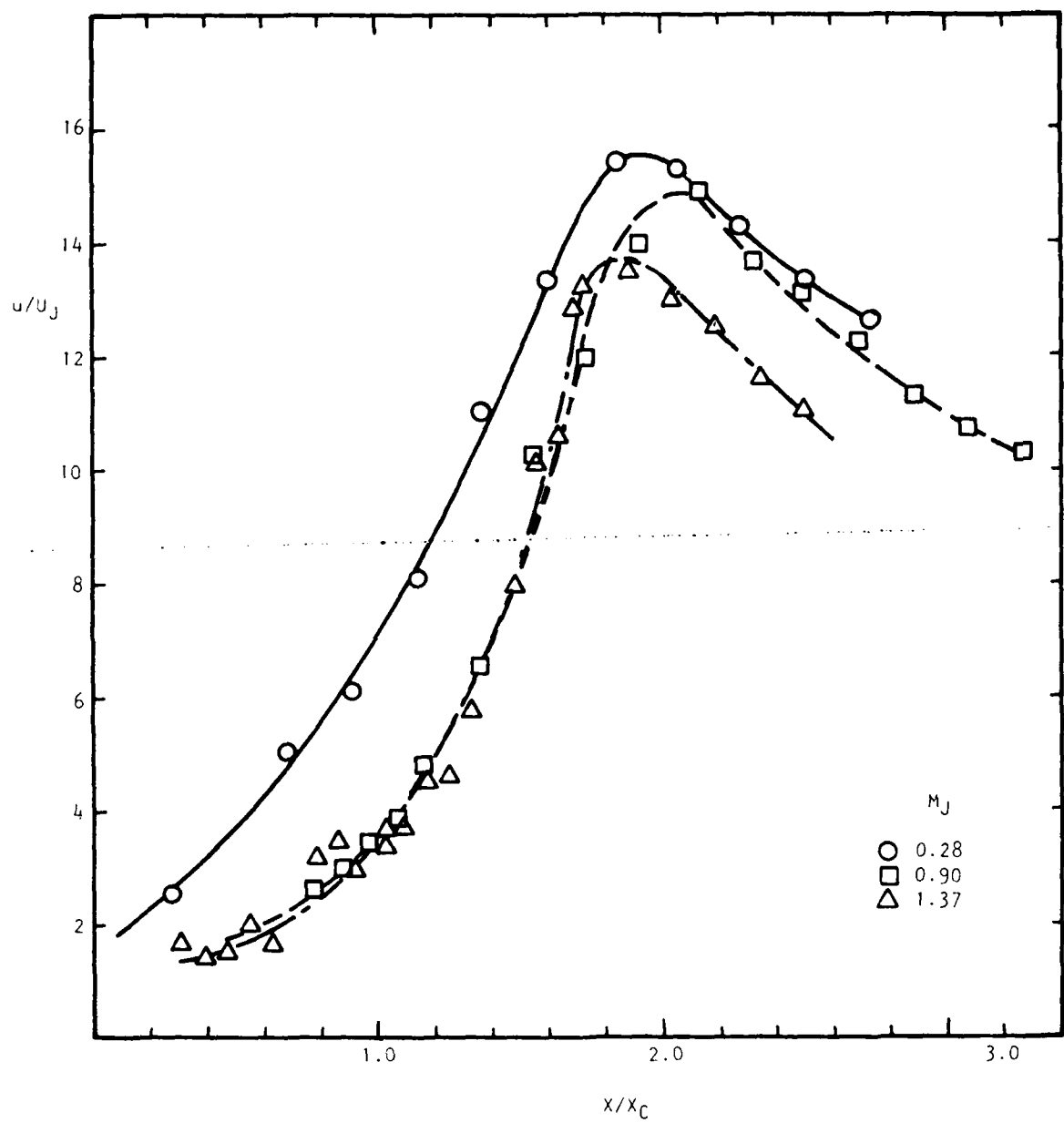


Figure 6.45  $u/u_J$  vs  $X/X_D$

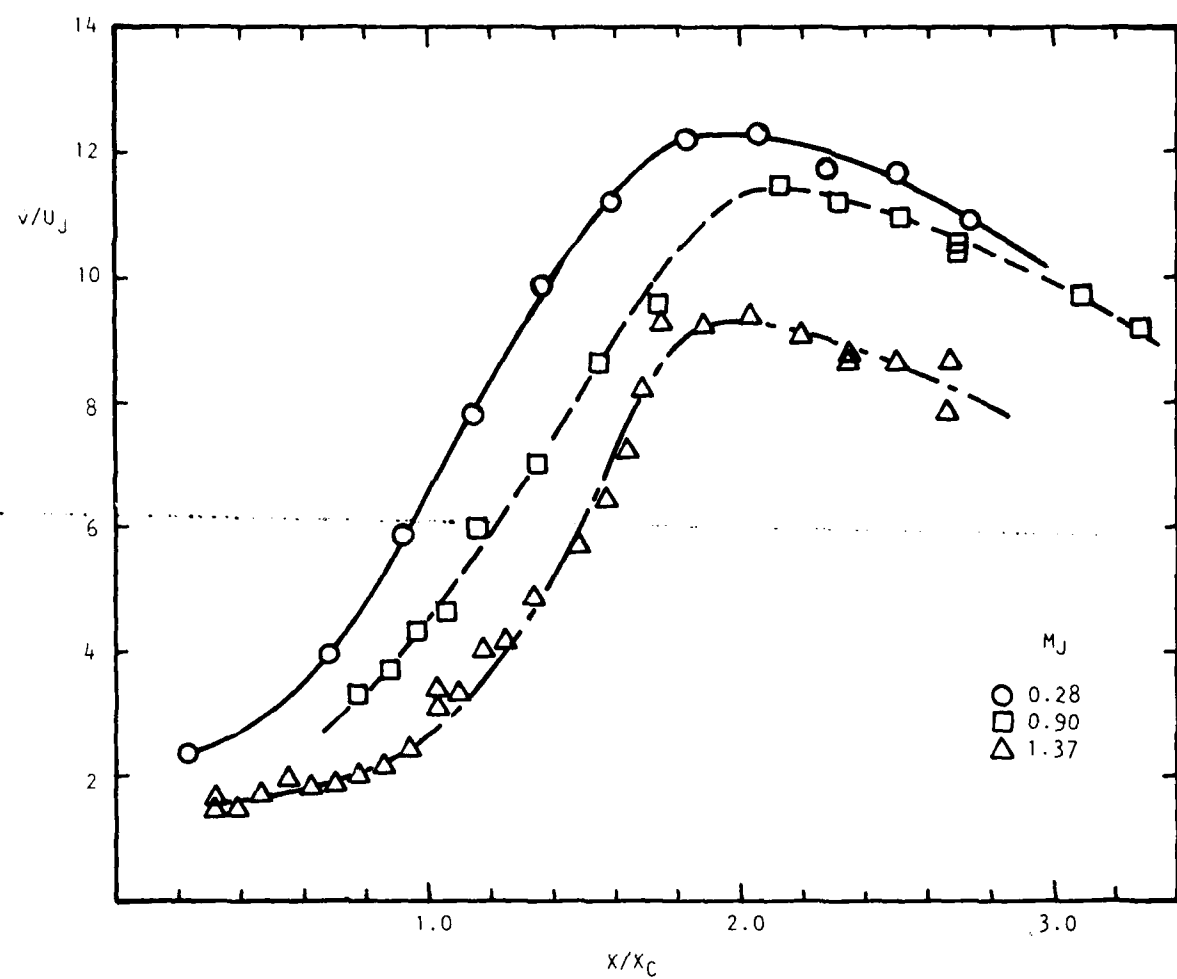


Figure 6.46  $v/v_J$  vs  $X/X_C$

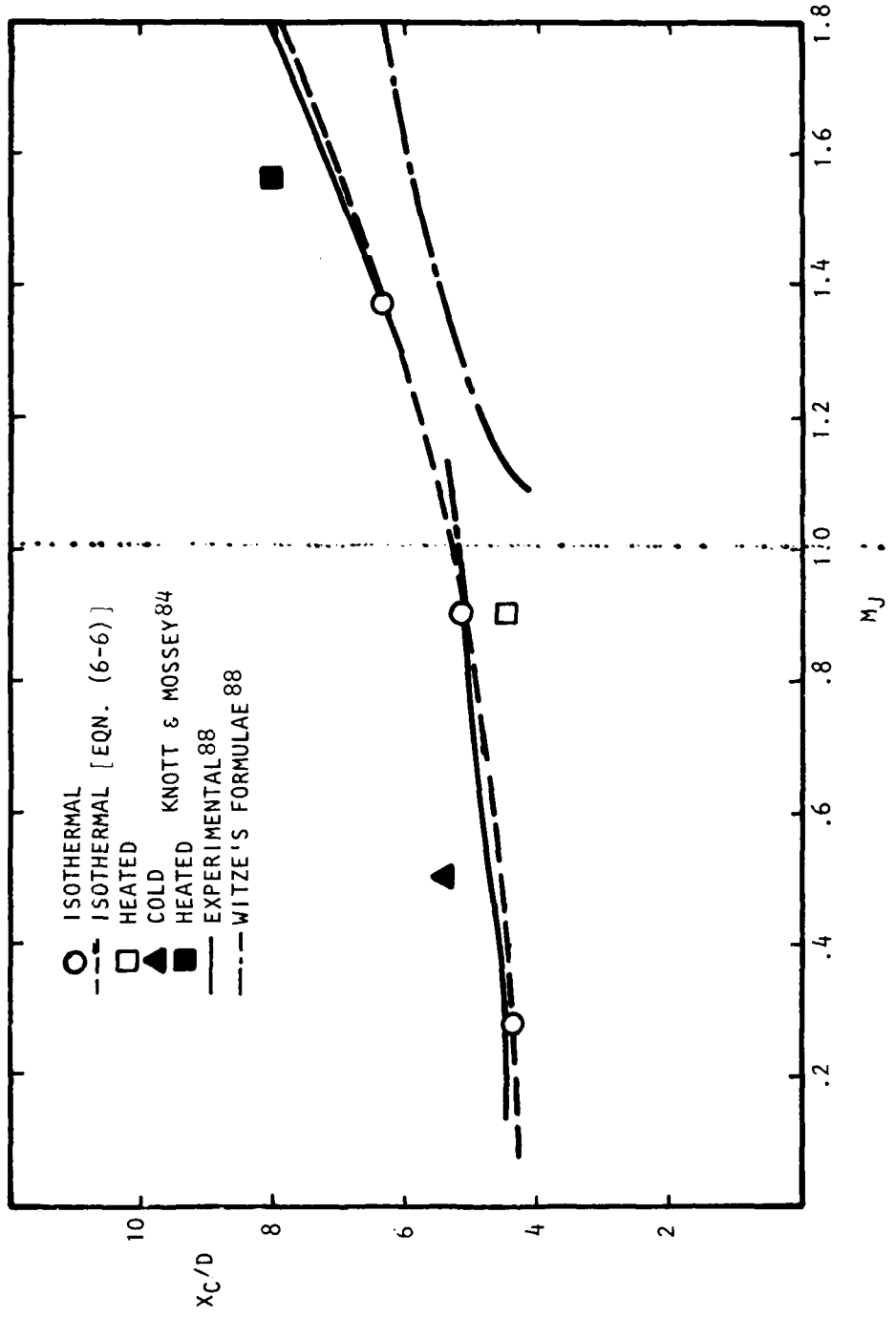


Figure 6.47  $X_{C/D}$  vs  $M_j$

variation of potential core length with Mach number for isothermal jets, based on this formula, is also shown in Figure 6.47. The prediction for the subsonic range passes through the data points. However, in the supersonic range, the predicted curve falls below the experimental results. It should be emphasized that his formula for this range was obtained from results of unheated jets. It would appear that Witze's empirical formulation does not adequately take account of the effects due to density differences caused by heating.

Since the present and earlier results have indicated a continuous trend in the change of the potential core length, a continuous curve extending from the subsonic to the supersonic range would appear to be a more appropriate representation of the changes in the potential core length for the range of Mach numbers studied. Such a curve passing through the data points for isothermal jets, is shown in the figure and has the form:

$$\frac{x_c}{D} = 1.1 M_j^2 + 4.3 \quad (6-6)$$

The curve may be seen to merge with the results from the other experimental studies. This equation suggests that there is a lower limiting value of the potential core length of 4.3 nozzle diameters; and that the value of the potential core length varies little within the lower range of Mach numbers, which appears to be borne out by the many studies of round jets at low subsonic speeds.

The present results for the heated jet is shown to lie below the curve for isothermal jets, suggesting, as in the previous results, that heating has the effect of shortening the potential core. The implication is that cooling the jet would cause the potential core to lengthen. Knott and Mossey's<sup>84</sup> result for a cold jet at Mach 0.5 would tend to agree with this suggestion. However, their result for the heated jet at a supersonic speed does not follow the same trend.

#### 6.4.4.2 Spreading rate $\delta_n$ versus $M_j$

When plotted in terms of the normalized parameter  $n^*$ , the radial distribution of the mean velocity, and particularly the radial extent of such a distribution, gives some measure of the spreading rate of the jet. However, it is difficult to define the real extent of the distribution because this would depend on what is chosen as the cut-off point. In an earlier discussion, a cut-off point was arbitrarily chosen to be that at which the value of  $U/U_j$  dropped to 0.05. Such a definition is subject to quite large errors, since the curve for the mean velocity tapers off very gradually in the outer region of the jet. An approach which has found common usage in the definition of the shear layer thickness is to determine the reciprocal of the maximum velocity gradient and to define this quantity as the thickness of the shear layer. In a normalized mean velocity distribution such as that shown in Figure 6.34, the reciprocal of the maximum gradient would give  $\delta_n$ , which is some measure of the spreading rate (Brown and Roshko<sup>39</sup>). The definition of  $\delta_n$  is shown in the inset of Figure 6.48. The advantage of this approach over the previous one is that there is less ambiguity, since the maximum slopes in the mean velocity distribution are better defined than the cut-off points on the curves.

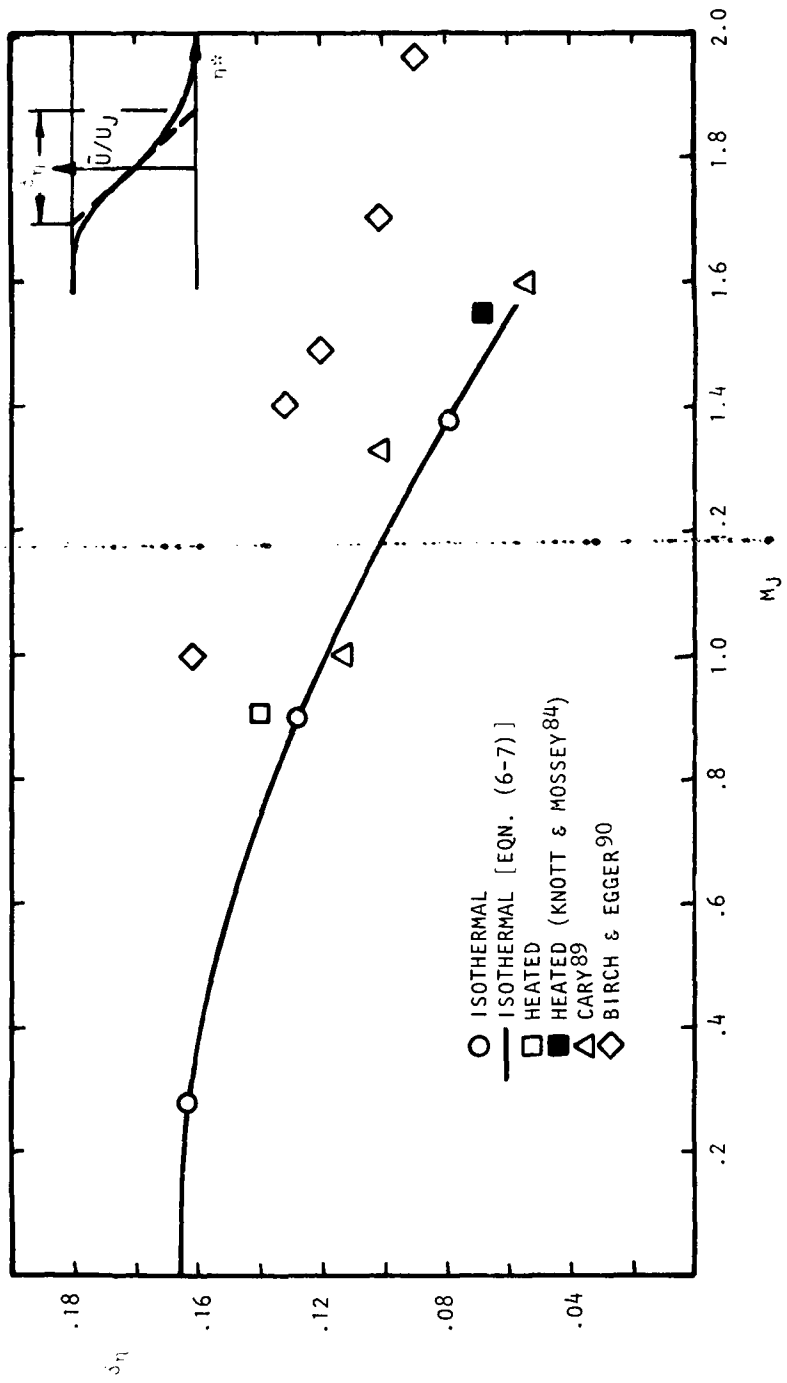


Figure 6.48  $\delta_\eta$  vs  $M_J$

Figure 6.48 shows the variation of  $\delta_n$  with Mach number. Also shown are results of Cary<sup>89</sup> and other researchers referenced by Birch and Eggers<sup>90</sup>. In all cases, the values of  $\delta_n$  fall with increasing Mach number.

The agreement is best between the present results and those of Cary<sup>89</sup>. The values of  $\delta_n$  obtained in the present study and by Cary<sup>89</sup> tend to be generally lower than those obtained by the other researchers. It is noted that an interferometer was used by Cary.<sup>89</sup> The discrepancy between the results obtained by optical methods and those of other researchers using probes might infer that the insertion of an external instrument into the flow region alters the spreading rate of mixing layer. The spreading rate derived from Knott and Mossey's<sup>84</sup> data for a supersonic jet is also shown and it falls close to the present results and those of Cary.

A curve is drawn through the present results for isothermal jets and it has an equation of the form:

$$\delta_n = 0.165 - 0.045 M_j^2 \quad (6-7)$$

The curve passes through the points given by Cary<sup>89</sup>. This curve implies a lower limiting spreading rate of 0.165 which is not far from the figure of 0.162 given by Liepmann and Laufer<sup>66</sup> for a two-dimensional shear layer at subsonic speed. Brown and Roshko<sup>39</sup> suggested that the spreading rate of two-dimensional shear layers might fall at very high Mach numbers as  $1/M$ . However, in the range which is now investigated, it appears that the quadratic form of the equation adequately describes the change.

#### 6.4.4.3 Relative changes in spreading on the two sides of the shear layer

The product of  $\delta_n$  and  $x_c$  is an interesting quantity to be considered. This is a measure of the shear-layer thickness at the point where the potential core ends, and it should be a constant if there is a balance in the movement of the two boundaries of the shear layer as the Mach number is increased. Figure 6.49 shows that there is a general decrease in the value of this product with Mach number, which suggests that the shear layer is contracting much faster on the outside than on the inside of the jet. The difference in the apparent movement of the two boundaries may best be seen in Figure 6.50, which gives the loci of points where the axial turbulence intensity is 8%, an arbitrarily chosen level. If the lines are taken to be an indication of the shear-layer boundary, the outer boundary tends to move through a larger distance than the inner boundary when the Mach number is increased. It seems therefore that an increase in the Mach number causes a compression of the fan which represents the shear layer, and that the compression is more pronounced on the outer side of the jet than on the inner side.

#### 6.4.4.4 Movement of the turbulence intensity peaks

In the discussion of the distribution of the turbulence along the jet centerline, it was indicated that the peaks of the turbulence intensities for the axial and radial components of velocity tended to be positioned at about the same distance downstream of the nozzle for the same Mach number condition. Moreover, it appeared that this distance bore some relationship with the length of the potential core. The downstream distance  $x_u$ -peak/D of the peaks

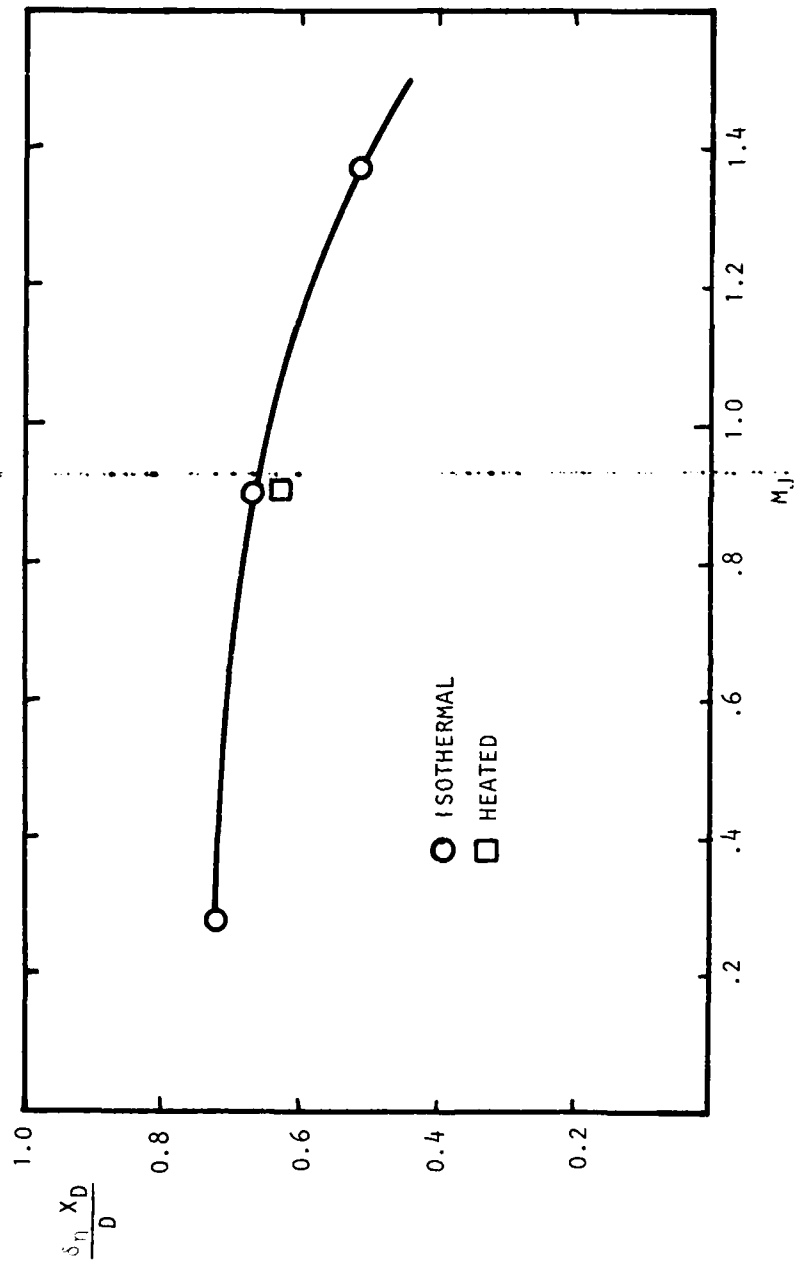


Figure 6.49  $\delta\eta \chi_D$  vs  $M_{Jz}$

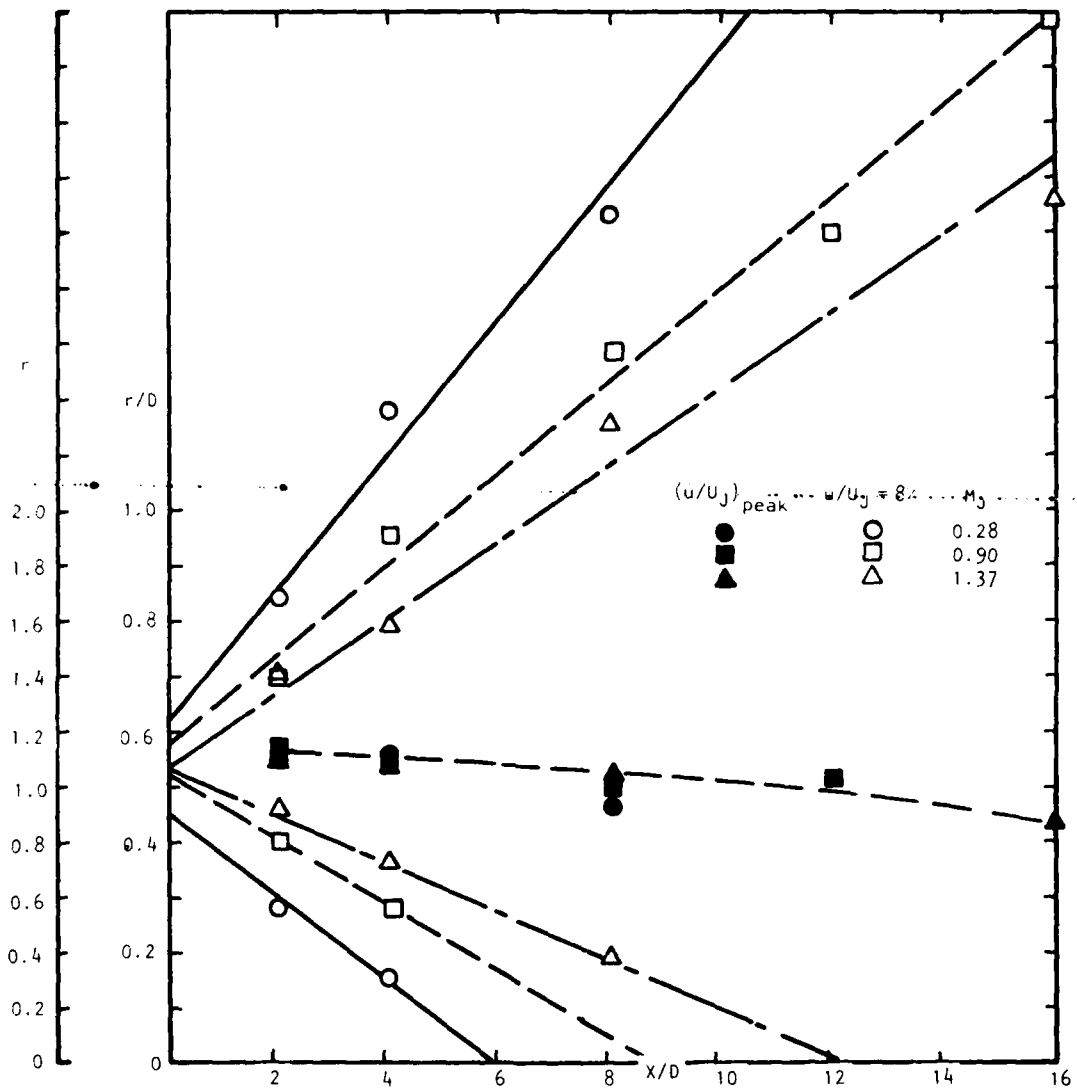


Figure 6.50 Loci of  $\tilde{u}/U_J = 8\%$  and  $(\tilde{u}/U_J)_{peak}$

in the turbulence intensity is plotted as a function of the Mach number in Figure 6.51, and the variation of  $x_c/D$  is also shown. From these curves, a ratio of the two quantities was determined, and it gave a factor of about two. It is interesting to recall that, when the similarity of the mean velocity distribution was considered in subsection 6.4.2.1, it was found that, as the Mach number was increased, the axial distance through which similarity was preserved was also increased. It was then estimated that the ratio of this distance to the potential core length would be about two, also.

#### 6.4.4.5 Equation for the centerline velocity distribution

As seen earlier, Witze's<sup>88</sup> general formula for the centerline velocity distribution appears in the form:

$$\frac{U}{U_J} = 1 - \exp \left\{ \frac{1}{2a} \frac{D}{x_c - x} \right\}$$

in which "a" and  $x_c$  are dependent on Mach number. It suggests that if the functional dependency of " $x_c$ " and "a" is known, an equation may be derived for the mean velocity distribution which explicitly takes account of Mach number effects. The variation of  $x_c$  with Mach number was given earlier in Figure 6.47, and the variation of  $1/2a$  is shown in Figure 6.52. The results lead to an expression for "a" of the form,  $1/2a = 2.5 M_J + 5.0$ . From the trends indicated by these two figures, the following general equation is derived for the mean centerline velocity distribution of isothermal jets:

$$\frac{U}{U_J} = 1 - \exp \left\{ (2.5 M_J + 5.0) \frac{D}{(1.1 M_J^2 + 4.3) D - x} \right\} \quad (6-8)$$

Curves which represent the distribution of mean velocity on the jet centerline at Mach numbers of 0.5 and 1.55 were calculated and are shown in Figure 6.53. The data of Knott and Mossey<sup>84</sup>, also included, show that their cold-jet results lie downstream of the corresponding curve for the isothermal jet, as expected. However, their heated supersonic jet results also lie downstream of the corresponding curve for the isothermal jet, which would disagree with the trends suggested by the present study.

#### 6.4.4.6 Normalization of the radial distribution

It was shown in the discussion of the radial distributions of the various flow quantities that at any given Mach number, good collapse of the data could be achieved for distances from the nozzle of up to twice the potential core length, if the radial distance was normalized according to the definition of  $\eta^*$ . However, at different Mach numbers, the data tended to be spread out differently. If the Mach number effect is taken into account and a new parameter is introduced to represent the radial position, it is conceivable that the data for all Mach numbers could be brought to a common curve. The ratio of  $\eta^*/\delta_\eta$  appears to be a good candidate for this, and if the relationship which has been derived between  $\delta_\eta$  and the Mach number is used, this parameter would be

$$\eta^* (0.165 - 0.045 M_J^2)^{-1}$$

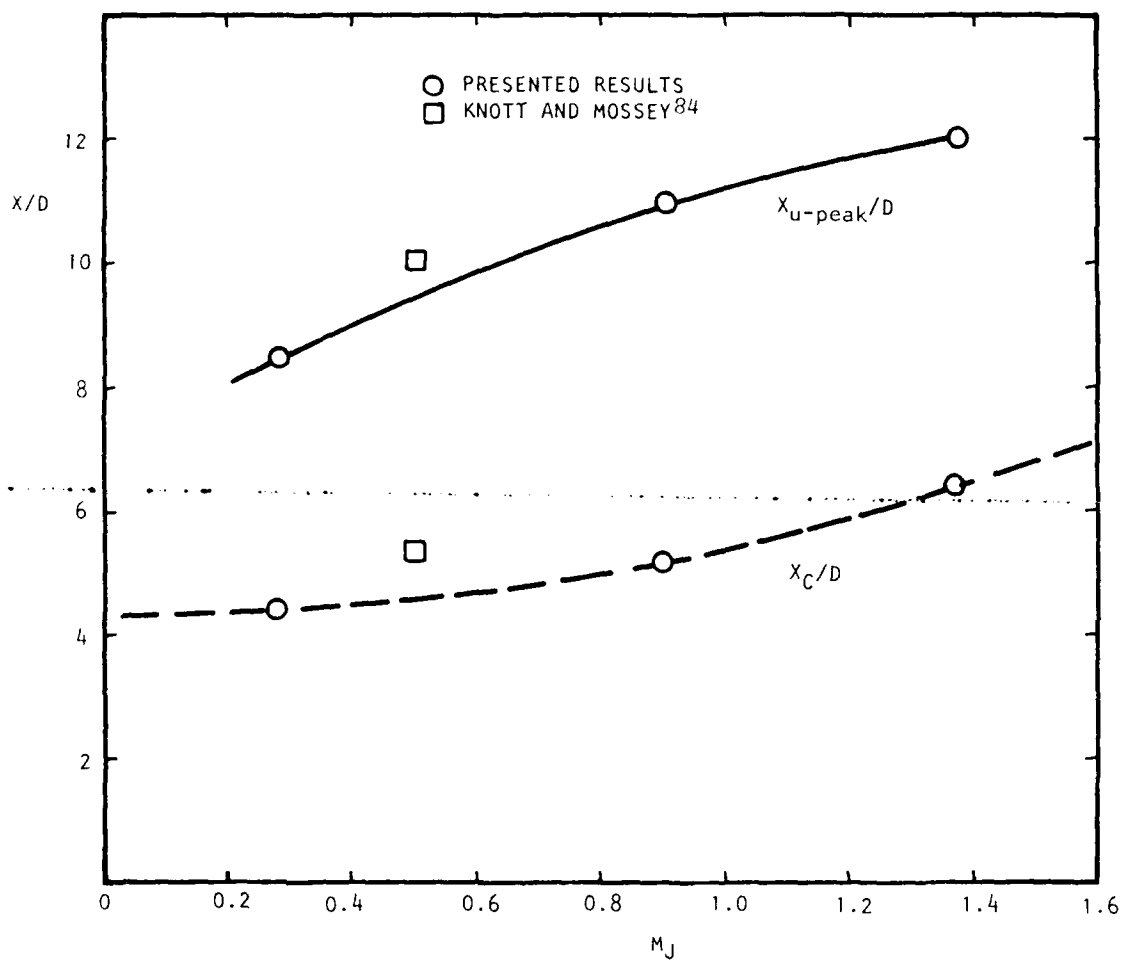


Figure 6.51  $X_{u\text{-peak}}/D$  and  $X_C/D$  vs  $M_J$

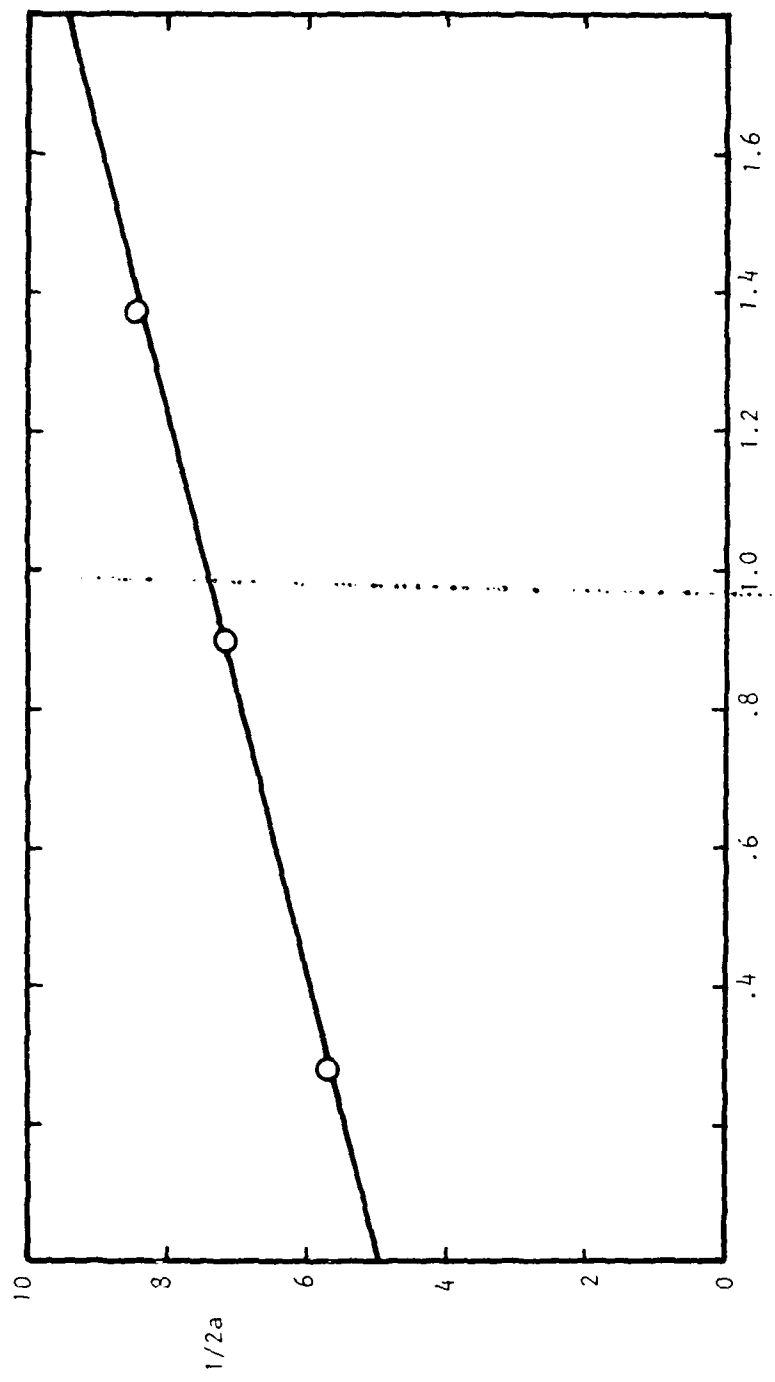


Figure 6.52  $1/2a$  vs  $M_J$

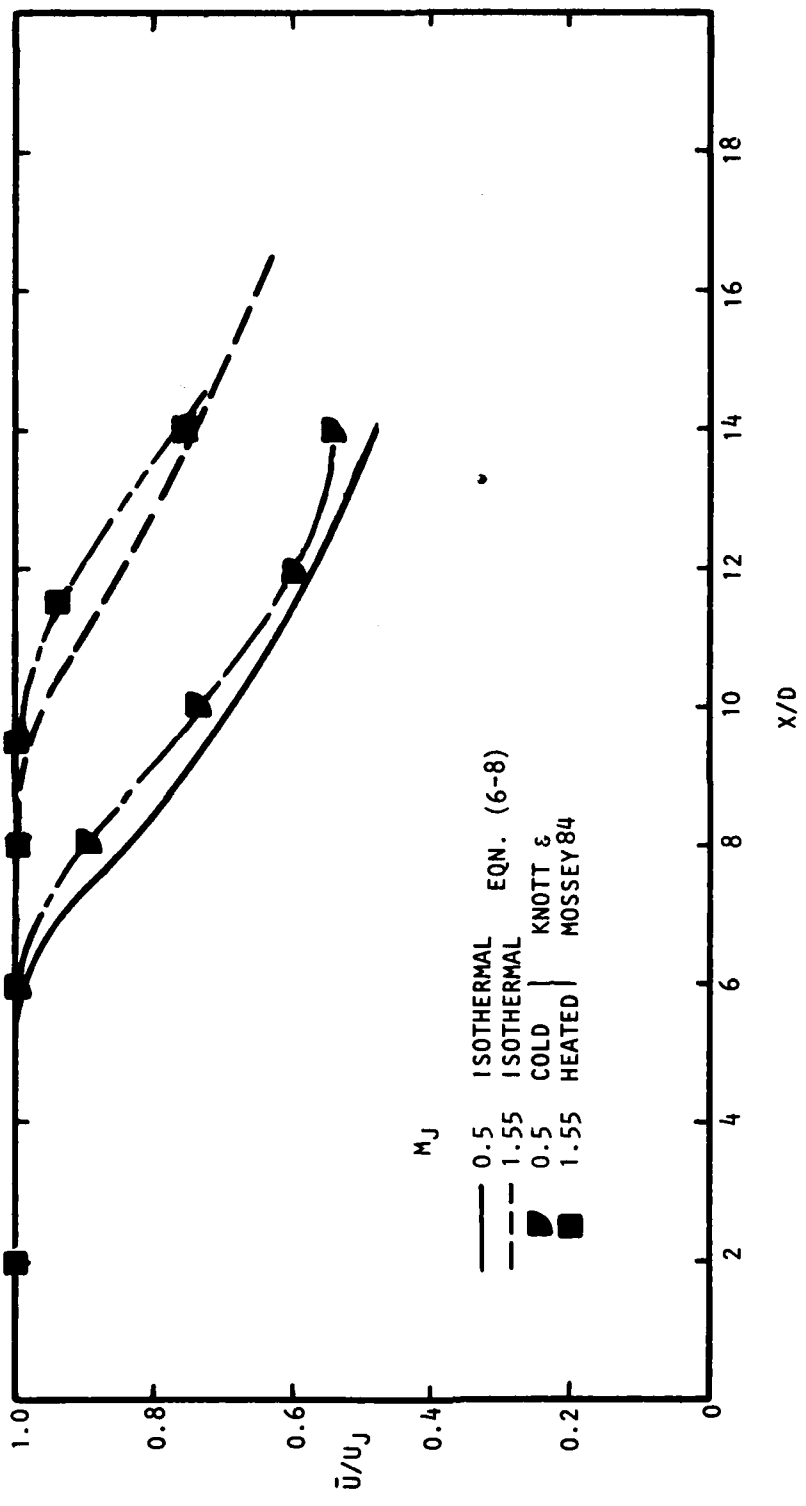


Figure 6.53  $\bar{u}/u_J$  vs  $x/D$  (Centerline)

Figures 6.54 to 6.56 show the radial distributions of the mean velocities and turbulence intensity plotted in terms of this parameter. For clarity, the display in each case is restricted to conditions at the axial station two diameters from the nozzle. However, this should not detract from the main aim of the exercise, since the results at different axial positions have been shown to collapse if they are plotted in terms of  $n^*$ . It is evident that there is a good degree of collapse of the results of the mean velocities, but the collapse is poorer for the turbulence intensity; which is in agreement with earlier comments on normalization of the centerline turbulence intensity distributions.

## 6.5 CONCLUSIONS

### 6.5.1 The LV as an Instrument

This work has shown that the LV used in the study is a viable instrument for the measurement of the various flow quantities in the jet. Some problems remain to be solved, but on the basis of the data which have been made available, the LV appears to have at least the capability of any conventional instrument (e.g., the hot-wire anemometer), even in its present form. The advantage of the LV is the capability it has, as evidenced in these experiments, for measurements at the higher subsonic and supersonic velocities, and in high-temperature environments.

One of the more obvious questions asked about the use of the LV relates to how much the presence of the seeds in the flow alters the physical structure of the flow. This question cannot be satisfactorily answered within the scope of the present study. However, there seems to be no unexpected behavior in the flow as a result of seeding the fluid with particles, and even in the supersonic case, the measurements do conform well with expectation.

This study has raised what is probably a more relevant question with regard to seeding: How should the flow be seeded to obtain meaningful results? It was found that, for an unbiased velocity to be measured, it was necessary to have a balanced seeding of the jet from inside and outside. Otherwise, the readings would show consistently higher or lower values than the true value, depending on whether the lack of seeding was from the outside or the inside of the jet. However, it was found that, as long as seeding was entering the measurement volume from the two sides, the readings of mean velocity fell within acceptable limits. Experiments of simple flow configurations are planned to examine in more detail the effects of seeding in mixing flows.

On assessing and comparing instrument capabilities, it was found that the LV was capable of giving all the kinds of experimental data which are currently obtained with hot-wire anemometers. The only exception may be in the application of conditional sampling techniques which have recently become very popular with hot-wire anemometers, and in intermittency measurements, because the LV itself works on a sampling principle, and the velocities do not appear as a continuous plot on a time history. The velocities, turbulence intensities, correlograms, and spectra obtained with the LV compare satisfactorily with similar measurements made with hot-wire anemometers. With regard to the measurement of the velocity component perpendicular to the mean flow, the LV is much superior, giving an

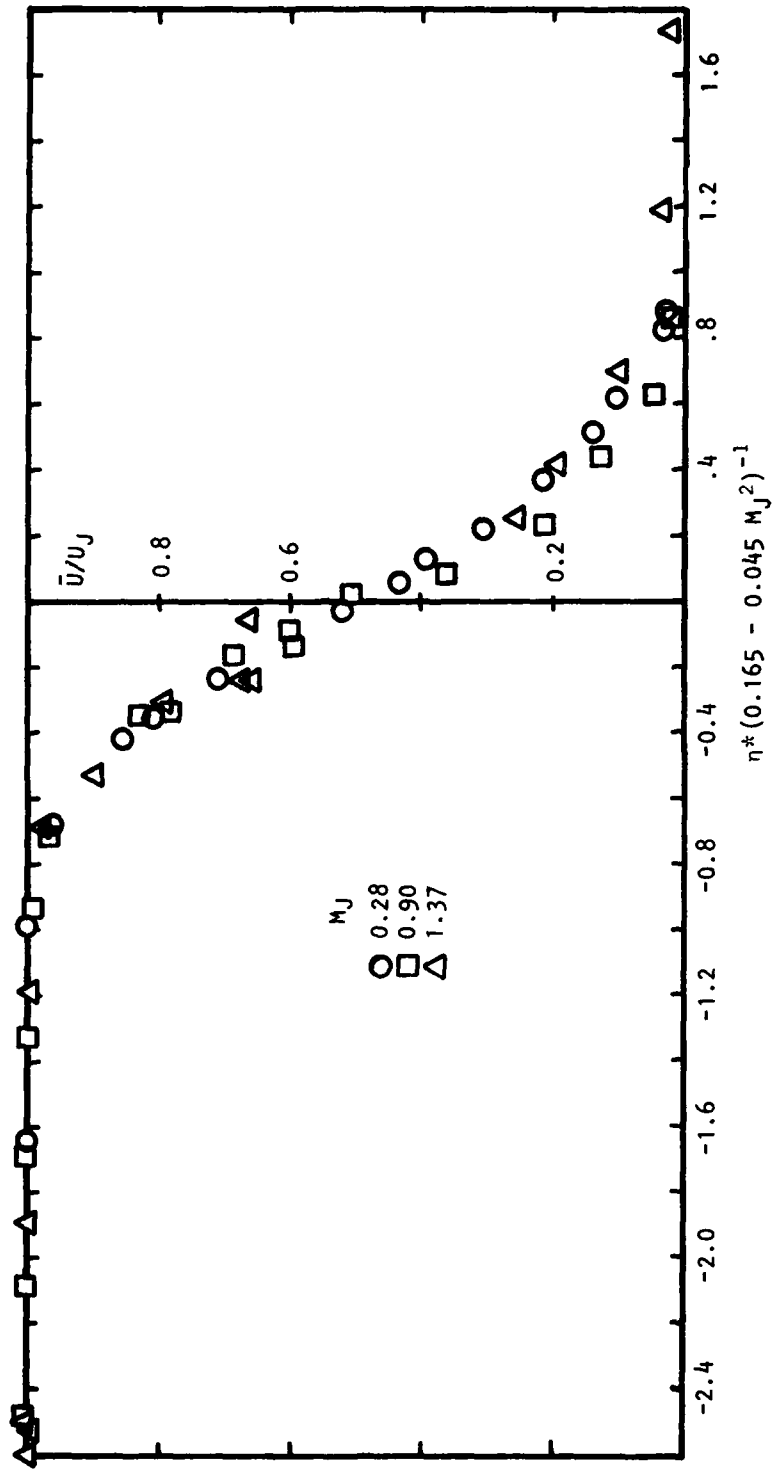


Figure 6.54  $\bar{U}/U_J$  vs  $\eta^* (0.165 - 0.045 M_J^2)^{-1}$

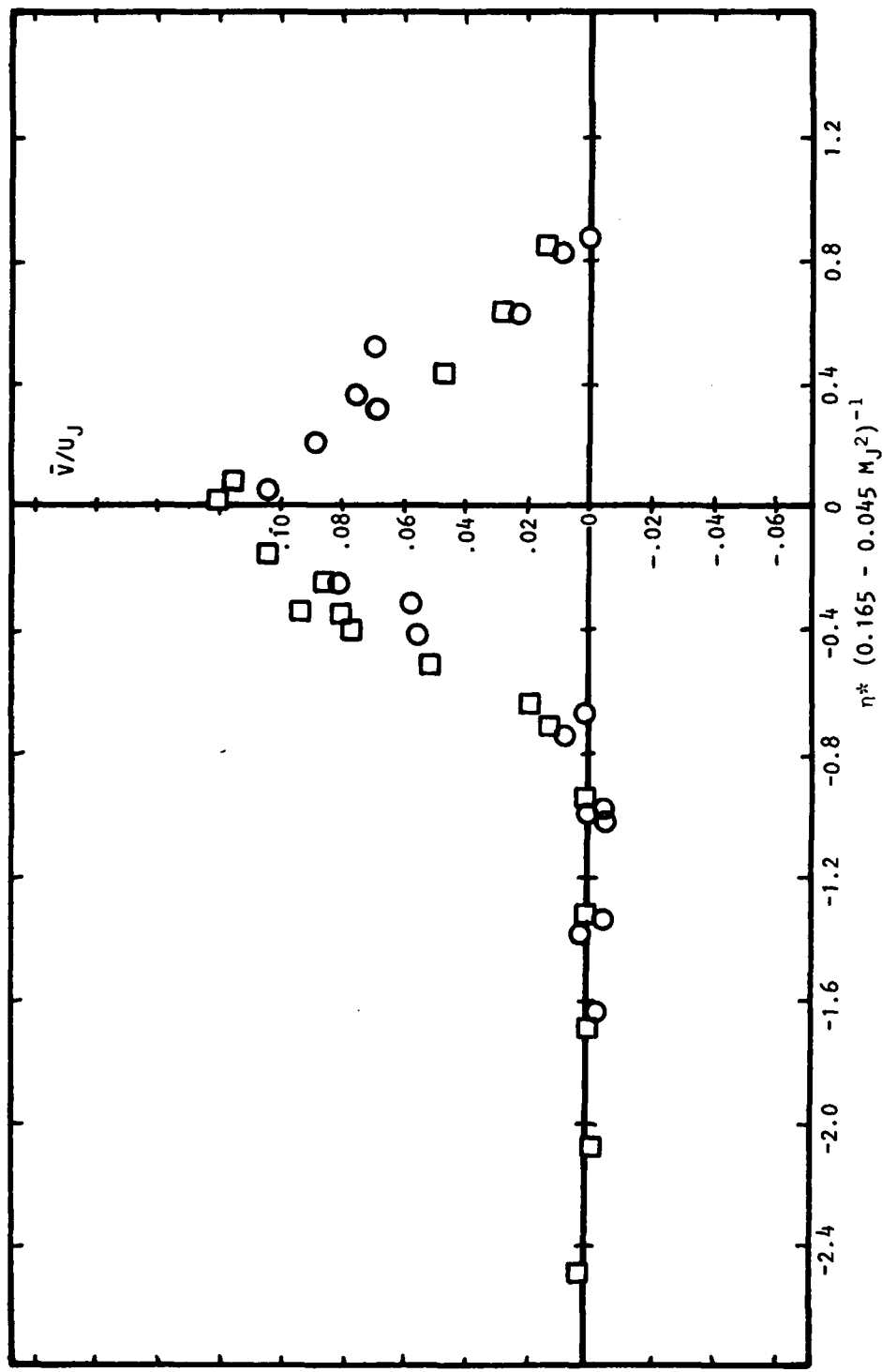


Figure 6.55  $\bar{V}/U_J$  vs  $\eta^* (0.165 - 0.045 M_J^2)^{-1}$

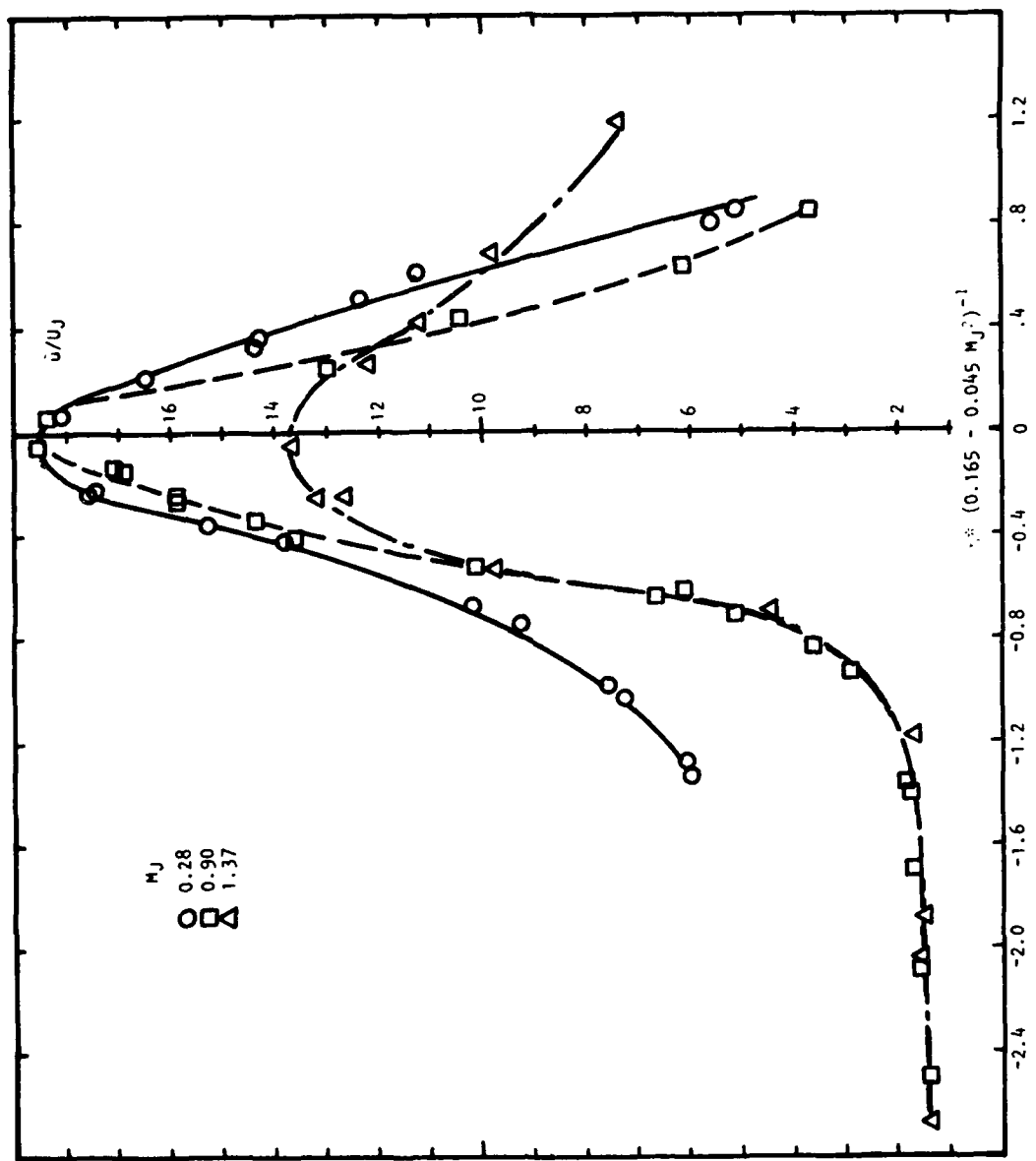


Figure 6.56  $\tilde{u}/U_J$  vs  $\eta^* (0.165 - 0.045 M_J^2)^{-1}$

unambiguous measurement of the velocity component. Another significant advantage of the LV is its capability in measuring reversed flow.

A consistent unaccountable difference of about 2% appears in the values of the axial turbulence intensity across the jet, depending on whether an LV or a hot-wire anemometer is used to carry out the measurement. The LV data tend to be higher. It is believed that a noisy signal from the photomultiplier and the consequent error in the triggering of the zero crossings in the LV processor could cause the LV to give an incorrectly high reading of turbulence. However, the recent discovery of inconsistencies between static calibrations of hot-wire anemometers and their use in dynamic measurements would suggest that the hot-wire measurements interpreted in the traditional way may be unrealistically low. Therefore, the accuracy of hot-wire data is as much in question as the LV data.

#### 6.5.2 The Jet Flow Field

With regard to the specific measurements to identify the characteristics of the jet, it was observed that increasing the jet speed from low subsonic to supersonic did not cause any drastic change in the flow structure. This may be due to the fact that, although the jet efflux velocity was supersonic, the speeds encountered within the shear layer, where the mixing process took place were predominantly subsonic. Apparently if no shocks are present, the shear layer of supersonic jets behaves essentially the same as that of subsonic jets.

Increasing the Mach number in an isothermal jet seems to cause the shear layer of the jet to decrease in spreading rate, and it would appear that the reduction is greater on the outer side of the jet than on the inner side. This reduction in the spreading rate causes the potential core of the jet to lengthen with increasing Mach number. The change in the potential core length,  $x_c$ , with Mach number,  $M_j$ , was found to be given by:

$$x_c/D = 1.1 M_j^2 + 4.3.$$

Changes in the spreading rate of the jet as a result of a change in the Mach number were also assessed. The spreading rate was defined by  $\delta_n$ , the reciprocal of the maximum velocity gradient of a normalized velocity distribution. The results also indicate a quadratic relationship between  $\delta_n$  and the Mach number. Specifically, it was found that the variation followed the equation  $\delta_n = 0.165 - 0.045 M_j^2$ .

Attempts to bring the data of radial distributions of mean velocity for all Mach numbers into a common curve proved to be successful if the normalized radial position parameter ( $n^*$ ) was divided by  $\delta_n$  and the plots made in terms of  $n^*/\delta_n$ . Substitution of the equation for  $\delta_n$  results in a parameter given by  $n^* (0.165 - 0.045 M_j^2)^{-1}$ .

The axial distributions of the mean velocity and the turbulence intensities on the jet centerline were found to move progressively downstream as the Mach number was increased. This trend is in agreement with the concept of an extending potential core resulting from an increasing Mach number. The two orthogonal components of turbulence intensity were found to rise with

increasing axial distance initially, reaching a peak somewhere downstream of the end of the potential core. The ratio of the distance of this peak to that of the end of the potential core is about 2.

The radial distributions of mean velocity are similar in the part of the shear layer where the potential core exists, and this similarity is found to be preserved for an appreciable distance downstream. The present results fall on the same normalized curve as that derived from two-dimensional shear layers. This may seem strange since the flow field of the circular jet, especially in the region downstream of the potential core, is expectedly axisymmetric. However, as previous hot-wire measurements have shown, this appears to be characteristic of round jets and the radial distribution of the mean velocity is expected to be preserved even downstream of the potential core. The distance to which similarity of the radial distributions is preserved appears to be about two times the potential-core length, irrespective of the jet Mach number.

There is at present only a limited amount of data which might shed light on the effects of temperature on the jet flow structure. However, it is clear even now that jet heating would increase the spreading rate of the jet shear layer. The accompanying effect of a shortened potential core is also apparent in the results.

It was found that there was no exactly consistent way in which the turbulence changed with Mach number. However, in the majority of cases there appeared a tendency for the turbulence intensity values to fall with Mach number. This was perhaps more strongly brought out in the falling off of the peaks in the axial distributions of the turbulence intensities.

In reviewing the current results, one deficiency has been the lack of sufficient data to quantify the effects of temperature on the jet structure. The acquisition of such quantifying data, therefore, must form the basis for the beginning of the next phase of work. It may be recalled that previous hot-wire anemometer studies have indicated that the jet scales on a Strouhal number, i.e. on  $FD/U_j$ . The heated-jet results seem to show that, at least as far as the jet spread rate is concerned, it does not scale on the jet efflux velocity. Therefore, it would be interesting to obtain spectra of velocity fluctuations of heated jets to see whether, in spite of an apparent alteration of the boundaries of the mixing layer, the basic jet structure still remains essentially the same as suggested by the Strouhal number criterion. Moreover, to furnish a complete set of data on the flow field of the jet, it would be necessary to fill in the gaps in data which were left because of time limitations. For example, the measurement of the covariance of the axial and radial velocity fluctuations must still be exploited.

The success which has been achieved with the use of the LV in this study prompts more ambitious application. Plans are well along the way to build a four-channel, two-point LV facility to make measurements of two-point cross-correlation in the jet. However, the potential of this instrument for even broader roles may be envisioned. For example, there are some regions in other

flow configurations in which the insertion of an instrument could conceivably change the whole structure of the flow. The LV would be ideally suited in such a region. There are many more situations where the LV could effectively be used, but in the continuing search for a solution to the jet-noise problem, the LV is likely to prove extremely useful. It holds the special promise of being a means by which better knowledge may be gained of the supersonic jet structure and might also hold the key to an understanding of the noise generating mechanism of supersonic jets.

## 7. SHOCK-ASSOCIATED NOISE

## SUMMARY

*The characteristics of the sound field of shock-containing, under-expanded jet flows are studied by measuring the noise from a convergent nozzle operated over a large envelope of supercritical jet operating conditions. The results from shock-containing jets are compared directly with the corresponding results from shock-free jets, and the effects of nozzle pressure ratio and jet exhaust temperature on broadband shock-associated noise are assessed independently.*

The experimentally observed characteristics of sound radiation from subsonic jets and fully-expanded (shock-free) supersonic jets were described in detail in Section 2 of this Volume. The work described in the present section deals with a complementary study of the noise from shock-containing jet flows. In particular, the characteristics of broadband shock-associated noise from under-expanded jets are examined over an extensive envelope of supercritical jet operating conditions.

The experimental program is defined in Figure 7S.1. A two-inch diameter convergent nozzle was operated at supercritical pressure ratios (up to 7.4) over the range of stagnation temperature ratios from unity to 3.7. The measurements were conducted in the anechoic facility. The test points were chosen carefully to be compatible with the turbulent mixing noise experiments, so that, whenever possible, the results from under-expanded (shock-containing) jets can be compared directly with the corresponding results from fully-expanded (shock-free) jets. The results from the entire test program are presented in the form of narrowband spectra in Volume IV of this report. Taken together with the results of the mixing noise experiments given in Volume III, it is possible to define accurately the jet operating conditions, the observer angles, and the frequencies over which the shock-associated noise dominates over the turbulent mixing noise from a supersonic jet.

The overall SPL results from shock-containing jets are compared directly with the corresponding results from shock-free jets, and the effects of nozzle pressure ratio and jet exhaust temperature on shock-associated noise are assessed independently. It is confirmed that the shock-associated noise trends, observed previously from a limited amount of measurements (mainly from unheated jets), are valid throughout the engine operating conditions of practical interest. The overall intensity of shock-associated noise is essentially independent of both the jet efflux temperature (Figure 7S.2) and observer angle (Figure 7S.3); it is primarily a function of jet pressure ratio only. The relevant scaling laws are derived.

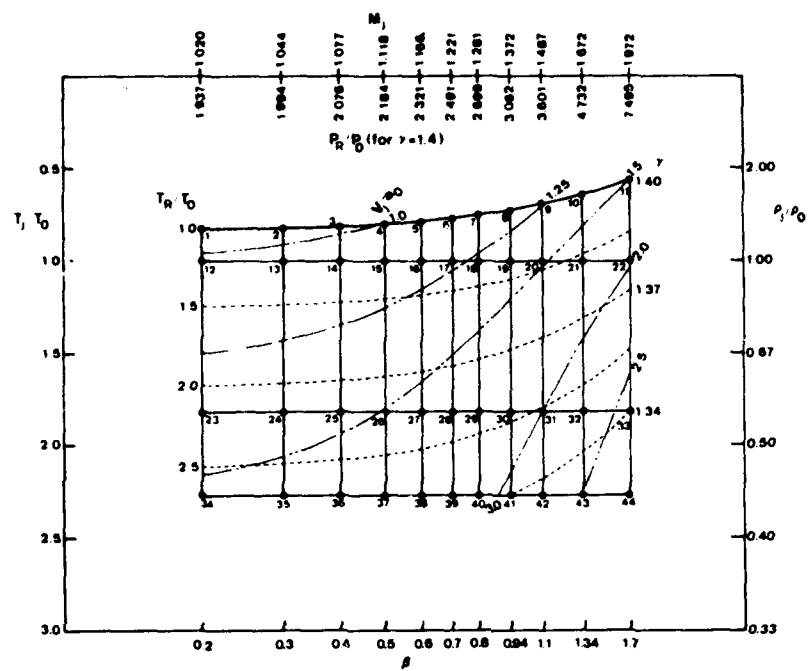


Figure 7S.1 Experimental Program Chart

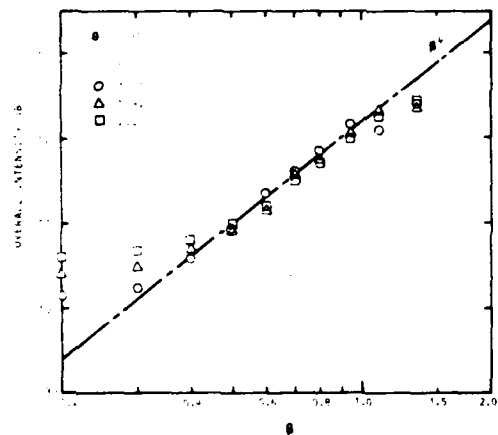


Figure 7S.2 Variation of Overall Intensity with  $\beta$  and  $T_j/T_0$

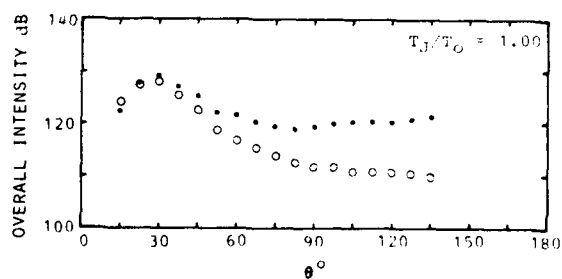


Figure 7S.3 Directivity of Overall Intensity

---

*The peak frequencies in the spectral results are examined with the aid of an existing theoretical model in order to infer some important characteristics of shock-containing jet flows. Finally, the measured spectra are compared in a preliminary manner with the spectra predicted by the same theoretical model, and specific areas for future research are highlighted.*

---

The presence of Doppler shift with angle in the measured peak frequencies (Figure 7S.4), and the variations of the measured peak frequencies with pressure ratio and temperature ratio, are all found to be in good qualitative agreement with the theoretical model proposed by Harper-Bourne and Fisher<sup>91</sup>. Further comparison of measured peak frequencies with theoretical scaling formulae provide several useful implications regarding the characteristics of shock-containing jet flows. It is inferred that the average value of turbulence or eddy convection speed in a jet flow is approximately 0.7 times the jet efflux velocity, and this fraction remains nominally independent of pressure ratio (Figure 7S.5). This observation therefore agrees with the measured value of  $V_c$ , obtained mainly from unheated jets by several investigators. The values of shock spacing constant  $K$  (shock cell length  $L = KBD$ ) are also calculated, and it is inferred that this constant increases with pressure ratio parameter  $\beta$ . It remains to be seen whether this trend can be verified experimentally.

A computer program for the prediction of shock-associated noise, based on the same semi-empirical model, is developed, and a preliminary comparison of measured and predicted spectra is conducted. Although the agreement between measured and predicted spectra is found to be reasonable (Figures 7S.6 and 7S.7), it has not been possible to derive any specific conclusion, since the comparison was not extensive. Furthermore, it is suggested that such a comparison will become more meaningful if values of various jet flow parameters, required for input to the prediction scheme, are obtained experimentally. A considerable amount of future effort is therefore required on various specific aspects of shock-associated noise. A brief discussion of the future work aimed at (i) evaluating the prediction capability in greater detail, and (ii) obtaining a fundamental understanding of various phenomena associated with the generation and radiation of shock-associated noise, is presented at the end of this section.

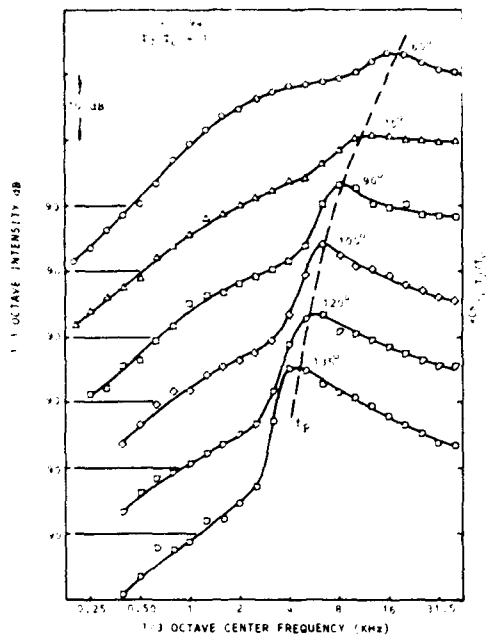


Figure 7S.4 Variation of Peak Frequency with Angle

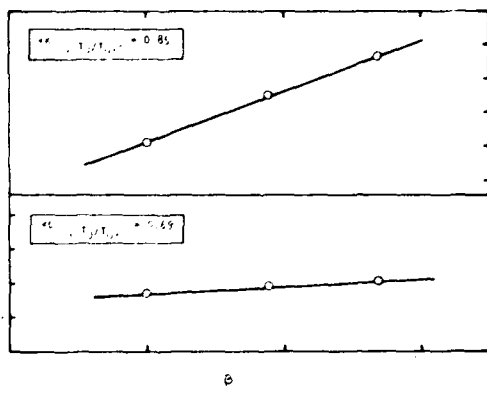


Figure 7S.5 Values of Eddy Convection Velocity Constant ( $C$ ) and Shock Spacing Constant ( $K$ ) Inferred from Noise Measurements

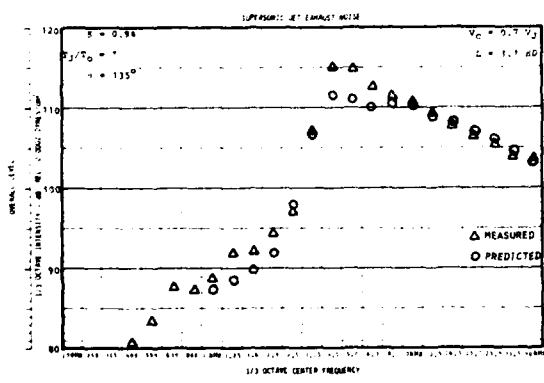


Figure 7S.6 Comparison of Measured and Predicted Spectra

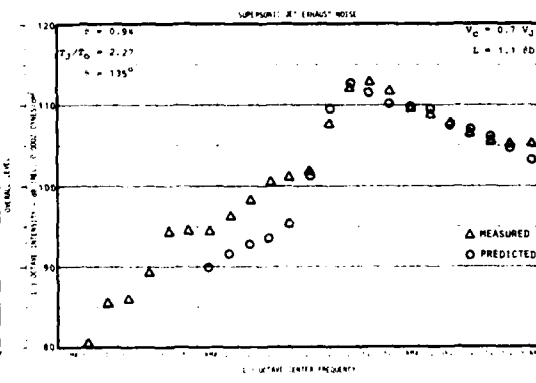


Figure 7S.7 Comparison of Measured and Predicted Spectra

## 7.1 INTRODUCTION

The experimentally observed characteristics of sound radiation from subsonic jets and fully-expanded (shock-free) supersonic jets were described in detail in Section 2 of this Volume. The work described in the present section deals with a complementary study of the noise from shock-containing jet flows. In particular, the characteristics of broadband shock-associated noise from under-expanded jets are examined over an extensive envelope of supercritical jet operating conditions.

The broadband shock-associated noise is defined in Figure 7.1, where the spectrum from an under-expanded jet is compared with the corresponding spectrum from a correctly expanded jet at identical jet operating conditions. When a convergent nozzle is operated at subcritical pressure ratio or when a convergent-divergent nozzle is operated at design pressure ratio, the acoustic spectrum is broad and smooth, and consists of pure turbulent mixing noise. On the other hand, when a convergent nozzle is operated at supercritical pressure ratio (under-expanded) or when a convergent-divergent nozzle is operated at off-design Mach number (under-expanded or over-expanded), the resulting acoustic spectrum contains an extra noise contribution, due to the presence of shock structure in the jet flow, in addition to the basic turbulent mixing noise. The shock-related noise can be divided into two distinct types, each having its own characteristic properties. The first component is discrete in nature, usually with several harmonics, and is often referred to as the "screech" component. The second component is broadband in nature with a well-defined peak frequency. The former has been studied fairly extensively in the past, whereas the broadband shock-associated noise component has not been examined in great detail. In the present study, it is this broadband component that is investigated; and in order to examine its trends and dependencies accurately, the contribution from the screech component to the total sound field is suppressed, as described in later paragraphs.

In considering the total noise radiated from a supersonic jet, it is worthwhile to summarize the roles played by shock-associated noise and turbulent mixing noise. If the sound field from a jet exhaust is characterized by three basic parameters, namely the pressure ratio  $P_R/P_o$ , the temperature ratio  $T_R/T_o$ , and the observer angle  $\theta$ , then the variations of these two noise contributions with the three parameters can be illustrated in a qualitative manner as shown in Figure 7.2. Also, shown in this figure are the regimes of  $P_R/P_o$ ,  $T_R/T_o$ , and  $\theta$  over which the shock-associated noise dominates the turbulent mixing noise. For fixed  $T_R/T_o$  and  $\theta$  (top part of Figure 7.2), the turbulent mixing noise increases as  $P_R/P_o$  decreases; the shock-associated noise is generated at supercritical pressure ratios only, and its magnitude also increases as  $P_R/P_o$  increases; at supercritical pressure ratios, the shock noise contribution normally dominates over the mixing noise contribution. For fixed supercritical  $P_R/P_o$  and  $\theta$  (middle part of Figure 7.2), the magnitude of shock-associated noise remains nominally independent of  $T_R/T_o$ ; in contrast, as  $T_R/T_o$  is increased, the turbulent mixing noise increases due to the increase in jet velocity with heating; the net result is that at low temperatures, the shock noise dominates over the mixing noise, and as the jet temperature is increased, the increasing contribution from mixing noise eventually becomes larger than the shock noise contribution. Finally, for fixed supercritical  $P_R/P_o$  and  $T_R/T_o$ , the bottom part of Figure 7.2 indicates the variations of noise levels with observer angle  $\theta$ . For emission angles beyond the peak radiation angle  $\theta_p$ , the shock-associated noise contribution is essentially uniform, whereas the

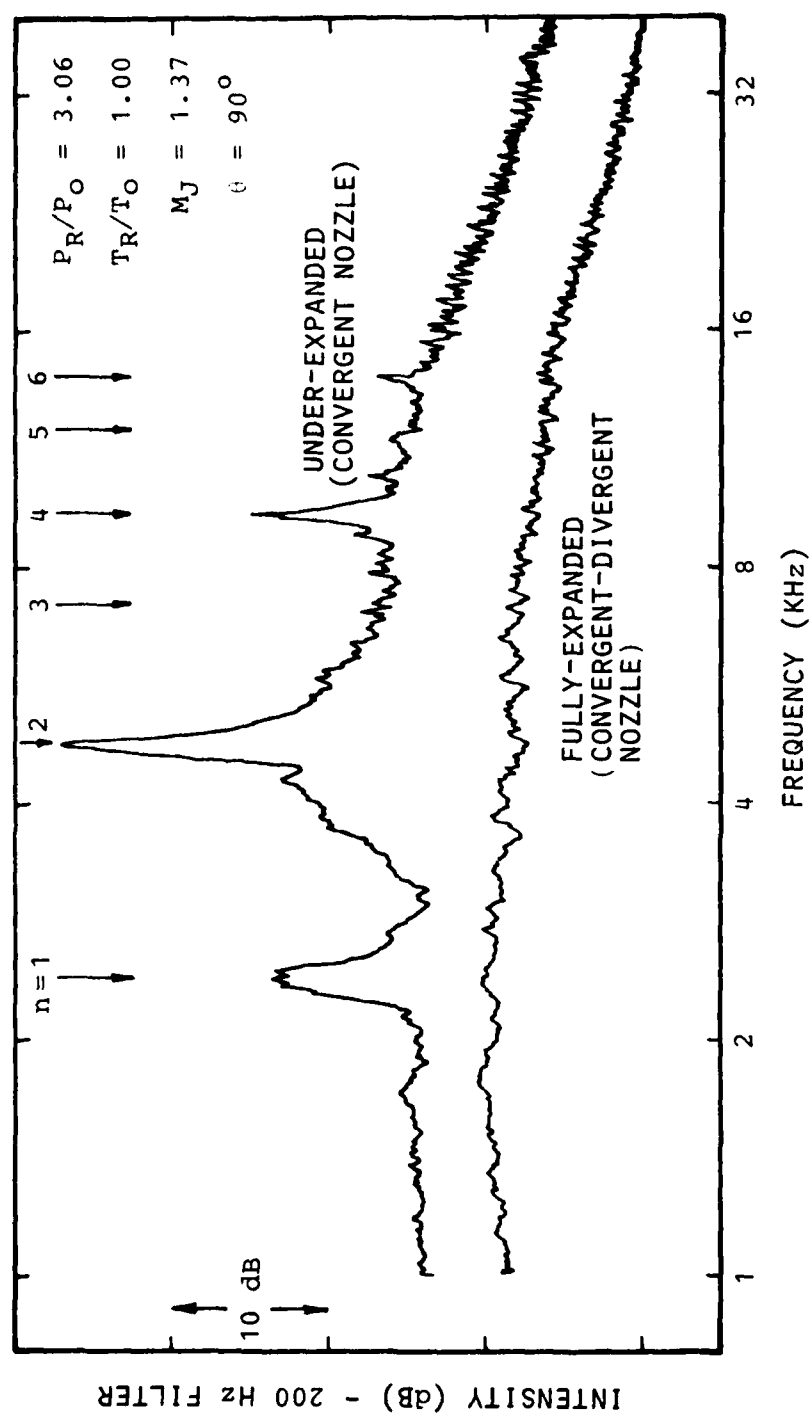


Figure 7.1 Comparison of Spectra from Fully-Expanded and Under-Expanded Jets

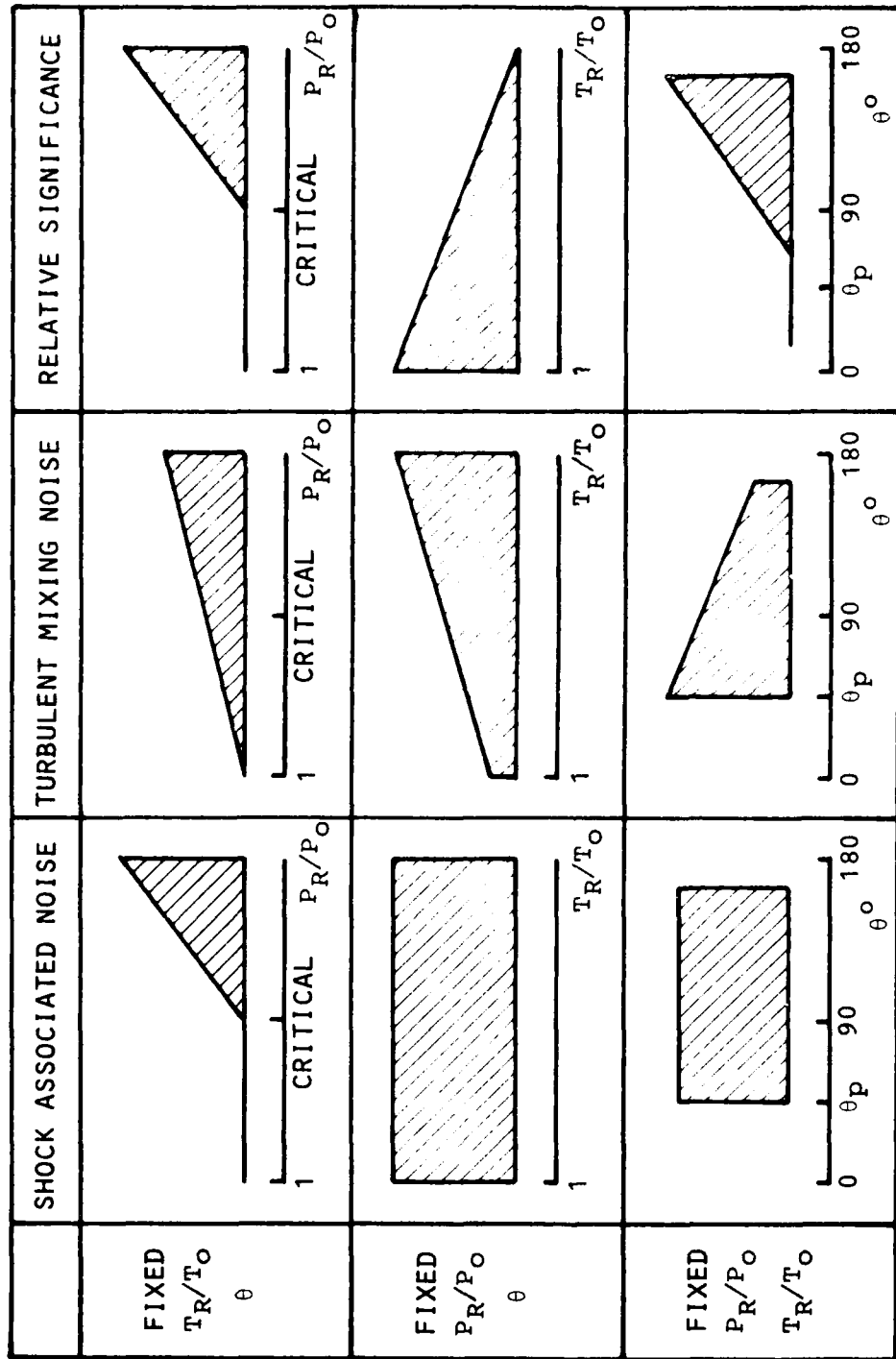


Figure 7.2 Overall Qualitative Significance of Shock-Associated Noise  
 (The height of the shaded area represents the noise level in a qualitative manner.)

turbulent mixing noise level decreases as the observer moves from the peak angle into the forward arc; hence, in this region, shock noise becomes increasingly significant, especially at large values of  $\theta$  (relative to jet exhaust) in the forward arc.

In summary, therefore, if we combine the trends discussed above, it becomes evident that the contribution of shock-associated noise to the total noise is significant (i) at supercritical pressure ratios, (ii) at low temperatures, and (iii) at large angles to the downstream jet axis. The shock-associated noise trends illustrated in Figure 7.2 were derived from the limited amount of data published in the literature. Later in this section, it will be seen that these trends are valid over an extensive envelope of supercritical jet operating conditions.

The main objectives of the present shock-associated noise study are as follows: (i) to obtain accurate shock-associated noise data over a wide range of practical jet operating conditions; (ii) to establish whether or not the trends observed from the limited amount of previous measurements are valid throughout the engine operating conditions of interest, and to quantify the major dependencies; (3) to compare the results with existing theoretical and/or semi-empirical models of shock-associated noise; (4) to identify the problem areas where further quantification and physical understanding are required; and (5) to define future work.

The experimental program is described in detail in paragraph 7.2. The data from the entire test program are presented in the form of narrowband spectra in Volume IV of this report. In the present section, the results are analyzed in detail. The overall results are presented and scaled in paragraph 7.3. The peak frequencies in the spectral results, when examined in the light of an existing theoretical model<sup>91</sup>, provide several important implications concerning some of the properties of shock-containing jet flows. These are discussed in paragraph 7.4. Following this, a preliminary comparison of the measured spectra with the spectra predicted by using the model proposed by Harper-Bourne and Fisher<sup>91</sup>, is discussed in paragraph 7.5.

## 7.2 EXPERIMENTAL PROGRAM

The characteristics of the sound field of shock-containing under-expanded jets are studied by measuring the noise from a two-inch diameter convergent nozzle operated at supercritical pressure ratios (up to 7.4) over the range of stagnation temperature ratios from unity to 3.7. The measurements were conducted in the Lockheed anechoic facility. The jet operating conditions were chosen carefully to be compatible with the turbulent mixing noise experiments so that, whenever possible, the results from under-expanded (shock-containing) jets can be compared directly with the corresponding results from fully-expanded (shock-free) jets.

### 7.2.1 Experimental Program Chart

The experimental program chart for shock-associated noise, somewhat similar to the experimental program chart for turbulent mixing noise (presented in Section 2), is shown in Figure 7.3. It contains all the information pertinent to the shock-associated noise experiments.

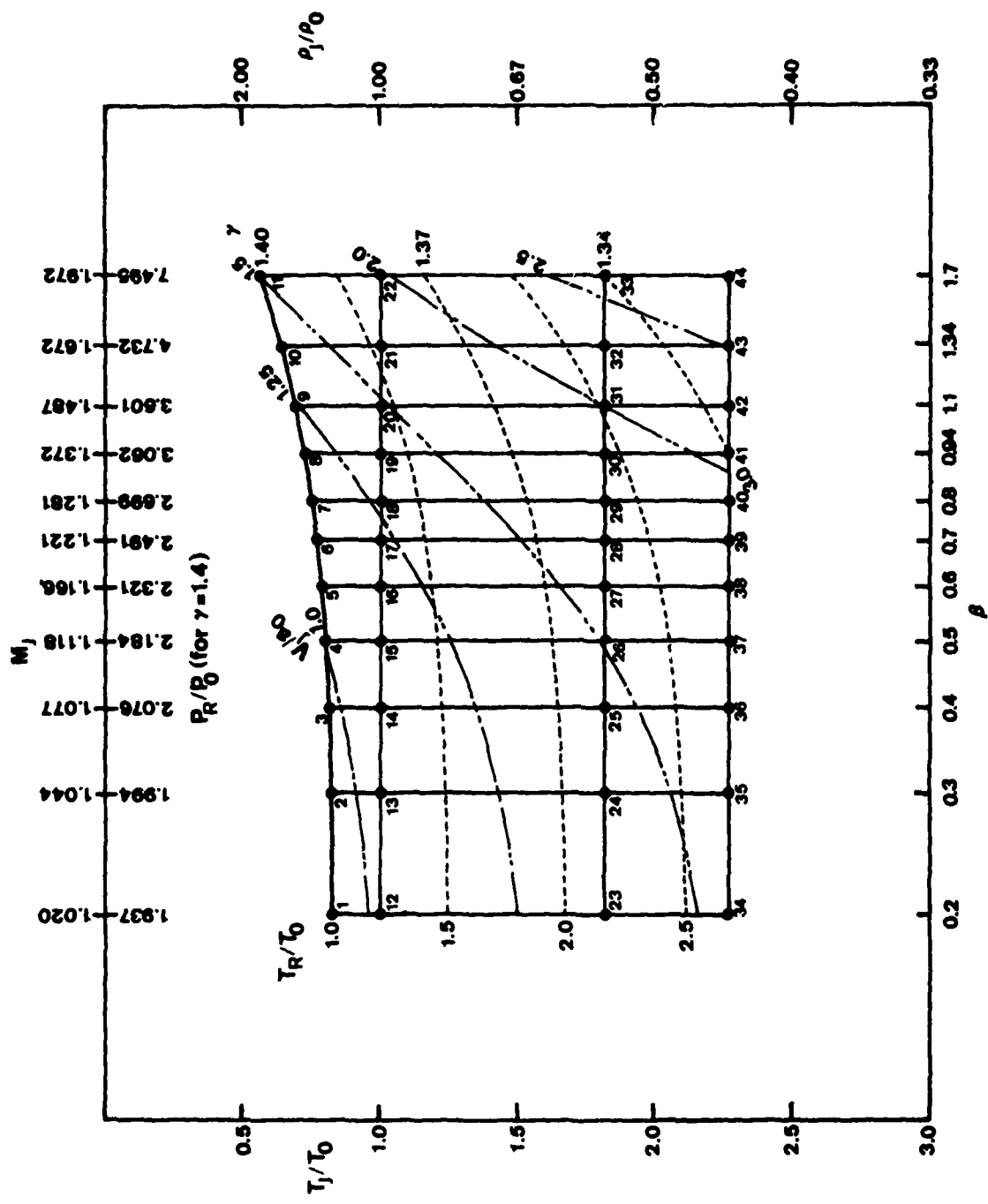


Figure 7.3 Experimental Program Chart for Shock-Associated Noise

The major difference between this chart and the previous chart for mixing noise experiments, arises from the observation that while the intensity of turbulent mixing noise (for a fixed measurement configuration) is essentially a function of jet exit velocity ratio [ $I \propto (V_j/a_0)^8$ ], the intensity of broadband shock-associated noise is primarily a function of the nozzle operating pressure ratio,  $P_R/P_o$ . For the latter, the measured intensity has been observed to vary according to  $I \propto \beta^4$ , where  $\beta = (M_j^2 - 1)^{1/2}$ . The experimental program has therefore been designed such that the jet operating conditions ( $T_R/T_o$ ,  $P_R/P_o$ ) chosen yield test points at reasonably spaced values of  $\log_{10}\beta$ .

The chart shows the values of  $\beta$  (and hence  $M_j$  and  $P_R/P_o$ ) on the X-axis and the values of jet static temperature ratio  $T_j/T_o$  (assuming ideal expansion) on the Y-axis for the 44 test points that constitute the complete experimental program. By considering test points on each horizontal line, the jet efflux temperature is kept constant while varying the pressure ratio parameter  $\beta$ . Conversely, on each vertical line, a constant value of  $\beta$  is maintained while jet exit temperature is varied. Also shown on the chart are lines of constant total (or stagnation) temperature ratio,  $T_R/T_o$ , and constant jet exit velocity ratio,  $V_j/a_0$ . These two parameters have been calculated using the isentropic flow equations and therefore include the assumption that the jet flow is correctly expanded. The main reasons for including these lines of constant  $T_R/T_o$  and constant  $V_j/a_0$  in the experimental program chart is to give an overall indication of the ranges of these parameters. But in addition, they serve to provide approximate values of these quantities for each test point, simply by a quick glance at the diagram.

The values of the parameter  $\beta$  were chosen such that in addition to obtaining reasonably spaced values of  $\log_{10}\beta$ , the twelve test points on the three vertical lines for  $\beta = 0.94$ ,  $1.34$ , and  $1.70$ , are identical to the jet operating conditions used in the turbulent mixing noise tests for the three convergent-divergent nozzles (of nominal design Mach numbers  $1.4$ ,  $1.7$ , and  $2.0$ ).

The values of the parameter  $T_j/T_o$  chosen for this test program are also identical to those utilized in the mixing noise tests. The four nominal values of  $T_j/T_o$  are  $T_j/T_o = \text{unheated}$  (i.e.  $T_R/T_o = 1$ ),  $1.00$ ,  $1.82$ , and  $2.27$ . For unheated tests (TP's 1 through 11), the contribution of the broadband shock-associated noise relative to the contribution from mixing noise (which, for fixed pressure ratio, increases with increasing temperature due to the increase in jet exit velocity) to the total sound field is at a maximum, and therefore the variation of shock-associated noise with  $P_R/P_o$  can be highlighted accurately. The test points (12 through 22) at isothermal jet operating conditions provide minimum effects of temperature, and hence form a base line for studying the effects of temperature on shock-associated noise. Finally, test points 23 through 44 provide data at high temperatures.

To summarize, the experimental program chart for shock-associated noise readily provides all the information relevant to this phase of the experimental program. Taken together with the results of the turbulent mixing noise experiments given in Volume III, it is possible to define accurately the jet operating conditions, the observer angles, and the frequencies over which the shock-associated noise dominates over the turbulent mixing noise from a supersonic jet exhaust.

The procedures adopted for the acquisition and the reduction of noise data are described in Volume IV. In essence, the complete experimental program was executed in two parts. The measurements in the rear arc were conducted first, where twelve microphones were placed at  $7\frac{1}{2}^{\circ}$  intervals from  $15^{\circ}$  to  $105^{\circ}$  to the downstream jet axis. The entire test program was then repeated to obtain results in the forward arc, where ten microphones were again located at  $7\frac{1}{2}^{\circ}$  intervals over the angular range from  $82\frac{1}{2}^{\circ}$  to  $150^{\circ}$  to the jet exhaust. The signals were recorded on a multi-channel FM tape recorder, and all data were analyzed to obtain narrow-band frequency spectra as well as one-third octave band spectra. In the narrow-band analysis, a constant filter bandwidth of 200 Hz was used, and the analysis was conducted over the frequency range from 1 KHz to 40 KHz. The 1/3-octave spectra were obtained over the frequency range from 200 Hz to 40 KHz, and the overall SPL was computed over this frequency range.

It should be noted that all results discussed in this Section are obtained from a two-inch diameter nozzle with the measurement points at 72 nozzle diameters. For application to other measurement configurations, the results must be scaled accordingly.

### 7.2.2 Screech Suppression

The total noise spectrum from an incorrectly expanded jet flow contains discrete components (or screech) in addition to the basic turbulent mixing noise and the broadband shock-associated noise. In order to study the trends and dependencies of the broadband component accurately, it is vital to keep the contamination by screech to a minimum in the experimental program. In the present experiments, screech suppression was successfully achieved by wrapping all surfaces surrounding the nozzle exit with sound absorbing material, and incorporating a small projection inside the nozzle lip. This projection interrupts the feedback loop between the first shock and the nozzle exit plane, which has been previously proposed and verified as the physical mechanism of screech generation.

The effectiveness of the two screech suppression measures, namely the wrapping around the nozzle exit and the nozzle lip projection, was investigated in detail by conducting several calibration tests, where the far-field noise data were recorded at  $90^{\circ}$  to the jet axis and the resulting spectra (from 1 KHz to 40 KHz) were analyzed with a 200 Hz constant bandwidth filter. The jet operating conditions for these tests were selected so as to evaluate the performance of the screech suppression technique as a function of pressure ratio,  $P_R/P_o$ , as well as temperature ratio,  $T_R/T_o$ . For most test conditions, the following four configurations were examined:

- (1) Convergent nozzle, without lip projection and without wrapping.
- (2) Convergent nozzle, without lip projection and with wrapping.
- (3) Convergent nozzle, with lip projection and with wrapping.
- (4) Con-div nozzle at the same pressure ratio, without lip projection and without wrapping.

The corresponding spectra, labelled A, B, C and D, respectively, should consist of (both theoretically and according to previous experience) the following combinations of the individual contributions:

- A Mixing Noise + Screech + Broadband Shock Noise
- B Mixing Noise + Reduced Screech + Broadband Shock Noise
- C Mixing Noise + Broadband Shock Noise
- D Basic Turbulent Mixing Noise

The results from two typical tests, one unheated and the other at high temperature, are shown in Figures 7.4 and 7.5, respectively. The jet Mach number  $M_j$  is kept constant at 1.372 in both cases. Examination of the spectra presented in these figures reveals that, in essence, covering the surfaces in the vicinity of the nozzle exit plane with sound absorbing material reduces the intensity of screech significantly (compare spectra A and B), and at the same time makes it more unstable (i.e., increases the bandwidth of the screech peaks). Addition of the nozzle lip projection minimizes the screech magnitude even further (compare spectra B and C) until the peaks are no longer visible over and above the "mixing noise plus broadband shock noise" spectrum C.

To summarize, therefore, it can be safely concluded that the screech suppressor has been successful in minimizing the intensity of screech to magnitudes well below the spectrum levels under examination. In addition, the basic mixing noise spectrum at low frequencies is not affected to any significant extent by the presence of the lip projection. Based on the results of these calibration tests, the shock-associated noise data obtained from the experimental program are considered to be essentially uncontaminated by the presence of screech.

### 7.3 Overall SPL Results

The overall characteristics of shock-associated noise are presented in this paragraph, where the results from shock-containing under-expanded jet flows are compared directly with the corresponding results from shock-free jets. In particular, the variation of overall SPL with pressure ratio (and hence  $\beta$ ), jet exit temperature ratio  $T_j/T_o$ , and observer angle  $\theta$  are examined in sufficient detail.

The noise characteristics of under-expanded jets are presented in a preliminary manner in Figure 7.6, where the variation of overall intensity with jet exit velocity ratio,  $V_j/a_0$ , is examined at three angles ( $\theta = 30^\circ, 90^\circ, 135^\circ$ ), for two values of jet exit temperature ( $T_j/T_o = 1.00, 2.27$ ). The corresponding results from shock-free jets are also shown for comparison. At  $\theta = 30^\circ$ , the contribution from shock-associated noise does not appear to be significant at both values of  $T_j/T_o$ , and hence the levels from shock-containing and shock-free jets essentially follow the same velocity dependence. However, for a fixed value of  $T_j/T_o$ , as the observer moves from the rear arc into the forward arc, the significance of shock-associated noise increases progressively, and at  $\theta = 135^\circ$ , the levels at supercritical pressure ratios are dominated by the contribution from shock noise. The effect of jet exit temperature ratio,  $T_j/T_o$ , on the relative significance of shock-associated noise can also be examined in Figure 7.6. For a fixed value of observer angle  $\theta$ , the significance of shock-associated noise decreases as  $T_j/T_o$  increases.

In order to determine the scaling of shock-associated noise with pressure ratio, the results at  $\theta = 135^\circ$  from under-expanded and fully-expanded jets at

FULL ARROW: PEAK FREQUENCIES OF SCREECH  
BROKEN ARROWS: PEAK FREQUENCIES OF BROADBAND SHOCK-ASSOCIATED NOISE

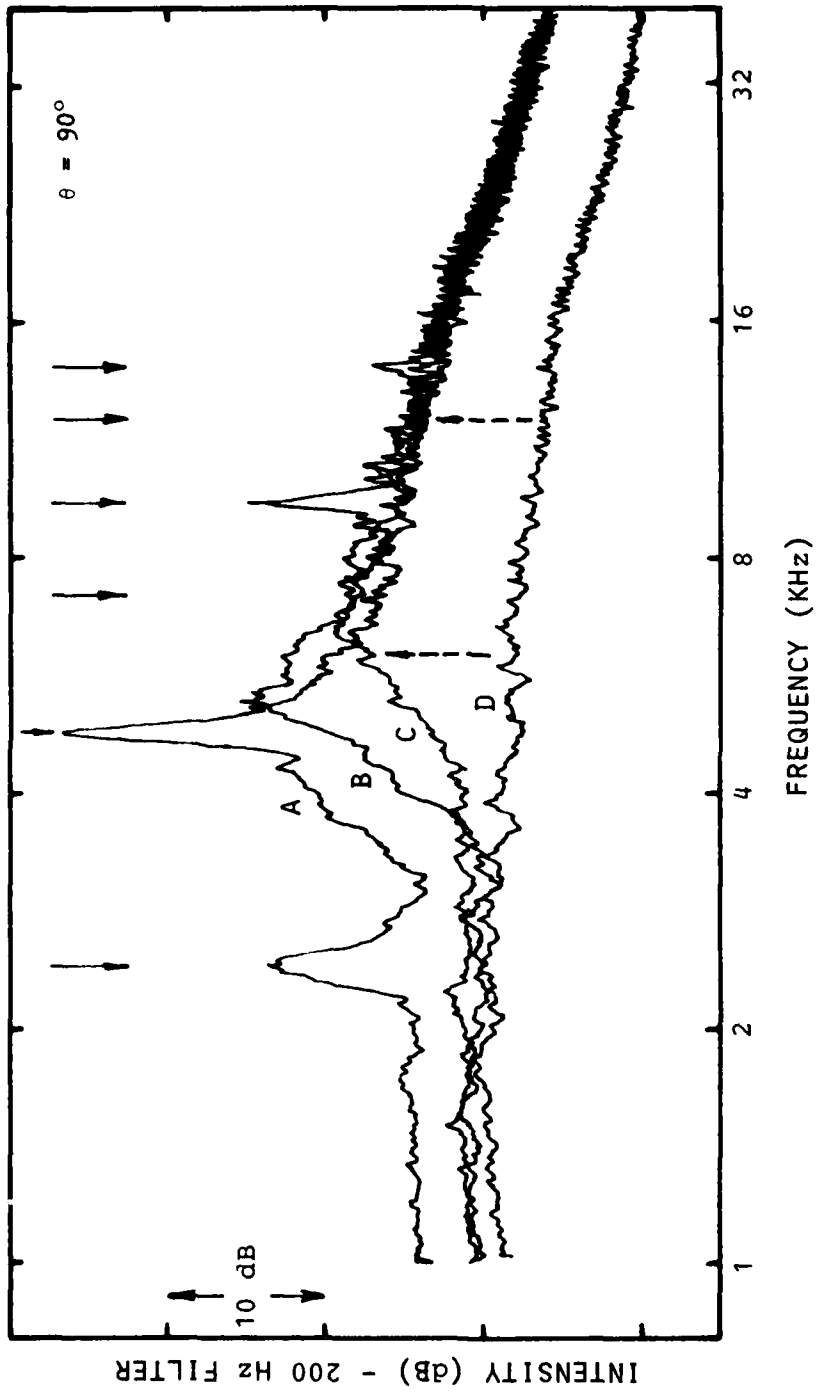


Figure 7.4 Results of Shock-Associated Noise Calibration Test  
 $P_R/P_O = 3.062$ ,  $T_R/T_O = 1.0$ ,  $M_J = 1.372$

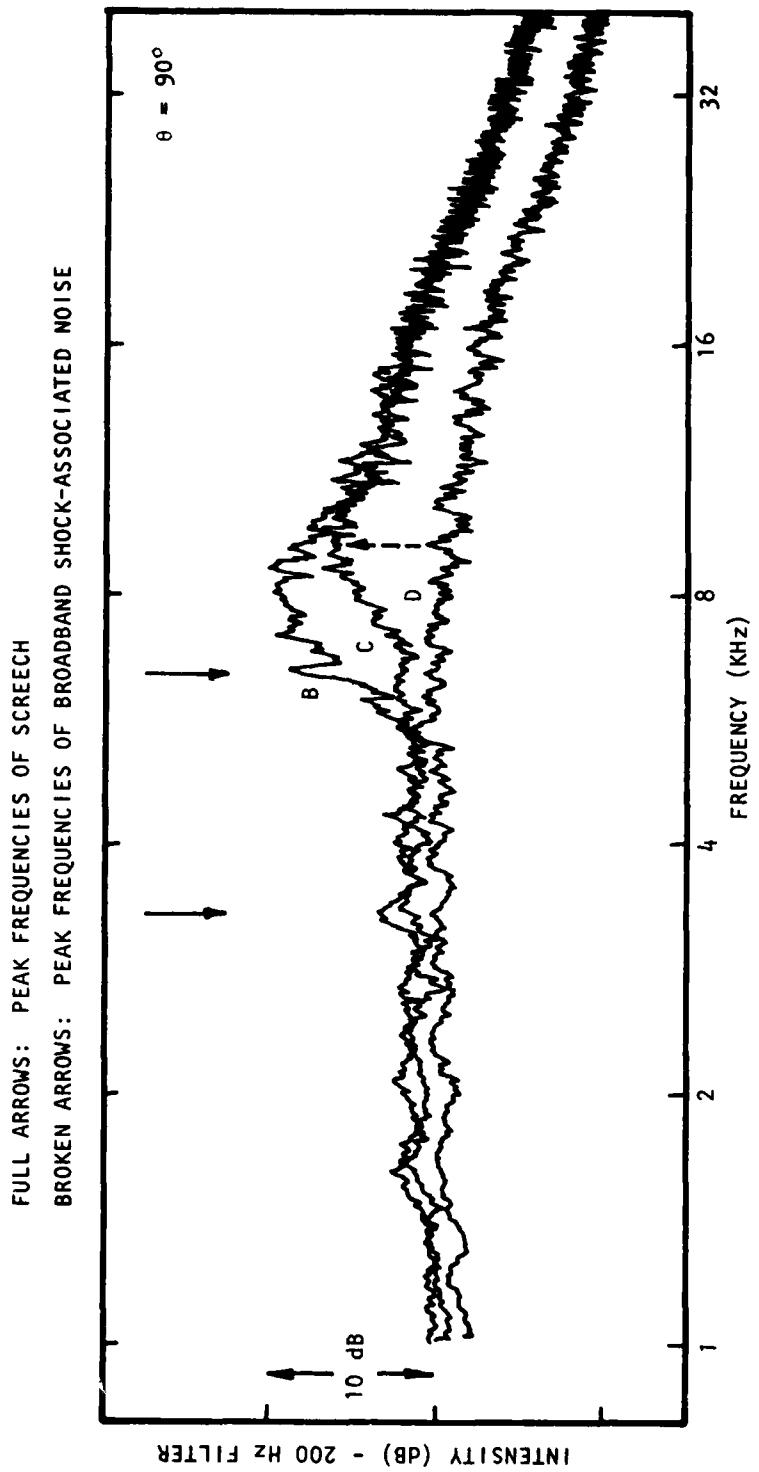


Figure 7.5 Results of Shock-Associated Noise Calibration Test  
 $P_R/P_O = 3.013$ ,  $T_R/T_O = 2.437$ ,  $M_J = 1.372$

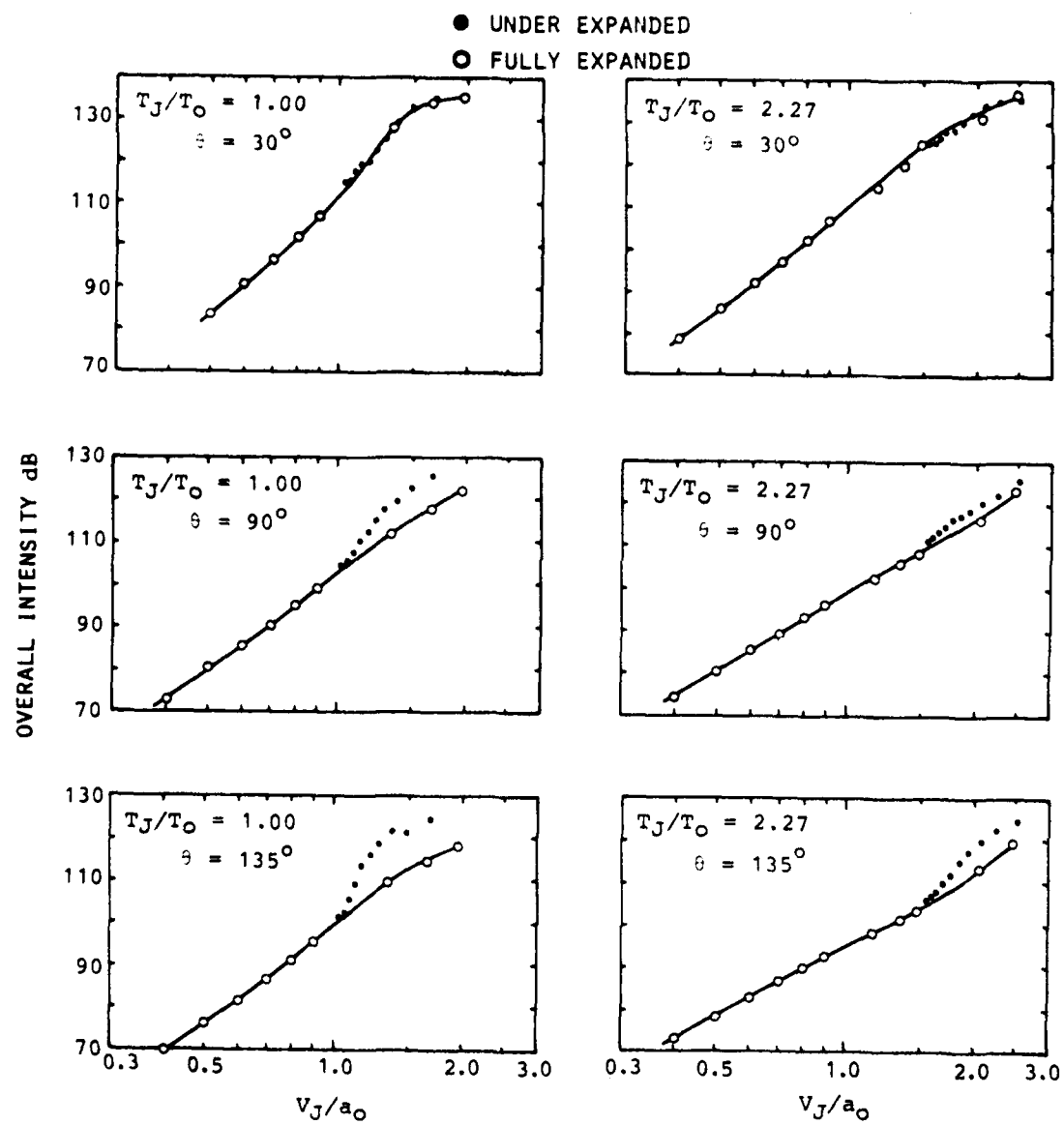


Figure 7.6 Overall Characteristics of Shock-Associated Noise

four values of  $T_j/T_0$  are plotted against the pressure ratio parameter  $\beta$  in Figure 7.7. At high values of  $\beta$ , the fully-expanded levels, which represent the contribution from turbulent mixing noise, are much lower in magnitude than the under-expanded noise levels. Over this regime, the overall intensity scales as  $I \propto \beta^4$  at all temperatures considered here. As  $\beta$  decreases, the mixing noise contribution to the total noise level becomes increasingly significant, and hence the under-expanded jet noise levels begin to depart from the  $\beta^4$  dependence. The value of  $\beta$ , at which this departure from  $\beta^4$  dependence commences, increases as  $T_j/T_0$  is increased. In other words, for unheated jets, the overall intensity from under-expanded jets conforms to the  $\beta^4$  dependence over a larger range of  $\beta$  values, and as the jet exit temperature is increased, this range diminishes. The reason for this is that for a fixed value of  $\beta$  (or pressure ratio), the mixing noise contribution increases with heating due to the increase in jet exit velocity. This is evident in Figure 7.7.

It should be noted that for  $\beta > 1$  (which corresponds to pressure ratios greater than approximately 3.5), the noise levels deviate from the  $\beta^4$  dependence at all temperatures, and there is a tendency for the shock-associated noise levels to saturate as  $\beta$  is increased beyond unity. The reason for this is not apparent at the present time.

The  $\beta^4$  dependence of shock-associated noise intensity observed above suggests that the amplitude of the effective source strength producing this noise varies as  $\beta^2$ . Examination of the normal shock relationships reveals that this is precisely the dependence of the pressure difference across a normal shock of upstream Mach number  $M_j$ . Thus, it appears that the effective source strength associated with the generation of shock-associated noise is proportional to the pressure difference across the shock waves.

The influence of jet temperature on the overall intensity scaling of shock-associated noise can be examined conveniently by superimposing the graphs presented in Figure 7.7 for various values of  $T_j/T_0$  onto a single graph. This is shown in Figure 7.8. It can be seen that at larger values of  $\beta$ , where the shock-associated noise dominates and scales on  $\beta^4$ , the levels are essentially independent of jet efflux temperature ratio  $T_j/T_0$ , and at lower pressure ratios (lower values of  $\beta$ ), the levels increase above the  $\beta^4$  dependence, as discussed earlier.

Finally, the variation of shock-associated noise with observer angle  $\theta$  is examined in Figure 7.9, where the results from under-expanded and fully-expanded jets for  $\beta = 0.94$  are compared at four values of  $T_j/T_0$ . For the unheated case ( $T_j/T_0 = 0.73$ ), the shock-associated noise dominates over the turbulent mixing noise levels at all angles greater than the peak angle. As the jet efflux temperature is increased, the turbulent mixing noise contribution increases, while the shock noise remains essentially unaltered. The relative significance of shock-associated noise therefore diminishes as  $T_j/T_0$  increases, and at the highest temperature considered ( $T_j/T_0 = 2.27$ ), the directivity in the rear arc is primarily controlled by the mixing noise, whereas in the forward arc the total noise levels are dominated by shock-associated noise. For all values of  $T_j/T_0$ , the directivities from under-expanded jets in the forward arc are essentially flat, indicating that the sound radiated by the presence of shocks in a jet flow is fairly omnidirectional.

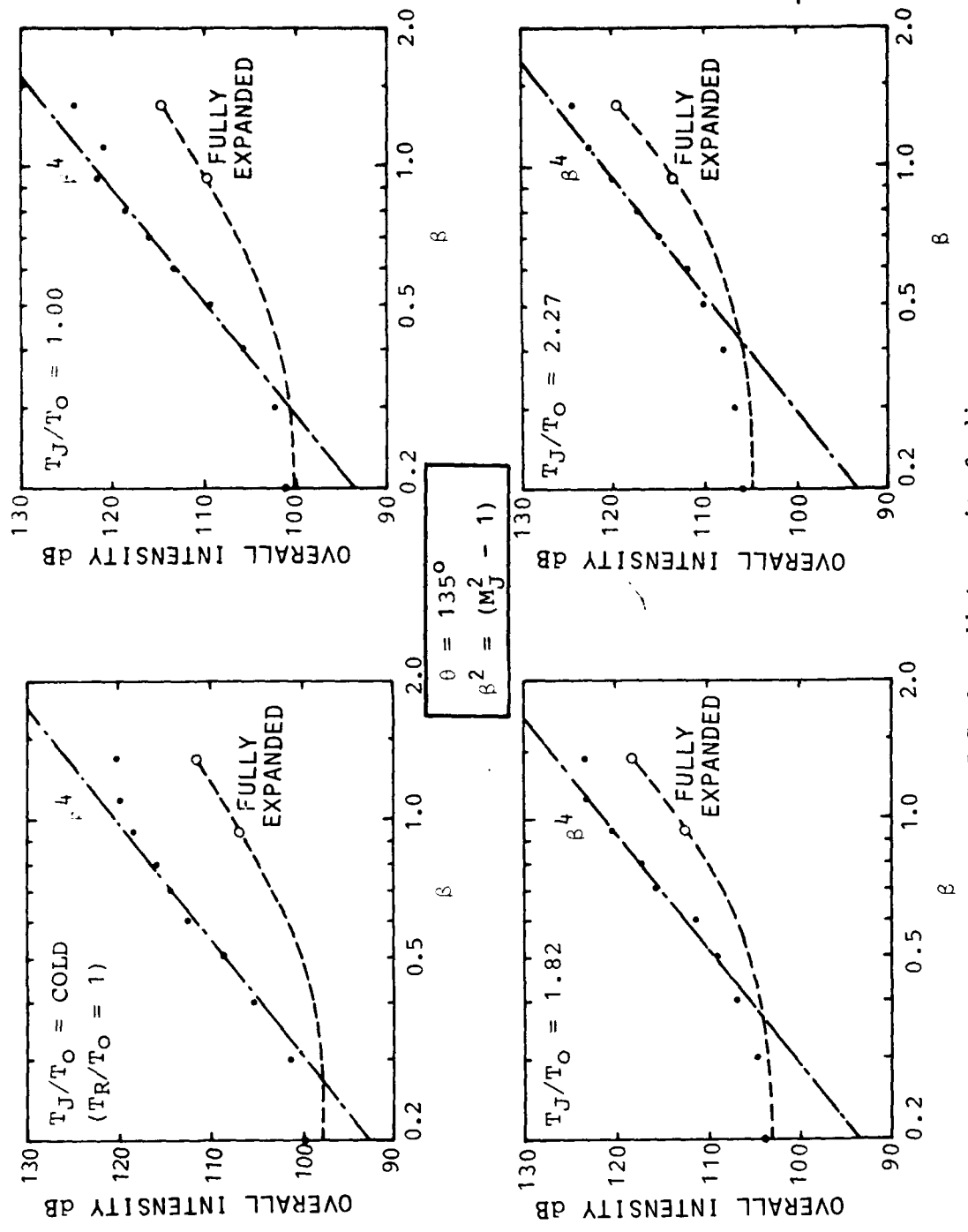


Figure 7.7 Overall Intensity Scaling

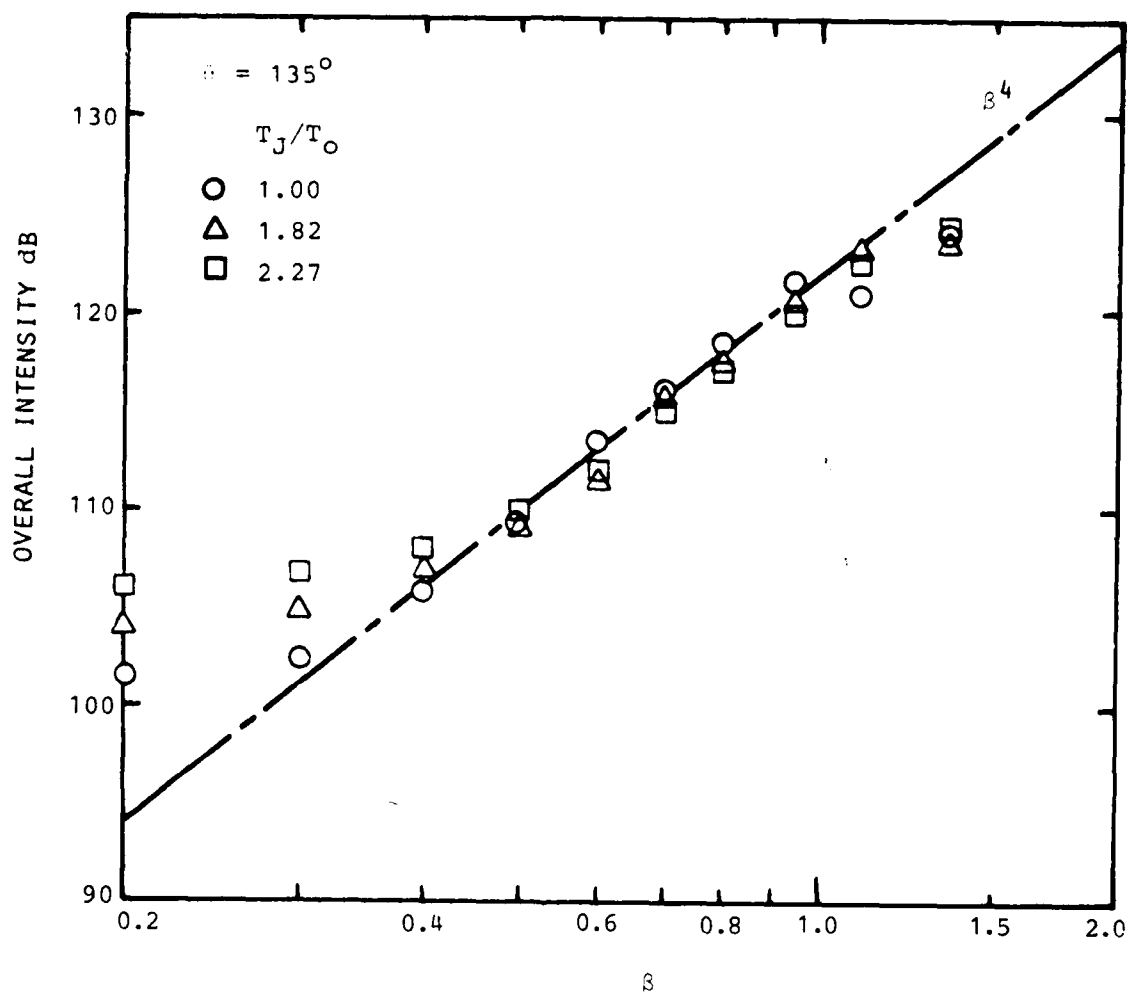


Figure 7.8 Effect of Jet Temperature

$R = 0.94$   
 $M_J = 1.372$

- UNDER EXPANDED
- FULLY EXPANDED

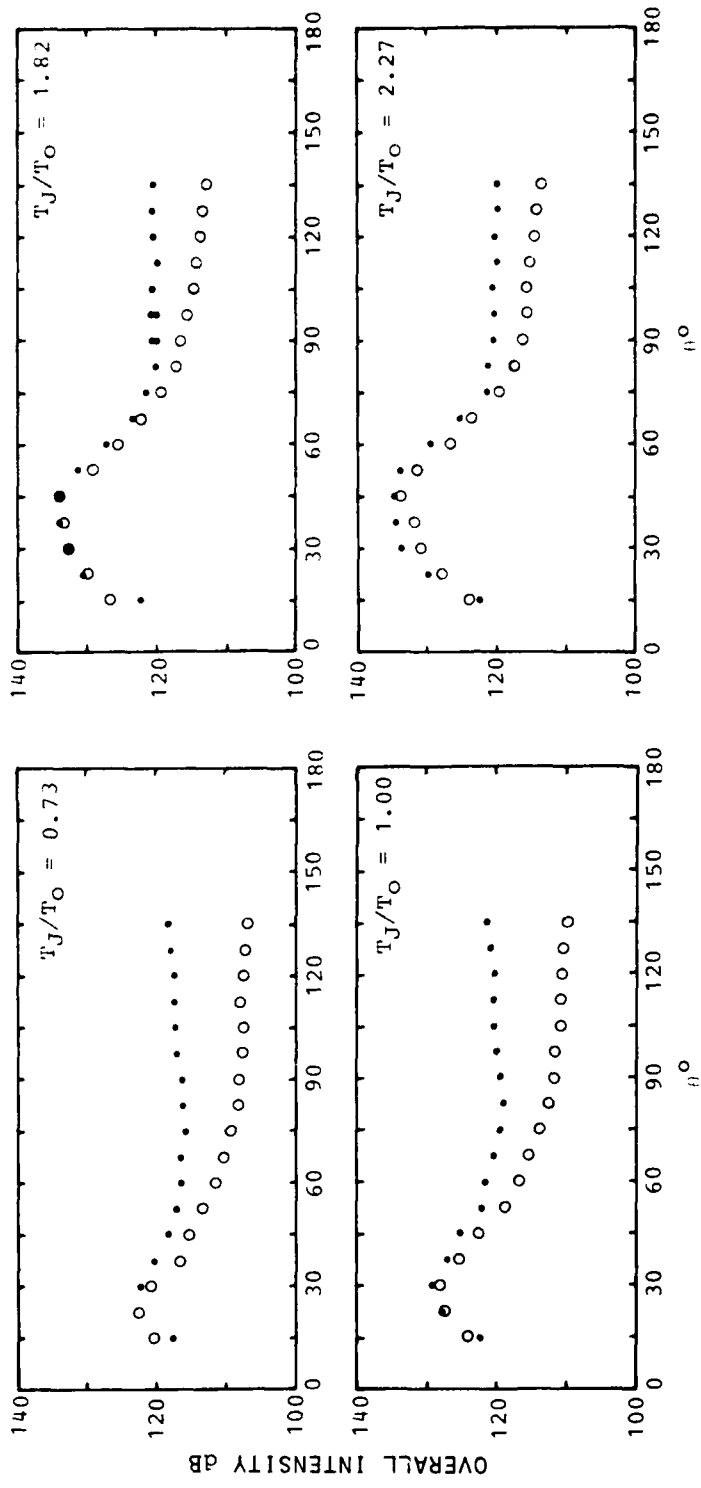


Figure 7.9 Directivity of Overall Intensity

In summary, therefore, it appears that the overall intensity of shock-associated noise is relatively independent of jet efflux temperature and emission angle. The overall level is principally a function of jet pressure ratio, and scales as  $1 \propto \beta^4$ .

#### 7.4 PEAK FREQUENCY AND IMPLICATIONS

The spectral results from under-expanded jet flows are examined first by studying the peak frequency of broadband shock-associated noise in detail. The variation of peak frequency,  $f_p$ , with observer angle  $\theta$ , pressure ratio parameter  $\beta$ , and jet temperature ratio  $T_j/T_o$ , provides several important implications regarding the characteristics of shock-containing jet flows, and these are discussed below.

A typical variation of peak frequency with observer angle  $\theta$  is shown in Figure 7.10 for an isothermal jet ( $T_j/T_o = 1$ ) operated at  $\beta = 0.94$ . For clarity the 1/3-octave spectra at various angles are plotted on a sliding vertical scale, and the peak frequencies are joined by a broken curve. It can be seen that the peak frequency of shock-associated noise decreases as the observer angle (relative to the downstream jet axis) increases. Thus, it appears that the peak frequency exhibits a Doppler shift phenomenon, at least in a qualitative manner.

Further evidence for this Doppler shift in the peak frequency is presented in Figure 7.11, where the variation of  $f_p$  with  $\theta$  is examined at several values of  $\beta$  and  $T_j/T_o$ . The peak frequency exhibits the Doppler shift at all jet operating conditions (combinations of  $\beta$  and  $T_j/T_o$ ). The variation of  $f_p$  with  $\beta$  and  $T_j/T_o$  at fixed value of  $\theta$  is also worth noting. For constant jet exit temperature, the peak frequency decreases with increasing pressure ratio parameter  $\beta$ ; on the other hand, at a fixed pressure ratio, the peak frequency increases as the jet efflux temperature is raised.

In order to explain the presence of Doppler frequency shift with angle for sound radiated from a choked jet, where the shocks have been observed to remain stationary when the nozzle operating conditions are held constant, a theoretical model for shock-associated noise was proposed by Harper-Bourne and Fisher<sup>91</sup>, and this model is introduced here with the help of the sketch shown in Figure 7.12.

##### 7.4.1 Theoretical Model for Shock-Associated Noise

The model was evolved by extending Powell's original model<sup>92</sup> for the discrete components, but without the feedback mechanism between the nozzle lip and the first shock. In this model, the end of each shock cell is taken as a compact source of sound and the relative phasing between the sources is determined by the convection of turbulent eddies between them. The model therefore consists of an array of shock-turbulence interaction sources in line with the nozzle lip and almost equally spaced with separation  $L$ . It is assumed that the convection of a turbulent eddy along this line of sources causes each to emit sound at the time of arrival of the eddy.

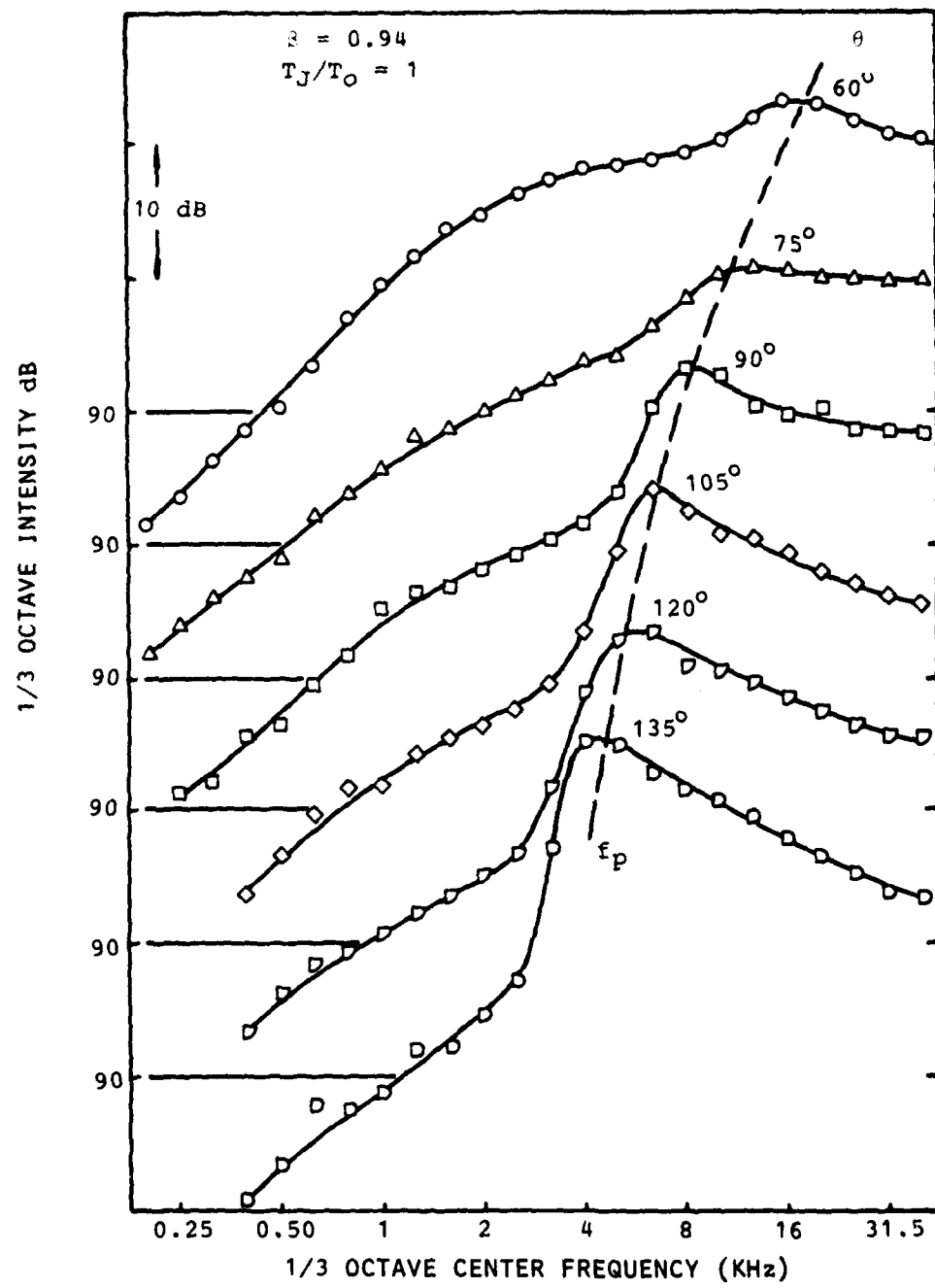


Figure 7.10 Variation of Peak Frequency with Angle

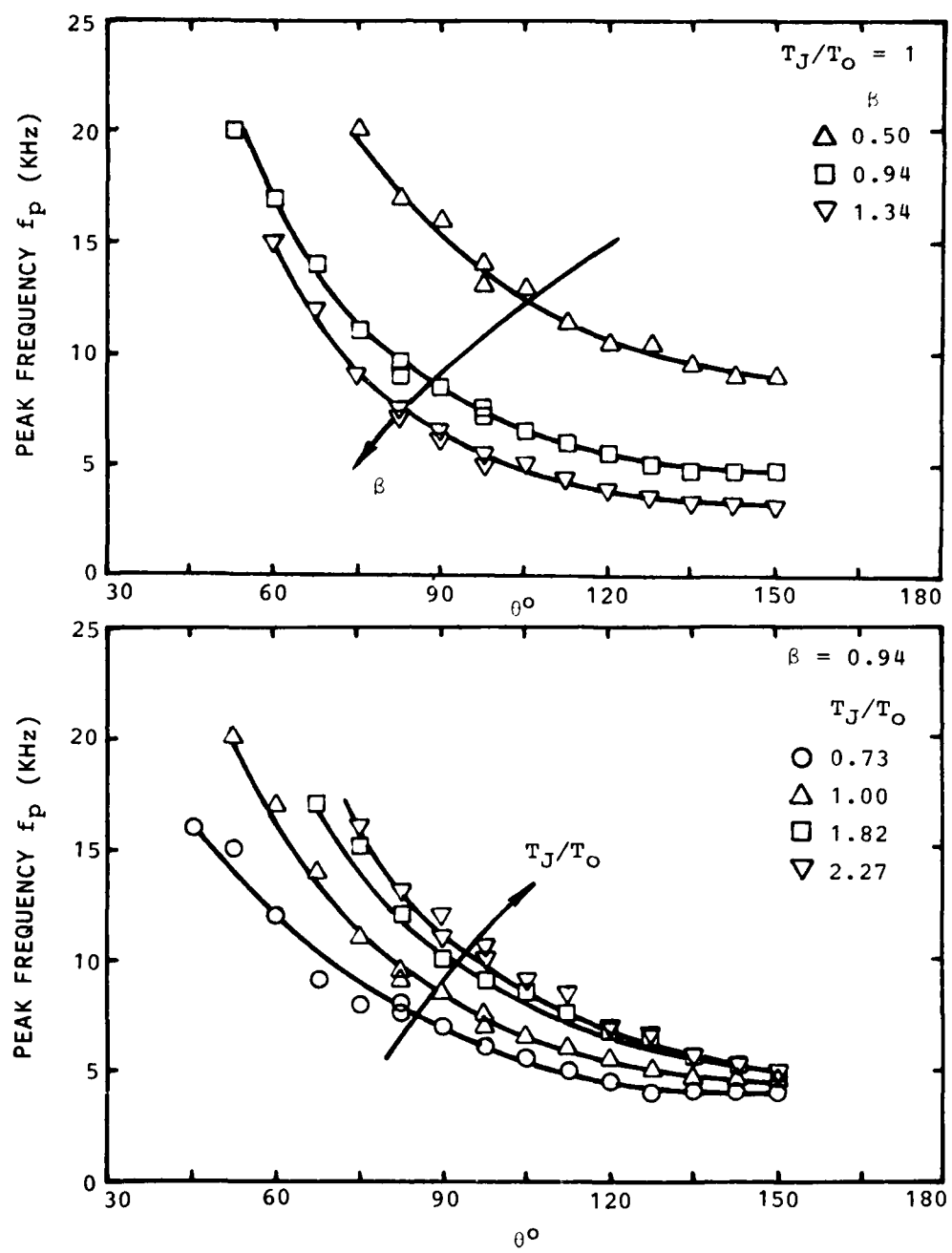


Figure 7.11 Variation of Peak Frequency with  $\beta$  and  $T_J/T_O$

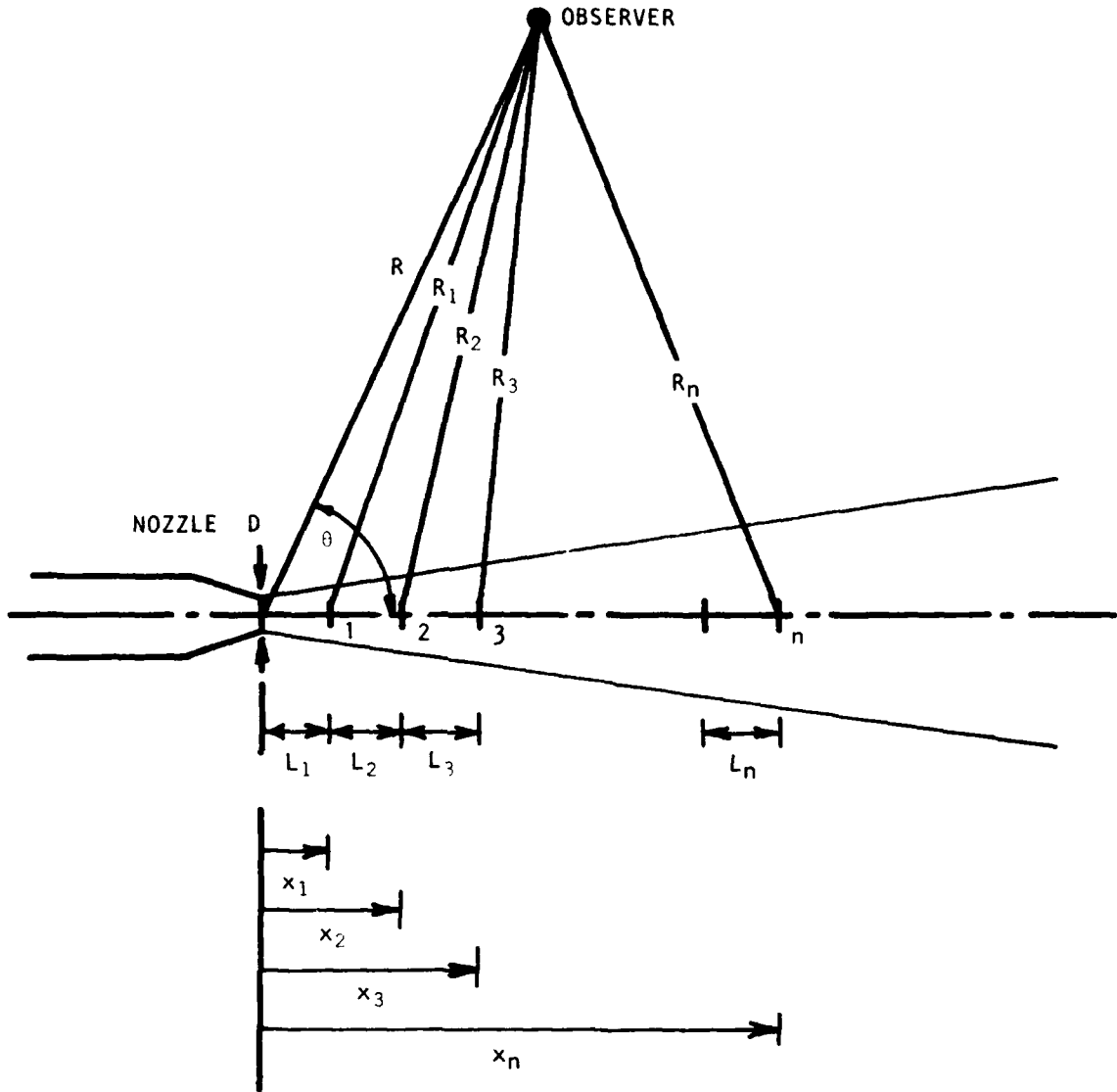


Figure 7.12 Sketch Illustrating Geometry Used in Theoretical Model for Shock-Associated Noise

The far-field sound pressure emitted by the  $n$ th source, located at a distance  $x_n$  from the nozzle exit plane, can be written as

$$p_n(R, \theta, t) = \frac{[F_n(t)]}{R}, \quad (7-1)$$

where  $F_n$  is the random source fluctuation and the square brackets denote evaluation at retarded time

$$[t] = (t - R_n/a_0). \quad (7-2)$$

The corresponding spectral density of this source,  $G_{nn}(\omega)$ , is a continuous function of frequency, and the source is assumed to be isotropic (i.e., it radiates equally in all directions).

The total intensity from an array of  $N$  such sources is then obtained by squaring and time averaging as

$$\langle p^2(R, \theta, t) \rangle = \frac{1}{R^2} \sum_{m=1}^N \sum_{n=1}^N \left\langle F_m \left( t - \frac{R_m}{a_0} \right) F_n \left( t - \frac{R_n}{a_0} \right) \right\rangle. \quad (7-3)$$

Since the sound pressure generated by the shock-turbulence interaction process is stationary in the statistical sense, the source fluctuations must also be stationary. It follows that

$$\left\langle F_m \left( t - \frac{R_m}{a_0} \right) F_n \left( t - \frac{R_n}{a_0} \right) \right\rangle = \left\langle F_m(t) F_n \left( t + \frac{R_m - R_n}{a_0} \right) \right\rangle, \quad (7-4)$$

where the time delay term can be written approximately as

$$\frac{R_m - R_n}{a_0} \approx \frac{x_n - x_m}{a_0} \cos\theta. \quad (7-5)$$

The spectral density (i.e., intensity per unit bandwidth  $\Delta\omega$ ) of sound pressure corresponding to the intensity given by Equation (7-3) can now be written as

$$G_{pp}(R, \theta, \omega) = \frac{1}{R^2} \sum_{m=1}^N \sum_{n=1}^N \frac{\left\langle F_m(t) F_n \left( t + \frac{x_n - x_m}{a_0} \cos\theta \right) \right\rangle}{\Delta\omega}. \quad (7-6)$$

The characteristics of the source fluctuations occurring at two separate shock locations,  $m$  and  $n$ , were examined by Harper-Bourne and Fisher<sup>91</sup> using a crossed beam schlieren system, and the results were cross-correlated. It was found that the peak values in the cross-correlations occurred at time delays given by

$$\tau_c = \frac{x_n - x_m}{V_c}, \quad (7-7)$$

where  $V_c$  is the eddy convection velocity. Further examination of the cross-correlations in a narrow frequency band  $\Delta\omega$  centered on frequency  $\omega$  revealed that the cross-correlation function tends to oscillate indefinitely in this case. In the limit as  $\Delta\omega \rightarrow 0$ , a standard statistical result was obtained, and this is given by

$$\frac{\langle F_m(t) F_n(t+\tau) \rangle}{\Delta\omega} = G_{mn}(\omega) \cos \left[ \omega \left\{ \tau - \frac{x_n - x_m}{V_c(\omega)} \right\} \right] \quad (7-8)$$

where  $G_{mn}(\omega)$  is the cross-power spectral density of the fluctuations at sources  $m$  and  $n$ . The above result peaks at a time delay which varies only slightly with frequency, and therefore  $V_c(\omega)$  is nominally equal to the group convection velocity  $V_c$ .

Inserting (7-8) into (7-6), a general expression for the spectral density of shock-associated noise is obtained as

$$G_{pp}(R, \theta, \omega) = \frac{1}{R^2} \sum_{m=1}^N \sum_{n=1}^N G_{mn}(\omega) \cos \left[ \frac{\omega(x_n - x_m)}{V_c} (1 - M_c \cos\theta) \right] \quad (7-9)$$

where  $M_c$  is the eddy convection Mach number ( $= V_c/a_0$ ), and  $(1 - M_c \cos\theta)$  is a Doppler factor.

If the spacing between adjacent shock locations is assumed to be constant, denoted by  $L$ , then the above equation becomes

$$G_{pp}(R, \theta, \omega) = \frac{1}{R^2} \sum_{m=1}^N \sum_{n=1}^N G_{mn}(\omega) \cos \left[ \frac{(n-m)\omega L}{V_c} (1 - M_c \cos\theta) \right]. \quad (7-10)$$

Examination of this equation shows that the spectral density of sound pressure will have a maximum value whenever the argument of the cosine term (in square brackets) is either zero or equal to an integer multiple of  $2\pi$  for non-zero values of  $(n-m)$ . The former condition occurs only at the Mach angle, given by  $\theta_M = \cos^{-1}(1/M_c)$ , and at this angle, the total radiation is usually dominated by turbulent mixing noise. The latter condition suggests that the shock-associated noise might exhibit a peak value at a frequency given by

$$f_p(\theta) = \frac{V_c}{L(1 - M_c \cos\theta)} \quad (7-11)$$

and harmonics thereof. At this frequency, the combination of eddy convection speed, shock cell spacing and angle of observation is such that the radiation from all sources interferes constructively. At other frequencies, this constructive interference is less complete and hence lower levels of noise are anticipated.

The theoretical model, described so far, has been extended by Harper-Bourne and Fisher to predict the detailed spectral characteristics of shock-

associated noise. We will return to this model in paragraph 7.5. For the moment, however, it should be recognized that the above equation for peak frequency provides several important implications regarding the eddy convection velocity and the shock spacing in an incorrectly-expanded jet flow. These are discussed below.

#### 7.4.2 Inferences from Measured Peak Frequencies

The validity of the theoretical model described above can be examined directly by calculating the peak frequencies using Equation (7-11) and comparing with the measured values. However, in order to do this, it is necessary to have the values of eddy convection speed  $V_c$  and shock spacing  $L$  for all jet operating conditions at which the comparison is to be conducted. Unfortunately, measured values of these two quantities are not available at the present time, except for the special case of unheated under-expanded jets 91. At this stage, therefore, it was decided to infer the values of these parameters using measured values of peak frequency, and to see whether or not they scale in a reasonable and consistent manner.

If the eddy convection velocity is expressed as some fraction  $C$  of the jet exit velocity, then

$$V_c = C V_j \quad \text{and} \quad M_c = C V_j / a_0, \text{ where } C = \text{constant.} \quad (7-12)$$

Furthermore, the shock spacing can be taken to be proportional to the pressure ratio parameter  $\beta$  and the jet diameter  $D$  91,93, i.e.

$$L = K \beta D, \text{ where } K = \text{constant.} \quad (7-13)$$

Incorporating results (7-12) and (7-13) into Equation (7-11), the peak frequency at  $90^\circ$  can be written as

$$f_p(90^\circ) = \frac{V_c}{L} = \frac{C}{K} \frac{V_j}{\beta D}. \quad (7-14)$$

Now if the constants  $C$  and  $K$  are assumed to be independent of  $\beta$  and  $T_j/T_o$ , at least for the present purposes, then the measured peak frequencies at  $90^\circ$  should follow a linear variation with  $V_j/\beta D$ , provided the model is valid.

The result of this exercise is shown in Figure 7.13, where the measured peak frequencies at  $\theta = 90^\circ$  over a large envelope of jet operating conditions ( $\beta$  and  $T_j/T_o$ ) are scaled according to Equation (7-14). Although there is some scatter in the results, the peak frequencies do scale linearly with  $V_j/\beta D$  in a convincing manner, and the value of the combined constant  $C/K$  is obtained as 0.8.

The scaling presented in Figure 7.13 appears quite encouraging, and it provides a certain amount of confidence in the validity of the theoretical model. However, it would additionally be very informative if individual values of eddy convection velocity constant  $C$  and shock spacing constant  $K$  can be inferred from measured peak frequencies of shock-associated noise. This

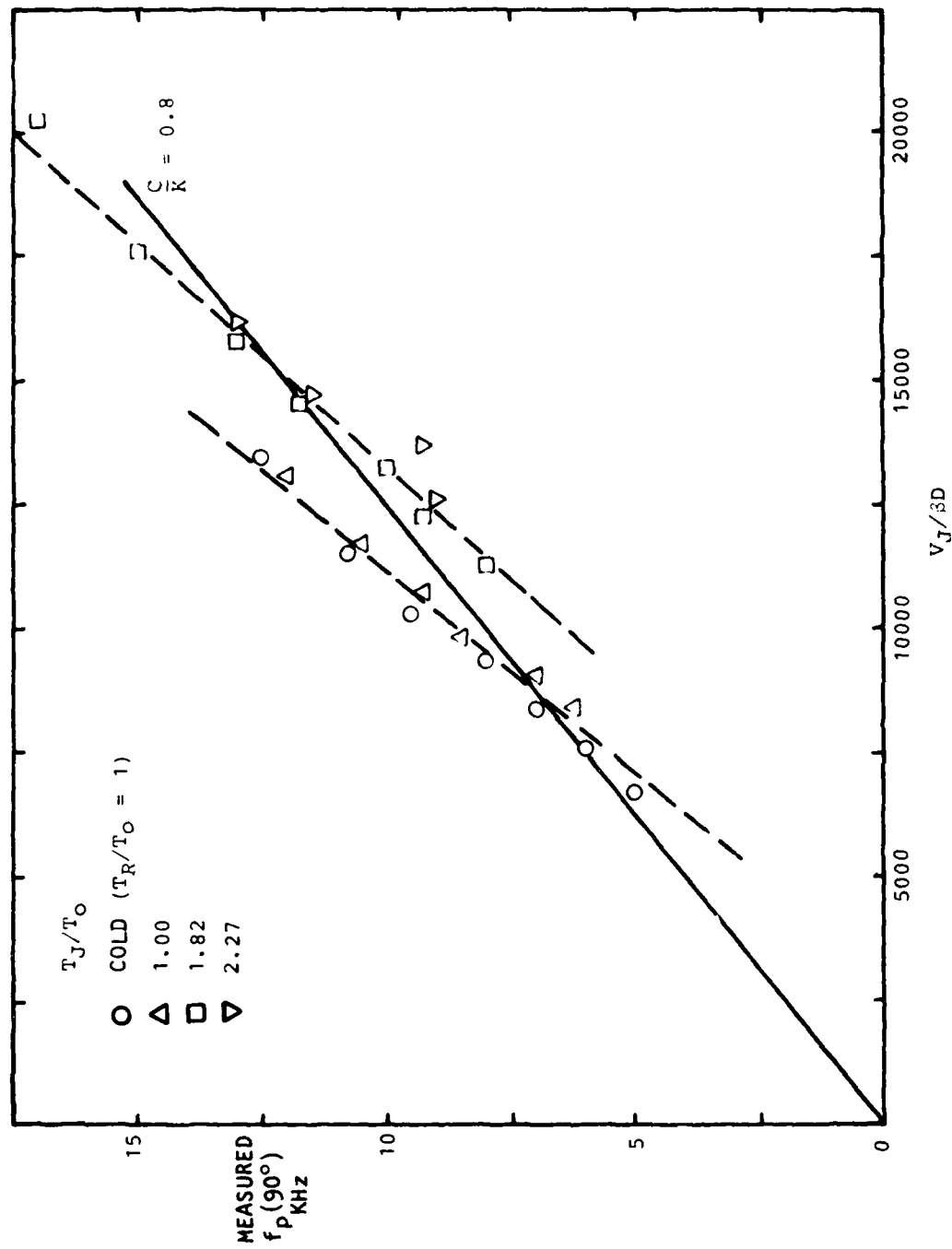


Figure 7.13 Peak Frequency Scaling

can be achieved by simple manipulation of Equation (7-11), which can be written as

$$f_p(\theta) = \frac{CV_J}{KBD \left[ 1 - C \left( \frac{V_J}{a_0} \right) \cos \theta \right]}. \quad (7-15)$$

Combining Equations (7-14) and (7-15), the eddy convection velocity constant can be obtained from

$$C = \frac{\left\{ 1 - \frac{f_p(90^\circ)}{f_p(\theta)} \right\}}{\left( \frac{V_J}{a_0} \right) \cos \theta}, \quad (7-16)$$

and once the value of  $C$  is determined, the shock spacing constant is given by

$$K = \frac{CV_J}{\beta D f_p(90^\circ)}. \quad (7-17)$$

Thus, using the measured values of peak frequency for any jet operating conditions, the values of  $C$  and  $K$  can be computed individually by using Equations (7-16) and (7-17).

The measured values of peak frequency at three pressure ratios ( $\beta = 0.50, 0.94, 1.34$ ) and four jet exit temperature ratios were used to determine the values of  $C$  and  $K$  according to this procedure. For a set of jet exit conditions ( $\beta, T_J/T_0$ ), the values of  $C$  and  $K$  obtained by using  $f_p$  at several values of  $\theta$  were averaged, and the results, denoted by  $\langle C \rangle_\theta$  and  $\langle K \rangle_\theta$ , respectively, are shown in Figure 7.14. Although it can be argued that since the results are examined at only three values of  $\beta$ , it might be misleading to derive any specific conclusions from this figure, it is still clear that the results do exhibit reasonably consistent trends. For a fixed jet efflux temperature ratio  $T_J/T_0$ , the eddy convection velocity constant  $\langle C \rangle_\theta$  appears to be fairly independent of the pressure ratio parameter  $\beta$ , whereas the shock spacing constant  $\langle K \rangle_\theta$  has a tendency to increase with increasing  $\beta$ . Also shown in Figure 7.14 are values of  $K$  calculated from the shock spacing measurements reported by Harper-Bourne and Fisher for an unheated jet. These values also have a tendency to increase with increasing  $\beta$ , although the actual magnitudes differ significantly from those inferred from the present measured values of peak frequency.

Finally, the results were arithmetically averaged over all jet exit temperatures considered in the present experiments, and the variations of the two constants, denoted by

$$\langle C \rangle_\theta, T_J/T_0 \quad \text{and} \quad \langle K \rangle_\theta, T_J/T_0,$$

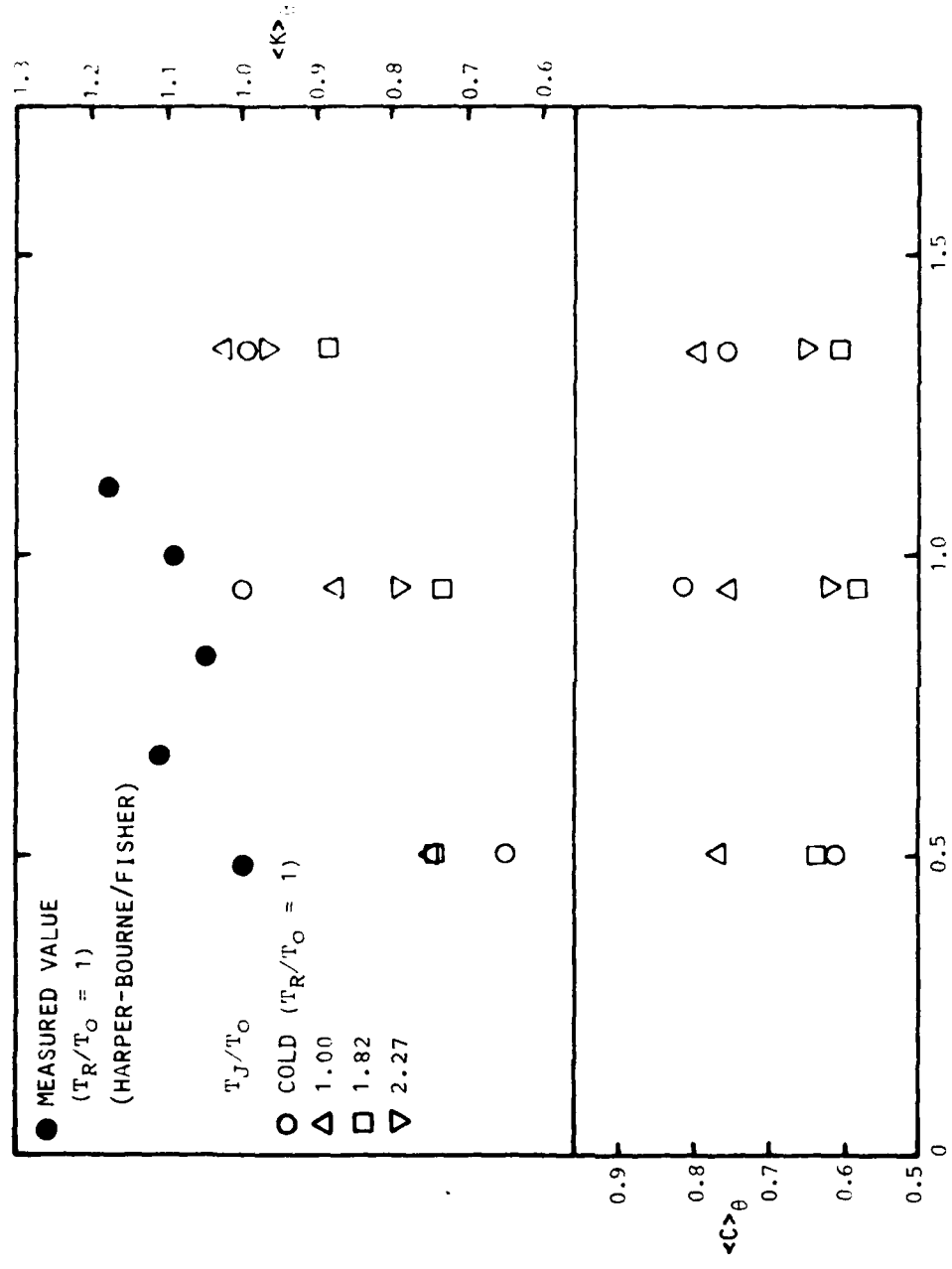


Figure 7.14 Values of  $\langle C \rangle_\theta$  and  $\langle K \rangle_\theta$  From Measured  $f_p(\theta)$

with  $\beta$  are presented in Figure 7.15. The linear variation with  $\beta$  is remarkably accurate in this case. The eddy convection velocity constant is nearly independent of the pressure ratio parameter  $\beta$ . The mean value of this constant calculated over the range of  $\beta$  considered here is 0.69, which is in very good agreement with the measured values published in the literature. The shock spacing constant increases with  $\beta$ , as noted previously. It remains to be seen whether or not the values of  $K$ , inferred here from the measured peak frequencies of shock-associated noise, agree with actual shock spacing measurements at various pressure ratios and jet efflux temperatures.

### 7.5 Comparison of Measured and Predicted Spectra

The theoretical model for shock-associated noise, introduced in paragraph 7.4, was extended by Harper-Bourne and Fisher<sup>91</sup> to predict the detailed spectral characteristics in the far field. In the present program, the results of this model were used, and a computer program was developed to predict the spectrum of shock-associated noise. A preliminary comparison of the measured and predicted spectra is discussed in this paragraph.

The theoretical model predicts the far-field spectral density of sound pressure,  $G_{pp}(R, \theta, \omega)$ , as a product of three terms in the following manner:

$$\underbrace{\text{Far-Field Intensity Spectrum}}_{G_{pp}(R, \theta, \omega)} = \underbrace{\text{Mach Number Dependence}}_{\left(\frac{D}{R}\right)^2 \left(\frac{D}{a_0}\right) \beta^5} \times \underbrace{\text{Source Spectrum}}_{H_o(\sigma)} \times \underbrace{\text{Interference Weighting}}_{f\{N, L_n, \theta, C_{m-n}(\sigma), \omega, V_c\}}, \quad (7-18)$$

where

$H_o(\sigma)$  = group source strength spectrum

$C_{m-n}(\sigma)$  = correlation coefficient spectrum between fluctuations at  $m^{th}$  and  $n^{th}$  shocks

$N$  = number of shocks

$L_n$  = shock spacing for  $n^{th}$  shock

$V_c$  = turbulence or eddy convection velocity

and  $\sigma = \text{Strouhal number, } \omega L/a_0$ .

The first term includes the basic Mach number or pressure ratio dependence discussed previously for the overall intensity results. The second term is defined as the normalized group source strength spectrum, and it effectively represents the combined strength of the shock-turbulence interactions occurring at several shock locations. The final term represents the magnitude of the constructive or destructive interference that occurs when sound waves emitted

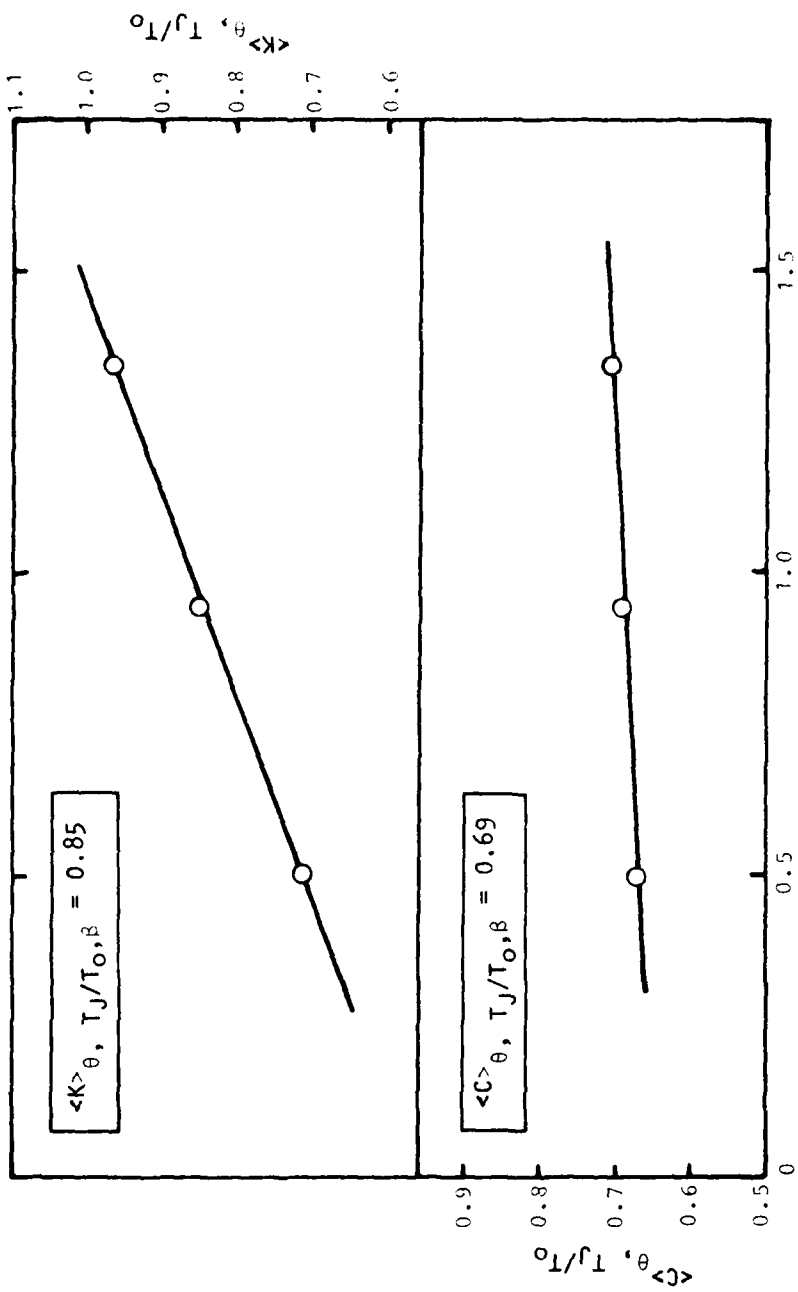


Figure 7.15 Values of  $\langle C \rangle_{\theta}$  and  $\langle K \rangle_{\theta}$  Averaged Over All  $T_J/T_o$

from various sources arrive simultaneously at the observation point  $(R, \theta)$ . This interference weighting is a function of several parameters as shown in Equation (7-18). The significance of the four parameters  $L_n$ ,  $\theta$ ,  $\omega$ , and  $V_c$  was discussed previously when the peak frequency results were examined. The additional quantity  $C_{m-n}(\sigma)$  is the correlation coefficient spectrum between fluctuations occurring at sources  $m$  and  $n$ , and it represents the degree of coherence that exists between the acoustic signatures emitted from various shock-turbulence interaction locations.

Using a crossed beam schlieren system, Harper-Bourne and Fisher examined the shock-containing jet flow from an unheated jet, and derived two relationships which can be incorporated in the prediction procedure. The first relationship gives the shock spacing  $L_n$  for the  $n$ th shock cell in terms of the shock spacing  $L_1$  for the first cell as

$$\frac{L_n}{L_1} = \left\{ 1 - \frac{\Delta L}{L_1} (n-1) \right\}, \quad \frac{\Delta L}{L_1} = 0.06. \quad (7-19)$$

That is, it was observed that the shock spacing decreases linearly by approximately 6% from one shock to the next. In a similar manner, measurements of cross-correlations of density gradient fluctuations between various shock locations indicated an empirical relationship of the form

$$C_{m-n}(\sigma) = C_1^{(m-n)^2}(\sigma), \quad \sigma = \frac{\omega L}{a_0} \quad (7-20)$$

which gives the correlation coefficient spectrum between fluctuations at sources  $m$  and  $n$  in terms of the correlation coefficient spectrum between fluctuations at adjacent ( $m - n = 1$ ) sources.

Incorporating the two relationships given by Equations (7-19) and (7-20) in the general prediction Equation (7-18), the spectral density of shock-associated noise can in principle be computed for any condition, providing the normalized group source strength spectrum  $H_0(\sigma)$  and the correlation coefficient spectrum  $C_1(\sigma)$  are known.

In reference 91, these two spectra were evaluated computationally by using measured shock-associated noise spectra, i.e.  $G_{pp}(R, \theta, \omega)$ , from unheated jets. Putting  $N=8$ ,  $\Delta L/L_1 = 0.06$  and  $V_c = 0.7 V_J$ , all other parameters being readily available, the directivities for a wide range of frequencies and different pressure ratios were processed using Equations (7-18), (7-19), and (7-20). The resulting spectra,  $H_0(\sigma)$  and  $C_1(\sigma)$ , contained a considerable amount of scatter, especially the latter. The mean variations were taken to be the "universal source spectral characteristics" for the shock-associated noise of a choked jet, and these two master spectra are shown as solid curves in Figure 7.16. Both spectra are plotted against the Strouhal number,  $\sigma = \omega L/a_0$ .

In the current investigation, a computer program, based on this semi-empirical model, was developed, and the shock-associated noise spectra at selected jet operating conditions were computed using the master  $H_0(\sigma)$  and  $C_1(\sigma)$  spectra given in Figure 7.16. The predicted spectra were compared with the corresponding measured spectra in a preliminary manner.

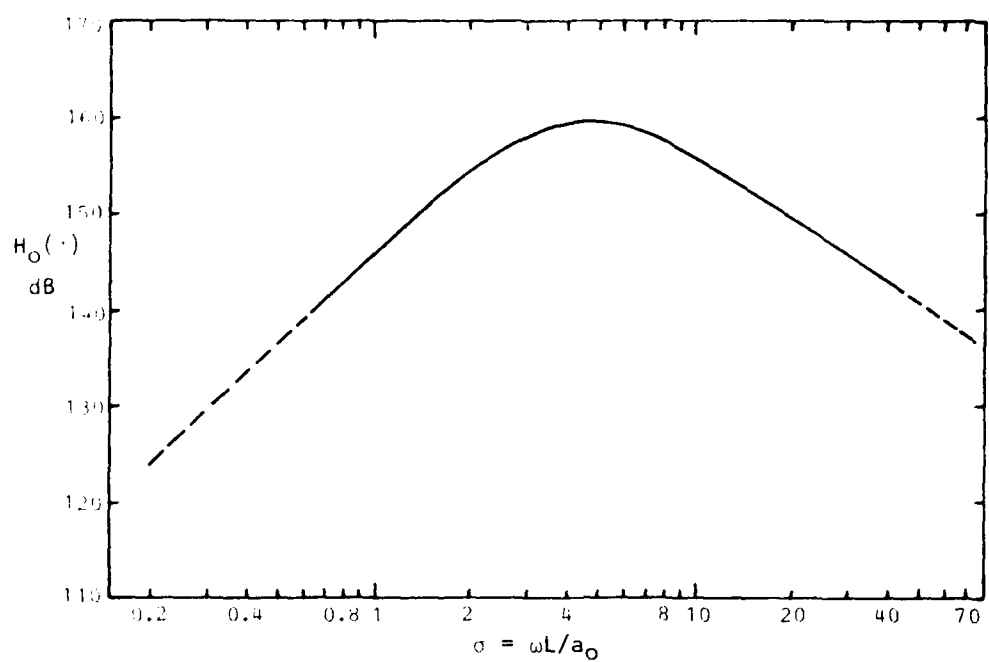


Figure 7.16(a) Normalized Group Source Strength Spectrum

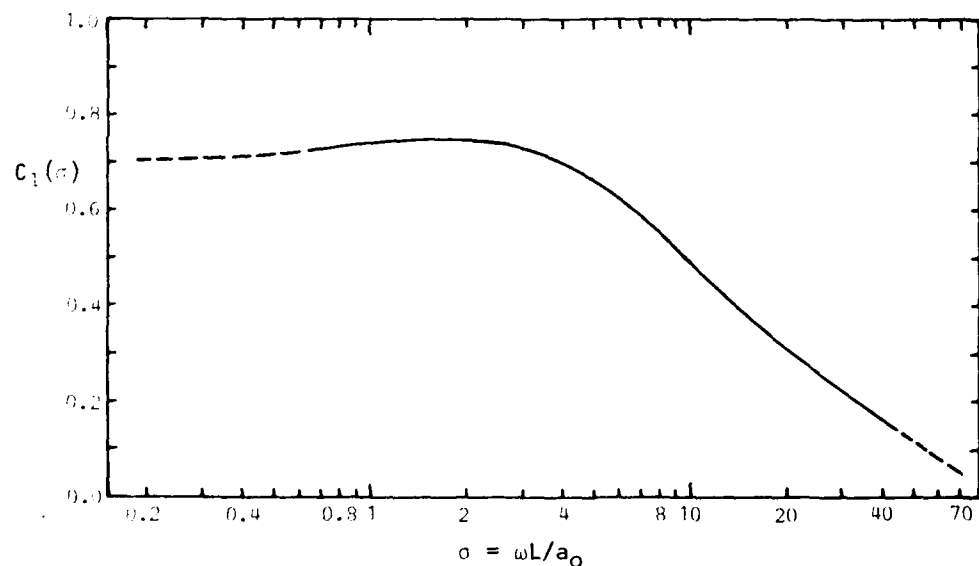


Figure 7.16(b) Correlation Coefficient Spectrum for Adjacent Shock Locations

Two typical comparisons at  $\psi = 135^\circ$  are presented in Figures 7.17 and 7.18 for a jet operated at  $K = 0.94$ . The first comparison is for an isothermal jet, while the second comparison is for a high temperature jet. In both predictions the eddy convection velocity was taken to be 0.7 times the jet efflux velocity, and the shock spacing constant  $K$  was taken to be 1.1, as suggested by Harper-Bourne and Fisher<sup>91</sup> using their unheated jet flow measurements.

The comparison of measured and predicted spectra shows that the agreement is good at all frequencies except near the peak frequency, where a slight underestimation occurs, especially for the isothermal case. It should be noted that in both comparisons, the measured spectrum levels at frequencies below approximately 3 kHz are dominated by turbulent mixing noise, and hence, over these frequencies, the predicted levels of shock-associated noise should be expected to be lower than the measured levels. This is seen to be true in both cases.

With the limited amount of comparisons carried out to date, it is not possible to derive any specific conclusions at this stage. Furthermore, for the heated conditions, the comparisons should strictly be carried out using measured values of the relevant jet flow parameters [ $V_c$ ,  $L_n$ ,  $C_{m-n}(\sigma)$ , etc.] rather than using the values derived mainly from unheated jet flow measurements, as has been done in the present comparison. Further work is therefore required in several areas, and this is discussed in the following paragraph.

## 7.6 CONCLUSIONS AND FUTURE WORK

The characteristics of broadband shock-associated noise were examined experimentally over an extensive envelope of supercritical pressure ratios and jet efflux temperatures. The results, both overall and spectral, were analyzed in detail, and comparisons with an existing semi-empirical model were conducted where possible.

The overall SPL results from shock-containing under-expanded jet flows were compared directly with the corresponding results from fully-expanded supersonic jets. It was confirmed that the shock-associated noise trends, observed previously from a limited amount of measurements (mainly from unheated jets), are valid throughout the engine operating conditions of practical interest. The overall intensity of shock-associated noise is essentially independent of both the jet efflux temperature and observer angle; it is primarily a function of jet pressure ratio only, and scales according to

$$I \propto \beta^4 \quad \text{where } \beta = (M_j^2 - 1)^{\frac{1}{2}}.$$

The peak frequencies of shock-associated noise were examined in the light of the theoretical model proposed by Harper-Bourne and Fisher. The presence of Doppler shift with angle in the measured peak frequencies, and the variations of measured peak frequencies with pressure ratio (or  $\beta$ ) and temperature ratio, are all found to be in good qualitative agreement with the theoretical model. This gives a certain amount of confidence in the model. Further comparison of measured peak frequencies with theoretical scaling formulae provided several useful implications regarding the characteristics of shock-containing jet flows. It was inferred that the average value of turbulence or eddy convection speed

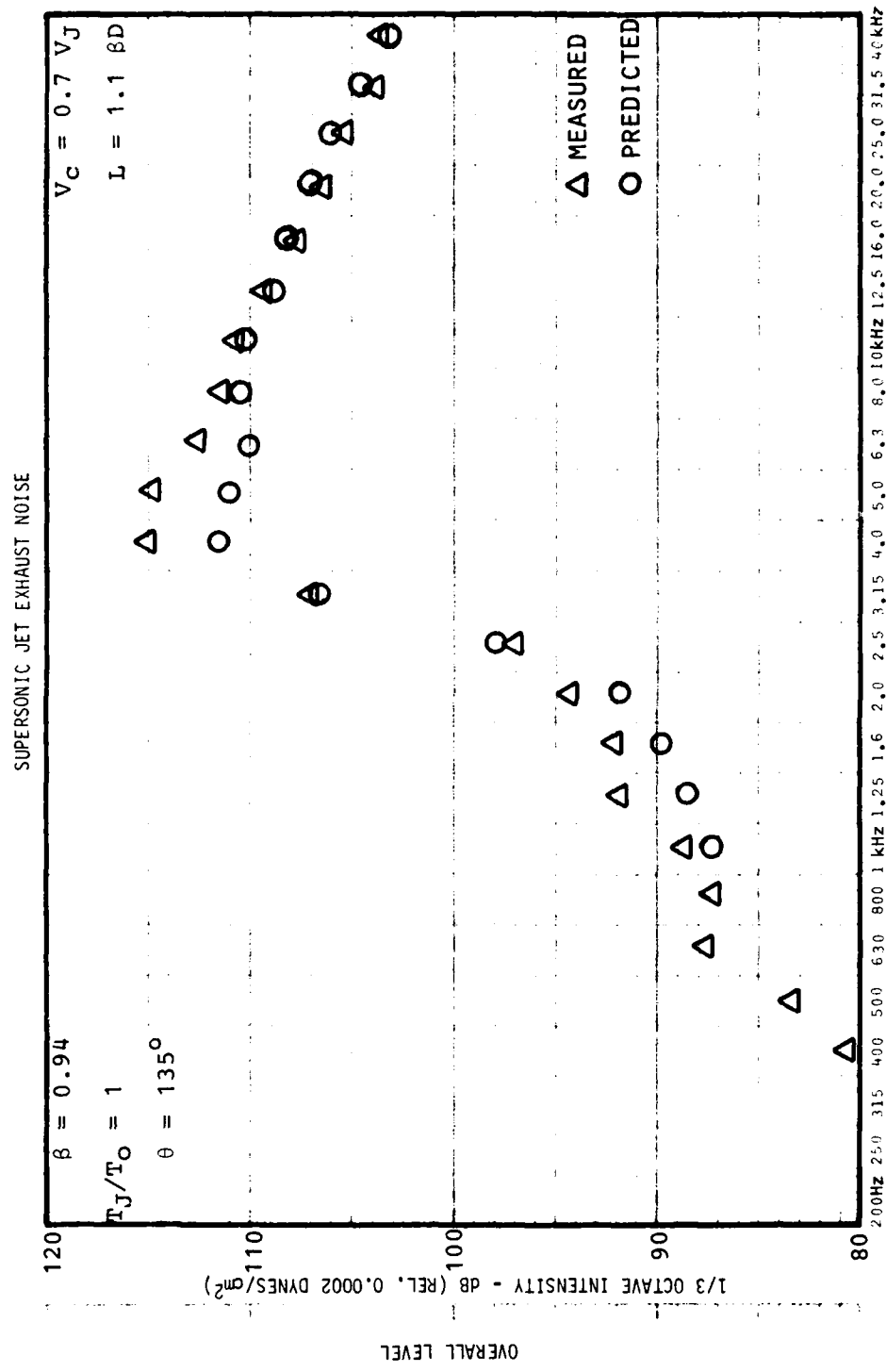


Figure 7.17 Comparison of Measured and Predicted Spectra

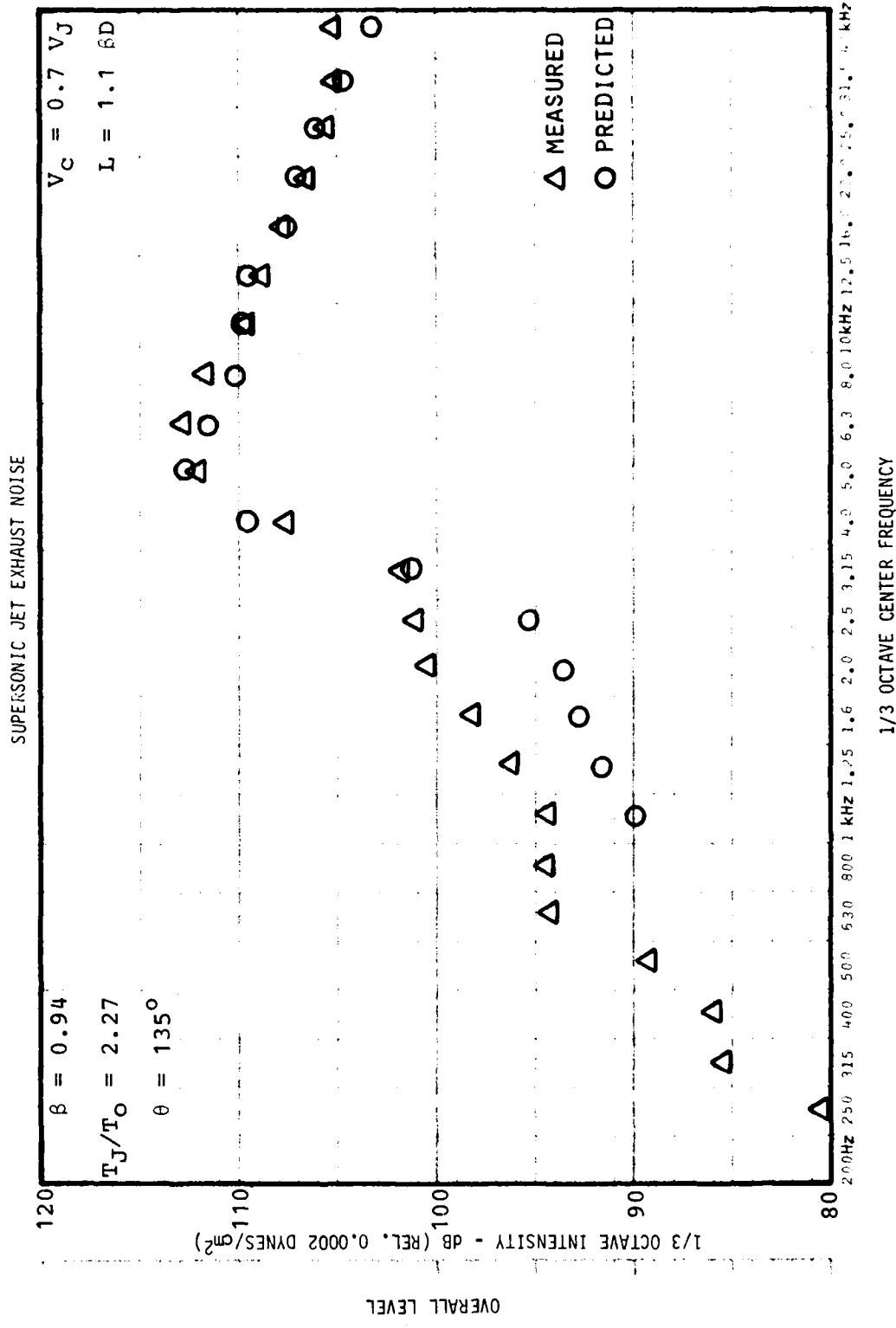


Figure 7.18 Comparison of Measured and Predicted Spectra

in a jet flow is approximately 0.7 times the jet efflux velocity, and this fraction remains nominally independent of the pressure ratio. This observation therefore agrees with the measured values of  $V_c$ , obtained mainly from unheated jets by several investigators. The values of shock spacing constant  $K$  (shock cell length  $L = KBD$ ) were also calculated, and it was inferred that this constant increases with pressure ratio parameter  $\beta$ . It remains to be seen whether this trend can be verified experimentally.

A computer program for the prediction of shock-associated noise, based on the same semi-empirical model, was developed, and a preliminary comparison of measured and predicted spectra was conducted. The predicted spectra were in good agreement with the measured spectra. However, since the comparison was not extensive, it has not been possible to derive any specific conclusion. Furthermore, it is suggested that such a comparison will become more meaningful if values of various jet flow parameters, required for input to the prediction scheme, are obtained experimentally. A considerable amount of future effort is therefore required on various specific aspects of shock-associated noise, and a brief discussion is given below.

The future work on shock-associated noise falls into two separate but complementary categories. The work under the first category is designed to evaluate in greater detail the semi-empirical prediction method<sup>91</sup> discussed throughout this section. In the second category, further effort is required in order to obtain a fundamental understanding of various phenomena associated with the generation and radiation of shock-associated noise.

For prediction purposes, it has become obvious that there is an urgent need to increase our knowledge of the flow properties of shock-containing jets. In particular, the variations of shock spacing  $L$  and turbulence convection speed  $V_c$  should be measured at several pressure ratios (or  $\beta$ ) and jet exit temperatures of practical interest. It is also necessary to measure the correlation coefficient spectra  $C_{m-n}(\omega)$  between fluctuations at shock locations  $m$  and  $n$ , for various jet operating conditions. These measurements can be accomplished by using either a laser velocimeter system or a crossed beam schlieren system. Once this information becomes available, the preliminary comparison between measured and predicted spectra, conducted during the present program, should be extended to cover the entire envelope of jet operating conditions for which acoustic measurements are already available.

On a more fundamental basis, it is necessary to obtain a thorough understanding of the physical significance of shock-turbulence interaction, which has been proposed as the possible mechanism of shock noise generation. In particular, it is necessary to identify and quantify the physical quantity (for example, density gradient fluctuations, turbulent velocity fluctuations, etc.) which plays the dominant role in the shock-turbulence interaction process. It is felt that any attempt towards reducing the strength of shock-turbulence interactions, and hence the levels of shock-associated noise, will be more successful if such an understanding is available.

Finally, it must be emphasized that the role played by flow-acoustic interaction in the case of shock-associated noise has been completely neglected in the present investigation. In Section 3 of this Volume, the powerful effects of this flow-acoustic interaction phenomena were examined for the sound radiated from subsonic and fully-expanded supersonic jets. On physical

grounds, it should be argued that since the sound generated by the interaction between a stationary shock and oncoming turbulence has to propagate through the shear layer on its way to the far-field observer, the flow-acoustic interactions are expected to play a significant role. This aspect needs to be examined in detail, and if it is found to be significant, it should be incorporated in the prediction method.

## APPENDIX 3A

### LILLEY EQUATION DEVELOPMENTS

331

### 3A.1 DERIVATION OF GENERALIZED LILLEY EQUATION FOR SOUND GENERATION IN TURBULENT SHEAR FLOWS

For an inviscid, nonconducting fluid with no chemical reactions or mass diffusion, changes in density and pressure following a fluid element are related by

$$\frac{D\rho}{Dt} = \frac{1}{c^2} \frac{Dp}{Dt} \quad \left[ \left( \frac{\partial p}{\partial \rho} \right)_S = \frac{1}{c^2}, \quad \frac{Ds}{Dt} = 0 \right] \quad (3A-1)$$

where  $c$  is the isentropic sound speed at frozen composition. It follows that the continuity equation may be written as

$$\frac{\partial v_i}{\partial x_i} = - \frac{1}{\rho c^2} \frac{Dp}{Dt}. \quad (3A-2)$$

The momentum equation for such a fluid is

$$\frac{Dv_j}{Dt} = - \frac{1}{\rho} \frac{\partial p}{\partial x_j}. \quad (3A-3)$$

By operating on (3A-3) with  $\partial/\partial x_j$  and on (3A-2) with  $D/Dt$ , and subtracting, a type of wave equation in  $p$  is obtained. Since the flows of interest are characterized by having an almost constant mean pressure, we treat the difference  $p'$  between  $p$  and its average value throughout the flow as a small quantity. Thus, the  $(Dp'/Dt)^2$  term which arises from (3A-2) is neglected, and we have

$$\frac{1}{\rho c^2} \frac{D^2 p'}{Dt^2} - \frac{\partial}{\partial x_j} \left( \frac{1}{\rho} \frac{\partial p'}{\partial x_j} \right) \doteq \frac{\partial v_i}{\partial x_j} \frac{\partial v_j}{\partial x_i}. \quad (3A-4)$$

A further  $D/Dt$  operation, applied to Equation (3A-4) gives to the same approximation

$$\frac{1}{\rho c^2} \frac{D^3 p'}{Dt^3} - \frac{D}{Dt} \frac{\partial}{\partial x_j} \left( \frac{1}{\rho} \frac{\partial p'}{\partial x_j} \right) \doteq 2 \frac{\partial v_i}{\partial x_j} \frac{\partial}{\partial x_i} \left( \frac{Dv_j}{Dt} \right) - 2 \frac{\partial v_i}{\partial x_j} \frac{\partial v_j}{\partial x_k} \frac{\partial v_k}{\partial x_i},$$

or, using (3A-3) to substitute for  $Dv_j/Dt$ ,

$$\frac{1}{\rho c^2} \frac{D^3 p'}{Dt^3} - \frac{D}{Dt} \frac{\partial}{\partial x_j} \left( \frac{1}{\rho} \frac{\partial p'}{\partial x_j} \right) + 2 \frac{\partial v_i}{\partial x_j} \frac{\partial}{\partial x_i} \left( \frac{1}{\rho} \frac{\partial p'}{\partial x_j} \right) \doteq -2 \frac{\partial v_i}{\partial x_j} \frac{\partial v_j}{\partial x_k} \frac{\partial v_k}{\partial x_i}. \quad (3A-5)$$

So far, the only approximation has been the neglect of quadratic and higher-order terms in  $p'$  arising from

$$\frac{D}{Dt} \left( \frac{1}{\rho c^2} \right), \quad \frac{D^2}{Dt^2} \left( \frac{1}{\rho c^2} \right).$$

We now introduce the notation

$$v'_i = v_i - \bar{v}_i, \quad (3A-6)$$

and proceed to neglect all terms of order  $p'v'$  or  $v'^3$  on the basis that in turbulent shear flows of constant mean pressure, we expect  $p'$  and  $(v')^2$  to be of the same order locally.

The basic flow field defined by the velocity components  $\bar{v}_i$  is taken in the analysis which follows to be steady and unidirectional; specifically,

$$\bar{v} = \{\bar{v}_1(x_2, x_3), 0, 0\} \quad (3A-7)$$

consistently with the equations of motion (3A-1) to (3A-3) and the association of  $\bar{p}$  with the pressure in the basic flow. Using Equation (3A-7), together with the approximation that  $v'^3$  is negligible, gives

$$\frac{\partial v_i}{\partial x_j} \frac{\partial v_j}{\partial x_k} \frac{\partial v_k}{\partial x_i} = 3 \frac{\partial \bar{v}_i}{\partial x_j} \frac{\partial v'_j}{\partial x_k} \frac{\partial v'_k}{\partial x_i}. \quad (3A-8)$$

Thus, Equation (3A-5) may be written, to the accuracy described, as

$$L(p') = \bar{\rho}Q, \quad (3A-9)$$

where the linear differential operator  $L$  is defined by

$$L \equiv \frac{1}{\bar{\epsilon}^2} \frac{\bar{D}^3}{Dt^3} - \bar{\rho} \frac{\bar{D}}{Dt} \frac{\partial}{\partial x_j} \frac{1}{\bar{\rho}} \frac{\partial}{\partial x_j} + 2\bar{\rho} \frac{\partial \bar{v}_i}{\partial x_j} \frac{\partial}{\partial x_i} \frac{1}{\bar{\rho}} \frac{\partial}{\partial x_j}, \quad (3A-10)$$

and the source term  $Q$  by

$$Q = -6 \frac{\partial \bar{v}_i}{\partial x_j} \frac{\partial v'_j}{\partial x_k} \frac{\partial v'_k}{\partial x_i} - \left( \delta_{ij} \frac{\bar{D}}{Dt} - 2 \frac{\partial \bar{v}_i}{\partial x_j} \right) \frac{\partial f'_j}{\partial x_i}. \quad (3A-11)$$

In (3A-11), the quantity  $f'_j = -V' \frac{\partial p'}{\partial x_j}$  may be interpreted as an equivalent force field; it represents  $V'p'$  interaction effects, where  $V'$  is the fluctuation in the specific volume  $1/\rho$ . (Note that  $\bar{D}/Dt = \partial/\partial t + \bar{v}_i \partial/\partial x_i$ .)

Without introducing any further approximations or assumptions, the expressions for  $L$  and  $Q$  above may be arranged in various alternative forms. It follows from the continuity equation applied to the basic flow defined by (3A-7) that  $\bar{\rho}$ , the density in the basic flow field, is a function only of  $(x_2, x_3)$ ; thus the Lilley equation operator becomes

$$L = \frac{1}{\bar{\epsilon}^2} \frac{\bar{D}^3}{Dt^3} - \frac{\bar{D}}{Dt} V^2 + \frac{\bar{D}}{Dt} \left( \frac{1}{\bar{\rho}} \frac{\partial \bar{\rho}}{\partial x_i} \right) \frac{\partial}{\partial x_i} + 2 \frac{\partial \bar{v}_1}{\partial x_j} \frac{\partial}{\partial x_1} \frac{\partial}{\partial x_j}. \quad (3A-12)$$

The source term  $Q$  may be rearranged to give (details are given in Section 3A.2 below, "Acceleration Quadrupole Source Derivation")

$$Q \doteq \frac{3}{2} \frac{\bar{D}}{Dt} \frac{\partial^2 v_i' v_j'}{\partial x_i \partial x_j} + 3 \frac{\partial^2 \bar{v}_i}{\partial x_j \partial x_k} v_j' \frac{\partial v_k'}{\partial x_i} - \left( \hat{\epsilon}_{ij} \frac{\bar{D}}{Dt} - 2 \frac{\partial \bar{v}_i}{\partial x_j} \right) \frac{\partial f_j'}{\partial x_i}, \quad (3A-13)$$

where the second term is zero if the basic flow is axisymmetric (including as a special case the two-dimensional shear layer).

An alternative form is, to the same accuracy (see Sections 3A.3 and 4 below, "Displacement Quadrupole" and "Displacement Dipole Source Derivation")

$$Q \doteq \frac{\bar{D}^3}{Dt^3} \left( \frac{1}{2} \frac{\partial^2 \xi_i' \xi_j'}{\partial x_i \partial x_j} - \frac{\partial \xi_i''}{\partial x_i} \right) \quad (3A-14)$$

where there is no restriction to axisymmetric basic flows. The perturbations  $\xi'$ ,  $\xi''$  are defined by

$$\frac{\bar{D} \xi_i'}{Dt} - \frac{\partial \bar{v}_i}{\partial x_k} \xi_k' = v_i', \quad \frac{\bar{D}^2 \xi_i''}{Dt^2} = f_i'; \quad (3A-15)$$

$\xi'$  represents to 1st order the displacement of a fluid particle relative to the basic flow. For modeling turbulence as a source of sound, the displacement description (3A-14) is preferred to the velocity description (3A-13) on grounds of simplicity; moreover it is shown in Section 3.3.2 that the velocity description leads to an asymptotic  $U_j^6$  dependence for isothermal jet noise intensity at low Mach numbers and is therefore unrealistic.

#### LINEARIZED LILLEY EQUATION WITH EXTERNAL FORCING

As an aid to interpreting Equations (3A-13 and 14), we consider the form of  $Q$  that results from external inputs when only first-order terms are retained. The input quantities are a volume displacement  $z$  per unit volume, a volume acceleration  $a$  per unit volume, and an applied force  $f_j$  per unit volume.

The resulting equations of momentum and continuity, with the external forcing terms approximated to first order, are

$$\frac{Dv_i}{Dt} \doteq f_j - \frac{1}{\rho} \frac{\partial p}{\partial x_j} \quad (3A-16)$$

and

$$\frac{D}{Dt} \left( \frac{\partial v_i}{\partial x_i} \right) \doteq \frac{D^2 z}{Dt^2} + a - \frac{D}{Dt} \left( \frac{1}{\rho c^2} \frac{Dp}{Dt} \right). \quad (3A-17)$$

Following through the derivation of the Lilley equation as previously, but with only first-order terms retained, gives finally

$$Q \triangleq \frac{\bar{D}^3 z}{Dt^3} + \frac{\bar{D} a}{Dt} - \left( \xi_{ij} \frac{\bar{D}}{Dt} - 2 \frac{\partial \bar{v}_i}{\partial x_j} \right) \frac{\partial f_i}{\partial x_j}. \quad (3A-18)$$

Comparison of Equations (3A-13) and (3A-14) with (3A-18) provides a physical interpretation of the various turbulent source terms. Thus, in (3A-14), for example, the first term (associated with turbulent velocity fluctuations) is equivalent to a volume-displacement distribution  $z = 1/2 \partial^2 (\xi_i' \xi_j') / \partial x_i \partial x_j$ , which is of quadrupole order with a quadrupole strength  $\xi_i' \xi_j' / 2$  per unit volume. Likewise, the second term in (3A-14) is equivalent to a volume-displacement distribution of dipole order, with a dipole strength of  $\xi_i''$  per unit volume related to the specific-volume fluctuation  $V'$ .

#### COMPARISON OF LILLEY AND LIGHTHILL EQUATIONS

Strictly, in the special case where  $\bar{v}_i = 0$  and  $\bar{\rho} = \rho_0$ , the LHS of the Lilley equation reduces to  $\square \beta p / \beta t$ , i.e.  $\partial / \partial t$  of the standard wave equation. Thus, a full RHS of the Lilley equation must reduce in this case to  $\partial / \partial t$  of the Lighthill source distribution.

However, our interest in the Lilley equation is limited to situations where mean flow variations play an important role. For this reason, we seek in this analysis to simplify the source terms by retaining on the right-hand side only those terms which contain bilateral interactions between fluctuating velocities. This immediately precludes any reduction to the unsheared case, since the RHS in that case can be expressed entirely in terms of third and higher order interactions among the fluctuating velocity components [see Equation (3A-8)] for flows with negligible density fluctuations.

Note that although  $p'$  can be related to given values of  $(y', V')$  by the Lilley equation, it is not possible to relate  $V'$  itself to  $y'$ , as can be seen by recognizing the possibility of a convected  $V'$  disturbance with  $y' = 0$ . Thus,  $V'p'$  terms must be included, but  $V'V'p'$  terms are discarded.

#### 3A.2 ACCELERATION QUADRUPOLE SOURCE DERIVATION

The first term in the basic Lilley equation source term,  $Q$ , which is given by Equation (3A-11) as

$$- 6 \frac{\partial \bar{v}_i}{\partial x_j} \frac{\partial v_j'}{\partial x_k} \frac{\partial v_k'}{\partial x_i}, \quad (3A-19)$$

can be rearranged to give, with certain assumptions, a volume acceleration quadrupole source, plus another source term:

$$\frac{3}{2} \frac{\bar{D}}{Dt} \frac{\partial^2 v_i' v_j'}{\partial x_i \partial x_j} + 3 \frac{\partial^2 \bar{v}_i}{\partial x_i \partial x_k} v_j' \frac{\partial v_k'}{\partial x_i}. \quad (3A-20)$$

Note that the second term is zero if the basic flow is axisymmetric. To prove this result, the first term is expanded as follows:

$$\begin{aligned}\frac{\bar{D}}{Dt} \frac{\partial^2}{\partial x_i \partial x_j} (v_i' v_j') &= \frac{\partial^2}{\partial x_i \partial x_j} \frac{\bar{D}}{Dt} (v_i' v_j') - \frac{\partial^2 \bar{v}_k}{\partial x_i \partial x_j} \frac{\partial}{\partial x_k} (v_i' v_j') \\ &\quad - 2 \frac{\partial \bar{v}_k}{\partial x_j} \frac{\partial^2}{\partial x_k \partial x_i} (v_i' v_j').\end{aligned}\quad (3A-21)$$

Consider the first term in (3A-21): from Equation (3A-35) below, it follows that

$$\frac{\bar{D}}{Dt} (v_i' v_j') = - \frac{\partial \bar{v}_i}{\partial x_k} v_k' v_j' - \frac{\partial \bar{v}_j}{\partial x_k} v_k' v_i' + O(p' v', v'^3). \quad (3A-22)$$

Hence

$$\begin{aligned}\frac{\partial}{\partial x_j} \frac{\bar{D}}{Dt} (v_i' v_j') &= - \frac{\partial \bar{v}_i}{\partial x_k} \frac{\partial}{\partial x_j} v_k' v_j' - \frac{\partial \bar{v}_i}{\partial x_k} \frac{\partial v_k'}{\partial x_j} v_j' \\ &\quad - \cancel{\frac{\partial \bar{v}_j}{\partial x_k} \frac{\partial v_k'}{\partial x_j} v_i'} - \frac{\partial \bar{v}_j}{\partial x_k} v_k' \frac{\partial v_i'}{\partial x_j} + O(p' v', v'^3),\end{aligned}$$

and therefore

$$\begin{aligned}\frac{\partial^2}{\partial x_i \partial x_j} \frac{\bar{D}}{Dt} (v_i' v_j') &= - \frac{\partial^2 \bar{v}_i}{\partial x_k \partial x_j} \left( \frac{\partial v_k'}{\partial x_i} v_j' + v_k' \frac{\partial v_j'}{\partial x_i} \right) \\ &\quad - \frac{\partial \bar{v}_i}{\partial x_k} \left( \frac{\partial^2 v_k'}{\partial x_i \partial x_j} v_j' + 2 \frac{\partial v_k'}{\partial x_j} \frac{\partial v_i'}{\partial x_i} \right) \\ &\quad - \frac{\partial^2 \bar{v}_j}{\partial x_k \partial x_i} v_k' \frac{\partial v_i'}{\partial x_j} \\ &= - 2 \frac{\partial \bar{v}_i}{\partial x_k} \frac{\partial v_j'}{\partial x_i} \frac{\partial v_k'}{\partial x_j} - v_j' \frac{\partial}{\partial x_j} \left( \frac{\partial \bar{v}_i}{\partial x_k} \frac{\partial v_k'}{\partial x_i} \right) \\ &\quad - 2 \frac{\partial^2 \bar{v}_i}{\partial x_j \partial x_k} \frac{\partial v_k'}{\partial x_i} v_j' + O(p' v', v'^3),\end{aligned}\quad (3A-23a)$$

where the crossed-out terms are  $O(p' v', v'^3)$  by virtue of  $\partial v_n'/\partial x_1 = O(p', v'^2)$ , Equation (3A-35b).

The second term in (3A-21) can be rewritten as

$$\begin{aligned} - \frac{\partial^2 \bar{v}_k}{\partial x_i \partial x_j} \frac{\partial}{\partial x_k} (v_i' v_j') &= - \frac{\partial^2 \bar{v}_k}{\partial x_i \partial x_j} \left( \frac{\partial v_i'}{\partial x_k} v_j' + v_i' \frac{\partial v_j'}{\partial x_k} \right) \\ &= - 2 \frac{\partial^2 \bar{v}_i}{\partial x_j \partial x_k} \frac{\partial v_k'}{\partial x_i} v_j', \end{aligned} \quad (3A-23b)$$

and the third term as

$$\begin{aligned} - 2 \frac{\partial \bar{v}_k}{\partial x_j} \frac{\partial^2}{\partial x_k \partial x_i} (v_i' v_j') &= - 2 \frac{\partial \bar{v}_k}{\partial x_j} \frac{\partial}{\partial x_k} \left( v_i' \frac{\partial v_j'}{\partial x_i} \right) + O(p' v', v'^3) \\ &= - 2 \frac{\partial \bar{v}_k}{\partial x_j} \frac{\partial v_i'}{\partial x_k} \frac{\partial v_j'}{\partial x_i} - 2 \frac{\partial \bar{v}_k}{\partial x_j} v_i' \frac{\partial v_j'}{\partial x_i} + O(p' v', v'^3) \\ &= - 2 \frac{\partial \bar{v}_k}{\partial x_j} \frac{\partial v_i'}{\partial x_k} \frac{\partial v_j'}{\partial x_i} - 2 v_i' \left[ \frac{\partial}{\partial x_i} \left( \frac{\partial \bar{v}_k}{\partial x_j} \frac{\partial v_j'}{\partial x_k} \right) - \frac{\partial^2 \bar{v}_k}{\partial x_i \partial x_j} \frac{\partial v_j'}{\partial x_k} \right] \\ &\quad + O(p' v', v'^3). \end{aligned} \quad (3A-23c)$$

Again the crossed-out term is  $O(p' v', v'^3)$  from Equation (3A-35b) below.

Combining Equations (3A-23a-c) with Equation (3A-21) gives

$$\begin{aligned} \frac{D}{Dt} \frac{\partial^2}{\partial x_i \partial x_j} (v_i' v_j') &= - 4 \frac{\partial \bar{v}_i}{\partial x_k} \frac{\partial v_j'}{\partial x_i} \frac{\partial v_k'}{\partial x_j} - 2 \frac{\partial^2 \bar{v}_i}{\partial x_j \partial x_k} \frac{\partial v_k'}{\partial x_i} v_j' \\ &\quad + O(p' v', v'^3), \end{aligned} \quad (3A-24)$$

which proves the equivalence of (3A-19) and (3A-20) to the indicated approximation. Note that the  $\partial^2 \bar{v}_i / \partial x_j \partial x_k$  term vanishes for an *axisymmetric* basic flow field (which includes a two-dimensional shear layer as a special case).

### 3A.3 DISPLACEMENT QUADRUPOLE SOURCE DERIVATION

Alternatively, the first term on the right of Equation (3A-11), i.e.

$$-6 \frac{\partial \bar{v}_i}{\partial x_j} \frac{\partial v_j'}{\partial x_k} \frac{\partial v_k'}{\partial x_i}, \quad (3A-25)$$

can be rearranged to give, with certain assumptions, a volume displacement quadrupole source term of the form

$$\frac{\partial^3}{\partial t^3} \left( \frac{1}{2} \frac{\partial^2 \xi'_i \xi'_j}{\partial x_i \partial x_j} \right). \quad (3A-26)$$

To prove this result the analysis given below, headed "Proposed Aerodynamic Source Term" starts with the expression (3A-26) (omitting the factor 1/2) and works back to the basic source term (3A-25). However, a number of special relations are required in the proof and these are developed first in the following three sub-sections.

#### KINEMATICS OF SMALL PERTURBATIONS TO A PARALLEL STEADY FLOW

We are concerned here with the displacement of a fluid element relative to an idealized basic flow field  $\bar{v}$ , measured between times  $t^0$  and  $t$ , where  $t^0$  is some fixed starting time.

The basic flow field is taken as a steady parallel flow in the  $x_1$  direction; i.e.  $\bar{v} = (\bar{v}_1, 0, 0)$ , where  $\bar{v}_1$  is independent of  $x_1$  and  $t$ . We define the displacement perturbation  $\eta$  as<sup>\*</sup>

$$\eta(x, t; t^0) = (x - x^0) - \bar{v}^0(t - t^0), \quad (3A-27)$$

where  $\bar{v}^0 = \bar{v}(x^0)$  is the basic flow velocity at the starting position  $x^0(t^0)$ , (i.e. the position of the particle at  $t = t^0$ ).

Operating on Equation (3A-27) with  $D/Dt$  gives

$$\frac{D\eta}{Dt} = v - \bar{v}(x^0), \quad (3A-28)$$

since  $x^0$  and  $t^0$  are constant following a fluid element. The component of Equation (3A-28) in the direction of the  $\bar{v}_1$  gradient ( $n$ ), normal to the mean flow direction, is

$$\frac{D\eta_n}{Dt} = v_n; \quad (3A-29)$$

---

\*In this section  $\eta$  replaces  $\xi'$  as the symbol for the displacement perturbation. Strictly,  $\xi'$  as defined by Equation (3A-15) is a first-order approximation to  $\eta$  as defined above.

while the component in the basic flow direction of Equation (3A-27) is

$$\frac{Dn_1}{Dt} = v_1 - \bar{v}_1 (x_n - n_n), \quad (3A-30)$$

since  $x_n^o = x_n - n_n$  from Equation (3A-27).

#### SMALL PERTURBATION ASSUMPTIONS

We are interested in the asymptotic form of the above relations for small velocity perturbations about the basic flow. Equation (3A-29) gives

$$\frac{\bar{D}n_n}{Dt} = v_n' + O(v'^2), \quad (\bar{D}/Dt = \partial/\partial t + \bar{v}_1 \partial/\partial x_1), \quad (3A-31)$$

and from Equation (3A-30) we get

$$\frac{\bar{D}n_1}{Dt} = v_1' + \frac{\partial \bar{v}_1}{\partial x_n} n_n + O(v'^2). \quad (3A-32)$$

A compact form which applies to all displacement components is

$$\frac{\bar{D}n_i}{Dt} = v_i' + \frac{\partial \bar{v}_i}{\partial x_k} n_k + O(v'^2). \quad (3A-33)$$

A further useful relation follows from the  $i$ -momentum equation,

$$\frac{Dv_i}{Dt} = - \frac{1}{\rho} \frac{\partial p'}{\partial x_i}, \quad (3A-34)$$

where the pressure in the basic flow, being constant, disappears from the right-hand side. The left-hand side of Equation (3A-34) may be written as

$$\frac{Dv_i}{Dt} = \frac{\bar{D}v_i}{Dt} + \frac{\partial \bar{v}_i}{\partial x_k} v_k' + O(v'^2);$$

since  $\bar{D}\bar{v}_i/Dt = 0$  by definition, it follows that

$$\frac{\bar{D}v_i'}{Dt} = - \frac{\partial \bar{v}_i}{\partial x_k} v_k' + O(p', v'^2). \quad (3A-35)$$

The reasonableness of grouping  $p'$  and  $v'^2$  terms together will be assumed for the time being (from experimental evidence,  $p' \sim v'^2$  is reasonable).

Finally, taking the divergence of Equation (3A-35) gives

$$\frac{\bar{D}}{Dt} \frac{\partial v_i'}{\partial x_i} + \frac{\partial \bar{v}_j}{\partial x_i} \frac{\partial v_i'}{\partial x_j} = - \frac{\partial \bar{v}_i}{\partial x_k} \frac{\partial v_k'}{\partial x_i} + O(p', v'^2)$$

and since  $\partial v_i' / \partial x_i = O(p')$  when diffusion effects are neglected, it follows that for small perturbations to a parallel basic flow

$$\frac{\partial \bar{v}_i}{\partial x_k} \frac{\partial v_k'}{\partial x_i} = O(p', v'^2), \quad (3A-35a)$$

or, equivalently,

$$\frac{\partial v_n'}{\partial x_1} = O(p', v'^2). \quad (3A-35b)$$

Note that it does not follow that  $\partial n_n / \partial x_1 = O(p', v'^2)$ , only that  $(\bar{D}/Dt)(\partial n_n / \partial x_1) = O(p', v'^2)$ .

#### VOLUME CHANGE OF A FLUID ELEMENT

The displacement  $\xi(x, t; t^0)$  of a fluid element is given by

$$\xi = (x - x^0) = \bar{v}(x^0) \cdot (t - t^0) + n(x, t), \quad (3-36)$$

using Equation (3A-27). Replacing  $\bar{v}(x^0) = \bar{v}(x - \xi)$  by a series expansion about  $x$ , which is permissible since  $\bar{v}$  depends only on  $(x_2, x_3)$  and the displacement components  $(\xi_2, \xi_3)$  are perturbation quantities, gives

$$\xi_i = \bar{v}_i(t - t^0) - n_k \frac{\partial \bar{v}_i}{\partial x_k} (t - t^0) + n_i + O(v'^2) \quad (3-37)$$

where the second term on the right has been further approximated by replacing  $n_k$  with  $\eta_k$  [see Equation (3A-39) below]. The velocities and displacements in Equation (3A-37) are all evaluated at  $(x, t)$ .

Now the ratio of initial and current volumes of the fluid element at  $(x, t)$  is given by the determinant

$$\begin{vmatrix} 1 - \frac{\partial \xi_1}{\partial x_1} & - \frac{\partial \xi_1}{\partial x_2} & - \frac{\partial \xi_1}{\partial x_3} \\ - \frac{\partial \xi_2}{\partial x_1} & 1 - \frac{\partial \xi_2}{\partial x_2} & - \frac{\partial \xi_2}{\partial x_3} \\ - \frac{\partial \xi_3}{\partial x_1} & - \frac{\partial \xi_3}{\partial x_2} & 1 - \frac{\partial \xi_3}{\partial x_3} \end{vmatrix} = J. \quad (3A-38)$$

$t, t^0 = \text{const.}$

We require a relation, accurate to 1st order in the perturbations  $v_i'$ , between  $J$  and the displacement perturbation  $n_i$ . For this purpose we note from Equation (3A-37) in the  $n$  direction that

$$\xi_n = n_n + O(v'^2); \quad (3A-39)$$

thus, we may rewrite Equation (3A-37) as

$$\xi_i = \bar{v}_i(t - t^o) - n_n \frac{\partial \bar{v}_i}{\partial x_n} (t - t^o) + n_i + O(v'^2). \quad (3A-40)$$

The value of  $J$  follows as

$$J = \begin{vmatrix} 1 + \frac{\partial n_n}{\partial x_1} \frac{\partial \bar{v}_1}{\partial x_n} (t - t^o) - \frac{\partial n_1}{\partial x_1} & - \frac{\partial \bar{v}_1}{\partial x_2} (t - t^o) & - \frac{\partial \bar{v}_1}{\partial x_3} (t - t^o) \\ - \frac{\partial n_2}{\partial x_1} & 1 - \frac{\partial n_2}{\partial x_2} & - \frac{\partial n_2}{\partial x_3} \\ - \frac{\partial n_3}{\partial x_1} & - \frac{\partial n_3}{\partial x_2} & 1 - \frac{\partial n_3}{\partial x_3} \end{vmatrix} + O(v'^2)$$

$$= 1 - \frac{\partial n_i}{\partial x_i} + O(v'^2). \quad (3A-41)$$

But the relative volume change of a given fluid element is  $O(p')$ , apart from diffusion effects which are neglected in this analysis. It follows from Equation (3A-41) that

$$\frac{\partial n_i}{\partial x_i} = O(p', v'^2), \quad (3A-42)$$

which is the required form of the continuity equation.

It is readily checked that Equation (3A-42) above is consistent with the divergence of Equation (3A-33).

#### PROPOSED AERODYNAMIC SOURCE TERM

We now investigate the quantity

$$S = \frac{\bar{D}^3}{Dt^3} \frac{\partial^2}{\partial x_i \partial x_j} (n_i n_j),$$

using the relations developed above. First, from Equation (3A-42) it follows that

$$\frac{\partial^2}{\partial x_i \partial x_j} (\eta_i \eta_j) = \frac{\partial \eta_i}{\partial x_j} \frac{\partial \eta_j}{\partial x_i} + O(p' v'). \quad (3A-43)$$

Also, from Equation (3A-33)

$$\bar{\frac{D}{Dt}} \left( \frac{\partial \eta_i}{\partial x_j} \right) = \frac{\partial v_i'}{\partial x_j} + \frac{\partial \bar{v}_i}{\partial x_k} \frac{\partial \eta_k}{\partial x_j} - \frac{\partial \bar{v}_k}{\partial x_j} \frac{\partial \eta_i}{\partial x_k} + \frac{\partial^2 \bar{v}_i}{\partial x_j \partial x_k} \eta_k + O(v'^2) \quad (3A-44)$$

so that

$$\begin{aligned} \bar{\frac{D^2}{Dt^2}} \left( \frac{\partial \eta_i}{\partial x_j} \right) &= \bar{\frac{D}{Dt}} \left( \frac{\partial v_i'}{\partial x_j} \right) + \frac{\partial \bar{v}_i}{\partial x_k} \left( \frac{\partial v_k'}{\partial x_j} + \cancel{\frac{\partial \bar{v}_k}{\partial x_\ell} \frac{\partial \eta_\ell}{\partial x_j}} - \cancel{\frac{\partial \bar{v}_\ell}{\partial x_j} \frac{\partial \eta_k}{\partial x_\ell}} + \cancel{\frac{\partial^2 \bar{v}_k}{\partial x_j \partial x_\ell}} \eta_\ell \right) \\ &\quad - \frac{\partial \bar{v}_k}{\partial x_j} \left( \frac{\partial v_i'}{\partial x_k} + \frac{\partial \bar{v}_i}{\partial x_\ell} \frac{\partial \eta_\ell}{\partial x_k} - \cancel{\frac{\partial \bar{v}_\ell}{\partial x_k} \frac{\partial \eta_i}{\partial x_\ell}} + \cancel{\frac{\partial^2 \bar{v}_i}{\partial x_k \partial x_\ell}} \eta_\ell \right) \\ &\quad - \frac{\partial^2 \bar{v}_i}{\partial x_j \partial x_k} \left( v_k' + \cancel{\frac{\partial \bar{v}_k}{\partial x_\ell} \eta_\ell} \right) + O(v'^2), \end{aligned} \quad (3A-45)$$

in which the crossed-through terms vanish by virtue of the basic flow assumption. However  $(\partial/\partial x_j)$  of Equation (3A-35) gives the relation

$$\bar{\frac{D}{Dt}} \left( \frac{\partial v_i'}{\partial x_j} \right) = - \frac{\partial \bar{v}_k}{\partial x_j} \frac{\partial v_i'}{\partial x_k} - \frac{\partial \bar{v}_i}{\partial x_k} \frac{\partial v_k'}{\partial x_j} - \frac{\partial^2 \bar{v}_i}{\partial x_j \partial x_k} v_k' + O(p', v'^2) \quad (3A-46)$$

which may be combined with Equation (3A-45) to give

$$\bar{\frac{D^2}{Dt^2}} \left( \frac{\partial \eta_i}{\partial x_j} \right) = - 2 \frac{\partial \bar{v}_k}{\partial x_j} \frac{\partial v_i'}{\partial x_k} - 2 \frac{\partial \bar{v}_k'}{\partial x_j} \frac{\partial \bar{v}_i}{\partial x_\ell} \frac{\partial \eta_\ell}{\partial x_k} + O(p', v'^2). \quad (3A-47)$$

Hence, using Equations (3A-46), (3A-44), and (3A-33),

$$\begin{aligned} \bar{\frac{D^3}{Dt^3}} \left( \frac{\partial \eta_i}{\partial x_j} \right) &= 2 \frac{\partial \bar{v}_k}{\partial x_j} \left( \cancel{\frac{\partial \bar{v}_\ell}{\partial x_k} \frac{\partial v_i'}{\partial x_\ell}} + \frac{\partial \bar{v}_i}{\partial x_\ell} \frac{\partial v_\ell'}{\partial x_k} + \cancel{\frac{\partial^2 \bar{v}_i}{\partial x_k \partial x_\ell} v_\ell'} \right) \\ &\quad - 2 \frac{\partial \bar{v}_k}{\partial x_j} \frac{\partial \bar{v}_i}{\partial x_\ell} \left( \cancel{\frac{\partial v_\ell'}{\partial x_m} \frac{\partial \eta_m}{\partial x_k}} - \cancel{\frac{\partial \bar{v}_m}{\partial x_k} \frac{\partial \eta_\ell}{\partial x_m}} + \cancel{\frac{\partial^2 \bar{v}_\ell}{\partial x_k \partial x_m} \eta_m} \right) \\ &\quad + O(p', v'^2) \\ &= O(p', v'^2) \end{aligned} \quad (3A-48)$$

since the crossed-through terms vanish by virtue of the basic flow assumption.  
Now, from Equation (3A-43)

$$S = \frac{\bar{D}^3}{Dt^3} \left( \frac{\partial \eta_i}{\partial x_j} \frac{\partial \eta_j}{\partial x_i} \right);$$

i.e.

$$S = \frac{\bar{D}^3}{Dt^3} \left( \frac{\partial \eta_i}{\partial x_j} \right) \cdot \frac{\partial \eta_j}{\partial x_i} + 3 \frac{\bar{D}^2}{Dt^2} \left( \frac{\partial \eta_i}{\partial x_j} \right) \cdot \frac{\bar{D}}{Dt} \left( \frac{\partial \eta_j}{\partial x_i} \right) + (\text{same with } i, j \text{ reversed})$$

$$= 3 \frac{\bar{D}^2}{Dt^2} \left( \frac{\partial \eta_i}{\partial x_j} \right) \cdot \frac{\bar{D}}{Dt} \left( \frac{\partial \eta_j}{\partial x_i} \right) + (i, j \text{ reversed}) + O(p'v', v'^3), \quad (3A-49)$$

using Equation (3A-48) above. Moreover, from Equations (3A-47) and (3A-44)

$$\begin{aligned} \frac{\bar{D}^2}{Dt^2} \left( \frac{\partial \eta_i}{\partial x_j} \right) \cdot \frac{\bar{D}}{Dt} \left( \frac{\partial \eta_j}{\partial x_i} \right) &= -2 \frac{\partial \bar{v}_k}{\partial x_j} \left( \frac{\partial v_i'}{\partial x_k} + \frac{\partial \bar{v}_i}{\partial x_\ell} \frac{\partial \eta_\ell}{\partial x_k} \right) \left( \frac{\partial v_j'}{\partial x_i} + \frac{\partial \bar{v}_j}{\partial x_m} \frac{\partial \eta_m}{\partial x_i} \right) \\ &\quad - \frac{\partial \bar{v}_m}{\partial x_i} \frac{\partial \eta_j}{\partial x_m} + \frac{\partial^2 \bar{v}_i}{\partial x_j \partial x_m} \eta_m \Big) + O(p'v', v'^3) \end{aligned}$$

where the crossed-through terms vanish by virtue of the basic flow field assumed; thus on multiplying out, we get

$$\begin{aligned} \frac{\bar{D}^2}{Dt^2} \left( \frac{\partial \eta_i}{\partial x_j} \right) \cdot \frac{\bar{D}}{Dt} \left( \frac{\partial \eta_j}{\partial x_i} \right) &= -2 \frac{\partial \bar{v}_k}{\partial x_j} \frac{\partial v_i'}{\partial x_k} \frac{\partial v_j'}{\partial x_i} + 2 \frac{\partial \bar{v}_k}{\partial x_j} \frac{\partial \bar{v}_m}{\partial x_i} \frac{\partial v_i'}{\partial x_k} \frac{\partial \eta_j}{\partial x_m} \\ &\quad - 2 \frac{\partial \bar{v}_k}{\partial x_j} \frac{\partial \bar{v}_i}{\partial x_\ell} \frac{\partial \eta_\ell}{\partial x_k} \frac{\partial v_j'}{\partial x_i} + 2 \frac{\partial \bar{v}_k}{\partial x_j} \frac{\partial \bar{v}_i}{\partial x_\ell} \frac{\partial v_m}{\partial x_i} \frac{\partial \eta_\ell}{\partial x_k} \frac{\partial \eta_j}{\partial x_m} \\ &\quad + O(p'v', v'^3). \end{aligned} \quad (3A-50)$$

Again the last term vanishes as above. In addition, in the second and third terms on the right the factors  $\partial v_i'/\partial x_k$  and  $\partial v_j'/\partial x_i$  both reduce to  $\partial v_n'/\partial x_1$  because of the basic flow field assumed, and are therefore  $O(p')$  from Equation (3A-35b).

Thus finally, combining Equations (3A-49) and (3A-50), we get

$$S \doteq -12 \frac{\partial \bar{v}_k}{\partial x_j} \frac{\partial v_i'}{\partial x_k} \frac{\partial v_j'}{\partial x_i}, \quad (3A-51)$$

which is the first term, multiplied by a factor of two, in the basic Lilley equation source term. Hence, its equivalence with a volume displacement quadrupole source term is established (to the indicated approximation).

### 3A.4 DISPLACEMENT DIPOLE SOURCE DERIVATION

The second term in the basic Lilley equation source term,  $Q$ , as given by Equation (3A-11) is

$$-\left(\delta_{ij}\frac{\bar{D}}{Dt} - 2\frac{\partial \bar{v}_i}{\partial x_j}\right)\frac{\partial f'_j}{\partial x_i}; \quad (3A-52)$$

it is shown below that this can be expressed as a volume displacement dipole source, of the form

$$-\frac{\bar{D}^3}{Dt^3}\left(\frac{\partial \xi_i''}{\partial x_i}\right). \quad (3A-53)$$

To prove this result, the assumption is made that  $f'_j$  is related to some quantity  $\phi_j$  by

$$f'_j = \frac{\bar{D}^2 \phi_j}{Dt^2}; \quad (3A-54)$$

then expression (3A-52) becomes

$$-\left(\delta_{ij}\frac{\bar{D}}{Dt} - 2\frac{\partial \bar{v}_i}{\partial x_j}\right)\frac{\partial}{\partial x_i}\frac{\bar{D}^2 \phi_j}{Dt^2}. \quad (3A-55)$$

To simplify this expression, the following relations are utilized, which follow from the definition  $\bar{D}/Dt \equiv \partial/\partial t + \bar{v}_k \partial/\partial x_k$ .

$$\frac{\partial}{\partial x_i}\left(\frac{\bar{D} \phi_j}{Dt}\right) = \frac{\bar{D}}{Dt}\left(\frac{\partial \phi_j}{\partial x_i}\right) + \frac{\partial \bar{v}_k}{\partial x_i}\frac{\partial \phi_j}{\partial x_k} \quad (3A-56)$$

$$\frac{\bar{D}}{Dt}\frac{\partial}{\partial x_i}\left(\frac{\bar{D} \phi_j}{Dt}\right) = \frac{\bar{D}^2}{Dt^2}\left(\frac{\partial \phi_j}{\partial x_i}\right) + \frac{\partial \bar{v}_k}{\partial x_i}\frac{\bar{D}}{Dt}\frac{\partial \phi_j}{\partial x_k}. \quad (3A-57)$$

Using Equation (3A-56) the final factor in expression (3A-55) is rearranged as

$$\frac{\partial}{\partial x_i}\left(\frac{\bar{D}^2 \phi_j}{Dt^2}\right) = \frac{\bar{D}}{Dt}\frac{\partial}{\partial x_i}\left(\frac{\bar{D} \phi_j}{Dt}\right) + \frac{\partial \bar{v}_l}{\partial x_i}\frac{\partial}{\partial x_l}\left(\frac{\bar{D} \phi_j}{Dt}\right);$$

again using Equation (3A-56) together with Equation (3A-57), it follows that

$$\frac{\partial}{\partial x_i}\left(\frac{\bar{D}^2 \phi_j}{Dt^2}\right) = \frac{\bar{D}^2}{Dt^2}\left(\frac{\partial \phi_j}{\partial x_i}\right) + \frac{\partial \bar{v}_k}{\partial x_i}\frac{\bar{D}}{Dt}\left(\frac{\partial \phi_j}{\partial x_k}\right) + \frac{\partial \bar{v}_l}{\partial x_i}\frac{\bar{D}}{Dt}\left(\frac{\partial \phi_j}{\partial x_l}\right) + \cancel{\frac{\partial \bar{v}_l}{\partial x_i}\frac{\partial \bar{v}_k}{\partial x_l}\frac{\partial \phi_j}{\partial x_k}} \quad (3A-58)$$

where the last term vanishes by virtue of the basic flow field assumed.

Hence, the first term in Equation (3A-55) becomes [from (3A-58)]

$$\begin{aligned} - \frac{\bar{D}}{Dt} \frac{\partial}{\partial x_j} \left( \frac{\bar{D}^2 \phi_j}{Dt^2} \right) &= - \frac{\bar{D}^3}{Dt^3} \left( \frac{\partial \phi_j}{\partial x_j} \right) - 2 \frac{\bar{D}}{Dt} \frac{\partial \bar{v}_k}{\partial x_j} \frac{\bar{D}}{Dt} \left( \frac{\partial \phi_j}{\partial x_k} \right) \\ &= - \frac{\bar{D}^3}{Dt^3} \left( \frac{\partial \phi_j}{\partial x_j} \right) - 2 \frac{\partial \bar{v}_k}{\partial x_j} \frac{\bar{D}^2}{Dt^2} \left( \frac{\partial \phi_j}{\partial x_k} \right), \end{aligned} \quad (3A-59)$$

again by virtue of the basic flow field assumed. For the same reason when Equation (3A-58) is used to evaluate the second term in Equation (3A-55), the only surviving term is

$$2 \frac{\partial \bar{v}_i}{\partial x_j} \frac{\bar{D}^2}{Dt^2} \left( \frac{\partial \phi_j}{\partial x_i} \right).$$

This cancels the second term in Equation (3A-59), so that only

$$- \frac{\bar{D}^3}{Dt^3} \left( \frac{\partial \phi_j}{\partial x_j} \right)$$

remains from the two source terms and the equivalence of equations (3A-52) and (3A-53) is established, with  $\phi_j \equiv \xi_j''$ .

## APPENDIX 3B

TRANSFER OF THE QUADRUPOLE OPERATOR FROM  
THE SOURCE FUNCTION TO THE GREEN FUNCTION  
[ DERIVATION OF EQUATION (3-17) ]

The method by which the quadrupole operator,  $\tilde{M}_{\alpha\beta}$ , in Equation (3-16) is transferred from the source strength function,  $\tilde{B}_{\alpha\beta}^{(v)}$ , to one operating on the Green function,  $G^{(v)}$ , is illustrated with an example, the axial-radial quadrupole case, where

$$\tilde{M}_{xr} \equiv k_o^2 \frac{(-jk_x/k_o)}{R} \frac{d}{dR} R . \quad (3B-1)$$

In this case Equation (3-16) can be written as

$$\tilde{p}(R) = (-jk_x/k_o) \int_0^\infty G^{(v)}(R|R') \frac{d}{dR'} [R' \tilde{B}_{xr}^{(v)}(R')] dR' \quad (3B-2)$$

or

$$\begin{aligned} \tilde{p}(R) = & (-jk_x/k_o) \left\{ \int_0^\infty \frac{d}{dR'} [G^{(v)}(R|R') R' \tilde{B}_{xr}^{(v)}(R')] dR' \right. \\ & \left. - \int_0^\infty \tilde{B}_{xr}^{(v)}(R') R' \frac{dG^{(v)}(R|R')}{dR'} dR' \right\} \end{aligned} \quad (3B-3)$$

Since  $G^{(v)}(R|R')$  and  $\tilde{B}_{xr}^{(v)}(R')$  must remain finite as  $R' \rightarrow 0$  and  $\tilde{B}_{xr}^{(v)}(R')$  must vanish at a finite distance from the jet axis, the first integral, which reduces to

$$[G^{(v)}(R|R') R' \tilde{B}_{xr}^{(v)}(R')]_0^\infty \quad (3B-4)$$

can be ignored. The second is rewritten as

$$\tilde{p}(R) = \int_0^\infty \tilde{B}_{xr}^{(v)}(R') N_{xr}(R') G^{(v)}(R|R') R' dR' \quad (3B-5)$$

where

$$N_{xr}(R) \equiv j(k_x/k_o) \frac{d}{dR} \quad (3B-6)$$

Equation (3B-5) with (3B-6) is the required result for this example [Equation (3-17) is the general result, with (3-18)]. When, the corresponding radial-radial quadrupole result is derived, the steps illustrated above have to be repeated twice in order to obtain the required result.

## APPENDIX 3C

NUMERICAL RESULTS OUTSIDE THE CONE OF SILENCE

In paragraph 3.2.4 numerical results for the SIPQ flow factor have been given as a function of  $k_0\delta$  and  $\delta/r_0$  (or  $k_0r_0$ ) for a fixed Mach number; here the Mach number dependence of the two types of SIPQ flow factor are illustrated for fixed values of a Strouhal number and of the profile parameter,  $\delta/r_0$ . Results are given for the fully developed profile, as well as for the error function profile; the former is again characterized by the distance,  $r_1$ , from the center line at which  $U/U_i = 0.663$ , but now  $r_1$  is no longer equal to the nozzle radius,  $r_0$ .

Results presented in this way demonstrate quite clearly that the volume acceleration SIPQ flow factor appears to have a Mach number dependence, in the low Mach limit, which is inconsistent with observation. The volume displacement SIPQ flow factor on the other hand is relatively well behaved and exhibits an almost constant departure from the geometric acoustics limit for a given Strouhal number over a wide Mach number range. The approximate analytic descriptions of the low Mach number behavior of  $F^{(1)}$  and  $F^{(3)}$  are used in paragraph 3.3.2 to show that the corresponding mean velocity dependence is  $U_j^6$  and  $U_j^8$ , hence attention here is confined mainly to the volume displacement source which exhibits the  $U_j^8$  dependence observed in practice.

Some parameter definitions and typical values differ from those adopted in the main text. The modified Doppler factor here is the one developed by Morfey and Szewczyk\*

$$D_m = \left\{ D_s^2 \left[ 1 + (\alpha_1 U_i / c_0)^2 \right] + (\beta_1^2 - \alpha_1^2) (U_i \cos \theta_0 / c_0)^2 \right\}^{1/2} \quad (3C-1)$$

where

$$D_s = (1 - \phi_s U_i \cos \theta_0 / c_0) \quad (3C-2)$$

$$\phi_s = 0.6$$

and

$$\alpha_1 = 0.25 \quad \beta_1 = 0.55 \quad (v = 1)$$

$$\alpha_1 = 0.20 \quad \beta_1 = 0.40 \quad (v = 3)$$

In place of the radiation angle,  $\theta_0$ , the source emission angle,  $\theta_s$ , is held constant;  $\theta_0$  is related to  $\theta_s$  by

$$\cos \theta_0 = \cos \theta_s / (1 + \phi_s U_i \cos \theta_s / c_0) \quad (3C-3)$$

$$= D_s \cos \theta_s \quad (3C-4)$$

---

\*Personal communication.

since

$$D_s = (1 - \phi_s U_i \cos\theta_o/c_o) = (1 + \phi_s U_i \cos\theta_s/c_o)^{-1}. \quad (3C-5)$$

Thus,  $\theta_o$  varies with  $U_i/c_o$  for a fixed value of  $\theta_s$ ; the  $\theta_o$  variation with  $U_i/c_o$  is indicated in each graph of this appendix. In Figure 3C.1, which refers to the fully developed profile, the modified Strouhal number  $S_m'$  replaces  $S_m$  where

$$S_m' = S_m (r_1/r_o) (U_j/U_i) \quad (3C-6)$$

i.e.  $S_m'$  is independent of jet exit conditions. In Figures 3C.2 through 3C.5 the Strouhal number  $S_s$  replaces  $S_m$  where

$$S_s = S D_s. \quad (3C-7)$$

The corresponding results are therefore independent of the semi-empirical wavenumber scaling parameters  $\alpha_1$ ,  $\beta_1$ .

Figures 3C.6 and 3C.7 allow a comparison to be made between the mean velocity dependence for two source types at the conditions indicated. The modified Strouhal numbers of 0.5 and 1.0 span the frequency range that corresponds to the nominal four diameter flow profile (where  $\delta/r_o = 1.05$ ) according to effective source location measurements

The asymptotic low Mach behavior of the volume acceleration SIPQ flow factor is accentuated when the source emission angle is changed from  $60^\circ$  in Figure 3C.6 to  $30^\circ$  in Figure 3C.8. The corresponding results for the volume displacement SIPQ flow factor in Figure 3C.9 are quite different, staying close to the geometric acoustics limit and giving a finite result, of under 1 dB, at zero Mach number.

In Figures 3C.1 and 3C.10 the main features of those results are shown to be independent of flow profile; in Figure 3C.1 the fully developed profile is used, with  $\delta/r = 1.82$ . In Figure 3C.10 the profile parameter for the initial mixing region profile (error function profile) is chosen to be  $\delta/r_o = 0.26$ , i.e. the nominal one diameter flow profile, with appropriately higher values of  $S_m$ .

Figure 3C.2 through 3C.5 illustrate the way in which the differences between the calculated volume displacement flow factor and the geometric acoustics limit vary with source emission angle. For a given Strouhal number the largest difference occur at  $\theta_s = 0$ , i.e. on the boundary of the cone of silence; the largest difference is 4.7 dB in the range  $0.5 \leq S_s \leq 1.0$ . In the forward arc at  $\theta_s = 120^\circ$  there is almost no departure at all from the geometric acoustics limit.

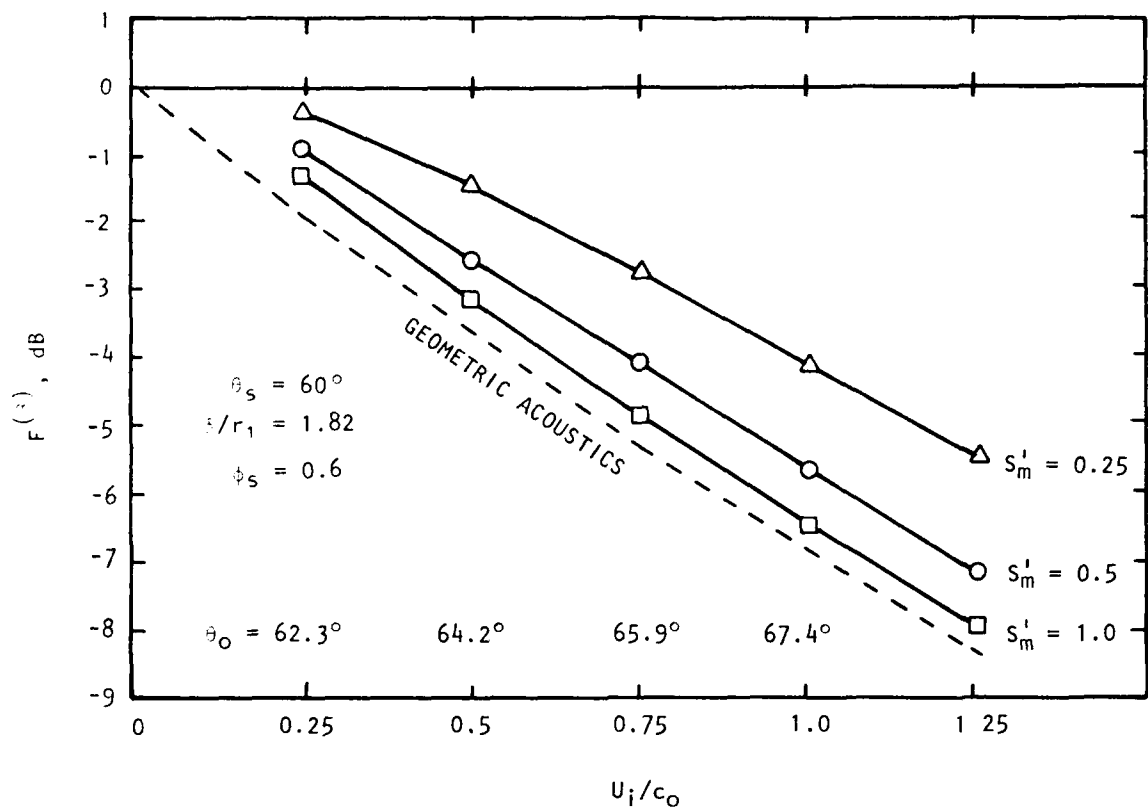


Figure 3C.1 Isothermal Flow Factor Variation with Mach Number for SIPQ Volume Displacement Source at Source Emission Angle  $\theta_s = 60^\circ$ ; Profile Parameter  $\delta/r_1 = 1.82$  (Fully Developed Profile),  $\phi_s = 0.6$ . Code:  
 ○  $S_m^i = 0.5$ ; □  $S_m^i = 1.0$ ; △  $S_m^i = 0.25$ ; --- Geometric Acoustics  
 Limit  $F^{(3)} = D_S^{-6}$ .

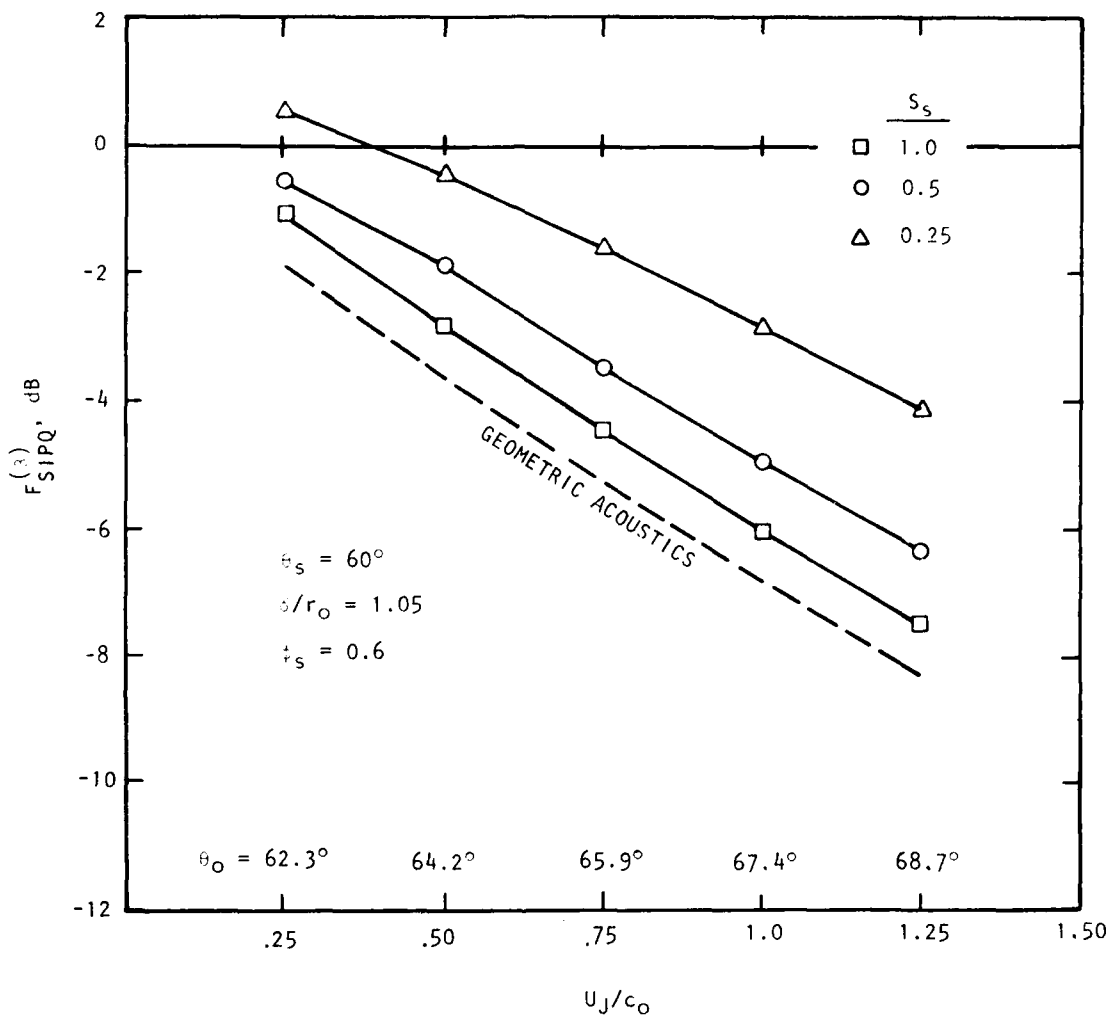


Figure 3C.2 Isothermal Flow Factor Variation with Mach Number for SIPQ Volume Displacement Source at Source Emission Angle  $\theta_S = 60^\circ$ ; Profile Parameter  $\delta/r_O = 1.05$ ,  $\phi_S = 0.6$ . Code:  $\square S_S = 1.0$ ;  $\circ S_S = 0.5$ ;  $\Delta S_S = 0.25$ ; --- Geometric Acoustics Limit  $F^{(3)} = D_S^6$ .

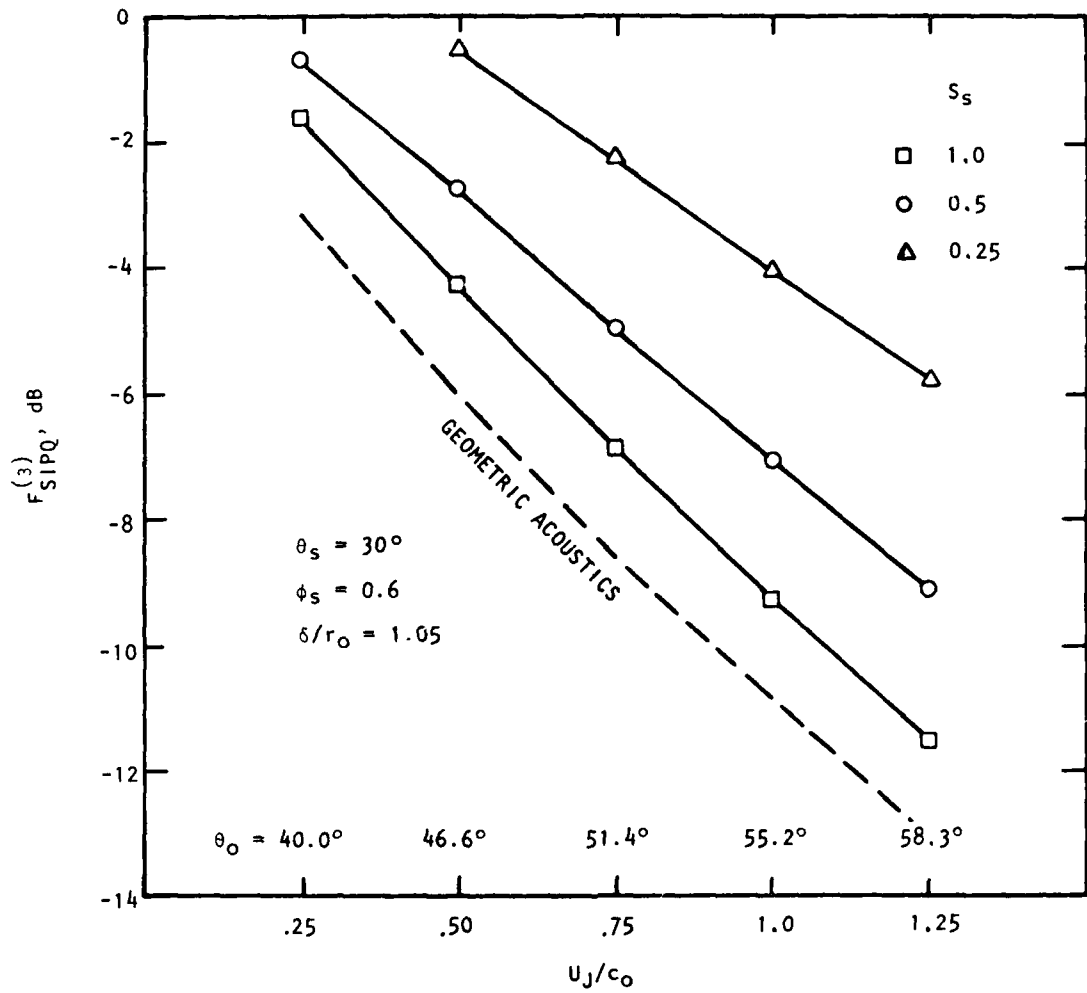


Figure 3C.3 Isothermal Flow Factor Variation with Mach Number for SIPQ Volume Displacement Source at Source Emission Angle  $\theta_s = 30^\circ$ ; Profile Parameter  $\delta/r_o = 1.05$ ,  $\phi_s = 0.6$ . Code:  $\square S_s = 1.0$ ;  $\circ S_s = 0.5$ ;  $\Delta S_s = 0.25$ ; --- Geometric Acoustics Limit  $F^{(3)} = D_s^6$ .

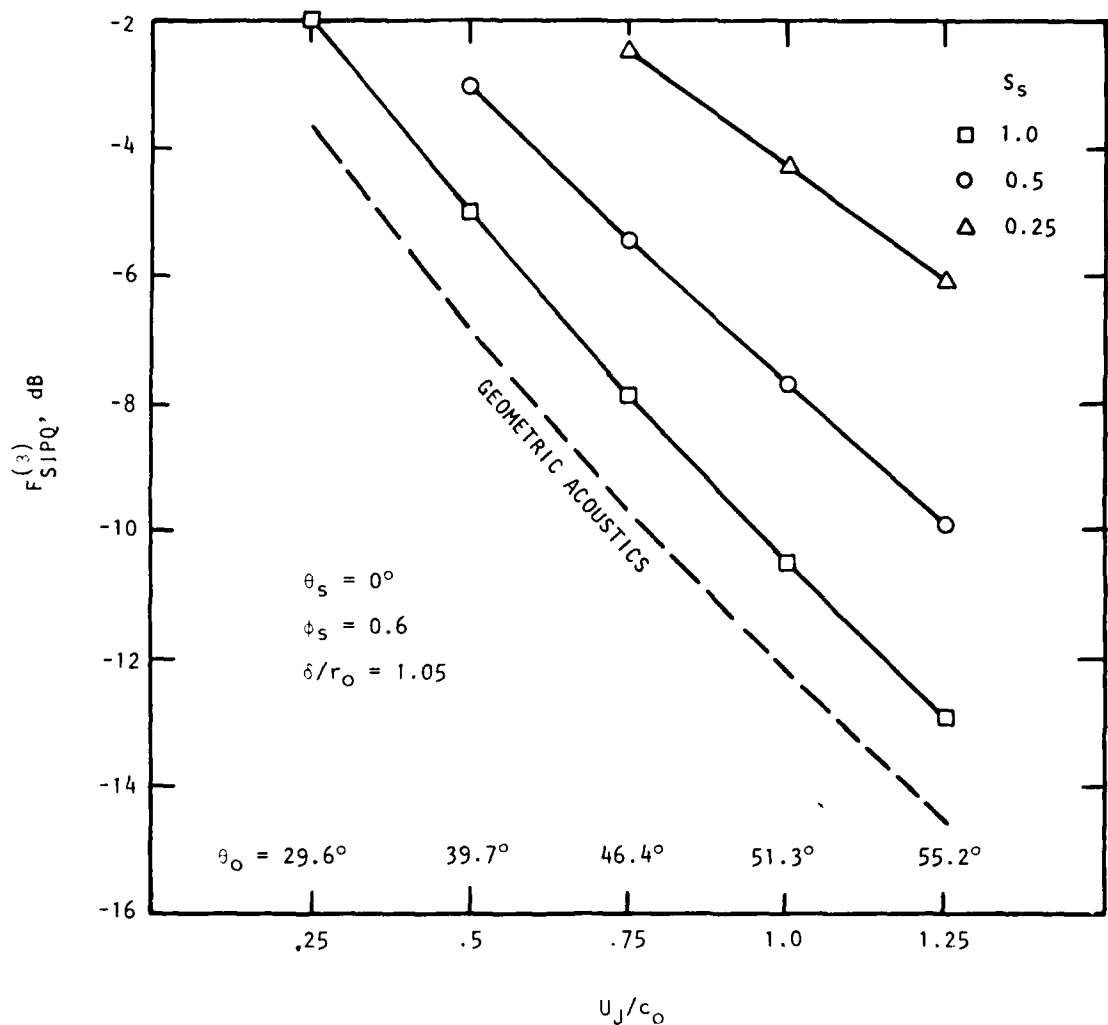


Figure 3C.4 Isothermal Flow Factor Variation with Mach Number for SIPQ Volume Displacement Source at Source Emission Angle  $\theta_s = 0^\circ$ ; Profile Parameter  $\delta/r_o = 1.05$ ,  $\phi_s = 0.6$ . Code:  $\square S_s = 1.0$ ;  $\circ S_s = 0.5$ ;  $\Delta S_s = 0.25$ ; --- Geometric Acoustics Limit  $F^{(3)} = D_s^6$ .

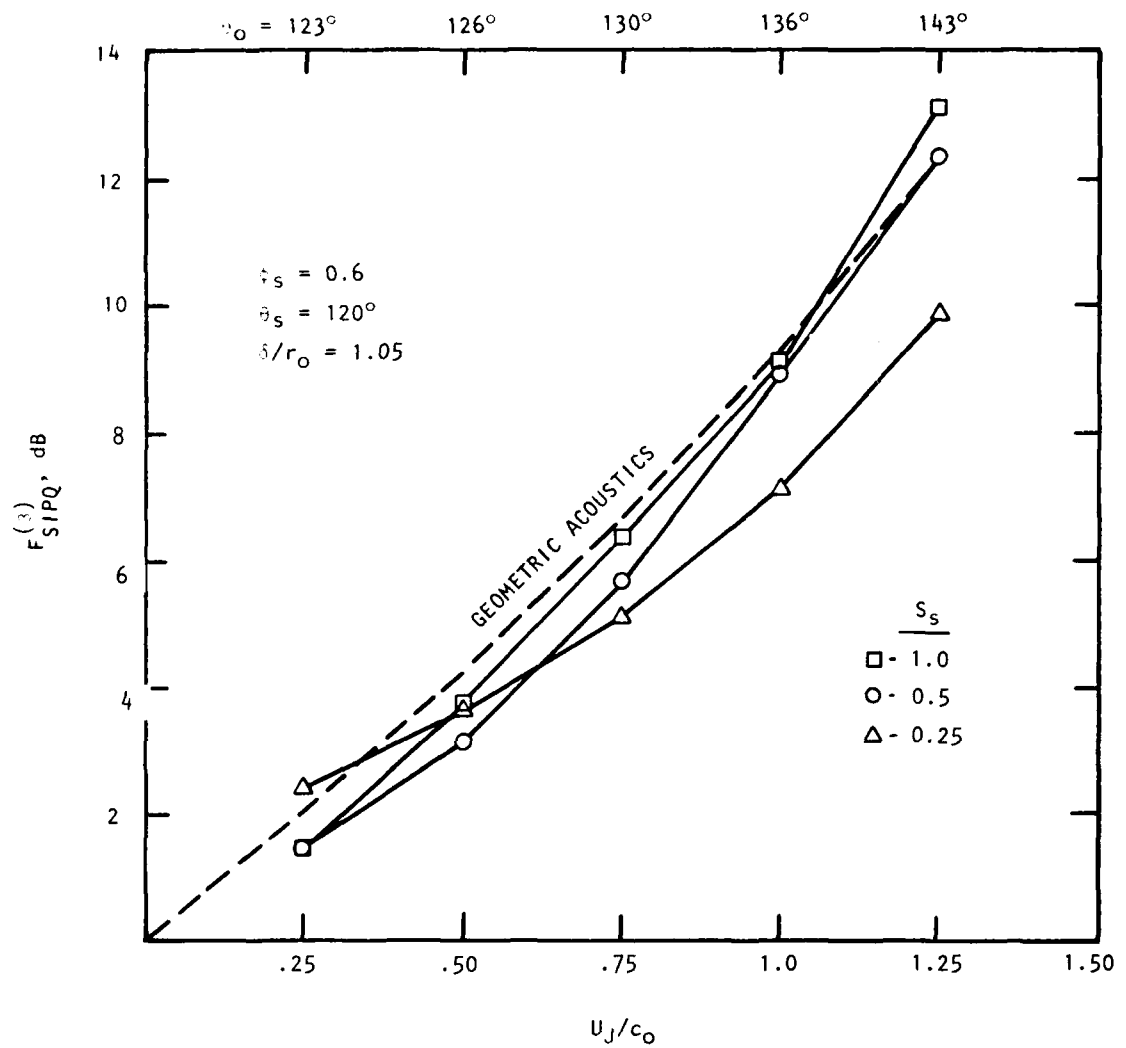


Figure 3C.5 Isothermal Flow Factor Variation with Mach Number for SIPQ Volume Displacement Source at Source Emission Angle  $\theta_s = 120^\circ$ ; Profile Parameter  $\delta/r_o = 1.05$ ,  $\phi_s = 0.6$ . Code:  $\square - S_s = 1.0$ ;  $\circ - S_s = 0.5$ ;  $\Delta - S_s = 0.25$ ; --- Geometric Acoustics Limit  $F^{(3)} = D_s^6$ .

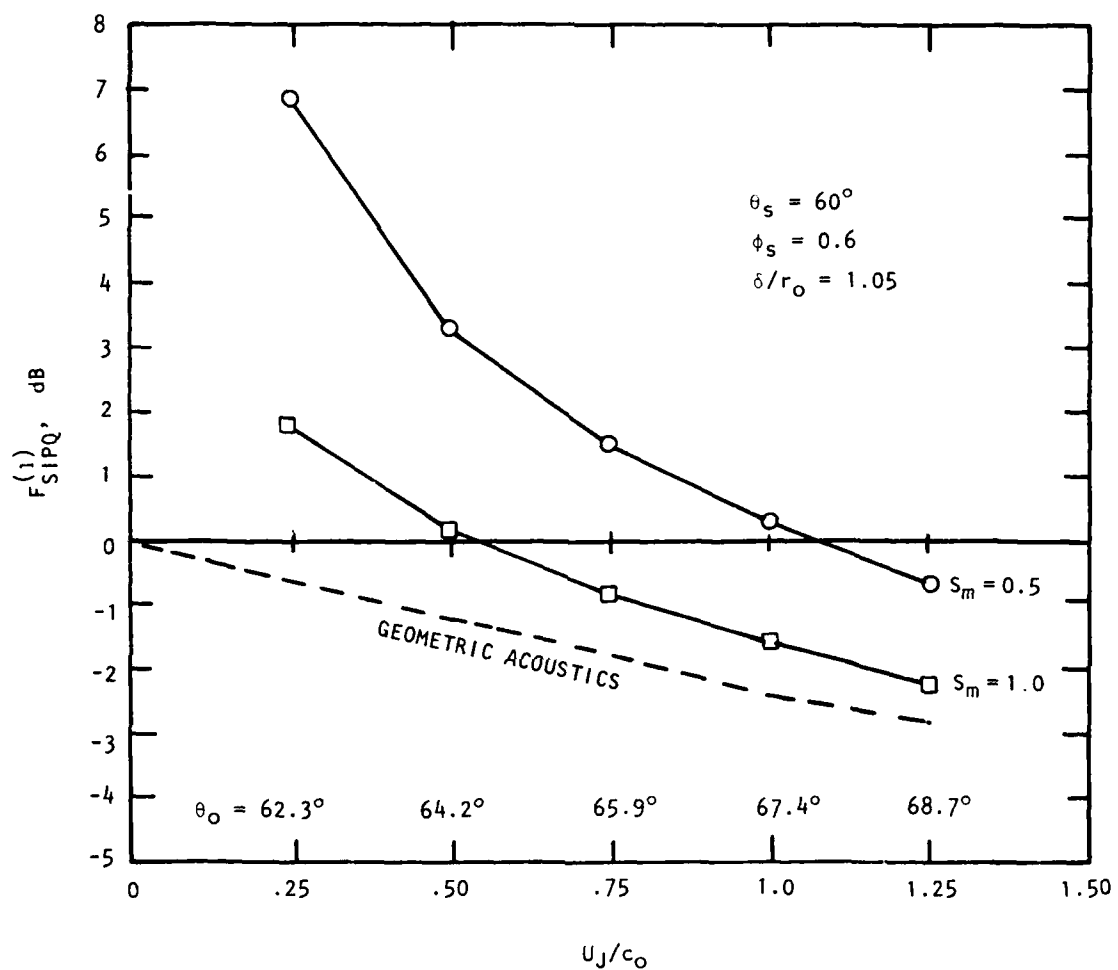


Figure 3C.6 Isothermal Flow Factor Variation with Mach Number for SIPQ Volume Acceleration Source at Source Emission Angle  $\theta_s = 60^\circ$ ; Profile Parameter  $\delta/r_o = 1.05$ ,  $\phi_s = 0.6$ . Code:  $\circ$   $S_m = 0.5$ ;  $\square$   $S_m = 1.0$ ; --- Geometric Acoustics Limit  $F^{(1)} = D_s^2$ .

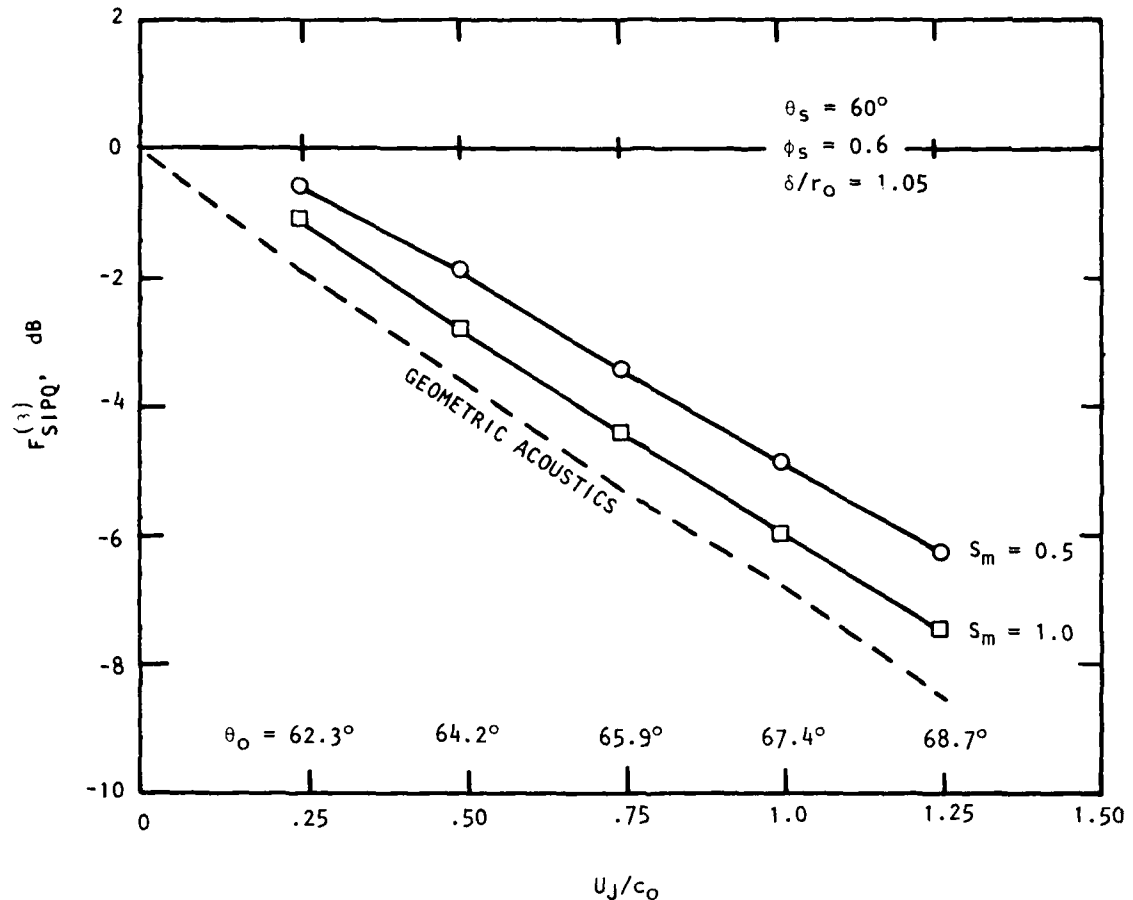


Figure 3C.7 Isothermal Flow Factor Variation with Mach Number for SIPQ Volume Displacement Source at Source Emission Angle  $\theta_s = 60^\circ$ ; Profile Parameter  $\delta/r_o = 1.05$ ,  $\theta_s = 0.6$ . Code:  $\bullet$   $S_m = 0.5$ ;  $\square$   $S_m = 1.0$ ; --- Geometric Acoustics Limit  $F^{(3)} = D_s^6$ .

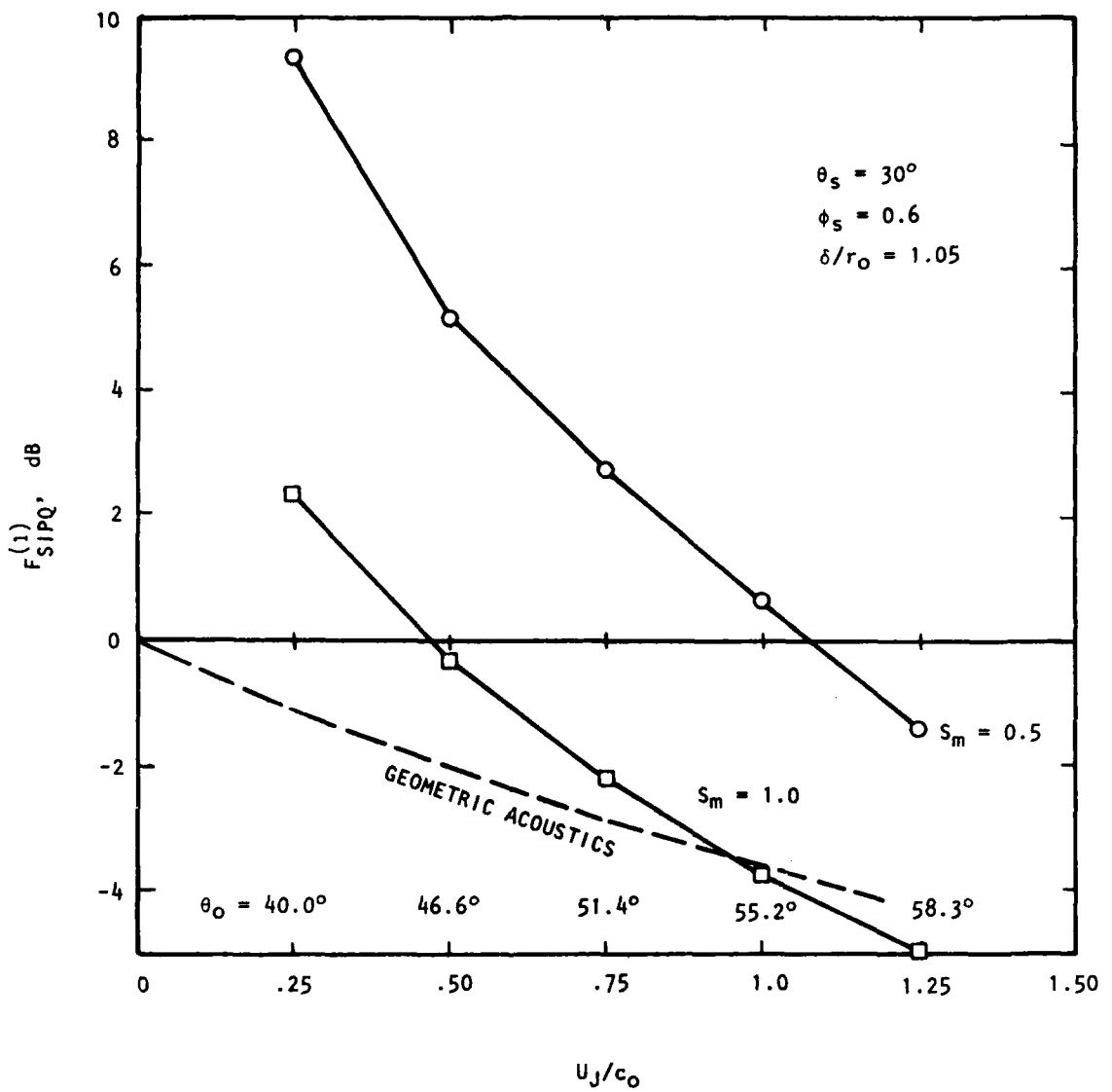


Figure 3C.8 Isothermal Flow Factor Variation with Mach Number for SIPQ Volume Acceleration Source at Source Emission Angle  $\theta_s = 30^\circ$ ; Profile Parameter  $\delta/r_o = 1.05$ ,  $\phi_s = 0.6$ . Code:  $\circ$   $S_m = 0.5$ ;  $\square$   $S_m = 1.0$ ; --- Geometric Acoustics Limit  $F^{(1)} = D_s^2$ .

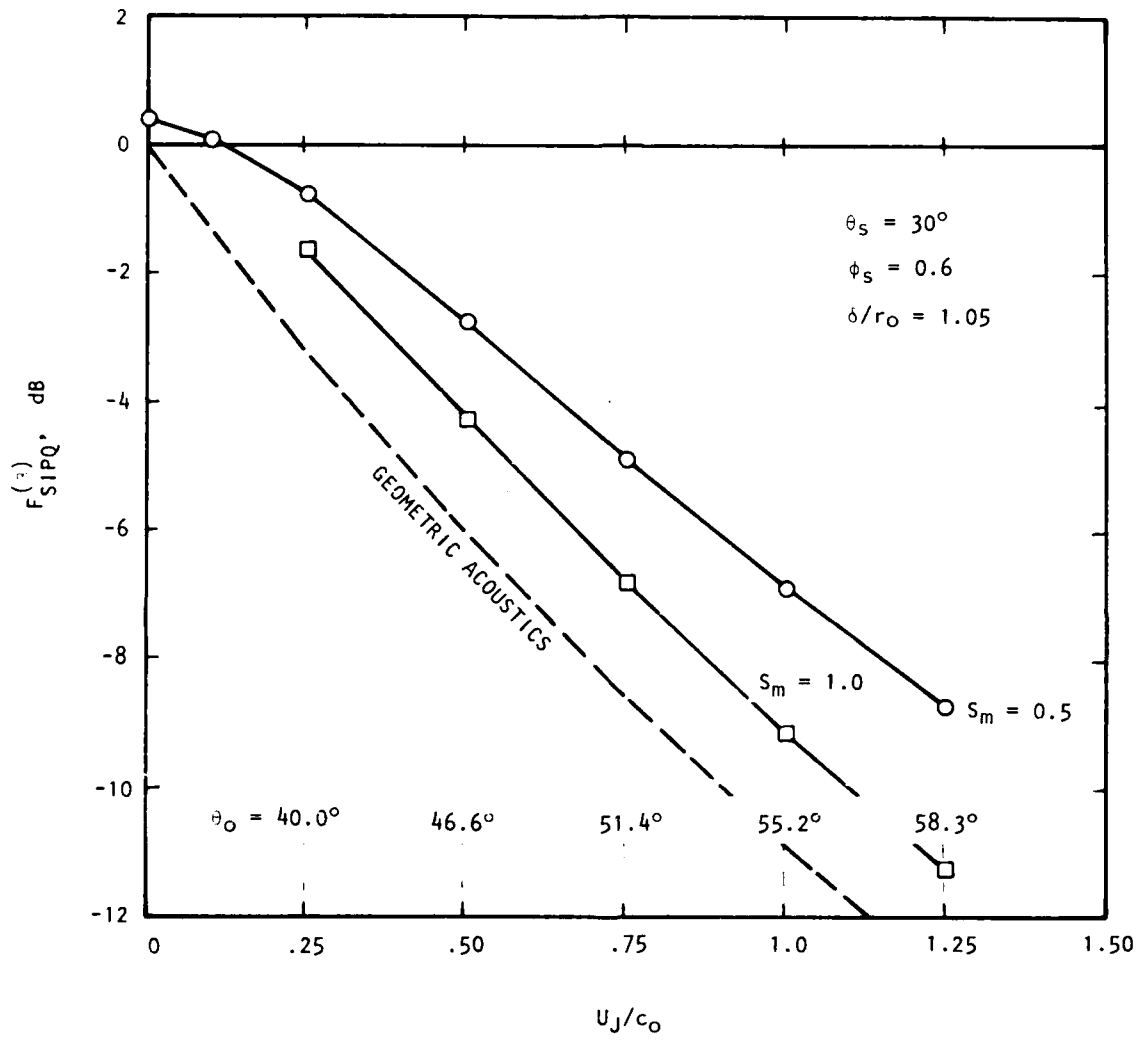


Figure 3C.9 Isothermal Flow Factor Variation with Mach Number for SIPQ Volume Displacement Source at Source Emission Angle  $\theta_s = 30^\circ$ ; Profile Parameter  $\delta/r_o = 1.05$ ,  $\phi_s = 0.6$ . Code:  $\circ$   $S_m = 0.5$ ;  $\square$   $S_m = 1.0$ ; --- Geometric Acoustics Limit  $F^{(3)} = D_s^6$ .

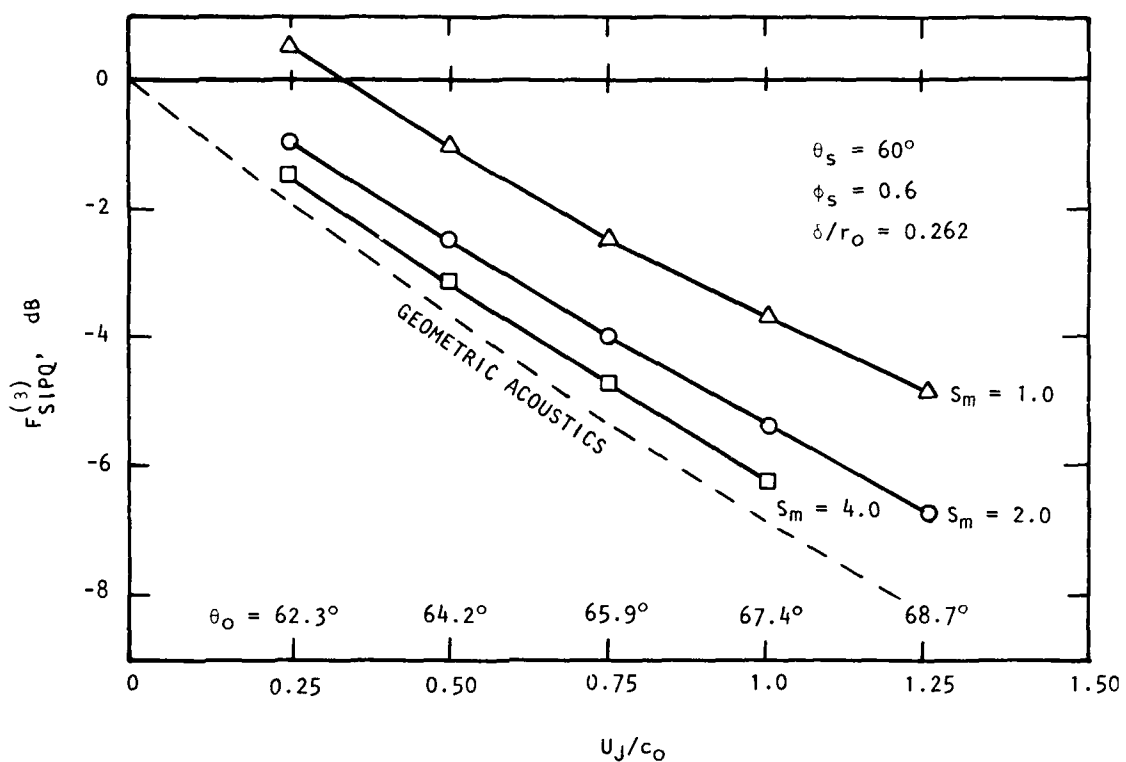


Figure 3C.10 Isothermal Flow Factor Variation with Mach Number for SIPQ Volume Displacement Source at Source Emission Angle  $\theta_s = 60^\circ$ ; Profile Parameter  $\delta/r_o = 0.262$ ,  $\phi_s = 0.6$ . Code:  $\circ$   $S_m = 2.0$ ;  $\square$   $S_m = 4.0$ ;  $\Delta$   $S_m = 1.0$ ; --- Geometric Acoustics Limit  $F^{(3)} = D_s^6$ .

## APPENDIX 3D

NUMERICAL RESULTS INSIDE THE CONE OF SILENCE  
("EFFECTIVE DEPTH" INVESTIGATION)

The high frequency analytic result for monopole radiation into the cone of relative silence, given by Equation (3-68) in Section 3.2.5.1 indicates that the radiation suffers an exponential decay as it propagates from the source position to the transition point. Fisher\* has advocated the use of an effective depth concept in order to understand certain jet suppressor mechanisms. That is, the exponential decay factor in Equation (3-68), for example, is approximated as follows

$$\int_{R_S}^{R_T} |q| dR \Rightarrow |q_s| h_0 \quad (3D-1)$$

i.e. the nondimensional wavenumber is replaced by a constant equal to its value at the source position, while  $h_0$  is a "depth constant" of order  $(R_T - R_S)$ . Fisher\* uses the two-dimensional expression

$$|q_s| = |\kappa_s| \quad (3D-2)$$

so that the exponential decay factor can be written as

$$|\kappa_s| (k_0 r_0) (\bar{y}/r_0), \quad (3D-3)$$

where  $\bar{y}$ , given by,

$$\bar{y}/r_0 = h_0/(k_0 r_0) \quad (3D-4)$$

is the effective depth (normalized by the nozzle radius). Fisher\* has demonstrated the usefulness of the effective depth concept and it is therefore of interest to present numerical results inside the cone of silence on that basis. Exact numerical solutions to the Lilley equation can be calculated for the monopole flow factor and used to infer effective depth values through an approximate expression of the type employed by Fisher\*. In principle this exercise should have been carried out with the quadrupole flow factor but the corresponding effective depth expressions were not derived until after this work had been initiated. Those new quadrupole flow factor expressions and corresponding effective depth calculations will be described in future reports.

Summation of Equation (3-68) over the azimuthal mode number  $n$  gives the monopole flow factor, in the high frequency limit, for radiation into the cone of silence. The infinite sum

$$F_m(v) = \sum_{n=-\infty}^{+\infty} c_n(v) c_n(v)^* \equiv \sum_{n=0}^{\infty} \epsilon_n c_n(v) c_n(v)^* \quad (3D-5)$$

$$(\epsilon_0 = 1; \epsilon_n = 2, n \neq 0)$$

\*M. J. Fisher, 1974, personal communication.

may be replaced by<sup>\*94</sup>

$$2 \int_0^\infty c_n^{(v)} c_n^{(v)*} dn \quad (3D-6)$$

the error being of order

$$d|c_n^{(v)}|^2/dn|_{n=0} \quad (3D-7)$$

which, from numerical results, appears to be extremely small, if not zero. When the approximation (3D-1) is substituted into Equation (3-68), with the restriction that  $h_0$  be independent of  $n$ , the integration (3D-6) yields

$$F_m^{(v)} \doteq \frac{D_s^{2v-6}}{\pi} \left\{ \frac{\bar{\rho}_s}{\rho_o} D_s^2 \right\} K_0(2\sigma_o) \quad (3D-8)$$

where  $K_0$  is the modified Bessel function of order zero and where

$$\sigma_o = h_0 |k_s|^2 + 1/4R_s^2|^{\frac{1}{2}}. \quad (3D-9)$$

If  $2\sigma_o$  is sufficiently large, the asymptotic expression for  $K_0$  may be used

$$K_0(2\sigma_o) \rightarrow \sqrt{\frac{\pi}{4\sigma_o}} e^{-2\sigma_o} \quad (3D-10)$$

and to a good approximation

$$\sigma_o \doteq h_0 |k_s| = (k_o r_o) |k_s| (\bar{y}/r_o) \quad (3D-11)$$

Thus, the exponential decay feature reappears via Equation (3D-10), containing the normalized effective depth parameter  $\bar{y}/r_o$ . From Equations (3D-8) and (3D-10) the flow factor expression is, approximately,

$$F_m^{(v)} \doteq \frac{D_s^{2v-6}}{2\pi^{\frac{1}{2}}} \left\{ \frac{\bar{\rho}_s}{\rho_o} D_s^2 \right\} \frac{e^{-2\sigma_o}}{\sigma_o^{\frac{1}{2}}}; \quad (3D-12)$$

the exact computed values of  $F_m^{(v)}$  can be used to calculate effective  $\sigma_o$  values from Equation (3D-12) (by iteration); effective depths,  $\bar{y}/r_o$ , follow from Equation (3D-11). A useful result from these calculations would be a simple relation between the effective depth and some actual depth that can be easily determined, i.e. without recourse to Lilley equation solutions. With

<sup>\*</sup>Abramowitz and Stegun, p. 376.

the effective depth results given below the actual depth  $(R_{T_K} - R_s)/k_{oro}$  is shown for comparison, where  $R_{T_K}$  is the transition point of

$$\kappa(R_{T_K}) = 0$$

or

$$\frac{U(R_{T_K})}{U_J} = \left( \frac{U_J}{c_0} \right)^{-1} \left\{ \frac{1}{\cos\theta_0} - 1 \right\}$$

As in Appendix 3C the source emission angle,  $\theta_s$ , is held constant and the effective/actual depth results are displayed as a function of  $U_J/c_0$  (here only the nominal four diameter profile is used where  $\delta/r_0 = 1.05$  and  $U_i = U_J$ ). The Strouhal number,  $S_s$ , is held constant at a value of unity, which is a realistic value for the flow profile used and should yield a flow factor behavior similar to that of the high frequency analytic limit, if the results of Appendix 3C (outside the cone of silence) can be extrapolated to inside the cone of silence. Figures 3D.1, 3D.2, and 3D.3 refer to source emission angle cosines  $\cos\theta_s = 1.18$ , 1.42, and 1.82, respectively. Clearly the effective and actual depths are of similar order for all three angles, while in Figure 3D.2 the two depths are virtually identical over the whole Mach number range. However, the other results in Figures 3D.1 and 3D.3 indicate that the agreement in Figure 3D.2 could be fortuitous. It could be a "cross-over" condition since in Figure 3D.1 the effective depths are larger than the actual depths while in Figure 3D.3 the situation is almost exactly reversed.

Further results are now required, particularly further inside the cone of silence, to establish the relation(s) between effective and actual depths and to expose important new effects that may occur at and near the radiation Mach angle.

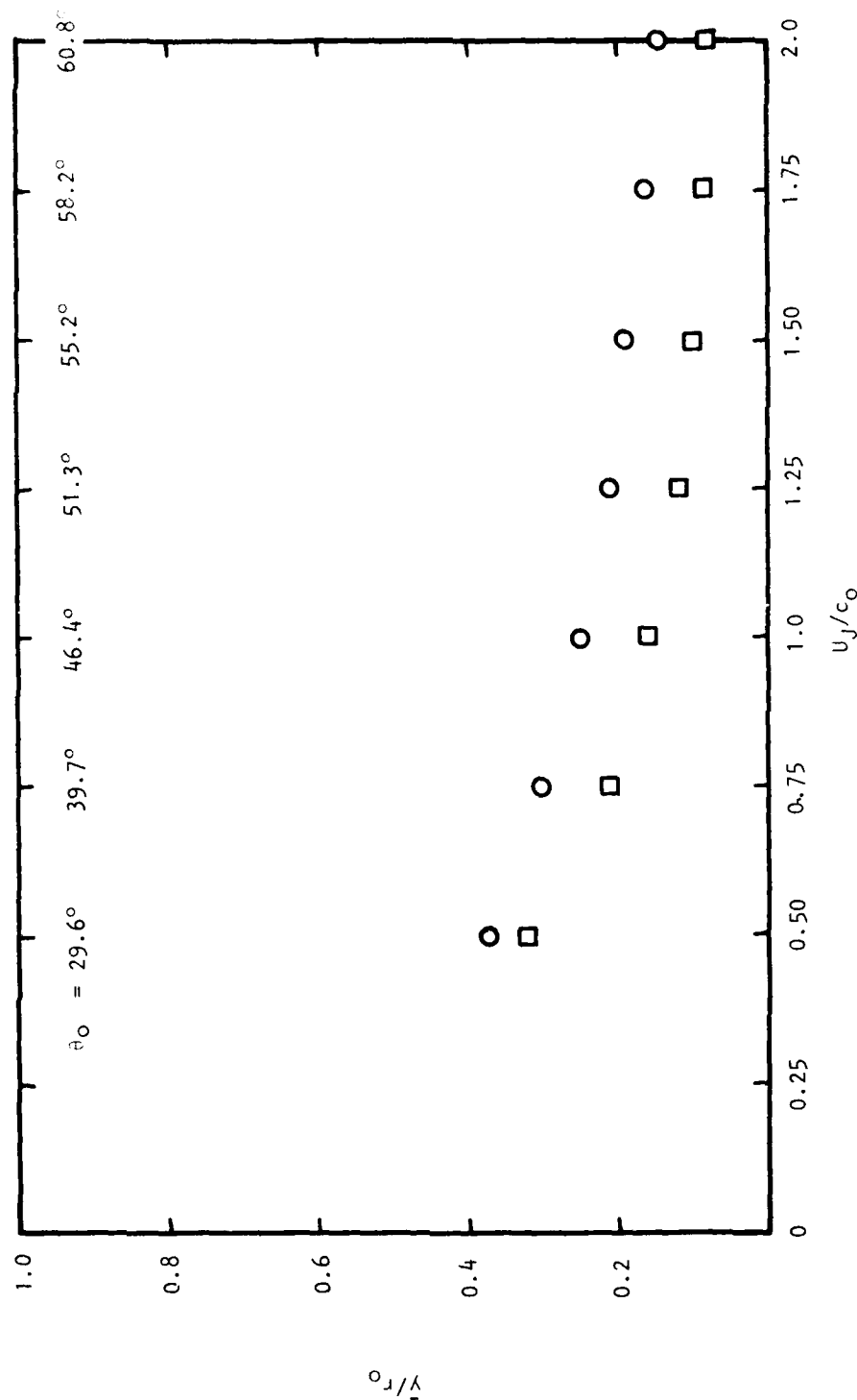


Figure 30.1 Effective and Actual Depth Mach Number Dependence for  $\cos\theta_s = 1.18$ ;  $s_s = 1.0$ ;  $\delta/r_0 = 1.05$ ,  $\phi_s = 0.6$ . Code:  $\circ$  Lilliey Equation - High Frequency Solution Effective Depth;  $\square$  Actual Depth re:  $\kappa$  Transition Point.

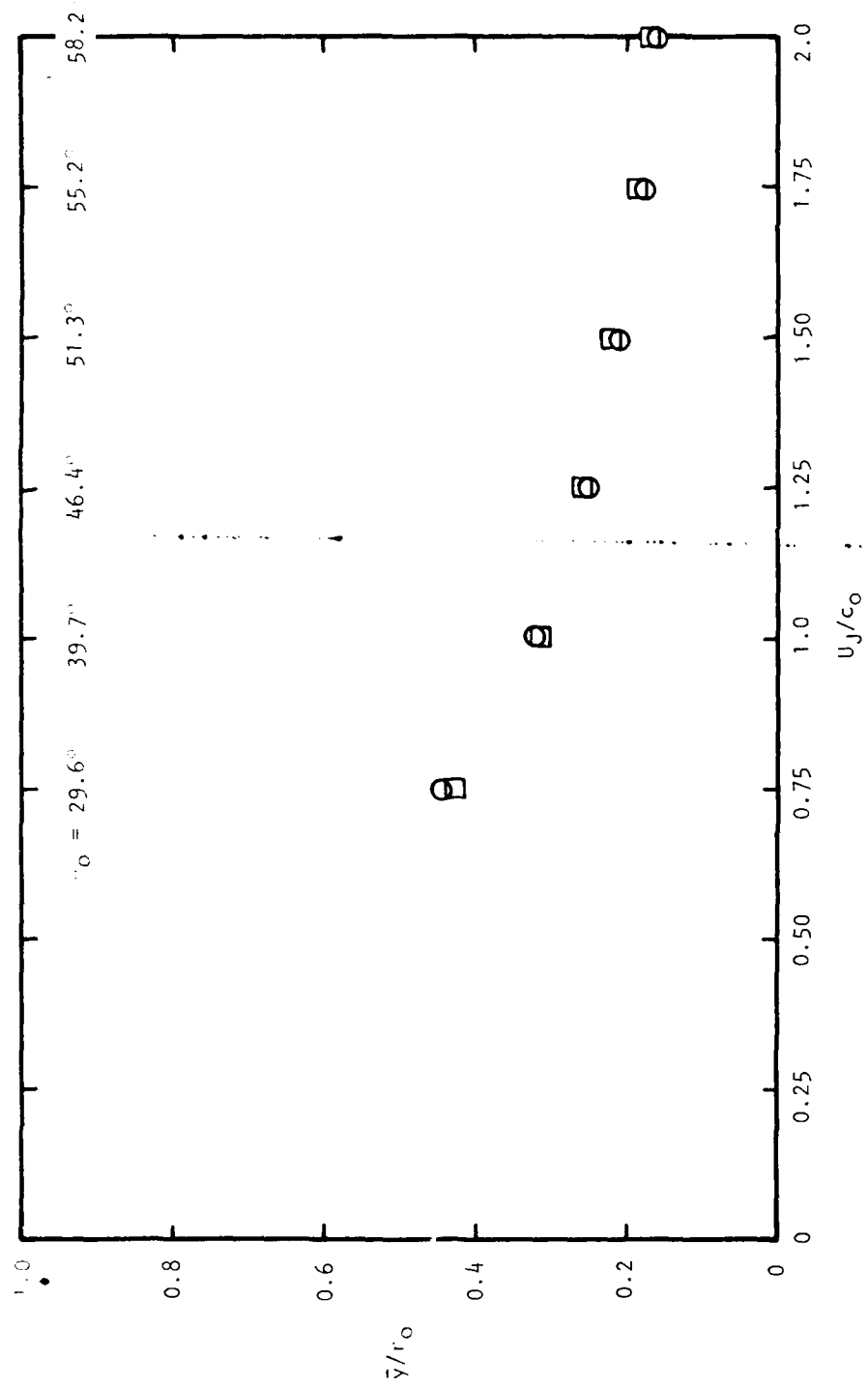


Figure 3D.2 Effective and Actual Depth Mach Number Dependence for  $\cos\theta_0 = 1.42$ ,  
 $S_s = 1.0$ ,  $\delta/r_0 = 1.05$ ,  $\psi_s = 0.6$ . Code:  $\circ$  Lillie Equation – High Frequency Solution Effective Depth;  $\square$  Actual Depth re: Transition Point.

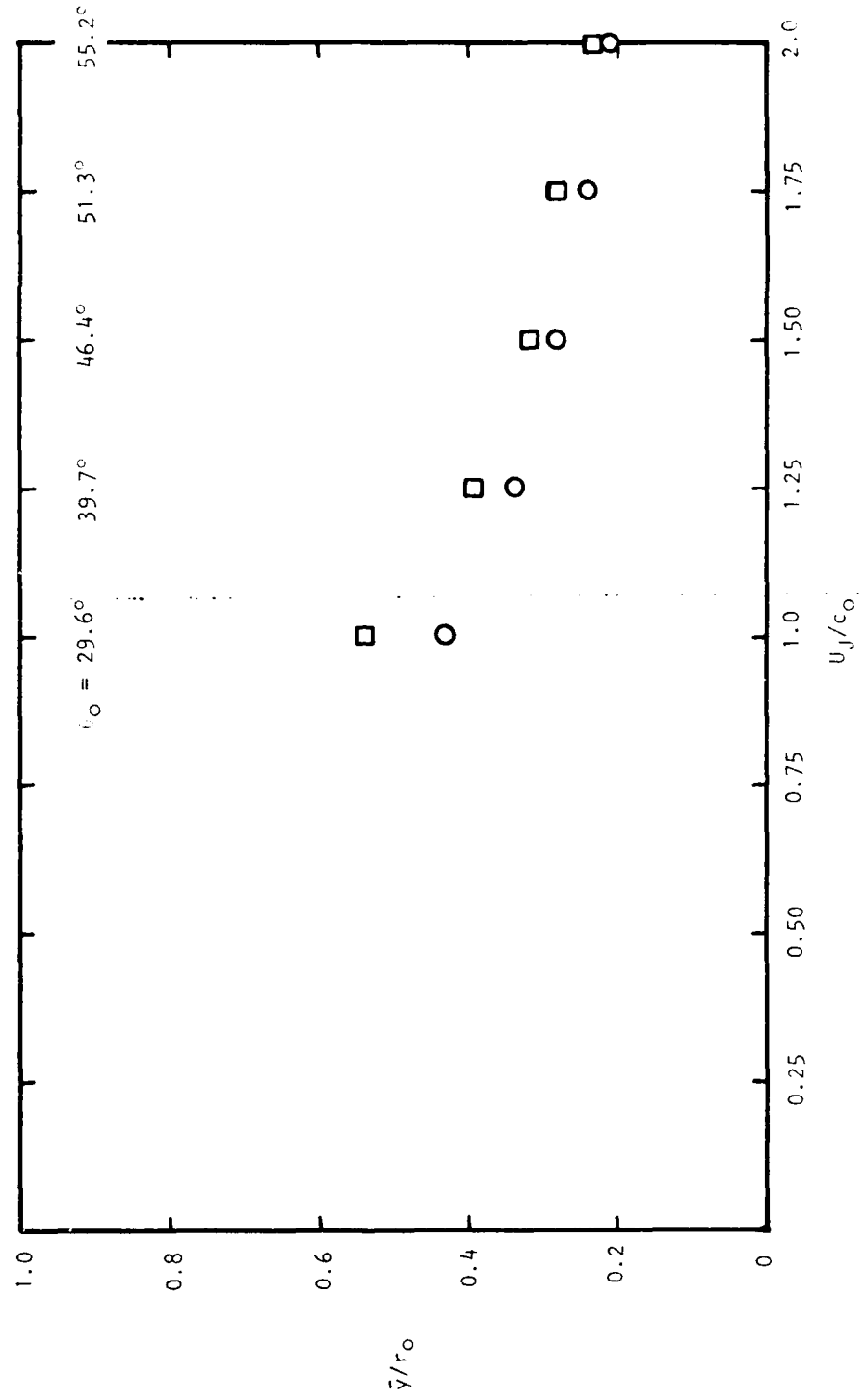


Figure 3D.3 Effective and Actual Depth Mach Number Dependence for  $\cos \varsigma = 1.82$ ,  
 $S_s = 1.0$ ,  $r_0 = 1.05$ ,  $\psi_s = 0.6$ . Code:  $\circ$  Lille Equation — High  
 Frequency Solution Effective Depth;  $\square$  Actual Depth re:  $\circ$   
 Transition Point.

## APPENDIX 3E

THE INFLUENCE OF TEMPERATURE ON JET NOISE AT  
90° TO THE JET AXIS: A COMPARISON BETWEEN  
MEASURED DATA AND A MODEL BASED ON THE  
UNSTEADY DENSITY SCATTERING, DIPOLE SOURCE

## INTRODUCTION

The influence of temperature on shock-free jet noise at  $90^\circ$  to the jet axis has been described in detail by Tanna *et al*<sup>13</sup> using measurements taken in the Lockheed-Georgia anechoic facility<sup>7</sup>. Tanna *et al*<sup>14</sup> analyzed the measured data on the basis of a Lighthill type analogy proposed by Lush<sup>8</sup> and derived scaling laws for the noise spectrum variation with mean jet velocity and temperature ratio. That work certainly provides an adequate basis for hot jet noise prediction, although it needs to be tested for parameter values that fall outside the range covered in the analysis.

One of the aims of the present work is to improve our understanding and to extend jet noise modeling techniques beyond the Lighthill stage, in particular, to incorporate flow-acoustic interactions with the aid of the Lilley equation. Progress in this direction, for nonisothermal jets, beyond that described in paragraph 3.3.1 of the main text, is described here; the theoretical framework is the modified Lilley equation given by Equations (3-1) and (3-4).

## DISCUSSION

The new dipole source term [in Equation (3-4)] arises through scattering of the turbulent pressure fluctuations by turbulent fluctuations in the specific volume at constant pressure. The working hypothesis is that when this source is used in conjunction with the usual quadrupole source (the result of turbulent velocity or displacement fluctuations) the resulting model will reproduce the major trends observed in practice. The hypothesis is tested here by direct comparisons with measurements taken at a true radiation angle of  $90^\circ$  to the jet axis (where mean velocity-acoustic interactions are absent). A basic assumption in this combined source model is that the turbulent velocity/displacement fluctuations are *temperature independent*. In the model the temperature effects on acoustic radiation arise in two ways, first through the dipole source strength: both the specific volume fluctuations at constant pressure and the turbulent pressure fluctuations can be temperature dependent. Second, through the mean temperature-acoustic interactions that occur as sound is emitted and propagates away from the quadrupole and dipole source regions within the flow. The dipole strength dependence on the fluctuating or mean temperature is not assumed; instead, it is obtained as one of the results of the comparison between measurement and model calculations given below. The mean temperature-acoustic interactions are calculated directly from solutions to the Lilley equation, expressed in terms of flow factor values [ $F(\cdot)$ ] as in the main text. These interactions include the mean density gradient scattering effects discussed in paragraph 3.3.1 of the main text.

## THE THEORETICAL MODEL

The far-field intensity,  $I$ , radiated by the SIPQ source at constant modified Strouhal number,  $S_m$ , takes the form

$$I(\omega, T_J/T_O) \propto F^{(v)}(\omega, T_J/T_O) D_m^{-(2v+3)} (U_J/c_O)^8 \quad (3E-1)$$

where  $\omega$  is given by

$$\omega r_O/c_O = \kappa S_m (U_J/c_O)/D_m \quad (3E-2)$$

and  $D_m$  is defined by Equation (3-51). Similarly, the statistically-isotropic point (SIPD) far-field intensity is given by (quantities distinguished by subscript d)

$$I_d(\omega, T_J/T_O) \propto F_d^{(v)}(\omega, T_J/T_O) D_m^{-(2v+1)} (U_J/c_O)^6 \\ \times \Omega(S_m, T_J/T_O) \quad (3E-3)$$

The observed velocity exponents may differ from those given in Equations (3E-2) and (3E-3); if the reason is a diminishing turbulence intensity the above exponents 8, 6 may be replaced by  $\ell$ ,  $\ell-2$ , and the following analysis is unaffected. The main assumption then is that the turbulent pressure fluctuations scale on the mean velocity in the same way as the square of the turbulent velocity fluctuations.

The dipole coefficient  $\Omega$  in Equation (3E-3) represents, at a given Strouhal number, the influence of temperature on the dipole source strength (through specific volume and pressure fluctuations) and is assumed to be negligibly small at the experimental isothermal condition  $T_J = T_O$ . It also incorporates the ratio of the dipole and quadrupole source strengths (apart from the mean velocity and mean temperature dependencies) which is assumed to depend only upon Strouhal number.

If the two sources are assumed to be independent then, the ratio, A, of the far-field intensity to that at isothermal conditions predicted by the model (at constant  $S_m$ ) follows from Equations (3E-1), (3E-3), and the constraint on  $\Omega$  that it be zero at the isothermal condition:

$$A = \frac{F(\omega, T_J/T_O) + F_d(\omega, T_J/T_O) D_m^2 (U_J/c_O)^{-2} (S_m, T_J/T_O)}{F(\omega, T_J/T_O = 1)} \quad (3E-4)$$

or

$$A = B + C D_m^2 (U_J/c_O)^{-2} \Omega(S_m, T_J/T_O) \text{ say}$$

where

$$B = F(\omega, T_J/T_O)/F(\omega, T_J/T_O = 1) \quad (3E-5)$$

$$C = F_d(\omega, T_J/T_O)/F(\omega, T_J/T_O = 1) \quad (3E-6)$$

The source type distinction, indicated by superscript (v), can be dropped at this stage since the flow factors are independent of v at  $\theta_0 = 90^\circ$  and so is the ratio A in Equation (3E-4)

#### COMPARISONS WITH MEASURED DATA

Values of the intensity ratio A in dB ( $\Delta$ ) have been derived from the Lockheed measured data at a true radiation angle of  $\theta_0 = 90^\circ$  by correcting for estimated source location effects. The  $\Delta$  values are shown as a function of  $T_j/T_0$  in Figures (3E-1) through (3E-4) for nominal Mach number values of  $U_j/c_0 = 0.5, 0.9, 1.47$  and at Strouhal numbers  $S_m = 0.1, 0.3, 1.0$  and  $3.0$ . (For reference purposes the density exponent lines  $C = -1, 1, 2$  and  $3$  are drawn in Figures 3E.1 and 3E.4, i.e.  $A \propto \rho_j^C = T_j^{-C}$ .)

The corresponding calculated flow factor ratios B and C, in dB, are shown in the same figures. They are not meant to agree with the measured  $\Delta$  values although where  $10 \log_{10} B$  does so, for example in Figure 3E.3c, it follows that the second term in the theoretical expression for A must be negligible compared with the first (even though its coefficient, C, is not).

From these measurement-based  $\Delta$  or A values and the calculated values of B, C and  $D_m$  a value of  $\Omega$  has been calculated at each "test point;" the results for each Strouhal number are shown in Figures 3E.5(a) through 3E.5(d) allowing a comparison to be made between values from each Mach number condition at a given temperature ratio. The range of each result, indicated by a vertical line, corresponds to an assumed  $\pm 1/2$  dB error in the measured data.

#### CONCLUSIONS

If the dipole coefficient,  $\Omega$ , is independent of Mach number,  $U_j/c_0$ , at a given temperature ratio, then the dipole order of the additional nonisothermal source is confirmed by the measured data. This feature is exhibited by the results at the highest temperature ratio for  $S_m = 0.3$  and  $1.0$  in Figures 3E.5(b) and 3E.5(c). At the lower temperature ratio ( $T_j/T_0 \approx 2.2$ ) only the subsonic  $\Omega$  values are independent of  $U_j/c_0$ . The cold temperature ratio ( $\approx 0.5$  only occurs when  $U_j/c_0 = 1.5$ ; there the  $\Omega$  values are not unrealistic at  $S_m = 0.1$  and  $0.3$  in Figures 3E.5(a) and 3E.5(b), but the large negative values for  $S_m = 1.0$  and  $3.0$  (the latter is not shown) in Figures 3E.5(c) and 3E.5(d) indicate that the model in its present simple form breaks down at these conditions.

In general, though,  $\Omega$  is positive and the existence of an additional source in nonisothermal jets is confirmed even when mean density gradient scattering effects (automatically included in the two flow factors F,  $F_d$ ) are taken properly into account. The dipole order of the additional source at almost all subsonic velocity test points is also substantially confirmed; the discrepancies at the supersonic Mach number may indicate that the turbulence structure is temperature dependent, contrary to one of the basic assumptions.

Further comparisons between measured data and predictions from the present model are given in Appendix 3G.

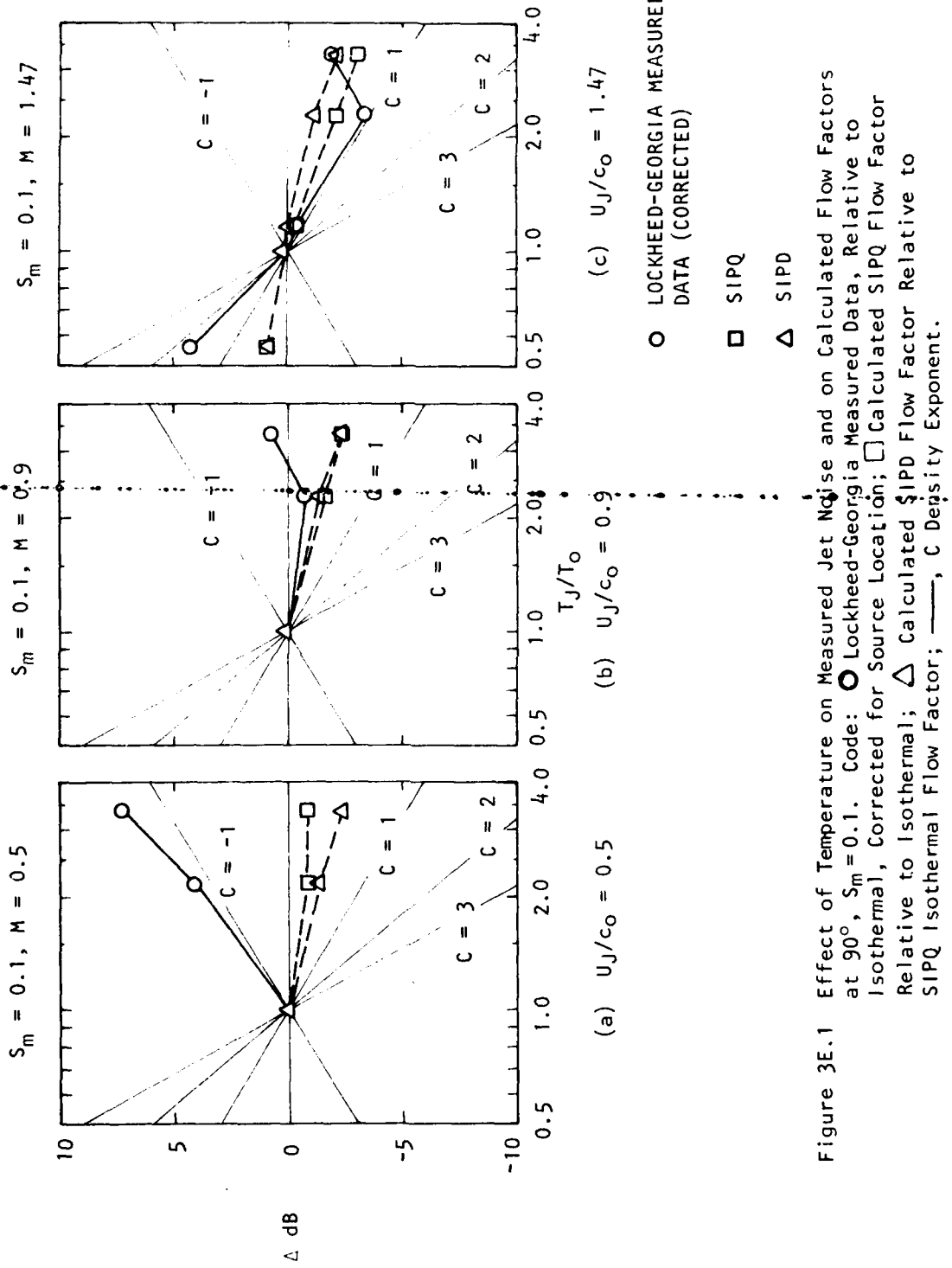


Figure 3E.1 Effect of Temperature on Measured Jet Noise and on Calculated Flow Factors at  $90^\circ$ ,  $S_m = 0.1$ . Code: ○ Lockheed-Georgia Measured Data, Relative to Isothermal, Corrected for Source Location; □ Calculated SIPQ Flow Factor Relative to Isothermal; △ Calculated SIPD Flow Factor Relative to SIPQ Isothermal; —,  $C$  Density Exponent.

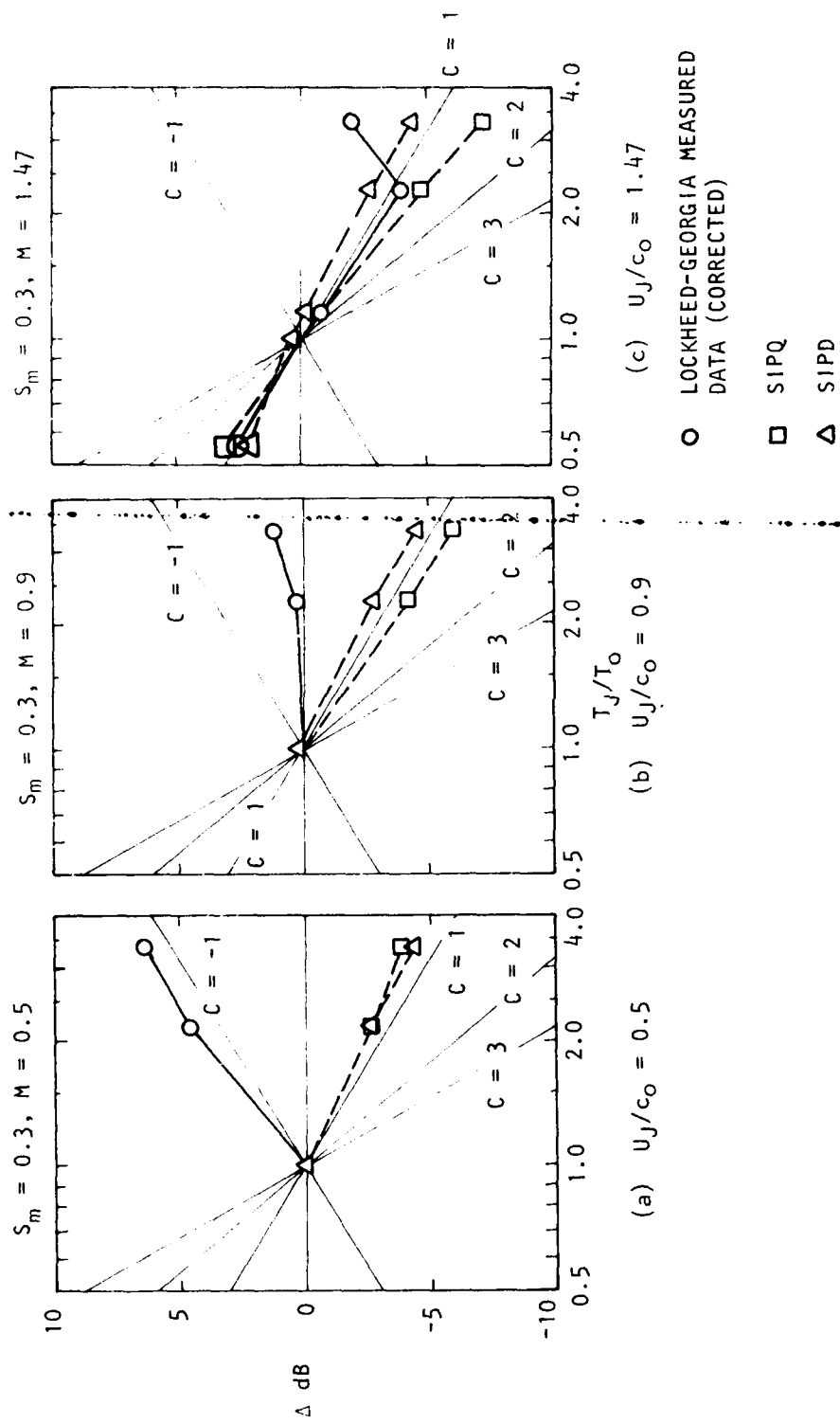


Figure 3E.2 Effect of Temperature on Measured Jet Noise and on Calculated Flow Factors at  $90^\circ$ ,  $S_m = 0.3$ . Code:  $\circ$  Lockheed-Georgia Measured Data, Relative to Isothermal, Corrected for Source Location;  $\square$  Calculated SIPQ Flow Factor Relative to Isothermal;  $\triangle$  Calculated SIPD Flow Factor Relative to SIPQ Isothermal Flow Factor; —,  $C$  Density Exponent.

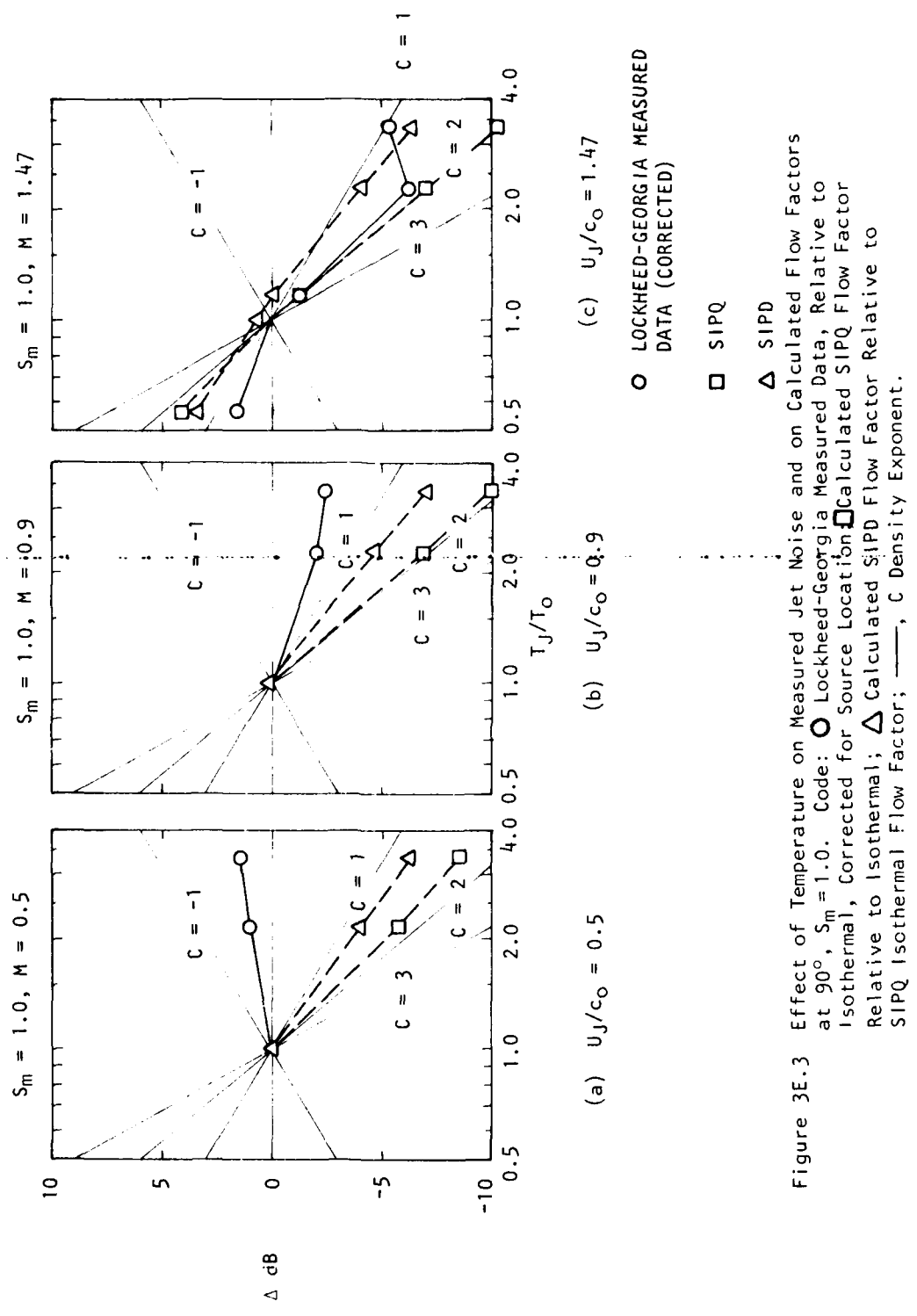


Figure 3E.3 Effect of Temperature on Measured Jet Noise and on Calculated Flow Factors at  $90^\circ$ ,  $S_m = 1.0$ . Code:  $\circ$  Lockheed-Georgia Measured Data, Relative to Isothermal, Corrected for Source Location;  $\square$  Calculated SIPQ Flow Factor Relative to Isothermal;  $\Delta$  Calculated SIPD Flow Factor Relative to SIPQ Isothermal Flow Factor;  $-$ ,  $C$  Density Exponent.

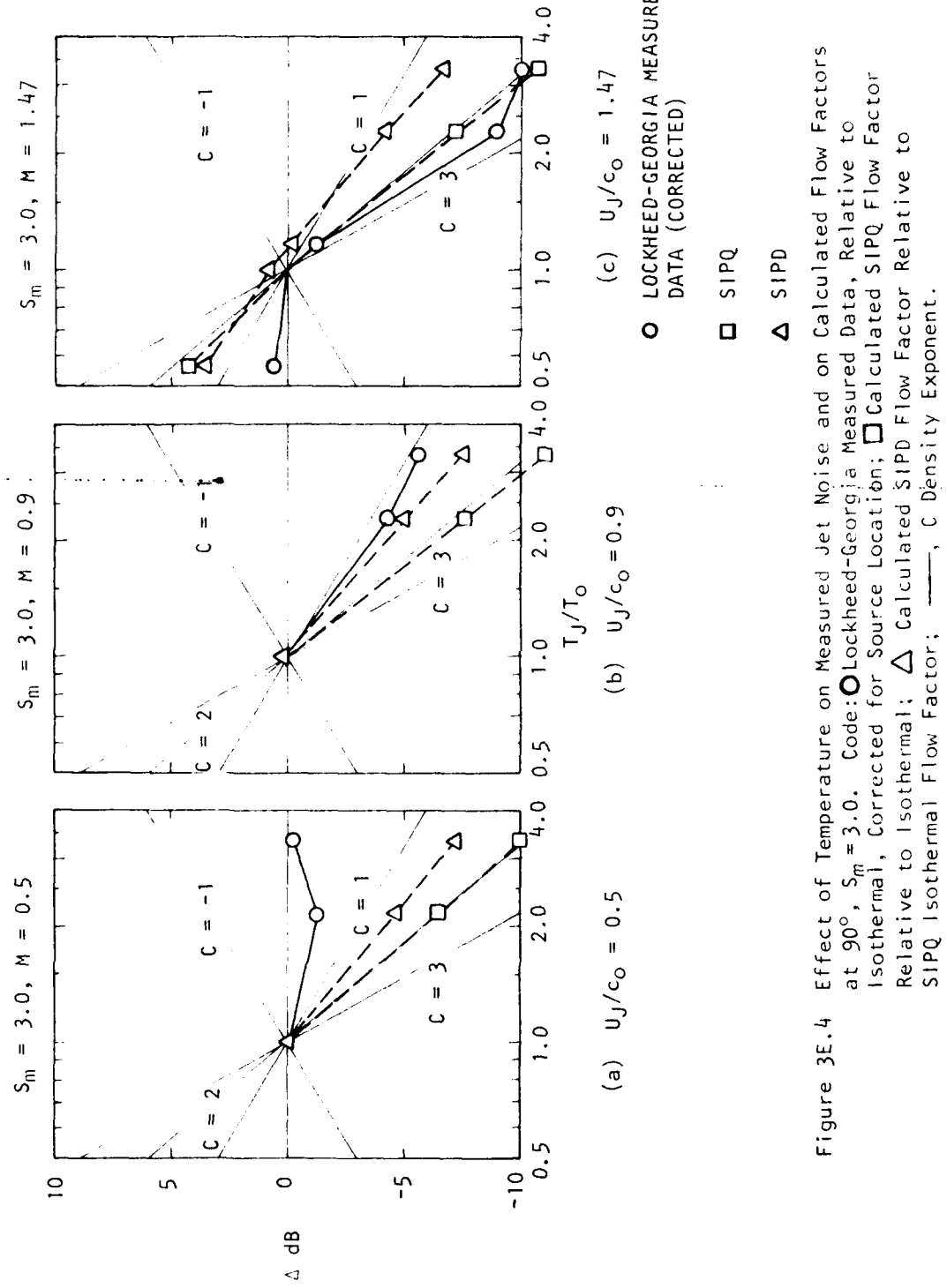


Figure 3E.4 Effect of Temperature on Measured Jet Noise and on Calculated Flow Factors at  $90^\circ$ ,  $S_m = 3.0$ . Code: ○ Lockheed-Georgia Measured Data, Relative to Isothermal, Corrected for Source Location; □ Calculated SIPQ Flow Factor Relative to Isothermal; △ Calculated SIPD Flow Factor Relative to SIPQ Isothermal Flow Factor; ◇ Calculated SIPD Flow Factor Relative to SIPQ Isothermal Flow Factor; —,  $C$  Density Exponent.

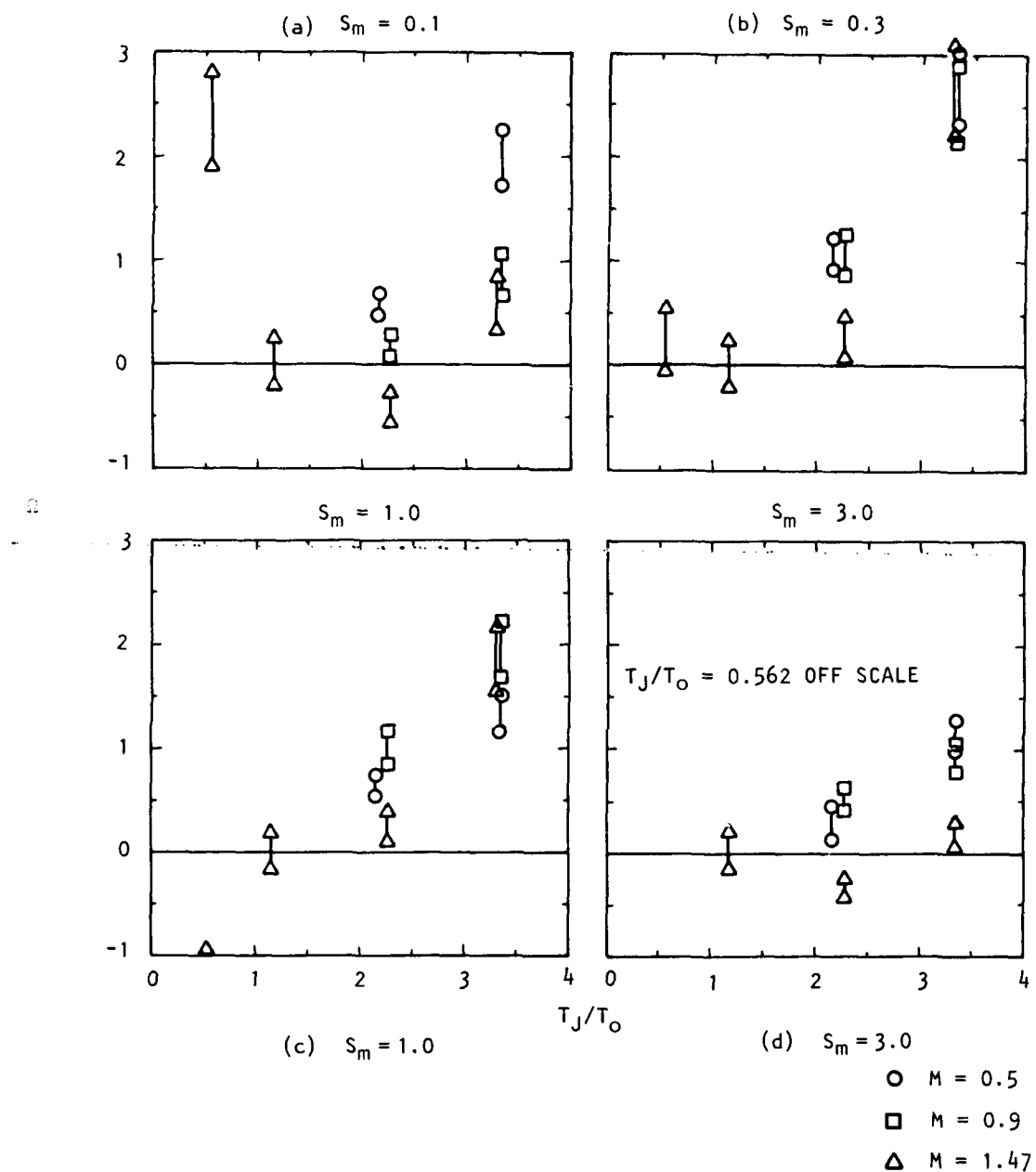


Figure 3E.5 Effect of Temperature on the Dipole Coefficient  $\Omega$ , Derived from Lockheed-Georgia Measured and Calculated Flow Factor, at  $90^\circ$ .  
 Code: ○  $U_J/c_0 = 0.5$ , □  $U_J/c_0 = 0.9$ , △  $U_J/c_0 = 1.47$ .

APPENDIX 3F

ISOTHERMAL JET NOISE DIRECTIVITY:  
DETAILED COMPARISONS WITH THEORY

The comparisons in paragraph 3.3.3 between measured and calculated isothermal jet noise directivities (for  $S_m = 1.0$  and  $3.0$  at  $U_j/c_0 = 0.5$  and  $0.9$ ) are extended here to include the lower Strouhal numbers  $0.1$  and  $0.3$  and the supersonic jet conditions  $U_j/c_0 = 1.33$  and  $1.95$ .

The discrepancies between measured directivities for low Strouhal numbers at subsonic Mach numbers and existing calculation methods based on the Ribner/Ffowcs Williams<sup>11,10</sup> extension of the Lighthill analogy typically are largest at small angles to the jet axis, as noted by Lush<sup>8</sup>. An example is shown in Figure 3F.1. The difference between the Lockheed-Georgia measured data and the  $D_m^{-5}$  directivity law is shown in the lower curve. The small angle differences have been attributed, in the past to the neglect of flow-acoustic interactions. Here, with the new volume displacement quadrupole source model, attention is focused on one particular test condition,  $U_j/c_0 = 0.9$ , for  $S_m = 0.1$ , in order to explore more carefully the possible reasons for the small angle discrepancy.

First, the measured data is corrected for source location effects, as described in reference<sup>15</sup>. The maximum discrepancy is thereby reduced from  $6$  dB to just over  $4$  dB as shown in Figure 3F.2.

Second, the classical  $D_m^{-5}$  law is replaced by the existing theoretical result  $D_m^{-3} F(3)$  as in Figure 3F.3; the convective amplification factor  $D_m^{-9}$  is also shown separately. The flow profile for this Strouhal number is chosen to correspond to a nominal 13 diameter axial station where  $U_i/U_j = 0.5$ . Now the discrepancies are equally large but of opposite sign.

The only remaining unrealistic feature in the theoretical calculation and in the processed data is the eddy convection velocity value of  $0.67 U_j$ . Since the centerline velocity is  $0.5 U_j$ , the source convection velocity exceeds that of the mean flow everywhere at this axial location. When the measured data is reprocessed and the theory recalculated, both with  $U_c = U_i$ , the magnitude of the discrepancies is reduced but the sign changes twice over the given angle range, as shown in Figure 3F.4.

Finally, the same exercise is repeated with  $U_c = 0.67 U_i$  and the results shown in Figure 3F.5. There is now almost perfect agreement between measurement and theory over the range  $135^\circ \geq \theta_0 \geq 60^\circ$  and then for smaller angles the two diverge, the difference reaching a maximum of just under  $9$  dB. The agreement in the forward arc is particularly striking in contrast to the previous comparisons. The calculation method in its present form and the parameter values used cannot be improved in any significant and realistic way. Hence, the comparison as shown in Figure 3F.5 must stand for the present and the reason(s) for the small angle discrepancy must be found elsewhere. Flow-acoustic interactions cannot be responsible for this feature within the present theoretical and physical framework.

To conclude this detailed investigation of one test condition-Strouhal number combination, the comparison is repeated for the volume acceleration SIPQ source in Figure 3F.6. Although the small angle discrepancy is all but eliminated, the degradation elsewhere is unacceptable. For reference purposes the uncorrected and corrected measured data are shown for comparison in Figure 3F.7 and in Figure 3F.8 the old  $D_m^{-5}$  law is shown along side the existing theoretical directivity calculations.

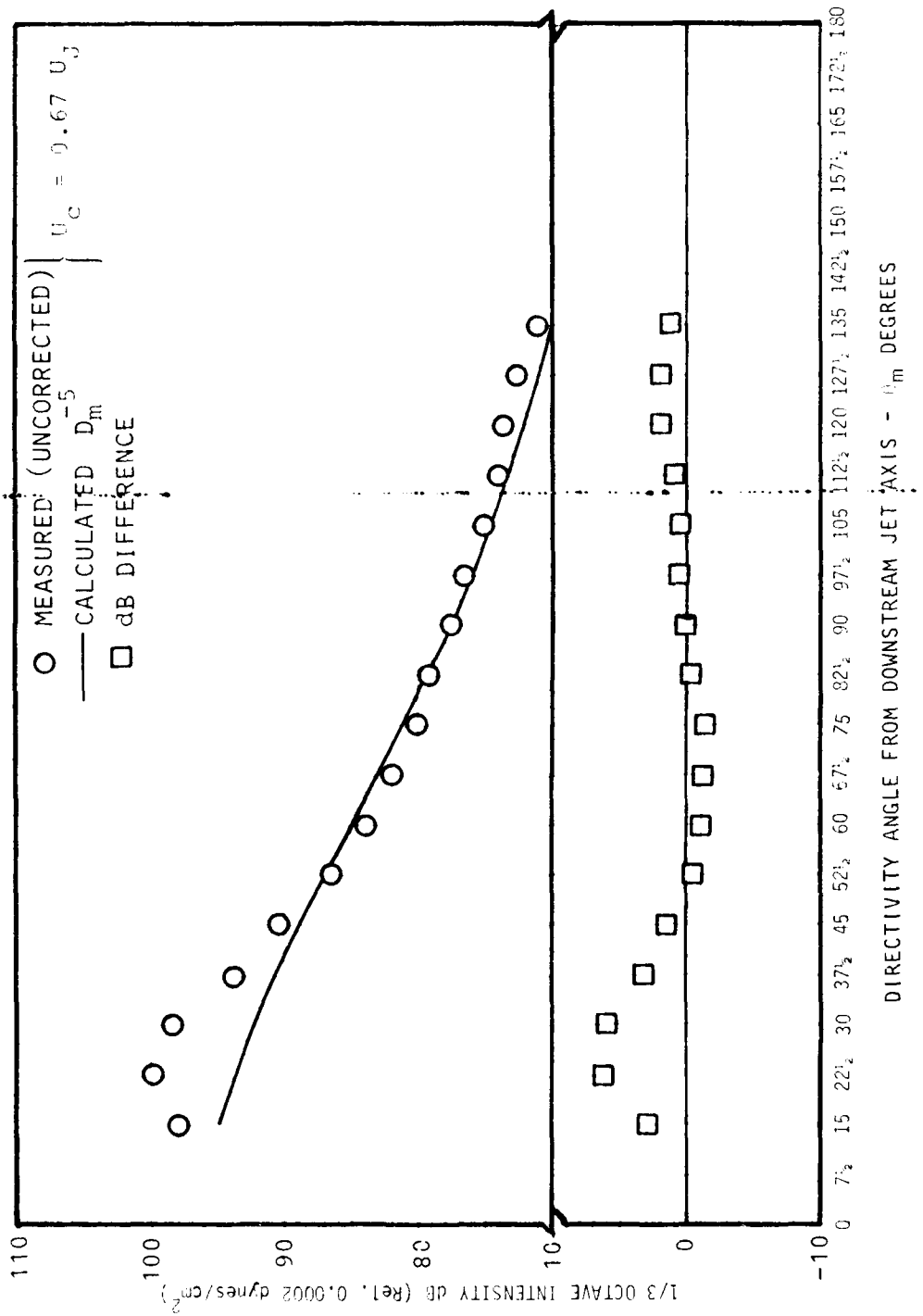


Figure 3F.1 Directivity of Isothermal Jet Noise: Comparison of Theoretical Models with Measured 1/3-Octave Data, for  $S_m = 0.1$ ,  $U_j/c_o = 0.9$

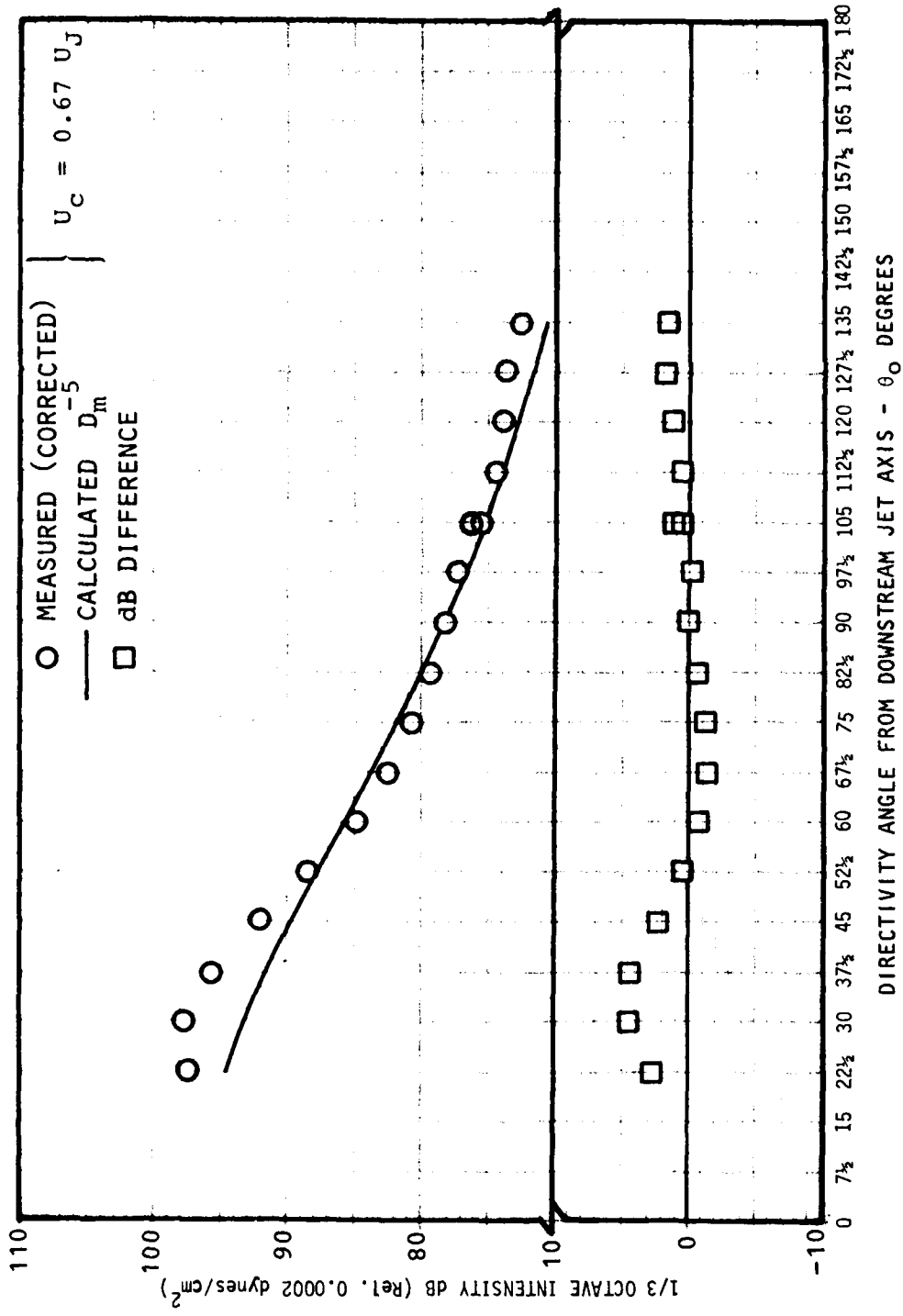


Figure 3F.2 Directivity of Isothermal Jet Noise: Comparison of Theoretical Models with Measured 1/3-Octave Data, for  $S_m = 0.1$ ,  $U_J/c_o = 0.9$

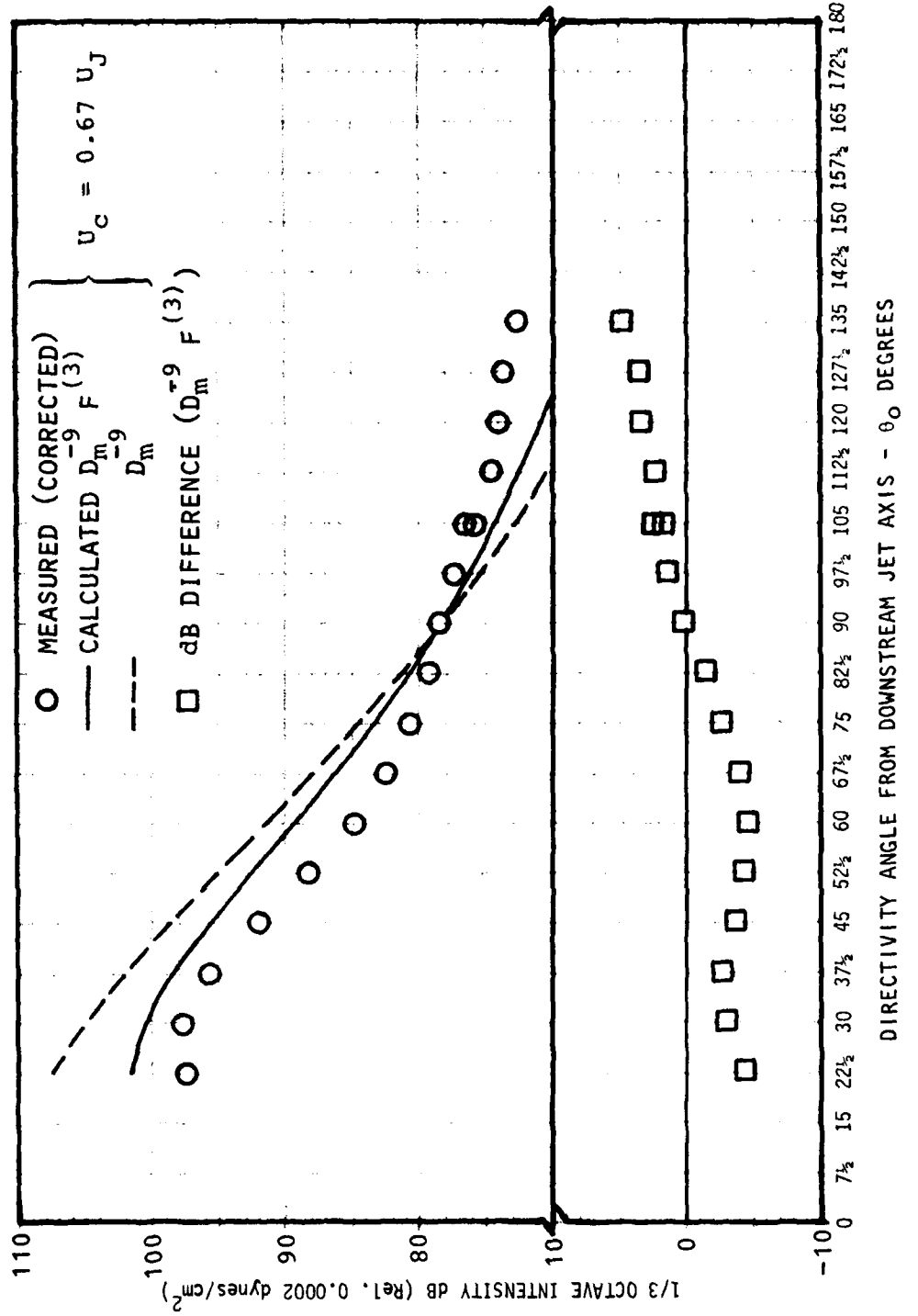


Figure 3F.3 Directivity of Isothermal Jet Noise: Comparison of Theoretical Models with Measured 1/3-Octave Data, for  $S_m = 0.1$ ,  $U_j/c_0 = 0.9$

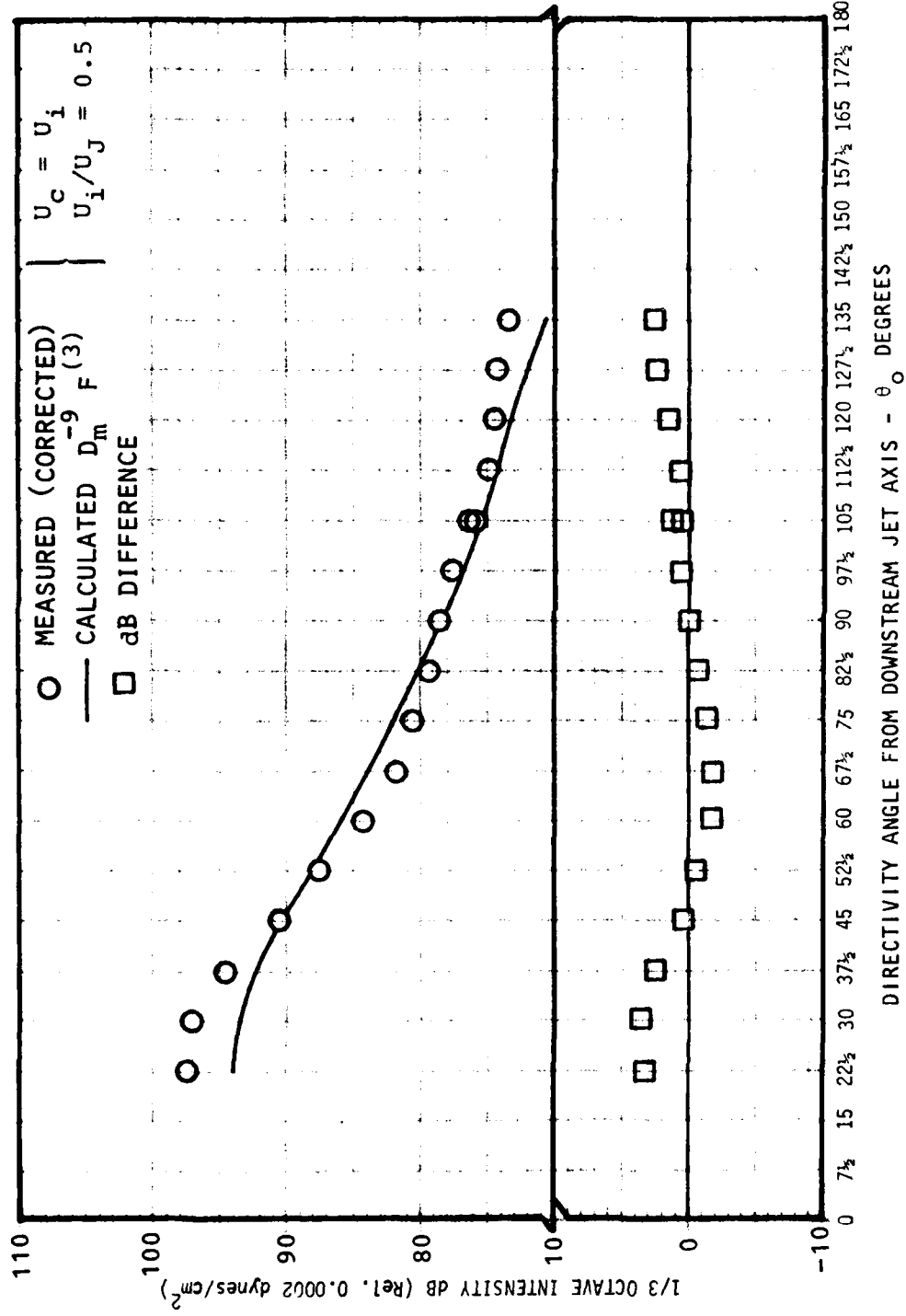


Figure 3F.4 Directivity of Isothermal Jet Noise: Comparison of Theoretical Models with Measured 1/3-Octave Data, for  $S_m = 0.1$ ,  $U_j/c_o = 0.9$

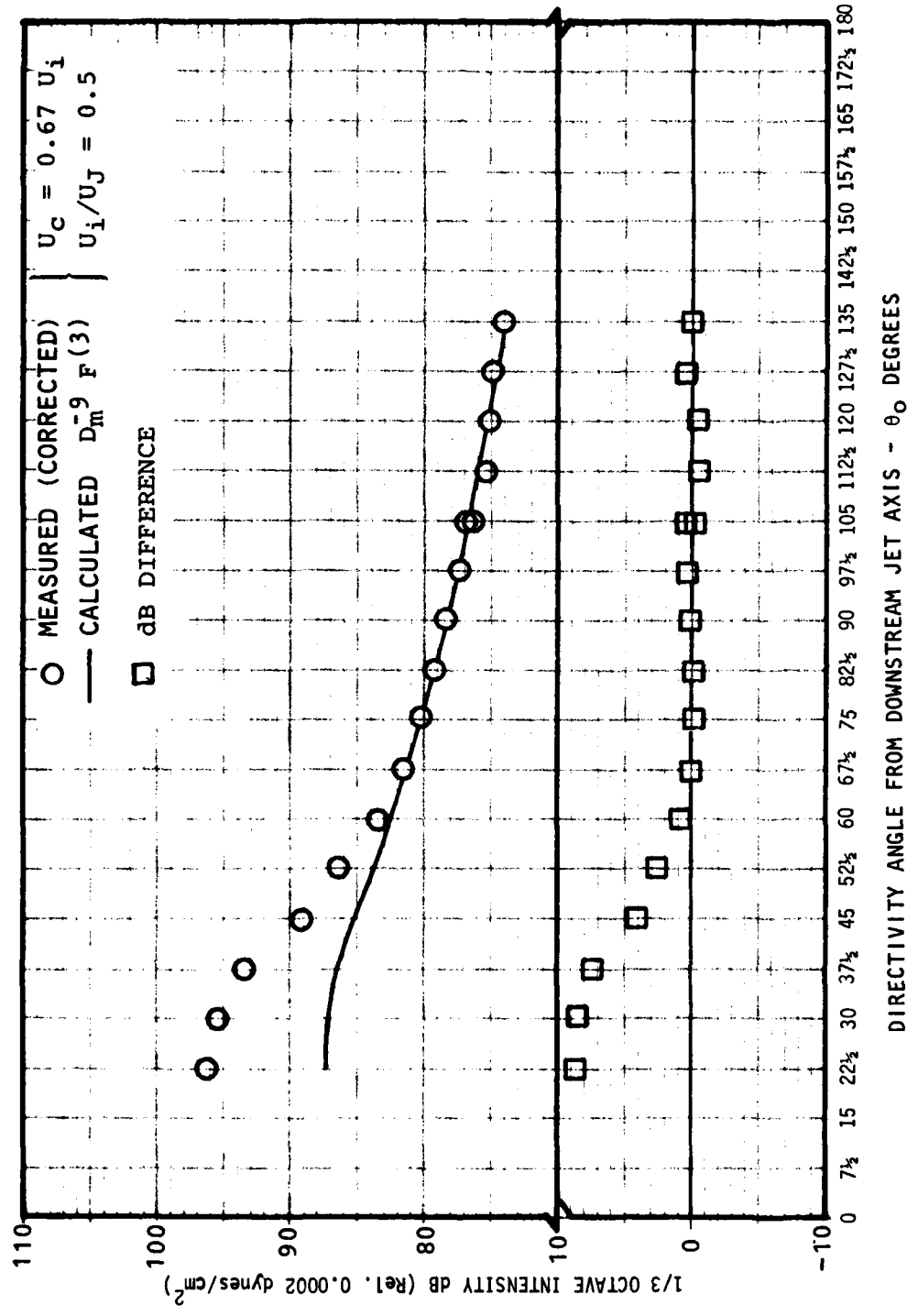


Figure 3F.5 Directivity of Isothermal Jet Noise: Comparison of Theoretical Models with Measured 1/3-Octave Data, for  $S_m = 0.1$ ,  $U_j/U_c = 0.9$

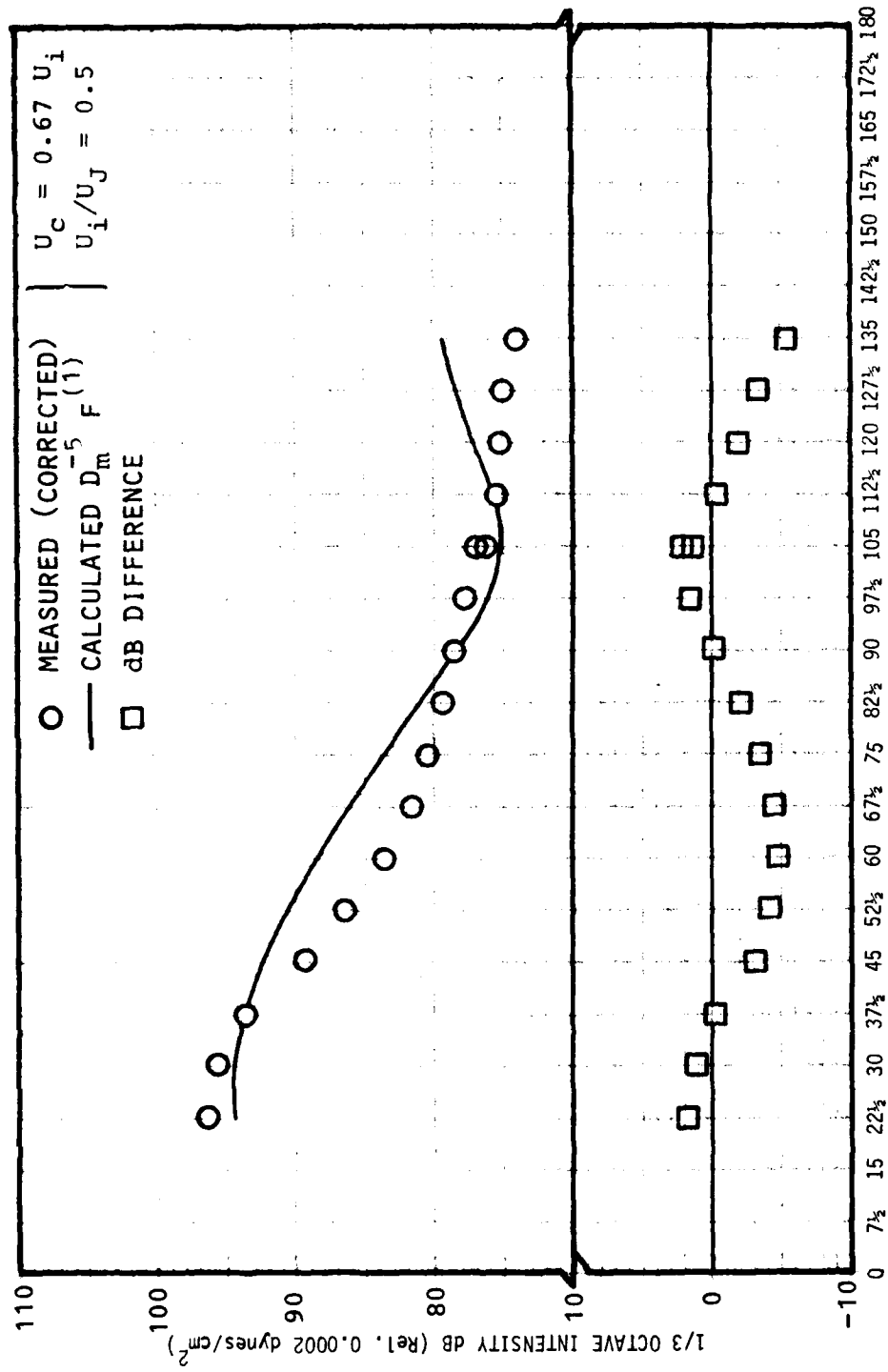


Figure 3F.6 Directivity of Isothermal Jet Noise: Comparison of Theoretical Models with Measured 1/3-Octave Data, for  $S_m = 0.1$ ,  $U_J/c_o = 0.9$

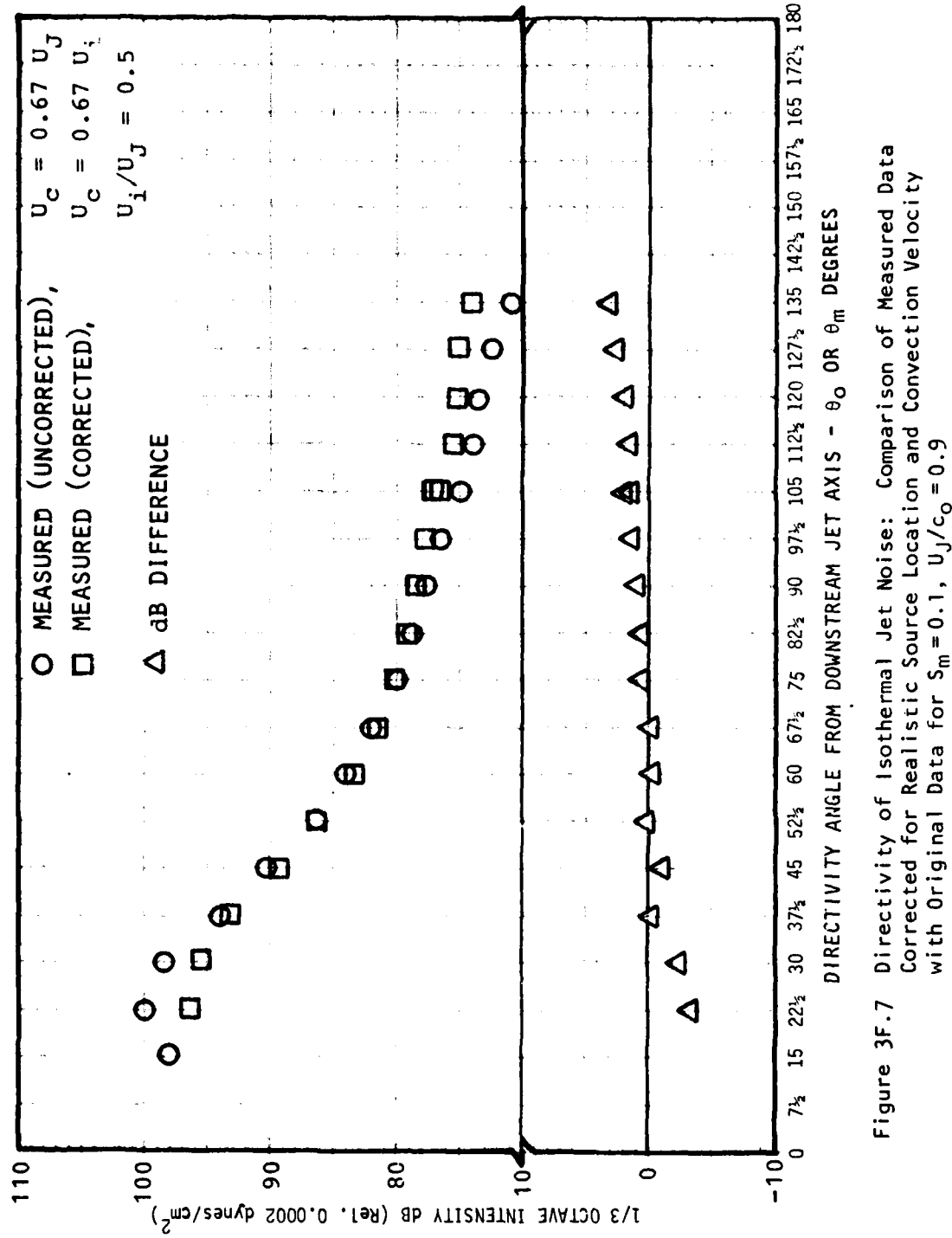


Figure 3F.7 Directivity of Isothermal Jet Noise: Comparison of Measured Data Corrected for Realistic Source Location and Convection Velocity with Original Data for  $S_m = 0.1$ ,  $U_j/c_o = 0.9$

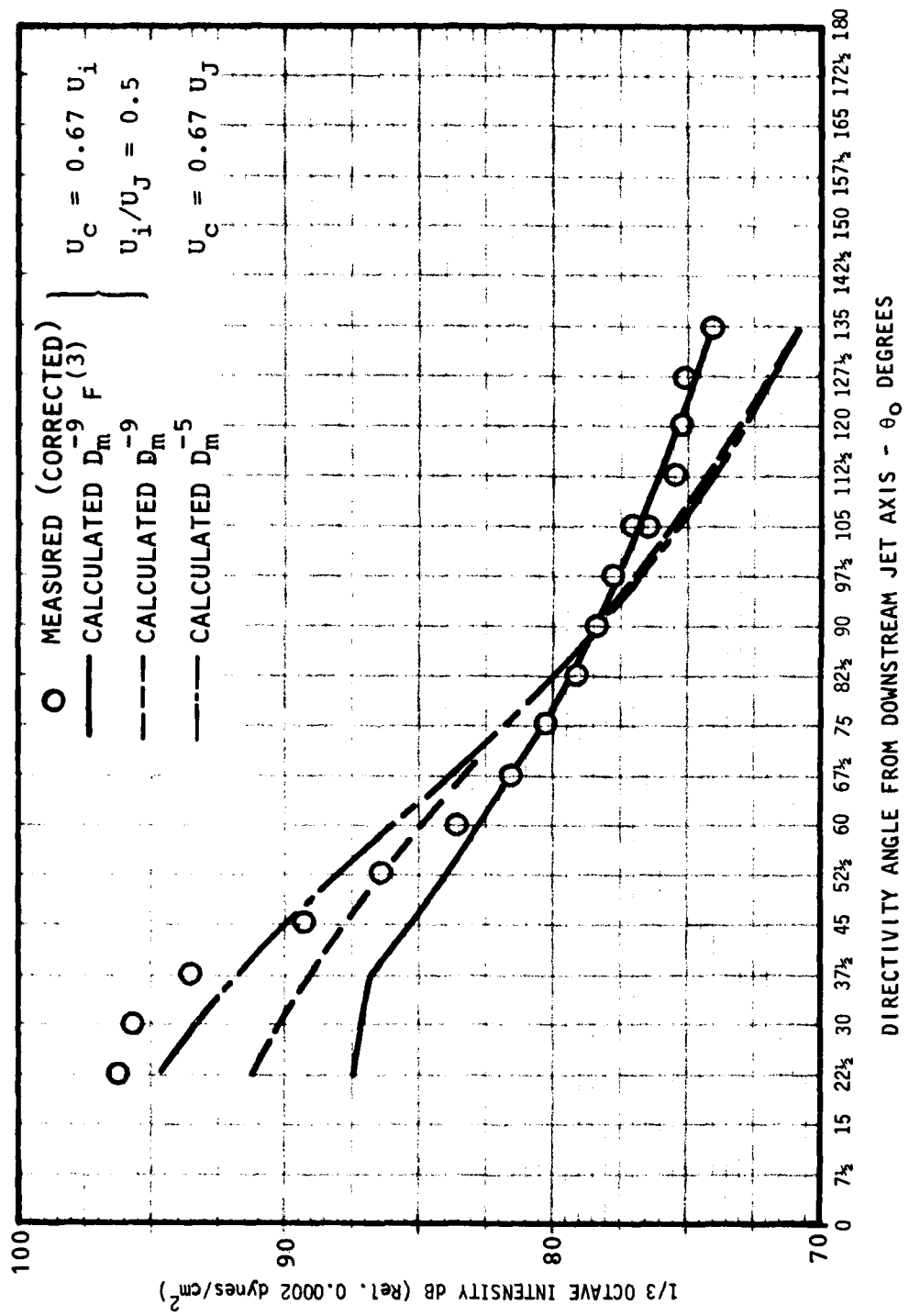


Figure 3F.8 Directivity of Isothermal Jet Noise: Comparison of Theoretical Models with Measured 1/3-Octave Data, for  $S_m = 0.1$ ,  $U_j/c_o = 0.9$

Returning to the small angle discrepancy in order to test potential mechanisms, it is usually necessary to establish the Mach number dependence of the phenomenon. In Figures 3F.9, 3F.10, and 3F.11 the comparison is repeated for  $U_j/c_0 = 0.5$ , 1.33, and 1.95 at the same Strouhal number,  $S_m = 0.1$ . In general the agreement is remarkably good except over the expected range which tends to broaden with increasing Mach number:  $22\frac{1}{2}^\circ \leq \theta_o \leq 40^\circ$  for  $U_j/c_0 = 0.5$ ,  $22\frac{1}{2}^\circ \leq \theta_o \leq 70^\circ$  for  $U_j/c_0 = 1.33$  and  $22\frac{1}{2}^\circ \leq \theta_o \leq 70^\circ$  for  $U_j/c_0 = 1.95$ . The difference between measurement and theory for the four Mach numbers is shown as a function of the cosine of the source emission angle (see Appendix 3C for definition) in Figure 3F.12. If the main reason for the differences is an inherent source directivity (e.g. stronger axial-axial quadrupoles as suggested by Lush<sup>8</sup>), then the data in Figure 3F.12 should exhibit the same dependence on  $\cos\theta_s$ , independent of  $U_j/c_0$ . Here this does not appear to be the case.

When the corrected measurement versus present theory comparison is repeated for a higher Strouhal number of 0.3 as in Figures 3F.13 through 3F.16, some significantly different trends emerge (compared with  $S_m = 0.1$ ). Now the powerful cone of silence effects begin to play a more significant role in the calculated directivity especially at the supersonic conditions and although the discrepancy at small angles may be linked with that at the lower Strouhal number, equally it could be the result of a lack of realism in the present theoretical model. That is, the real radial source distribution has been replaced by one concentrated at a radial point. If the discrepancy had appeared again at the subsonic condition  $U_j/c_0 = 0.9$  for this higher Strouhal number, there would have been reason to believe that the same mechanism is completely responsible. As it is, the agreement at subsonic conditions is rather good and if anything the theory over-predicts the measured level. Hence, the theoretical model needs to be improved before Strouhal number effects can be properly investigated at least in the direction of increasing Strouhal number. Values less than 0.1 have not been investigated as yet.

The main reason for the large low Strouhal number differences between measured isothermal jet noise directivities and calculations based on the Lilley equation is believed to be as follows. Acoustic radiation is generated by the large scale structure, i.e. by the unstable modes of the turbulent jet through an essentially linear process of flow divergence-mode interaction. The unstable modes are described by solutions of the homogeneous Lilley equation. These solutions have not been included within the immediate framework of this investigation but are being investigated separately as described in Section 4. Estimates of the acoustic radiation levels are calculated there and these will be combined with the results from this investigation in due course. When that is done, it is expected that almost all the low Strouhal number differences between theory and experiment will be removed.

At the next Strouhal number,  $S_m = 1.0$ , results in Figures 3F.17 and 3F.18 for the two subsonic Mach numbers are virtually the same as those shown in Figure 3.11 of paragraph 3.3.3. The only difference is the minor correction (at this Strouhal number) to the measured data. For the two supersonic Mach numbers, Figures 3F.19 and 3F.20 are the most extreme examples of how the present source model (radial-point) can yield unrealistic flow factor results inside the cone of silence. Elsewhere though the agreement between measured

and calculated levels remains substantially the same as at lower Strouhal numbers.

At the highest Strouhal number,  $S_m = 3.0$ , complete measured directivity results can be obtained only for subsonic conditions; Figures 3F.21 and 3F.22 repeat Figure 3.12 of section 3.3 except for measured data corrections.

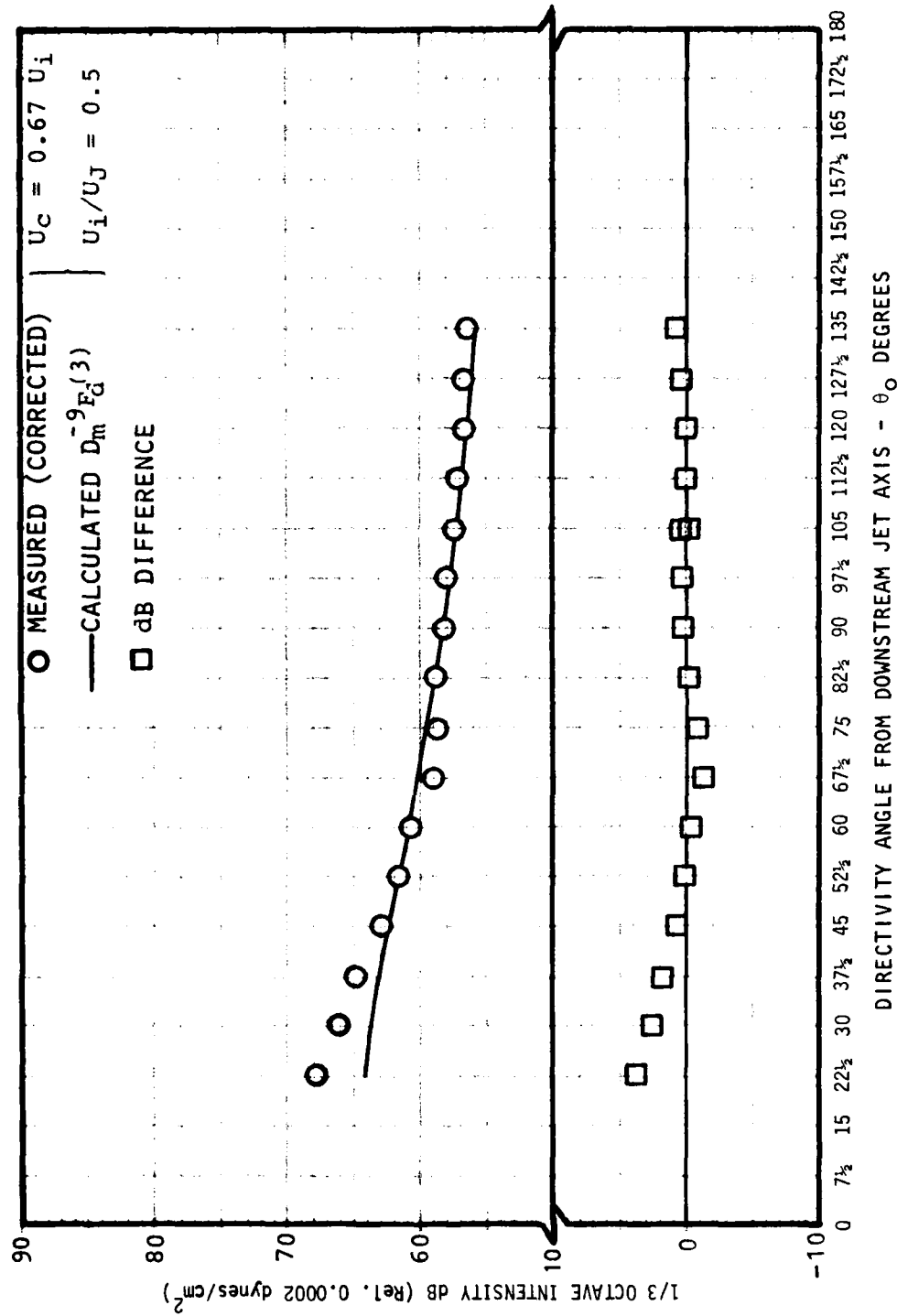


Figure 3F.9 Directivity of Isothermal Jet Noise: Comparison of Theoretical Models with Measured 1/3-Octave Data, for  $S_m = 0.1$ ,  $U_j/c_o = 0.5$

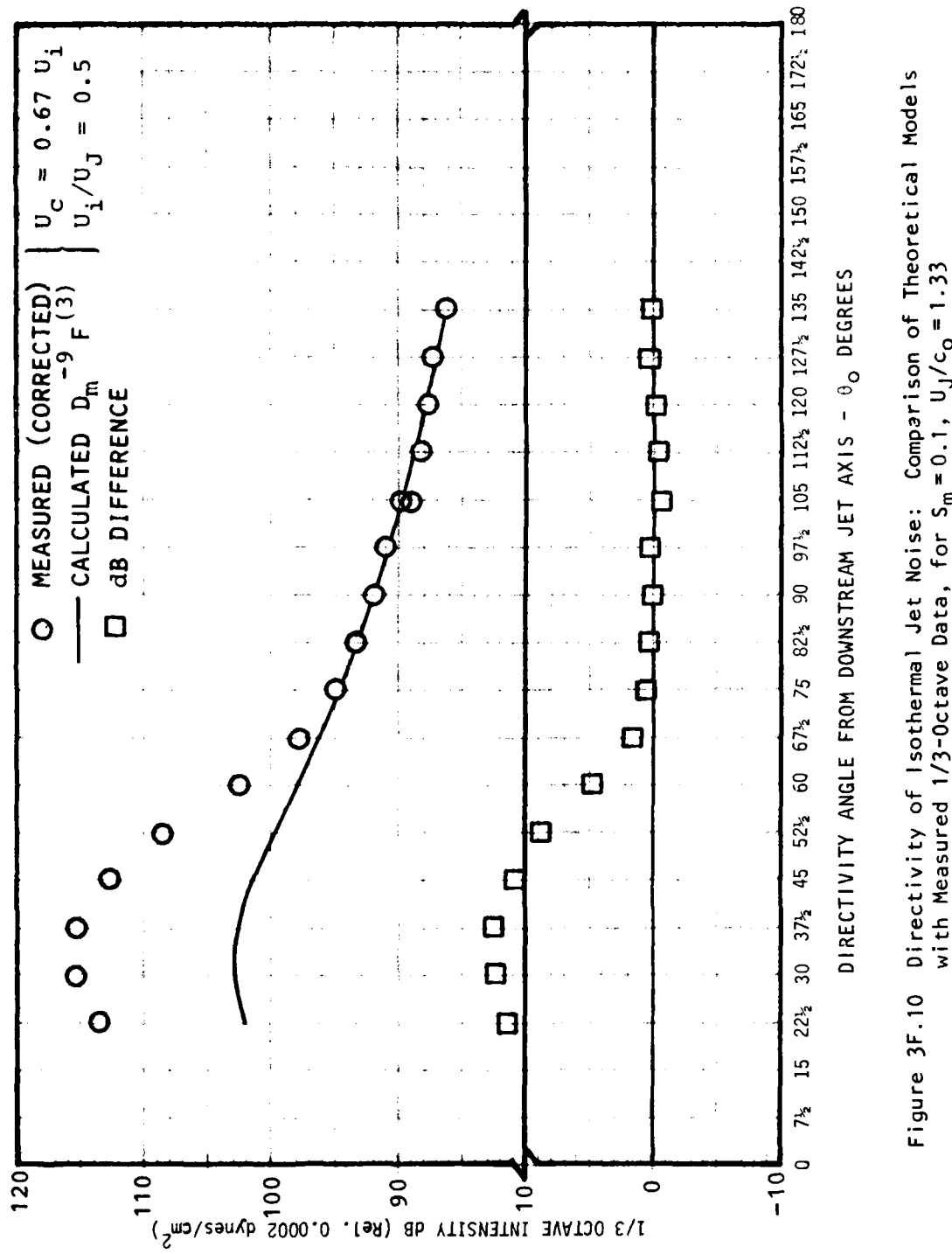


Figure 3F.10 Directivity of Isothermal Jet Noise: Comparison of Theoretical Models with Measured 1/3-Octave Data, for  $S_m = 0.1$ ,  $U_j/c_o = 1.33$

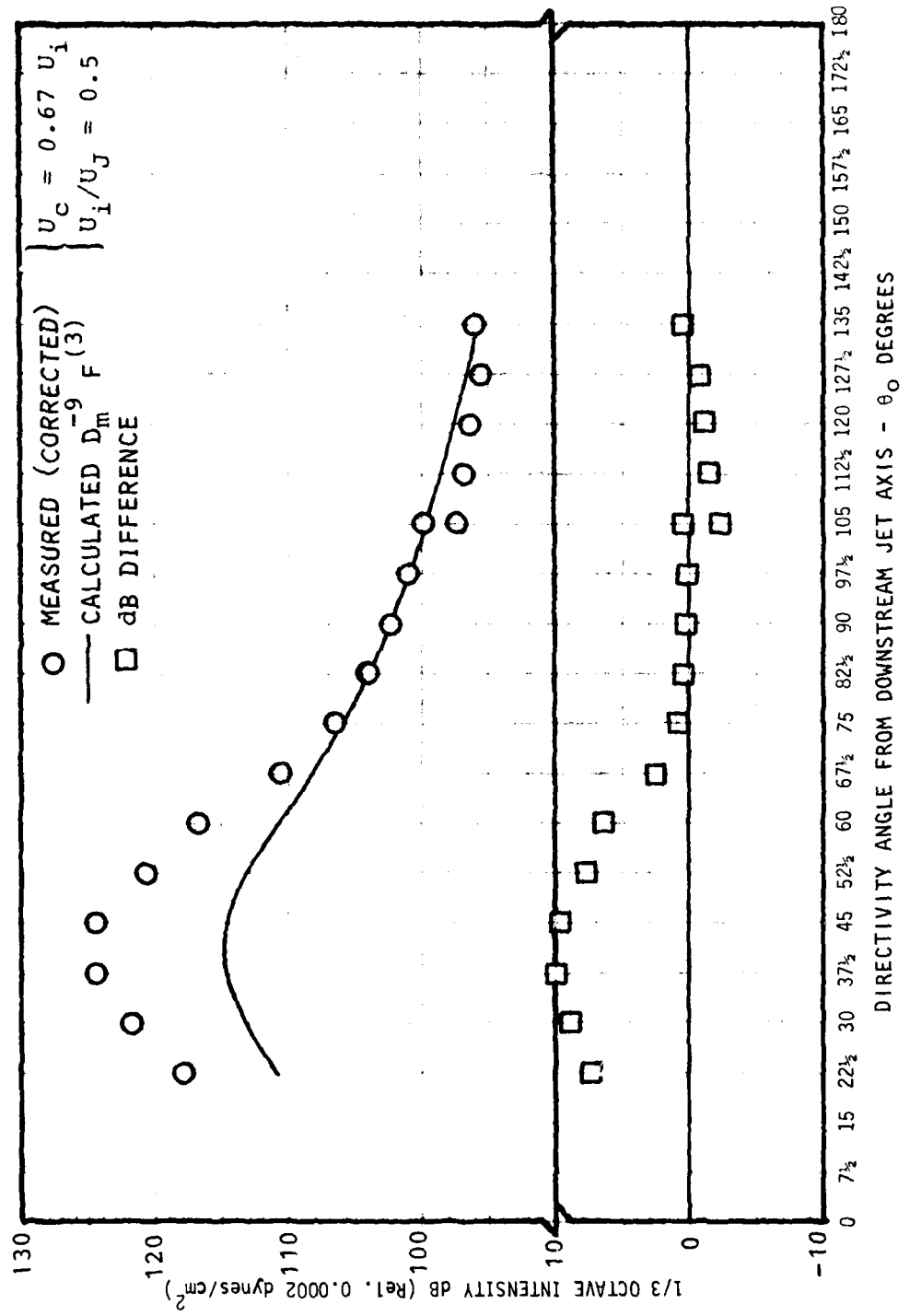


Figure 3F.11 Directivity of Isothermal Jet Noise: Comparison of Theoretical Models with Measured 1/3-octave Data, for S<sub>m</sub> = 0.1, U<sub>J</sub>/c<sub>0</sub> = 1.95

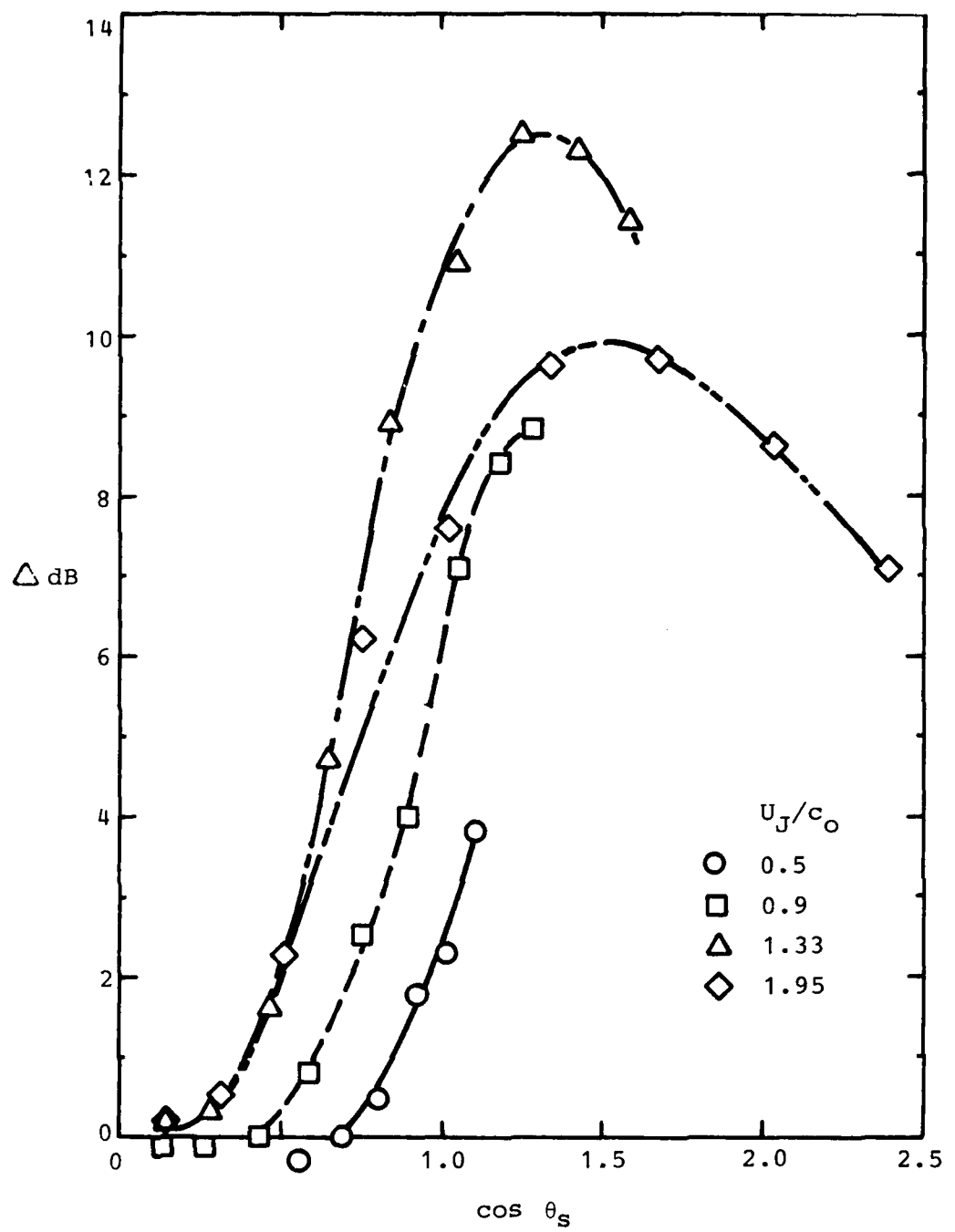


Figure 3F.12 Directivity of Isothermal Jet Noise: Variation of dB Difference Between Present Theory and Measured Data with Cosine of Source Emission Angle, for  $S_m = 0.1$

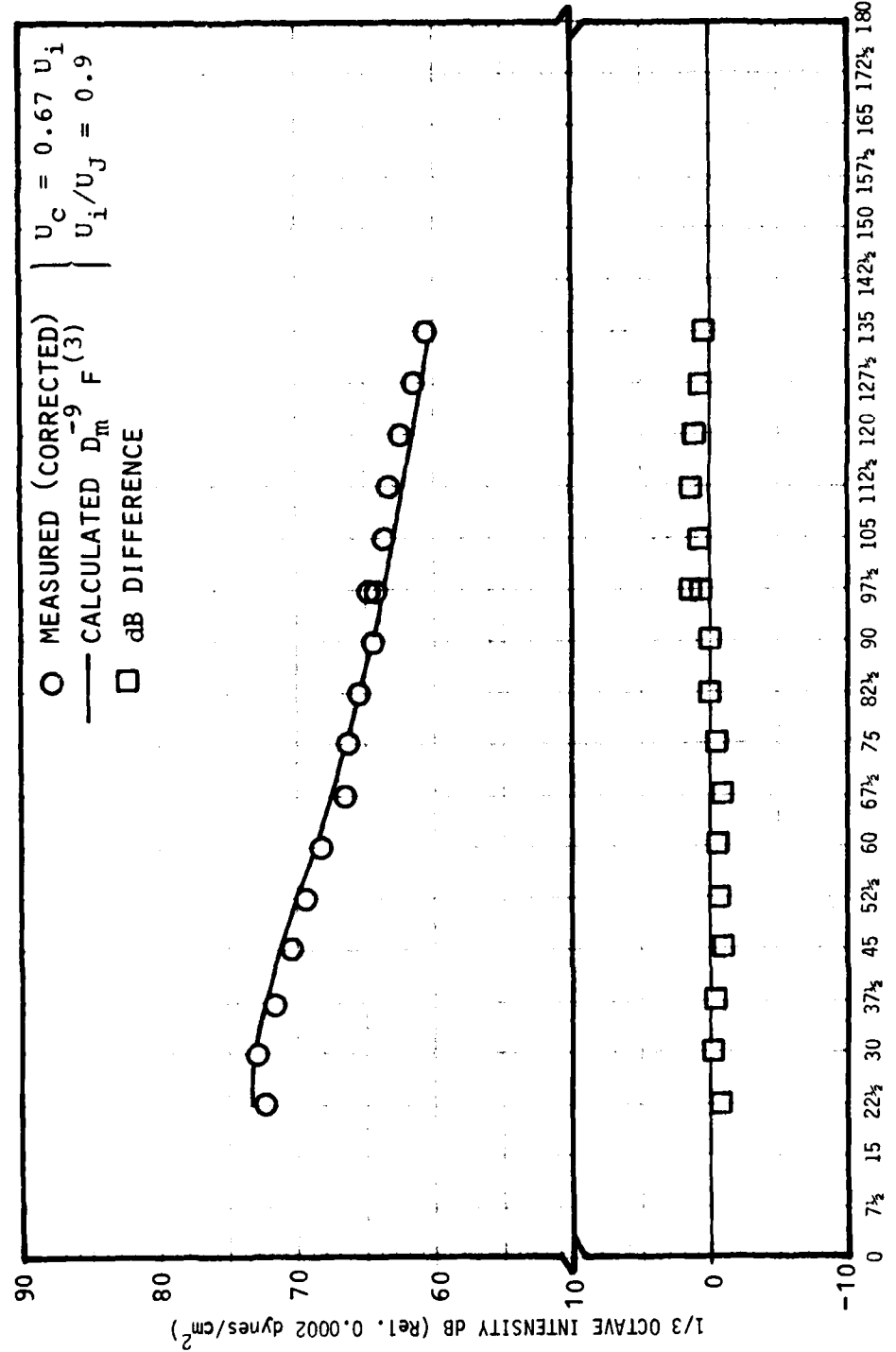


Figure 3F.13 Directivity of Isothermal Jet Noise: Comparison of Theoretical Models with Measured 1/3-Octave Data, for  $S_m = 0.3$ ,  $U_j/c_o = 0.5$

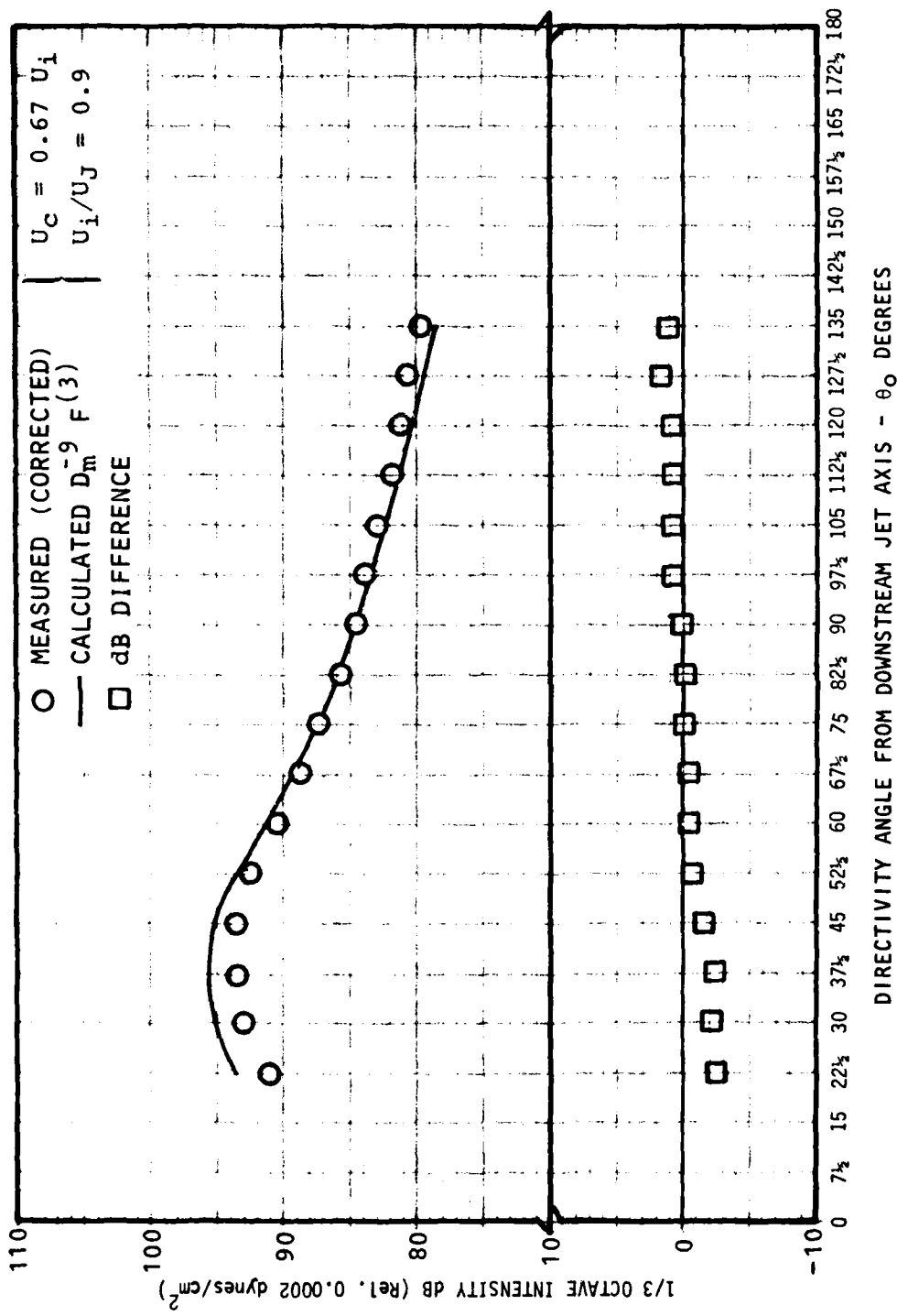


Figure 3F.14 Directivity of Isothermal Jet Noise: Comparison of Theoretical Models with Measured 1/3-Octave Data, for  $S_m = 0.3$ ,  $U_j/c_o = 0.9$

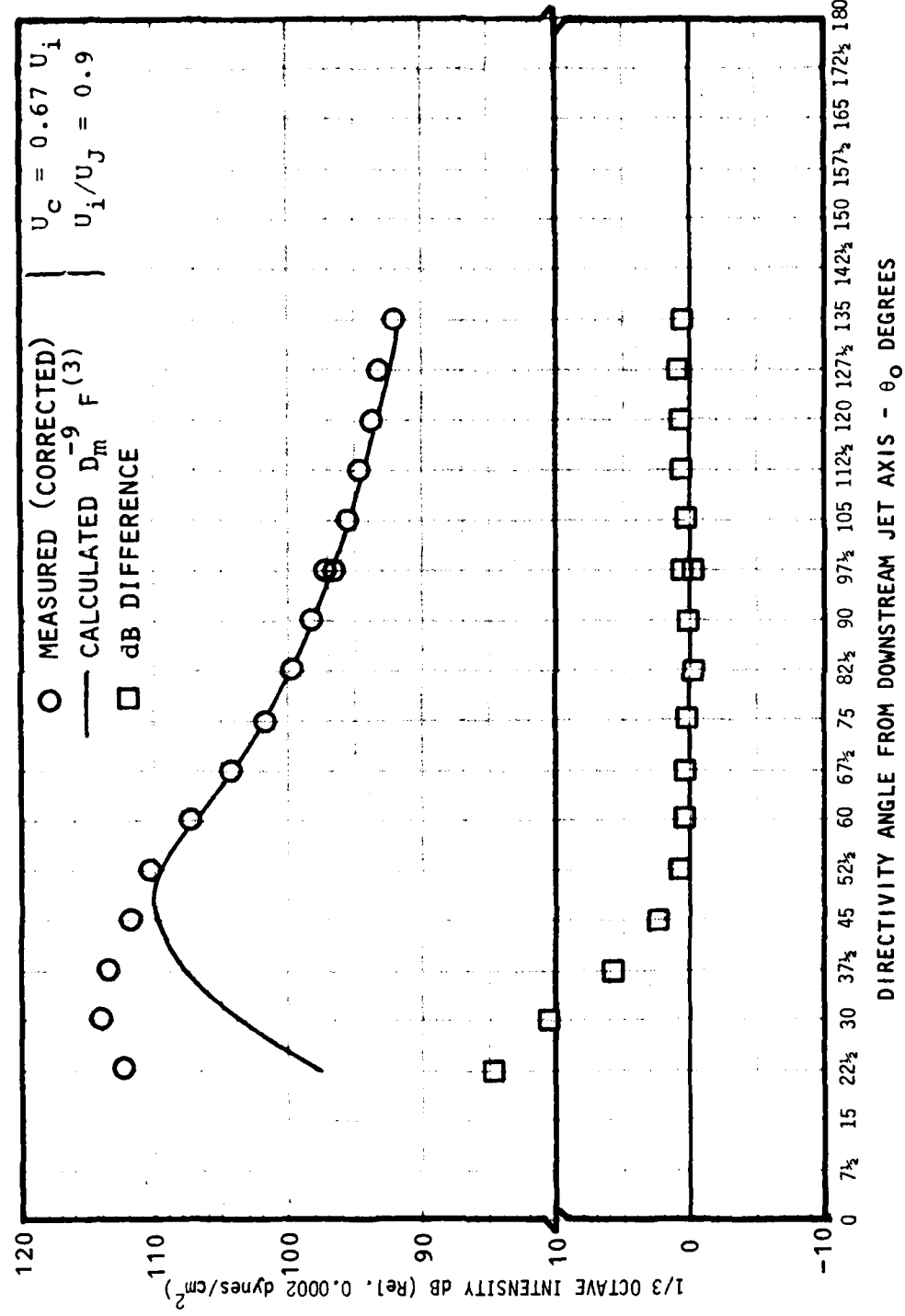


Figure 3F.15 Directivity of Isothermal Jet Noise: Comparison of Theoretical Models with Measured 1/3-Octave Data, for  $S_m = 0.3$ ,  $U_J/c_o = 1.33$

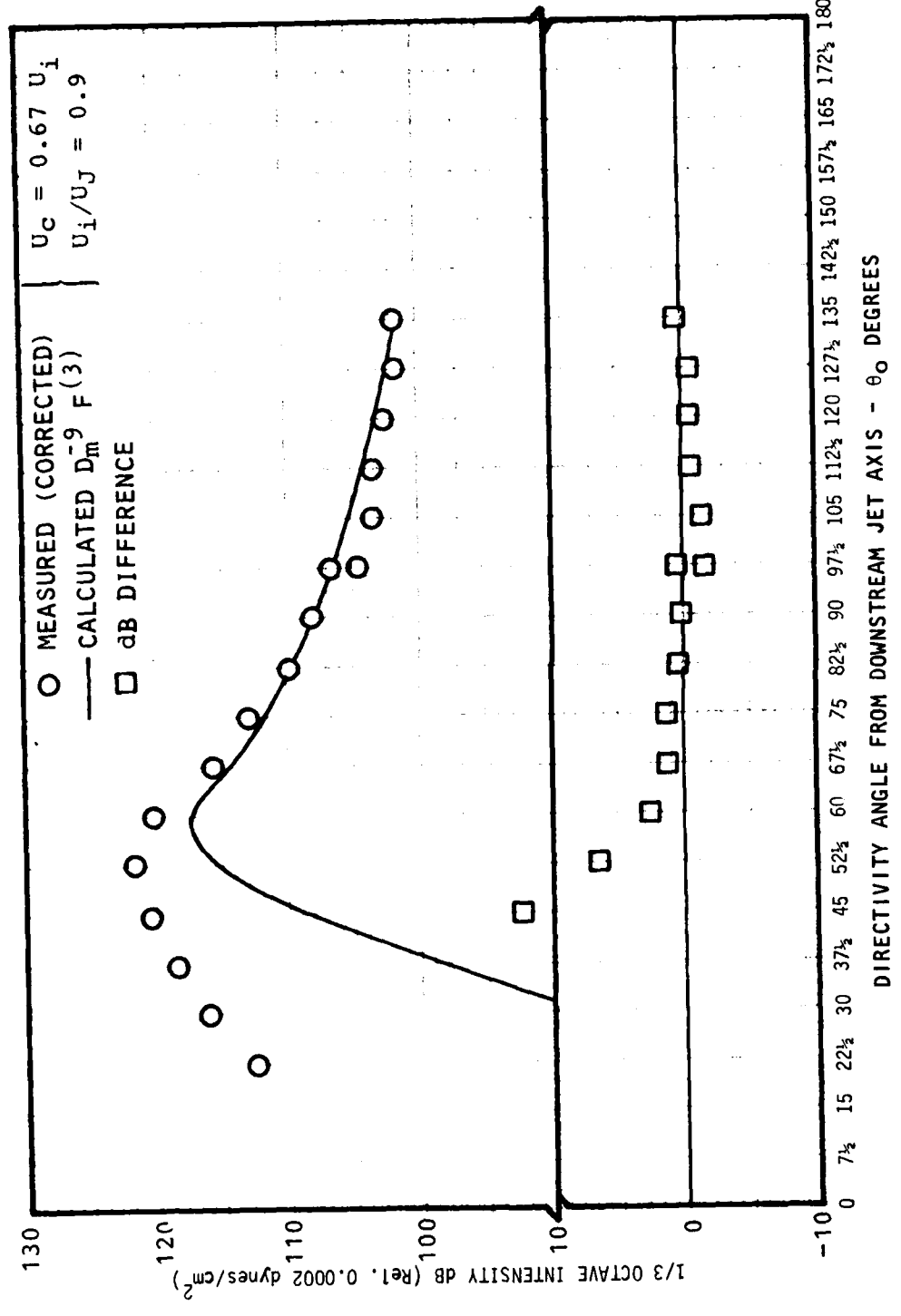


Figure 3F.16 Directivity of Isothermal Jet Noise: Comparison of Theoretical Models with Measured 1/3-Octave Data, for  $S_m = 0.3$ ,  $U_j/c_o = 1.95$

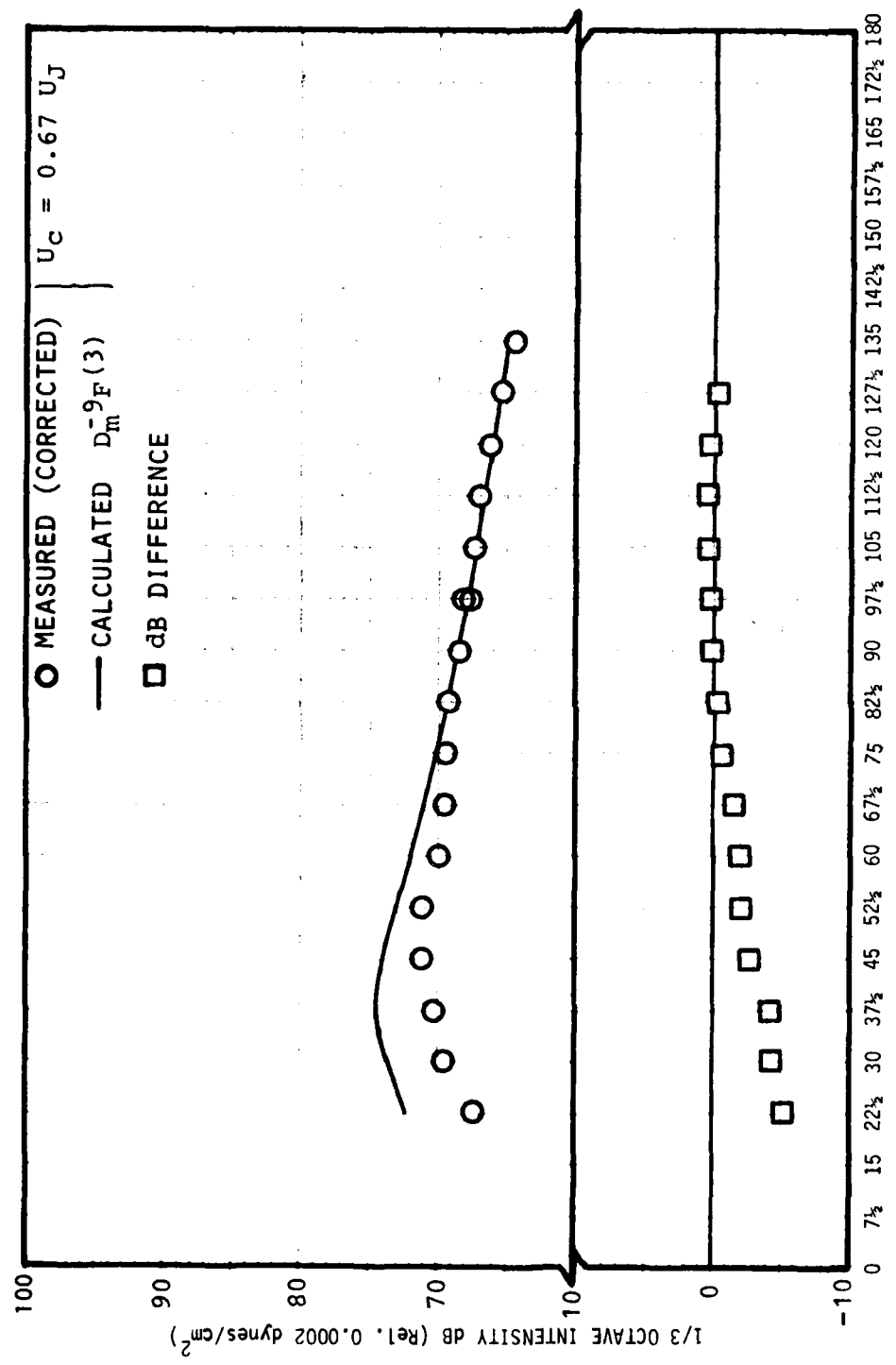


Figure 3F.17 Directivity of Isothermal Jet Noise: Comparison of Theoretical Models with Measured 1/3-Octave Data, for  $S_m = 1.0$ ,  $U_J/c_o = 0.5$

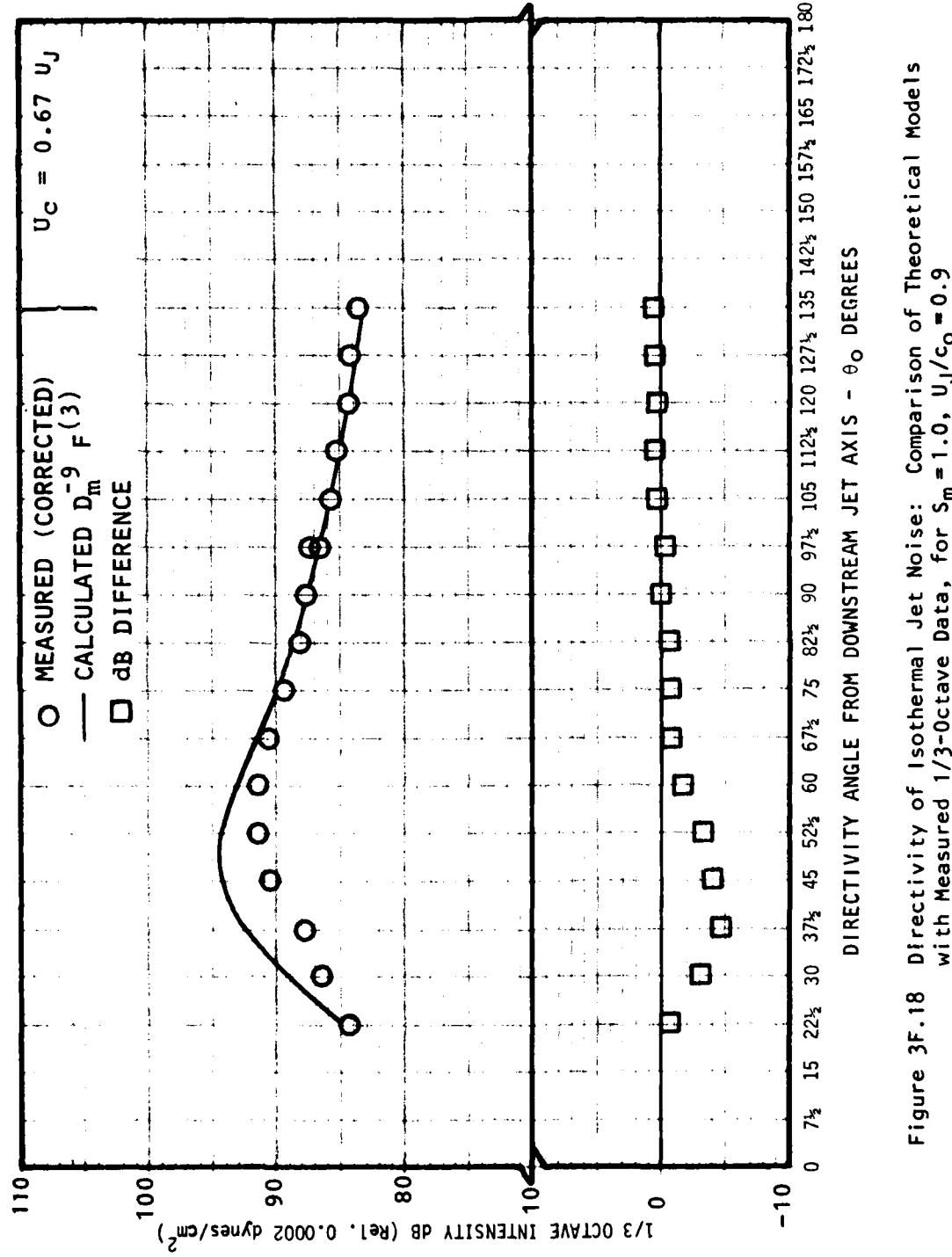


Figure 3F.18 Directivity of Isothermal Jet Noise: Comparison of Theoretical Models with Measured 1/3-Octave Data, for  $S_m = 1.0$ ,  $U_j/c_o = 0.9$

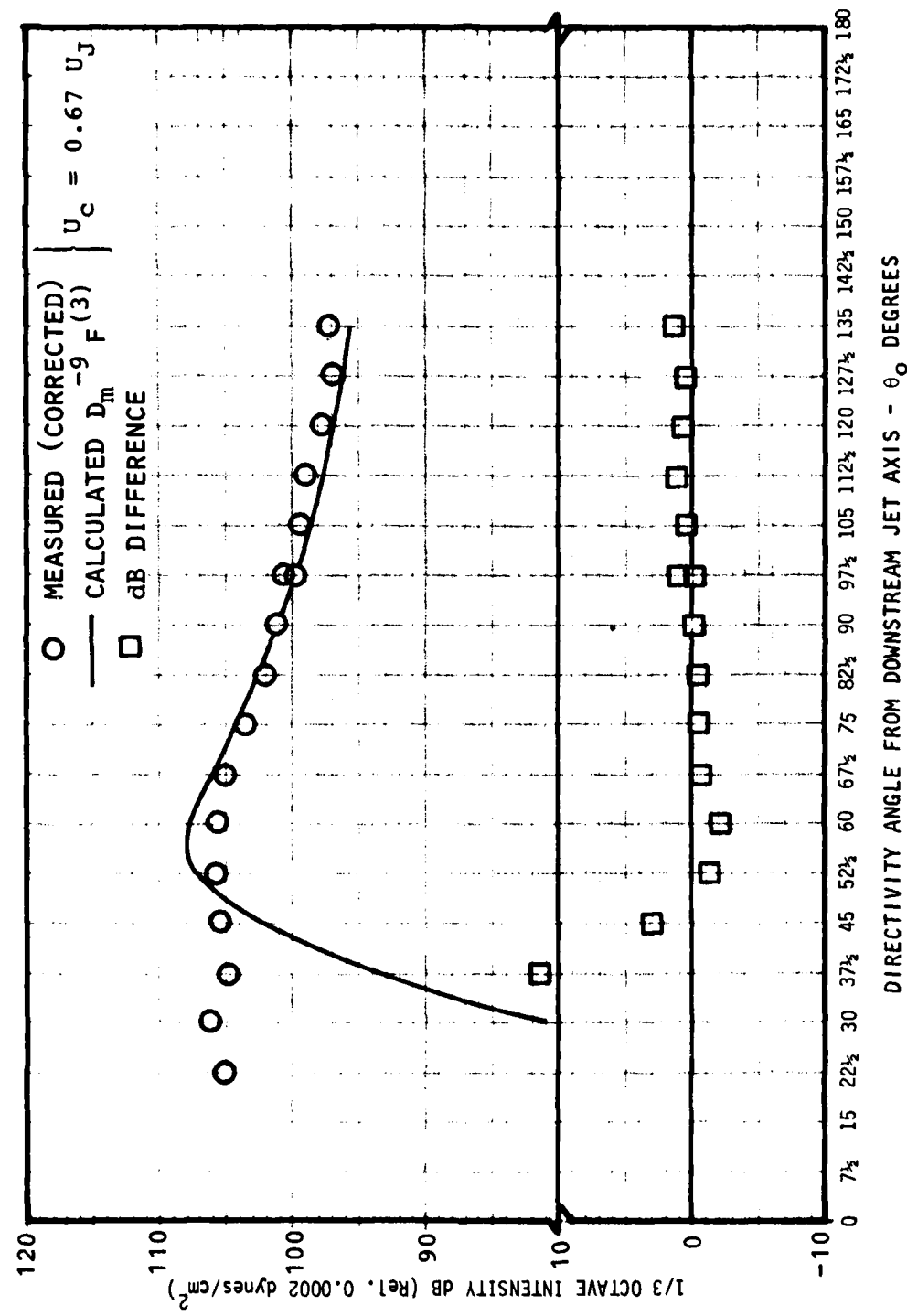


Figure 3F.19 Directivity of Isothermal Jet Noise: Comparison of Theoretical Models with Measured 1/3-Octave Data, for  $S_m = 1.0$ ,  $U_j/U_c = 1.33$

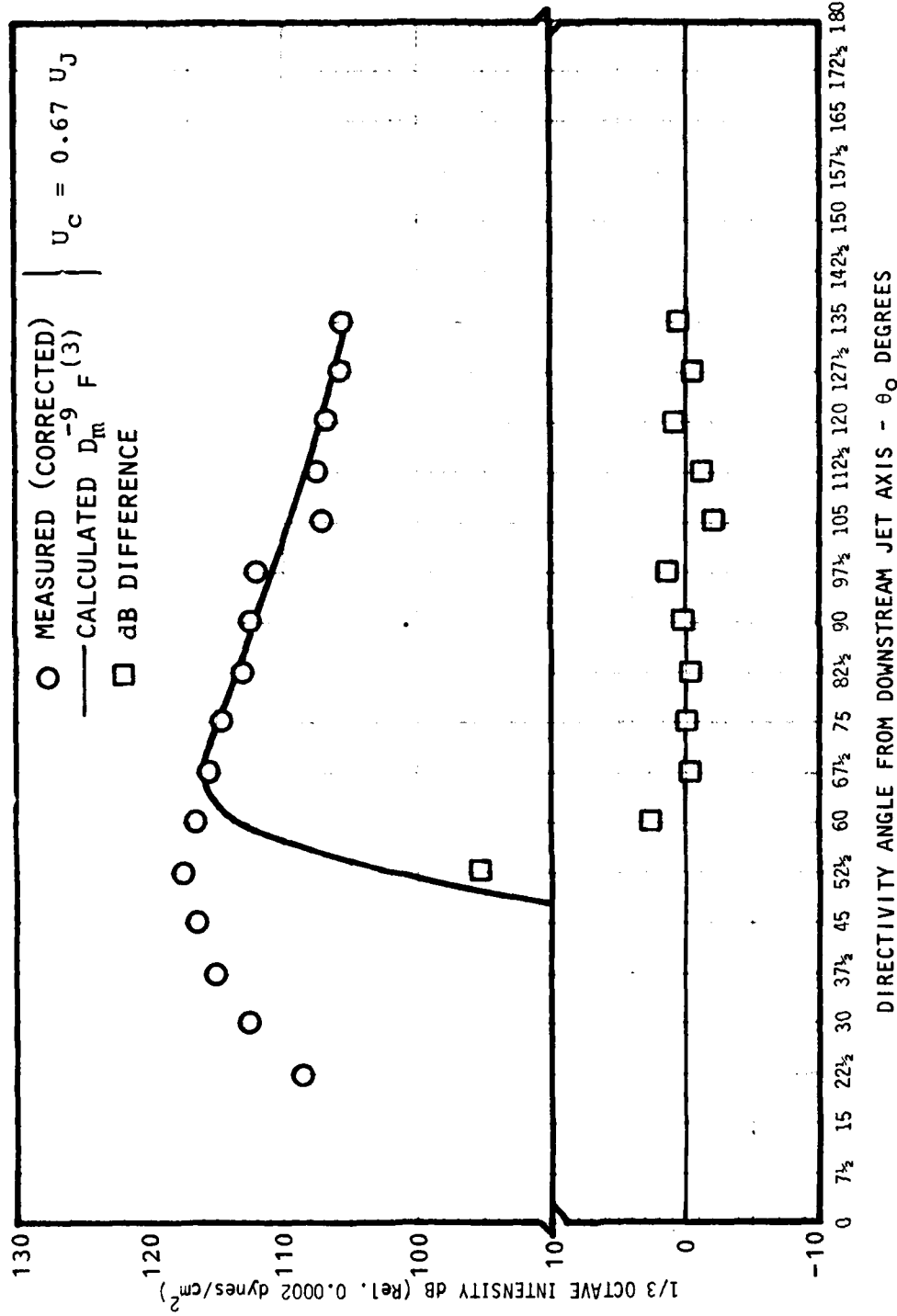


Figure 3F.20 Directivity of Isotermal Jet Noise: Comparison of Theoretical Models with Measured 1/3-Octave Data, for  $S_m = 1.0$ ,  $U_J/c_0 = 1.95$

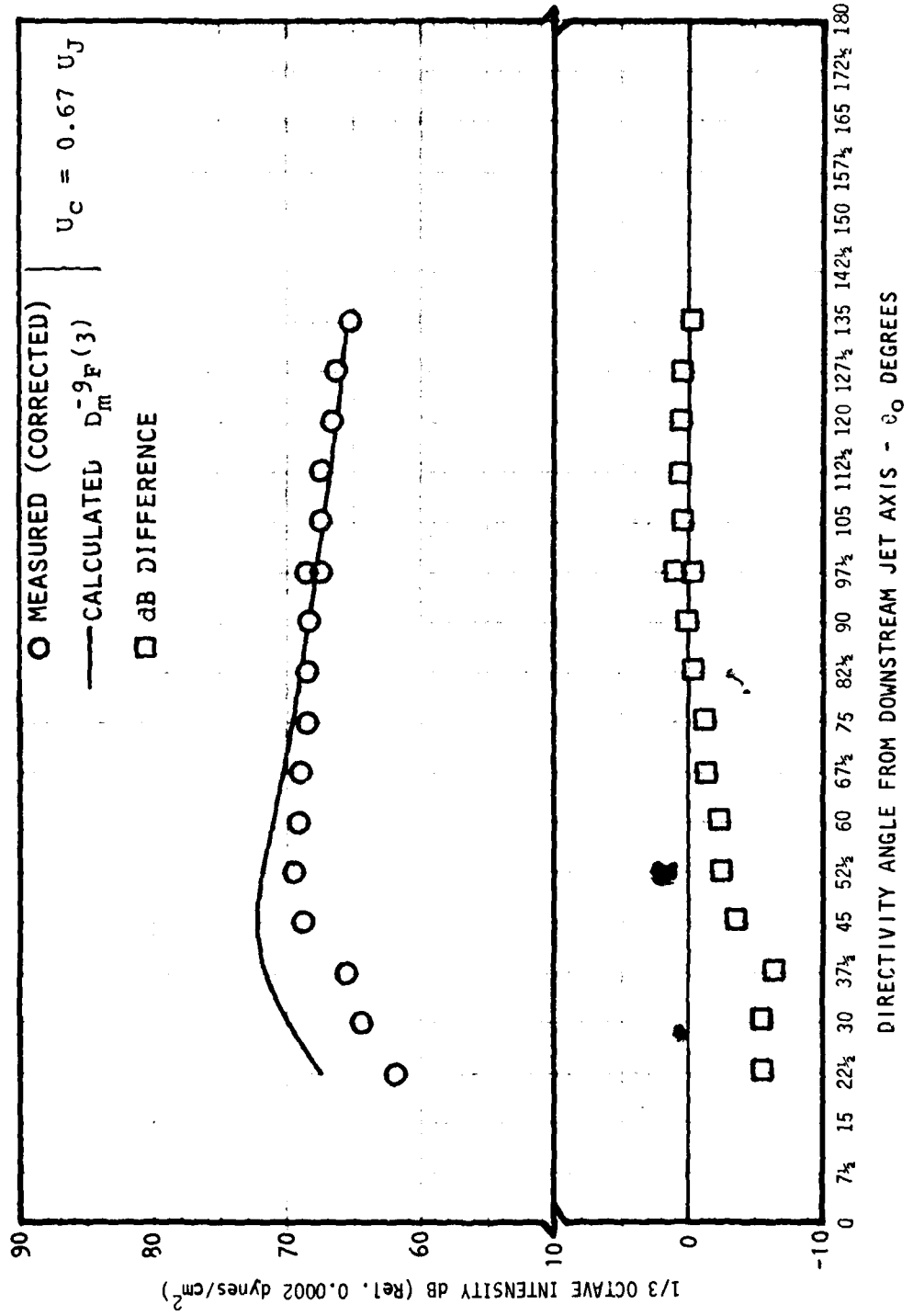


Figure 3F.21 Directivity of Isothermal Jet Noise: Comparison of Theoretical Models with Measured 1/3-Octave Data, for  $S_m = 3.0$ ,  $U_j/c_o = 0.5$

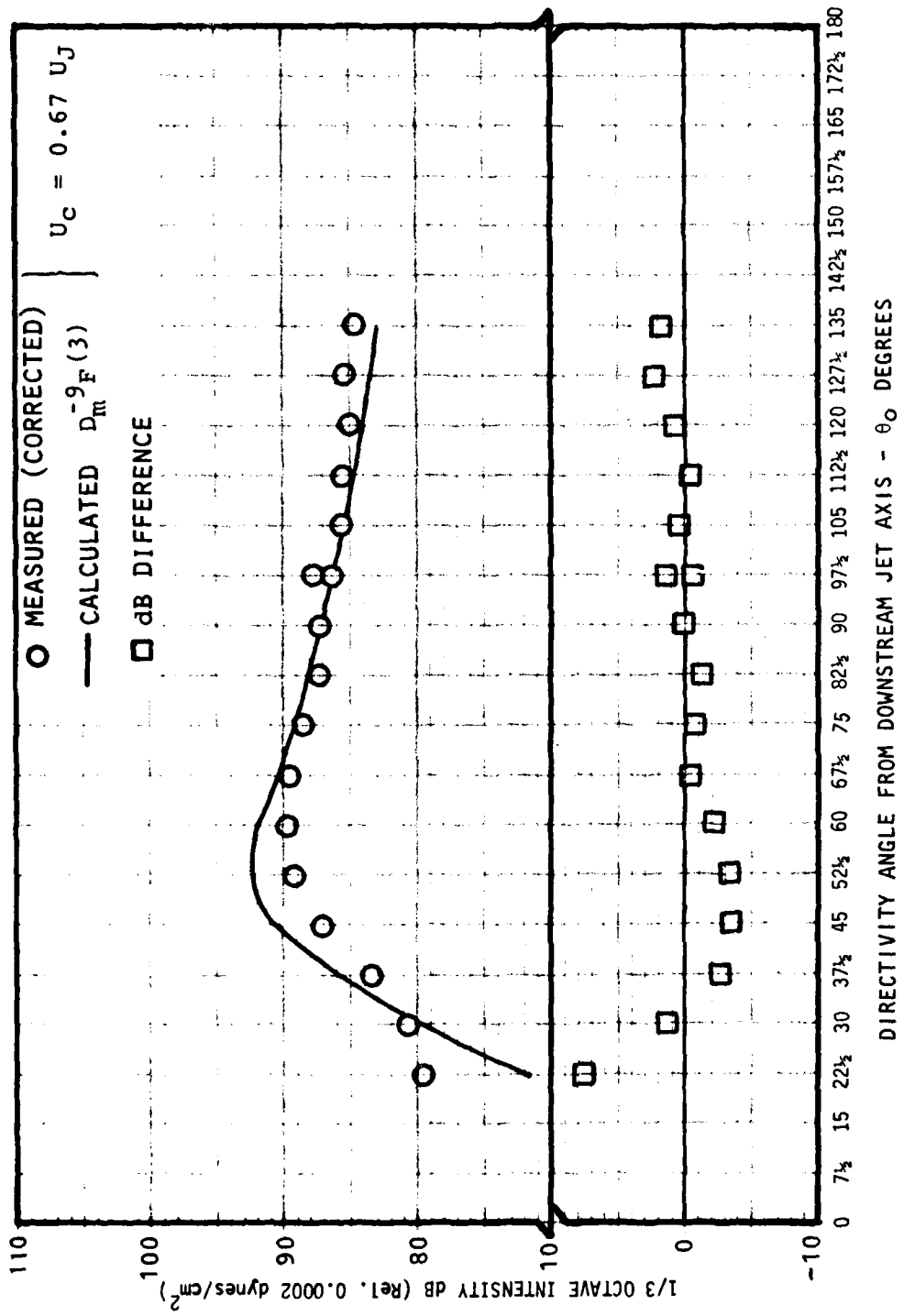


Figure 3F.22 Directivity of Isothermal Jet Noise: Comparison of Theoretical Models with Measured 1/3-Octave Data, for  $S_m = 3.0$ ,  $U_j/c_o = 0.9$

## APPENDIX 3G

### HOT-JET NOISE DIRECTIVITY: DETAILED COMPARISONS WITH THEORY

In Appendix 3F it is demonstrated that a combined quadrupole-dipole theoretical source model can, in general, account for the influence of temperature on jet noise radiation at  $90^\circ$  to the jet axis. The relative, mean square, temperature dependent, dipole source strength,  $\Omega(S_m, T_J/T_0)$ , is deduced from data measured at  $90^\circ$ . For other angles that value of  $\Omega$  and calculated flow factors can be used to predict the ratio of the far-field intensity to that at isothermal conditions (at the same angle), referred to in Appendix 3E as 'A':

$$I(\theta_0, \omega, T_J/T_0) / I(\theta_0, \omega, T_J/T_0 = 1) \equiv A(\theta_0)$$

$$= \frac{F^{(3)}(\theta_0, \omega, T_J/T_0) + F_d^{(3)}(\theta_0, \omega, T_J/T_0) D_m^2(U_J/c_0)^{-2} \Omega(S_m, T_J/T_0)}{F^{(3)}(\theta_0, \omega, T_J/T_0 = 1)}$$

Rather than compare calculated values of A with corresponding measured values a predicted absolute intensity,  $I(\theta_0, \omega, T_J/T_0)$ , is derived from

$$I(\theta_0, \omega, T_J/T_0) = I(\theta_0, \omega, T_J/T_0 = 1) |_{\text{measured}}$$

$$\times A(\theta_0) |_{\text{calculated}}$$

[Of course  $A(\theta_0)$  does depend on measured data at  $90^\circ$  via the value deduced for  $\Omega$ ]. That predicted value, in dB, is then compared with measured hot-jet noise levels over the angle range  $15^\circ \leq \theta_0 \leq 135^\circ$  in Figures 3G.1 through 3G.6. At  $S_m = 0.1$  in Figures 3G.1 and 3G.2, the agreement is not good; one of the most likely reasons is that it has not been possible at this time to correct the measured data for source location effects nor to process the measured data and calculate numerical results with a realistic value of the eddy convection velocity. Both effects are important at low Strouhal numbers. At a higher Strouhal number of 0.3 there is a marked improvement. In Figure 3G.3 for  $U_J/c_0 = 0.5$  the 5 dB increase at  $90^\circ$  with heating contrasts with an 8 dB increase at  $135^\circ$  and almost no change at all at  $22\frac{1}{2}^\circ$ ; these features are substantially reproduced by the theoretical prediction. In Figure 3G.4 for  $U_J/c_0 = 0.9$  the situation is reversed — no change at  $135^\circ$  and  $5\frac{1}{2}$  dB decrease at  $22\frac{1}{2}^\circ$ ; again, the calculations reproduce the result, even though the change at  $90^\circ$  is only 1/2 dB. Keeping the Mach number at 0.9 the results for  $S_m = 1.0$  and 3.0 in Figures 3G.5 and 3G.6 are visually the most striking examples to date which confirm that the modified Lilley equation model contains an excellent physical description of temperature effects. That automatically includes the new temperature dependent dipole source first introduced<sup>19</sup> as an extension to the Lighthill analogy.

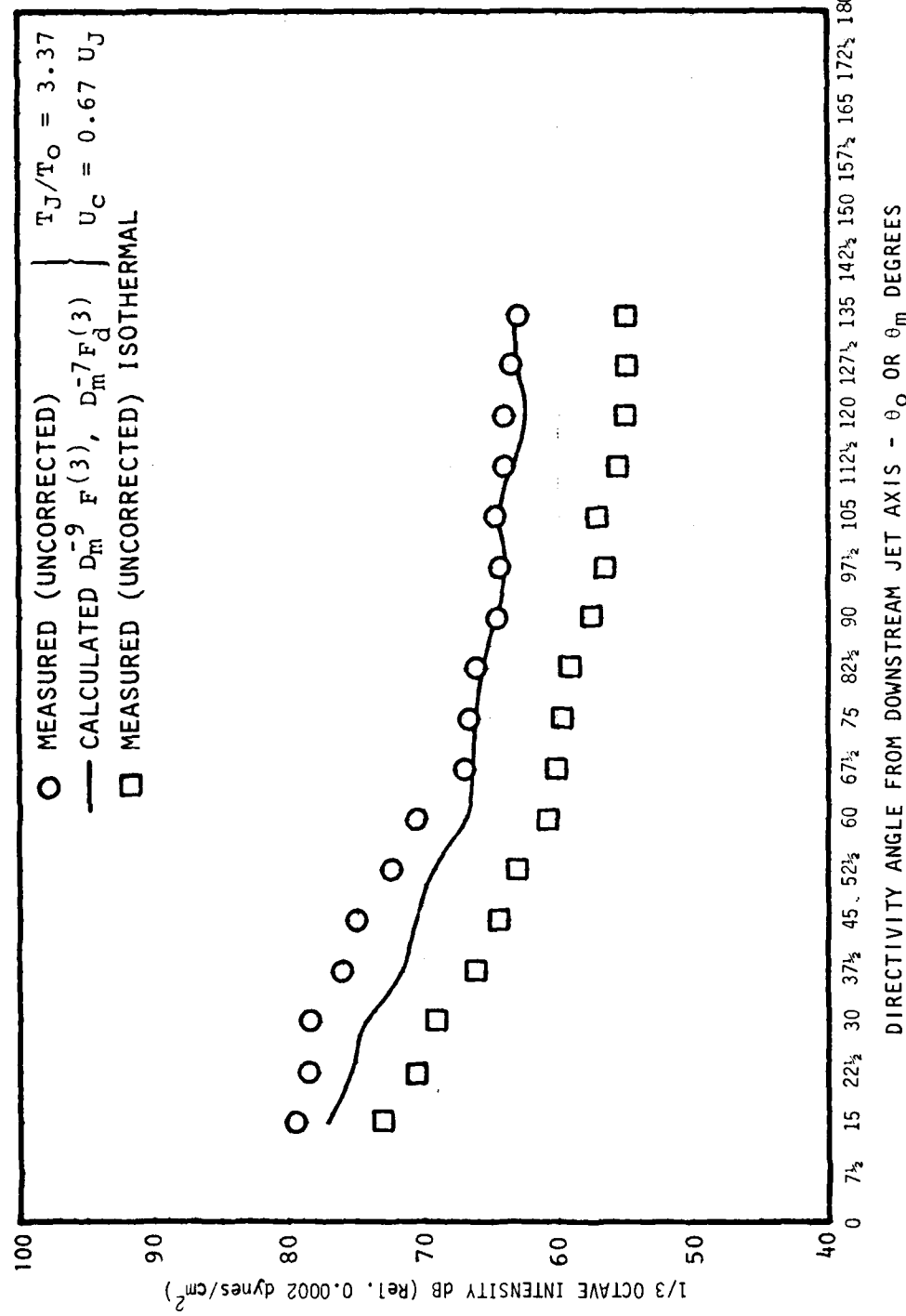


Figure 3G.1 Directivity of High Temperature Jet Noise: Comparison of Theoretical Models with Measured 1/3-Octave Data, for  $S_m=0.1$ ,  $U_J/c_0=0.5$ ,  $T_J/T_0=3.37$

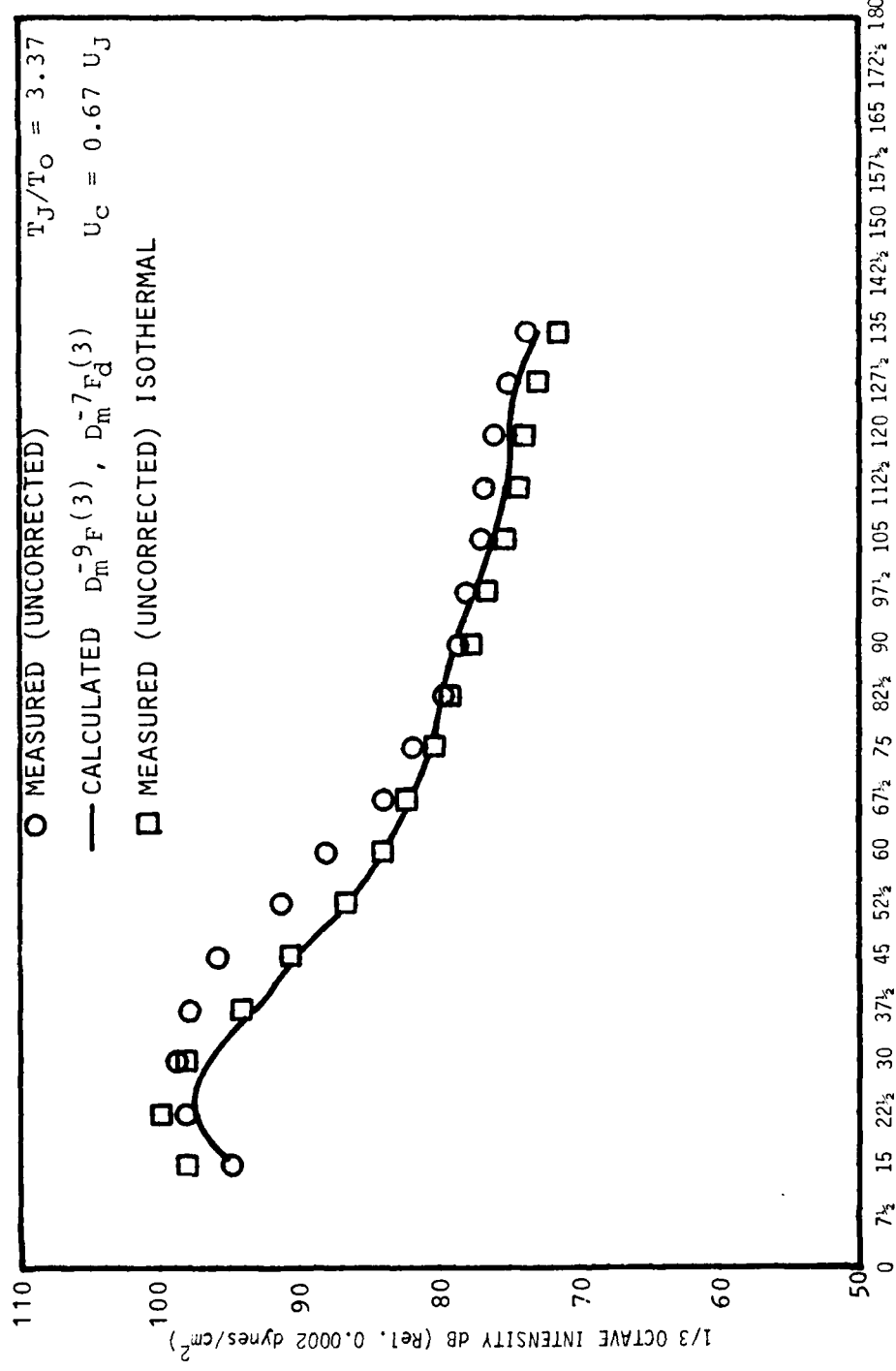


Figure 3G.2 Directivity of High Temperature Jet Noise: Comparison of Theoretical Models with Measured 1/3-Octave Data, for  $S_m = 0.1$ ,  $U_J/c_o = 0.9$ ,  $T_J/T_O = 3.37$

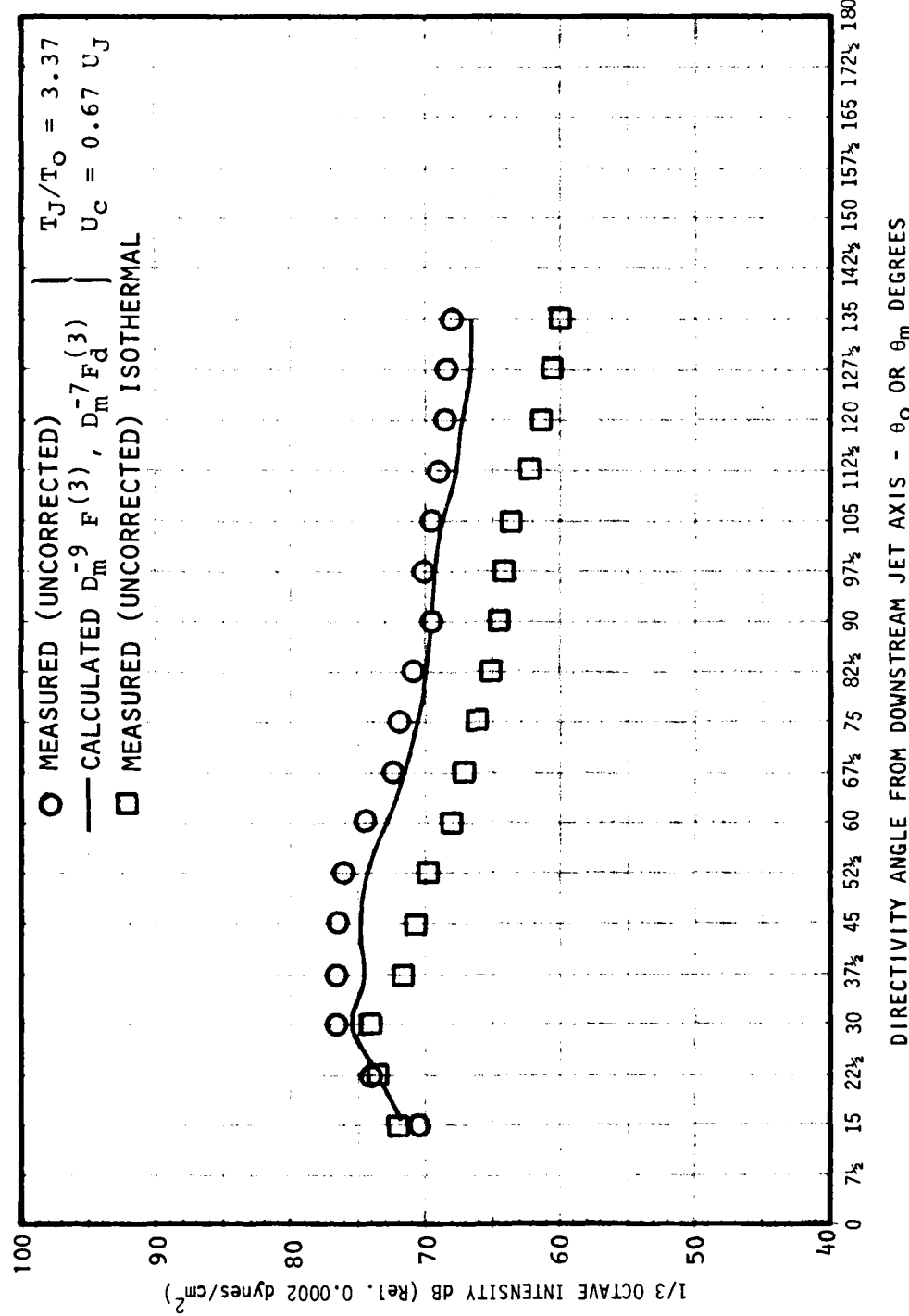


Figure 36.3 Directivity of High Temperature Jet Noise: Comparison of Theoretical Models with Measured 1/3-Octave Data, for  $S_m = 0.3$ ,  $U_j/c_o = 0.5$ ,  $T_j/T_o = 3.37$

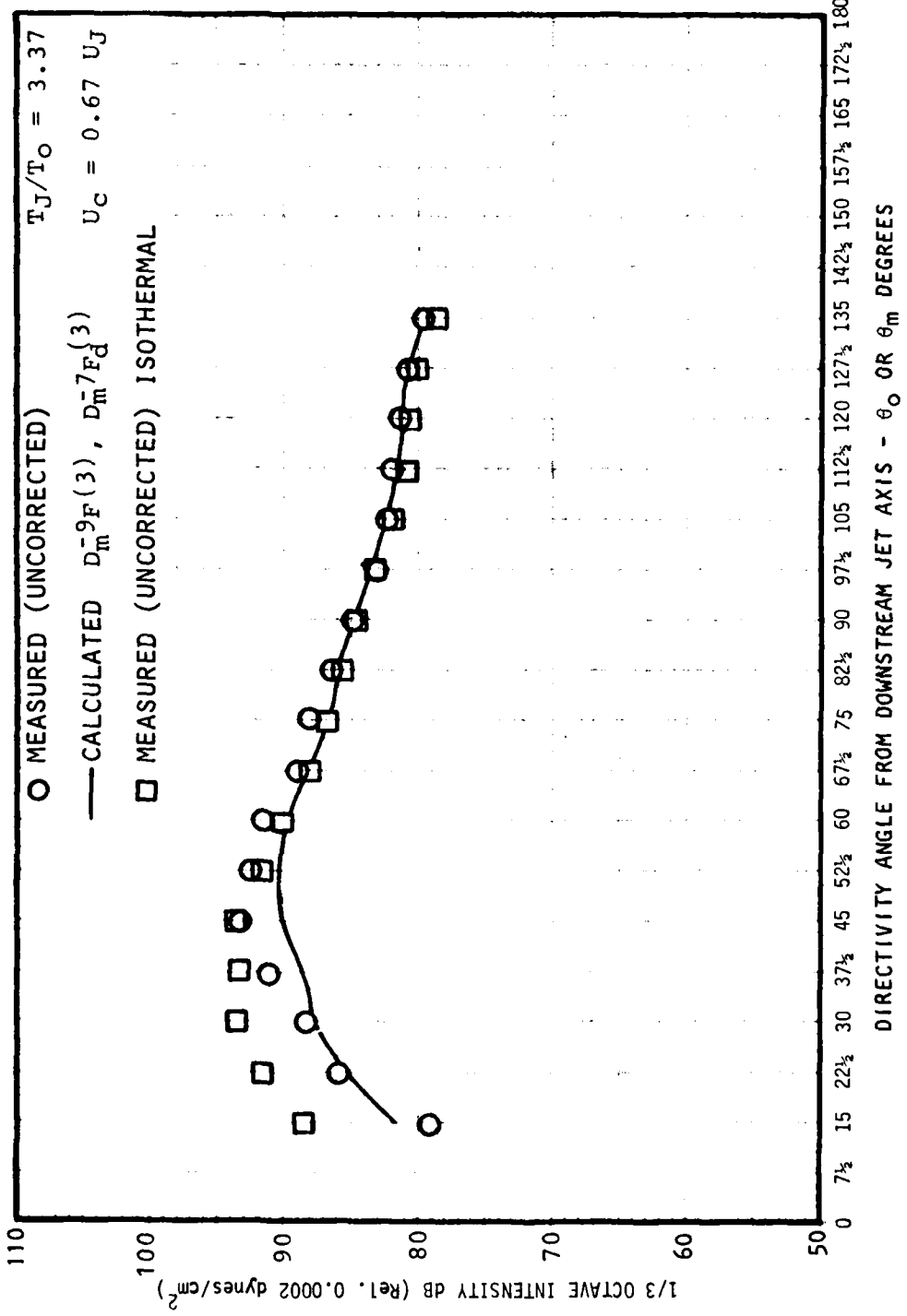


Figure 3G.4 Directivity of High Temperature Jet Noise: Comparison of Theoretical Models with Measured 1/3-Octave Data, for  $S_m = 0.3$ ,  $U_J/c_o = 0.9$ ,  $T_J/T_O = 3.37$

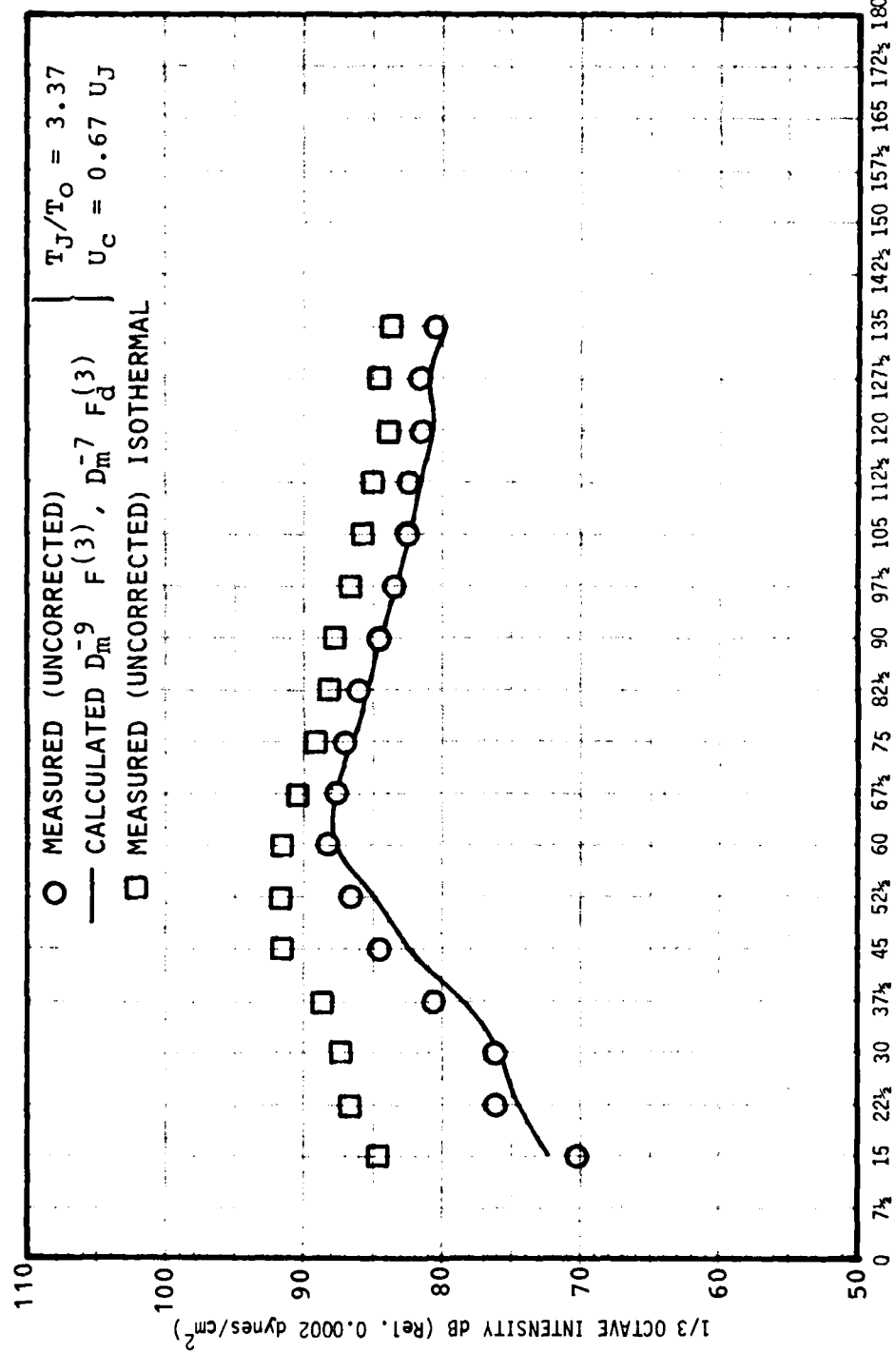


Figure 3G.5 Directivity of High Temperature Jet Noise: Comparison of Theoretical Models with Measured 1/3-Octave Data, for  $S_m = 1.0$ ,  $U_J/c_o = 0.9$ ,  $T_J/T_O = 3.37$

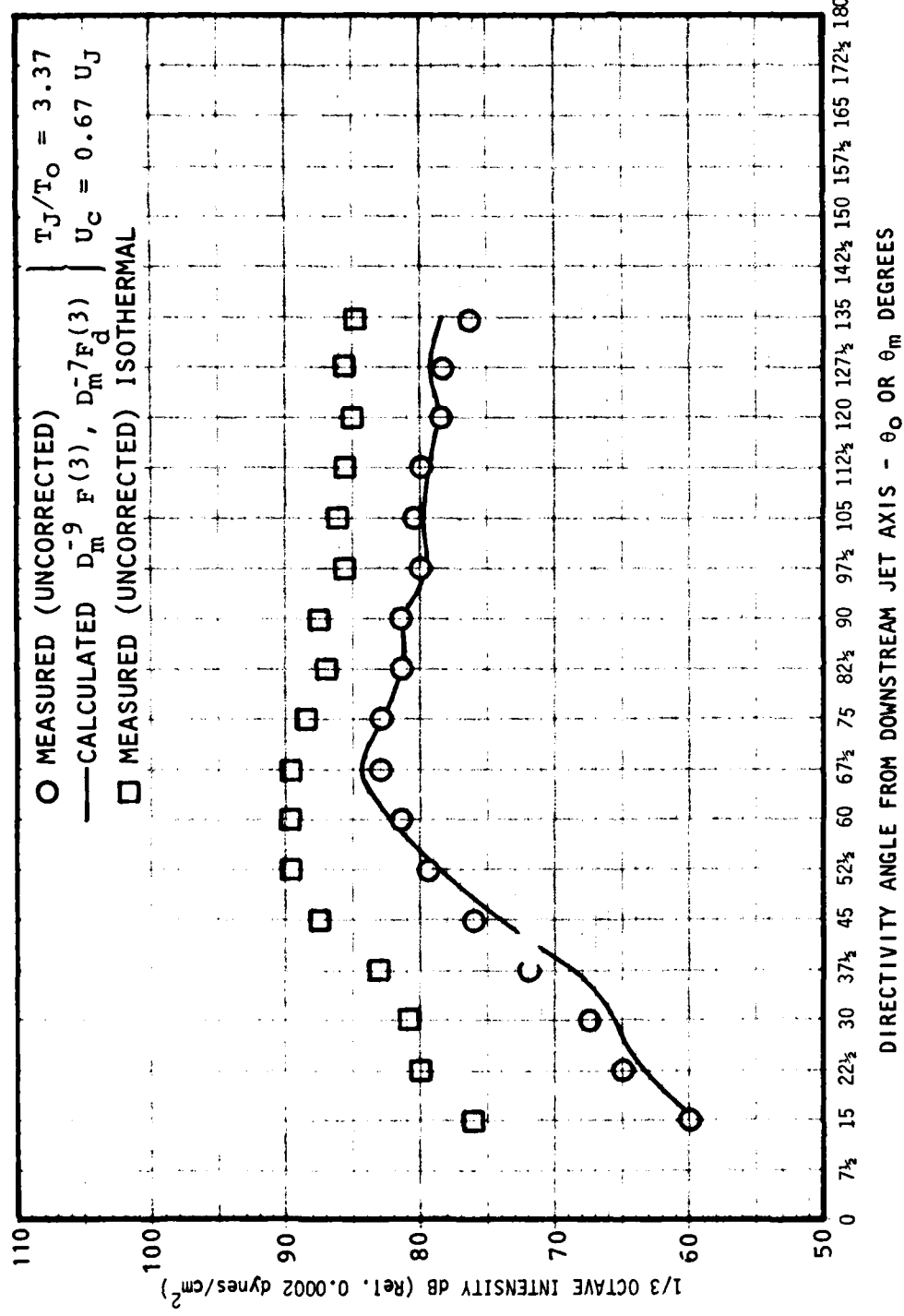


Figure 3G.6 Directivity of High Temperature Jet Noise: Comparison of Theoretical Models with Measured 1/3-Octave Data, for  $S_m = 3.0$ ,  $U_j/c_o = 0.9$ ,  $T_j/T_o = 3.37$

## APPENDIX 4A

### THE NONLINEAR INTEGRAL EQUATIONS FOR A COMPRESSIBLE AXISYMMETRIC JET

In the following analysis it has been found to be convenient to use tensor notation. The physical components of the tensors for cylindrical coordinates and other relevant tensor relationships are given in Appendix 4B.

The continuity and momentum equations for an inviscid compressible fluid can be written in the form,

$$\frac{\partial p}{\partial t} + (\rho u^i)_{,i} = 0, \quad (4A-1)$$

and

$$\rho \left\{ \frac{\partial u_i}{\partial t} + u^j u_{i,j} \right\} = - [p \delta_i^j]_{,j} \quad (4A-2)$$

respectively. Making use of the continuity equation, the momentum equation may be rewritten in the form,

$$\frac{\partial(\rho u_i)}{\partial t} + (\rho u^j u_{i,j})_{,j} = - [p \delta_i^j]_{,j} \quad (4A-3)$$

The velocity, density and pressure are written in component form as,

$$\begin{aligned} u_i &= \bar{u}_i + u'_i + \tilde{u}_i, \\ \rho &= \bar{\rho} + \rho' + \tilde{\rho}, \\ \text{and } p &= \bar{p} + p' + \tilde{p}, \end{aligned} \quad (4A-4)$$

where an overbar denotes the time-independent component, a prime denotes the random turbulent time-dependent component and a tilde denotes a periodic component. The averaging properties of these components are given by Reynolds and Hussain<sup>37</sup>. Substitution of Equation (4A-4) into Equation (4A-3) and phase-averaging, which removes the linear contribution of the random turbulent component, leads to

$$\begin{aligned} &\frac{\partial}{\partial t} (\bar{\rho} \bar{u}_i + \bar{\rho} \tilde{u}_i + \tilde{\rho} \bar{u}_i + \tilde{\rho} \tilde{u}_i + \langle \rho' u'_i \rangle) \\ &+ [(\bar{\rho} + \tilde{\rho}) (\bar{u}^j \bar{u}_i + \bar{u}^j \tilde{u}_i + \tilde{u}^j \bar{u}_i + \tilde{u}^j \tilde{u}_i)]_{,j} \\ &+ [\langle \rho u'^j u'_i \rangle + \langle u^j \rho' u'_i \rangle + \langle u_i \rho' u'^j \rangle - 2 \langle \rho' u'^j u'_i \rangle]_{,j} \\ &= - (\bar{p} \delta_i^j)_{,j} - (\tilde{p} \delta_i^j)_{,j}, \end{aligned} \quad (4A-5)$$

where  $\langle \cdot \rangle$  denotes the phase average.

The time average of Equation (4A-5) is

$$\begin{aligned} & [\bar{\rho}\bar{u}^j\bar{u}_i + \bar{\rho}\bar{u}^j\bar{u}_i + \bar{u}^j\bar{\rho}\bar{u}_i + \bar{u}_i\bar{\rho}\bar{u}^j + \bar{\rho}\bar{u}^j\bar{u}_i],_j \\ & + [\bar{\rho}u^j u_i' + u^j \rho' u_i' + u_i \rho' u^j - 2\rho' u^j u_i'],_j \\ & = - (\bar{\rho} \delta_i^j),_j \end{aligned} \quad (4A-6)$$

In order to seek a realistic closure to this problem, it will be assumed that the contribution of the time independent shear stresses, given by the second bracketed term on the left hand side of Equation (4A-6), may be represented by an isotropic eddy viscosity  $\bar{\epsilon}$  such that,

$$[\bar{\rho}u^j u_i' + u^j \rho' u_i' + u_i \rho' u^j - 2\rho' u^j u_i'] = -2\bar{\rho}\bar{\epsilon} \bar{d}_i^j \quad (4A-7)$$

where  $\bar{d}_i^j$  is the time averaged deviatoric stress tensor, which is related to the time averaged rate of strain tensor  $\bar{e}_i^j$  by the relationship,

$$\bar{d}_i^j = \bar{e}_i^j - \frac{1}{3} \Delta \delta_i^j,$$

where

$$\Delta = \bar{e}_k^k. \quad (4A-8)$$

The covariant differentiation of Equation (4A-6) may be carried out after substitution of Equations (4A-7) and (4A-8). Denoting the physical velocity components by  $v$ ,  $w$  and  $u$  in the physical coordinates  $r$ ,  $\phi$  and  $z$ , the resulting equations may be written, for an axisymmetric flow,

$$\begin{aligned} & \frac{1}{r} \frac{\partial}{\partial r} \{ \bar{\rho}\bar{v}^2 + \bar{\rho}\bar{v}^2 + 2\bar{v}\bar{p}\bar{v} + \bar{\rho}\bar{v}^2 \} r + \frac{\partial}{\partial z} \{ \bar{\rho}\bar{u}\bar{v} + \bar{\rho}\bar{u}\bar{v} + \bar{u}\bar{p}\bar{v} + \bar{v}\bar{p}\bar{u} + \bar{\rho}\bar{u}\bar{v} \} \\ & - \bar{\rho} \frac{\bar{w}^2}{r} + \frac{\bar{\rho}\bar{w}^2}{r} = - \frac{\partial \bar{p}}{\partial r} + \frac{1}{r} \frac{\partial}{\partial r} \{ 2 \bar{\rho}\bar{\epsilon} r \frac{\partial \bar{v}}{\partial r} \} \\ & + \frac{\partial}{\partial z} \left| \bar{\rho}\bar{\epsilon} \left[ \frac{\partial \bar{v}}{\partial z} + \frac{\partial \bar{u}}{\partial r} \right] \right| + \frac{2\bar{\rho}\bar{\epsilon}\bar{v}}{r^2} - \frac{1}{r} \frac{\partial}{\partial r} \left\{ \frac{2}{3} \bar{\rho}\bar{\epsilon}\bar{\Gamma} \right\} r, \end{aligned} \quad (4A-9)$$

$$\begin{aligned} & \frac{1}{r} \frac{\partial}{\partial r} \{ \bar{\rho}\bar{v}\bar{w} + \bar{v}\bar{p}\bar{w} + \bar{\rho}\bar{v}\bar{w} \} r + \frac{\partial}{\partial z} \{ \bar{\rho}\bar{u}\bar{w} + \bar{u}\bar{p}\bar{w} + \bar{\rho}\bar{u}\bar{w} \} \\ & + \bar{\rho} \frac{\bar{v}\bar{w}}{r} + \frac{\bar{v}\bar{p}\bar{w}}{r} + \frac{\bar{\rho}\bar{v}\bar{w}}{r} = 0, \end{aligned} \quad (4A-10)$$

and

$$\begin{aligned} \frac{1}{r} \frac{\partial}{\partial r} & \{ \bar{\rho} \bar{u} \bar{v} + \bar{\rho} \bar{u} \bar{v} + \bar{v} \bar{\rho} \bar{u} + \bar{u} \bar{\rho} \bar{v} + \bar{\rho} \bar{u} \bar{v} \} r + \frac{\partial}{\partial z} \{ \bar{\rho} \bar{u}^2 + \bar{\rho} \bar{u}^2 + 2 \bar{u} \bar{\rho} \bar{u} + \bar{\rho} \bar{u}^2 \} \\ = - \frac{\partial \bar{p}}{\partial z} + \frac{1}{r} \frac{\partial}{\partial r} & \left\{ \bar{\rho} \bar{\epsilon} r \left| \frac{\partial \bar{u}}{\partial r} + \frac{\partial \bar{v}}{\partial z} \right| \right\} + \frac{\partial}{\partial z} \left| 2 \bar{\rho} \bar{\epsilon} \frac{\partial \bar{u}}{\partial z} \right| - \frac{\partial}{\partial z} \left| \frac{2}{3} \bar{\rho} \bar{\epsilon} \bar{r} \right|, \end{aligned} \quad (4A-11)$$

where

$$\bar{r} = \left| \frac{1}{r} \frac{\partial}{\partial r} (\bar{v} r) + \frac{\partial \bar{u}}{\partial z} \right| \quad (4A-12)$$

Application of an order of magnitude analysis using the boundary layer approximation leads to

$$\begin{aligned} \frac{1}{r} \frac{\partial}{\partial r} & \{ \bar{\rho} \bar{u} \bar{v} + \bar{\rho} \bar{u} \bar{v} + \bar{v} \bar{\rho} \bar{u} + \bar{u} \bar{\rho} \bar{v} + \bar{\rho} \bar{u} \bar{v} \} r \\ + \frac{\partial}{\partial z} & \{ \bar{\rho} \bar{u}^2 + \bar{\rho} \bar{u}^2 + 2 \bar{u} \bar{\rho} \bar{u} + \bar{\rho} \bar{u}^2 \} = - \frac{\partial \bar{p}}{\partial z} + \frac{1}{r} \frac{\partial}{\partial r} \{ \bar{\rho} \bar{\epsilon} r \frac{\partial \bar{u}}{\partial r} \}, \end{aligned} \quad (4A-13)$$

and

$$\frac{1}{r} \frac{\partial}{\partial r} \{ \bar{\rho} \bar{v}^2 + \bar{\rho} \bar{v}^2 \} r - (\bar{\rho} + \tilde{\rho}) \frac{\tilde{w}^2}{r} = - \frac{\partial \bar{p}}{\partial r}. \quad (4A-14)$$

Integrating Equation (4A-14) with respect to  $r$ , differentiating with respect to  $z$ , and substituting into Equation (4A-13) leads to,

$$\begin{aligned} \frac{1}{r} \frac{\partial}{\partial r} & \{ \bar{\rho} \bar{u} \bar{v} + \bar{\rho} \bar{u} \bar{v} + \bar{v} \bar{\rho} \bar{u} + \bar{u} \bar{\rho} \bar{v} + \bar{\rho} \bar{u} \bar{v} \} r \\ + \frac{\partial}{\partial z} & \{ \bar{\rho} \bar{u}^2 + \bar{\rho} (\bar{u}^2 - \bar{v}^2) + 2 \bar{u} \bar{\rho} \bar{u} + (\bar{\rho} \bar{u}^2 - \bar{\rho} \bar{v}^2) - \int^r \frac{(\bar{\rho} + \tilde{\rho})(\bar{v}^2 - \tilde{w}^2)}{\gamma} d\gamma \} \\ = \frac{1}{r} \frac{\partial}{\partial r} & \{ \bar{\rho} \bar{\epsilon} r \frac{\partial \bar{u}}{\partial r} \}. \end{aligned} \quad (4A-15)$$

Multiplying Equation (4A-15) throughout by  $r$  and integrating with respect to  $r$  leads to a homogeneous ordinary differential equation with dependent variable  $z$ . This equation may be integrated with respect to  $z$  to give,

$$\begin{aligned} \int_0^\infty & \left[ \bar{\rho} \bar{u}^2 + \bar{\rho} (\bar{u}^2 - \bar{v}^2) + 2 \bar{u} \bar{\rho} \bar{u} + (\bar{\rho} \bar{u}^2 - \bar{\rho} \bar{v}^2) + \int^r \frac{(\bar{\rho} + \tilde{\rho})(\bar{v}^2 - \tilde{w}^2)}{\gamma} d\gamma \right] r dr \\ = \left[ \int_0^\infty & \bar{\rho} \bar{u}^2 r dr \right]_{z=0}. \end{aligned} \quad (4A-16)$$

The differences of small quantities in  $(\bar{u}^2 - \bar{v}^2)$  will be neglected and due to the periodic nature of the disturbance time-averaged third order products of the periodic fluctuation are zero. This leads finally to

$$\int_0^\infty [\bar{\rho}\bar{u}^2 + 2\bar{u}\bar{\rho}\bar{u}] r dr = \left[ \int_0^\infty \bar{\rho}\bar{u}^2 r dr \right]_{z=0}. \quad (4A-17)$$

In order to obtain the mean mechanical energy equation, Equation (4A-15) is multiplied throughout by  $\bar{u}(r)$ . Then integrating across the jet, and neglecting differences of small quantities and time averaged third order products of periodic fluctuations, gives

$$\begin{aligned} \frac{d}{dz} \int_0^\infty & \left[ \frac{\bar{u}^2}{2} (\bar{\rho}\bar{u} + 3\bar{\rho}\bar{u}) \right] r dr \\ &= \int_0^\infty \left[ \bar{\rho}\bar{u} \bar{u} \frac{\partial \bar{u}}{\partial z} \right] r dr + \int_0^\infty \bar{\rho}\bar{u}\bar{v} \frac{\partial \bar{u}}{\partial r} r dr - \int_0^\infty \bar{v}\bar{\rho}\bar{u} \frac{\partial \bar{u}}{\partial r} r dr - \\ &\quad - \int_0^\infty \bar{\rho}\bar{\epsilon} \left( \frac{\partial \bar{u}}{\partial r} \right)^2 r dr \end{aligned} \quad (4A-18)$$

The periodic fluctuation kinetic energy flux equation is obtained by multiplying Equation (4A-5) throughout by  $\bar{u}^i$ .

Now if the time dependent component of the random shear stresses is related to the periodic diviatoric stress tensor,  $\bar{d}_i^j$ , through an isotropic eddy viscosity  $\bar{\epsilon}$ , and that,

$$[\langle \rho u^i j u_i^j \rangle + \langle u^j \rho' u_i^j \rangle + \langle u_i \rho' u^j \rangle - 2 \langle \rho' u^i j u_i^j \rangle] - \overline{[ ]} = -2\bar{\epsilon} \bar{d}_i^j, \quad (4A-19)$$

where  $\overline{[ ]}$  denotes the time average of the first bracketed term on the left-hand side of Equation (4A-19), then, making use of Equation (4A-7), it follows that

$$\begin{aligned} \bar{u}^i & \left[ \langle \rho u^i j u_i^j \rangle + \langle u^j \rho' u_i^j \rangle + \langle u_i \rho' u^j \rangle - 2 \langle \rho' u^i j u_i^j \rangle \right] \\ &= -2\bar{u}^i (\bar{\rho}\bar{\epsilon}\bar{d}_i^j + \bar{\rho}\bar{\epsilon}\bar{d}_i^j). \end{aligned} \quad (4A-20)$$

Using Equation (4A-20) in Equation (4A-5) after multiplication by  $\bar{u}^i$  and taking the time average leads finally to

$$\begin{aligned}
& \frac{1}{2} \{ \bar{\rho} \bar{u}^j \bar{u}_i \bar{u}^i + \bar{u}^j \bar{\rho} \bar{u}_i \bar{u}^i + \bar{\rho} \bar{u}^j \bar{u}_i \bar{u}^i + \bar{\rho} \bar{u}^j \bar{u}_i \bar{u}^i \}_{,j} \\
& + \{ \bar{\rho} \bar{u}^j \bar{u}^i + \bar{u}^j \bar{\rho} \bar{u}^i + \bar{\rho} \bar{u}^j \bar{u}^i + \bar{\rho} \bar{u}^j \bar{u}^i \}_{,j} \\
& = - \bar{u}^i [\bar{\rho} \delta_i^j]_{,j} + \frac{1}{2} [\bar{\rho} \bar{\epsilon} (\bar{u}^i \bar{u}_i)^{,j}]_{,j} + [\bar{\rho} \bar{\epsilon} \bar{u}^i \bar{u}^j]_{,j} \\
& - \bar{\rho} \bar{\epsilon} \bar{u}^i_{,j} [\bar{u}_i^{,j} + \bar{u}^j_{,i}] - \frac{2}{3} [\bar{\rho} \bar{\epsilon} e_k^k \delta_i^j]_{,j} \quad (4A-21)
\end{aligned}$$

The tensors in Equation (4A-21) may be replaced by their physical components and after applying the boundary layer approximations to the resulting scalar equation, Equation (4A-21) becomes

$$\begin{aligned}
& \frac{1}{r} \frac{\partial}{\partial r} \left[ \frac{1}{2} \left\{ \bar{\rho} \bar{v} (\bar{u}^2 + \bar{v}^2 + \bar{w}^2) + \bar{\rho} \bar{v} (\bar{u}^2 + \bar{v}^2 + \bar{w}^2) \right\} r \right] + \\
& + \frac{\partial}{\partial z} \left[ \frac{1}{2} \left\{ \bar{\rho} \bar{u} (\bar{u}^2 + \bar{v}^2 + \bar{w}^2) + \bar{\rho} \bar{u} (\bar{u}^2 + \bar{v}^2 + \bar{w}^2) \right\} \right] = - \left\{ \bar{v} \frac{\partial \bar{p}}{\partial r} + \frac{\bar{w}}{r} \frac{\partial \bar{p}}{\partial \phi} + \bar{u} \frac{\partial \bar{p}}{\partial z} \right\} \\
& - \left\{ \bar{\rho} \bar{v}^2 \frac{\partial \bar{v}}{\partial r} + \bar{\rho} \bar{u}^2 \frac{\partial \bar{u}}{\partial z} + \bar{\rho} \bar{u} \bar{v} \frac{\partial \bar{u}}{\partial r} + \bar{v} \bar{\rho} \frac{\bar{w}^2}{r} + \bar{\rho} \bar{u} \left( \bar{v} \frac{\partial \bar{u}}{\partial r} + \bar{u} \frac{\partial \bar{u}}{\partial z} \right) \right\} + \\
& + \frac{1}{r} \frac{\partial}{\partial r} \left\{ \bar{\rho} \bar{\epsilon} r \left[ \frac{\partial}{\partial r} \left( \frac{\bar{u}^2 + \bar{v}^2 + \bar{w}^2}{2} \right) + \frac{1}{3} \bar{v} \frac{\partial \bar{v}}{\partial r} + \bar{w} \frac{\partial \bar{v}}{\partial \phi} - \frac{\bar{w}^2}{r} + \bar{u} \frac{\partial \bar{v}}{\partial z} \right. \right. \\
& \left. \left. - \frac{2}{3} \frac{\bar{v}}{r} \frac{\partial \bar{w}}{\partial \phi} - \frac{2}{3} \frac{\bar{v}^2}{r} - \frac{2}{3} \bar{v} \frac{\partial \bar{u}}{\partial z} \right] \right\} - \phi, \quad (4A-22)
\end{aligned}$$

where,

$$\begin{aligned}
\phi = & \bar{\rho} \bar{\epsilon} \left[ 2 \left\{ \left( \frac{\partial \bar{v}}{\partial r} \right)^2 + \frac{1}{r^2} \left( \frac{\partial \bar{w}}{\partial \phi} + \bar{v} \right)^2 + \left( \frac{\partial \bar{u}}{\partial z} \right)^2 \right\} \right. \\
& + \left\{ \frac{1}{r} \left( \frac{\partial \bar{u}}{\partial \phi} \right) + \frac{\partial \bar{w}}{\partial z} \right\}^2 + \left\{ \left( \frac{\partial \bar{u}}{\partial r} \right) + \left( \frac{\partial \bar{v}}{\partial z} \right) \right\}^2 + \left\{ \frac{1}{r} \left( \frac{\partial \bar{v}}{\partial \phi} \right) - \frac{\bar{w}}{r} + \left( \frac{\partial \bar{w}}{\partial r} \right) \right\}^2 \\
& \left. - \frac{2}{3} \left\{ \left( \frac{\partial \bar{v}}{\partial r} \right) + \frac{1}{r} \left( \frac{\partial \bar{w}}{\partial \phi} + \bar{v} \right) + \left( \frac{\partial \bar{u}}{\partial z} \right) \right\}^2 \right] \quad (4A-23)
\end{aligned}$$

Multiplying Equation (4A-22) throughout by  $r$  and integrating with respect to  $r$  across the jet, neglecting time averaged third order products of periodic fluctuations and including only the most significant terms leads to,

$$\begin{aligned}
 \frac{d}{dz} \int_0^\infty \frac{1}{2} \bar{\rho} \bar{u} (\bar{u}^2 + \bar{v}^2 + \bar{w}^2) r dr = & - \int_0^\infty \left| \bar{v} \frac{\partial \bar{p}}{\partial r} + \frac{\bar{w}}{r} \frac{\partial \bar{p}}{\partial \phi} + \bar{u} \frac{\partial \bar{p}}{\partial z} \right| r dr - \\
 & - \int_0^\infty \bar{\rho} \bar{u} \bar{v} \frac{\partial \bar{u}}{\partial r} r dr - \int_0^\infty \phi r dr
 \end{aligned} \tag{4A-24}$$

## APPENDIX 4B

### TENSOR NOTATION AND PHYSICAL NOTATION

The following definitions, notation, and relationships are useful in the derivation of the equations of motion to be found in this report.

In a cylindrical coordinate system the physical components of a velocity tensor  $u_i$  are given by,  $u_1 = v$ ,  $u_2 = wr$ , and  $u_3 = u$ , for the physical coordinate system,  $x^1 = r$ ,  $x^2 = \phi$ , and  $x^3 = z$ .

The covariant derivative of a tensor  $u_i$  with respect to  $x^j$  is defined by

$$u_{i,j} = \frac{\partial u_i}{\partial x^j} - \left\{ \begin{matrix} s \\ i \ j \end{matrix} \right\} u_s .$$

The covariant derivative of a tensor  $u^i$  with respect to  $x^j$  is defined by

$$u^{i,j} = \frac{\partial u^i}{\partial x^j} + \left\{ \begin{matrix} i \\ j \ s \end{matrix} \right\} u_s .$$

For a cylindrical coordinate the only non-zero Christoffel symbols,  $\left\{ \begin{matrix} s \\ p \ q \end{matrix} \right\}$ , are

$$\left\{ \begin{matrix} 1 \\ 22 \end{matrix} \right\} = -r \quad \text{and} \quad \left\{ \begin{matrix} 2 \\ 12 \end{matrix} \right\} = \left\{ \begin{matrix} 2 \\ 21 \end{matrix} \right\} = \frac{1}{r} .$$

Using these definitions for the cylindrical coordinate system leads to,

$$\begin{aligned} u_{1,1} &= \frac{\partial u_1}{\partial x^1} \equiv \frac{\partial v}{\partial r}, \quad u_{1,2} = \frac{\partial u_1}{\partial x^2} - \frac{u_2}{r} \equiv \frac{\partial v}{\partial \phi} - w, \quad u_{1,3} = \frac{\partial u_1}{\partial x^3} \equiv \frac{\partial v}{\partial z} \\ u_{2,1} &= \frac{\partial u_2}{\partial x^1} - \frac{u_2}{r} \equiv \frac{\partial w}{\partial r} - w, \quad u_{2,2} = \frac{\partial u_2}{\partial x^2} + ru_1 \equiv \frac{\partial w}{\partial \phi} + vr, \quad u_{2,3} = \frac{\partial u_2}{\partial x^3} \equiv \frac{\partial w}{\partial z} \\ u_{3,1} &= \frac{\partial u_3}{\partial x^1} \equiv \frac{\partial u}{\partial r}, \quad u_{3,2} = \frac{\partial u_3}{\partial x^2} \equiv \frac{\partial u}{\partial \phi}, \quad u_{3,3} = \frac{\partial u_3}{\partial x^3} \equiv \frac{\partial u}{\partial z} . \end{aligned}$$

The covariant tensor  $u_i$  may be related to the contravariant tensor  $u^j$  through the metric tensor  $g_{ij}$  and its conjugate  $g^{ij}$ , such that

$$u_i = g_{ij} u^j \quad \text{and} \quad u^j = g^{ji} u_i .$$

For cylindrical coordinates

$$g_{11} = 1, \quad g_{22} = r^2, \quad g_{33} = 1, \quad g_{pq} = 0, p \neq q$$

and

$$g^{11} = 1, \quad g^{22} = 1/r^2, \quad g^{33} = 1, \quad g^{pq} = 0, p \neq q .$$

Thus,  $u_1 = u^1$ ,  $u_2 = r^2 u^2$ ,  $u_3 = u^3$ .

There exists a summation convention such that whenever an index is repeated in a given term, the term is to be summed over that index from 1 to N.

$$\text{i.e. } u_j x^j = \sum_{j=1}^N u_j x^j = u_1 x^1 + u_2 x^2 + \dots + u_N x^N.$$

- As an example of the use of tensor notation, consider the equation of continuity which may be written,

$$\frac{\partial p}{\partial t} + (\rho u^i)_{,i} = 0.$$

Using the summation convention this becomes

$$\frac{\partial p}{\partial t} + (\rho u^1)_{,1} + (\rho u^2)_{,2} + (\rho u^3)_{,3}.$$

Using the expression for the covariant derivative of a contravariant tensor and omitting zero Christoffel symbols, gives,

$$\frac{\partial p}{\partial t} + \frac{\partial \rho u^1}{\partial x^1} + \frac{\partial \rho u^2}{\partial x^2} + \left[ \begin{matrix} 2 & 1 \\ 1 & 3 \end{matrix} \right] \rho u^1 + \frac{\partial \rho u^3}{\partial x^3} = 0.$$

Introducing the physical components of the velocity tensor gives,

$$\frac{\partial p}{\partial t} + \frac{\partial \rho v}{\partial r} + \frac{\partial \rho w/r}{\partial \phi} + \frac{\rho v}{r} + \frac{\partial \rho u}{\partial z} = 0,$$

or

$$\frac{\partial p}{\partial t} + \frac{1}{r} \frac{\partial \rho vr}{\partial r} + \frac{1}{r} \frac{\partial \rho w}{\partial \phi} + \frac{\partial \rho u}{\partial z} = 0.$$

## APPENDIX 4C

LINEARIZED EQUATIONS OF MOTION FOR A COMPRESSIBLE,  
VISCOUS, HEAT-CONDUCTING FLUID IN CYLINDRICAL  
COORDINATES AND INVISCID STABILITY EQUATIONS

In this section the equations of motion for a compressible axisymmetric flow are derived. The viscous terms are derived in full though no solution to the complete equations is attempted in this report. These complete equations do provide the basis for compressible, viscous stability solutions.

The equation of continuity was derived in Appendix 4B and may be written,

$$\frac{\partial p}{\partial t} + \frac{1}{r} \frac{\partial pvr}{\partial r} + \frac{1}{r} \frac{\partial pw}{\partial \phi} + \frac{\partial pu}{\partial z} = 0 \quad (4C-1)$$

The momentum equations may be written in tensor form as,

$$p \left\{ \frac{\partial u_i}{\partial t} + u_j u_{i,j} \right\} = \sigma_{i,j}^j, \quad (4C-2)$$

where

$$\sigma_{i,j}^j = - p \delta_{i,j}^j + [2\mu e_i^j + (\zeta - \frac{2}{3} \mu) e_k^k \delta_{i,j}^j] \quad (4C-3)$$

and

$$e_i^j = \frac{1}{2} g^{jq} \left\{ u_{i,q} + u_{q,i} \right\}. \quad (4C-4)$$

The thermal energy equation may be written,

$$\rho C_v \left\{ \frac{\partial T}{\partial t} + u_j T_{,j} \right\} = \sigma_{i,j}^k u_{i,k}^j + g^{ij} (K T_{,j}),_i \quad (4C-5)$$

The equation of state for a perfect gas is,

$$p = \rho RT. \quad (4C-6)$$

Expanding the convection, viscous and heat-conduction terms in Equations (4C-2) and (4C-5) and writing the velocity tensors in their physical components leads finally to

$$\begin{aligned} p \left\{ \frac{\partial v}{\partial t} + v \frac{\partial v}{\partial r} + \frac{w}{r} \frac{\partial v}{\partial \phi} + u \frac{\partial v}{\partial z} - \frac{w^2}{r} \right\} &= - \frac{\partial p}{\partial r} + \frac{1}{r} \frac{\partial}{\partial r} \left\{ 2\mu r \frac{\partial v}{\partial r} \right\} + \\ &+ \frac{1}{r} \frac{\partial}{\partial \phi} \left\{ u \left[ \frac{1}{r} \frac{\partial v}{\partial \phi} + \frac{\partial w}{\partial r} - \frac{w}{r} \right] \right\} + \frac{\partial}{\partial z} \left\{ u \left[ \frac{\partial v}{\partial z} + \frac{\partial u}{\partial r} \right] \right\} + \\ &+ \frac{\partial}{\partial r} \left\{ (\zeta - \frac{2}{3} \mu) \Delta \right\} - \frac{2\mu}{r^2} \left\{ \frac{\partial w}{\partial \phi} + v \right\}, \end{aligned} \quad (4C-7)$$

$$\begin{aligned} p \left\{ \frac{\partial w}{\partial t} + v \frac{\partial w}{\partial r} + \frac{w}{r} \frac{\partial w}{\partial \phi} + u \frac{\partial w}{\partial z} + \frac{vw}{r} \right\} &= - \frac{1}{r} \frac{\partial p}{\partial \phi} + \frac{1}{r} \frac{\partial}{\partial r} \left\{ \mu r \left[ \frac{\partial w}{\partial r} + \frac{1}{r} \frac{\partial v}{\partial \phi} - \frac{w}{r} \right] \right\} + \\ &+ \frac{2}{r^2} \frac{\partial}{\partial \phi} \left\{ u \left[ \frac{\partial w}{\partial \phi} + v \right] \right\} + \frac{\partial}{\partial z} \left\{ u \left[ \frac{\partial w}{\partial z} + \frac{1}{r} \frac{\partial u}{\partial \phi} \right] \right\} + \end{aligned}$$

$$+ \frac{1}{r} \frac{\partial}{\partial \phi} \left| \left( \zeta - \frac{2}{3} \mu \right) \Delta \right| + \frac{\mu}{r} \left| \frac{\partial w}{\partial r} + \frac{1}{r} \frac{\partial v}{\partial \phi} - \frac{w}{r} \right|, \quad (4C-8)$$

$$\rho \left| \frac{\partial u}{\partial t} + v \frac{\partial u}{\partial r} + \frac{w}{r} \frac{\partial u}{\partial \phi} + u \frac{\partial u}{\partial z} \right| = - \frac{\partial p}{\partial z} + \frac{1}{r} \frac{\partial}{\partial r} \left| \mu r \left| \frac{\partial u}{\partial r} + \frac{\partial v}{\partial z} \right| \right| + \\ + \frac{1}{r} \frac{\partial}{\partial \phi} \left| \mu \left| \frac{1}{r} \frac{\partial u}{\partial \phi} + \frac{\partial w}{\partial z} \right| \right| + \frac{\partial}{\partial z} \left| 2\mu \frac{\partial u}{\partial z} \right| + \frac{\partial}{\partial z} \left| \left( \zeta - \frac{2}{3} \mu \right) \Delta \right|, \quad (4C-9)$$

and

$$\rho C_v \left| \frac{\partial T}{\partial t} + v \frac{\partial T}{\partial r} + \frac{w}{r} \frac{\partial T}{\partial \phi} + u \frac{\partial T}{\partial z} \right| = - p \Delta + \left( \zeta - \frac{2}{3} \mu \right) \Delta^2 + \\ + 2\mu \left| \left( \frac{\partial v}{\partial r} \right)^2 + \left( \frac{1}{r} \frac{\partial w}{\partial \phi} + \frac{v}{r} \right)^2 + \left( \frac{\partial u}{\partial z} \right)^2 \right| + \\ + \mu \left| \left( \frac{1}{r} \frac{\partial v}{\partial \phi} + \frac{\partial w}{\partial r} - \frac{w}{r} \right)^2 + \left( \frac{\partial v}{\partial z} + \frac{\partial u}{\partial r} \right)^2 + \left( \frac{1}{r} \frac{\partial u}{\partial \phi} + \frac{\partial w}{\partial z} \right)^2 \right| + \\ + \frac{1}{r} \frac{\partial}{\partial r} \left| K r \frac{\partial T}{\partial r} \right| + \frac{1}{r^2} \frac{\partial}{\partial \phi} \left| K \frac{\partial T}{\partial \phi} \right| + \frac{\partial}{\partial z} \left| K \frac{\partial T}{\partial z} \right|, \quad (4C-10)$$

where

$$\Delta = \left| \frac{1}{r} \frac{\partial vr}{\partial r} + \frac{1}{r} \frac{\partial w}{\partial \phi} + \frac{\partial u}{\partial z} \right| \quad (4C-11)$$

The case of an axisymmetric, parallel mean flow jet will now be considered. The equations above are separated into their time-independent and time-dependent components. The equations are linearized and the fluctuation equations are obtained by subtracting the time-averaged equations from the complete separated equations. For the axisymmetric parallel jet flow, the following simplifications are possible,

$$\frac{\partial}{\partial \phi} \overline{( )} = 0, \quad \frac{\partial}{\partial z} \overline{( )} = 0, \quad \bar{w} = 0, \quad \bar{v} = 0.$$

Nondimensionalizing the equations with respect to the jet exit velocity, the jet radius and the ambient density and pressure leads to,

$$\frac{\partial p'}{\partial t} + \bar{\rho} \left| \frac{1}{r} \frac{\partial v' r}{\partial r} + \frac{1}{r} \frac{\partial w'}{\partial \phi} + \frac{\partial u'}{\partial z} \right| + v' \frac{dp'}{dr} + \bar{u} \frac{\partial p'}{\partial z} = 0, \quad (4C-12)$$

$$\bar{\rho} \left| \frac{\partial v'}{\partial t} + \bar{u} \frac{\partial v'}{\partial z} \right| = - \frac{1}{\gamma M_J^2} \frac{\partial p'}{\partial r} + \frac{1}{R_J} \left| \frac{2}{r} \frac{\partial}{\partial r} \left[ \bar{\mu} r \frac{\partial v'}{\partial r} \right] \right| + \\ + \frac{1}{r} \frac{\partial}{\partial \phi} \left| \bar{\mu} \left( \frac{1}{r} \frac{\partial v'}{\partial \phi} + \frac{\partial w'}{\partial r} - \frac{w'}{r} \right) \right| + \frac{\partial}{\partial z} \left| \bar{\mu} \left( \frac{\partial v'}{\partial z} + \frac{\partial u'}{\partial r} \right) + \mu' \frac{d\bar{u}}{dr} \right| + \\ + \frac{\partial}{\partial r} \left| \left( \bar{\zeta} - \frac{2}{3} \bar{\mu} \right) \Delta' \right| - \frac{2\bar{\mu}}{r^2} \left| \frac{\partial w'}{\partial \phi} + v' \right|, \quad (4C-13)$$

$$\begin{aligned} \bar{\rho} \left[ \frac{\partial w'}{\partial t} + \bar{u} \frac{\partial w'}{\partial z} \right] = & - \frac{1}{\gamma M_J^2 r} \frac{\partial p'}{\partial \phi} + \frac{1}{R_J} \left[ \frac{1}{r} \frac{\partial}{\partial r} \left[ \bar{u} r \left( \frac{\partial w'}{\partial r} + \frac{1}{r} \frac{\partial v'}{\partial \phi} - \frac{w'}{r} \right) \right] + \right. \\ & + \frac{2}{r^2} \frac{\partial}{\partial \phi} \left[ \bar{u} \left( \frac{\partial w'}{\partial \phi} + v' \right) \right] + \frac{\partial}{\partial z} \left[ \bar{u} \left( \frac{\partial w'}{\partial z} + \frac{1}{r} \frac{\partial u'}{\partial \phi} \right) \right] + \\ & \left. + \frac{1}{r} \frac{\partial}{\partial \phi} \left[ \left( \bar{z} - \frac{2}{3} \bar{u} \right) \Delta' \right] + \frac{\bar{u}}{r} \left[ \frac{\partial w'}{\partial r} + \frac{1}{r} \frac{\partial v'}{\partial \phi} - \frac{w'}{r} \right] \right], \quad (4C-14) \end{aligned}$$

$$\begin{aligned} \bar{\rho} \left[ \frac{\partial u'}{\partial t} + \bar{u} \frac{\partial u'}{\partial z} + v' \frac{d\bar{u}}{dr} \right] = & - \frac{1}{\gamma M_J^2} \frac{\partial p'}{\partial z} + \frac{1}{R_J} \left[ \frac{1}{r} \frac{\partial}{\partial r} \left[ \bar{u} r \left( \frac{\partial u'}{\partial r} + \frac{\partial v'}{\partial z} \right) + u' r \frac{d\bar{u}}{dr} \right] + \right. \\ & + \left. \frac{1}{r} \frac{\partial}{\partial \phi} \left[ \bar{u} \left( \frac{1}{r} \frac{\partial u'}{\partial \phi} + \frac{\partial w'}{\partial z} \right) \right] + 2 \frac{\partial}{\partial z} \left[ \bar{u} \frac{\partial u'}{\partial z} \right] + \frac{\partial}{\partial z} \left[ \left( \bar{z} - \frac{2}{3} \bar{u} \right) \Delta' \right] \right], \quad (4C-15) \end{aligned}$$

$$\begin{aligned} \bar{\rho} \left[ \frac{\partial T'}{\partial t} + \bar{u} \frac{\partial T'}{\partial z} + v' \frac{d\bar{T}}{dr} \right] = & - (\gamma - 1) \bar{p} \Delta' + \\ & + \frac{\gamma(\gamma-1)M_J^2}{R_J} \left[ 2\bar{u} \left[ \frac{d\bar{u}}{dr} \frac{\partial v'}{\partial z} + \frac{d\bar{u}}{dr} \frac{\partial u'}{\partial r} \right] + u' \left( \frac{d\bar{u}}{dr} \right)^2 \right] \\ & + \frac{\gamma}{\sigma R_J} \left[ \frac{1}{r} \frac{\partial}{\partial r} \left[ \bar{K} r \frac{\partial T'}{\partial r} + K' r \frac{d\bar{T}}{dr} \right] + \frac{1}{r^2} \frac{\partial}{\partial \phi} \left[ \bar{K} \frac{\partial T'}{\partial \phi} \right] + \frac{\partial}{\partial z} \left[ \bar{K} \frac{\partial T'}{\partial z} \right] \right], \quad (4C-16) \end{aligned}$$

and

$$\frac{p'}{\bar{\rho}} = \frac{\rho'}{\bar{\rho}} + \frac{T'}{\bar{T}}, \quad (4C-17)$$

where primes denote fluctuating quantities and,

$$R_J = \frac{\bar{\rho}_o \bar{u}_J \bar{r}_J}{\bar{\mu}_o}, \quad M_J = \frac{\bar{u}_J}{\bar{a}_o}, \quad \sigma = \frac{\mu_o}{\bar{K}_o}.$$

In order to derive the inviscid stability equations the equations are Fourier transformed with respect to  $z$  and  $t$  and the azimuthal variation is decomposed into a Fourier series such that, typically,

$$\sum_{n=0}^{\infty} \hat{q}(r; \alpha, n, \omega) e^{in\phi} = \frac{1}{4\pi^2} \int_{-\infty}^{\infty} \int_{-\infty}^{\infty} e^{i(\omega t - \alpha z)} q'(r; z, \phi, t) dz dt \quad (4C-18)$$

The inviscid transformed form of equations (4C-12) through (4C-17) are,

$$i(\alpha\bar{u} - \omega)\hat{\rho} + \bar{\rho} \left[ \frac{d\hat{v}}{dr} + \frac{\hat{v}}{r} + \frac{in}{r}\hat{w} + i\alpha\hat{u} \right] + \frac{d\bar{\rho}}{dr}\hat{v} = 0, \quad (4C-19)$$

$$i\bar{\rho}(\alpha\bar{u} - \omega)\hat{v} = -\frac{1}{\gamma M_J^2} \frac{d\hat{\rho}}{dr}, \quad (4C-20)$$

$$i\bar{\rho}(\alpha\bar{u} - \omega)\hat{w} = -\frac{in}{\gamma M_J^2 r} \hat{\rho}, \quad (4C-21)$$

$$i\bar{\rho}(\alpha\bar{u} - \omega)\hat{u} + \bar{\rho} \frac{d\bar{u}}{dr}\hat{v} = -\frac{i\alpha}{\gamma M_J^2} \hat{\rho}, \quad (4C-22)$$

$$i\bar{\rho}(\alpha\bar{u} - \omega)\hat{T} + \bar{\rho} \frac{dT}{dr}\hat{v} = -(\gamma-1)\bar{\rho}\bar{T} \left[ \frac{d\hat{v}}{dr} + \frac{\hat{v}}{r} + \frac{in\hat{w}}{r} + i\alpha\hat{u} \right], \quad (4C-23)$$

and

$$\frac{\hat{\rho}}{\bar{\rho}} = \frac{\hat{\rho}}{\rho} + \frac{\hat{T}}{\bar{T}}$$

Assuming the static pressure is constant, these equations may be reduced to a pair of simultaneous ordinary differential equations for the transformed pressure and radial velocity fluctuations:

$$i\bar{\rho} \left\{ (\alpha\bar{u} - \omega) \frac{1}{r} \frac{d\hat{v}_r}{dr} - \alpha \frac{d\bar{u}}{dr} \hat{v} \right\} = -\left\{ \lambda^2 + \left( \frac{n}{r} \right)^2 \right\} \frac{\hat{\rho}}{\gamma M_J^2}, \quad (4C-25)$$

and

$$i\bar{\rho}(\alpha\bar{u} - \omega)\hat{v} = -\frac{1}{\gamma M_J^2} \frac{d\hat{\rho}}{dr}, \quad (4C-20)$$

where

$$\lambda^2 = \alpha^2 - \frac{(\alpha\bar{u} - \omega)^2}{\bar{a}^2}, \quad (4C-26)$$

and  $\bar{a}$  is the speed of sound in the ambient medium nondimensionalized with respect to the jet exit velocity. Equations (4C-25) and (4C-20) are in a convenient form for numerical integration and this form is used in the present calculations. However, the radial velocity fluctuation may be eliminated leading to a second order differential equation for  $\hat{\rho}$ , in the form,

$$\frac{1}{r} \frac{\partial}{\partial r} \left[ r \frac{d\hat{\rho}}{dr} \right] + 2 \left[ \frac{1}{\bar{a}} \frac{d\bar{a}}{dr} - \frac{\alpha}{(\alpha\bar{u} - \omega)} \frac{d\bar{u}}{dr} \right] \frac{d\hat{\rho}}{dr} - \left\{ \lambda^2 + \left( \frac{n}{r} \right)^2 \right\} \hat{\rho} = 0. \quad (4C-27)$$

Equation (4C-27) is recognized as the homogeneous form of Lilley's equation (ref. 4) which characterizes the propagation of a pressure fluctuation through a parallel flow with radial velocity and speed of sound gradients. The solutions to Equation (4C-27) in regions where  $\bar{a}$  and  $\bar{u}$  are constant provide the boundary conditions in the numerical eigenvalue problem.

## APPENDIX 4D

### ANALYTICAL AND NUMERICAL REPRESENTATION OF THE MEAN FLOW SHAPE FUNCTIONS

In this appendix several different shape functions, used to describe the mean flow profile, will be discussed. It will be found that the most satisfactory representation uses an analytic expression in the annular mixing region and a numerical solution of the boundary layer equations downstream of the end of the potential core.

Firstly, some of the physical characteristics of the jet flow and some of the numerical requirements will be discussed. It is convenient, for the purposes of computation to divide the jet into two regions, the annular mixing region and the flow downstream of the end of the potential core. In the annular mixing region the mean velocity may be defined in terms of two local characteristic parameters, the jet width,  $b$ , that is the radial distance from the edge of the potential core to the radial point at which  $\bar{U} = .5$ , and the potential core radius. Downstream of the end of the potential core the mean velocity is conveniently described in terms of the local half width, that is the radial location at which the mean velocity is one half its centerline value, and the jet centerline velocity. The mean velocity profile is characteristic of a two-dimensional shear layer close to the jet exit. The mean velocity is constant and its radial derivatives are zero in the potential core region. At the end of the annular mixing region a transition region exists which matches the flow in the annular mixing region with the true fully developed jet flow. In this region the curvature of the mean velocity profile on the jet centerline adjusts from its zero value in the potential core to its fully preserved, finite value. Similarity solutions based on an eddy viscosity hypothesis lead to an error function profile close to the jet exit and a rational function in the fully developed jet. The characteristics of the mean velocity profile in the annular mixing region are also observed experimentally to be preserved downstream of the end of the potential core. From the numerical computation standpoint it is most convenient to have an analytic definition of the mean velocity shape function. In order to properly integrate the inviscid stability equations, it is necessary to integrate along a contour in the complex space plane. Such an excursion requires the definition of the mean velocity and its derivative at that point. These values can be evaluated using a Taylor expansion about a point on the real axis. The accuracy of the computed mean velocity depends on both the distance of the complex point to the point on the real axis and the accuracy with which the higher order derivatives of the mean velocity may be evaluated. Calculations have shown that eight or more derivatives of the mean velocity are required to permit significantly decaying solutions to be properly obtained. However, if the mean velocity is an analytic function, its value is exactly obtained at any point in the complex plane.

For these reasons the mean velocity in the mixing region may be described in terms of an error function. This function has only a minimal discontinuity in derivatives at the edge of the potential core and is known to be a solution for the turbulent mixing layer based on an eddy viscosity approach. Townsend<sup>54</sup> defines the velocity profile as

$$\bar{U} = (A/2\pi)^{\frac{1}{2}} \int_{\zeta_0}^{\infty} \exp [-A(\zeta - \zeta_0)^2/2] d\zeta, \quad (4D-1)$$

where  $A = 300$ ,  $\zeta_0 = .03$ , and  $\zeta = (r-1)/x$ . If it is assumed that the potential core length in this case is 8 radii, then the velocity profile may be written in terms of the half width,  $b$ , and the potential core radius,  $h$ , as

$$\bar{u} = .5 [1 - \operatorname{erf}\{\psi\}] \quad (4D-2)$$

where

$$\operatorname{erf}\{\psi\} = \frac{2}{\sqrt{\pi}} \int_0^{\psi} e^{-t^2} dt, \quad (4D-3)$$

$$\psi = 1.8984 (n - 1), \quad (4D-4)$$

and

$$n = (r - h)/b. \quad (4D-5)$$

Far downstream of the end of the potential core the mean velocity profile may be given analytically in the form,

$$\bar{u} = \bar{u}_c / (1 + .4142 \xi^2)^2 \quad (4D-6)$$

where

$$\xi = r/b. \quad (4D-7)$$

Experiments have shown that a good fit to the data is also given by the curves,

$$\bar{u} = \bar{u}_c \exp[-.6931 \xi^2]. \quad (4D-8)$$

In order to maintain continuity in the axial direction the two types of profile, (4D-2) and (4D-6), must be matched in the transition region. Two separate approaches are considered in order to carry out this matching.

Since similarity of mean velocity and turbulence profiles is observed to extend past the end of the potential core, the first matching procedure continues the error function profile downstream of the end of the potential core. This clearly requires a new evaluation of the half-velocity radius. In terms of  $\xi$  the equivalent value of  $n$  is found to be

$$n = [n_1 (1 - \xi) + \xi n_{.5}] \quad (4D-9)$$

where  $n_1$  is the value of  $n$  at which  $\bar{u}(n) = \bar{u}_c$  and  $n_{.5}$  is the value of  $n$  at which  $\bar{u}(n) = .5 \bar{u}_c$ . Now from the integral form of the momentum equation,

$$\int_0^{\infty} \bar{\rho} \bar{u}^2 r dr = 1/2 T_J, \quad (4D-10)$$

we obtain,

$$b^2 = (2T_J \psi_2)^{\frac{1}{2}}, \quad (4D-11)$$

where

$$\psi_2 = \int_0^\infty \bar{\rho} \bar{u}^2(n) \xi d\xi \quad (4D-12)$$

where  $n$  is given by (4D-9). The values of  $n_1$  and  $n_{1.5}$  are only implicitly defined in terms of  $\bar{u}_c$ . However, it is more convenient to describe the mean velocity profile everywhere in terms of  $b$ . Thus, an iterative search is used to define  $\bar{u}_c$  and hence  $n_1$  and  $n_{1.5}$  in terms of  $b$ . This transitional profile is continued until the second derivative on the jet axis matches that of Equation (4D-8). Then Equation (4D-8) is used to define the mean flow further downstream. The mean velocity profiles defined in this way are shown in Figure 4D.1 for three different values of  $b$ , corresponding to a profile in the annular mixing region, the transition region and the fully developed jet flow. The main difficulty with this procedure is that it leads to a finite mean velocity radial derivative on the jet centerline which is physically impossible. It is also found that the transition is not smooth enough to prevent discontinuous axial changes in the stability characteristics. In this region wave components of nearly all azimuthal mode numbers and frequencies are decaying. A decaying solution is extremely sensitive to changes in the mean velocity profile.

Matching the annular mixing region with the developed jet flow, for both the mean velocity and its derivative, with analytic shape functions is thus clearly seen to be a complicated procedure. It may be concluded that the best description of the mean velocity profiles downstream of the end of the potential core can be obtained by numerically solving the boundary layer equations. The two equation turbulence models described by Launder *et al* 56 has been used. This model uses a system of differential equations for the axial mean velocity, the stagnation enthalpy, the turbulence kinetic energy, and the decay rate of turbulence energy. Use of the last equation eliminates the need to provide an algebraic formula for the turbulence length scale. The equations have been solved using the finite-difference procedure of Patankar and Spalding<sup>95</sup>. The initial value of the mean velocity profile is given by Equation (4D-2) at the end of the potential core. The first four radial derivatives of the axial mean velocity are also calculated at the same time to permit evaluation of the mean velocity on small excursions into the complex space plane. The calculated shape functions, which are now functions of the jet width as well as the coordinate,  $\xi = r/b$ , are shown in Figure 4.3 for several values of  $b$ .

Thus, the mean velocity shape function is described by an analytic function in the annular mixing region and a numerical solution of the boundary layer equations downstream of the end of the potential core.

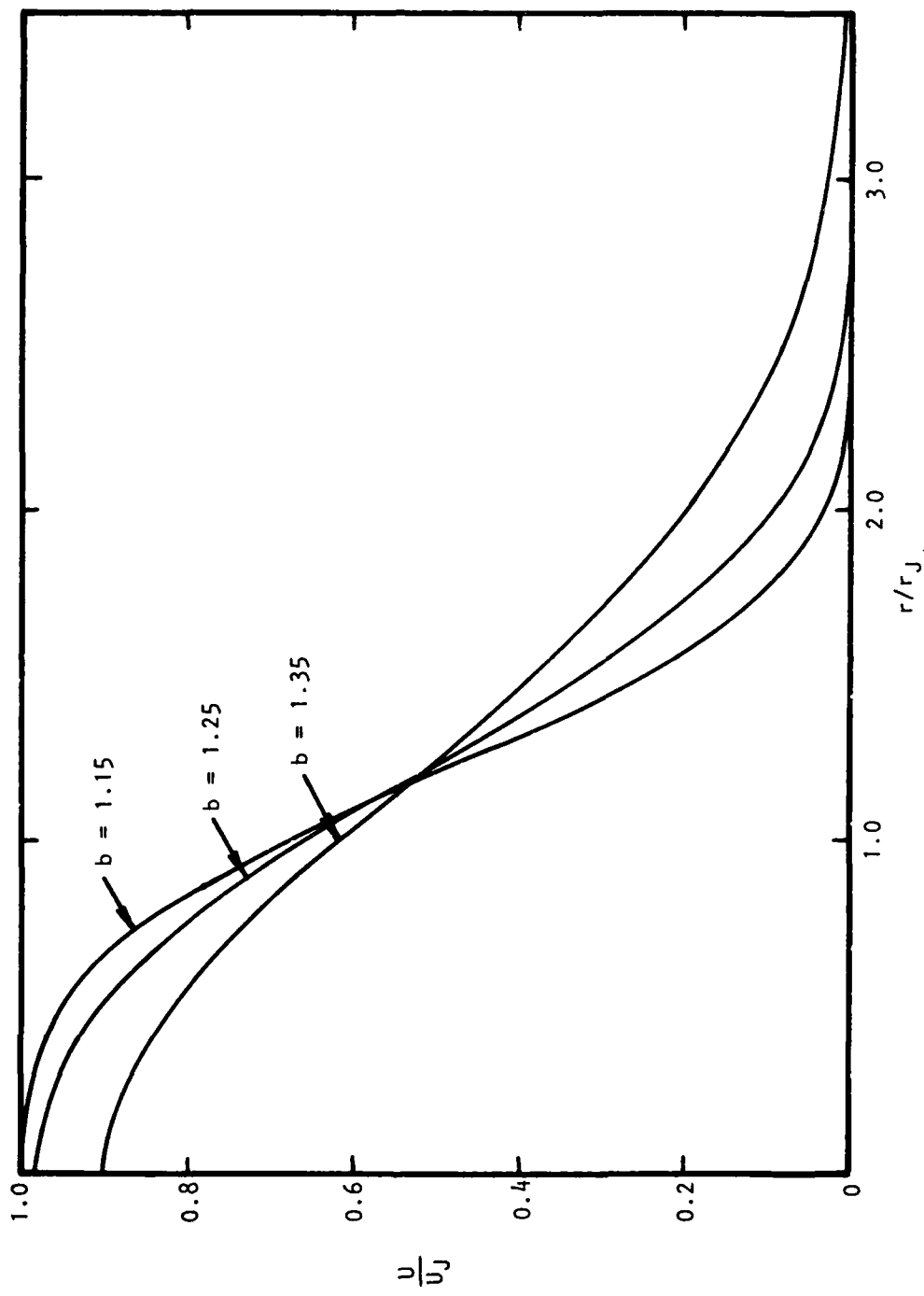


Figure 4D-1 Mean Velocity Profiles Obtained from Literature Search

APPENDIX 4E

EIGENFUNCTION DISTRIBUTIONS AT  $b = .2$

In this appendix the radial distributions of the velocity and pressure fluctuations for three azimuthal mode numbers, 0, 1, and 2; and three Strouhal numbers, .1, .3, and 1 are presented for a jet thickness of  $.2 r_j$ . This thickness corresponds to an axial location between one and two diameters from the jet exit. The distributions are shown in Figures 4E.1 through 4E.12. The corresponding local conditions and eigenvalues are given in Table I.

$$M_0 = 1.4$$

$$T_J = 1$$

$$b = .2$$

$$h = .84494$$

$$\bar{u} = 1$$

$$r < h$$

$$c = .5 [1 - \text{erf } (1.8984 (r - b - h)/b)] \quad r \geq h$$

Azimuthal Mode No. n	Strouhal Number St	Local Frequency $\omega = \beta b$	Local Wave Number $\alpha = kb$
0	.1	.06283	.06823 - .01884i
0	.3	.18850	.26061 - .12470i
0	1	.62832	1.19038 - .01820i
1	.3	.18850	.29100 - .15543i
2	.3	.18850	.30785 - .17043i

Table I Local Eigenvalues at  $b = .2$

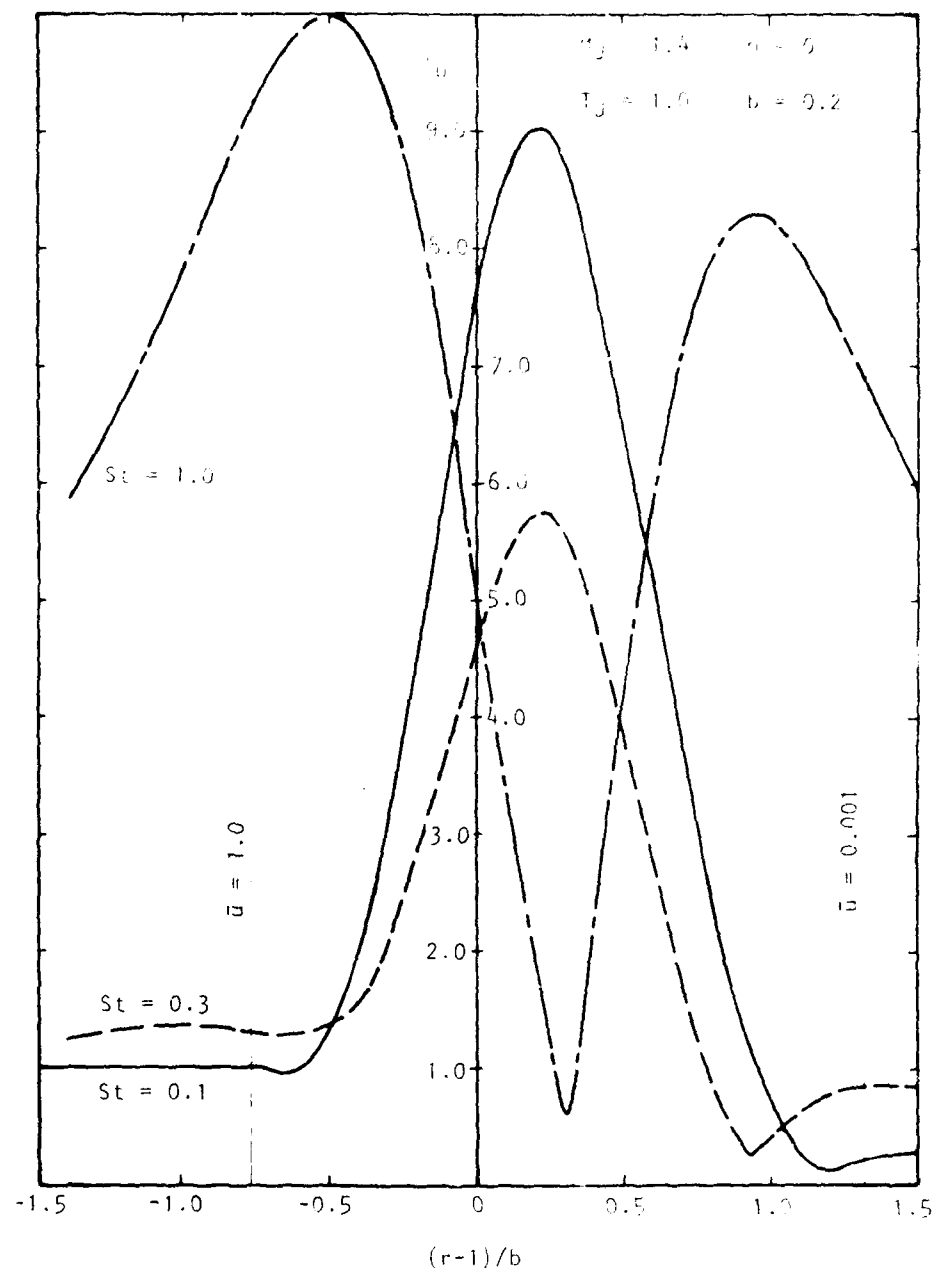


Figure 4E.1 Amplitude of Axial Velocity Fluctuation:  $n = 0$

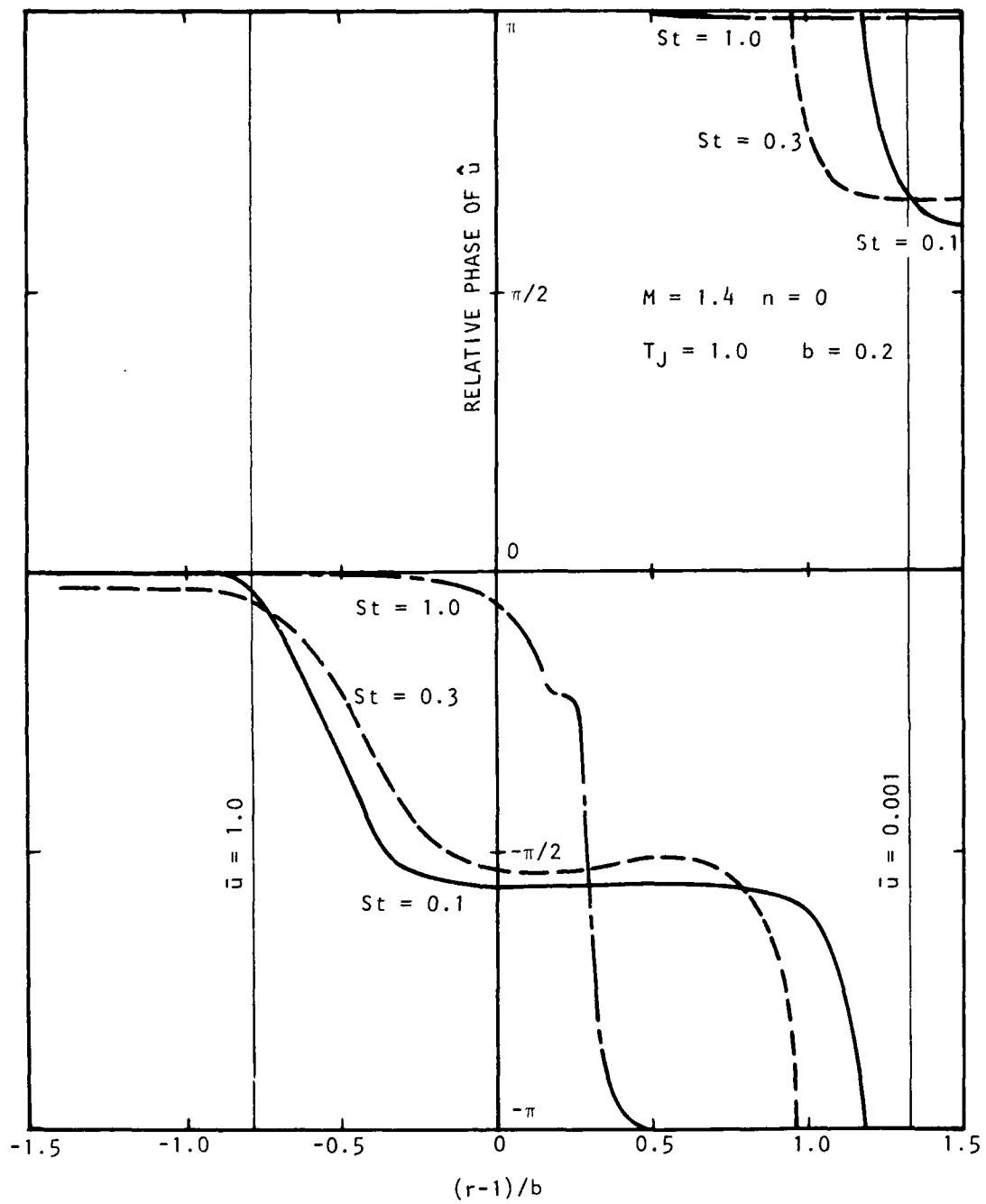


Figure 4E.2 Relative Phase of Axial Velocity Fluctuation:  $n = 0$

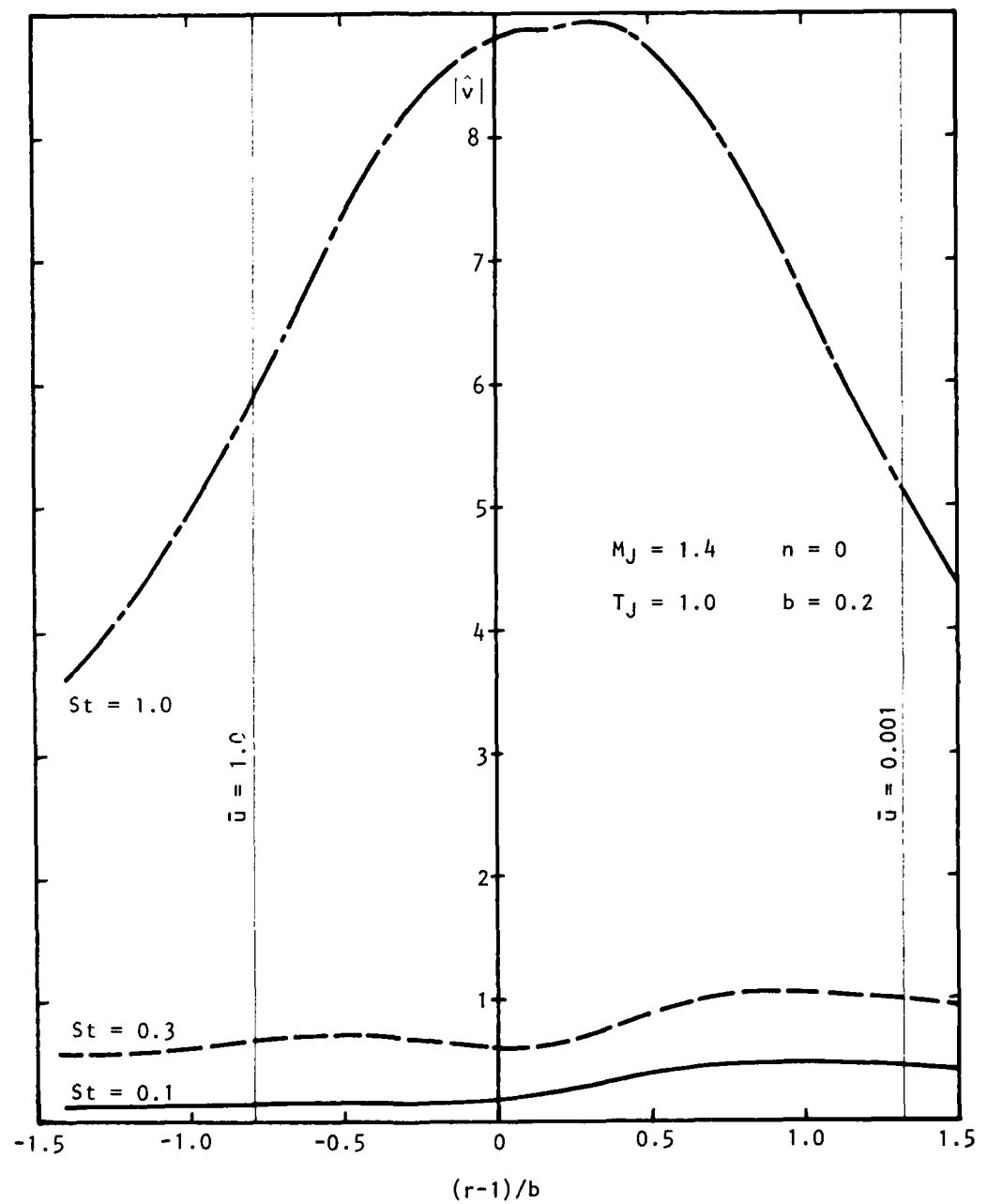


Figure 4E.3 Amplitude of Radial Velocity Fluctuation:  $n = 0$

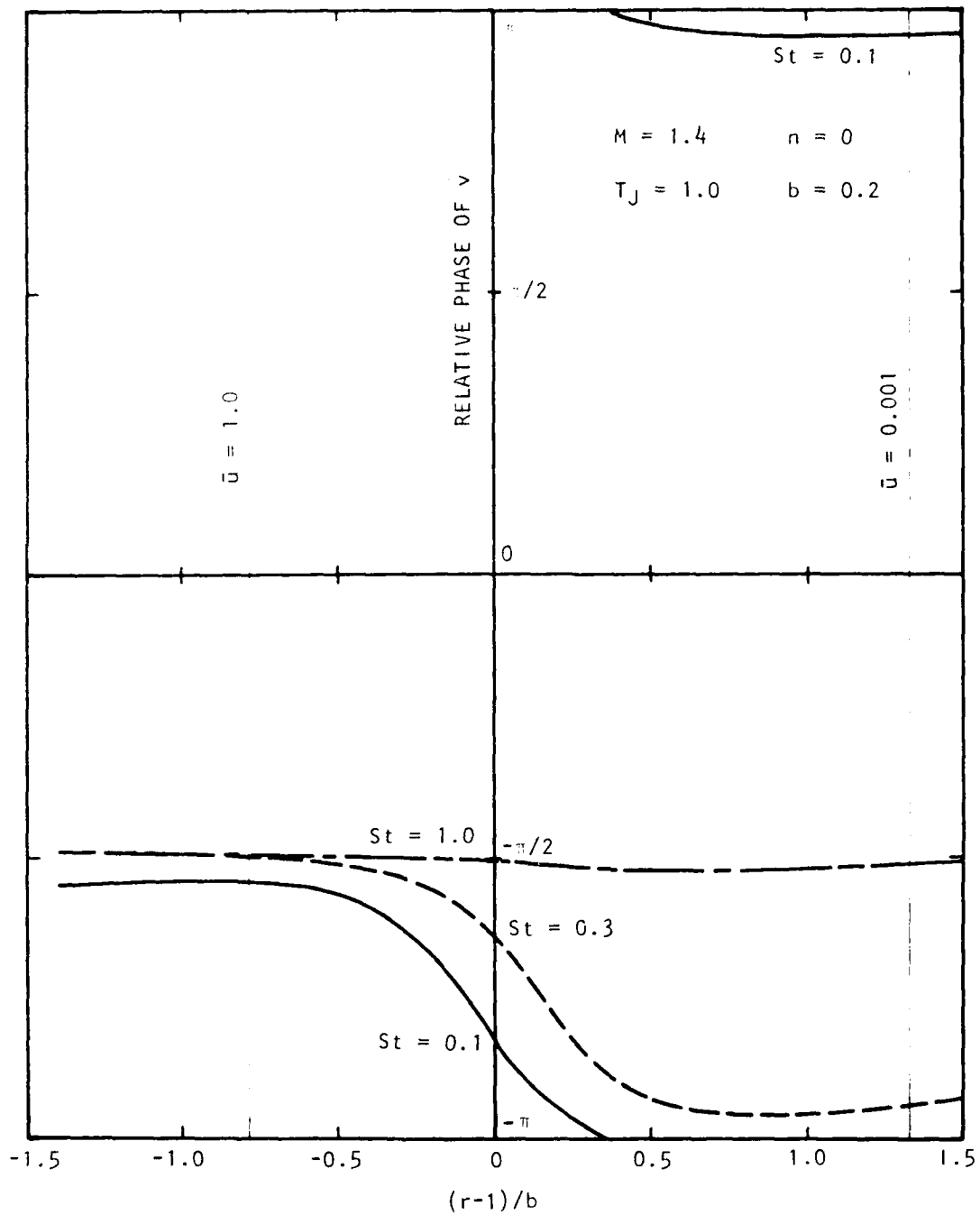


Figure 4E.4 Relative Phase of Radial Velocity Fluctuation:  $n = 0$

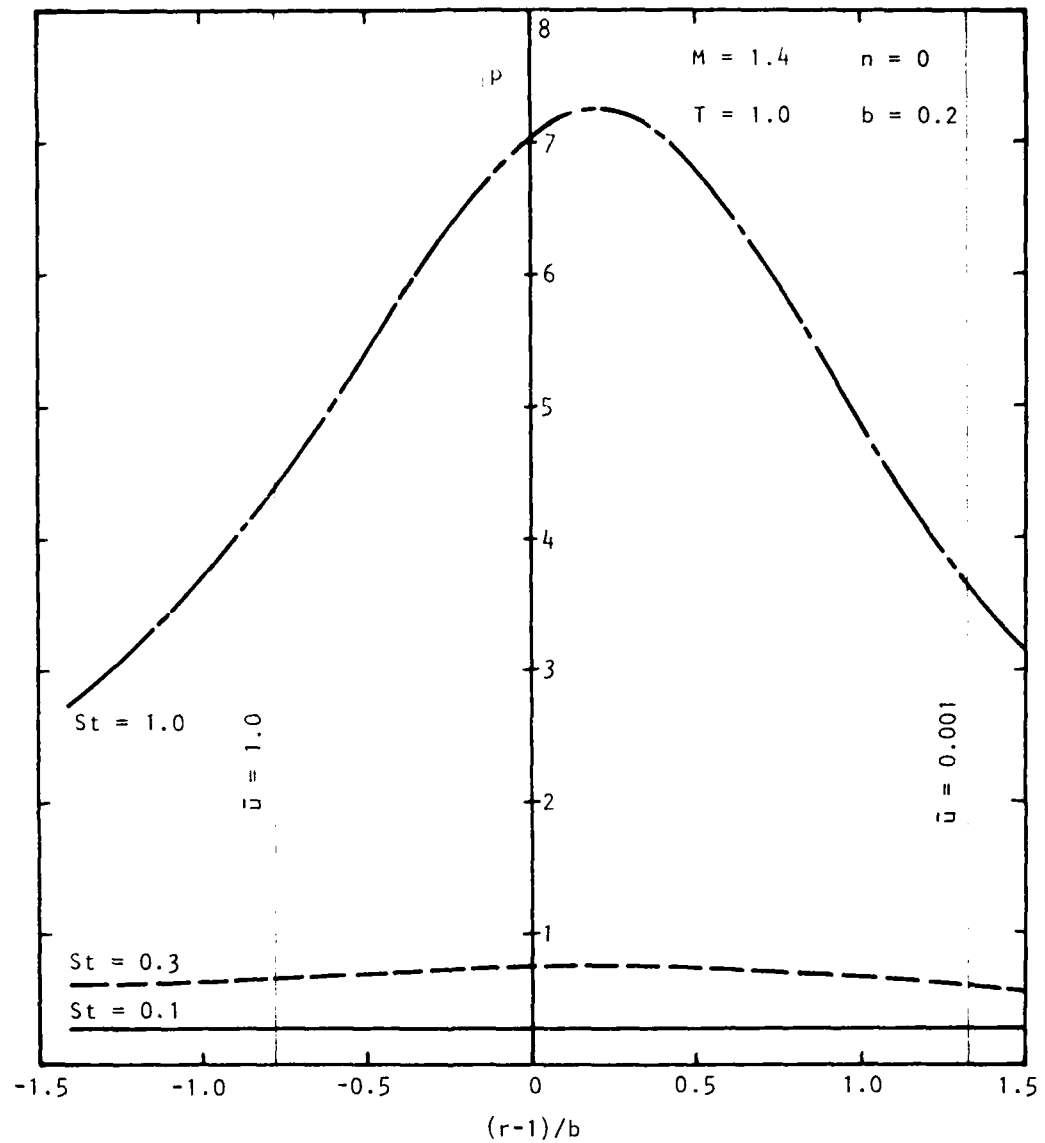


Figure 4E.5 Amplitude of Pressure Fluctuation:  $n = 0$

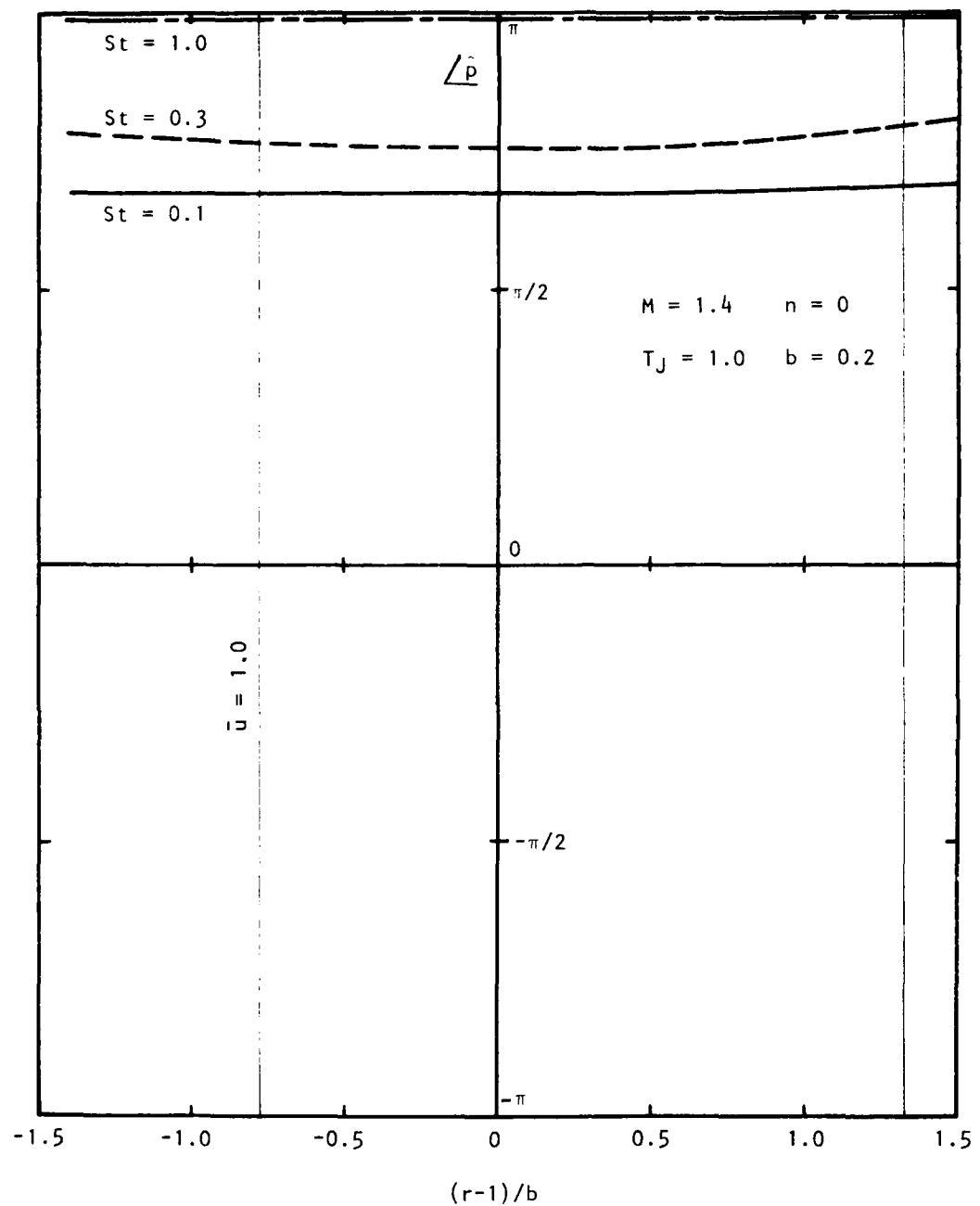


Figure 4E.6 Relative Phase of Pressure Fluctuation:  $n = 0$

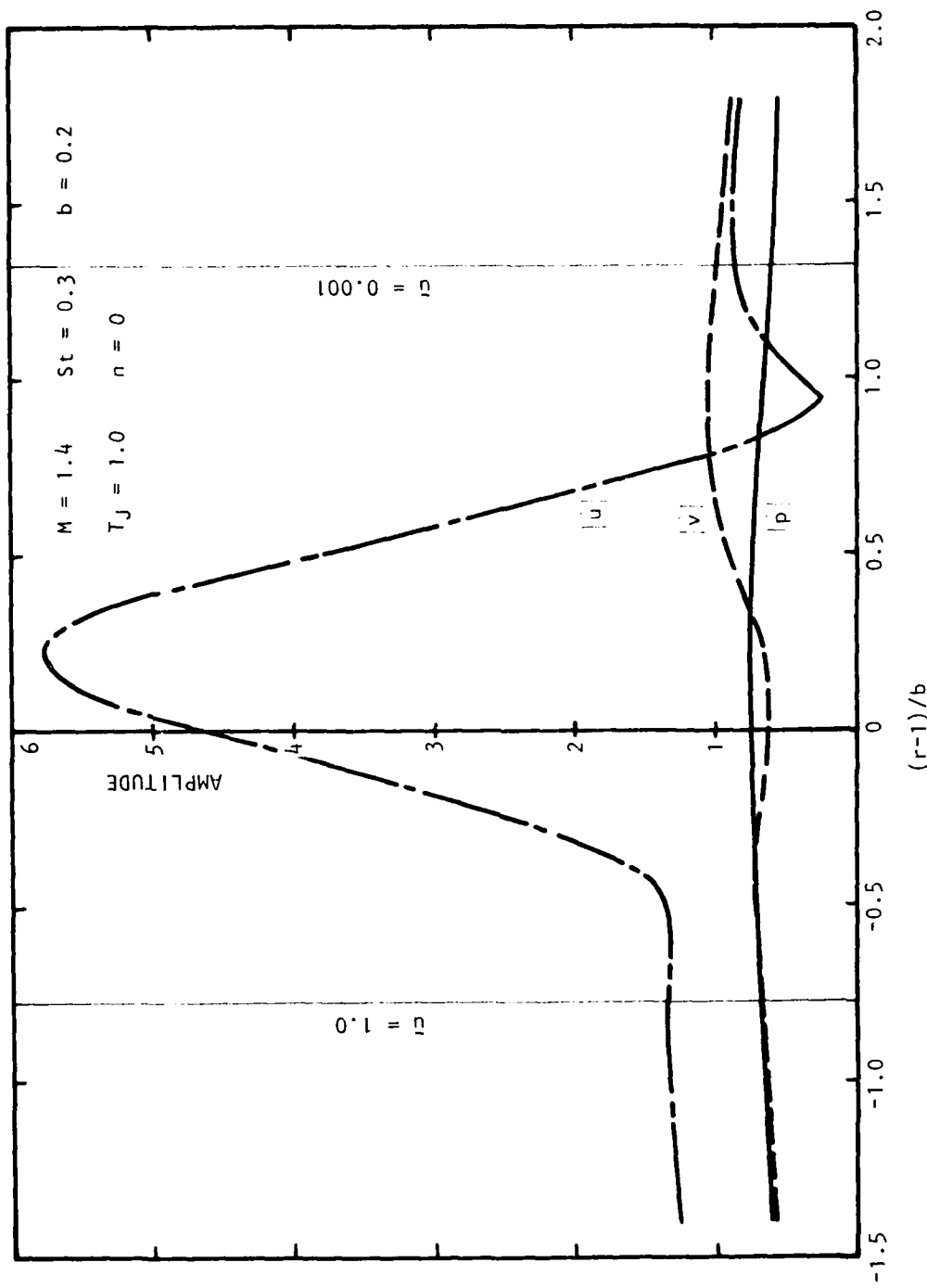


Figure 4E.7 Radial Distribution of Fluctuation Amplitude:  $n = 0$ ,  $St = .3$

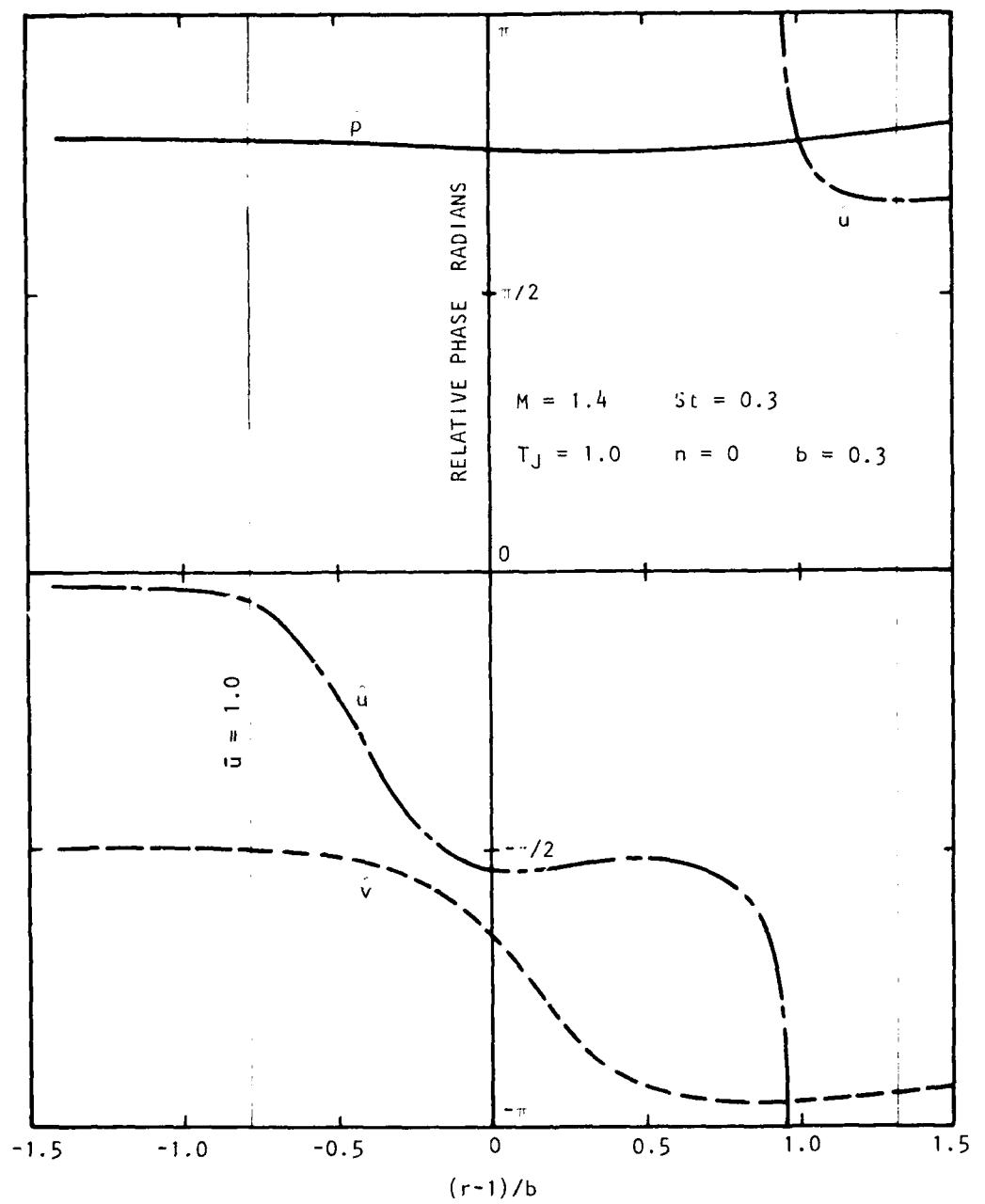


Figure 4E.8 Radial Distributions of Relative Phase:  $n = 0$ ,  $St = .3$

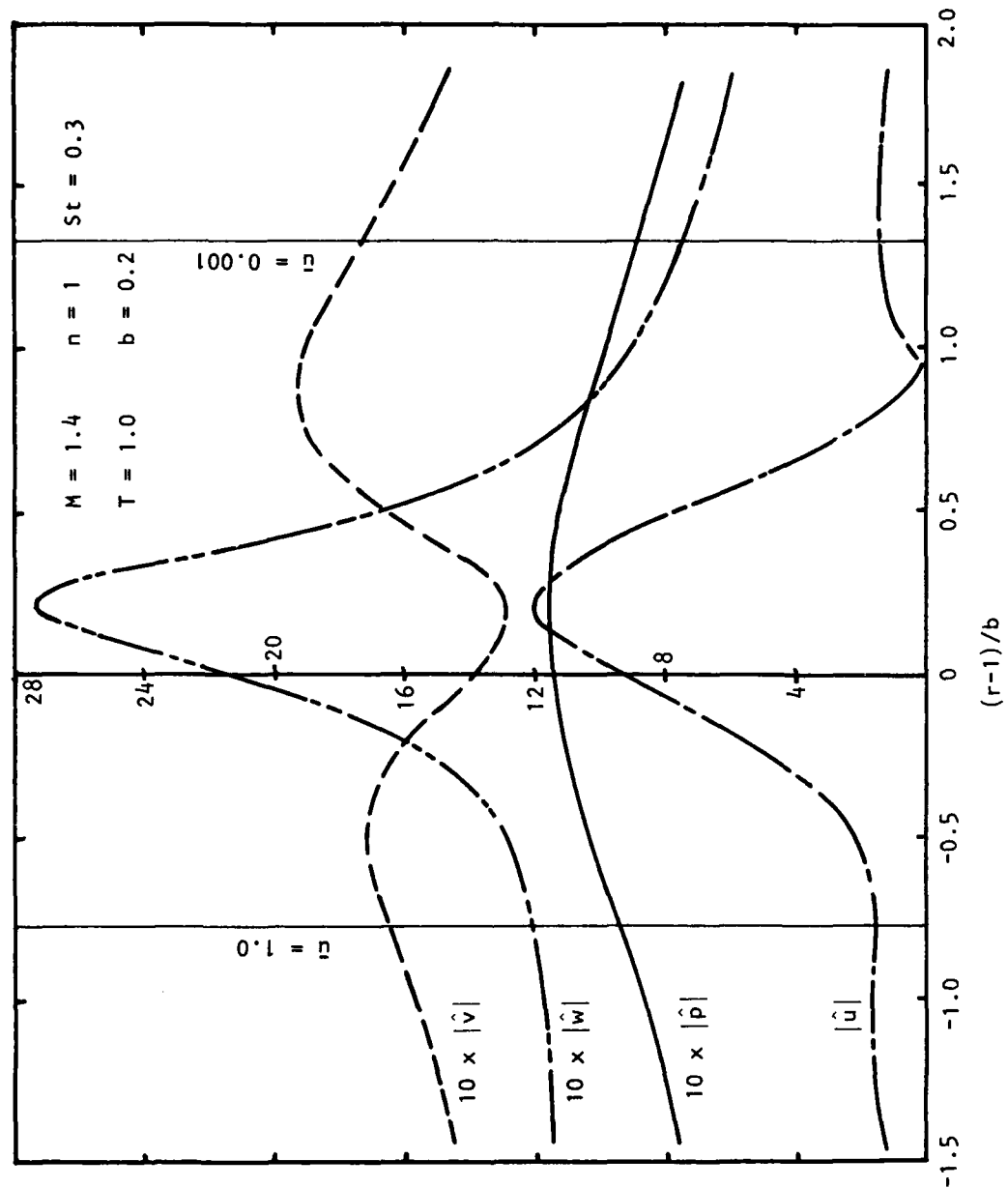


Figure 4E.9 Radial Distributions of Fluctuation Amplitude:  $n = 1$ ,  $St = .3$

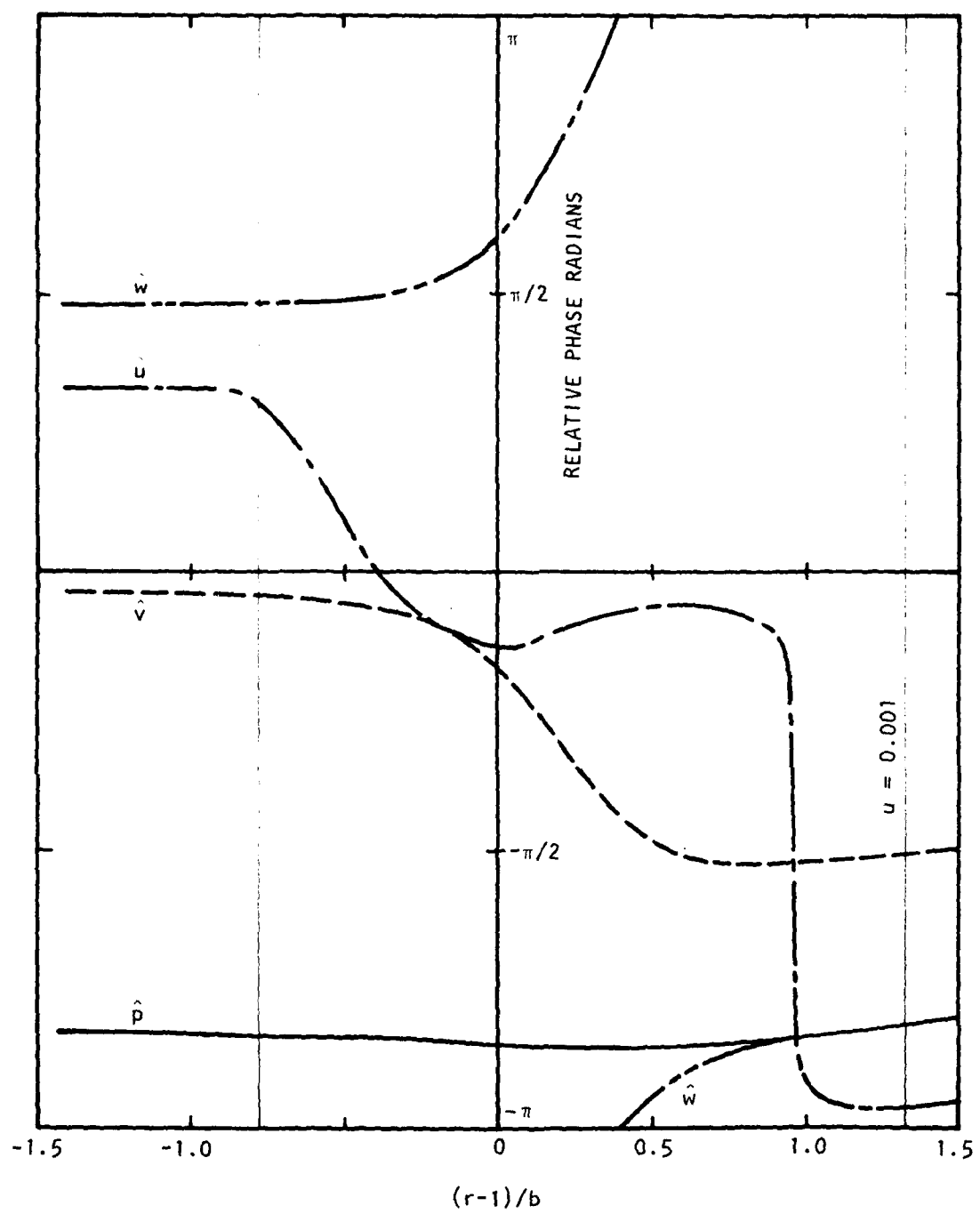


Figure 4E.10 Radial Distribution of Fluctuation Relative Phase:  
 $n = 1, St = .3$

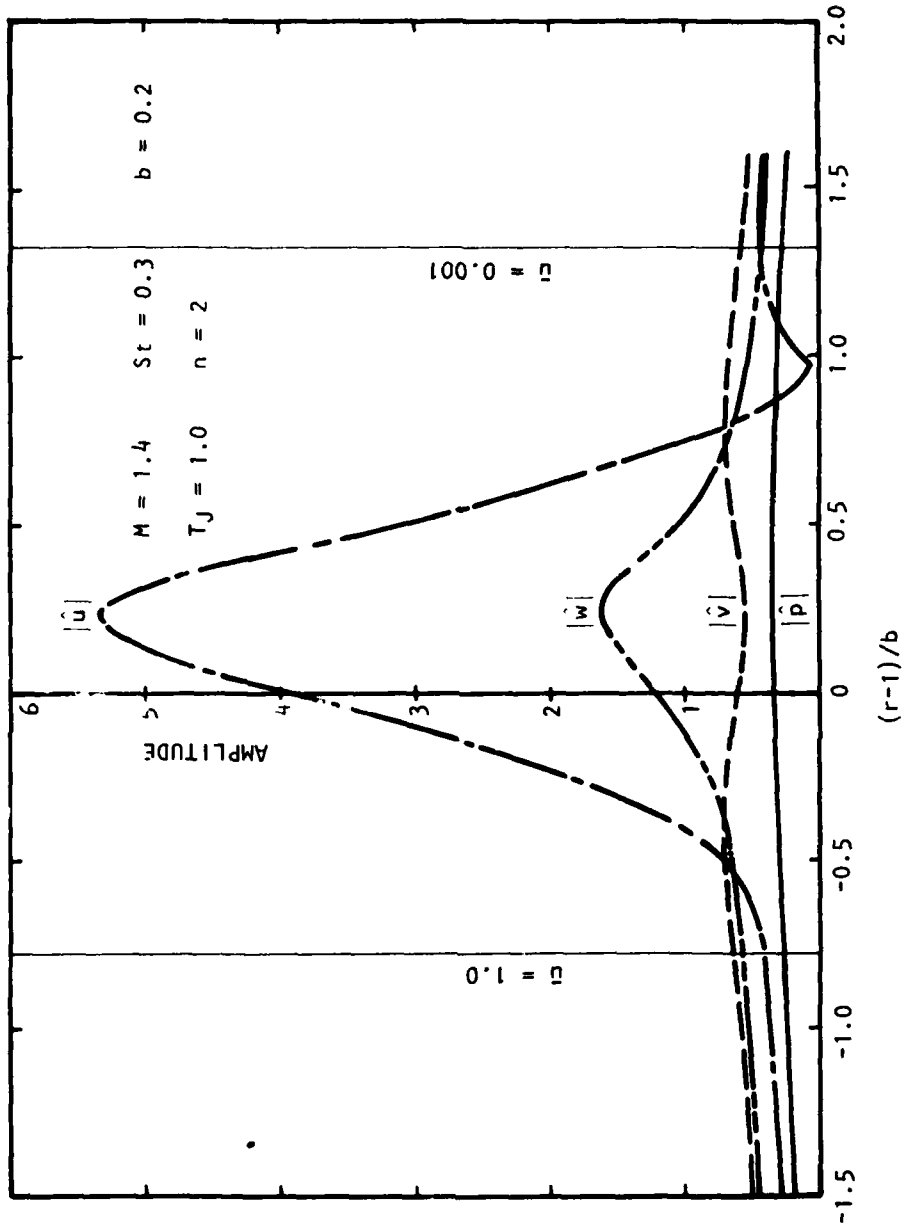


Figure 4E.11 Radial Distributions of Fluctuation Amplitude:  $n = 2$ ,  $St = .3$

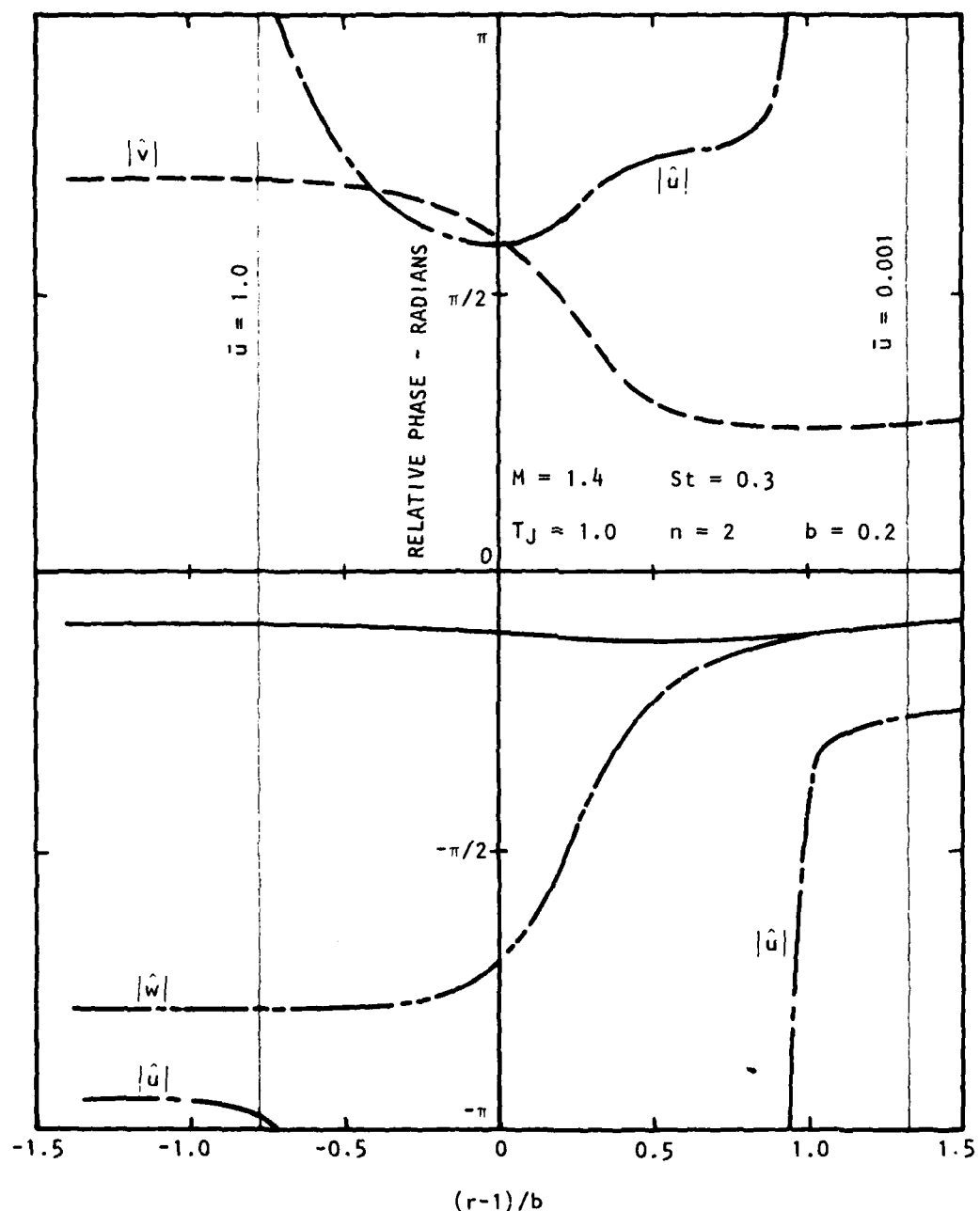


Figure 4E.12 Radial Distribution of Fluctuation Relative Phase:  
 $n = 2, St = .3$

## APPENDIX 6A

THE EFFECT OF VELOCITY MEASUREMENT INACCURACY  
ON THE MEASURED FLOW STATISTICS

This discussion addresses the effect of error in each individual velocity measurement upon the flow statistics derived from such a measurement. The flow being measured is presumed to be a stochastic signal,  $x$ , with arbitrary probability distribution  $f_x(x)$  which gives rise to the mean velocity  $\eta$  and variance  $\sigma^2$ . Standard relationships from Papoulis<sup>96</sup> are:

$$\eta = \int_{-\infty}^{\infty} xf_x(x) dx$$

$$\sigma^2 = \int_{-\infty}^{\infty} (x-\eta)^2 f_x(x-\eta) dx$$

For convenience in the subsequent algebra, the variable  $X$  will be changed to  $X^1$  where  $X^1 = X - \eta$ .

The effect of measurement inaccuracy will be modelled as a second stochastic signal,  $y$ , added to the actual flow characteristics. The probability distribution of  $y$ ,  $f_y(y)$  is presumed to be uniform in the range  $(-a, a)$ :

$$f_y(y) = 1/2a \text{ for } |y| < a \\ = 0 \quad \text{elsewhere}$$

This results in a mean  $\eta_y = 0$  and variance  $\sigma_y^2 = 1/3 a^2$ . It is further assumed that the disturbance  $y$  is statistically independent of the flow  $x^1$ .

A further relationship from Papoulis<sup>96</sup> is that the probability density  $f_z(z)$  of the sum of two independent random variables is the convolution of their individual probability densities:

If  $z = x^1 + y$ ,

$$f_z(z) = \int_{-\infty}^{\infty} f_x(x^1) f_y(z-x^1) dx^1$$

If  $y$  is uniformly distributed in the range  $(-a, a)$ , this reduces to:

$$f_z(z) = \frac{1}{2a} \int_{z-a}^{z+a} f_x(x^1) dx^1$$

It will be shown that the mean of this new signal is the mean of  $n$  of  $x$  and the variance  $\sigma_z^2$  is the sum of the variances of the two contributing signals.

First an expression for the mean of this distribution,  $\eta_z$ , will be derived:

$$\begin{aligned}\eta_z &= \int_{-\infty}^{\infty} zf(z)dz \\ &= \frac{1}{2a} \int_{-\infty}^{\infty} z \int_{z-a}^{z+a} f(x')dx' dz\end{aligned}$$

Interchanging the order and limits of integration:

$$\begin{aligned}\eta_z &= \frac{1}{2a} \int_{-\infty}^{\infty} f(x') \int_{x'-a}^{x'+a} z dz dx' \\ &= \frac{1}{2a} \int_{-\infty}^{\infty} f(x') \frac{z^2}{2} \Big|_{x'-a}^{x'+a} dx' \\ &= \int_{-\infty}^{\infty} x' f(x') dx' = \eta_{x'} = 0.\end{aligned}$$

The variance of this distribution may then be computed:

$$\sigma_z^2 = \frac{1}{2a} \int_{-\infty}^{\infty} z^2 \int_{z-a}^{z+a} f(x') dx' dz$$

which by the same process of inversion reduces to:

$$\begin{aligned}&= \frac{1}{2a} \int_{-\infty}^{\infty} f(x') \frac{z^3}{3} \Big|_{x'-a}^{x'+a} dx' \\ &= \int_{-\infty}^{\infty} x'^2 f(x') dx' + \frac{a^2}{3} \int_{-\infty}^{\infty} f(x') dx' \\ &= \sigma^2 + a^2/3\end{aligned}$$

This result indicates that the variance of two independent random signals is the sum of their individual variances. It is possible to show that this relationship extends to measurement error characteristics of arbitrary distribution.

## REFERENCES

1. Plumblee, H. E.; and Doak, P. E.: Summary of Supersonic Jet Noise Studies. Vol. I, The Generation and Radiation of Supersonic Jet Noise. AFAPL-TR-72-53, July 1972.
2. Plumblee, H. E.; and Burrin, R. H.: Future Studies for Definition of Supersonic Jet Noise Generation and Reduction Mechanisms. Vol. II, The Generation and Radiation of Supersonic Jet Noise. AFAPL-TR-72-53, July 1972.
3. Doak, P. E.: Progress Toward a Unified Theory of Jet Engine Noise. Vol. III, The Generation and Radiation of Supersonic Jet Noise. AFAPL-TR-72-53, July 1972.
4. Lilley, G. M.; Plumblee, H. E.; Strahle, W. C.; Ruo, S. Y.; and Doak, P. E.: Theory of Turbulence Generated Jet Noise, Noise Radiation from Upstream Sources, and Combustion Noise. Vol. IV, The Generation and Radiation of Supersonic Jet Noise. AFAPL-TR-72-53, July 1972.
5. Lush, P. A.; and Burrin, R. H.; An Experimental Investigation of Jet Noise Variation with Velocity and Temperature. Vol. V, The Generation and Radiation of Supersonic Jet Noise. AFAPL-TR-72-53, July 1972.
6. Fisher, M. J.; Mayo, W. T.; Meadows, D. M.; Burrin, R. H.; and Beisel, G. E.: Jet Flow Measurement and Analysis with Special Emphasis on Remote Sensing Devices. Vol. VI, The Generation and Radiation of Supersonic Jet Noise. AFAPL-TR-72-53, July 1972.
7. Plumblee, H. E., ed., et al, A Progress Report on Studies of Jet Noise Generation and Radiation, Turbulence Structure and Laser Velocimetry. The Generation and Radiation of Supersonic Jet Exhaust Noise. AFAPL-TR-74-24, June 1974.
8. Lush, P. A.: Measurements of Subsonic Jet Noise and Comparison with Theory. *J. Fluid Mech.*, Vol. 46, pp. 477-500, 1971.
9. Lighthill, M. J.: The Bakerian Lecture, Sound Generated Aerodynamically. *Proc. Roy. Soc.*, Vol. A267, pp. 147-182, 1962.
10. Ffowcs Williams, J. E.: Noise from Turbulence Convected at High Speed. *Phil. Trans. Roy. Soc.*, Vol. A255, 1963, pp. 469-503.
11. Ribner, H. S.: The Generation of Sound by Turbulent Jets. *Adv. in Applied Mech.*, Vol. 8, 1964, pp. 103-182.
12. Burrin, R. H.; Dean, P. D.; and Tanna, H. K.: A New Anechoic Facility for Supersonic Hot Jet Noise Research at Lockheed-Georgia. In *The Generation and Radiation of Supersonic Jet Noise*, U. S. Air Force Aero Propulsion Laboratory Technical Report AFAPL-TR-74-24, 1974.

13. Tanna, H. K.; Fisher, M. J.; and Dean, P. D.: Effect of Temperature on Supersonic Jet Noise. AIAA Paper No. 73-991, 1973.
14. Tanna, H. K.; Dean, P. D.; and Fisher, M. J.: The Influence of Temperature on Shock-Free Supersonic Jet Noise. *J. Sound Vib.*, Vol. 39, No. 4, pp. 429-460, 1975.
15. Tester, B. J.; and Morfey, C. L.: Developments in Jet Noise Modeling - Theoretical Predictions and Comparisons with Measured Data. AIAA Paper No. 75-477, 1975.
16. Davies, P.O.A.L.; Fisher, M. J.; and Barratt, M. J.: The Characteristics of the Turbulence in the Mixing Region of a Round Jet. *J. Fluid Mech.*, Vol. 15, pp. 337-367, 1963.
17. Fisher, M. J.; Lush, P. A.; and Bourne, M. Harper: Jet Noise. *J. Sound Vib.*, Vol. 28, 1973, pp. 563-585.
18. Hoch, R. G.; Duponchel, J. P.; Cocking, B. J.; and Bryce, W. D.: Studies of the Influence of Density on Jet Noise. *J. Sound and Vib.*, Vol. 28, 1973, pp. 649-668.
19. Morfey, C. L.: Amplification of Aerodynamic Noise by Convected Flow Inhomogeneities. *J. Sound Vib.*, Vol. 31, 1973, pp. 391-397.
20. Lilley, G. M.: Generation of Sound in a Mixing Region. In Vol. IV, Theory of Turbulence Generated Jet Noise, Noise Radiation from Upstream Sources and Combustion Noise. 1972, AFAPL-TR-72-53.
21. Lilley, G. M.; Morris, P. J.; Tester, B. J.: On the Theory of Jet Noise and Its Application. AIAA Paper No. 73-987, 1973.
22. Tester, B. J.; Burrin, R. H.: On Sound Radiation from Sources in Parallel Sheared Jet Flows. AIAA Paper No. 74-57, 1974.
23. Michalke, A.: An Expansion Scheme for the Noise from Circular Jets. *Zeitschrift für Flugwissenschaften*, Vol. 20, 1972, pp. 229-237.
24. Crighton, D. G.: Basic Principles of Aerodynamic Noise Generation. *Prog. in Aerospace Sci.*, Vol. 16, 1975.
25. Csanady, G. T.: The Effect of Mean Velocity Variations on Jet Noise. *J. Fluid Mech.*, Vol. 26, 1966, pp. 183-197.
26. Krishnappa, G.: Effect of Temperature on the High-Frequency Component of the Jet Noise. *J. Acous. Soc. Am.*, Vol. 41, 1967, pp. 1208-1211.
27. Pao, S. P.: Aerodynamic Noise Emission from Turbulent Shear Layers. *J. Fluid Mech.*, Vol. 59, 1973, pp. 451-479.
28. Mani, R.: A Moving Source Problem Relevant to Jet Noise. *J. Sound Vib.*, Vol. 25, 1972, pp. 337-347.

29. Mani, R.: The Jet Density Exponent Issue for the Noise of Heated Subsonic Jets. *J. Fluid Mech.*, Vol. 64, 1974, pp. 611-622.
30. Morfey, C. L.: The Sound Field of Sources in Motion. *J. Sound Vib.*, Vol. 23, 1972, pp. 291-295.
31. Blokhintsev, D. I.: *Acoustics of a Nonhomogeneous Moving Medium*. (Gostekhizdat), Translated in NACA-TM-1399, 1956.
32. Tanna, H. K.; and Dean, P. D.: An Experimental Study of Shock-Free Supersonic Jet Noise. AIAA Paper No. 75-480, 1975.
33. Grosche, F. R.: Distributions of Sound Source Intensities in Subsonic and Supersonic Jets. AGARD CP-131, Noise Mechanisms (see also AIAA Paper No. 73-989), 1973.
34. Laufer, J.; Kaplan, R. E.; and Chu, W. T.: On Noise Produced by Subsonic Jets. Proceedings of the Second Interagency Symposium on University Research in Transportation Noise, Vol. 1, 1974, pp. 50-58.
35. Goldstein, M. E.: Aeroacoustics. NASA SP-346, 1974.
36. Landahl, M. T.: A Wave-Guide Model for Turbulent Shear Flow. *J. Fluid Mech.*, Vol. 29, Pt. 3, 1967, pp. 441-459.
37. Reynolds, W. C.; and Hussain, A.K.M.F.: The Mechanics of an Organized Wave in Turbulent Shear Flow. Part 3, Theoretical Models and Comparisons with Experiments. *J. Fluid Mech.*, Vol. 54, Pt. 2, 1972, pp. 263-288.
38. Sharma, R.: The Structure of Turbulent Shear Flow. Ph.D. Thesis, University of Southampton, 1968.
39. Brown, G. L.; and Roshko, A.: On Density Effects and Large Structure in Turbulent Mixing Layers. *J. Fluid Mech.*, Vol. 64, Pt. 4, 1974, pp. 775-816.
40. Crow, S. C.; and Champagne, F. H.: Orderly Structure in Jet Turbulence. *J. Fluid Mech.*, Vol. 48, Pt. 3, 1971, pp. 547-591.
41. Liepmann, H. W.: Free Turbulent Flows. In *The Mechanics of Turbulence*, Int. Symp. Nat. Sci. Res. Center, Gordon and Breach, pp. 211-227, 1961.
42. Ko, D.R.S.; Kubota, T.; and Lees, L.: Finite Disturbance Effect in the Stability of Laminar Incompressible Wake Behind a Flat Plate. *J. Fluid Mech.*, Vol. 40, Pt. 2, 1970, pp. 315-341.
43. Stuart, J. T.: On the Non-linear Mechanics of Hydrodynamic Stability. *J. Fluid Mech.*, Vol. 4, Pt. 1, 1958, pp. 1-21.
44. Liu, J.T.C. and Lees, L.: Finite Amplitude Instability of the Compressible Laminar Wake. Strongly Amplified Disturbances. *Physics of Fluids*, Vol. 13, No. 12, 1970, pp. 2932-2938.

45. Liu, J.T.C.: Non-linear Development of an Instability Wave in a Turbulent Wake. *Physics of Fluids*, Vol. 14, No. 11, 1971, pp. 2251-2257.
46. Morris, P. J.: The Structure of Turbulent Shear Flow. Ph.D. Thesis, University of Southampton, 1971.
47. Chan, Y. Y.: Non-linear Spatial Wave Development in an Axisymmetrical Turbulent Jet. National Research Council of Canada, Aero. Report, LR-585, 1975.
48. Liu, J.T.C.: Developing Large-Scale Wave-like Eddies and the Near Jet Noise Field. *J. Fluid Mech.*, Vol. 62, Pt. 3, 1974, pp. 437-464.
49. Morris, P. J.: A Model for the Structure of Jet Turbulence as a Source of Noise. AIAA Paper No. 74-1, 1974.
50. Merkine, L-O.; and Liu, J.T.C.: On the Development of Noise-Producing Large-Scale Wave-like Eddies in a Plane Turbulent Jet. *J. Fluid Mech.*, Vol. 70, Pt. 2, 1975, pp. 353-368.
51. Tam, C.K.W.: Directional Acoustic Radiation from a Supersonic Jet Generated by Shear Layer Instability. *J. Fluid Mech.*, Vol. 46, Pt. 4, 1971, pp. 757-768.
52. Tam, C.K.W.: Supersonic Jet Noise Generated by Large-Scale Disturbances. AIAA Paper 73-992, 1973. (Also *J. Sound Vib.*, 1975.)
53. McLaughlin, D. K.; Morrison, G. L.; and Troutt, T. R.: Experiments on the Instability Waves in a Supersonic Jet and Their Acoustic Radiation. *J. Fluid Mech.*, Vol. 69, Pt. 1, 1975, pp. 73-95.
54. Townsend, A. A.: *The Structure of Turbulent Shear Flow*. 1956, Cambridge University Press.
55. Reynolds, W. C.: Large-Scale Instabilities of Turbulent Wakes. *J. Fluid Mech.*, Vol. 54, Pt. 3, 1972, pp. 481-488.
56. Launder, B. E.; Morse, A., Rodi, W.; and Spalding, D. B.: Prediction of Free Shear Flows, A Comparison of the Performance of Six Turbulence Models. Proc. of Conf. on Free Turbulent Shear Flows. NASA SP-321, Vol. 1, pp. 361-426, 1972.
57. Brekhovskikh, L. M.: *Waves in Layered Media*. Academic Press (New York), 1960.
58. Eggers, J. M.: Velocity Profiles and Eddy Viscosity Distributions Downstream of a Mach 2.22 Nozzle Exhausting into Quiescent Air. NASA TN D-3601, 1966.
59. Michalke, A.: On Spatially Growing Disturbances in an Inviscid Shear Layer. *J. Fluid Mech.*, Vol. 23, Pt. 3, 1965, pp. 521-544.
60. Peters, C. E.; and Phares, W. J.: An Integral Turbulent Kinetic Energy Analysis of Free Shear Flows. Proc. of Conf. on Free Turbulent Shear Flows. NASA SP-321, Vol. 1, pp. 577-662, 1972.

61. Crow, S. C.: Acoustic Gain of a Turbulent Jet. Meeting of Division of Fluid Dynamics, American Physical Society, Paper IE-6, Univ. Colorado, Boulder, Nov. 1972.
62. Crighton, D. G.: Basic Principles of Aerodynamic Noise Generation. *Progress in Aerospace Sciences*, Vol. 16, 1975.
63. Michalke, A.; and Fuchs, H. V.: On Turbulence and Noise of an Axisymmetric Shear Flow. *J. Fluid Mech.*, Vol. 70, Pt. 1, 1975, pp. 179-205.
64. Bouthier, M.: Stabilité Linéaire des Écoulements presque Parallèles. *J. de Mécanique*, Vol. 11, 1972, pp. 599-621.
65. Stevenson, W. H.: Redijo, M. K.; and Gammitt, R. E.: Bibliography on Laser Doppler Velocimeters: Theory, Design and Applications. Laser Doppler Velocimeter Workshop, Purdue Univ., March 1972.
66. Liepmann, H.; and Laufer, J.: Investigation of Free Turbulent Mixing. NACA Tech. Note 1257, 1947.
67. Corrsin, S.: Investigation of the Flow in an Axially Symmetric Heated Jet. NACA Report No. W-94, 1947.
68. Corrsin, S.; Uberoi, M. S.: Further Experiments on the Flow and Heat Transfer in a Heated Turbulent Air Jet. NACA Tech. Note 1865, 1949.
69. Laurence, J. C.: Intensity, Scale and Spectra of Turbulence in the Mixing Region of a Subsonic Jet. NACA Report 1292, 1956.
70. Bradshaw, P.; Ferris, D. H.; and Johnson, R. F.: Turbulence in the Noise-Producing Region of a Circular Jet. *J. Fluid Mech.*, Vol. 19, 1964, p. 591.
71. Wygnanski, I.; and Fiedler, H.: Some Measurements in the Self-Preserving Jet. *J. Fluid Mech.*, Vol. 38, 1969, p. 577.
72. Lau, J. C.; and Fisher, M. J.: The Vortex-Street Structure of "Turbulent" Jets. Part I. *J. Fluid Mech.*, Vol. 67, 1975, p. 299.
73. Champagne, F. H.; and Scleicher, C. A.: Turbulence Measurements with Inclined Hot Wires. Part 2, Hot-Wire Response Equations. *J. Fluid Mech.*, Vol. 28, 1967, p. 177.
74. Rose, W. G.: Some Corrections to the Linearized Response of a Constant-Temperature Hot-Wire Anemometer in a Low-Speed Flow. *J. of Appl. Mech.*, Vol. 29, 1962, p. 554.
75. Hesketh, G.: Hot-Wire Measurements in a Plane Turbulent Jet. *J. Fluid Mech.*, Vol. 32, 1965, p. 721.
76. Perry, A.: Oral report at 5th Australasian Conference on Hydraulics and Fluid Mechanics (New Zealand), Dec. 1974. (See also Proceedings of 5th Australasian Conference on Hydraulics and Mechanics, Vol. 1, p. 356, 1974.)

77. Kolpin, M. A.: The Flow in the Mixing Region of a Jet. *J. Fluid Mech.*, Vol. 18, 1964, p. 529.

78. Lau, J. C.; Fisher, M. J.; and Fuchs, H. V.: The Intrinsic Structure of Jet Turbulence. *J. Sound Vib.*, Vol. 22, 1972, p. 379.

79. Bradbury, L.J.S.: The Structure of a Self-Preserving Turbulent Plane Jet. *J. Fluid Mech.*, Vol. 23, 1965, p. 31.

80. Plumblee, H. E. Jr. (ed.): A Study of the Effects of Forward Velocity on Turbulent Jet Mixing Noise. Contract No. NAS3-18540 (To be published), July 1975.

81. Lau, J. C.: The Coherent Structure of Jets. Ph.D. Thesis, University of Southampton, 1971.

82. Fisher, M. J.; and Davies, P.O.A.L.: Correlation Measurements in a Non-frozen Pattern of Turbulence. *J. Fluid Mech.*, Vol. 18, 1964, p. 99.

83. Davies, P.O.A.L.: Turbulence Structure in Free Shear Layers, *AIAA Journal*, Vol. 4, 1966, p. 1971.

84. Knott, P.; and Mossey, P.: Parametric Laser Velocimeter Studies of High-Velocity, High-Temperature, Turbulent Jets. Vol. II, Supersonic Jet Exhaust Noise Investigation. AFAPL-TR- , Aug. 1975, p. 413.

85. Sami, S.; Carmody, T.; Rouse, H.: Jet Diffusion in the Region of Flow Establishment. *J. Fluid Mech.*, Vol. 27, 1967, p. 231.

86. Haldeen, R. M.: A Literature Review on Subsonic Free Turbulent Shear Flows, AFOSR-TN-5494, U. S. Air Force, Apr. 1964.

87. Görtler, H., Berechnung von Aufgaben der Freien Turbulenz auf grund eines Neun Naherungsansatzes. *ZAMM*, v22, Pt. 5, p. 244, 1942.

88. Witze, P. O.: Centerline Velocity Decay of Compressible Jets. *AIAA Journal*, Vol. 12, 1974, p. 417.

89. Cary, B. B.: An Optical Study of Two-Dimensional Jet Mixing. Ph.D. Thesis, Univ. of Maryland, 1954.

90. Birch, S. F.; and Eggers, J. M.: A Critical Review of the Experimental Data for Developed Free Turbulent Shear Layers. Proceedings of Conf. on Free Turbulent Shear Flows, NASA SP-321, Vol. 1, 1972, p. 11.

91. Harper-Bourne, M.; and Fisher, M. J.: The Noise from Shock Waves in Supersonic Jets. Proceedings of the AGARD Conference on "Noise Mechanisms" (Brussels, Belgium), September 1973.

92. Powell, A.: On the Mechanism of Choked Jet Noise. *Proc. Phys. Soc. B.*, Vol. 66, 1953, pp. 1039-1056.

93. Pack, D. C.: A Note on Prandtl's Formula for the Wave-Length of a Supersonic Gas Jet. *Qtrly. J. of Mech., and Appl. Math.*, Vol. 3, Pt. 2, 1950.

94. Abramowitz, M.; and Stegun, I. A.: *Handbook of Mathematical Functions*. National Bureau of Standards, Applied Mathematics Series 55, June 1964.

95. Patankar, S. V.; and Spalding, D. B.: *Heat and Mass Transfer in Boundary Layers*. Second ed., Int. Textbook Co. Ltd. (London), 1970.

96. Papoulis, A.: *Probability, Random Variables, and Stochastic Processes*, McGraw-Hill, 1965.